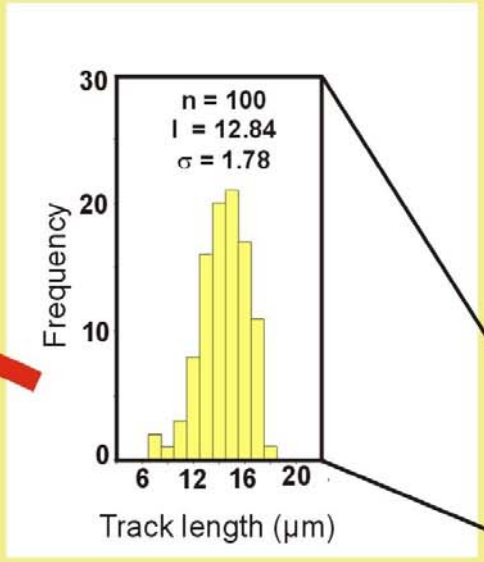

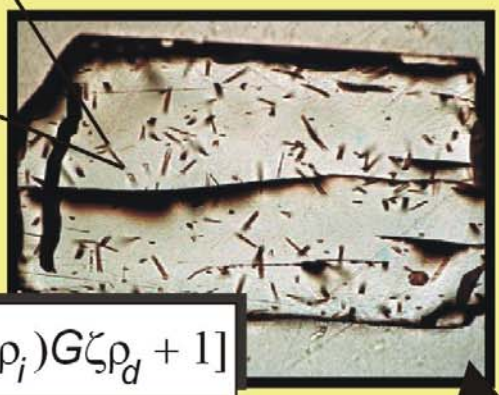

$$t = \lambda_\alpha \ln[\lambda_\alpha(\rho_s / \rho_i)G\zeta\rho_d + 1]$$

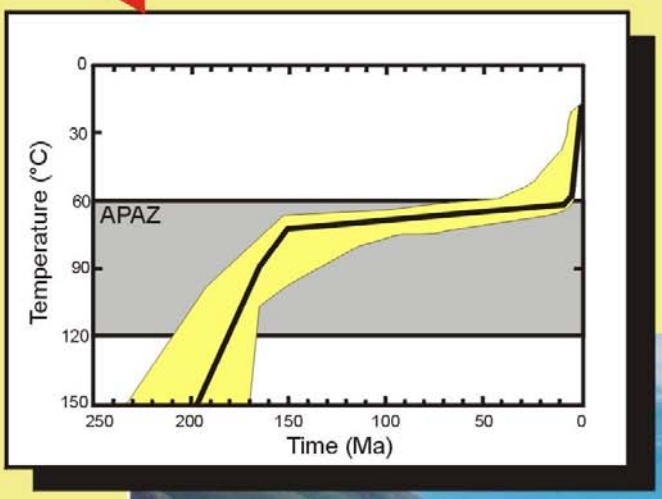

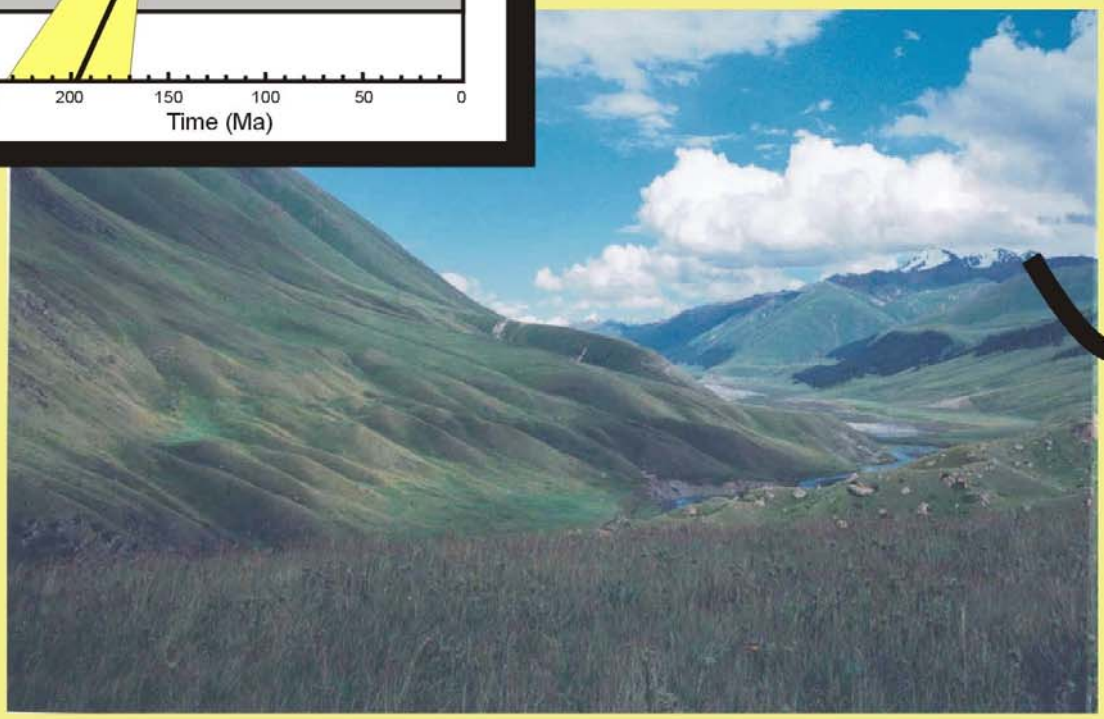

За Язулу!

Faculteit Wetenschappen
Vakgroep Geologie en Bodemkunde
Laboratorium voor Mineralogie, Petrologie en Micropedologie
Universiteit Gent

Apatite fission-track thermochronology of the Altai Mountains (South Siberia, Russia) and the Tien Shan Mountains (Kyrgyzstan): relevance to Meso-Cenozoic tectonics and denudation in Central Asia

Apatiet fissiesporen thermochronologie van het Altai gebergte (Zuid-Siberië, Rusland) en het Tien Shan gebergte (Kirgizië): relevantie voor de Meso-Cenozoïsche tektonische evolutie en denudatie in Centraal-Azië

JOHAN DE GRAVE

Proefschrift voorgelegd tot het behalen van de graad van
Doctor in de Wetenschappen, richting Geologie

Promotor: Prof. Dr. Peter Van den haute

Academiejaar 2002-2003

TABLE OF CONTENTS

DANKWOORD - ACKNOWLEDGEMENTS

Het is een voorrecht geweest om gedurende meer dan vier jaar te mogen werken op interessante vraagstukken aangaande de geologie en de thermochronologische evolutie van de prachtige streken van Siberië en Centraal-Azië. Het is dan ook voor mij een uiterst boeiende en leerrijke periode geweest waarin ik vele mensen heb ontmoet en veel hulp heb gekregen om dit onderzoek tot een goed einde te brengen. In het wetenschappelijk onderzoek streven wij ernaar de zaken met een zo groot mogelijke nauwkeurigheid te reconstrueren. Niettegenstaande moeten wij onderkennen dat er steeds een fouten- of onzekerheidsmarge blijft bestaan. Ik vrees dat dit voor dit dankwoord niet anders is. Het is onmogelijk om iedereen te bedanken die mij gedurende dit onderzoek op allerhande vlakken heeft gesteund en aangemoedigd. Maar toch deze poging.

Eerst en vooral wens ik mijn promotor Prof. Dr. Peter Van den haute hartelijk te bedanken voor zijn deskundige bijstand, zijn enthousiasme en voor de vele leerrijke discussies en besprekingen die wij gedurende dit onderzoek hebben gevoerd.

De opbouwende kritieken van de leescommissarissen Prof. Dr. Peter Van den haute, Prof. Dr. Frans De Corte, Prof. Dr. Marc De Batist en Dr. Raymond Jonckheere hebben ontegensprekelijk de kwaliteit van het werk, zowel op inhoudelijk als op tekstueel vlak bevorderd. Daarvoor mijn oprechte dank.

Em. Prof. Dr. Stoops wens ik te bedanken voor de mogelijkheid die hij mij bood om aan het Laboratorium voor Mineralogie, Petrologie en Micropedologie van de Vakgroep Geologie en Bodemkunde (Universiteit Gent) dit onderzoek uit te voeren. Ook alle andere collega's ben ik dankbaar voor de aangename werkomgeving in ons laboratorium, en in de Vakgroep in het algemeen.

Een belangrijke en uitermate aangename schakel in dit onderzoek wordt gevormd door het veldwerk en de monsternames die in Siberië, Kazakhstan en Kirgizstan werden uitgevoerd in de zomers van 1998, 1999 en 2000. Onmisbaar hierbij was de onuitputtelijke inzet van Dr. Michael M. Buslov. Ik wil hem hiervoor uiteraard hartelijk bedanken, ook voor de vriendschappelijke sfeer waarin alles is kunnen gebeuren. Evenzeer gaat mijn dank uit naar de collega's die van dit veldwerk een overgetelijke ervaring hebben gemaakt: Dr. Boris Dehandschutter, Dr. Eugene Vysotsky, Dr. Karel Theunissen, Dr. Laryssa Smirnova, Dr. Elia Vassilieva, Dr. Damien Delvaux, Dr. Kanaathbek Y. Abdrakhmatov. Ook Rob Hus, Birgit Theunissen, Dima Kokh, Kostya Kokh en vele andere collega's, studenten en vrienden zijn ten zeerste bedankt voor de leuke "veld-momenten", de hulp op het veld,

en de geologische en andere discussies. Vele Russische studenten, geologen en gidsen hebben hun uiterste best gedaan om de praktische en logistieke aspecten van het veldwerk in vaak moeilijke omstandigheden mogelijk te maken.

Dit onderzoek en het veldwerk is mede tot stand kunnen komen door de intense samenwerking met het Departement Geologie en Mineralogie van het Koninklijk Museum voor Midden-Afrika uit Tervuren. Prof. Dr. Jean Klerkx wil ik hiervoor speciaal bedanken.

Het fissiesporen onderzoek was slechts mogelijk dankzij de vlotte samenwerking met het Instituut voor Nucleaire Wetenschappen (Laboratorium voor Analytische Scheikunde, Universiteit Gent). Ik ben Prof. Dr. Frans De Corte en Ing. Antoine Dewispelaere zeer erkentelijk voor hun hulp en raadgevingen bij bestralingen en fluentiebepalingen uitgevoerd in het kader van dit onderzoek.

Dr. Raymond Jonckheere verdient een specifieke vermelding voor zijn nooit aflatende en deskundige hulp die hij mij verleende inzake verschillende aspecten van fissiesporen-onderzoek. Prof. Dr. Günther Wagner ben ik zeer erkentelijk voor het beschikbaar stellen van de infrastructuur van het Departement Archeometrie van het Max Planck Instituut voor Kernfysica in Heidelberg.

Voor bijstand in velerlei administratieve en technische aspecten wens ik eerst en vooral Arlette Bavay-Calle te bedanken. Ik wil haar via deze weg ook veel beterschap en moed toewensen. Ook Nicole Selen, Hubert Bourdin en Julien Van Hende wil ik graag bedanken.

Uiteraard was de steun en het vertrouwen van mijn ouders, familie en vrienden gedurende mijn studies en dit onderzoek essentieel. Zonder hun steun en vertrouwen gedurende de afgelopen jaren was deze doctoraatsscriptie nooit tot stand gekomen. In het bijzonder veel kussen aan Geertrui met de belofte om de tijd die het schrijven van deze scriptie heeft gekost ruimschoots goed te maken.

Dit doctoraat kwam tot stand met financiële steun van het IWT.

It was a privilege for me to have been able to work during four years on the interesting topics of the geological and thermochronological evolution of the beautiful regions of Siberia and Central Asia. It has been a very instructive and fascinating period during which I met many people and received a lot of help to accomplish this study. In scientific research we strive to reconstruct the questions put to us as precisely as possible. Nevertheless we have to recognize that there always exists a margin of error or uncertainty. I fear these acknowledgements do not form an exception to the rule. It is impossible to thank everybody who helped me in various issues during my research. Yet I will attempt to be as complete as possible.

Firstly, I wish to thank my promotor, Prof. Dr. Peter Van den haute for his expert assistance, his enthusiasm and the many instructive discussions we had during this study.

The constructive remarks by the reading committee, Prof. Dr. Peter Van den haute, Prof. Dr. Frans De Corte, Prof. Dr. Marc De Batist and Dr. Raymond Jonckheere, undoubtedly improved the quality of this work both on the level of contents as on the textual level. I therefore sincerely thank the committee.

Em. Prof. Dr. Stoops is acknowledged for the possibility he offered me to conduct this research at the Laboratory for Mineralogy, Petrology and Micropedology at the Department of Geology and Soil Sciences (University of Gent). I would also like to thank the other colleagues very much for the great working atmosphere at the Laboratory and the Department as a whole.

An important and very pleasurable aspect of this research was the fieldwork and sampling which were carried out in Siberia, Kazakhstan and Kyrgyzstan during the summers of 1998, 1999 and 2000. The inexhaustible enthusiasm of Dr. Michael Buslov was indispensable. Spasiba bolshoi Misha! The fieldwork was a wonderful experience where many friendships originated, I would like to thank all the participants: Dr. Boris Dehandschutter, Dr. Eugene Vysotsky, Dr. Karel Theunissen, Dr. Laryssa Smirnova, Dr. Elia Vassilieva, Dr. Damien Delvaux, Dr. Kanaathbek Y. Abdrakhmatov. Also a lot of gratitude to Rob Hus, Birgit Theunissen, Dima Kokh, Kostya Kokh and many other colleagues and friends for the several unforgettable "field-moments", the help in the field and the geological and other discussions. Many Russian students, geologists and guides have done their utmost best to organize the practical and logistical aspects of the fieldwork, which was often carried out in difficult circumstances.

This research was also made possible owing to an intense and fruitful co-operation with the Department of Geology and Mineralogy of the Royal Museum for Central Africa in Tervuren. I would especially like to show my appreciation to Prof. Dr. Jean Klerkx.

This fission-track study could not have been achieved without the smooth co-operation with the Institute for Nuclear Sciences (Laboratory of Analytical Chemistry, University of Gent). I wish to thank Prof. Dr. Frans De Corte and Ing. Antoine Dewispelaere for their help and advice with the irradiations and fluence measurements performed in this work.

Dr. Raymond Jonckheere is specifically acknowledged for his expert advice on many issues concerning fission-track analysis. I am grateful to Prof. Dr. Günther Wagner for allowing me to use the infrastructure and equipment of the Department of Archeometry at the Max Planck Institute for Nuclear Physics in Heidelberg, Germany.

For the help with administrative and technical questions I am thankful to Arlette Bavay-Calle, who I wish a lot of courage and strength. I am also thankful to Nicole Selen, Hubert Bourdin and Julien Van Hende.

Last, but not least, I should thank my parents, family and friends, without whose support and confidence during my studies and my research, this work would never have been accomplished. Especially loads of kisses to Geertrui, with the promise of making up for the time invested in the writing of this dissertation.

This research was made possible with financial support of the IWT.

INTRODUCTION

The Central Asian mountain belt forms the world's largest intracontinental mountain chain, stretching over a distance of more than 5000 km north of the Himalayan-Tibetan deformation zone, from the Pamir mountains in the western part to the Sea of Okhotsk in East Siberia. It includes a.o. the Pamir mountains, the Tien Shan mountains, the Altai-Sayan mountains, the Baikal Rift Zone and the Stanovoy mountains. The entire region is currently subjected to widespread active deformation, resulting in processes of intracontinental mountain building and basin formation. The whole area is known as the Central Asian Deformation Zone (CADZ).

It was only after the introduction of the theory of plate tectonics in the 1970's that the driving forces that are responsible for the development of the CADZ were identified. In the light of this new geodynamic view, it was recognized that the continent-continent collision of India and Eurasia in the Early Cenozoic and particularly the ongoing indentation of India into the Eurasian plate, were responsible for the active tectonic processes observed in the CADZ. It was envisaged that the strain and stress build-up at the collision zone due to continuing convergence was in part released as movements and deformation along inherited zones of lithospheric weakness far into the interior of Eurasia.

These pre-existing zones of lithospheric weakness are represented by older sutures and structures, mainly strike-slip fault zones, which carve up the intricate blocky-mosaic tectonic architecture of the Central Asian and South Siberian basement. The basement of the CADZ was mainly formed in the Palaeozoic as the result of a complex accretionary history. During much of the Palaeozoic era the Siberian craton acted as the continental core around which many tectonic units of various type and dimension assembled. The tectonic units docked with the growing orogenic rim of Siberia along the sutures and structures that are reactivated at present. In this way, a vast mobile belt running through the entire area was formed. Besides the accretion of these tectonic units, the continental growth was further achieved through intrusion of large volumes of crustal magma. In the Mesozoic, accretion continued primarily on the southern rims of Eurasia and acted as a precursor to the huge collision of India and Eurasia during or soon after the Meso-Cenozoic transition.

It is the aim of this study to contribute to the understanding and knowledge of the tectonic evolution of the CADZ both with respect to its Mesozoic accretionary history as to its Cenozoic and present reactivation. It is important to quantify and constrain the movements of the various units composing the CADZ both in space and in time. The strain partitioning in the heterogenous and anisotropic Central Asian crust induced a variety of movements and deformation styles. The tectonic regimes range from pure extension, as is in the Baikal Rift Zone, to transpression in the Altai-Sayan and Tien Shan mountains. Transpressional mountain belts are a striking characteristic of intracontinental deformation. Study of the transpressional Altai-Sayan and Tien Shan mountains within the CADZ hence not only has an important regional geological and geodynamic significance, but equally augments our understanding of intracontinental deformation in general.

A transpressional process is defined by both convergent and lateral horizontal movements as well as by vertical movements. This study focusses on the age, rate and magnitude of the vertical tectonic movements within two major units of the CADZ: the Altai-Sayan mountain belt in South Siberia and the Tien Shan mountain belt in Kyrgyzstan. Low-temperature thermochronological techniques are the most suitable tools for investigating these issues. Low-temperature thermochronology relies on both chronological and thermal information contained in mineral-specific isotopic systems. The apatite fission-track (AFT) method is one of the most succesful and most widely applied low-temperature thermochronological techniques. Owing to its radiometric dating potential and its specific closure temperature, the AFT system is able to record rock movements in the top 4 km of the earth's crust relative to the vertical structure and position of the isotherms in the crust, and that within an absolute time frame. The number of fission tracks contained in an apatite sample yields its AFT age, while the length of the tracks are a measure for the thermal information registered in the AFT system. Combining both data sets, AFT thermal history modelling for the Altai-Sayan and Tien Shan mountain belts was carried out.

In the first chapter of this work the AFT method is outlined in some detail. The basic principles of the method are discussed in a historical perspective and extensive literature references are provided. Furthermore chapter one provides insight in more recent methodological developments and includes the derivation of the fundamental age equations used to calculate AFT ages.

The second chapter deals with the thermal stability of fission tracks and the thermal annealing models for fission tracks in apatite. Again, the basic principles are outlined in a historical perspective and an attempt is made to elucidate the range of models that are available today. The main aim of this chapter is to explain the reader how thermal information is derived from AFT length analysis and how this information can be interpreted in a geological and tectonic context.

In the third chapter attention is directed toward the important aspect of calibration of the AFT method. In this work both the absolute and the so-called zeta (ζ) calibration approach were used. Results of the applied calibration procedures are presented. This includes an extensive data set of apatite age standard analysis performed during our study of the Central Asian and Siberian apatites.

In chapter four, the geological and geodynamic setting of the Altai-Sayan and the Tien Shan mountains is discussed within the broader setting of the CADZ. Chapter five focusses on the study areas in more detail and elaborates on the fieldwork and sampling of the apatites used in this work.

Finally, in chapter six we present our AFT data and the thermal histories that we have modelled from the AFT data for the Altai-Sayan and Tien Shan mountains. The data and models are discussed and interpreted within the tectonic framework outlined in chapters four and five. We arrive to an overall thermo-tectonic model for both study areas. These models are also compared to each other and to studies performed by other authors in the region. In chapter 7 our general conclusions are summarized.

CHAPTER 1

THE APATITE FISSION TRACK DATING METHOD

1.1. Fission tracks: Definition, structure and formation

Radioactive isotopes are characterized by an energetically unstable atomic nucleus. In order to attain a more favourable energetic state the nucleus will disintegrate into a stable daughter atom by emitting one or more of its nuclear particles. This is what we call radioactive decay. A very specific mode of nuclear disintegration is *fission*. In this nuclear reaction the nucleus splits into two daughter fragments that are usually unstable and disintegrate further to stable isobars by β-emission. Fission only occurs with heavy nuclides (atomic number $Z \geq 90$ and atomic mass $A \geq 230$). The reaction is generally binary and asymmetric, implying that the fissioning nucleus splits into two dissimilar (unequal mass and atomic number) fragments. Nuclear fission can occur spontaneously due to the existing instability within the nucleus itself, or it can occur when the nucleus is irradiated or bombarded with certain subatomic particles. Each fission reaction also produces several neutrons and a large amount of energy (~200 MeV). A significant portion of that energy (~170 MeV) appears as kinetic energy of the fission fragments. As they both carry a strong positive charge, the repulsive Coulomb force propels the fragments in opposite directions with high velocity. This velocity exceeds the orbital speed of the electrons, and the particle is launched through the medium as a nucleus partially stripped of its orbital electrons. When a fissioning nuclide (e.g. ^{238}U) is embedded in a solid (the *detector*), for example as a trace element in a crystal lattice, the fission fragments create a narrow trail of damage along their trajectories. This damage trail is called the *Fission Track* (FT). In the core of the track the crystal lattice is completely destroyed and altered into an amorphous state (the so-called thermal spike model, e.g. Toulemonde et al., 2000), although the classical model for fission track formation (the ion explosion spike model, see further) describes the fission track as an evacuated core zone (Fleischer et al., 1975). According to most models, the fission track is essentially a continuous structure, although alternative (discontinuous structure) models (the so-called *gap* model or *Orsay* model, e.g. Dartyge et al., 1981) have been proposed. The simplified formation model of latent fission tracks, known as the *ion explosion spike* theory (Fleischer et al., 1975), states that the charged fission fragments induce ionization along their path in a dielectric solid, creating an array of positive lattice ions which expel one another in interstitial positions, and leaving a set of lattice vacancies. The consequential lattice stress is smoothed out by elastic relaxation (figure 1.1). Although this theory is at present strongly debated by physicists, it is still widely used in general papers and textbooks on the FT-dating method (e.g. Wagner and Van den haute, 1992). As a general comment, the Wagner and Van den haute (1992) textbook *Fission-Track Dating* was used as a

general reference. For more details concerning specific topics discussed in this chapter, the reader is referred to this work and references therein.

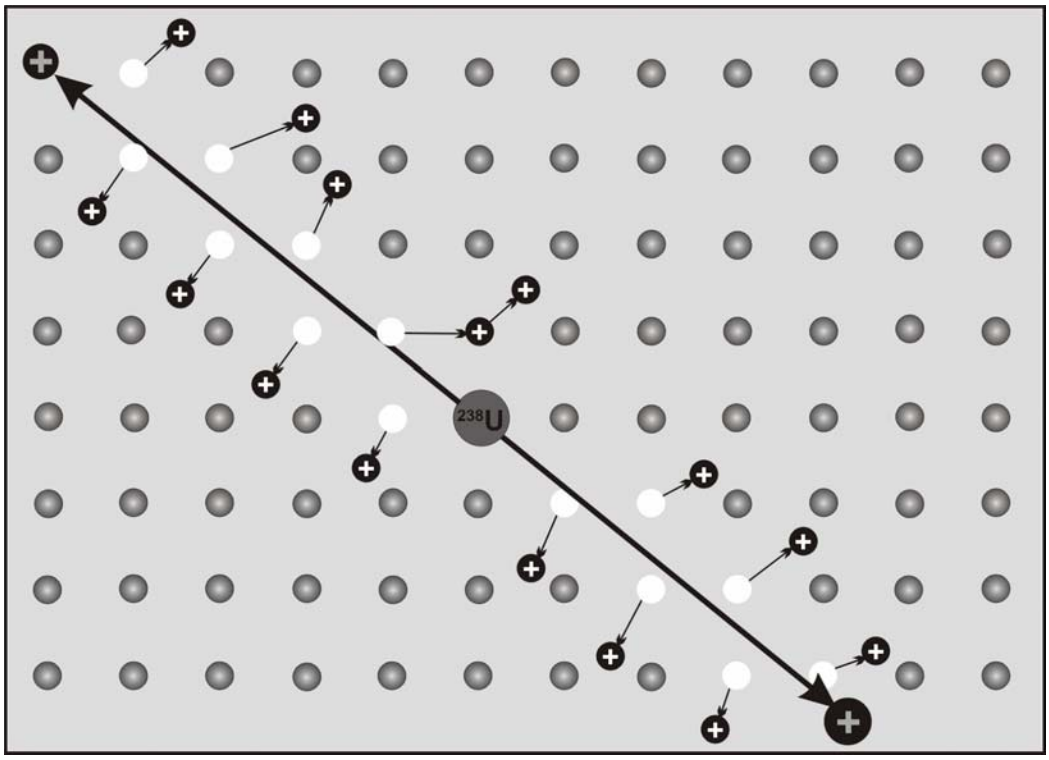

Figure 1.1: Simplified scheme for the formation of a fission track according to the ion explosion spike theory (after Fleischer at al., 1975). A ^{238}U nucleus fissions, projecting two high-energy fission fragments through the lattice. Ionization, Coulomb explosion and subsequent elastic relaxation create a permanent trail of lattice damage, the fission track, along the linear trajectory of each of the fission fragments.

The initial velocity of a fission fragment is a function of its kinetic energy, inherited from the fission reaction. As the fragment is propelled through the detector, its energy and thus its velocity decreases by interactions with the solid medium. The energy loss, or the linear energy transfer along the trajectory (-dE/dx) is termed the *stopping power* of the medium. The distance travelled by the fission fragment is the *range*. The range vectors of both fission fragments meet in the original lattice site of the parental nuclide and form one linear trail.

Depending on the energy of the fission fragments and the type of detector, a FT reaches lengths from less than 1 μm to several mm. In general, the FT width is a few nm and hence it is submicroscopic. Such a track, invisible under an optical microscope, is called a *latent track*. Latent tracks can only be observed using high-resolution electron microscopy (figure 1.2). However, as is the case for any lattice defect, a FT forms a site for preferential attack by a chemical etchant. Etching of a latent FT with a suitable chemical etchant for an appropriate time and at a selected temperature reveals the track for observation with an optical microscope.

Table 1.1: Abundances and half-lives of the natural isotopes exhibiting spontaneous fission (from Wagner & Van den haute, 1992). * Geochemical average.

Isotope	Relative abundance (compared to ^{238}U)	Total $T_{1/2}$ (in a)	Spontaneous fission $T_{1/2}$ (in a)
^{232}Th	4^{*}	1.40×10^{10}	1.0×10^{21}
^{234}U	5.44×10^{-5}	2.46×10^{5}	1.5×10^{16}
^{235}U	7.25×10^{-3}	7.04×10^{8}	1.0×10^{19}
^{238}U	1	4.47×10^{9}	8.2×10^{15}

Natural fission tracks in minerals in the earth's crust are terrestrial and not cosmogenic in origin (Fleisher et al., 1975). Naturally induced fission occurred in rare cases and under extraordinary conditions (in the Oklo uranium ore deposits in Gabon; e.g. Loss et al., 1988). Hence, it is fair to state that fission tracks detected in minerals are entirely the result of spontaneous fission processes. From table 1.1 it can furthermore be deduced that nearly all FTs observed in minerals are the result of fission of ^{238}U. The other natural isotopes displaying spontaneous fission have too low abundances or too long half-lives to produce significant quantities of FTs compared to ^{238}U.

Figure 1.2: A latent fission track in Durango apatite as observed with high-resolution transmission electron microscopy (Wang et al., 1999).

Depending on the uranium content of the sample and the thermal stability of the tracks in the investigated material (see next chapter), it is possible to date geological samples of hundreds of millions of years old up to archeological glasses stemming from recent human history. The applicability of the method is limited by the product of the U-content (U) of the sample on one hand and its age (t) on the other hand. The FT method is not applicable when this product is too low. A too low track density is the result and thus is first of all very time consuming to count, and secondly, the uncertainty margin is too broad. On the other hand, when the $t \times U$ value is too high, the method is also unusable as tracks are not sufficiently resolvable under the microscope (due to overlap). For

rapid and efficient counting of tracks in apatite, densities between 10^5 and 10^7 tracks/cm^2 are required (figure 1.3).

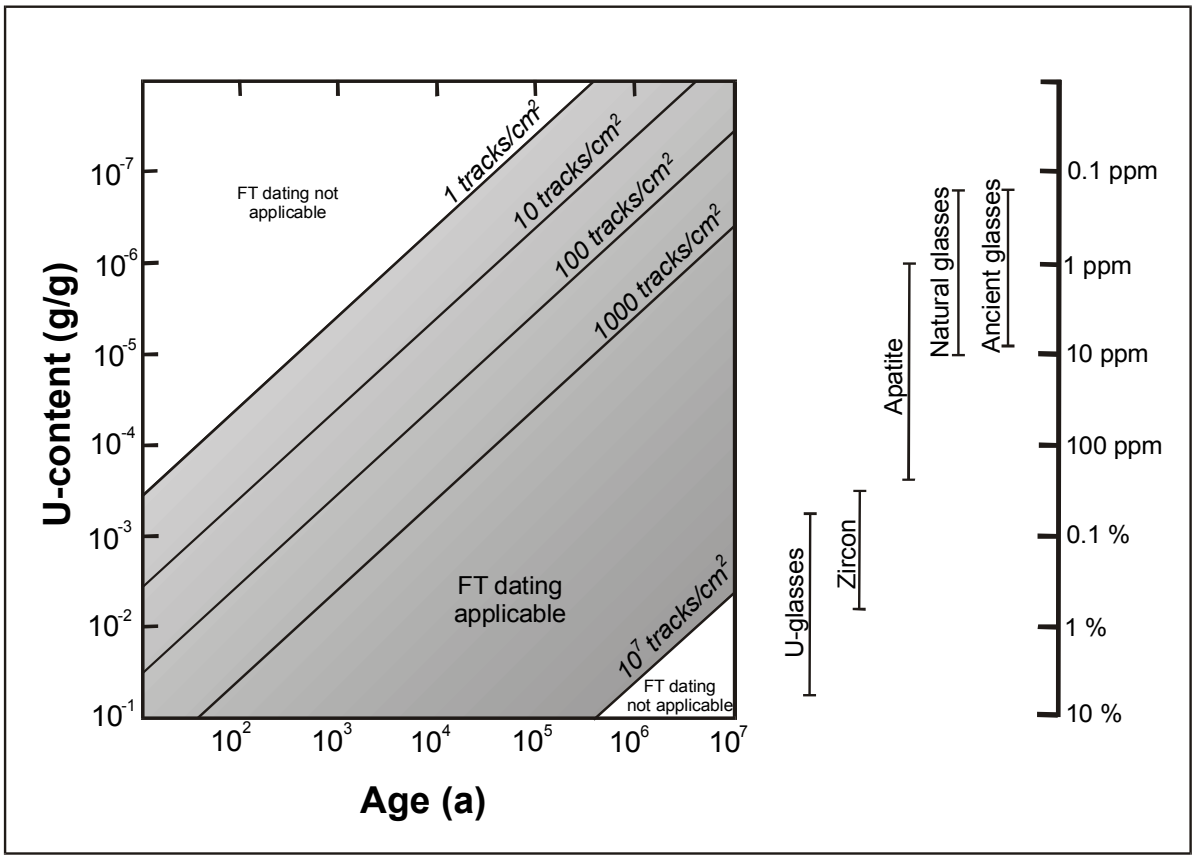

Figure 1.3: Applicable time-span of the FT dating method as a function of the sample's uranium content (after Wagner and Van den haute, 1992).

1.2. Fission track revelation

1.2.1. Surface tracks

In order to observe FTs with an optical microscope, so-called *revelation* methods have been developed. The chemical etching technique is by far the most widely used revelation method in FT dating. The mineral is treated with a chemical etchant that attacks the mineral surface on one hand and crystal defects on the other. A FT is a lattice defect and is hence a preferential site for chemical etching. In particular the track diameter will be widened to an extent that eventually the track becomes observable with an optical microscope. Because of the non-etchability of the track ends, the etchant is generally not capable of revealing the entire range of a fission fragment. Consequently the etchable length of a FT is shorter than the combined range of the two fission fragments. This is called the *range deficit* (Fleischer et al., 1975) (figure 1.4).

Etched FTs in crystals have complex shapes due to the anisotropic character of the detector. In general, the etching rate along the track (V_t) is much larger than the bulk etching rate (V_b) of the undamaged detector surface. As a consequence, etched FTs exhibit a needle-like appearance. Radial enlargement of the track channel causes the track to become revealed. At the surface/track interface of some crystal surfaces the etching process creates an etch pit or opening with a characteristic geometry, that reflects the crystal symmetry and the crystallographic orientation of the etched surface. In this case the etched FT has a funnel shape. It is however the channel that remains the true diagnostic part of the track. In addition, the composition and concentration of the etchant has an influence on the shape and appearance of an etched FT.

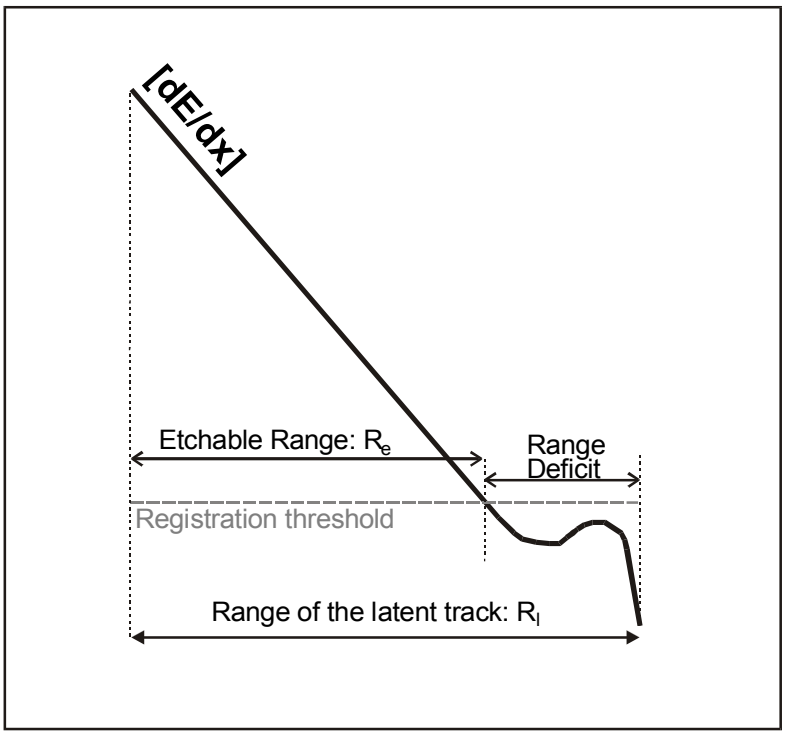

Figure 1.4: Schematic illustration of the energy loss (dE/dx) along the trajectory of a fission fragment through a solid medium. The detector-specific registration threshold defines the etchable range (R_e) of the fission track. The difference between the true range of the latent fission track (R_l) and R_e is the range deficit. Due to this range deficit for a specific detector, the ends of a latent fission track cannot be revealed (from Jonckheere, 1995).

1.2.2. Fission tracks in apatite

This thesis reports on an apatite FT (AFT) investigation in Central Asia. It is therefore logical to focus the discussion in the following sections on the specific case of fission tracks in apatite. However, some aspects of the FT dating method will be dealt with in a general fashion. The phosphate apatite $Ca_5(PO_4)_3(F, Cl, OH)$ is the most common mineral used in FT analyses and hence its properties and behaviour as a FT chronometer are the best studied. Fluorapatite is by far the most widespread member of the isomorphous apatite solid solution series (Deer et al., 1962; McConnell, 1973). Apatite is a common accessory mineral in numerous rock types (in general from 0.1 to 1 % in

most acidic igneous rocks) with the important exception of calcareous sediments. Uranium is a common trace element in the apatite lattice where it replaces Ca (in the order of 1 to 100 ppm), and FTs are fairly easily revealed (nitric acid solution at room temperature). It has become a valuable geothermochronometer in the study of thermotectonic history of rocks based on the low thermal stability of FTs in apatite. Other minerals, such as zircon and sphene and natural glasses are also commonly used in FT analysis. The first AFT ages were reported by Fleischer and Price (1964), Naeser (1967) and Wagner (1968).

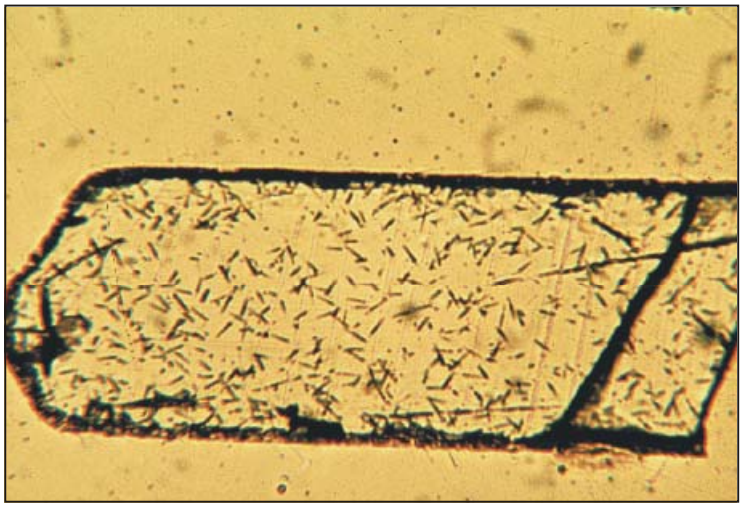

Figure 1.5: Etched spontaneous fission tracks in apatite (magnification 1250×). Etching conditions: 2.5% HNO_3 at 20°C for 70 seconds.

Latent FT diameters in apatite are 5 to 10 nm (Paul and Fitzgerald, 1992), while the observed length of an etched induced track in apatite is 16 µm on average (e.g. Green, 1980; Gleadow et al., 1986). However, based on theoretical assumptions Jonckheere (1995) calculated that the length of latent induced tracks in apatite may amount to 20 µm. For AFT revelation, HNO_3 is used as an etchant. Depending on the HNO_3 concentration (from 0.5 to 65%) apatite is etched within 10 to 80 seconds, generally at temperatures of 20-30°C. An example of etched FTs in apatite is presented in figure 1.5. Figure 1.6 shows hexagonal etch pits of the FTs on a basal [0001] apatite surface.

Track revelation characteristics in apatite (Durango) were studied extensively by Jonckheere and Van den haute (1996). These authors identified three types of etched internal surfaces. These are P-type (Pitted), S-type (Smooth) and T-type (Textured) surfaces. P-type surfaces, after acquiring an initial roughness, grow smoother with etching time. S-type surfaces remain smooth for long etching times, while T-type surfaces develop a progressively coarser texture. It was found that internal crystallographic sections parallel to $\{0001\}$ and $\{11\bar{2}1\}$ correspond to P-type, $\{10\bar{1}0\}$ and $\{10\bar{1}1\}$ to T-type, and $\{11\bar{2}0\}$ to S-type surfaces. In P-type $\{0001\}$ surfaces, and also in some S-type surfaces, FTs exhibit a funnel shape with hexagonal etch pit opening and needle-like track channel. In these surfaces, lattice defects other than FTs are easily revealed during etching. This is not the case in S- and T-type surfaces, where tracks are simple channels. The bulk etching velocity perpendicular to the surface increases from P-, to S-, to T-type surfaces. FT densities were found to be more or less

equal in all surface types near the limit of track revelation, but with prolonged etching times, FT density decreased in P-type surfaces, increased in S-type surfaces, while remaining constant for T-type surfaces.

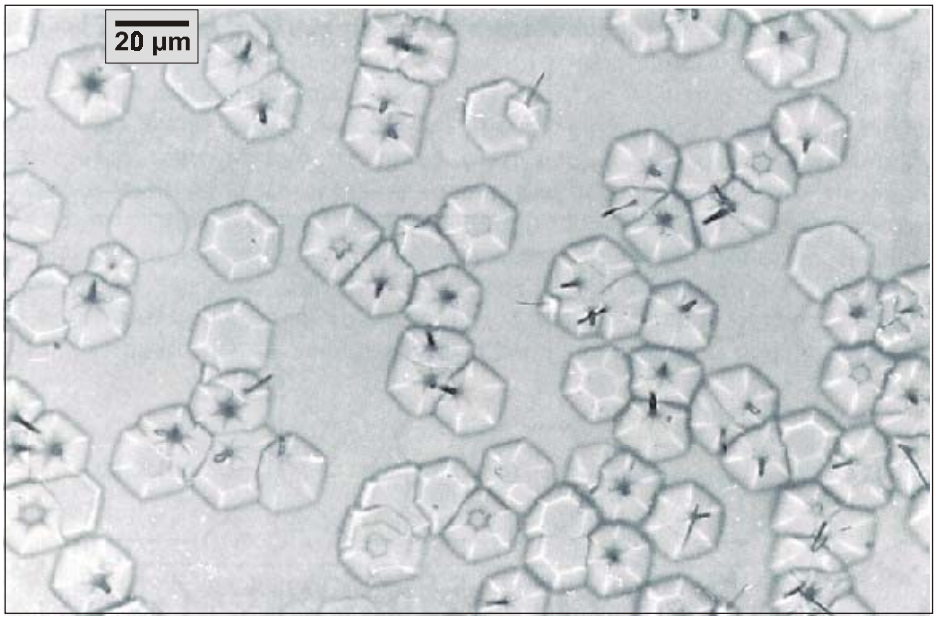

Figure 1.6: Typical funnel shape of etched fission tracks on the basal plane (parallel to the c-axis) in apatite. The hexagonal crystal symmetry of apatite is clearly reflected by the shape of the etch pits. The channel is the diagnostic part of the fission track, flat bottomed pits represent tracks that are completely etched through. Etching conditions: 4N HNO_3 at 25°C for 60 seconds (from Wagner and Van den haute, 1992).

The classic (V_b-V_t)-model for FT revelation (see section 1.2.1) fails to explain these revelation characteristics and track geometries as found for apatite by Jonckheere and Van den haute (1996). These authors propose a model based on the concept of radial shift velocity (V_r), which is a property of macroscopic surfaces and is represented by a vector normal to the surface, equal in magnitude to its rate of translation during dissolution. This translation involves the plane surface as a whole, contrary to V_b. In this way a (V_r-V_t)-model takes the crystallographic orientation of the etched surface into account and is able to predict the complex FT geometries in an anisotropic detector such as apatite. The authors further showed that the etching efficiency (η, see next section) cannot be expressed as a function of the etching velocities. Also, they introduce the q factor or the observation factor depending on FT analyst, FT observation and identification (also see next section). They unite the etching and observation characteristics, as they mutually influence one and other, into a combined track counting efficiency, or ηq-factor.

1.2.3. Areal and spatial track densities

The areal density of surface intersecting tracks (ρ; tracks/cm^2) stands in relation with the spatial density of latent tracks (tracks/cm^3 = N_f) and thus of fissioned atoms in a unit volume of the apatite detector. The mathematical relationship between N_f and ρ has been derived by Fleischer et al., (1975) (figure 1.7). They assumed that U is distributed in a homogeneous fashion in the detector, that there does not exist a preferential track orientation and that track length is constant. A fissioning nuclide in position O (see figure 1.7) creates a latent track of length $l = 2R_l$ (R_l represents the average range of a fission fragment in the investigated detector). The $l = 2R_l$ relationship is actually a simplification because fission is generally asymmetric and hence the two fission fragments have a different mass and velocity, which results in different ranges. But when adopting the $l = 2R_l$ relationship, the track defines a sphere with radius R_l and centre O. If N_f is the areal density of the fissioned nuclides, then $N_f dz$ represents the number of fissioned nuclides in a layer of unit area and infinitesimal thickness dz at distance z ($\leq R_l$) below the considered surface. Only tracks at an angle $\theta \geq \arcsin(z/R_l)$ intersect the surface. The probability P(z) of a track having an angle greater than or equal to θ is given by the ratio of the area of the sphere above the considered detector surface to the area of the semi-sphere above the position O of the fissioned nuclide.

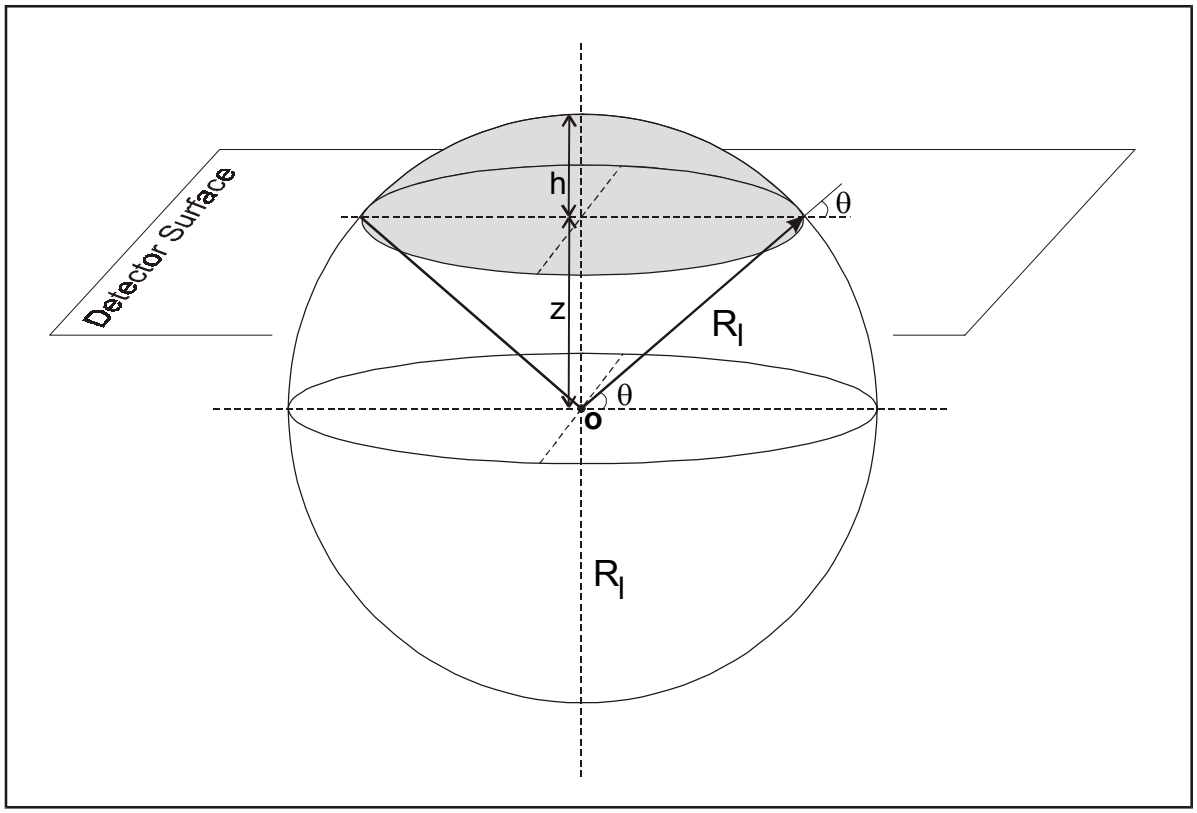

Figure 1.7: When a ^{238}U nuclide (at location o) within a crystal lattice fissions, a fission track with a length $l = 2R_l$ (R_l is the range of one fission fragment) is created. When the position of the U isotope was at a distance z ($z \leq R_l$) under the detector surface, only tracks with upper ends in the gray zone of the sphere (with radius R_l) will cut that surface.

Thus:

$$P(z) = 2\pi R_l h/2\pi R_l^2 = R_l(R_l - R_l\sin\theta)/R_l^2 = (1 - \sin\theta) \quad 1.1$$

The number of tracks intersecting the considered surface is hence $(1 - \sin\theta)N_f dz$, and the areal latent track density ρ_l is:

$$\rho_l = \int_0^{R_l} (1 - \sin\theta) N_f dz = \int_0^{R_l} N_f (1 - z/R_l) dz \quad 1.2$$

This integral yields the following simple relationship between the areal and the spatial track densities:

$$\rho_l = N_f R_l/2 \text{ or } \rho_l = N_f l/4 \quad 1.3$$

This is the case for an external mineral surface, in which tracks only originate from fissioning nuclides in one semi-sphere on one side of the surface. This is the so-called 2π-geometry (corresponding to a solid angle of 2π). An internal surface (a polished internal section of an apatite crystal for example), is intersected by tracks resulting from both side of the surface (4π-geometry; solid angle of 4π). In this case ρ_l is:

$$\rho_l = N_f R_l = N_f l/2 \quad 1.4$$

Equations (1.3) and (1.4) can be written as:

$$\rho_l = gN_f R_l = gN_f l/2 \quad 1.5$$

in which g is a factor referring to the track registration geometry; being $g = 1$ for the 4π- and $g = 0.5$ for the 2π-geometry.

The etched track density (ρ_e) is not equal to the latent track density (ρ_l) as calculated above. A main reason for this is the range deficit (section 1.2.1; figure 1.4). Furthermore, additional etching effects should be taken into account and an *etching efficiency factor* (η) must be included in the expression for ρ_e (Green and Durrani, 1978). This factor can be defined as the ratio of the number of tracks that are effectively revealed within a certain etch time to the number of latent tracks intersecting a given surface. The etching efficiency factor η depends on the material. For anisotropic detectors, such as minerals, a simple equation for η cannot be given. The etched track density can finally be written as:

$$\rho_e = \rho_l\eta = gN_f R_e\eta = gN_f l_e\eta/2 \quad 1.6$$

R_e represents the etchable range of the FT; the etchable length of the fission track is $l_e = 2R_e$.

1.2.4. Confined tracks

Occasionally tracks that do not intersect the surface are also etched. These tracks are localized entirely in the interior of the crystal. They are etched when the etchant can reach them through a surface track or through a fracture in the crystal that traverses the confined track (figure 1.8). As a result, the entire etchable length of the fission track is revealed and these *confined tracks* are ideal for use in track length analysis. Confined tracks are called TINTs (Track IN Tracks) or TINCLEs (Track IN CLEavage) depending on how the etchant reached it (Lal et al., 1968; Bhandari et al., 1971). Confined tracks are used in FT analysis for measurements of the tracks lengths. Their FT length distribution (typically composed of about 100 tracks per sample), are used in the FT method as a thermochronological tool (section 2.6).

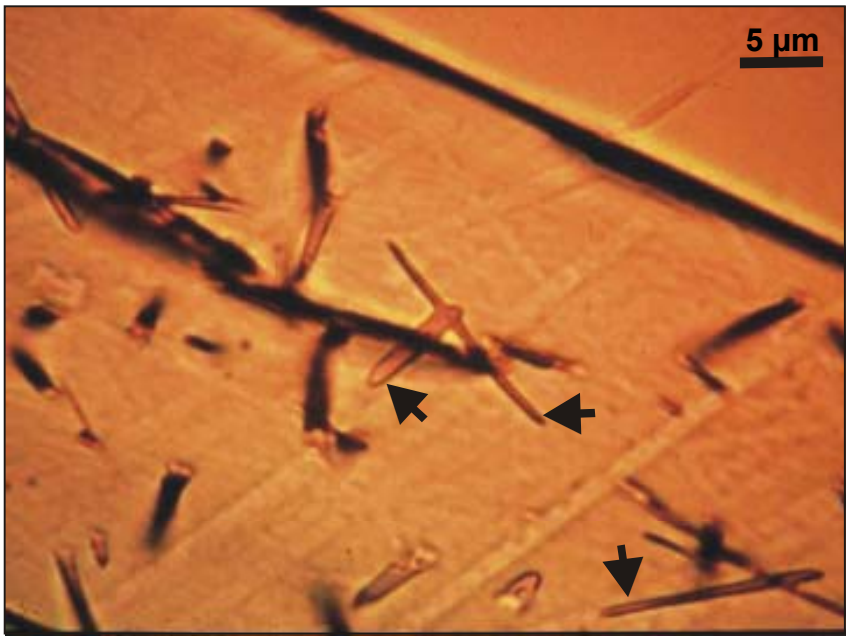

Figure 1.8: Example of confined fission tracks in an apatite crystal. These tracks are etched over their entire etchable length crystal because the etchant was able to reach them passing through a fracture in the crystal or through a surface track.

In principle, the projected track lengths and the true lengths of surface tracks can be used for FT length analysis as well, although at present all studies are based on horizontal confined tracks (Laslett et al., 1982). However, it should be noted that in the cases of high degrees of annealing (chapter 2), there is a bias against short tracks. In small samples or samples with low spontaneous track densities it can be difficult or impossible to measure a sufficient number of confined tracks and to construct a length distribution. In these cases or when experiments demand a high number of confined tracks, the samples can be irradiated with fission fragments from a ^{252}Cf-source. These fission fragments create host tracks, hence augmenting the probability of revealing confined tracks in the sample. Depending on the duration and intensity of the irradiation, and the sample-to-source distance, the number of confined FTs of the sample will be enlarged and more TINTs will be revealed. Repolishing the irradiated surface will erase these tracks and restore the sample (Donelick and Miller, 1991).

1.3. Fission track observation and identification

Etched FTs form straight channels of limited length that do not exhibit preferred orientations. Dislocations and other spurious defects on the other hand generally occur in clusters or in parallel arrays and often have a curved form. But in some cases the distinction between etched FTs and etched dislocations, surface defects or other spurious track-like features is difficult. FT identification is consequently to some extent a subjective matter with some variability associated with the observation equipment and with the FT researcher. This is illustrated by interlaboratory comparisons on reference materials (e.g. Naeser et al, 1981; Miller et al., 1985, 1990 and 1993; Van den haute and Chambaudet, 1990) that at times point to significant differences in absolute track densities. FT researchers have the tendency to only count the tracks that can be identified with certainty. Areal FT densities may therefore be underestimated. It seems sensible to acknowledge and quantify this behaviour by introducing an *observation factor* or *observation efficiency* $q \leq 1$, although its exact value is difficult to enumerate and depends on the researcher and the observation equipment (Wagner and Van den haute, 1992). Comprehensive discussions on this matter are given by Jonckheere and Van den haute (1998, 1999 and 2002). The factor q can be defined as the ratio of the observed areal density of etched FTs that are recognized as such by an individual analyst under certain observation conditions to the actual existing areal density of etched FTs.

In short, we can adjust the expression for the etched FT density (section 1.2.3; equation 1.6) to an observed density of etched FTs as follows:

$$\rho_e = gN_fR_e\eta q \qquad 1.7$$

The ηq-factor was defined by Jonckheere and Van den haute (2002) as the track counting efficiency.

1.4. Principles of the fission track dating method

The FT dating method is based on the fact that spontaneous FTs accumulate in a given mineral sample over time. If the value for the disintegration constant for the spontaneous FT reaction of ^{238}U is known and if the uranium concentration in the sample is known, a FT age can be calculated. Derivation of the fundamental FT age equation was first done by Price and Walker (1963). In this section the derivation by Wagner and Van den haute (1992) is followed.

In order to derive the fundamental age equation for the FT dating method, a first step is to start from the basic first-order differential equation of radioactive decay from parent isotope to a stable daughter. This relationship states that the disintegration rate is proportional to the number of parent nuclei (N_P) at time t:

$$dN_P/dt = -\lambda N_P \qquad 1.8$$

The factor λ is the decay-constant (in a^{-1}), which is the ratio of the number of individual disintegrations that occurs in a unit time (one year, 1 a), to a given number of parental nuclei. $(N_P)_o$ is the original number of parent isotopes at time t = 0; after integration equation (1.8) becomes:

$$N_P = (N_P)_o e^{-\lambda t} \text{ or } (N_P)_o = N_P e^{\lambda t} \quad 1.9$$

The number of stable daughter nuclei (N_D) is given by $N_D = (N_P)_o - N_P$, or:

$$N_D = N_P (e^{\lambda t} - 1) \quad 1.10$$

This equation for isotopic dating systems can also be applied to the FT dating method, where ^{238}U is the radioactive parent that decays by spontaneous fission. Each fission reaction creates a fission track and so the fission track can be considered as the stable daughter isotope. However ^{238}U predominantly decays to ^{206}Pb by successive α- and β-decays. The total decay-constant (λ_U) of ^{238}U is composed of the fission (λ_f) and the α (λ_α) decay-constant: $\lambda_U = \lambda_\alpha + \lambda_f$. So, if ^{238}N represents the present-day concentration of ^{238}U then the number of spontaneous fission tracks (N_s) per unit volume is:

$$N_s = (\lambda_f/\lambda_U)\ ^{238}N(e^{\lambda_U t} - 1) \quad 1.11$$

Because λ_α is several orders of magnitude greater than λ_f it is fair to state that $\lambda_U \approx \lambda_\alpha$ and then the solution (to t) of previous equation can be written as:

$$t = \lambda_\alpha^{-1} \ln[(\lambda_\alpha/\lambda_f)(N_s/^{238}N) + 1] \quad 1.12$$

Several physical methods can be used to measure the present ^{238}U concentration (^{238}N), but for the FT method an elegant procedure based on microscopic FT counting, was developed. When a sample is irradiated in a nuclear reactor with a precisely known (i.e. experimentally measured) fluence (ϕ) of thermal neutrons, nuclei of ^{235}U present in the sample are induced to fission. These induced fission reactions create induced FTs that can be counted. The number of induced FTs per unit of volume is given by $N_i = {}^{235}N\sigma\phi$, in which σ refers to the conventional effective cross-section of ^{235}U for thermal-neutron induced fission. The parameter σ can be considered a constant for a specific nuclear reaction given a certain neutron energy. It can be defined as the ratio of the number of neutrons that effectively produce fission of ^{235}U per unit of time to the total thermal neutron flux φ to which the sample is exposed. The cross-section is expressed in barn (b) with $1b = 10^{-24}cm$. The thermal neutron fluence (ϕ_{th}) is the thermal neutron flux (φ_{th}, specific to the irradiation facility used) multiplied by the irradiation time (t_{irr}), so $\phi_{th} = \varphi_{th} t_{irr}$ if we assume that the flux stays constant during irradiation. The fluence is a parameter that can be measured very accurately.

Apart from very rare exceptions (the Oklo deposits in Gabon) the present $^{235}U/^{238}U$ ratio in nature is a constant ($I = 7.2527 \times 10^{-3}$ Cowan and Adler, 1976). So the number of induced fission tracks per unit of volume is $N_i = {}^{238}NI\sigma\phi$ and thus equation (1.12) becomes:

$$t = \lambda_\alpha^{-1} \ln[(\lambda_\alpha/\lambda_f)(N_s/N_i)I\sigma\phi + 1] \qquad 1.13$$

The determination of a FT age consequently comes down to the measurement of the N_s/N_i ratio and of the thermal neutron fluence.

Counting of FTs with an optical microscope involves determining areal FT densities. The theoretical relationship between the areal and spatial FT densities is (section 1.2):

$$\rho_{s,i} = g_{s,i} N_{s,i} (R_e)_{s,i} \eta_{s,i}\, q_{s,i} \qquad 1.14$$

The subscript "s" refers to the spontaneous fission tracks, "i" to the induced fission tracks. Accordingly, the (N_s/N_i) ratio in equation (1.13) can be written as:

$$\frac{N_s}{N_i} = \frac{\rho_s}{\rho_i} \frac{g_i R_{e,i} \eta_i q_i}{g_s R_{e,s} \eta_s q_s} \qquad 1.15$$

Then two factors can be defined:

$$G = g_i/g_s \qquad 1.16$$

$$Q = \frac{R_{e,i} \eta_i q_i}{R_{e,s} \eta_s q_s} \qquad 1.17$$

The geometry ratio (G) is the ratio of the geometry factors for the registration geometries of the spontaneous and the induced FTs. In principle this factor is 0.5, 1.0 or 2.0. In practice, depending on the procedure used (section 1.2.2), this value is 0.5 (external detector method; Gleadow and Lovering, 1977) or 1.0 (population method; Green and Durrani, 1978).

The procedure factor (Q) incorporates several effects. It includes the observation factors, which depend on the FT researcher her- or himself and on the optics of the microscope. It also contains etching parameters (etching efficiency and etch time factor), so the Q-factor will also depend on the etching conditions used for revealing both spontaneous and induced tracks. Finally it includes the etchable range of the fission fragments and hence, in addition, Q depends on the range deficit. Furthermore, Q also depends on the registration geometries of the spontaneous and induced tracks and especially, when the external detector method is used (section 1.8.3), on the different length deficit in the mineral and the external detector (Jonckheere and Van den haute, 2002). Enkelmann and Jonckheere (2003, in press) present a recent discussion on this matter. To assign an exact value to Q depends on empiricism and personal calibration.

In conclusion, the general formulation of the FT age equation is:

$$t = \lambda_\alpha^{-1} \ln[(\lambda_\alpha/\lambda_f)(\rho_s/\rho_i)QGI\sigma\phi + 1] \qquad 1.18$$

In this formulation an FT age can be calculated if the areal track density ratio is determined by counting the tracks with the optical microscope, and if the thermal neutron fluence is carefully measured and finally, if the Q-value is known.

The remaining parameters in the age equation are nuclear constants and are:

$\lambda_\alpha = 1.55125 \times 10^{-10} a^{-1}$	(Jaffey et al., 1971; Steiger and Jäger, 1977)
$\lambda_f = 8.46 \times 10^{-17} a^{-1}$	(e.g. Galliker et al., 1970)
$I = 7.2527 \times 10^{-3}$	(Cowan and Adler, 1976; Steiger and Jäger, 1977)
$\sigma = 570.8$ b	(Wagner and Van den haute, 1992).

Values for λ_α and I are accepted values. Values for both other constants are not subject of a broad consensus. Elaboration on this topic will be a focus in the following section.

1.5. Relevant nuclear parameters and the problem of the ^{238}U fission decay constant

1.5.1. The fission decay constant of ^{238}U

Since the discovery of nuclear fission (Hahn and Strassmann, 1939; Meitner and Frisch, 1939) and spontaneous ^{238}U fission (Flerov and Petrzhak, 1940) various techniques have been applied to determine the fission decay-constant of ^{238}U, resulting in more than 50 λ_f values ranging from $7 \times 10^{-18} a^{-1}$ to $2.8 \times 10^{-16} a^{-1}$. The majority of λ_f values cluster around two modes: $7.0 \times 10^{-17} a^{-1}$ and $8.5 \times 10^{-17} a^{-1}$ (Bigazzi, 1981; Hurford and Green, 1981a; Wagner and Van den haute, 1992; and Van den haute et al., 1998, give a comprehensive overview on this matter). Within each of these two clusters, the most precise determination was adopted and two λ_f-values came into use: $(7.03 \pm 0.11) \times 10^{-17} a^{-1}$ (Roberts et al., 1968) and $(8.46 \pm 0.06) \times 10^{-17} a^{-1}$ (Galliker et al., 1970). This uncertainty created scepticism about the reliability of the FT method, and prompted some FT geochronologists to propose new calibration techniques (section 1.7.2), but it did not remove the ambiguity as such. Hence Holden (1989) and Wagner and Van den haute (1992), later supported by Iwano and Danhara (1998) and Holden and Hoffman (2000), recommended the value of $(8.46 \pm 0.06) \times 10^{-17} a^{-1}$. An important argument for this recommendation is that the lower λ_f values were obtained using so-called U-detector methods, based on track counting, and thus vulnerable to systematic uncertainties related to this method. In contrast, the values clustering around 8.46 were obtained with direct and more precise radiochemical and nuclear-physical methods and thus the $(8.46 \pm 0.06) \times 10^{-17} a^{-1}$ value seems to be the most reliable.

Van den haute et al. (1988) dated apatite fission-track (AFT) age-standards based on precise thermal neutron fluence measurements with different certified metal activation fluence monitors (section1.7.1.2). Rewriting the fundamental FT age equation and substitution of the known AFT age of the age-standards yielded a λ_f-value of $8.5 \times 10^{-17}a^{-1}$, supporting the Galliker-value. However Carpéna and Mailhé (1987) performed age standard analyses in support of the lower Roberts et al. (1968) value. A discussion of λ_f-values based on track analyses is also given in Jonckheere et al. (1993) and Van den haute et al. (1998).

Guedes et al. (2000) repeated the Roberts et al. (1968) experiments, but used a different calibration technique based on natural U thin films (Bigazzi et al., 1990, 1995 and 1999; Guedes et al., 2002 and 2003; Hadler et al., 2003). Their experiments allowed them to calculate a λ_f-value of $(8.35 \pm 0.24) \times 10^{-17}a^{-1}$. This result is in agreement with Garwin (1985) who gives a value of $8.7 \times 10^{-17}a^{-1}$. It seems clear from this synopsis that for the use in the FT age equation the value of $(8.46 \pm 0.06) \times 10^{-17}a^{-1}$ for the ^{238}U fission decay-constant (λ_f) is appropriate. The absolutely calibrated AFT ages from Central Asian mountain belts presented in this study are based on this value. Mainly for the reason that alternative calibration techniques relying on age standards have been developed (e.g. the zeta-calibration) the λ_f-problem was circumvented and was hence relegated to the background. Recently however the debate of improving the decay constants of various isotopic systems for geo- and cosmochronological use has been resumed (Begemann et al., 2001), and it is fair to say that the FT method is not the only technique prone to controversy on this point.

1.5.2. The effective fission cross-section of ^{235}U

The value of the cross-section for thermal neutron induced fission of ^{235}U, is not really debated, yet several values are used, mostly due to outdated references or unawareness of upgraded values. However, these small variations of the σ-values have an almost negligible effect on FT age calculation. It is nonetheless important that the use of the most accurate figures is adopted in FT geochronology. Note that in literature it is σ_o, i.e. the conventional 2200m/s cross section for fission of ^{235}U (section 1.6 and section 3.2.1), that is reported. The most recent version of the Evaluated Nuclear Data Files (ENDF-B VI, 1990) cites an evaluated value of $\sigma_o = 584.25$ barn ($\pm$ 0.19%). This value is recommended by Holden and Holden (1989) and Holden (1999). The ^{235}U (n,f) reaction shows a somewhat discrepant behaviour: it deviates from a $\sigma(v) \sim 1/v$ relationship (v is the neutron velocity) at thermal neutron energies. Therefore a temperature dependent correction factor should be applied. This correction factor was calculated as $g(T) = 0.977$ at a temperature of 20°C (Green and Hurford, 1984; Wagemans et al., 1988). This leads to an advized cross-section value of $\sigma = 570.8$ barn for perfectly thermalized neutrons at 20°C (Wagner and Van den haute, 1992; Van den haute et al., 1998).

1.6. The thermal neutron fluence

The nuclear fuel in a nuclear reactor fissions and produces neutrons. The total neutron flux (φ_{tot}) (i.e. the number of neutrons crossing a unit area in a unit time) consists of three components: $\varphi_{tot} = \varphi_f + \varphi_{epi} + \varphi_{th}$; these are respectively, the flux of fast, epithermal and thermal neutrons (figure 1.9). The fast neutrons are high-energy neutrons (0.5 – 10 MeV) and are the direct products of the fission reaction. The moderator (graphite, heavy water or normal water) surrounding the reactor fuel, absorbs the energy of the high-energy, fast moving neutrons, slowing them down to an epithermal state. When the neutron energy is in a state of thermal equilibrium with the moderator, the neutrons reach a slow or thermal stage and are called thermal neutrons. They exhibit a Maxwell-Boltzmann energy distribution and have energies from 0 to 0.25 eV. The epithermal neutrons have energies between those of fast and thermal neutrons. Epithermal neutrons are also capable of inducing fission of ^{235}U. The cross-section of this reaction is called the *resonance integral* I_o and is 275 barn for ^{235}U. It is therefore of great importance that the irradiation channel is well thermalized. The γ-activity of irradiated metal activation monitors is also induced in part by non-thermal neutrons (section 1.7.1.2 and section 3.2.1). In this case it is imperative to be capable of calculating exactly what the contribution of the epithermal flux amounts to. Given the σ_o and I_o values and the monitors used, the ratio of $\varphi_{th}/\varphi_{epi}$ should be > 50 in order to have a negligible amount (< 1%) of FTs induced by fission events due to epithermal neutrons. If this ratio is known, it is easy to calculate and correct for its effect on the γ-activity of the monitors (section 1.7.1.2 and section 3.2.1).

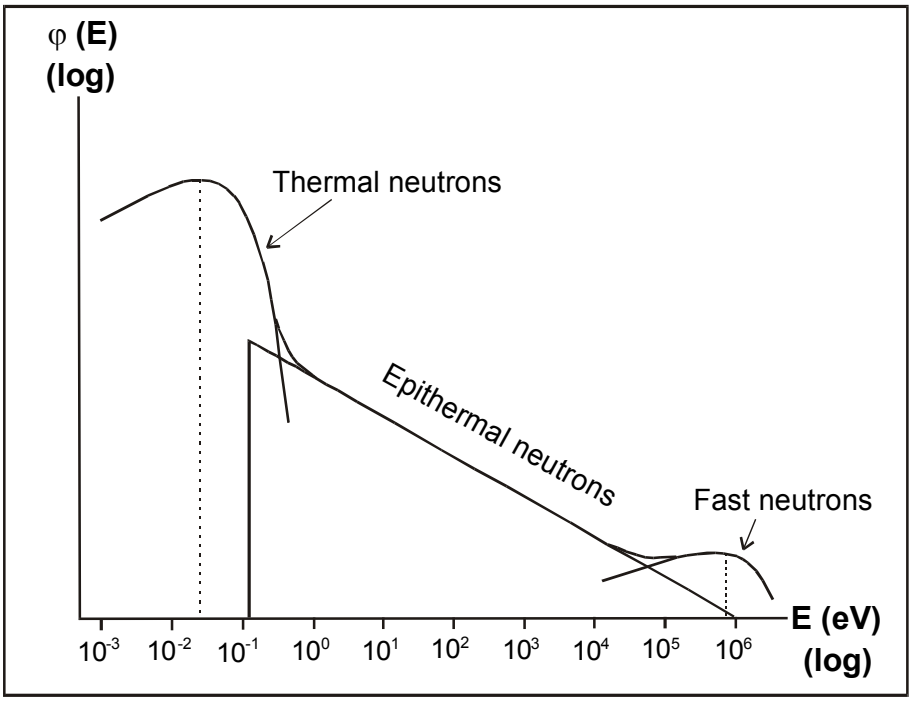

Figure 1.9: Thermal, epithermal and fast components of the neutron flux, φ (E) (in arbitrary units) in function of the neutron energy (E) (after Jonckheere, 1995; Bellemans, 1996).

Epithermal and fast neutrons are also capable of inducing ^{238}U and ^{232}Th fission, so the energy spectrum of the reactor neutrons should be well known. Moreover, the thermalization of the used irradiation channel should be guaranteed in order to determine an absolute FT age correctly (e.g. Hurford and Green, 1981a; Crowley, 1986; Tagami and Nishimura, 1989 and 1992). Care must be taken also with the sample irradiation geometry to minimize the effects of neutron flux gradients (e.g. Hurford and Gleadow, 1977; Wagner and Van den haute, 1992).

1.7. Calibration of the FT dating method

1.7.1. The absolute approach

The absolute approach relies on a direct and accurate determination of the thermal neutron fluence (ϕ_{th}) the apatite samples were exposed to during irradiation. The irradiation of the samples creates induced ^{235}U FTs that indirectly quantify the ^{238}U concentration in the sample. If we adopt a value for the ^{238}U fission decay-constant -e.g. the Galliker et al. (1970) value of $(8.46 \pm 0.06) \times 10^{-17} a^{-1}$ as used in this work- a FT age can readily be calculated. An absolute determination of ϕ_{th} can be obtained by co-irradiating fluence monitors with the samples. Different types of monitors can be used.

1.7.1.1. Uranium-fission monitors

One method for determining the thermal neutron fluence (ϕ_{th}), is to make use of uranium-fission monitors (Bigazzi et al., 1990; De Corte et al., 1995). However, the method is very laborious and therefore not used in FT dating. De Corte et al. (1995) have shown that ϕ_{th}-values obtained by using co-irradiated metal activation monitors agree with those obtained with U-fission monitors. The uranium-fission monitor calibration uses diluted Al-U-alloys, in analogy with metal activation monitors (e.g. Au-Al or Co-Al alloy; see next section). In fact, U-fission monitors can also be considered as a metal activation monitor. In the experiments by De Corte et al. (1995) the U-fission monitor was enriched in ^{235}U (93.22 atom%). During irradiation in the nuclear reactor, thermal neutrons induce the ^{235}U nuclei in the monitor to fission with a certain $^{235}U(n, f)$ reaction rate (R). It is this rate, R, that provides the most direct estimate for ϕ_{th}.

The induced fission of ^{235}U produces unstable isotopes (e.g. ^{88}Kr, ^{88}Rb, ^{134}I…) which emit γ-radiation during disintegration. Based on their fission yield and the energy and intensity of the characteristic γ-peaks, selected nuclides were analyzed with γ-spectrometry after irradiation. The detected characteristic γ-peak area of a selected fission nuclide with particular fission yield an estimate of the number of fissioned ^{235}U nuclei. This value then stands in direct relationship with ϕ_{th}. Of all investigated fission nuclides, ^{91m}Y, ^{95}Zr, ^{99}Mo, ^{140}Ba, ^{140}La and ^{142}La yielded the best results.

The uranium-fission rate (R) determined with metal-activation monitors (section 1.7.1.2), R_{metal}, and the value measured by γ-spectrometry of the fission products, R, were shown to be in excellent agreement. De Corte et al. (1995) obtained a ratio of $R/R_{metal} = 0.997 \pm 0.006$, showing that the much less laborious metal-activation monitor approach is also accurate and a more practical way to evaluate the thermal neutron fluence during irradiations.

1.7.1.2. Metal activation monitors

Another option in the absolute approach is to use *metal activation monitors*. These monitors, typically Au or Co (in the form of foil or wires), are activated during the irradiation and their γ-activity after irradiation is function of the neutron fluence they were exposed to. In the previous section it was mentioned that these monitors yield accurate fission rates and absolute fluences. The foils or wires are diluted Al-alloys to avoid shielding effects. This approach (and the former) requires a precise knowledge of the exact composition of the neutron flux in terms of thermal and epithermal neutrons and a well-calibrated measurement equipment. If all the necessary requirements are met, the absolute approach of calibrating ϕ_{th} by using these metal activation monitors is a powerful calibration method and leads to correct FT age determinations (Van den haute et al., 1988).

Only metal monitors for which the relevant nuclear parameters are precisely and accurately known can be used. In practice, only Au and Co (and to a lesser extent Mn) come into consideration. Additional advantages of the use of Co and/or Au is that both elements are mono-isotopic and their activated radio-isotopes disintegrate following simple decay schemes. Cu, which has been used in the past, does not meet the stringent requirements. Therefore it should no longer be utilized for absolute measurement of ϕ_{th} (Van den haute et al., 1988; De Corte et al., 1991). Cu is still used as a suitable monitor to determine relative fluence ratios; it is therefore useful for establishing the radial or longitudinal fluence gradient (Van den haute and Chambaudet, 1990; Wagner and Van den haute, 1992).

The neutron bombardment in the reactor will induce (n,γ) reactions in the abovementioned metals:

$^{197}Au\ (n,\gamma)\ ^{198}Au$ $\quad t_{1/2} = 2.696$ d $\quad E_\gamma = 411.8$ keV

$^{59}Co\ (n,\gamma)\ ^{60(m)}Co$ $\quad t_{1/2} = 5.271$ a $\quad E_\gamma = 1173.2$ and 1332.5 keV

Measurement of the γ-activity of the metal monitors by γ-spectroscopy gives a direct value of the thermal neutron fluence. Derivation of the relevant equations in this respect is discussed in detail in chapter 3.

In principle, single Au or Co monitoring is sufficient to accurately assess the thermal neutron fluence, but combined use of both metal monitors is recommended and provides a control on internal consistency of this method (Green and Hurford, 1984; Van den haute et al., 1988).

1.7.1.3. Uranium doped glass monitors

To reduce the complexity of the absolute approach, U-doped glass monitors were manufactured. A first set of glasses was produced by the former National Bureau of Standards (NBS) in the USA (now: NIST, National Institute of Standards and Technology). Four series of glass monitors (SRM961 to SRM964) with different U-contents (500, 50, 1 and 0.02 ppm U) were developed and a number of specimens were irradiated in the NBS reactor. The thermal neutron fluence was monitored with pure Au and Cu foils (Carpenter and Reimer, 1974). The irradiated glasses were distributed along with identical, non-irradiated specimens (SRM610-611, SRM612-613, SRM614-615 and SRM616-617 respectively; the two numbers refer to the thickness of the glass discs: the first numbers refer to discs of 3mm, the second to discs of 1 mm).

Co-irradiation of samples with non-irradiated glass monitors enables the calculation of the unknown ϕ_{th} when a comparison is made between the induced track density in the monitor (ρ_{UN}) and the induced track density in the pre-irradiated glass (ρ_{GL}) when both are etched under identical conditions:

$$\phi_{UN} = \frac{\phi_{GL}\rho_{UN}}{\rho_{GL}} \qquad 1.19$$

Counting of the induced tracks is done either in the glass itself (after etching) or in a muscovite external detector (after etching) in close contact with the glass during irradiation (the topic of external detectors will be discussed in section 1.8.2). Counting the tracks in an external detector has the advantage that the same glass mount can be used again in later irradiations.

The NBS-SRM glasses have several shortcomings: the calibration of the fluence with Au and Cu of the pre-irradiated glasses appears to be inconsistent, Cu has been found to be an unsuitable fluence monitor, the U is depleted in ^{235}U, the glasses contain significant concentrations of interfering Th isotopes and other elements (e.g. REE's). Consequently a new set of pre-irradiated SRM glasses (SRM962a and SRM963a) was manufactured as replacements for the original SRM962 and SRM963 (Carpenter, 1984). These sets nevertheless still posses several of the disadvantages of the earlier glasses.

Other glasses were distributed by the Corning Glassworks company: a first series, the U1-U7 glass monitor sets (Schreurs et al., 1971) which are no longer available and the CN1 (40 ppm U), CN2 (35 ppm U), CN5 (12 ppm U) and CN6 (1 ppm U) glasses. Other members of this glass monitor series, CN3 and CN4, are Th-doped. The CN glasses contain natural uranium, and proved of far more use to FT geochronology.

Critical studies of the SRM and/or CN glass monitors were made by Hurford and Green (1983), Green, (1985), Crowley (1986), Hurford (1990), Bellemans et al. (1995a), De Corte et al. (1995) and Hurford (1998).

In co-operation with the Institute of Reference Materials and Measurements (IRMM) of the European Commission, Ingelbrecht, De Corte and Van den haute developed a new certified U-doped glass monitor set (IRMM-540). Great care was taken to avoid the shortcomings of the older glass monitors (Bellemans et al., 1995b and De Corte et al., 1998). This glass was specifically made for use in FT dating, while the other glasses were originally conceived for other purposes. The IRMM-540 glass monitor has a homogeneously distributed certified (De Corte et al., 1998) U-content of 13.9 ± 0.5 ppm and a natural $^{235}U/^{238}U$ isotopic ratio of $(7.277 \pm 0.007) \times 10^{-3}$. The concentration of interfering elements such as Th and REE's are below the detection limit of the various analytical methods used. A set of IRMM-540 glasses consists of one pre-irradiated glass disc, the mica external detector (which was attached to the pre-irradiated disc) and two non-irradiated glass discs. The thermal neutron flux to which the pre-irradiated IRMM-540 glasses were exposed also has a certified value of $(1.070 \pm 0.011) \times 10^{17}$ cm^{-2} (De Corte et al., 1998).

The IRMM-540 glass is now out of stock, but work on successors for this neutron fluence monitor is far advanced. Two new reference glasses specifically for FT dating, are underway. They will have nominal U-contents of 15 ppm (IRMM-540R) and 55 ppm (IRMM-541), while for both the natural uranium isotopic ratio shall be observed. Sets will be similar to IRMM-540 sets, containing three glass discs (one pre-irradiated) and a mica external detector (Derbyshire et al., 2001).

1.7.2. The age standard approach: the zeta-method

1.7.2.1. Principles of the approach

Because of the controversy over the ^{238}U fission decay-constant (Bigazzi, 1981), the difficulty of accurate thermal neutron fluence determinations (Green and Hurford, 1984) and the possible interdependence of the two, a calibration based on analysis of FT age standards was promoted and elaborated by Hurford and Green (1981a), (1981b), (1982), and (1983) based on the principle proposed by Fleischer and Hart (1972).

If a mineral sample of unknown age (t_u) and a FT age standard sample of known age (t_S) are co-irradiated, both will be exposed to the same thermal neutron fluence, if we neglect a possible fluence gradient. The age equations for the sample and the age standard are respectively given by:

$$t_u = \lambda_\alpha^{-1} \ln[(\lambda_\alpha/\lambda_f)(\rho_s/\rho_i)_u QGI\sigma\phi_{th} + 1] \qquad 1.20$$

and

$$t_S = \lambda_\alpha^{-1} \ln[(\lambda_\alpha/\lambda_f)(\rho_s/\rho_i)_S QGI\sigma\phi_{th} + 1] \qquad 1.21$$

If we treat the sample and the standard under the same etching and observation conditions, a factor *Z* for the specific irradiation (specific ϕ_{th}) can be defined as:

$$Z = QI\sigma\phi_{th}/\lambda_f, \quad 1.22$$

It should be noted here that in equation (1.22) the Q-factor is also included, which was not the case in the original derivation of these equations by Hurford and Green (1983).

Equations (1.20) and (1.21) can now be rewritten as:

$$t_u = \lambda_\alpha^{-1}\ln[\lambda_\alpha(\rho_s/\rho_i)_u GZ + 1] \quad 1.23$$

and

$$t_S = \lambda_\alpha^{-1}\ln[\lambda_\alpha(\rho_s/\rho_i)_S GZ + 1] \quad 1.24$$

or:

$$Z = \frac{e^{\lambda_\alpha t_S} - 1}{\lambda_\alpha(\rho_s/\rho_i)_S G} \quad 1.25$$

Substitution of equation (1.25) in (1.23) gives t_u, without the need to know the λ_f and σ values and without having to calculate ϕ_{th}. The Z-parameter has a dimension of time (a). Z is dependent on the neutron fluence and cannot be used for other irradiations. Furthermore, as is shown from incorporation of the Q-factor in the expression for Z, the Z-parameter depends on the etching and observation conditions. Thus, Z-values obtained by one researcher cannot be adopted by others.

A more elaborate but practical alternative is provided by the zeta- or ζ-method (Hurford and Green, 1981a, 1981b, 1982 and 1983). It relies on age standard analyses as well, but also on the co-irradiation of U-doped glass monitors (SRM, U, CN or IRMM glasses; section 1.7.1.3). In this way a calibration factor, the ζ-*factor*, can be determined, which is independent of the irradiation.

FT age standards of a certain mineral (e.g. apatite) are irradiated together with a specific glass monitor. This produces fission tracks that can be etched and counted in the glass itself or in an external detector attached to the glass monitor during the irradiation. This induced track density (ρ_d) is proportional to the thermal neutron fluence, or $\phi_{th} = B\rho_d$, in which B is a proportionality constant, expressed in neutrons per track. The B-factor depends on the type of glass dosimeter, especially on the U-content, and on etching and observation conditions used by the individual researcher. The age equation for the age standard co-irradiated with the glass can be written as:

$$t_S = \lambda_\alpha^{-1}\ln[(\lambda_\alpha/\lambda_f)(\rho_s/\rho_i)_S QGI\sigma\, B(\rho_d)_S + 1] \quad 1.26$$

In the same manner as was done for the Z-factor, we now define a calibration factor, the ζ-factor:

$$\zeta = QI\sigma B/\lambda_f, \quad 1.27$$

resulting in:

$$t_S = \lambda_\alpha^{-1}\ln[\lambda_\alpha(\rho_s/\rho_i)_S G\zeta(\rho_d)_S + 1] \quad 1.28$$

or,

$$\zeta = \frac{e^{\lambda_\alpha t_S} - 1}{\lambda_\alpha(\rho_s/\rho_i)_S G(\rho_d)_S} \quad 1.29$$

The ζ calibration factor is expressed in (a cm^2) and includes the debatable parameters Q, σ, B and λ_f. It is therefore a calibration factor, only to be used by an individual FT researcher. The B-factor also implies that ζ is variable according to the U-concentration of the glass dosimeter used. Other implications of the fact that the Q-factor is embedded in the ζ-equation is that the ζ-value also depends on the mineral under investigation. In short, ζ-values vary with researcher, experimental set-up and conditions, mineral and glass dosimeter (Green, 1985; Tagami, 1987; Shin and Nishimura, 1991).

Also for different age standards of the same mineral slight variations in the ζ-values have been observed (Green, 1985), possibly due to different etching properties linked to compositional variation. A weighted average ζ-factor determined for a specific age standard is called a *sample weighted mean zeta* or *SWMZ*. When SWMZ-values acquired for different age standards (using the same glass dosimeter and under the same general conditions) are averaged, an *overall weighted mean zeta* or *OWMZ* is obtained (Hurford and Green, 1983). When ζ calibration factors are reported, generally they refer to an OWMZ-value, since accurate calibration involves several experiments, preferably with as many age standards as are available for a given mineral.

The FT age of an unknown sample is determined after co-irradiation with the same type of glass dosimeter from the following equation:

$$t_u = \lambda_\alpha^{-1}\ln[\lambda_\alpha(\rho_s/\rho_i)_u G\zeta(\rho_d)_u + 1] \quad 1.30$$

In this equation $(\rho_d)_u$ represents the induced track density for the glass dosimeter co-irradiated with the sample. This irradiation can be a different irradiation from the one(s) of the age standards from which the ζ-value was calculated. It can also be an interpolated value, calculated from several glasses in an irradiation package.

FT dating using the ζ-calibration method in combination with the external detector procedure (section 1.8.2) yields results that are comparable and reproduceable on an interlaboratory scale. It helped to re-establish the FT method from the stalemate it had reached due to the λ_f and ϕ_{th} problems, and it brought the method to where it is today, having a broad variety of applications in geoscience. But it should be noted that relying on age standard calibration implies calibration with other isotopic systems, making the FT method dependent on these other dating methods. One should also be aware that the "FT formation age" of apatite for example, even for carefully chosen standards is not in fact the true formation age as determined with these other isotopic systems. Moreover, the ζ-factor must be considered as a preliminary calibration system that acts as a kind of dustbin-factor incorporating all poorly known or understood parameters and concepts. Deconvolution of the ζ-factor, lifting out constants when they can be agreed upon and leaving a factor that may only depend on procedural aspects, should be aimed for (Wagner and Van den haute, 1992; Hurford, 1998). It is a secondary aim of this work to show that AFT dating can be carried out using the procedure factor (Q), entailing absolute ϕ_{th}-measurements, in combination with the external detector method and that these results obtained with the ζ-approach.

1.7.2.2. Apatite age standards

In the ζ-approach, the FT age of the unknown sample is determined relative to the reference age of age standards. So it is of considerable importance that in order to be considered as an age standard, a mineral sample must fulfill some essential requirements which can be summarized as follows (G.A. Wagner in Hurford and Green, 1981): (1) the rock formation containing the standard should be geologically well documented, (2) the mineral should be homogeneous in FT age (only crystals from one age population and none derived from older rock), (3) the age of the sample should be known unambiguously from stratigraphy as well as from independent isotopic dating, (4) this independent isotopic age should consistently refer to the formation of the mineral and not to some posterior event, (5) no correction for track fading should be necessary. Furthermore we can state an additional criterium: (6) spontaneous track density should not be too high or too low, and no U-heterogeneity should be present.

Age standards are only available for a limited amount of minerals. For apatite two standards are recognized by the Fission Track Working Group of the IUGS Subcommission on Geochronology (Hurford, 1990a and 1990b). The first one is apatite from the *Fish Canyon Tuff*, an Oligocene volcanic tuff from Colorado, USA (Hurford and Gleadow, 1977; Naeser et al, 1981; Hurford and Green, 1983; Green, 1985; Carpéna and Mailhé, 1987; Wagner and Van den haute, 1992; Hurford; 1998). Its age has been determined by $^{40}Ar/^{39}Ar$ (biotite) dating (Hurford and Hammerschmidt, 1985) as 27.9 ± 0.5 Ma. It was successfully studied in interlaboratory comparisons (Naeser et al., 1981; Miller et al., 1985) and it was used as an apatite age standard since the introduction and during the subsequent further development of the ζ-calibration method (e.g. Hurford and Green, 1983; Green, 1985).

The second is *Durango* apatite from the Durango martite (hematite variety) ore body in the Tertiary Carpintero volcanic group, Cerro de Mercado, Mexico (Young et al., 1969; Naeser and Fleischer, 1975; Hurford and Gleadow, 1977; Green, 1985; Wagner and Van den haute, 1992; Jonckheere et al., 1993; Hurford, 1998). A K-Ar study of the Carpintero group yielded an age of 31.4 ± 0.5 Ma (McDowell and Keizer, 1977, recalculated by Green, 1985). In contrast to the Fish Canyon, Durango apatite is available as large (cm-scale), gem-quality euhedral crystals.

A third apatite, the *Mount Dromedary* apatite from the Cretaceous Mount Dromedary quartz monzonite (banatite) intrusive complex, New South Wales, Australia (Green, 1985; Miller et al., 1985; Hurford, 1990a and 1990b; Shin and Nishimura, 1991; Wagner and Van den haute, 1992) is also sometimes used as a putative age standard, although it is not accepted as such (Jonckheere et al., 2000). Its reference age is 98.8 ± 0.6 Ma, obtained from biotite Rb-Sr analysis (Williams et al., 1982).

Analyses are being carried out on apatite from a phonolitic tuff from the *Kaiserstuhl* alkaline volcanic complex, near Freiburg, Germany to evaluate if this apatite is suitable as a standard. The $^{40}Ar/^{39}Ar$ age of the tuff is 16.2 ± 0.4 Ma corresponding well with the first FT ages and even (U/Th)-He ages obtained from this material (Kraml et al., 1996; Link et al., 2003 and Meinert Rahn, pers. comm.).

1.8. Dating procedures and techniques

For an exhaustive overview the reader is referred to Fleischer et al. (1975), Gleadow (1981), Hurford and Green (1982) and Wagner and Van den haute (1992).

The distinction between the various procedures is largely based on how the induced track density is determined. When induced track etching and/or observation characteristics differ from those of the spontaneous tracks, the procedure factor $Q \neq 1$ (section 1.4). These dating FT procedures are efficiently used in age standard calibration approaches. Procedures for which can be assumed that $Q \approx 1$, the absolute approach can be followed. The existing procedures can be subdivided in two categories: *multi-grain methods*, where track densities are averaged over a large number (population) of grains on the one hand and *single-grain methods*, where a track density ratio and thus an age can be determined for each individual grain separately on the other hand. An example of the latter procedure is the so-called external detector method that was used for the dating of the apatites from Central Asia and Siberia in this work. This procedure is therefore discussed in greater detail.

1.8.1. Multi-grain methods

In multi-grain or grain-population methods (Naeser, 1967; Wagner, 1968), the sample is split into two aliquots, one serving for the measurement of spontaneous track density (ρ_s), the other for that of the induced track density (ρ_i). Two methods can traditionally be classified in this section. The first is the *subtraction method* where the induced track aliquot is irradiated and etched. Counting of a statistically representative population from this aliquot gives a total track density of $\rho_s + \rho_i$. The aliquot for spontaneous tracks gives the ρ_s-value. Subtraction gives ρ_i. But by far the most important multi-grain procedure is the *population method s.s.*, where the aliquot for ρ_i-analysis is heated for a certain time before irradiation. This heating anneals the existing latent spontaneous tracks. Etching after irradiation hence only reveals the induced tracks. In this way ρ_s and ρ_i are measured directly, but in two different aliquots. For both these methods it can be assumed that $Q \approx 1$, at least if annealing of the samples in the population method does not influence the etching properties (which is usually not the case for apatite). The geometry ratio in this case is, $G = g_i/g_s = 1/1 = 1$.

1.8.2. Single-grain methods

As mentioned, in single-grain methods a ρ_s/ρ_i ratio is determined for each grain individually. This is of great value if samples contain grains with a great U-heterogeneity, if a sample contains grains of different age (common in detrital rocks) or if there simply is not enough material available.

A first example of this class of methods is the *re-etch method.* In this method the spontaneous tracks are etched before irradiation of the sample. The induced tracks are revealed during re-etching of the same sample after irradiation. Distinction (which is not always possible) between both types of tracks is made on the basis of their size, with the spontaneous tracks having a larger size due to the second etching step.

A second example is the *repolish method*. In this method the spontaneous tracks are etched and the spontaneous FT density is determined. Subsequently the sample is repolished to remove the layer of etched and counted spontaneous tracks. After irradiation and etching, the sample is counted again. This time the determined FT density will be the result of both the spontaneous and the induced tracks. Subtraction of the spontaneous FT density established prior to irradiation finally yields the induced FT density.

The *external detector method* (Price and Walker, 1963) is the most widely used dating method in FT geochronology at present. It is used succesfully in combination with the ζ-calibration technique. The induced tracks are registered, revealed and counted in an external detector (ED), while the spontaneous tracks are counted in a polished and etched internal surface of the mineral. During irradiation, the ED is placed in close contact with the mineral surface containing the spontaneous tracks (figure 1.10). The ED must be free of U so that the tracks in the ED originated in the sample. The tracks in the ED originate from ^{235}U nuclides at a depth $< R_i$ under the mineral surface (R_i is the

range of single induced fission fragment). Sometimes plastic foils (Lexan, Makrofol, Kapton) are used as ED, but in most geological applications low U muscovite mica is used. Mica, being a mineral, and thus an anisotropic detector in contrast to the polymere detectors, is preferred because track registration characteristics are more similar to the investigated mineral samples (Gleadow, 1981). On the other hand it should be stated that handling, preparation, attaching and storage of plasic foils is a lot easier. An example of etched FTs in muscovite mica is shown in figure 1.11.

The apatite/ED configuration necessitates a geometry correction: $g_s = 1$ (4π-geometry) and $g_i = 0.5$ (2π-geometry) and hence $G = g_i/g_s = 0.5$ (Gleadow and Lovering, 1977; equation 1.16). It is also clear that in the ED method $Q \neq 1$. Because many parameters characteristic for the dated mineral differ considerably from those of the ED. Comprehensive discussions on this matter have been provided by Iwano et al (1992) and (1993), Jonckheere (1995), Iwano and Danhara (1998), Jonckheere and Van den haute (1998), (1999) and (2002). We will discuss our determination of the Q-factor in section 3.5.

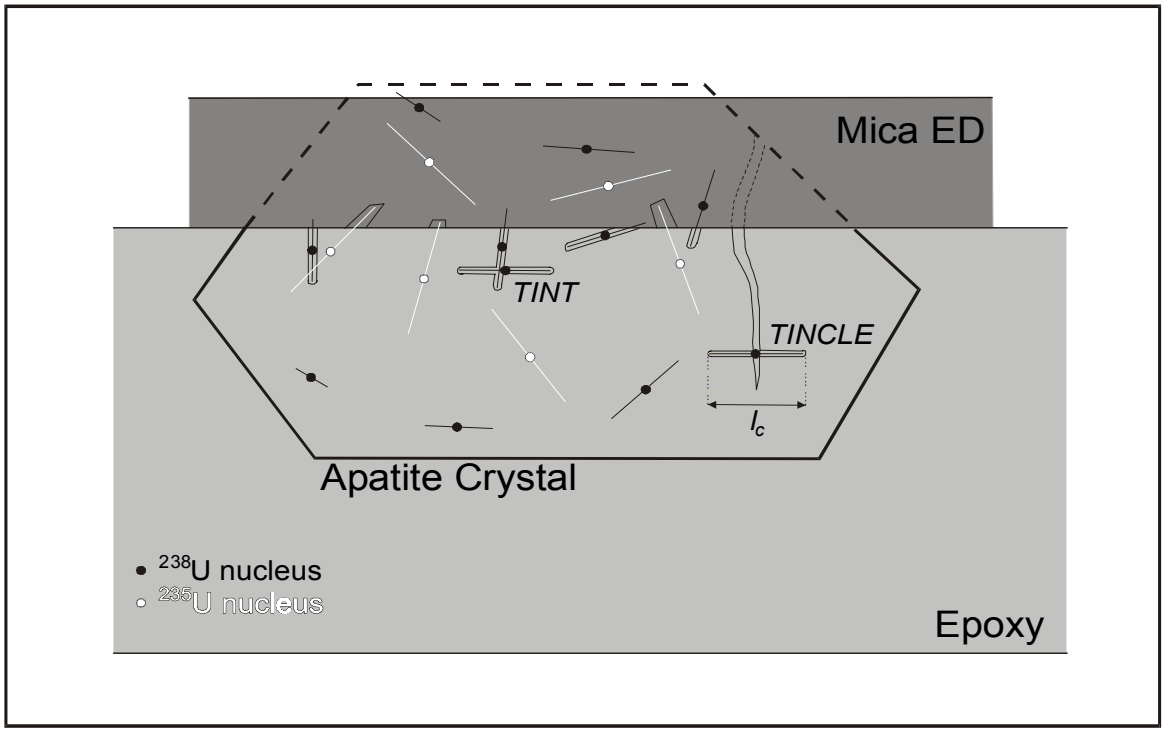

Figure 1.10: Scheme of a sample mount prepared for the external detector (ED) method. The apatite is fixed in epoxy and an internal surface is polished and etched. In this way the spontaneous tracks from ^{238}U fission intersecting this surface are revealed in the crystal. Afterwards an ED (in most cases muscovite mica) is attached. The mount is irradiated with thermal neutrons that induce fission of ^{235}U. Etching of the ED reveals the induced tracks intersecting the ED surface.

A Q-factor specific for the apatite/muscovite pair for an individual researcher using a certain experimental set-up can be calculated. In this way a personal calibration factor -in some analogy with the ζ-factor- can be assigned. If the Galliker-value ($\lambda_f = 8.46 \times 10^{-17} a^{-1}$) for the ^{238}U fission decay-constant is adopted, the ED method can effectively be used in combination with the absolute

calibration approach. In this study, AFT ages with ED will both be reported as traditional ζ-ages as recommended by Hurford (1990a and 1990b) and also as absolute Q-ages.

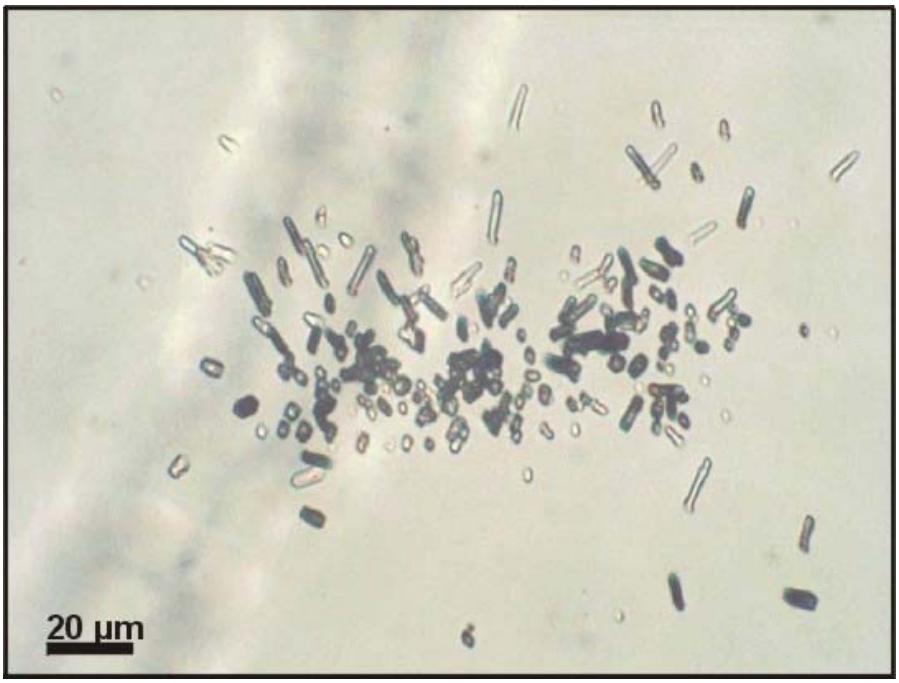

Figure 1.11: Fission tracks in a muscovite ED after etching in 40% HF for 30 minutes at 25°C.

CHAPTER 2

THERMAL STABILITY OF FISSION TRACKS AND GEOLOGICAL INTERPRETATION OF AFT ANALYSES

2.1. Fading of fission tracks: generalities

The radiation damage along a fission track constitutes a metastable state of the solid that, given time and external factors, will be restored. This process is called *fading* of fission tracks and results in the reduction of the etchable length of the fission track. Segmentation of the track, resulting in *unetchable gaps* (Dartyge et al., 1981; Paul, 1993; Hejl, 1995) precedes the ultimate stage of disappearance of the track (Green et al., 1986). The existence of these unetchable gaps may be an indication of the validity of the so-called Orsay model (Dartyge et al., 1981) of fission tracks with extended and point defects.

Because of the linear relationship between the etchable track length or etchable range and the areal density of fission tracks in minerals, fading of fission tracks causes reduction of the track density (figure 2.1) and as a consequence the apparent FT age is lowered and a sample is dated too young (Green, 1988). This 1:1 relationship is at least true for limited degrees of annealing ($l/l_o = \rho/\rho_o = 1.0$ to 0.65). Temperature is a major controlling factor in the fading process (e.g. Gleadow et al., 1983). In order to evaluate the thermal effect, FT lengths in an apatite sample are measured and a length distribution of confined FTs is constructed (e.g. Gleadow et al., 1986a). This distribution together with the FT age itself, represents a powerful research tool in thermochronology where temperature-time- or T-t-conditions of rocks are reconstructed. Especially the fact that apatite is sensitive to low temperatures (below ~150°C to even room temperature) has made AFT analysis (AFTA) an important instrument for investigating denudation histories of mountain belts or burial histories of sedimentary basins for example. This application of the FT method has been the main reason for its success in the last decade and will be discussed in this chapter.

The external factors that influence FT fading are hydrostatic rock pressure (Wendt et al., 2002), shock wave pressure, plastic deformation, ionizing radiation, but most of all it is temperature. Combining the effects of both temperature and time on FT fading, one speaks of *annealing* of fission tracks. FT annealing was already recognized shortly after the development of the FT method (Fleischer et al., 1965). In order to better understand FT annealing, numerous isochronal (when the annealing time is kept constant and experiments at different temperature are conducted) and

isothermal (when the temperature is kept constant and experiments are run at different annealing times) experimental studies have been carried out in the past, and different annealing models were proposed by different authors. Some of the most widely used models will be described in more detail in section 2.5.

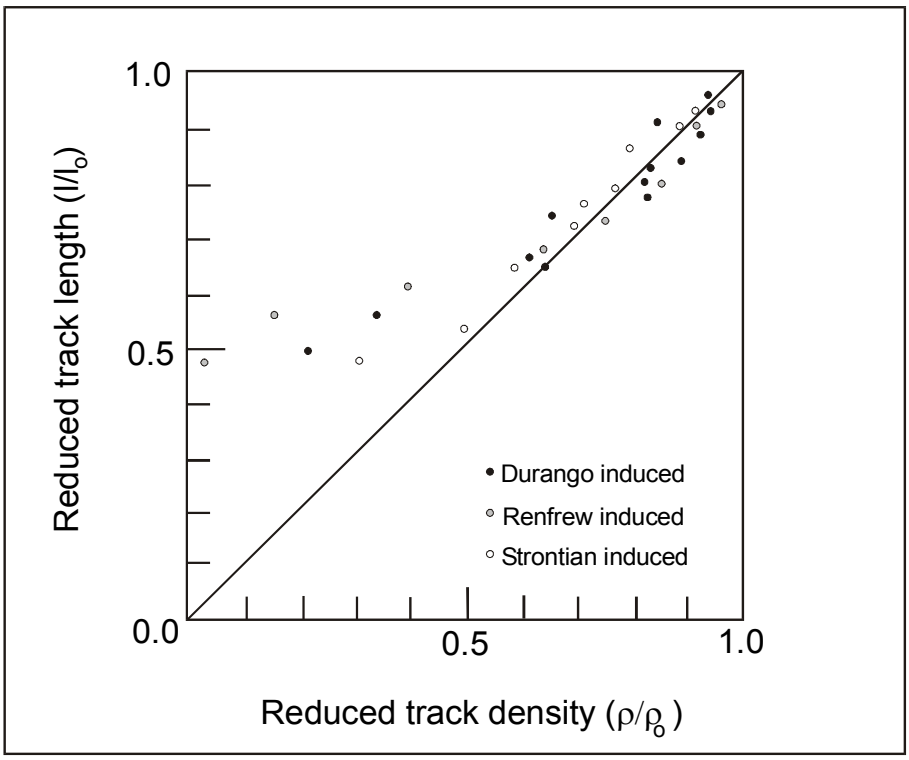

Figure 2.1: Linear relationship between track length reduction and track density reduction for induced tracks from several apatites (after Green, 1988).

It is generally thought that diffusional processes contribute to the restoration of the crystal damage and thus to the fading of fission tracks. Given time, this diffusion may cause the tracks to fade even at ambient temperatures. The diffusion rates increase greatly at elevated temperatures because the added thermal energy to the system exceeds the activation energy for the diffusion of the lattice atoms which can then leave their trap sites and move to regular lattice positions.

Since the fission fragments cause the most extensive damage in the central part of the fission track in the crystal lattice, the density of defects decreases towards the track ends. When annealing reduces the defect density, an increasing portion of the damaged channel becomes unetchable. The critical etching threshold is first reached at the track ends and thus annealing results in a progressive shortening of the fission tracks from both ends (Green et al., 1986).

2.2. Annealing kinetics, laboratory experiments and the diffusion law

The degree of annealing is often expressed as a reduction of FT length (l) or FT density (ρ) with respect to the original values l_o and ρ_o before annealing. In other words, the length ($r = l/l_o$) or density reduction ($r = \rho/\rho_o$) is a measure of the degree of annealing of the fission tracks. When there is no annealing ($l = l_o$ and $\rho = \rho_o$) the retention of the fission tracks is 100% or r = 1. When annealing progresses, tracks disappear and the retention decreases to a point when annealing is complete or 0% of the tracks are retained, in that case the retention, r = 0. In early FT annealing studies, the ρ-parameter was used to describe the retention of tracks, while in later work l was preferred because the $r = l/l_o$ approach is faster and more precise than the $r = \rho/\rho_o$ approach. Moreover, the length reduction is thought to be a direct response to annealing, while density reduction is a secondary response related to the length reduction.

As outlined, laboratory experiments have been carried out keeping either the annealing temperature (T) constant, i.e. *isothermal* annealing experiments, or the annealing time (Δt) constant, i.e. *isochronal* annealing experiments. The results of both isochronal and isothermal experiments are presented in *Arrhenius diagrams* with a logarithmic time axis and a reciprocal absolute temperature axis ($\log\Delta t$ vs. T^{-1} or vs. 10^3T^{-1}) (see figure 2.2 for an example). Because of a linear relationship between these annealing parameters lines of equal annealing or retention degrees are straight in an Arrhenius diagram (figure 2.2). This linear relationship has been proven on an empirical basis.

In early studies, FT annealing was simply considered as a diffusion process with first order kinetics. Based on this assumption the linear relationship in the Arrhenius diagrams was demonstrated (e.g. Märk et al., 1973).

In general, the first order reaction rate can be written as:

$$dn/dt = -\alpha n \qquad 2.1$$

where n denotes the concentration, in this case of the displaced atoms in the apatite lattice. The proportionality constant, α is temperature-dependent according to:

$$\alpha = \alpha_o e^{\frac{-E_a}{kT}} \qquad 2.2$$

in which α_o was regarded as a material specific resonance frequency, E_a as the activation energy for the diffusional process; T is the absolute temperature (in Kelvin), and k is Boltzmann's constant (= 8.616×10^{-5} eV/K).

Integration of equation 2.1 (at constant T, i.e. isothermal annealing) yields:

$$n = n_o e^{-\alpha t} \qquad 2.3$$

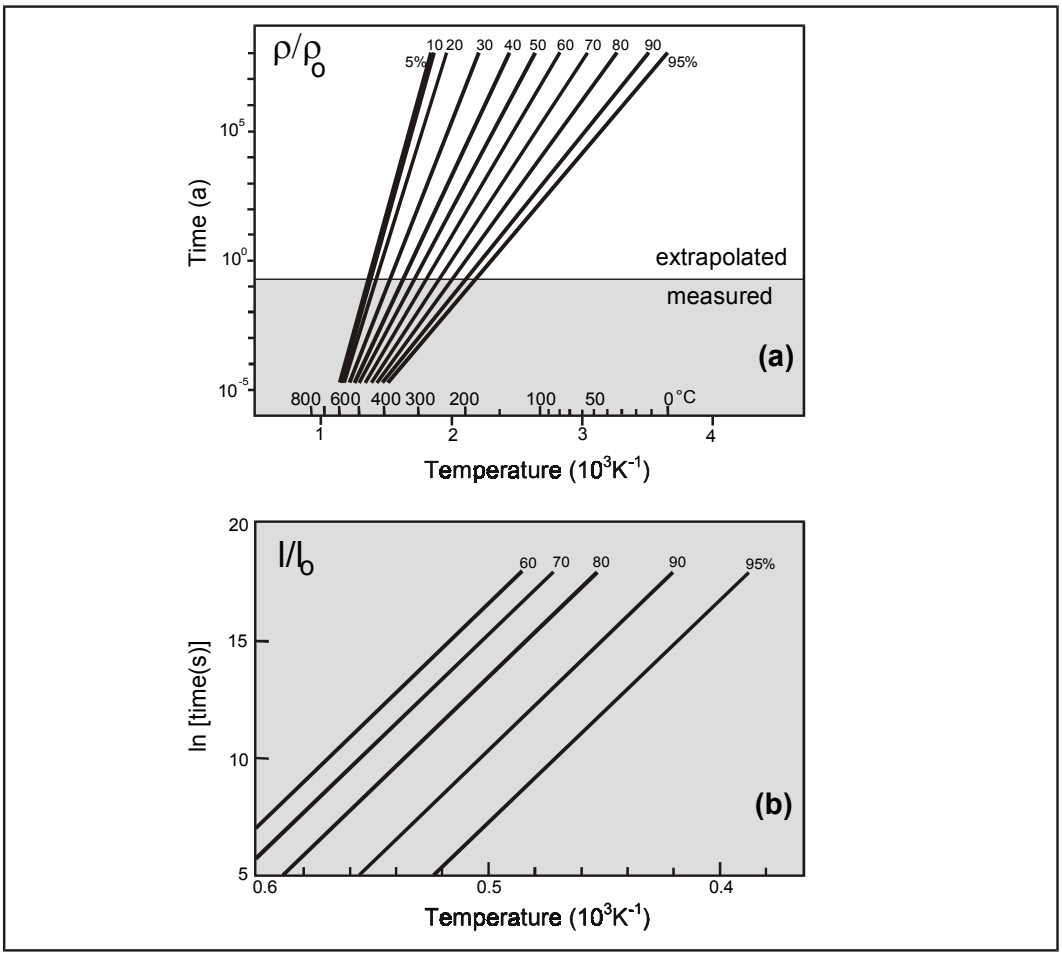

Figure 2.2: Example of Arrhenius plots obtained for laboratory annealing experiments (shaded area in a en b) with extrapolation to geological time scales (a). (a) Divergent Arrhenius plot on the basis of the ρ/ρ_o annealing parameter (see text for elaboration; after Wagner and Reimer, 1972). (b) Parallel Arrhenius plot on the basis of the l/l_o annealing parameter (after Green et al., 1985).

Where n_o can be considered the concentration of displaced apatite atoms before the onset of annealing. Combining equations 2.2 and 2.3 gives

$$n = n_o e^{-\alpha_o e^{\frac{-E_a}{kT}} t} \qquad 2.4$$

or

$$\ln t = \frac{E_a}{kT} + \ln\left[-\ln\left(\frac{n}{n_o}\right)\right] - \ln\alpha_o \qquad 2.5$$

In this equation the linear relationship between lnt and T^{-1} is obvious. In the case of FT density reduction we can propose an analogous relationship as in equation 2.3 to describe the annealing process by writing:

$$\rho/\rho_o = e^{-\alpha t} \qquad 2.6$$

and

$$\ln t = \frac{E_a}{kT} + \ln\left[-\ln\left(\frac{\rho}{\rho_o}\right)\right] - \ln\alpha_o \qquad 2.7$$

When considering the l/l_o retention parameter, equations 2.6 and 2.7 become:

$$l/l_o = e^{-\alpha t} \qquad 2.8$$

and:

$$\ln t = \frac{E_a}{kT} + \ln\left[-\ln\left(\frac{l}{l_o}\right)\right] - \ln\alpha_o \qquad 2.9$$

Describing FT annealing by first order kinetics was attempted in the early stages of the development of the FT method, mainly by Austrian FT scientists (e.g. Märk et al., 1973). In these early studies there existed some debate on the activation energy (E_a) for these diffusional processes. If it was regarded as a constant (e.g. by Märk et al., 1973) lines of equal FT retention would be represented by parallel straight lines in the Arrheniusdiagrams. Wagner and Reimer (1972) on the other hand considered that E_a would increase with increasing degrees of annealing, resulting in a fanning array of the lines of equal FT retention in an Arrheniusdiagram.

The early simple exponential diffusion law for FT annealing (equation 2.6) proved inadequate to describe the laboratory annealing data to their disposal. The Austrian research group (Bertel and Märk, 1983) generalized their model through a summation of a series of exponentials as described by:

$$\rho(t) = \sum_{j=1}^{n} \rho_j e^{-\alpha_j t} \qquad 2.10$$

This multi-exponential model fitted their data (obtained on Durango apatite) better than the simple exponential law. For apatites from the Armorican Massif (France) Chaillou et al. (1981) obtained a comparable equation.

However, in modern literature the physical model of first order kinetics on which these early assumptions were based is considered incorrect and too simplistic to describe the complex process of track annealing. Nowadays FT annealing is approached on an empirical basis and no physical meaning is attached to the parameters governing the empirical annealing equations.

2.3. Extrapolation to geological timescales and compositional effects

The linear relationship expressed by equations 2.5, 2.7 or 2.9 makes it in principle easy to extrapolate the results of the laboratory experiments to geological timescales. It is sufficient to simply extend the straight retention lines in the Arrhenius diagram to these geological timscales which are several orders of magnitude longer than the annealing times applied in the laboratory. In doing so it is assumed that the annealing is the same as in the laboratory. We also need to know exactly if fanning occurs in the Arrhenius diagram, and if so, to what extent.

The question of parallel or fanning Arrhenius plots was investigated thoroughly by Green et al. (1985). These authors use the l/l_o ratio, which, as mentioned earlier, is more precise compared to the ρ/ρ_o ratio used in the earlier studies. Another reason in favour of the length reduction parameter is that it represents a more fundamental parameter in the annealing process as it is this length reduction that causes the track density reduction. Green et al. (1985) come to the conclusion that, when annealing experiments are carried out on pure, single crystal apatites (e.g. Durango apatite), the parallel or near parallel Arrhenius plot is attained (figure 2.2). When these experiments are done using several different grains of apatite the plots may show slight or more marked fanning. Green et al. (1985) attribute this to an artifact caused by superposition of several narrow Arrhenius plots each with an individual activation energy. These different plots and activation energies represent a range of different chemical compositions of the apatite. This observation triggered more extensive research on the effects of apatite chemical composition on FT annealing.

It was then clear that the chemical composition of the apatite had a significant influence on the annealing characteristics of the apatite in question. As was outlined in chapter 1, the general crystal chemical formula of apatite is $Ca_5(PO_4)_3(OH,F,Cl)$. Depending on the single valence cation in the apatite structure we have hydroxy apatite (OH^-), fluorapatite (F^-) or chlorine apatite (Cl^-). The first variety is rare in nature. Fluorapatite is by far the most common type of apatite (Deer et al., 1962; McConnel, 1973). The widely used standard Durango apatite has a Cl/(Cl+F) ratio of ~ 0.12 for example (Young et al., 1969; Carlson et al., 1999). Chlorine apatites also exist as rock-forming minerals, but commonly these apatites will be members of a solid solution series having a specific Cl/F or Cl/(Cl +F) ratio. It was noticed by Green et al. (1985) that apatite FT ages of chlorine-rich volcano-sedimentary apatites from the Otway Basin in Australia approximate the actual depositional age the closest (figure 2.3), leading to the conclusion that chlorine apatites are more resistant to annealing than fluorapatites. This fact is corroborated by laboratory investigations. A supplementary factor having an influence on track annealing, is that the annealing process itself is anisotropic (Green et al., 1986 and 1988; Donelick, 1991). The latter effect is discussed later (section 2.5.8.2).

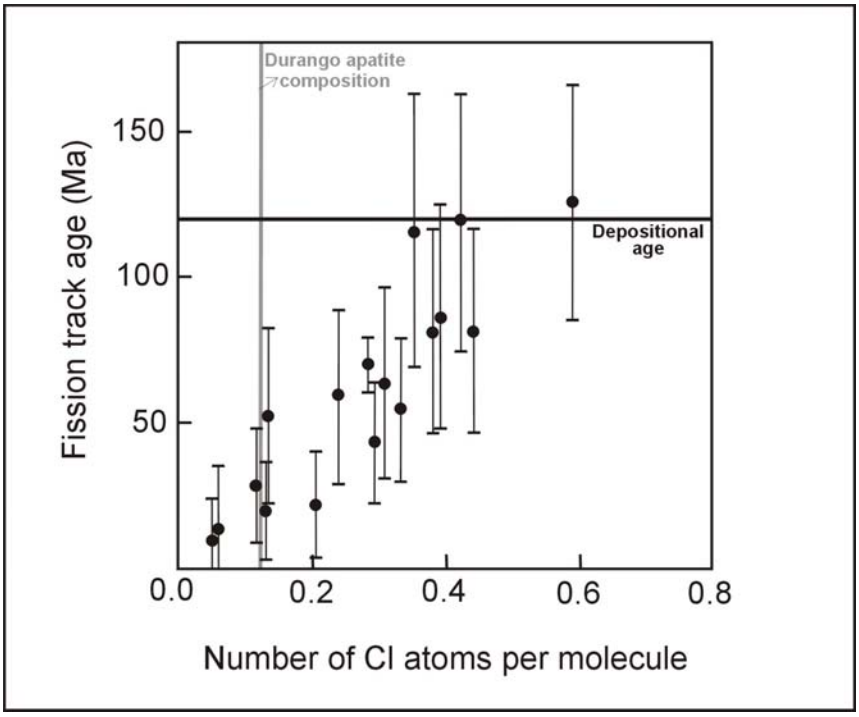

Figure 2.3: Relationship of apatite composition (Cl contents) on the annealing characteristics and hence apparent fission track age of apatite samples from the Otway basin (Australia). The depositional age of the apatites is shown in black, the composition of Durango apatite is indicated in grey as a reference (after Green et al., 1986).

2.4. Fission track annealing in the geological environment: borehole studies

Extrapolating results from laboratory FT annealing studies to geological timescales seems straightforward considering the linear character of the lines of equal FT retention in the Arrhenius diagrams. However it is of major importance to study the annealing behaviour of apatite in real geological conditions. Apatite samples from deep drill hole cores are an ideal subject for this purpose. Temperature increases with depth within the earth's crust. The average geothermal gradient amounts to about 25 to 30°C/km. So samples from deeper down the drill hole should show greater degrees of in-situ FT annealing and exhibit shorter mean track lenghts and hence lower track densities. The apparent apatite FT age is expected to decrease farther down the drill hole. Naeser and Forbes (1976) and Naeser (1979 and 1981) were the first researchers to test and confirm these hypotheses investigating samples from boreholes in the United States (Eielson, Alaska; Tejon oil field, California; Los Alamos borehole, New Mexico and Coso, California). Gleadow and Duddy (1981) and Gleadow et al. (1983) soon followed with their research on AFT annealing in volcanoclastic sandstones from deep drill holes in the Otway basin in Southern Victoria, Australia. These researchers showed that apparent AFT ages clearly start decreasing at around 60°C until about 125°C when a zero-FT age is reached. The mean confined FT lengths also gradually decreases with rising temperature down the boreholes. Moreover all borehole studies confirmed in principle the validity of the extrapolation of laboratory data to geological environments and timescales. In particular, borehole studies confirmed that annealing in the geological environment takes place in the

temperature range predicted from extrapolation of the laboratory models (Naeser, 1981; Gleadow and Duddy, 1981). As a consequence the divergence of the original annealing fans in the Arrhenius diagrams was corrected and reduced. The early borehole studies were corroborated by an extensive study of the 4 km deep KTB (Kontinentale Tiefbohrung der Bundesrepublik Deutschland) drill hole in the Variscan basement of the Bohemian Massif in Germany (Coyle et al., 1997). AFT data from this borehole shows a decreasing trend down the borehole (figure 2.4) into the higher temperature zones in the crust. This decline is manifest from ~60°C onwards. The FT ages gradually decrease until the tracks disappear completely at ~120-125°C where apatite samples show zero-FT ages.

Even at low ambient temperatures FT repair in apatite takes places (e.g. Green, 1988), a process called *ageing* by Gleadow et al. (1983). Vrolijk et al. (1992) observed reduced mean track lengths of 14.6 ± 0.1 μm from apatites from a deep-sea drill core that had an exclusively low temperature history. The samples are from a Cretaceous volcanoclastic sedimentary sequence at ODP site 800 (East Mariana Basin). Heat flow modelling and shallow burial history at the ocean bottom indicates the apatites never experienced temperatures over 16-21°C after post-volcanic cooling during the last 96 Ma. Yet there is clear evidence of FT length reduction. It is hence shown that, given time, even at low temperatures FT annealing occurs. This was also seen in apatite age standards as Durango.

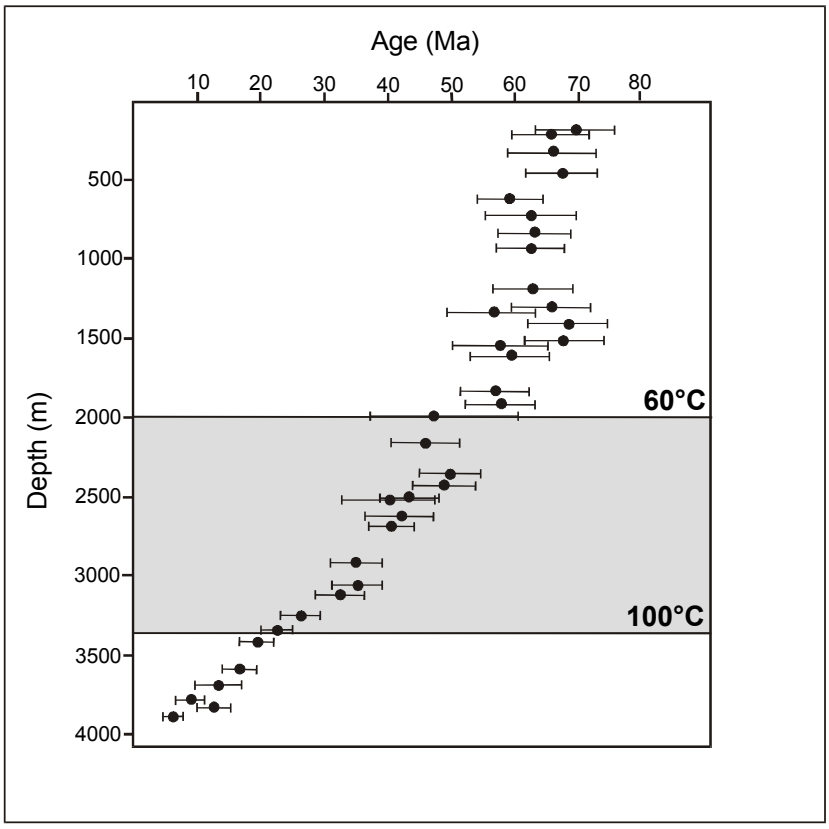

Figure 2.4: Decrease of apparent AFT age with depth from the 4000m deep KTB pilot drill hole (Germany; from Wagner and Van den haute, 1992). A more or less constant cooling age of about 65 Ma is observed in the upper part of the drill hole, until ~60°C (this is the Total Stability or Retention Zone, see text for discussion). The decrease towards a zero-AFT age attained at ~120°C becomes significant from 60°C onwards (identifying the so-called Partial Annealing Zone, PAZ).

2.5. The concept of equivalent time and AFT thermal annealing models

2.5.1. The concept of equivalent time

The notion of *equivalent time* was first introduced by Goswami et al. (1984) and developed and tested by Duddy et al. (1988). The equivalent time concept as described by Duddy et al. (1988) allows to express a variable temperature FT annealing formalism for apatite on the basis of the AFT annealing model of Laslett et al. (1987) (see section 2.5.2). The equivalent time concept postulates that a track annealed to a certain degree (r) behaves during further annealing in a manner independent of the time-temperature (t-T) conditions that caused the earlier annealing, but only determined by r and the reigning (t-T)-conditions.

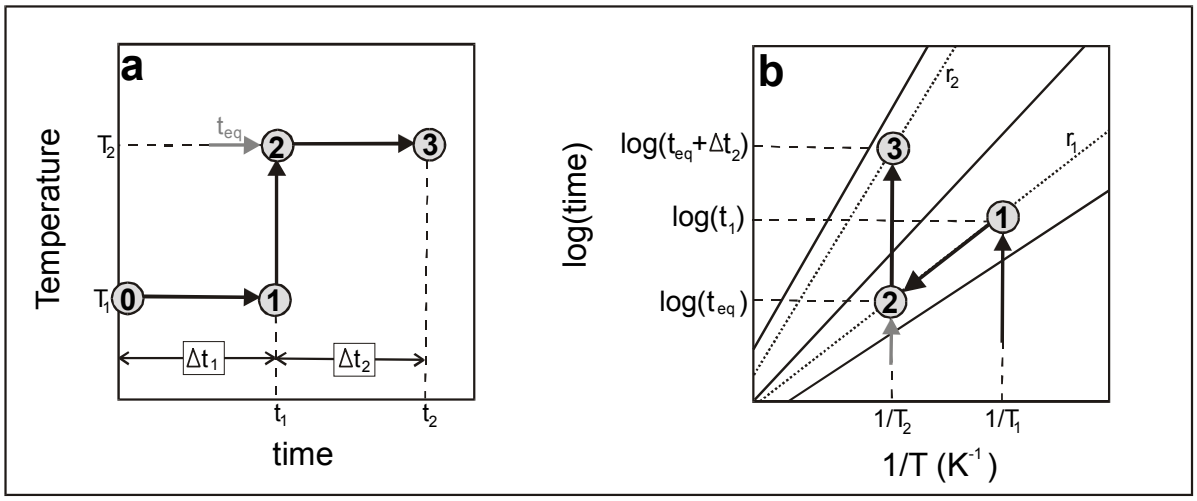

Figure 2.5: The principle of equivalent time for annealing in apatite at variable temperatures (Duddy et al., 1988). (a) Unannealed tracks (at starting position 0) are subjected to a temperature T_1 for a duration of Δt_1 and subsequently to T_2 for a duration of Δt_2 (until final position 3). (b) The annealing degree r_1 after the first heating step (position 1) is obtained from the Arrhenius diagram when plotting the conditions of the first heating step in a point with co-ordinates $(1/T_1, \log(\Delta t_1))$. At the start of the second step (position 2), the tracks still exhibit the r_1 annealing degree. The time to achieve this degree of annealing at temperature T_2 (opposed to Δt_1 for T_1) is called the equivalent time t_{eq}. The annealing degree r_2 achieved after both discrete heating steps (from position 0 to position 3) is obtained by heating the sample in one hypothetical step at temperature T_2 for a duration $(\Delta t_1 + teq)$. The point $(1/T_2, \log(\Delta t_1 + teq))$ in the Arrhenius diagram gives the value for r_2.

So, if we divide a thermal event into a series of time-intervals Δt_i of constant temperature T_i, we can envisage that at the start of an interval with temperature $T_i(t)$, a certain fission track has been shortened to $r_{i-1} = l_{i-1}/l_o$ during a former interval with duration Δt_{i-1} at a temperature T_{i-1} (figure 2.5). If this track had spent its entire previous history at temperature T_i, it would have achieved the degree of shortening r_{i-1} in an equivalent time t_{eq}, given by:

$$\ln(t_{eq}) = A + B(r_{i-1})T_i^{-1} \qquad 2.11$$

At the end of the interval Δt_i, the cumulative FT shortening r_i can then be calculated from a general Arrhenius relationship:

$$\ln(t_{eq} + \Delta t_i) = A + B(r_i)T_i^{-1} \qquad 2.12$$

2.5.2. The Laslett et al. (1987) annealing model

Laslett et al. (1987) used the more precise $r = l/l_o$ retention for their annealing research (e.g. Green et al., 1985; Gleadow et al., 1986a) to describe laboratory annealing experiments on the mono-compositional Durango apatite (e.g. Green et al., 1986). This research showed several shortcomings in the annealing models available at that time. As mentioned, borehole data showed that the chemical composition of the apatite plays a significant role in the annealing behaviour of the apatite and that the broad divergent fanning of lines of equal retention in the laboratory Arrhenius diagrams should be reinvestigated. Furthermore it became clear that the annealing process itself was much more complex than thought and that it cannot be described by a simple diffusion process and by first order kinetics (Green, 1988). Hence, as mentioned, the simple or multi- exponential laws (equation 2.6 or 2.10) were considered an oversimplification of reality. The model put forward by Laslett et al. (1987) took al these new findings into account and proved able to fit their annealing data very well. The model is purely empirical and is not based on any a priori theoretical assumptions.

2.5.2.1. Development of the model

Straight lines of equal FT annealing or equal FT retention in an Arrhenius diagram can be represented in a general form as:

$$\ln(t) = A + BT^{-1} \qquad 2.13$$

Where A and B are constants for a given r. As explained, the retention parameter used here is $r = l/l_o$ and is a function of ln(t) and the reciprocal absolute temperature value:

$$r = f\{\ln(t), T^{-1}\} \qquad 2.14$$

As outlined by Green et al. (1985) we can expect a parallel or slightly fanning Arrhenius diagram. In the former case all iso-annealing lines have the same slope and B is constant for all r. The parameter A can be regarded as a sole function of r and can be written as:

$$A(r) = \ln(t) - BT^{-1} \qquad 2.15$$

Equation 2.15 is constrained by the fact that if t = 0 and T = 0, there is no annealing and retention is complete, so r = 1. Laslett et al. (1987) show that the function A(r) should have the form of ln(1 - r) and thus that their parallel model in a general form can be written as:

$$\ln(1 - r) = c_o + c_1\ln(t) + c_2T^{-1} \qquad 2.16$$

Whereby c_o, c_1 and c_2 are constants to be determined on an empirical and numerical basis by fitting of the available annealing data (Green et al., 1985). The parameterization of equation (2.16) is only valid when t is expressed in seconds, and T in Kelvin. In doing so they found that:

$$\ln(1 - r) = 3.87 + 0.219[\ln(t) - 19270T^{-1}] \quad 2.17$$

Equation 2.16 gives the general form of the parallel Laslett annealing model, whereas equation 2.17 gives the numerical model after fitting of the extensive Green et al. (1986) apatite FT annealing dataset. The fit of these data is statistically very good with a multiple correlation factor of 96.7%.

In the case of a slightly fanning Arrhenius diagram, the slopes of the iso-retention lines represented by the parameter B in equation 2.13 should vary with the degree of FT annealing and hence should be a function of r. With this in mind, rewriting equation 2.11 gives:

$$\ln(t) = A(r) + B(r)T^{-1} \quad 2.18$$

Further development of the fanning model involves the assumption that the iso-retention lines meet in a common point (t_o, T_o) where we can write an expression for the A-function as:

$$A(r) = \ln(t_o) - B(r)T_o^{-1} \quad 2.19$$

In early experiments involving FT annealing in minerals and construction of fanning Arrhenius plots, it was already shown by Dakowski et al. (1974) that the aforementioned assumption is valid.

Solving equations 2.18 and 2.19 for A(r) and B(r) yields:

$$A(r) = \frac{[T\ln(t) - T_o\ln(t_o)]}{T - T_o} \quad 2.20$$

and

$$B(r) = \frac{[TT_o\ln(t_o) - T_oT\ln(t)]}{T - T_o} \quad 2.21$$

Laslett et al. (1987) show that the parameter $T_o^{-1} = -3.1 \times 10^{-6}$ K and consequently is near the zero-point of absolute temperature (0 K). This gives a corresponding value of $\ln(t_o) = -28.27$ in the Arrheniusplot. Given this, equations 2.20 and 2.21 can be simplified and equation 2.18 rewritten as:

$$B(r) = T[\ln(t) + 28.27] \quad 2.22$$

Fitting and statistical analysis of the experimental data yield an empirical numerical model in the general form of a power transform:

$$\frac{\left\{\left[\frac{1-r^{\alpha}}{\alpha}\right]^{\beta}-1\right\}}{\beta} = c_o + c_1 T\left[\ln(t) + c_2\right] \qquad 2.23$$

Again, c_o, c_1 and c_2 and also the powers α and β, are constants to be determined by fitting the available annealing data. Doing so with the Green et al. (1986) data in the same manner as for the parallel model, yields:

$$\frac{\left\{\left[\frac{1-r^{2.7}}{2.7}\right]^{0.35}-1\right\}}{0.35} = -4.87 + 0.000168T\left[\ln(t) + 28.12\right] \qquad 2.24$$

So, after data fitting, equation 2.24 gives the numerical fanning Laslett annealing model. The fit of these data with this model is statistically very good as well and even slightly better than the Laslett parallel model, with the multiple correlation factor here being 98.0 %.

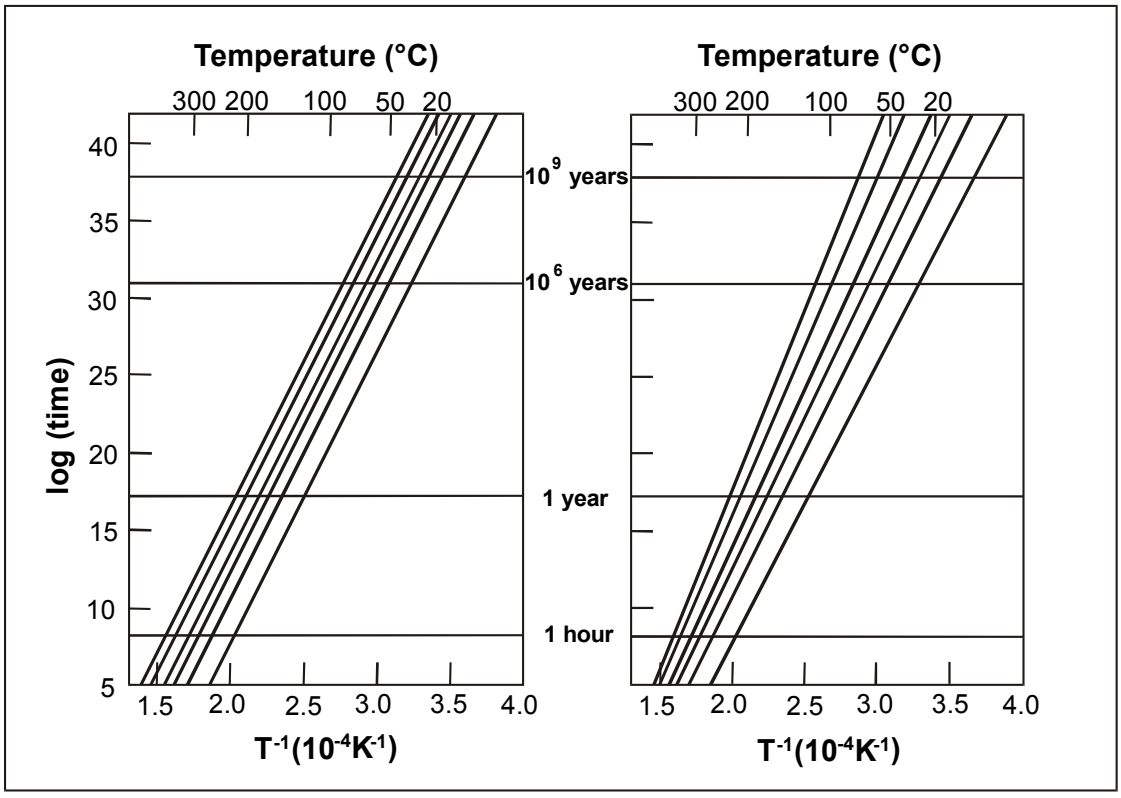

Figure 2.6: Parallel and divergent Arrhenius diagram obtained from the Laslett et al. (1987) annealing model.

Laslett et al. (1987) conclude that the rectilinear fanning model, described by equation 2.24, gives an adequate representation of the AFT annealing data at their disposal. Extrapolation of these models to geological timescales is presented in figure 2.6. It is clear that the very small differences at laboratory timescales are magnified by this extrapolation. The fanning might still be an artifact induced by the existence of small chemical composition differences (Laslett et al., 1987. It also should be noted that the apatite lattice itself is built by several different atoms altogether. Hence there might exist a difference between diffusion of displaced calcium atoms and of displaced phosphate atoms for example. An additional complicating factor is that track annealing in apatite and crystals in general, is shown to be anisotropic (Green and Durrani, 1977).

2.5.2.2. Testing the Laslett model in geological conditions

The FT annealing model by Laslett et al. (1987) is based on isothermal annealing data in apatite. The model was extended by Duddy et al. (1988) to deal with annealing in which temperature varies with time. This extension is is based on the principle of equivalent time as discussed in section 2.5.1.

The Laslett et al. (1987) annealing model describes the FT annealing as a function, g(r) (a so-called Box-Cox transformation) of time and temperature as shown in equation 2.24:

$$g(r) = \frac{\left\{\left[\frac{1-r^{2.7}}{2.7}\right]^{0.35} - 1\right\}}{0.35} = -4.87 + 0.000168T\left[\ln(t) + 28.12\right] \qquad 2.25$$

In terms of equivalent time, (figure 2.5) t_{eq} and r_i can be calculated from equations 2.12 and 2.25:

$$\ln(t_{eq}) = -28.12 + \left[\frac{g(r_{i-1} + 4.87)}{0.000168\ T_i}\right] \qquad 2.26$$

and

$$r_i = \sqrt[2.7]{1 - \sqrt[0.35]{1 + 0.35\left\{-4.87 + 0.000168T_i\left[\ln(t_{eq} + \Delta t_i) + 28.12\right]\right\}}} \qquad 2.27$$

Duddy et al. (1988) performed laboratory heating and cooling experiments and predicted FT length reduction in apatite on the basis of the equivalent time concept. The statistical agreement between predicted and observed confined track lengths is very good (figure 2.7). Using the equivalent time concept Duddy et al. (1988) extended the Laslett et al. (1987) model from a purely isothermal FT annealing model for apatite to a model capable of predicting FT annealing in apatite at variable temperature conditions.

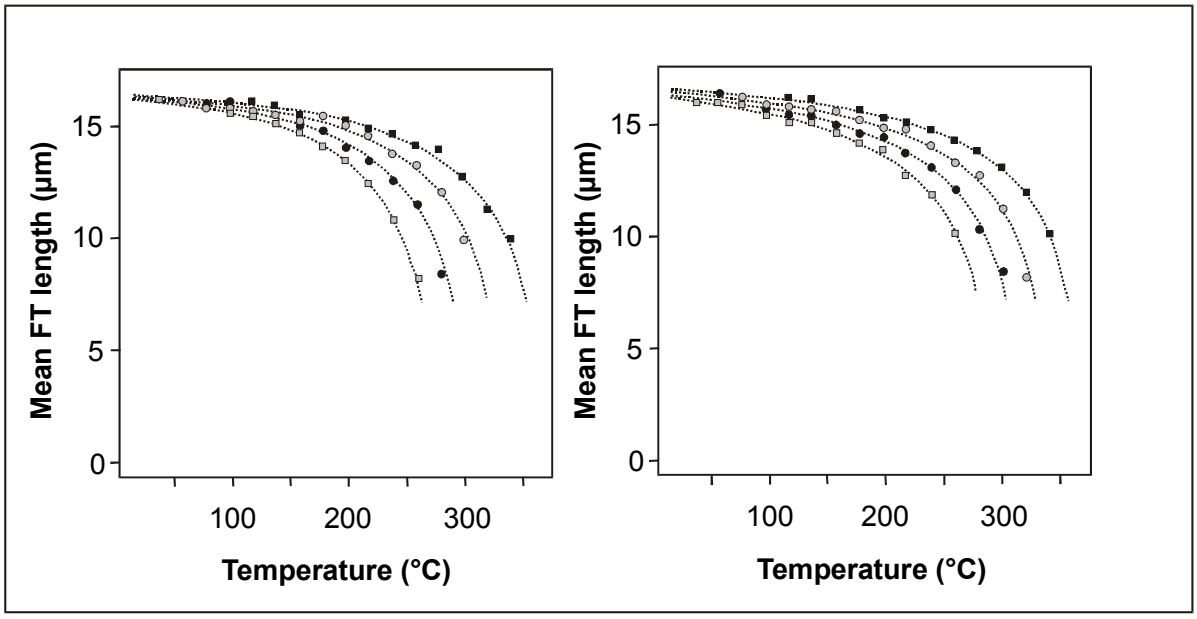

Figure 2.7: Illustriation of data fitting for testing annealing models to experimental FT data. Symbols depict different annealing times (isochronical symbols) which are plotted in function of varying temperatures and resulting track length reduction (from Laslett and Galbraith, 1996b). Dotted lines fitted to this laboratory data describe the model functions. This example depicts fitting data from two apatites in the Laslett and Galbraith (1996b) paper.

In this way, the Laslett et al. (1987) model is able to predict the mean confined FT length of an apatite sample, provided the (t, T)-history of annealing for that sample are given. Green et al. (1989a) tested this model for actual geological situations, thereby providing estimates for paleotemperature history of natural samples. It should be pointed out here that for the laboratory experiments at the basis of the Laslett et al. (1987) model, lengths of induced tracks were used for calculating l/l_o. In geological samples spontaneous track lengths are investigated. Green (1988) however argued that this does not have an influence on the model equations.

Using the described model and an appropriate thermal history or temperature-time (T, t)-path for apatite samples, Green et al. (1989a) were able to predict the apparent AFT age, mean confined fission track length and length distribution for that specific thermal history. These authors show the validity of this approach using so-called undisturbed volcanic apatites and undisturbed basement apatites (Gleadow et al., 1986a), they used well data by Gleadow and Duddy (1981) and Gleadow (1983) from the Otway basin. They also used experiments of heating, cooling and reheating to produce and predict bi-modal length distributions (Gleadow et al., 1986a). In this manner it was shown that thermal history reconstruction by forward modelling of AFT data was possible.

On the basis of this lies the quantitative isothermal description of the AFT annealing by Laslett et al. (1987) and the subdivision of a thermal history curve in time intervals of constant temperature and using the equivalent time concept (Duddy et al., 1988). Small discrepancies in observed and modelled AFT data could be attributed to apatite compositional effects. For the model is based on Durango apatite (having a Cl/(Cl + F) ratio of about 0.1) annealing data by Green et al. (1986), while apatites in geological evironments will mostly show a range of compositions reflecting the solid

solution series between clorine and fluorapatite. Bearing this in mind the modelled results in the Green et al. (1989a) paper correlate very well with the independently established thermal histories.

The Laslett model was worked out by Green into a software package, called *Supertrack*, which was able to perform forward AFT modeling. Later Green patented the software and further developed it: corrections for apatite composition were made and a multi-compositional kinetic model, AFTA® was subsequently written and extended to inverse modeling (see section 2.5.6) next to the original forward modelling approach. The AFTA® program demands an input of Cl-content of the investigated apatite sample and hence analytical chemical data on the samples is required. Thermal history solutions are extracted from data broken into discrete compositional groups, using separate kinetics for each group. This software is widely used in the FT research community to model their AFT data. In particular it is favoured by geologists in detrital apatite research to investigate thermal maturity of sedimentary basins and prospection of hydrocarbons (Green et al., 1989b).

When reconstructing thermal histories with the Laslett et al. (1987) model, and indeed also with the other models discussed below, results tend to exhibit a late cooling event. Because this was identified in many cases this apparent cooling was dubbed the "Worldwide Recent Cooling Event". It was soon recognized to be a modelling artifact with no geological significance. This artifact has to be taken into account and one should investigate if thermal histories showing late cooling events are in fact based on geological reality. Ketcham et al. (1999) argued that the initial mean track length (l_o) parameter of 16.35 µm (measured by Green et al., 1986, on induced confined tracks) used in the model is too high. Natural samples rarely exhibit these high lengths. A characteristic "long" track in a natural fluorapatite is typically in the 14.0-14.6 µm range (e.g. in Durango apatite, Green, 1988). To achieve this length the apatite would require at least 20 Ma of constant heating at temperatures around 40 to 50°C according to the Laslett et al. (1987) equations for example. As a result, samples with mean lengths <15 µm (i.e. in fact the majority of natural apatite outcrop samples) have to show recent cooling to bridge the gap between the 40-50°C threshold to ambient surface temperatures.

2.5.3. The Crowley et al. (1991) annealing model

One of the first alternatives for the apatite FT annealing model by Laslett et al. (1987) was proposed by Crowley et al. (1991). These authors use laboratory isothermal annealing data on fluorapatite to construct a general FT annealing model. They use the annealing data from Green et al. (1986) on Durango apatite and additional annealing data obtained from two other; fluor-rich apatite samples. One is a fluorapatite from a norite complex in Iowa (USA), and the other is a Sr-fluorapatite from the Kola peninsula (Russia). Crowley et al. (1991) fit these data using four possible annealing equations corresponding to, (equation 2.13 for the simplest formulation), i.e. (1) a parallel linear form, (2) a parallel curvilinear form, (3) a fanning linear form, and (4) a fanning curvilinear form. The best fit of the data was obtained by making use of the fanning linear form and confirms the work by Laslett et al. (1987). Their empirical model can be described by:

$$g(r;\alpha,\beta) = C_o + \frac{C_1 \ln(t) + C_2}{T^{-1} - C_3} \qquad 2.28$$

In equation 2.28, g(r; α, β) is a Box-Cox transform of $r = l/l_o$ as in equation 2.23 of the Laslett et al. (1987) model. The powers α and β, and the parameters C_o, C_1, C_2 and C_3 should be estimated from the annealing data. In fact equation 2.28 can be regarded as a generalized form of the fanning Laslett model described by equation 2.23. In "Crowley terms", equation 2.23 can be rewritten as:

$$g(r; \alpha, \beta) = C_o + C_1 T \ln(t) + C_2 T \qquad 2.29$$

With the generalized form by Crowley et al. (1991) as in equation 2.28, being an extended 6-parameter equation and fitting additional fluorapatite annealing data in respect to the Green et al. (1986) data set.

Crowley (1993) developed a forward modelling program, Lenmodel, which makes use of the equivalent time concept by Duddy et al. (1988) to estimate AFT data for a user-supplied thermal history. The forward model is in other words based on the semi-analytical solution of the annealing equations for this given thermal history approximated by isothermal increments as outlined in earlier work (Crowley, 1985).

2.5.4. The Laslett and Galbraith model

Laslett and Galbraith (1996b) made a revision of the fanning Arrhenius annealing equations by Laslett et al. (1987) and Crowley et al. (1991). The basis of their model is the same as described earlier, but they derive a six parameter equation in order to fit both the FT laboratory annealing datasets by Green et al. (1986) and Crowley et al. (1991). They also specify an error structure based on two components of variance that should make a better estimate of the uncertainty of the modelled results. The six parameter Laslett and Galbraith (1996b) model is given as:

$$\mu_i = \mu_{max}\left[1 - e^{c_o + c_1 \frac{\log(t_i) - \log(t_c)}{T_i^{-1} - T_c^{-1}}}\right]^{\lambda} \qquad 2.30$$

Where μ_i is the mean of the FT length (l) distribution (considered to be a normal distribution) of the apatite sample heated at temperature T_i for a time t_i and μ_{max} is the mean length of unannealed tracks. It differs from the mean original track length (l_o) as used in the first Laslett-model. In particular, μ_{max} represents the mean at exactly the moment of track formation. It is a value that takes track annealing at ambient temperatures in the time span between irradiation and etching into account, an observation made in the meantime by Donelick et al. (1990). Its value should be directly estimated from the data and not measured after irridiation and etching. In this way the initial mean track length is allowed to be a free parameter in the annealing model, in contrast to earlier descriptions where a fixed value was

utilized. T_c and log (t_c) are the co-ordinates of the intersection of the fanning iso-retention lines. The parameters c_o, c_1 and λ are to be derived empirically and depend on the composition of the apatite. Laslett and Galbraith (1996b) find a good fit for all available data for $\lambda = 1/3$.

2.5.5. The Carlson (1990) annealing model

Another AFT annealing model was published by Carlson (1990). His objective for the model was to depart from purely empirical annealing models and to develop a model based on a physical description of FT annealing. He hence uses an alternative parameterization for his FT annealing model. Carlson (1990) states that the annealing mechanisms for fission tracks should bear resemblance to well-known and understood mineralogical processes as topotactic mineral transformations and O-diffusion in silicates.

Carlson (1990) envisages a fission track as a zone of different defects, following to some extent the so-called Orsay model of the latent FT structure (Dartyge et al., 1981). The disrupted lattice zone around a latent FT is considered to be composed of a cylindrical core zone of certain width, wedging out toward the ends of the track (taper form). Over the entire length, there is a certain axial distribution of lattice defects and a radial defect distribution (which is approximated by a power-law function concentrating defects strongly near the radial center). During annealing, the defects are restored due to diffusional processes with a certain defect-elimination rate, which according to Carlson (1990) adheres to the physical laws governing the kinetics of topotactic mineral transformations. Hence this rate is constant over time, but depends exponentially on temperature. The restoration of the lattice due to repositioning of the lattice atoms, occurs both axially as well as radially and results in track length shortening and reduction of the track's diameter. For geometric reasons, radial shrinkage of the taper-formed disrupted zone alone also produces axial shortening and in later stage of annealing, as the diameter is decreased radically, segmentation of the track arises. This produces so-called unethable gaps.

From these physical laws, without testing to experimental data, Carlson derives following relationship between the length (l) of the track and its thermal history:

$$l = l_o - A\left(\frac{k}{h}\right)^n \left[\int_0^t T(\tau) e^{\frac{-Q}{RT(\tau)}} d\tau\right]^n \qquad 2.31$$

In which l_o is the initial (unannealed length), k is Boltzmann's constant, h is Planck's constant, R is the universal gas constant, T is absolute temperature, and t is the time elapsed since the onset of the annealing episode. The variable τ is a dummy variable of integration over time. There are three quantities, n, A and Q to be determined by experimental measurement. These quantities however have a physical meaning: n is a power-law exponent quantifying initial radial deffect distribution (it is a positive real number smaller than 1), A is an empirical rate constant for axial track shortening,

and Q is the activation energy for atomic motions within the lattice (corresponding to E_a which was used earlier).

For further stages of annealing Carlson extends the model by introducing a length parameter (which he calls $l_{as/sg}$) in terms of "l" in equation 2.31, designating the mean length of a population of tracks that have undergone both axial shortening and segmentation. Compositional effects for a given apatite would be reflected by the exact values of the n, A and Q parameters. Carlson argues that not the chemical composition as such is the driving factor influencing atomic repositioning, but it rather exerts an indirect impact via the total ionic porosity (Z) (e.g. Dahl, 1995). The ionic porosity is the percentage of the unit cell volume not occupied by ions. Therefore Z is dependent on the amount and nature of the ions and hence on the chemical composition. Anisotropy effects would be corrected for by establishing a parameter A_θ, being the shortening rate for a fission track at a certain angle θ to the crystallographic c-axis. The polythermal character of equation 2.30 implies that the concept of equivalent time should not be invoked in this model.

Purely from theory Carlson (1990) finds an expression which closely resembles the isothermal parallel Laslett et al. (1987) model described by equation 2.14, which was:

$$\ln(1 - r) = c_o + c_1\ln(t) + c_2T^{-1}$$

If we rewrite Carlson's law for isothermal annealing (T = constant) we find:

$$l = l_o - A\left(\frac{kT}{h}\right)^n e^{\frac{-nQ}{RT}} t^n \qquad 2.32$$

Dividing equation 2.32 by l_o and writing it in the logarithmic form, yields:

$$\ln(1-r) = \ln\frac{A}{l_o} + n\ln\frac{kT}{h} + n\left(\ln(t) - \frac{Q}{RT}\right) \qquad 2.33$$

Or in a generalized form:

$$\ln(1-r) = c_o + n\ln(T) + c_1\ln(t) + c_2T^{-1} \qquad 2.34$$

So, apart from a small temperature factor T^n ($0 < n < 1$) which Carlson attributes to a material characteristic vibrational frequency factor, equation 2.34 has the same form as the equations derived in the Laslett and Crowley models (equations 2.15 and 2.29 respectively).

Green et al. (1993) argued that the Carlson (1990) model is not a theoretical model, but also relies on an empirical approach. An issue admitted by Carlson (1993), but still the model is rooted in an explicit physical basis, leading Carlson (1993) to describe his model as semi-empirical. Nevertheless the underlying physical meaning has not yet been fully established and Green et al. (1993) argue that

therefore the Carlson (1990) model is based on axiomatic postulates and is not proven to have a specific physical basis. Green et al. (1993) also criticized the model for not giving a good fit to laboratory data, and for providing no consistent extrapolation with established geological annealing rates. Hence these authors advized against the use of the Carlson (1990) model.

2.5.6. Inverse modelling of FT annealing data

Software has been developed for reconstructing thermal histories of rocks using AFT age and length data. The first programs were able to perform forward modelling (e.g. Crowley, 1985 and 1993; Green et al, 1989). Forward modelling involves providing the software with a geological reasonable thermal history (T-t-data) for the sample under investigation. The program then predicts the AFT data for a given thermal history by using the specific model equations. By trial and error, fitting the observed and predicted AFT-data is used to refine the user-provided thermal history and to reconstruct it in more detail. Inverse modelling of the AFT data, i.e. reconstructing unknown thermal histories on the basis of observed AFT is an even more powerful tool in thermochronology and in the early 1990's the first methods were being explored (Lutz and Omar, 1991; Corrigan, 1991 and 1993; Jonckheere, 1992). The mathematical and statistical details of these models are clearly beyond the scope of this work, but a qualitative description of inverse modelling may be useful here.

Corrigan (1991) outlines a stochastic inversion method to quantify the thermal history information contained in synthetic AFT-data generated by forward modeling of a given thermal history. The concept of the method is independent of the specific annealing model used, but the problem is addressed in the continuous form of variable temperature T(t) and is hence somewhat biased towards the Carlson (1990) model that does not rely on the principle of equivalent time (Duddy et al., 1988). Nevertheless, as Corrigan (1991) points out, the Laslett et al. (1987) annealing equations can be treated by the same method. The annealing model is generalized as:

$$l(t) = f(B, l_o, T(t)) \qquad 2.35$$

Equation 2.33 describes the predicted etchable length (l(t)) of a fission track formed at time t as a function of the initial unannealed length (l_o) of the thermal history of that track (T(t)) and of a set of parameters, grouped as B, which can be derived empirically and depend upon the annealing model used and upon the apatite composition.

The nature of the dataset (FT age and FT length data) is nonlinear, nondeterministic and is associated with a significant degree of uncertainty characteristic of the FT method. As a consequence, the thermal history solution will not be unique and the goal of inverse modelling is to constrain a range of thermal histories compatible with the dataset. This is done by the so-called simulated annealing approach (Kirkpatrick et al., 1983) that is described as a kind of hybrid Monte Carlo optimization. It is a numerical method that relies on the input of a reasonable assumption of the expected thermal history. The algorithm recalculates the predicted AFT data and the resulting thermal history curve

until a good statistical agreement is obtained with the input of the observed AFT age and length data. This can be done using traditional goodness-of-fit statistics, such as calculation of χ^2 for example. Because of the inherent non-uniqueness of the solution, several possible permissible thermal histories may produce the same AFT data, so instead of a specific thermal history curve, thermal history envelopes of most probable histories are calculated. The results are contour plots of the probability density of time-temperature space compatible with the provided AFT data, and can be interpreted as an estimate of the probability distribution of temperature at any given time. Corrigan (1991) defines such an algorithm and presents a set of optimization parameters and prior constraints on the time-temperature space for inverse modelling by the Monte Carlo approach with the Carlson (1990) annealing equations. As was already reported by Green et al. (1989a), Corrigan (1991) also found that resolving thermal histories beyond a resolution smaller than 10°C is not possible given the various intrinsic uncertainties in the different steps of an AFT analysis. On the basis of the inverse algorithm presented here, several other computer modelling programs were developed for inverse thermal history reconstruction (Issler, 1996; Willet, 1997).

2.5.7. The Monte Trax program

The Monte Trax computer program was developed by Galagher (1995). It is a widely used software package for inverse thermal history modelling based on AFT data. The algorithm used shows some similarities to those described in the previous section, certainly in respect to the problem solving strategy.

Typically, the inverse problem is addressed in terms of a misfit function between observed and predicted AFT data. The idea is then to minimize the misfit by applying numerical techniques (iterative Monte Carlo simulation e.g.) until a statistically acceptable or good fit is achieved. The Monte Carlo procedure generates the candidate (t, T)-paths that are then tested for their goodness-of-fit. Gallagher (1995) inverts the problem. He defines a mathematical expression that iteratively should maximize the probability that a certain thermal history would yield the observed AFT data. Instead of a "misfit function" a "merit function" is defined. Mathematically this is equivalent to finding the thermal history that maximizes the log-function of the likelihood. This is the *maximum likelihood* approach. The log likelihood function mathematically describes the probability of obtaining the specific observed AFT data. Finding a thermal history that maximizes this function then corresponds to maximizing the probability of obtaining this data given that particular thermal history. The log likelihood function (L) should incorporate all aspects of an AFT dataset. This dataset consists of a series (j) of FT counts, N_s for the spontaneous tracks, and N_i for the induced tracks, and a series (k) of track lengths, l. Gallagher defines L as:

$$L = \sum_j \left[N_{s,j} \ln(\theta) + N_{i,j} \ln(1-\theta) \right] + \sum_k \ln(P[l_k]) \qquad 2.36$$

in which

$$\theta = \frac{\rho_s}{\rho_s + \rho_i} \qquad 2.37$$

Where ρ_s is the predicted spontaneous track density and ρ_i the predicted induced track density. $P[l_k]$ is the probability of obtaining that particular confined track length bin.

As in previous cases, the program, later named Monte Trax, actually consists out of two steps. A first step identifies a general thermal history that provides a reasonable fit to the observations. The second step is a refinement of that thermal history until a "best fit" option is found by maximization of the log-likelihood. Again, because of the non-uniqueness of the solution, a range of good fits will be attained, and so probability density envelopes can be calculated.

The first step consist of defining time-temperature (t-T)-points on the basis of a priori geological knowledge. These t-T-points are then connected by line segments by the program in order to have an initial thermal history curve. The program searches the t-T-space for possible thermal histories defined by the constraints and identifies the form or trend of the thermal histories that fit best to the data input. This can be done using a stochastic numerical method such as a Monte Carlo method, but Gallagher (1995) uses so-called *genetic algorithms*. Genetic algorithms are a special class of Monte Carlo methods that are very efficient for optimizing non-linear problems as is the case for FT annealing and reconstruction of thermal histories (Gallagher and Sambridge, 1994). Unlike random Monte Carlo, in which all models are independently generated and calculated, genetic algorithms uses information of the previously obtained set of candidate solutions to identify model types that are more successful in predicting the observed data. Continued iteration of this approach eventually leads to a general form of the thermal history to be reconstructed.

The second step uses the best thermal history generated by the genetic algorithms for a general thermal history to be used as a start-off model. This model is then improved using a numerical technique, i.e. the Powell's method. This is a multi-dimensional line search technique in which each (t, T)-point is taken in turn and a one-dimensional line search is performed to find a maximum in the L-function. The discrete (t, T)-points are the model parameters that are being refined and a confidence region around them is calculated by this systematic line search method. At each stage of this search the program re-optimizes all other model parameters to find the maximum likelihood model.

Gallagher (1995) used synthetic AFT data provided by forward modelling of a known thermal history curve using the Laslett et al. (1987) annealing equations. When using other annealing models he found the same overall thermal history solution, but the Laslett model yielded the best fits. The modelling strategy (to some extent trial and error) favoured, consists of starting with a minimal number of (t, T)-points to constrain the general model form and if needed, to progressively add points until observed and predicted AFT data show no significant discrepancies.

2.5.8. The Ketcham et al. (1999) annealing model and the AFTSolve program

Ketcham et al. (1999) developed an empirical, multi-kinetic FT annealing model and accompanying thermal history modelling software, AFTSolve (Ketcham et al., 2000) on the basis of extensive multi-compositional apatite annealing data of Carlson et al. (1999). It takes into account several aspects of AFT annealing such as chemical composition of the apatite (Carlson et al, 1999), crystallographic orientation of the fission tracks (Donelick, 1991 and Donelick et al., 1999) and FT annealing of apatite even at low ambient temperatures (Donelick et al., 1990; Vrolijk et al., 1992). Although it was recognized earlier that compositional and crystallographic orientation effects play a significant role in FT annealing in apatite, the Ketcham et al. (1999) model is the first one to actually quantify and incorporate model parameters to that effect. The model is able to handle different kinetic apatite populations, i.e. apatites having different annealing kinetics, simultaneously. These characteristics can be quantified by using specific kinetic parameters (see next section). Although statistical tests (e.g. Green, 1981) and statistically based graphical devices (e.g. Galbraith, 1990) can be used to distinguish between age populations, the multi-kinetic annealing model portrayed here distinguishes between kinetic populations. The model quantifies and uses sample specific kinetic parameters to model the AFT data, rather than using a (mono-kinetic) model based on the annealing behaviour of a single apatite standard as Durango for example. In this way the thermal history information contained in each kinetic subpopulation can be resolved separately. This enhances the resolution of thermal history reconstruction on one hand and avoids that two or more distinct subpopulations are mixed and obscure each other's individual data. Of course this is of great importance when studying clastic apatites in sediments, but samples containing kinetically different apatites have been recognized in crystalline rocks as well (O'Sullivan and Parrish, 1995).

2.5.8.1. Experimental results

The Ketcham et al. (1999) model is founded on a large dataset of 408 laboratory annealing experiments conducted on 15 different apatites, covering the whole range of possible apatite compositions, even including various types of cationic substituted specimens (Carlson et al., 1999). The dataset contains experimental results on apatites that were used in earlier annealing studies, such as Durango apatite (Green et al., 1986) and Tioga apatite (Donelick, 1991). All samples are characterized in terms of composition and homogeneity. As the most influential chemical marker, the chlorine-content (Cl) is especially of interest (e.g. Green et al., 1986). Track lengths were measured on horizontal confined (TINT) tracks and their angle to the crystallographic c-axis was determined. In addition, the so-called D_{par} parameter was determined. D_{par} is the mean maximum diameter of FT *etch figures* on prismatic surfaces of the hexagonal apatite crystals (Burtner et al., 1994). These etch figures are the cross-section of the FT etch pits with the etched apatite surface. Their maximum diameters are parallel to the c-axis. D_{par} depends on de etch rate, which is material dependent. It can be viewed as an indirect measure of composition in the same way as Carlson (1990) uses total ionic

porosity (Z) as explained in section 2.5.4 for example. In analogy with Cl, D_{par} can therefore be used to characterize a specific kind of apatite in terms of its annealing behaviour (figure 2.8). The relationship between the observed and modeled FT lengths and the Cl and D_{par} kinetic parameters respectively was determined and used to construct the Ketcham et al. (1999) multikinetic model. As an illustration of the broad range of annealing behaviour of apatites, Carlson et al. (1999) found closure temperatures of 81°C for an end-member hydroxy apatite sample, to over 200°C for Bamble apatite (a chlor-hydroxy apatite from Bamble, Norway) that was found to be the most resistant to FT annealing.

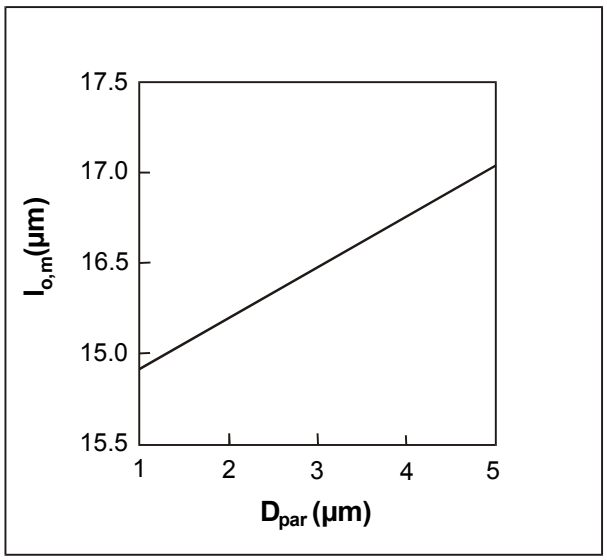

Figure 2.8: Linear relationship between the original unannealed mean track length in apatite ($l_{o,m}$) and the etchpit diameter on planes parallel to the c-axis (D_{par}). Both can be used as so-called kinetic parameters in the Ketcham et al. (1999) annealing model. (from Donelick et al., 1999).

2.5.8.2. Crystallographic orientation effects

The effect of crystallographic orientation on FT length in the Ketcham et al. (1999) annealing model for apatite is based on the work presented in a companion paper by Donelick et al. (1999), which in turn is largely based on earlier work by Donelick (1991). The latter author developed the so-called *elliptical model* for fission-track lengths in apatite exibiting low degrees of annealing. This is an equation expressing the mean etchable AFT length (l_{θ_i}) at an angle θ_i to the crystallographic c-axis as a function of the corresponding radius of an ellipse with maximum and minimum semi-axes, respectively, the mean track length parallel (l_c) and perpendicular (l_a) to the c-axis. In polar co-ordinates, the AFT length at an angle θ_i is given by the equation for the elliptical radius:

$$l_{\theta_i} = \sqrt{\frac{\sin^2\theta_i}{l_a^2} + \frac{\cos^2\theta_i}{l_c^2}} \qquad 2.38$$

Donelick et al. (1999) confirm and extend this elliptical model to all degrees of annealing. The authors also conclude that the process responsible for FT length anisotropy in the laboratory experiments is also operative over geological time scales as well. The length anisotropy increases as the degree of annealing increases. The elliptical model seems to hold well until mean lengths of about 11 μm are reached. At higher degrees of annealing tracks at high angles to the c-axes experience, accelerated length reduction. This phenomenon was attributed by Green et al. (1986) to the process of track segmentation. The extension of the elliptical model for highly annealed tracks exhibiting evidence of accelerated length reduction is quantified by determining a threshold angle (θ_{air}) to the c-axis above which accelerated length reduction dominates. Using their experimental data, the following empirical relationships were established by Donelick et al. (1999):

$$l_a = 1.632 l_c - 10.879 \quad 2.39$$

$$\theta_{air} = 0.304 e^{0.439 l_c} \quad 2.40$$

$$a_1 = 0.1035 \theta_{air} - 2.250 \quad 2.41$$

In equation 2.41 a_1 represents the intercept of an accelerated-length-reduction fission track with an axis perpendicular to the c-axis (in other words, the intercept with the axis along which l_a is measured).

2.5.8.3. The multi-kinetic annealing model

The multi-kinetic model by Ketcham et al. (1999) was established on the basis of experiments in which apatites of different composition were annealed simultaneously. In this way it was ensured that the apatites have all experienced the same thermal treatment. Care was taken to guarantee identical etching conditions. The relationship of one apatite to another at laboratory time scales can then be expressed as:

$$r_{lr} = \left(\frac{r_{mr} - r_{mr0}}{1 - r_{mr0}} \right)^{\kappa} \quad 2.42$$

Where r_{lr} and r_{mr} are the reduced lengths of the apatites that are less resistant and more resistant to annealing respectively. The parameters r_{mr0} and κ are empirically fitted parameters. In particular, r_{mr0} is the reduced length of the more resistant apatite at the point were the less resistant apatite first becomes totally annealed. Ketcham et al. (1999) found that equation 2.42 appears to describe the annealing behaviour of any pair of apatites, both with respect to mean length as to c-axis projected length data (as described by Donelick et al., 1999).

Furthermore it was found that:

$$r_{mr0} + \kappa \approx 1 \qquad 2.43$$

A single equation can now be used to describe the most-resistant apatite, and then calculated r_{mr0}-κ pairs can be used to infer the behaviour of the less-resistant apatites. Rather than having to measure all possible apatite compositions, it is sufficient to create functions that relate the measurable kinetic parameters (D_{par} and Cl) to r_{mr0} and κ values. The most resistant apatite from the Carlson et al. (1999) data set is the Bamble apatite as mentioned earlier. Its annealing behaviour was found to be adequately described by:

$$\frac{\left(\frac{1-r_{c,mod}^{-11.988}}{-11.988}\right)^{-0.12327}-1}{-0.12327} = -19.844 + 0.38951\left[\frac{\ln(t)+51.253}{\ln(T^{-1})+7.6423}\right] \qquad 2.44$$

With $r_{c,mod}$ being the modelled reduced length of a FT parallel to the c-axis (Donelick et al., 1999) after an isothermal annealing event at absolute temperature T and of duration t. So, $r_{c,mod} = l_{c,mod}/(l_{c,mod})_o$ where the lengths are c-axis projected track lengths modelled according to the extended Donelick et al. (1999) elliptical model. Equation 2.42 for the B2 apatite has the general "Box-Cox-form" $g(r; \alpha, \beta) = f(t, T, C_i)$ as used in many annealing models (Laslett et al., 1987; Crowley et al., 1991; Laslett and Galbraith, 1996b) and was obtained empirically by minimizing the misfit between the g and f functions by use of numerical methods (Ketcham et al., 1999 used conventional χ^2 statistics).

The model presented by Ketcham et al. (1999) was not only chosen to describe the Carlson et al. (1999) laboratory annealing data but also was adopted to adhere to geological benchmark conditions. The model is able to describe the high temperature annealing behaviour exhibited by the near end-member fluorapatites from the Otway Basin bore holes (e.g. Gleadow and Duddy, 1981; Green et al.; 1989b), as well as the ambient low temperature annealing as observed by Vrolijk et al. (1992). For the laboratory data the model approximates a slightly fanning Arrhenius form, but extrapolated to geological time scales the best fit is obtained by a slightly curvilinear form of the iso-retention lines. The authors suggest the physical properties of the defect-elimination model as outlined by Carlson (1990) as an explanation for this observation, although they acknowledge other physical processes might be at work.

As mentioned earlier, it is sufficient to relate measurable kinetic parameters to the model parameters to construct this multi-kinetic annealing model. Given the Carlson et al. (1999) data, Ketcham et al. (1999) obtain for the Cl and D_{par} kinetic parameters:

$$r_{mr0} = 1 - e^{0.647(D_{par} - 1.75) - 1.834} \quad 2.45$$

and

$$r_{mr0} = 1 - e^{2.107(1 - |Cl - 1|) - 1.834} \quad 2.46$$

Where D_{par} is in μm, Cl-content of the apatite is reported in atoms per formula unit (apfu). Once r_{mr0} is determined, equation 2.43 is used to calculate κ and the model equation 2.42 can be completed. A third kinetic parameter which can be used and for which equations are at hand is OH-content. Nevertheless Ketcham et al. (1999) point out that the uncertainties concerning OH are far greater than for the other two parameters. In addition to estimating the length reduction of a kinetic FT population after an annealing episode, it is also necessary to estimate the natural spread of lengths that will be observed. The Ketcham et al. (1999) model uses modelled standard deviations given by Donelick et al. (1999). An empirical function is provided for use of mean FT lengths and c-axis projected FT lengths:

$$\sigma_m = 0.02858(l_m)^2 - 0.8733 l_m + 7.464 \quad 2.47$$

and

$$\sigma_{c,mod} = 0.008452(l_{c,mod})^2 - 0.2442 l_{c,mod} + 2.312 \quad 2.48$$

Using the equations above, the multi-kinetic model will calculate a length distribution with a mean length and standard deviation that can be compared to the observed mean length and standard deviation. The equations 2.45 and 2.46, relating kinetic and model parameters is specific to the apatite etching conditions used by Carlson et al. (1999), which are 20s in 5.5M HNO_3 solution at 21°C. Researchers using the multi-kinetic model should use these exact conditions as well, or should derive similar equations based on their data and etching conditions.

2.5.8.4. The AFTSolve program

AFTSolve is a computer program developed by Ketcham et al. (2000) based on the Ketcham et al. (1999) FT annealing model for apatite. Both forward and inverse modelling is possible. Next to the Ketcham et al. (1999) equations that are set as default, other annealing models can be used, which is a great advantage of this program. In particular the annealing equations of Laslett et al. (1987) and Crowley et al. (1991) can be chosen. Input of AFT data is straightforward for both FT length and age data. When using the Ketcham equations, the program also requires input of kinetic parameters (Cl or D_{par}). The program subdivides discrete apatite grain populations on the basis of these kinetic parameters. Because of the specific etching conditions used by Carlson et al. (1999), the program allows to change coefficients related to equations 2.45 and 2.46 for different methodologies. The user

can adapt the program computing to ^{252}Cf TINTs (Donelick and Miller, 1991) if they were used in the determination of the observed FT length distribution. If desired AFTSolve calculates a vitrinite reflectance corresponding to the AFT data.

For a given (t, T)-history, AFTSolve approximates continuous track formation by subdividing the t-T-path into discrete isothermal steps. This is based on so-called optimal time step size selection (Issler, 1996). This is the so-called staircase approximation of the (t, T)-history, based on the concept of equivalent time (Duddy et al., 1988). The amount of annealing achieved in each time step is then summed over the entire thermal history, using a specific weighting factor (w). The w-factor takes into account relative track generation within each time step, observational bias and relative track retention by using an empirical function that relates measured FT length to measured FT density (Green, 1988). Furthermore, w is the product of the length of the time step and the average relative uranium concentration. In this way a track length distribution is predicted by the model. In addition, AFTSolve calculates the pooled FT age that would be obtained for a particular (t, T)-path. This is done by assuming that each time step of size Δt_j contributes that specific amount to the total FT age, modified for the track length reduction of the population in that time step relative to the age standard (Willet, 1992) used for determining the observed AFT age. So, the modelled age ($t_{AFT,mod}$) is then given by:

$$t_{AFT,mod} = \rho_S^{-1} \sum_j \rho_j \Delta t_j \qquad 2.49$$

With ρ_S the estimated FT density reduction in the age standard, ρ_j the FT density reduction for time step j with duration Δt_j (assuming FT density reduction is lineary proportional to FT length reduction). The program default reduction for the standard is set to 0.893 for Durango apatite and is based on an observed mean spontaneous FT length in Durango of 14.47 μm (Donelick and Miller, 1991) and a mean spontaneous FT length of 16.21 μm (Carlson et al., 1999). AFTSolve allows a user adapted age standard reduction value. The ρ_j-values are calculated by the program for each time step Δt_j.

In the inverse modelling algorithm, candidate thermal histories are generated by AFTSolve from user-entered constraints. These are fixed (t, T)-intervals (with time fixed) in the (t, T)-space. Two extremes, a high T starting point and an ambient low T are a minimal requirement to be defined by the user. The user can add additional constraints that further restrict the candidate thermal histories. Supplementary nodal points are produced along the (t, T)-path between two user-entered constraints. The nodal points are equally spaced in time, in sets of $(2^n - 1)$, where n is an integer specified in AFTSolve by the user. Naturally, these supplementary nodes are restrained to the temperature extremes defined by the bracketing user-entered constraints. The user can impose maximum cooling or heating rates in all segments of the (t, T)-path and can force them to be monotonic or not.

The thermal history numerical searching algorithm can be chosen by the user from either a traditional Monte Carlo method or a so-called Contrained Random Search (CRS) technique as presented by

Willet (1997). The latter is advized when the search space is ill-constrained, while the former is better for mapping out probability density envelopes in well-confined situations. The number of iterations can also be defined The statistical merit function that tests the degree of fit between the predicted AFTdata and the observed data is a so-called Kolmogorov-Smirnov (K-S) test for the length distribution, mean length and standard deviation, and a K-S based test for the individual single grain AFTages and the corresponding predicted and observed apparent pooled age (Ketcham et al., 2000). In this way, AFTSolve calculates (t, T)-envelopes that contain all individual paths that pass the statistical criteria and conform to the user-entered constraints. A broader envelope of acceptable fits (5% limit, K-S value of 0.05) and a narrower envelope of good fits (50% limit, K-S value of 0.5) appear in the AFTSove program output. The best fitting (t, T)-path is shown as a single curve within the good fit envelope.

Ketcham et al. (2000) suggest a general modelling strategy to be followed to ensure successful use of the AFTSolve program. First, a general thermal history can be generated by the program by fixing 2 constraints: the ambient (low surface or bore hole) temperature at time 0 and a high temperature ensuring total annealing at an initial point in time, guestimated from geological evidence. In subsequent runs the user can then define more constraints pursuing the general trend of the initial thermal history model or additional (t, T)-constraint evident from geological knowledge of the investigated area. Successive modelling by imposing or relaxing constraints will eventually refine the reconstructed thermal history until satisfactory results are obtained.

2.6. Fission track analysis as a thermochronological tool

2.6.1. General aspects

As soon as laboratory annealing studies were carried out and track annealing models were developed, it was attempted to extrapolate the results to geological environments and geological time scales and to apply these findings to develop a thermochronological tool based on FT analysis. Track length analysis was found to be a powerful tool to reconstruct thermal histories.

The shape of the FT length distribution, the mean track length and the standard deviation all provide information about the thermal history to which a sample was exposed. Progressive annealing results in a shorter mean track length (l_m), and also causes the FT length distribution to become broader, thus increasing the standard deviation (σ). This was shown by e.g. Green et al. (1986) and Gleadow et al. (1983) for laboratory annealed apatites as well as for deep drill hole samples. Gleadow et al. (1986a) and (1986b) found that freshly *induced* fission tracks in apatite exhibit a narrow, symmetrical distribution (figure 2.9a) centered around a l_m value of 16.3 µm with a σ of 0.9 µm. *Undisturbed volcanic type* samples, i.e. all apatites which cooled down fast after formation (like volcanic apatites) and were thereafter never affected by thermal events, also show a narrow, symmetrical distribution (figure 2.9b), but with a shorter l_m of 14.0 to 15.7 µm and σ between 0.8 and 1.3 µm. *Undisturbed basement type* apatites are characterized by slow cooling, reflecting the stable tectonic conditions of a

cratonic basement for example, not affected by thermal events. Intrusive and metamorphic rocks slowly cooled to ambient surface temperatures are typical for this type. Apatites extracted from these rocks have a somewhat broader length distribution (figure 2.9c), negatively skewed (due to old tracks formed at transitional temperatures between total annealing and total retention), with l_m between about 12.5 and 13.5 µm and σ between 1.3 and 1.7 µm. *Mixed distributions* (figure 2.9e) are characteristic of apatites with a thermal overprint. FT populations have then accumulated during two (or more) events. When these populations show no resolution, they form a mixed distribution with l_m generally < 11.5 µm and σ around 2.0 µm. Apatites with mixed length distribution have a mixed age with no geological significance. When a mixed distribution is resolved into two distinct populations, a *bimodal distribution* (figure 2.9d) is obtained. It is typified by l_m < 13µm and σ > 2µm. These mixed distributions are more common in sedimentary apatites. An AFT age alone can be interpreted in a number of ways in most cases, but the confined track length distribution allows to place firm constraints on the meaning of the apparent age. Figure 2.10 gives an overview of l_m versus σ plots (Gleadow et al., 1986a).

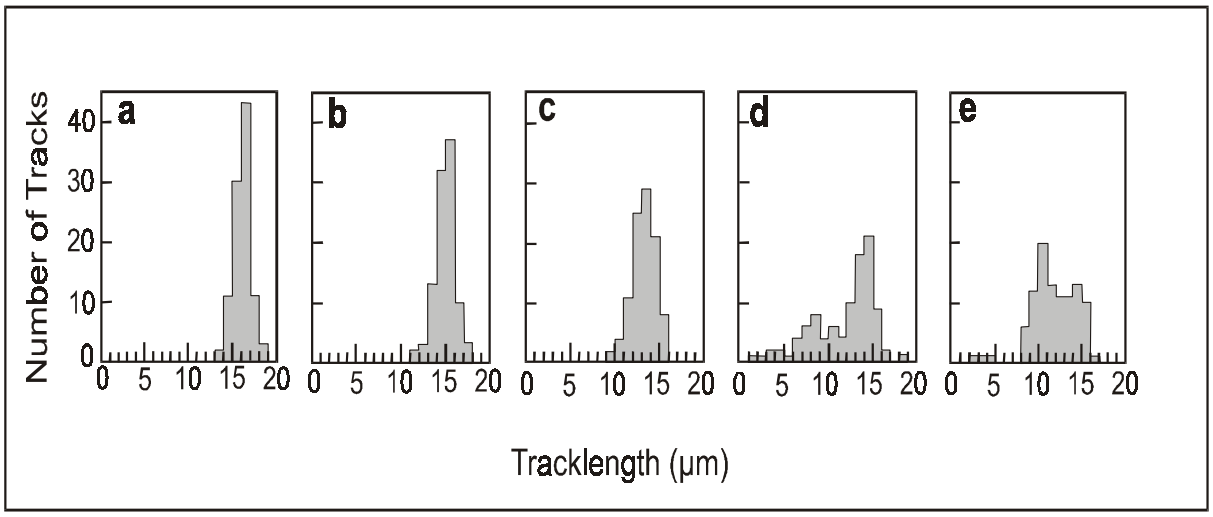

Figure 2.9: Track length distributions of confined fission tracks in apatite. (a) Fresh induced tracks, (b) distribution for so-called undisturbed volcanic type apatites, (c) undisturbed basement type apatites, (d) bimodal distribution due to two distinct and well-resolved length populations (linked to a thermal event) within an apatite sample, and (e) mixed distribution (after Gleadow et al., 1986).

The advances in the FT methodology on the issue of track length analysis confirmed and refined two important aspects in FT thermochronology. These are firstly the *closure temperature* concept and secondly, the *Partial Annealing Zone* concept.

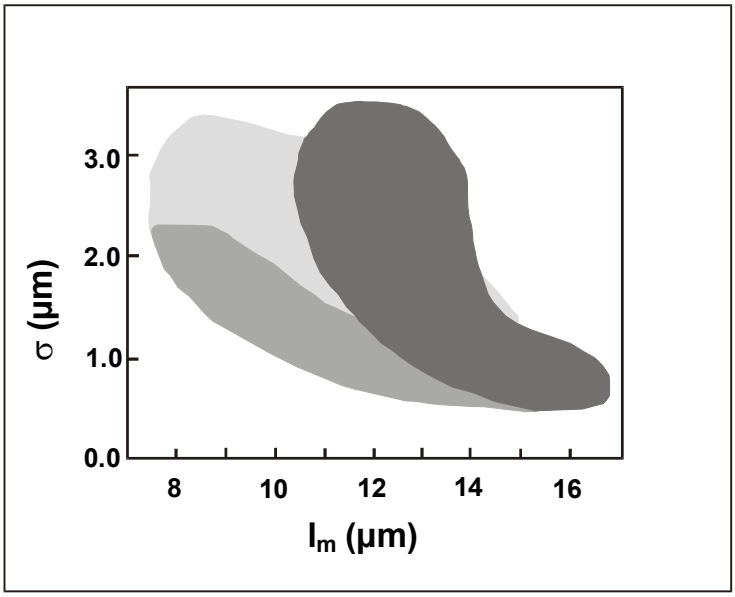

Figure 2.10: Mean track length (l_m) versus standard deviation (σ) trends for outcropping crystalline basement rock-apatites (dark grey shading), sedimentary apatites (light grey shading) and laboratory annealing data on Durango apatite (intermediate shading) (after Gleadow et al., 1986).

2.6.2. The closure temperature concept and cooling ages

Dodson (1973) and (1979) defined the closure temperature (T_C) associated with a steadily cooling isotopic system as the temperature at the time given by its apparent age. In this case, this is the apparent AFT age. Amongst others, James and Durrani (1986) devized a numerical method to calculate FT closure temperatures.

Most geochronological systems have a high- and a low-temperature state. In the high-temperature state, daughter products (in this case, fission tracks) cannot accumulate because diffusion (in this case, FT annealing) at these temperatures is too high. In FT terms, this high-temperature threshold is defined by the minimum temperature of total annealing (T_A) on a geological time scale. In the low-temperature state, loss of daughter products (annealing and shortening of fission tracks) is negligible and accumulation or retention is complete. This low-temperature state is defined to set in when a temperature threshold of total retention (T_R) is reached. In fact, for the case of fission tracks, because annealing continues even at ambient temperatures (Donelick et al., 1990; Vrolijk et al., 1992), total retention in geological conditions is not attained. Therefore Wagner and Van den haute (1992) defined T_R as the temperature above which the annealing rate increases markedly. There also exists a transitional state between both extremes, marked by a partial loss of daughter products (annealing and shortening of fission tracks). T_C is situated within this transition zone. In this respect, FT dating can be regarded to yield a cooling age, i.e. time passed since the mineral (apatite) cooled below a certain closure temperature. It should also be noted that $T_{A,C,R}$ are not a constant, but vary in function of the cooling rate; the higher this rate, the higher $T_{A,C,R}$. Because apatites in nature can in principle undergo multi-phase thermal histories in the upper parts of the Earth's crust, these samples are not

characterized by a single cooling rate. Wagner et al. (1977) defined the T_C for FT dating as the temperature at which 50% of the tracks are retained/annealed. For normal, constant cooling rates of around 10°C/Ma, Wagner and Van den haute (1992) listed several T_C-values cited in the literature for apatite and propose the value of 100 ± 20°C. These authors also cite values for T_R and T_A for apatite. These values depend on the composition (more specifically, the annealing properties) of the apatite and its cooling rate. In general, for the most prevalent types of apatite (fluorapatites) and given normal cooling rates, it is commonly accepted that T_R is about 60°C and T_A about 120°C to 125°C. These values are confirmed by borehole data (figure 2.4). AFT data in general will give information on paleotemperatures of up to 125°C (Gleadow et al., 1986a). Owing to these low crustal temperatures, AFT analysis has become an important tool in low temperature thermochronology.

2.6.3. The Partial Annealing Zone concept

Between the T_A and T_R temperature limits as defined above, a transitional zone exists where tracks are partially stable, i.e. they are formed and retained, but affected by temperature and hence shortened. In the geological environment, in the Earth's stable crust, these temperature states are reflected by three distinct depth zones. As described by the geothermal gradient, temperature increases with increasing depth. This results in a top crustal zone where fission tracks are considered stable and completely retained. This is called the *Total Retention Zone* (TRZ) or *Total Stability Zone* (TSZ). It is bounded by the ambient surface temperature at the top and an isotherm at depth corresponding to T_R as defined in the previous section (~60°C for apatite). Because of this retention, FT density from samples within this zone will increase with time. The lower crust bounded at the top by the isotherm corresponding to the total annealing temperature ($T_A \approx 120$°C for apatite) is the *Total Annealing Zone* (TAZ). Track accumulation is not complete in this zone. The crustal section between these two extremes (T_R and T_A) is called the *Partial Annealing Zone* (PAZ) or *Partial Stabilty Zone* (Wagner, 1972). The T_C isotherm is located somewhere in the centrally in the PAZ.

The *Apatite Partial Annealing Zone* (APAZ) is bounded by the ~60 and ~120°C isotherms. Given a normal geothermal gradient of about 30°C/km, this corresponds to the depth interval between 2 and 4 km in the crust (figure 2.11). Apparent AFT ages will consequently date the time at which the sample passed through the APAZ, and more specifically, through the T_C isotherm. Because in the APAZ tracks are partially annealed, they are shortened and the probability of intersecting the etched apatite surface decreases, hence the AFT age decreases and does not date the time at which bottom APAZ temperatures were reached. This prompted the use of the effective T_C concept corresponding to a 50% track retention isotherm in a stable crust (Wagner et al., 1977). This 50% value of Wagner et al. (1977) entails that $T_C \approx 90$°C in the APAZ for cooling rates of the order of magnitude of 10°C/Ma. The cooling age obtained in this manner can be interpreted by knowledge of the exact cooling history of the sample as it passes the APAZ; information which is contained in the length distribution. Of course independent geological information on the thermal history is of great help, but it may not always be available. In this respect four cooling models can be envisaged (Wagner, 1981; figure 2.11).

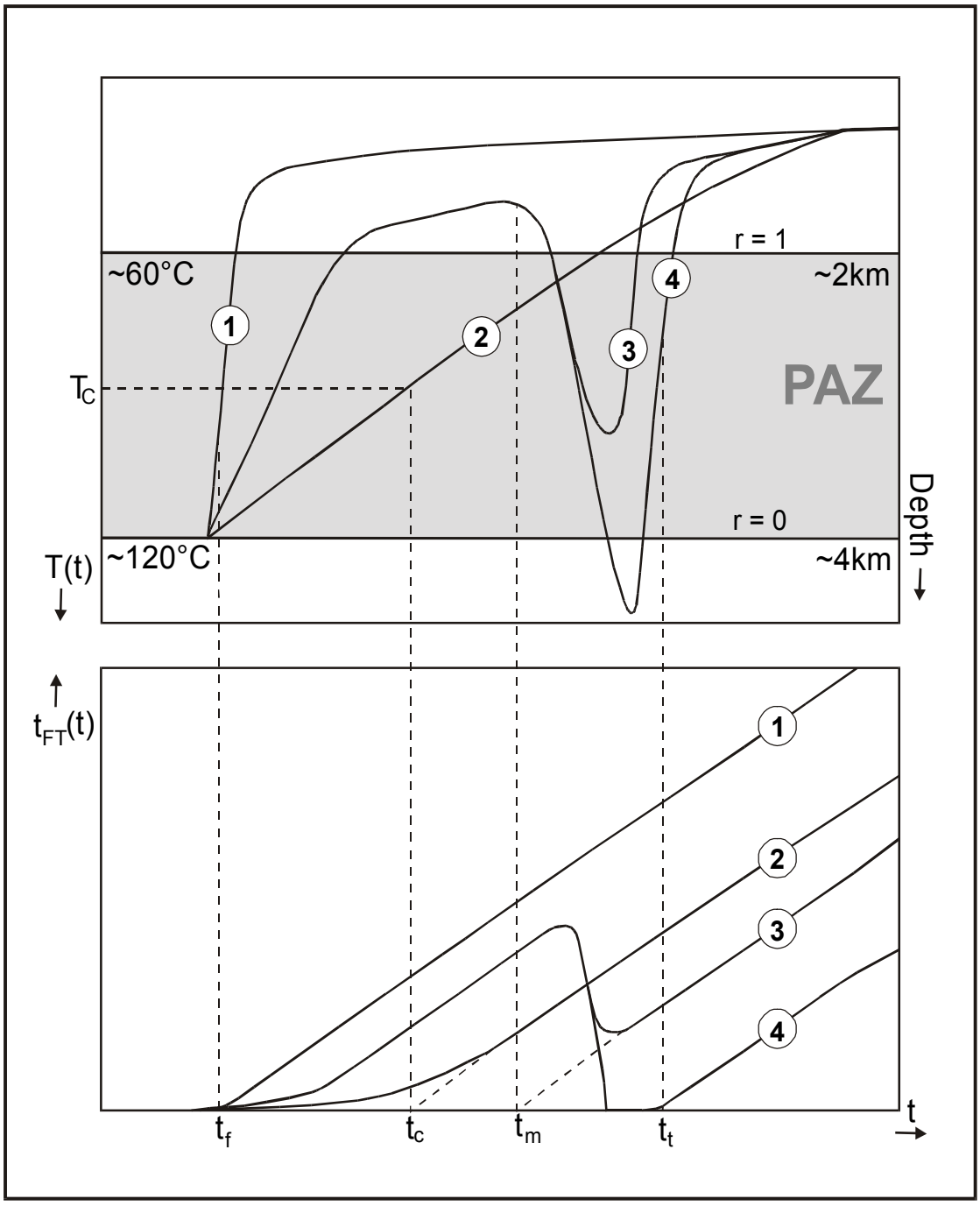

Figure 2.11: Potential cooling paths, T(t), and resulting apparent AFT ages of rocks cooling down through the Partial Annealing Zone (PAZ). The lower PAZ boundary for apatite, under which retention is 0% (r = 0), is at about 120°C, or at about a depth of 4km in the crust, given a geothermal gradient of 30°C/km. The upper limit, above which retention of tracks is 100% is at 60°C or 2 km depth. The closure temperature, T_C, lies in the PAZ, around 100°C. (1) Rapid cooling through the PAZ resulting in a formation or "fast cooling event" age t_f. (2) Slow cooling through the PAZ and T_C, recording a cooling age, t_c. (3) A moderate thermal overprint, taking apatites back in PAZ temperatures without erasing al pre-existing tracks, leading to a geological insignificant mixed age t_m. (4) Intense thermal overprint, resetting the AFT clock completely; fast cooling afterwards registers the time of the thermal event, t_t.

(1) In the case of fast cooling through the APAZ, an apatite formation age (t_f) can be determined when the apatite crystallizes from a melt as in volcanic apatites for example (used e.g. in tephrochronology). In general this case will date the rapid cooling event responsible for the youngest movement of the apatite from the APAZ bottom through the entire APAZ (figure 2.11, case 1). The rapid cooling implies an insignificant amount of partial track annealing. These samples will yield an undisturbed volcanic type AFT length distribution as was defined by Gleadow et al. (1986a) and (1986b).

(2) When the apatite sample cools down slowly through the APAZ more tracks are partially annealed and the time when the apatite sample passed the T_C isotherm in the crust gives the cooling age (t_C) of the apatite (figure 2.11, case 2). This thermal history will correspond to an undisturbed basement type length distribution. It is typical for crystalline basement rocks, where it may be caused by denudation of overlying strata for example.

(3) When the sample experienced a short thermal event that was not sufficient to reset the AFT thermochronometer completely, the thermal overprint will result in mixed ages (t_m) without geological significance and a mixed or bimodal length distribution (figure 2.11, case 3). This thermal event can be linked to sedimentary or tectonic burial, circulation of hot fluids or even a meteorite impact (Gleadow et al., 1986b).

(4) When this thermal event is intense enough, it might reset the AFT thermochronometer completely by annealing all pre-existing tracks and hence erasing the pre-existing thermal record of the sample. If cooling after the thermal event is fast enough, a thermal age (t_t) or the age of the thermal event will be obtained (figure 2.11, case 4). If it is followed by slow cooling, a cooling age as outlined in (2) is dated.

Because the above described concepts are dependent on the cooling rates and the apatite annealing behaviour, there is no discrete closing temperature at which fission tracks suddenly become retained in apatite (or other minerals for that matter). But for more or less linearly cooling systems, an effective AFT closure temperature of 100 ± 20°C is a reliable assumption (Wagner and Van den haute, 1992). For more complex cooling systems, the PAZ concept forms a firm base for AFT data interpretation. In this work we use an APAZ bounded by the 120 and 60°C isotherms, but reported values range from 120 to 140°C for the high temperature limit and 40 to 70°C for the low temperature limit (Wagner and Van den haute, 1992).

2.7. Geological interpretation of apatite fission track ages

2.7.1. Cooling through denudation

As outlined above (and disregarding the possibility of a mixed age), an AFT age (t_{AFT}) will represent a cooling age of the mineral and hence of its host rock. Its value will give an immediate estimate of the mean cooling rate (u_c) the sample experienced:

$$u_c = (T_C - T_o)t_{AFT}^{-1} \qquad 2.50$$

Where T_C is the effective closure temperature at cooling age t_{AFT}, and T_o is the ambient surface temperature of the sample.

When investigating orogenic systems, tectonic uplift is a main cause of cooling, but uplift alone does not cause cooling as the thermal structure of the rock column remains unaffected. It is actually denudation of the uplifted rock mass that disrupts the isotherms and causes the cooling. This denudation can be of erosional or of tectonic origin. However, uplift does not necessarily imply immediate denudation, and vice versa (Summerfield and Brown, 1998). However, when there is reason to believe that uplift is followed by denudation at a comparable rate, and provided the geothermal gradient (dT/dx) stays constant, an uplift rate (u_x) can be established:

$$u_x = u_c(dT/dx)^{-1} \qquad 2.51$$

In this case t_{AFT} will date the uplift of the rock column as it passed through the T_C isotherm. On geological time scales there might exist a non-negligible time lag between uplift and uplift-induced denudation and subsequent relaxation of the isotherms (figure 2.12). When there is no independent geological control on the fact whether there was an uplift event in the investigated region, it is much safer to interpret AFT ages in terms of cooling and denudation rather than uplift. Conversely, heating events may be interpreted by tectonic burial due to thrust movement or, in a sedimentary environment, by subsidence and sedimentary burial. Because the study areas dealt with in this work are located in active orogenic belts, the interpretation of AFT data will specifically focus on tectonically induced denudation and cooling.

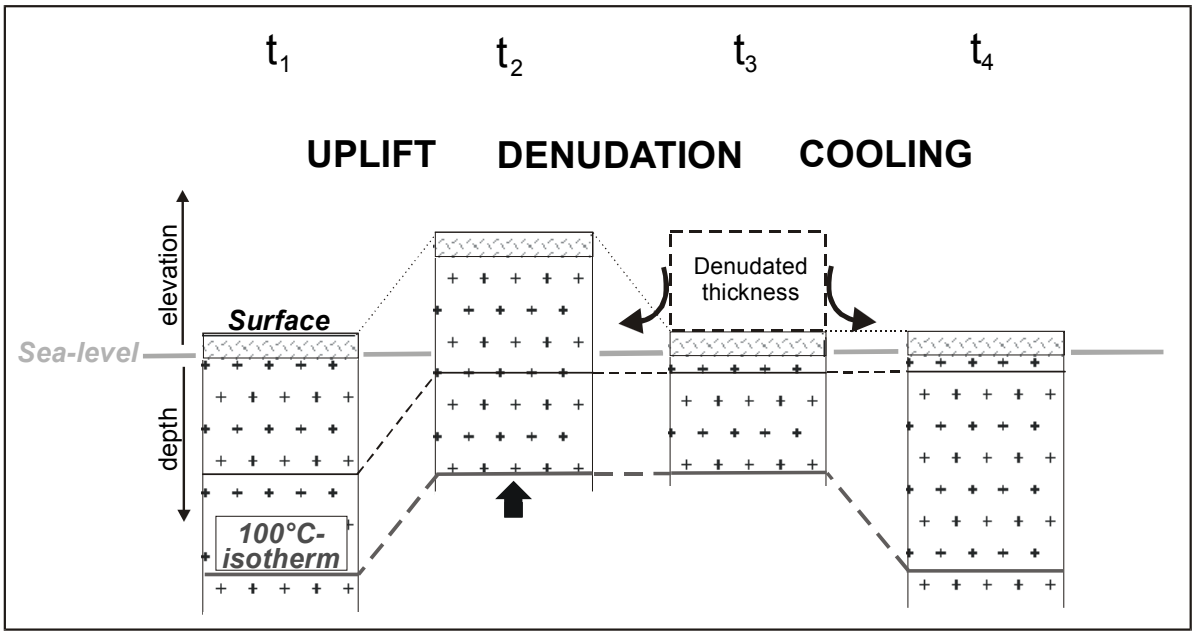

Figure 2.12: Cartoon illustrating the relationship between uplift, denudation and cooling of a crustal column with respect to the sea-level (in absence of isostatic adjustment).

2.7.2. Denudation, exhumation and uplift

From the previous it has become obvious that AFT cooling ages, even obtained in active mountainous regions, should not automatically be interpreted as being the result of tectonic uplift. In the past it has been assumed on several occasions that all episodes of accelerated denudation arise as a direct, and essentially geologically contemperaneous, response to tectonic uplift events.

The word *uplift* refers to an opposite displacement of rocks or a surface with respect to the gravity vector in a fixed reference framework. The earth's geoid for example, or the mean sea level, provided one corrects for eustatic sea level changes. In a tectonic context, a surface is the interface between rock and air (or water) of at least 10^3-10^4 km^2 according to England and Molnar (1990). *Surface uplift* and r*ock uplift* refer to, respectively, vertical displacement of the earth's surface or of rocks relative to the earth-geoid or mean sea level framework. Rock uplift can be either driven by tectonic forces or isostasy. Surface uplift refers to changes in mean surface elevation over an extensive area (10^3-10^4 km^2). Displacement of rocks with respect to the surface is called *exhumation* (e.g. England and Molnar, 1990; Abbott et al., 1997) or *denudation* (Summerfield and Brown, 1998), with the latter term preferred in FT thermochronology. Sometimes differentiation is made between both terms, in the sense that denudation refers to the vertical component of rocks moving to the surface, while exhumation is a vector in the sense of the actual rock mass movement. Both vectors do not automatically have the same sense, as is illustrated in figure 2.13.

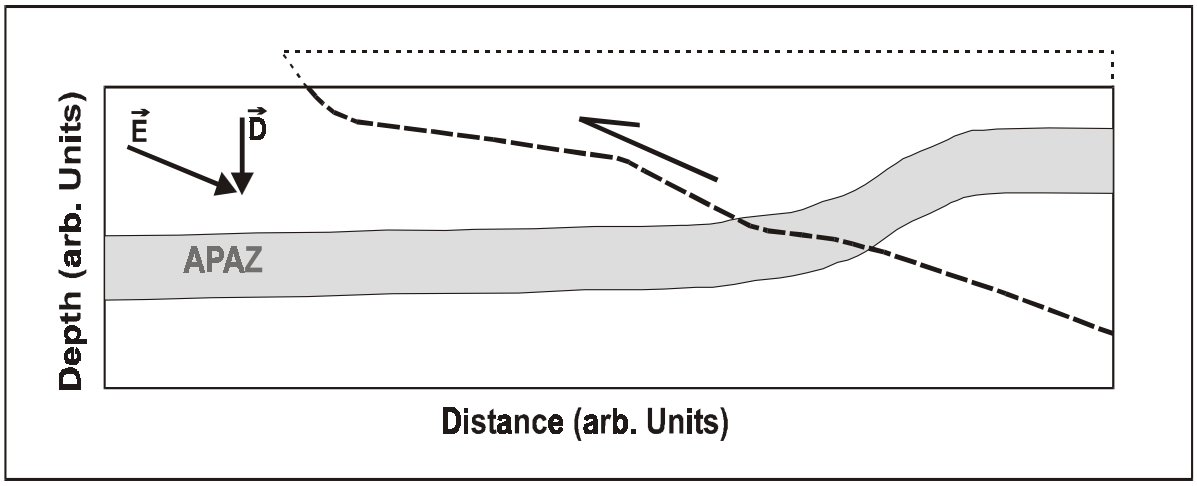

Figure 2.13: Cartoon showing the difference between the exhumation vector (E) and the denudation vector (D). Denudation is (only) the vertical movement of rocks with respect to the surface. The exhumation vector can be inclined with respect to the surface as illustrated in the figure by a thrust nappe movement. Depth and distance are in arbitrary units.

Surface uplift is the main factor measured in order to retrieve information about the tectonic forces acting in mountain belts (England and Molnar, 1990; Abbott et al., 1997). *Tectonic uplift* is used when the driving force for the uplift movement is of tectonic origin. In the majority of the cases tectonic uplift is achieved by crustal thickening with a horizontal shortening obeying plate tectonic rates (Harrison, 1994). All tectonic processes are driven by the force of gravity in the presence of density differences. At the largest scale of plate motion, this is manifested by circulation and convection in the mantle (England and Molnar, 1990). These density differences are compensated isostatically, and the consequent lateral variations of the average vertical normal stress on vertical planes are referred to as the *driving force* (England and Molnar, 1990).

Measuring rock uplift involves measuring the change in vertical position of a certain point with respect to the fixed reference level. This can be done using GPS data for example. A cooling age, measured with a geothermometer such as AFT analysis, on the other hand, gives information on the timing of denudation, when the rocks move relative to the surface, through the isotherms in the crust. These relative movements can still be triggered by tectonic uplift, but other explanations are also possible. For example, climatically controlled base level drops by drainage pattern shifts or eustatic pulses, or extensional tectonics and downfall of blocks are just as reasonable (see figure 2.14). Measurement of tectonic surface uplift rates however can only be achieved in rare cases (Abbott et al., 1997).

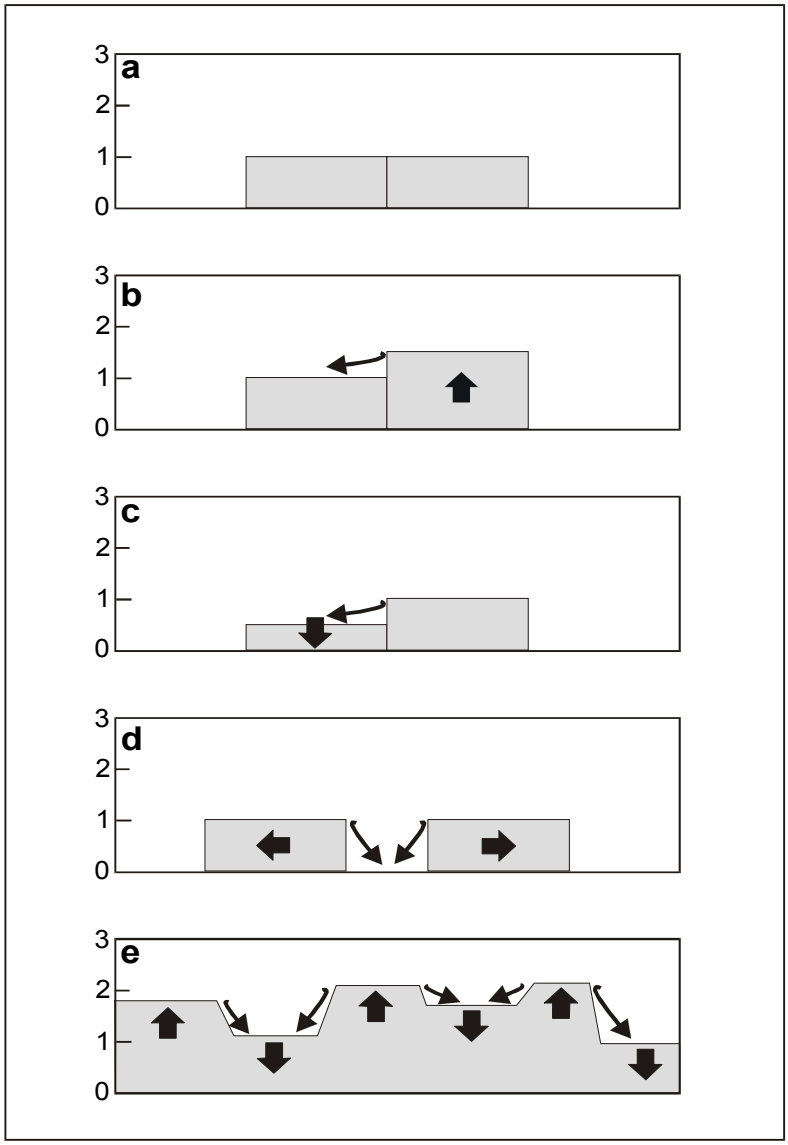

Figure 2.14: Uplift and denudation in a vertical reference frame (arbitrary units). (a) Initial situation of two different tectonic blocks (after Summerfield and Brown, 1998). (b) Uplift and denudation of one block with respect to the fixed reference frame. (c) Base level drop (e.g. due to downfall of a block) resulting in denudation of the adjacent block with same vertical dimensions as the previous case. (d) Extensional tectonics (e.g. a rifting process) can result in base level change and denudation of both adjacent blocks. (e) differential uplift (e.g. horst-graben structure) results in different base levels and internal drainage of parts of the uplifted terrain.

Denudation entails the removal of surface material by means of climatic or tectonic erosion. Removal of this surface material implies removal of mass from the crustal section of the lithosphere, creating a density disequilibrium that is then compensated by isostatic rebound. Hence it does not necessarily cause the mean surface elevation to depart from its isostatically balanced level. Denudation rates therefore tell nothing about surface uplift rates (England and Molnar, 1990). Moreover, high elevation in itself is not a major influential factor for high denudation rates. Actually the elevation differences seen over a certain horizontal distance (*relief*) play the key role in this issue. Relief is chiefly dependent on fluvial or glacial incision and hence is also climatically controlled (Sugai and

Ohmori, 1999). On the other hand, changing relief in combination with isostatic rebound may well induce so-called isostatic uplift of mountain summits or ridgetop uplift (figure 2.15). For example, this process is responsible for as much as 20 to 30% of the uplift of peaks in the Himalayan orogen (Montgomery, 1994). The isostatic component is due to erosional unloading of a certain rock column and can be specifically related to river incision in many cases, which in its turn can be linked to climatic changes sometimes induced by the growing orogen itself (Willett, 1999; Peizhen et al; 2001; Hartshorn et al., 2002).

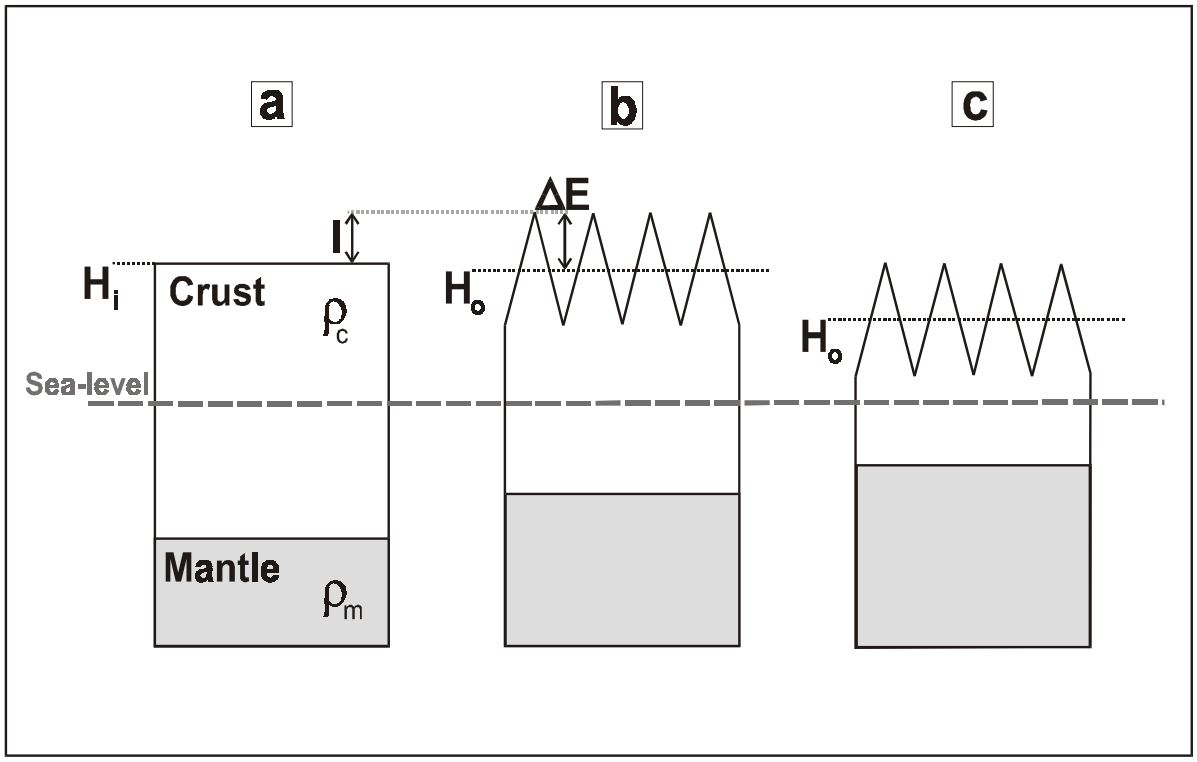

Figure 2.15: Isostatic uplift of mountain peaks in response to valley incision (after Montgomery, 1994). (a) Initial situation of a lithospheric column with crustal material, having a density ρ_c, and a mantle section with density ρ_m. Its initial elevation above sea level is H_i.(b) Valley incision (ΔE) lowers the mean elevation to H_o, but mountain peaks rise above H_i due to isostatic rebound (I). (c) Further erosion, which does not alter the landscape topography or relief, lowers both mean elevation as it does mountain peaks.

In general we can evaluate the contribution of the isostatic rebound as (Brown, 1991):

$$\vec{\Delta H} = \vec{U}_T + \vec{I} + \vec{\Delta E} \qquad 2.52$$

$\vec{\Delta H}$ represents the absolute elevation difference between the initial situation (prior to tectonic uplift) and the present situation (after tectonic uplift). $\vec{U}_T$ is the tectonic uplift vector, perpendicular to a reference level (the geoid), having a positive sense upward. $\vec{I}$ is the isostatic rebound component, also positive upward. $\vec{\Delta E}$ is the denudation vector, which has a positive sense downwards. Note that the initial and present elevations can be measured with respect to sea level, but that eustatic pulses may have occurred (figure 2.16). The tectonic uplift component can however only be resolved if independent evidence for the initial mean surface elevation is available, for example by constraints

from paleobotanical data or the presence of marine sequences in the rock column under investigation (Brown, 1991).

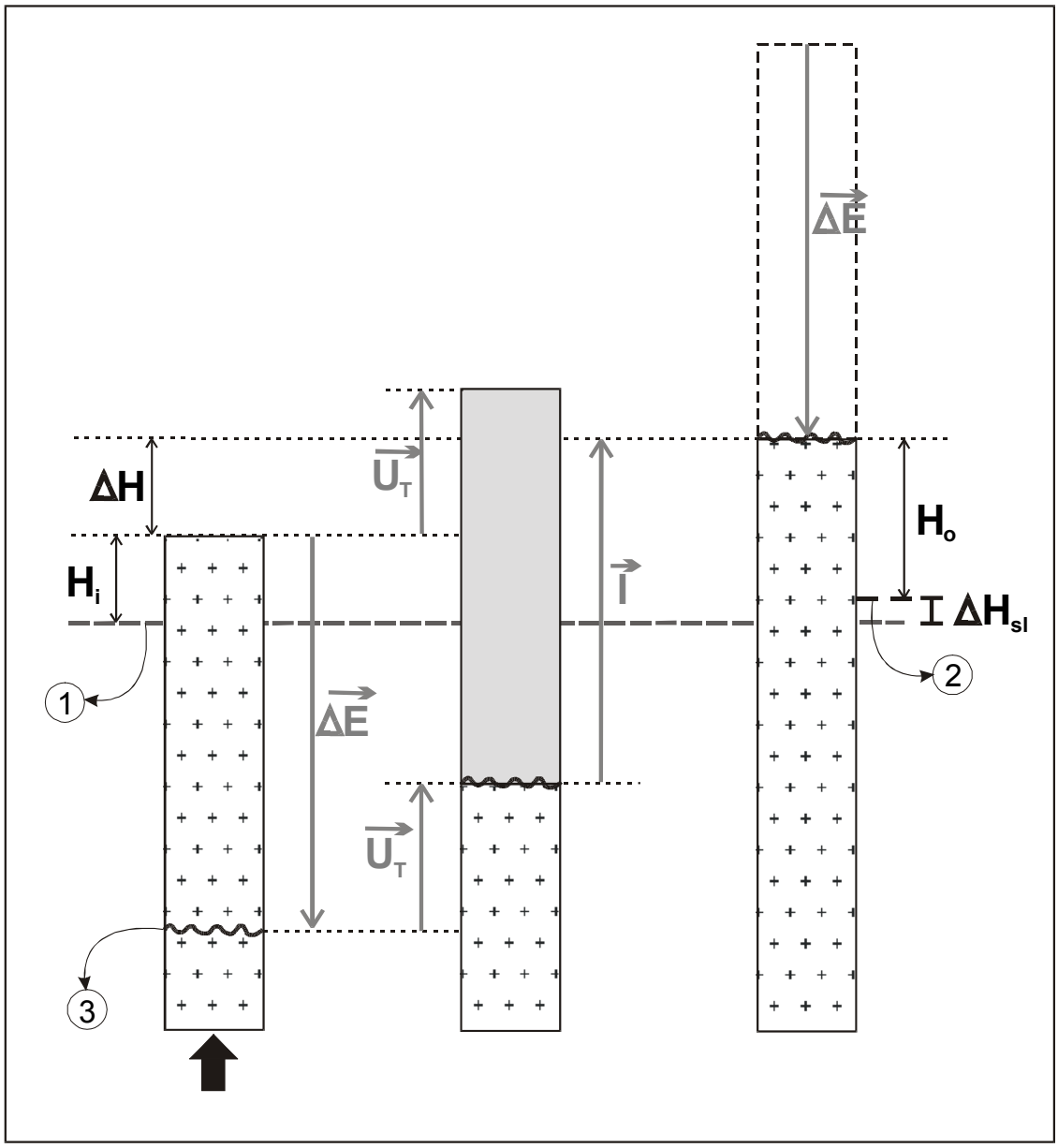

Figure 2.16: Backstacking concept showing the relationship between tectonic uplift (U_T), denudation (ΔE) and isostatic response (I) as described by Brown (1991). H_o is the present-day elevation of a surface (3) with respect to the present sea level (2). H_i is the paleo-elevation of the rock column with respect to the palaeo-sea level (1). ΔH is the elevation difference between the palaeo-surface and the present surface, ΔH_{sl} is a sea level change (see text for further elaboration).

Furthermore there is an additional denudational (sometimes called, erodibility) response to lithology to take into account. A further complication lies in the fact that many of the processes mentioned above are in an intricate dynamic interaction; large scale surface uplift for example may cause climatic changes, which in turn will change erosion rates and hence denudation rates. Uplift of the Tibetan Plateau is a marked illustration of this fact, imposing a drastic change of atmospheric

circulation patterns in Asia, resulting in a wet monsoonal climate in South East Asia and arid conditions in Central Asia.

Clearly mountain belts represent uplifted surfaces of the earth's crust. They can obviously only attain a high mean elevation if there is a certain time lag between an crustal uplift and a responding denudation. In this respect orogens may exhibit a varying morphological sensitivity, with broader ranges exhibiting longer time lags between uplift and denudation response because larger parts are internally drained (Summerfield and Brown, 1998). In any case, major tectonic events are often followed by regional episodes of accelerated erosion (e.g. Willett, 1999; Peizhen et al., 2001; Braun, 2002).

This implies that tectonic interpretation of AFT data in terms of uplift and mountain building is not a straightforward procedure and should involve incorporation of additional geological data. However it is clear that AFT data are a potentially useful tool in various fields of earth sciences, with climate and landscape evolution and assessing tectonic hazards being a promising new application of AFT as a thermchronometer (Burbank and Anderson, 2000). Table 2.1 places the AFT thermochronometer in the broader perspective of low-temperature thermochronology.

Table 2.1: List of isotopic systems applied to several minerals used in low-temperature thermochronology. T_C refers to their closure temperature.

Isotopic System	Mineral	T_C (°C)	Reference
$^{40}Ar/^{39}Ar$	Muscovite	360 ± 10	McDougall and Harrison (1988)
	Biotite	300 ± 20	
	K-Feldspar	150 - 300	
FT	Sphene	300 ± 20	Wagner and Van den haute (1992)
	Zircon	220 ± 20	
	Apatite	*100 ± 20*	
(U/Th)-He	Zircon	180 ± 20	Wolf et al. (1998)
	Apatite	60 ± 20	

2.7.3. Steady state isotherms and topography

As explained elsewhere, thermochronometers, like the AFT clock e.g., will give a cooling age, i.e. the time at which a rock column moved in the crust relative to a thermal reference frame. More specifically, the time when these rocks passed a certain retention threshold (the closure temperature isotherm) will be dated. The thermal reference frame is a set of isotherms within the crust, described by the geothermal gradient and with an upper boundary fixed to the earth's surface, described by the surface topography. During a period of relative tectonic quiescence and erosional stability, the surface topography typically has a regional wavelength and amplitude such that even low-temperature steady-state isotherm-planes in the crust are relatively parallel to the surface. AFT ages

will decrease with increasing depth through the APAZ until a zero-AFT age is obtained around the 120°C isotherm. The AFT ages will then typically depict a PAZ profile as will be explained in the next section. According to O'Sullivan and Brown (1998) there might be a non-negligible effect of surface cooling on the position of the isotherms with respect to that surface, that may have a significant influence on the AFT ages of outcrop samples. These authors infer Miocene climatic cooling to interpret AFT cooling data obtained from Alaskan apatite samples. Considering the uncertainty of the annealing equations in respect to recent cooling events in thermal history reconstruction (see section 2.5), the Alaskan "cooling" might be based on a modelling artifact. Whatever the correct interpretation, these authors have shown the sensitivity of the structure of low-temperature isotherms in the upper crustal section.

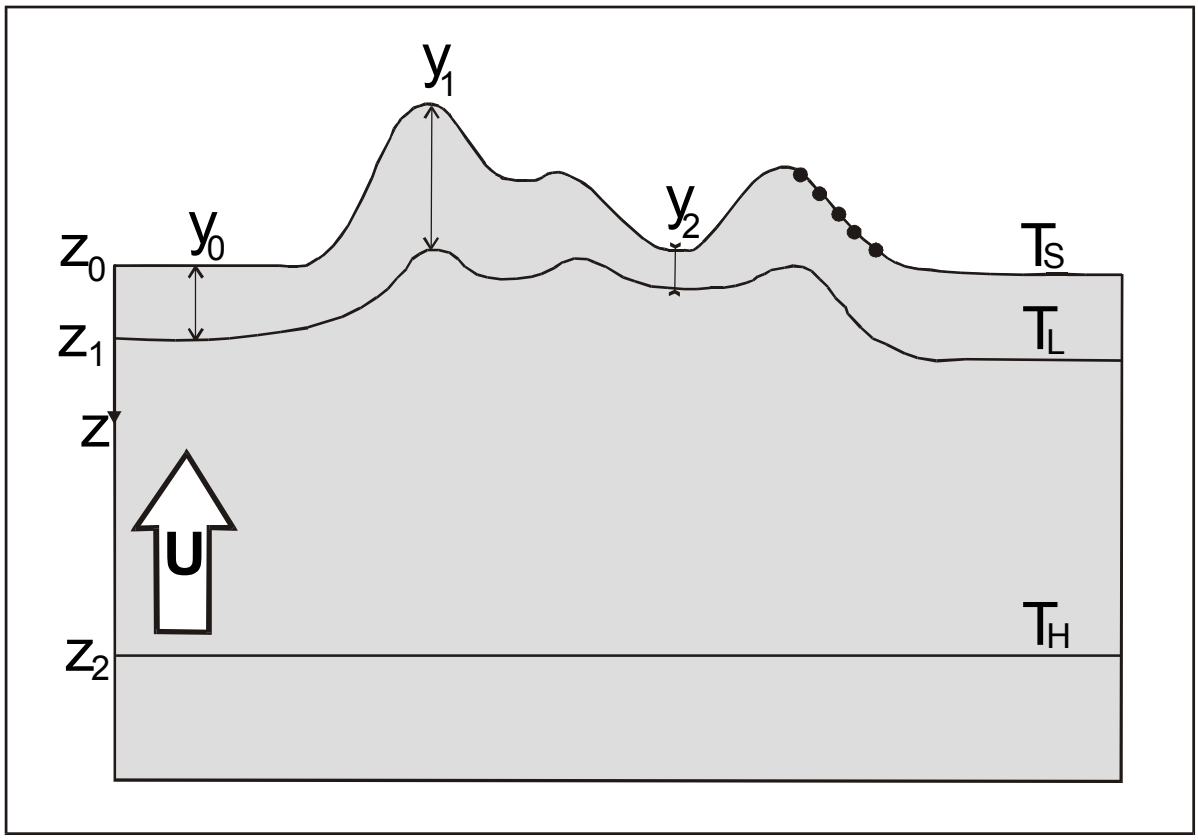

Figure 2.17: Acive erosion, possibly due to an uplift event (U) creates topography, at elevation z_o and with surface temperature, T_S. This will perturbes the isothermal structure of the crust, especially affecting low-temperature isotherms, T_L (at depth z_1), which will follow the surface topography in a dampened fashion. Under peaks (y_1) the isothermal structure will be stretched with respect to the normal situation (y_o), while under valley floors (y_2) the isotherms are condensed. High-temperature isotherms (T_H) deeper in the crust (at depth z_2) will remain unaffected. A vertical profile of AFT samples (black dots) for example will hence be vertical to the isotherms instead of cross-cutting them as would be the goal of vertical AFT profiling.

When however there is no steady state situation and hence no balance between erosion and rock movements (a possible effect of tectonic activity e.g.) the eroding topography will have an important influence on the steady-state isotherms (Stüwe et al., 1994). The developing topography will perturb the isotherms by diffusion advection of heat. This thermal perturbation by the finite topography will

decrease exponentially with depth (Braun, 2002) and hence especially the low-temperature isotherms will be affected. They will follow the surface topography in a dampened fashion (stretched under hills or mountainpeaks and compressed under valley floors for example) while deeper in the crust the isotherms will retain their flat planar shape (figure 2.17). It is then clear that this issue is of significance for AFT data interpretation. In particular, using a low-temperature thermochronometer as AFT and/or when in fast eroding areas, a plot of age versus elevation or depth (see next section), can significantly overestimate denudation rates according to Stüwe et al. (1994), Brown and Summerfield (1997), Moore and England, (2001), and Braun (2002). Braun (2002) argues that the sensitivity of the slope in age-elevation plots to relative relief change is a strong function of the wavelength of topography and the rate of surface landform changes. Stüwe et al. (1994) modelled that the perturbation affect for AFT data (perturbation of the 100°C isotherm) becomes significant (up to 1 km) for denudation rates larger than about 500 to 1000 m/Ma, and for topography with amplitudes exceeding 3km and wavelengths exceeding 20km.

2.7.4. Horizontal profiles and age-elevation profiles

In the thermo-tectonic application of the AFT method, sampling is done over a widespread region, preferably along horizontal profiles perpendicular to the regional structural features. This sampling strategy may yield different AFT data, even when sampled at more or less similar elevations. Different AFT ages may then be either interpreted as the result of differential denudation, possibly due to differential movements along certain fault planes, possibly even differential uplift. An alternative interpretation is based on regional variation in the geothermal palaeogradient (figure 2.18).

Age-elevation (or age-depth profiles) are also a useful tool in AFT thermochronology. Usually a geological age increases with depth, as is the case for a stratigraphic column for example where the stratigraphic age increases with depth (the principle of superposition). However, FT ages from crystalline terranes behave conversely in most cases; they decrease with depth, or increase with elevation as apatites higher in the rock column cooled down through the T_C isotherm earlier than those in lower positions. This trend can hence be clearly observed in vertical (depth or elevation) age profiles. In FT thermochronology it can therefore be useful to follow a double sampling strategy, namely to sample both vertical and horizontal profiles. A vertical profile can be sampled from a deep drill hole, or it can be an elevation profile where large elevation differences exist over relatively short horizontal distances ensuring that all samples belong to the same tectonic block.

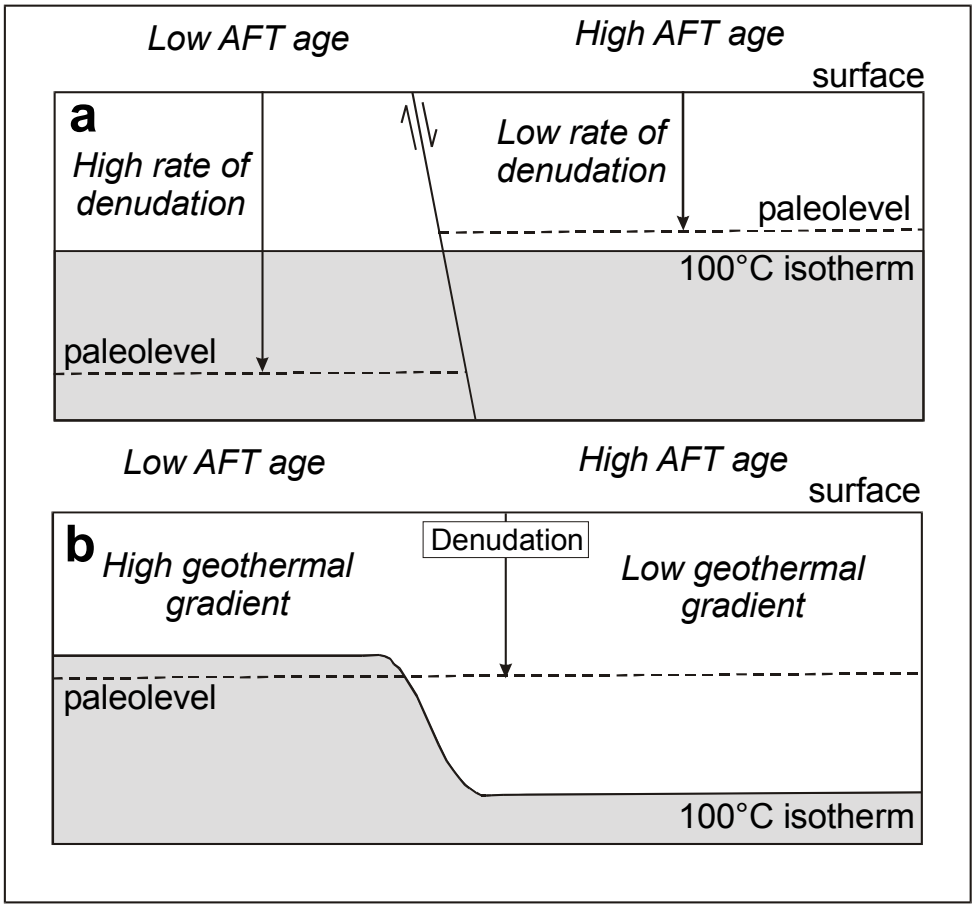

Figure 2.18: Varying AFT ages from horizontal profiles can be interpreted in a tectonic fashion (a) caused by differential denudation, possibly linked to differential fault movements. They can also be explained by a regional differential geothermal gradient (b).

Plotting AFT age vs. elevation in an orogenic terrane will yield a linear trend of increasing age with increasing elevation in most cases. The slope (θ) of the curve is a direct estimate of the denudation rate in the study area over the time interval given by the AFT age. Although AFT data may overestimate the rate in certain cases as discussed in the previous section. Given the geothermal gradient (which is assumed constant), this can be linked to a cooling rate. Such a *denudational profile* develops during steady cooling/denudation of the vertical rock column (figure 2.19a). The AFT clock starts running when the rocks pass through the T_C isotherm, whereby this isotherm is fixed at a constant depth. When the cooling event is rapid, the cooling rate will induce a steep slope for the vertical AFT age profile. When the slope is steep enough, in other words, when the cooling is rapid enough, a near vertical line can be obtained in the age-elevation plot (figure 2.19b). The intercept with the age axis in this case will approximate the cooling event (t_f) of the apatite, or more generally speaking, the rapid cooling age as outlined in case (1) of section 2.5. Steady, slower cooling or rapid cooling can be implied independently from the AFT length data (Gleadow et al., 1986a and 1986b) as was described in section 2.3. After a period of stability following a rapid uplift event, and provided that there is no subsequent cooling or denudation, in other words, when the region is in thermotectonic stability, a typical *PAZ profile* can be observed. Characteristic is a steeper upper part of more or less constant age and a less steep lower portion under the break-in-slope, approaching a

zero AFT age (figure 2.19c). The PAZ is bordered in the profile by the zero AFT age and the break-in-slope.

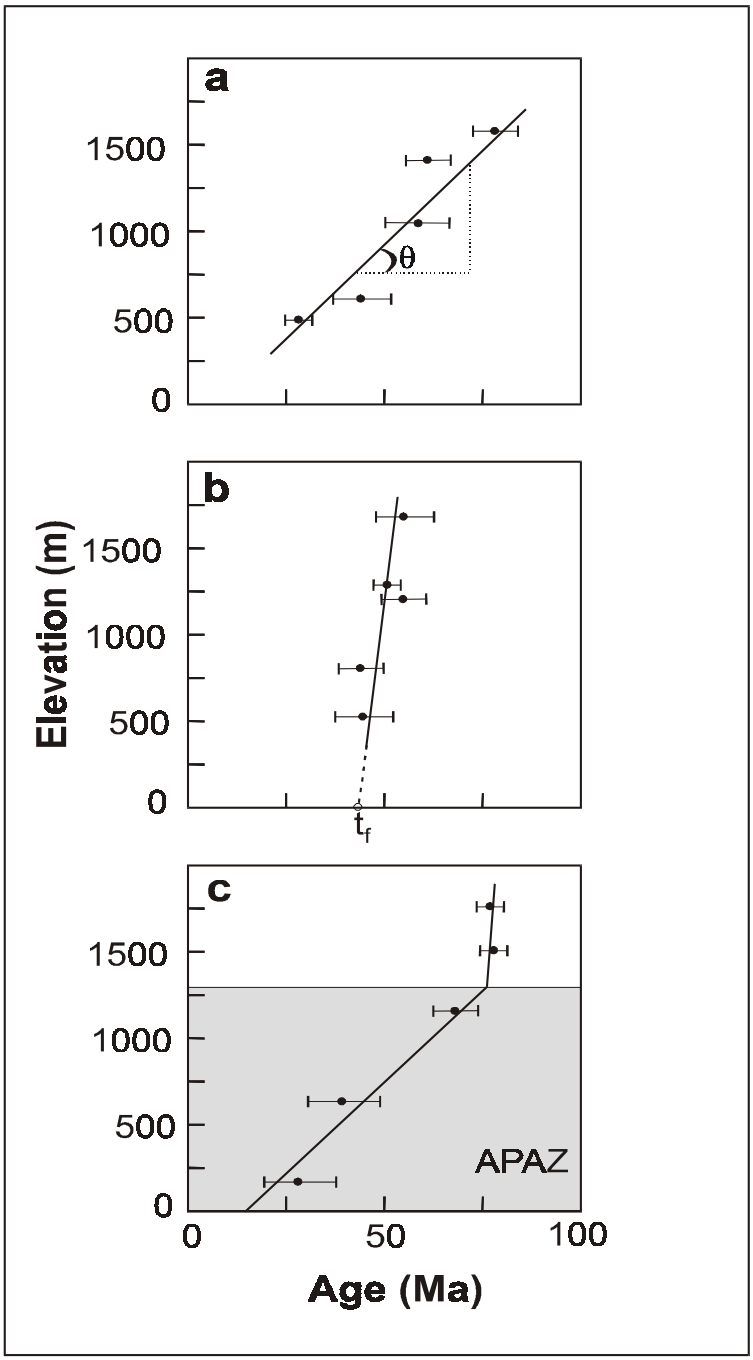

Figure 2.19: (a) Age-elevation plot giving a denudational profile. The slope (θ) can give a true or apparent denudation rate (see text for discussion). (b) In case of rapid cooling the slope in an age-elevation plot will be steep, almost vertical. The intercept with the time-axis in this case will yield a formation age (t_f). (c) When the crust is in thermal stability (tectonic and denudational quiescence) a PAZ profile develops in an age-elevation (or depth) plot; an upper part reflecting the Total Stability or Retention Zone for fission tracks, and a lower zone of decreasing FT ages in the PAZ as track annealing reaches higher and higher degrees.

In most cases however, changes in thermal regime due to thermal events will affect the age profile and more complex trends will develop. In some situations these can still give valuable thermchronological information. Wagner and Van den haute (1992) give an overview of resulting age-elevation plots from possible combinations of thermal events. One is of particular interest to this study. It is the case of the so-called "uplifted PAZ profile" (Gleadow and Fitzgerald, 1987; Wagner et al., 1989). The designation "uplift" to AFT cooling data of course should be approached with caution as it is actually denudation that causes the cooling under constant geothermal conditions.

The "uplifted PAZ profile" is created in a two-stage cooling history (figure 2.20). A first stage is one of thermotectonic stability that allows a typical PAZ profile to develop (figure 2.19c). In a second stage a cooling event sets in, resulting in a new PAZ within the crust and a shift of the former PAZ profile upwards in respect to the new, present PAZ. This relative upward shift is in fact a downward shift of the crustal isotherm-structure linked to thermal and/or tectonic events. In the case of tectonics, denudation, possibly induced by relative surface uplift can be responsible for the cooling. The fact that the "uplifted PAZ profile" is observed, does however imply that denudation has not been sufficient to have removed the entire section of the ancient PAZ profile and can hence imply a net surface uplift. So, depending on the amount of denudation and the intensity and timing of onset of the younger cooling event, lower parts of a fossil PAZ can presently be observed. Rocks with resident apatites at the boundary between the former PAZ and TAZ (having a zero AFT age at the time when the former PAZ conditions were in place) now, in the present conditions, are able to retain fission tracks. They are then located within the present PAZ or even in the TRZ. The zero AFT age adapted to the new conditions will be achieved in apatites further down the rock column in respect to the former zero AFT age apatites. In this manner it is possible to distinguish two PAZ intervals (a fossil and a present PAZ) in an age-elevation plot, each bounded by a break-in-slope in the plot (see figure 2.20). At present conditions that could mean that a fossil PAZ signature can be observed in rocks at a certain elevation, while the present PAZ would be observed at depth. Each section of the age-elevation plot will have experienced a different portion of the total cooling history and samples from these sections will hence possess a characteristic AFT length distribution.

Gleadow and Fitzgerald (1987) and Fitzgerald and Gleadow (1990) observed the base of a fossil PAZ in apatite samples from the Transantarctic Mountains (figure 2.20). Their age-elevation profiles are composed of a lower, steeper part, starting at around 50 Ma, and characterized by a narrow AFT length distribution with mean lengths above 14 μm, and an upper, more gently sloping part with a broader length distribution and mean length in the order of 12 to 13 μm. These authors interpreted the lower section as reflecting a Cenozoic rapid uplift-induced denudation of the Transantarctic basement. The upper section is believed to display a characteristic (fossil) APAZ signature with mixed AFT ages and length distributions. The break-in-slope between both segments is interpreted as the base of the fossil APAZ and approximating the onset of what Fitzgerald and Gleadow (1990) call "uplift" of the Transantarctic Mountains. In general, the break-in-slope occurs at approximately the time at which cooling began (Brown, 1991). Later these "uplifted PAZ profiles" were also recognized and described in other study areas (e.g. Fitzgerald et al., 1995, in the Alaska range and Fitzgerald et al., 1999, in the Pyrenean orogen).

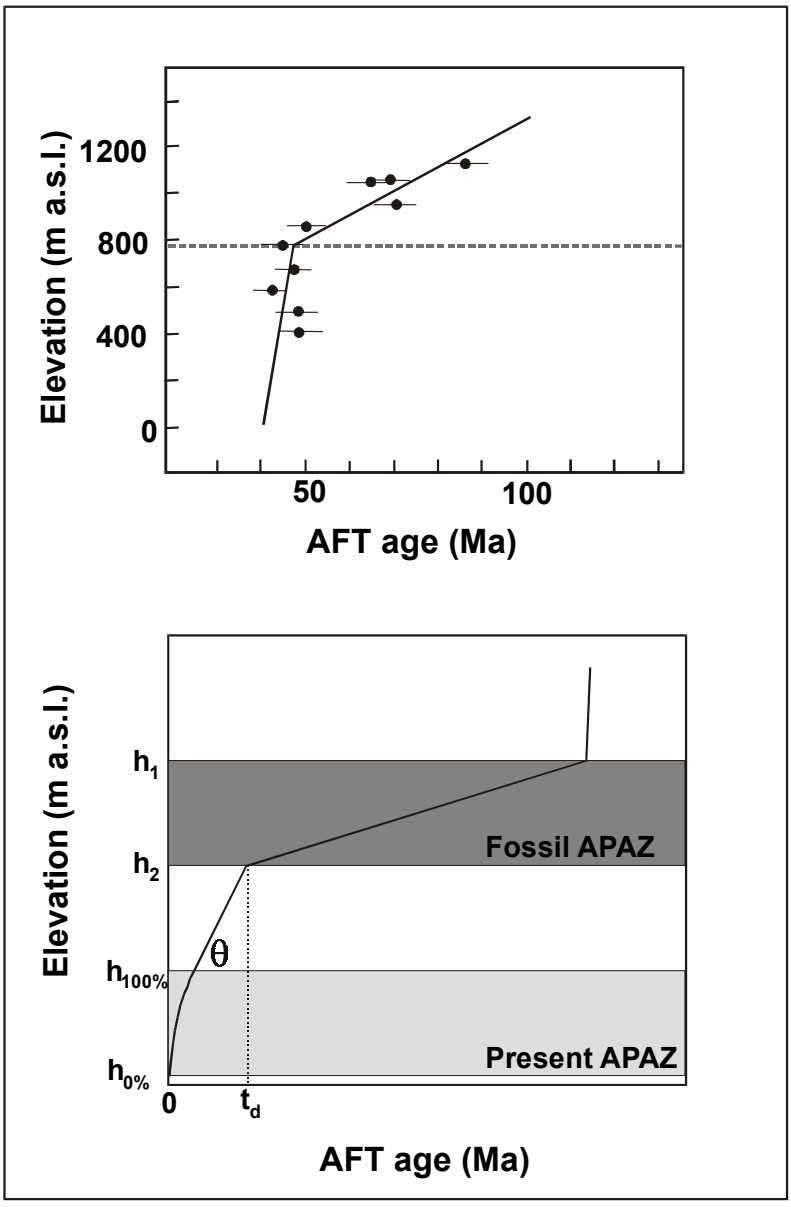

Figure 2.20: Top: AFT age-elevation profile from Gleadow and Fitzgerald (1987) from samples from the Transantarctic Mountains. A clear break-in-slope is observed around 50Ma, dividing the plot in a steep lower part and a more gentle sloping upper part. The latter is the lower section of an uplifted PAZ profile (see text for more details). The lower part reflects a ~50Ma rapid cooling event. Bottom: Theoretical concept of the uplifted PAZ profile (after Wagner and Van den haute, 1992) after a period of thermal stability. An uplifted block retains its inherited fossil PAZ "memory", while a present, new PAZ is developing (see text for explanation).

CHAPTER 3

CALIBRATION PROCEDURES

3.1. Irradiations

3.1.1. Irradiation packages

For this study a total of five irradiations (I to V) were carried out. For each irradiation an irradiation package was assembled. Each package consisted of a number of apatite mounts stacked in a cylindrical irradiation container or rabbit. In the stack, mounts of apatite age standards embedded together with glass fluence monitors, were arranged in an evenly spaced fashion. This allowed to interpolate the track density values arising from the glass fluence monitors for all samples and to determine the neutron flux gradient within one package. Totalled over the five irradiations the large number of age standards enabled determination of an accurate ζ-calibration factor (see section 1.7.2.1). On the top and bottom and in some cases also in the middle of each package, absolute metal activation monitors were placed for the determination of the absolute thermal neutron fluence. Circular foils (0.5 cm or 1.0 cm in diameter) of diluted Al-Au and Al-Co alloys were used.

After irradiation, the packages were left until radiation levels dropped below the safety thresholds. Then the packages were disassembled. The mica ED was taken off each mount and etched in a 40 or 48% HF solution at 20 to 25°C for 20 to 45 minutes (depending on the type of mica: table 3.1) to reveal the induced fission tracks.

Table 3.1: Etching conditions for the mica external detectors for each of the five (I to V) irradiations performed

Irradiation	HF concentration	Temperature	Etch time	Mica type
I	48%	25°C	20 minutes	Jahre
II	40%	20°C	45 minutes	Goodfellow
III	40%	20°C	45 minutes	Goodfellow
IV	40%	20°C	45 minutes	Goodfellow
V	40%	25°C	35 minutes	Goodfellow

3.1.2. Irradiation facility

All irradiations for this work were done in the Thetis research reactor of the Institute of Nuclear Sciences (INW) of the University of Gent (Belgium). The Thetis reactor (figure 3.1) is a small 250 kW research reactor containing light water and graphite blocks as a moderator. It has 17 irradiation channels. Channel 8 is predominantly used for FT purposes because it is the best thermalized channel in the reactor as it is at the largest distance from the reactor core. During the last decade the neutron flux in this channel gradually dropped from ~1.6 × 10^{11} cm^{-2} s^{-1} to ~1.0 × 10^{11} cm^{-2} s^{-1}. As a consequence the fluence that can be achieved during a single irradiation dropped to 2.5 × 10^{15} cm^{-2} (for a maximal irradiation time of 7 hours), which can be rather low for certain cases where the ED method is used. Four of the irradiations for this study were carried out in channel 8, and one in channel 7. Both irradiation channels meet the requirements for thermalization as put forward by Green and Hurford (1984) and Van den haute et al. (1988). As mentioned, channel 8 has a present nominal neutron flux (φ) of 1.0 × 10^{11} cm^{-2} s^{-1}; for channel 7 this value amounts to 1.7 × 10^{11} cm^{-2} s^{-1}. The epithermal/thermal flux ratio ($\varphi_{epi}/\varphi_{th}$) is 1/163.5 for channel 8 and 1/116 for channel 7. The samples were irradiated for 4 to 6 hours depending on the channel used.

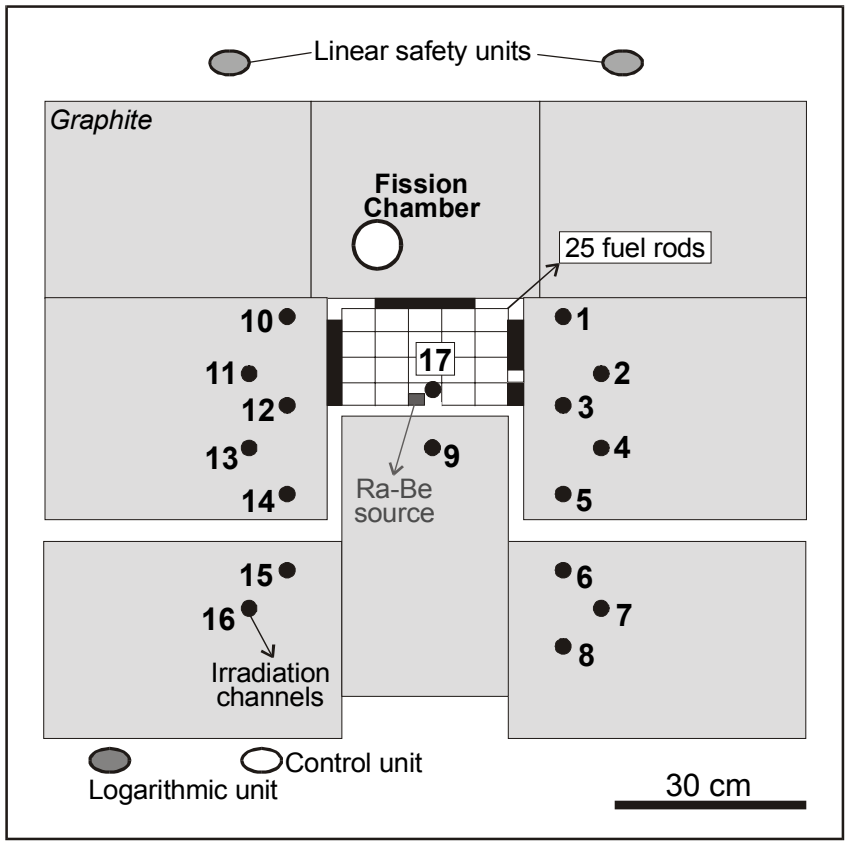

Figure 3.1: Schematic plan of the Thetis nuclear research reactor at the INW (Institute of Nuclear Sciences at the University of Gent). Numbered dots indicate irradiation channels. In this work channels 7 and 8 were used (after Moens, 1981).

Detailed studies over many years of irradiations in the Thetis research reactor has resulted in a reliable methodology for the accurate determination of absolute neutron fluences, with a relative error of 2.5%.

Table 3.2: Irradiations performed for apatite FT analysis of samples from the Altai and Tien Shan mountain belts. I to V represent the irradiation number, their dates and irradiation time (t_i) are given. TC is the irradiation channel used in the Thetis reactor, de flux ratio of epitermal to thermal neutrons for the channels is listed. Au en Co are the number of these metal activation monitors included in the specific irradiation package, DUR and FCT represent the number of mounts of apatite age standards (DURango and Fish Canyon Tuff) that were included in the irradiation. Finally the mean calculated thermal neutron fluence for each of the irradiations is presented.

	Date	t_i (min)	TC	$\varphi_{epi}/\varphi_{th}$	Au	Co	DUR	FCT	ϕ_m (neutrons/cm^2)
I	26/03/1999	405	8	1/163.5	3	3	5	2	2.782×10^{15}
II	20/03/2001	310	8	1/163.5	2	2	7	2	1.647×10^{15}
III	09/10/2001	360	8	1/163.5	3	2	5	2	1.977×10^{15}
IV	09/10/2001	226	7	1/116	3	2	6	0	2.088×10^{15}
V	11/04/2002	405	8	1/163.5	3	2	4	2	2.244×10^{15}

3.1.3. Performed irradiations

The description and details (the number and type of apatite age standards, metal activation monitors, U-doped glasses) for each of the five irradiations that were carried out are listed in table 3.2 and a schematic representation of the standards and monitors as well as of the apatite samples in the irradiation packages for each of these irradiations is given in figure 3.2.

3.2. Absolute thermal neutron fluence determination with metal activation monitors

3.2.1. Principles

As discussed in section 1.7.1.2, the thermal neutron fluence can be determined by measuring the γ-radiation of co-irradiated metal activation monitors. In this study Au and Co foils (diluted in Al to avoid self-shielding effects) were simultaneously used as monitors. Both monitors are certified reference materials for neutron dosimetry. The Au-monitor is a 0.1 mm thick (Al-0.1wt%Au)-foil certified as reference material IRMM-530 (Ingelbrecht et al., 1991; De Corte et al., 1995b and 1998) by the Institute for Reference Materials and Measurements of the European Commission. The Co-monitor is a 0.1 mm thick (Al-1.0%Co)-foil certified as reference material IRMM-528R (De Corte et al., 1995b) by the same institute. When irradiated in a nuclear reactor these metals experience the following (n,γ)-reactions:

$$^{197}Au + n \rightarrow {}^{198}Au \rightarrow {}^{198}Hg + \beta^- + \gamma \quad (E_\gamma = 411.8 \text{ keV})$$

$$^{59}Co + n \rightarrow {}^{60(m)}Co \rightarrow {}^{60}Ni + \beta^- + \gamma \quad (E_\gamma = 1173.2 \text{ and } 1332.5 \text{ keV})$$

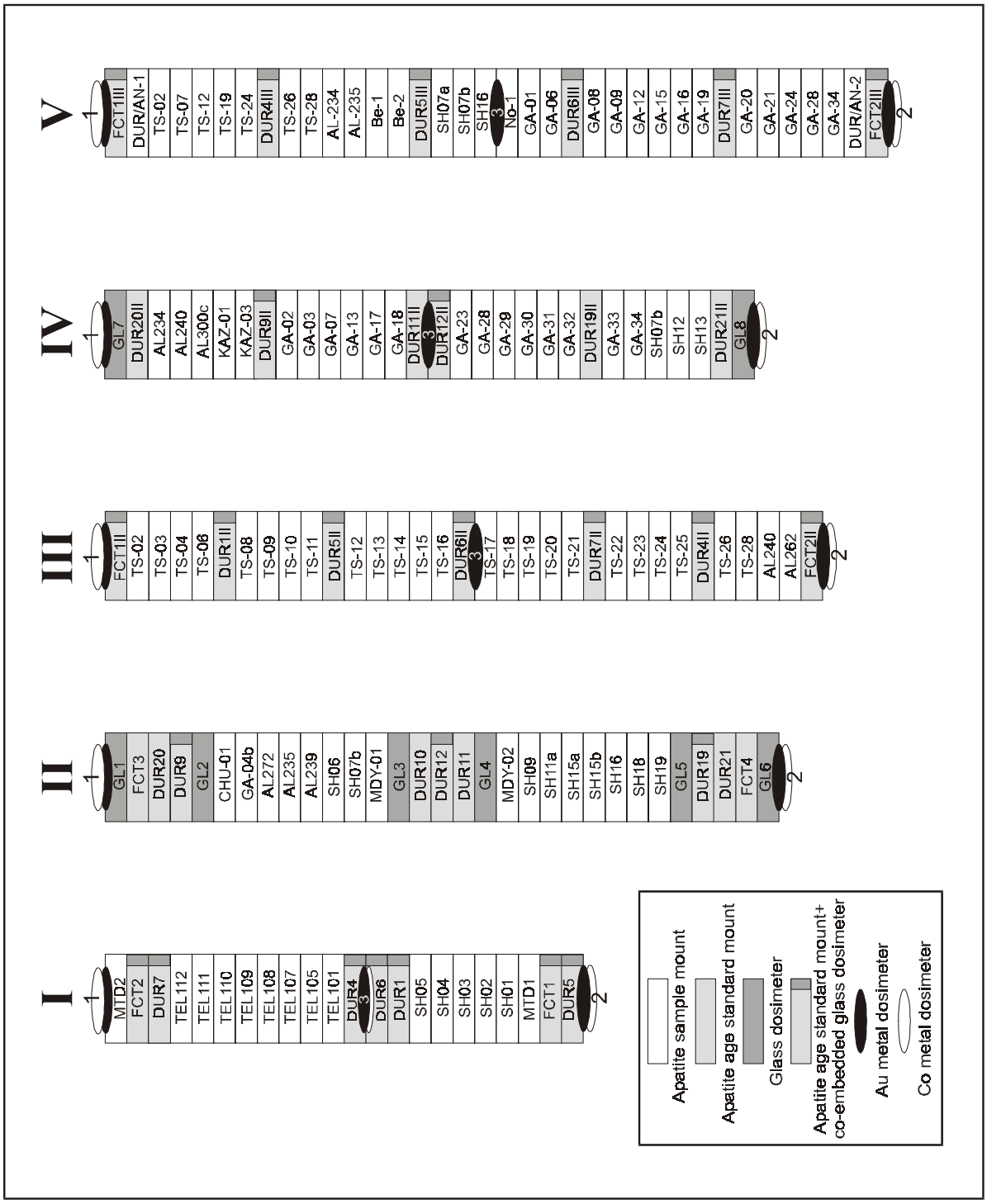

Figure 3.2: Schematic diagram of the five irradiation packages prepared for this study. The apatite mounts represented here correspond to 1.0 cm × 1.5 cm rectangles or 1.9 cm ∅ circular discs, all of about 1.0 to 1.5 mm thickness. Details of each irradiation are listed in table 3.1. See text for explanations of the metal and glass dosimeters and the apatite age standards.

The monitors included in the irradiation packages are circular foils punched from a larger sheet. Their diameter ranged from 0.5 to 1.2 cm. Each circular foil has a certain total mass (m_{tot}) and contains a specific weight percentage of the monitoring metal (1.00 ± 0.02 % for Co and 0.1000 ± 0.0006 % for Au in our case as cited above).

So, for example, for a Co-monitor, $m_{mon} = m_{Co} = m_{tot}/100$, while for the Au-monitor that would be, $m_{mon} = m_{Au} = m_{tot}/1000$. Consequently, the number of atoms (N) of the metal monitor isotope is given by:

$$N = m_{mon}N_a\theta/M \qquad 3.1$$

N_a is Avogadro's number ($N_a = 6.02252 \times 10^{23}$ atoms.mol^{-1}). The parameter M is the atomic weight of the element and θ is the isotopic abundance for the specific isotope. As Au and Co are mono-isotopic: $\theta = 1$ for both metals.

During the irradiation a certain fraction of the nuclei is activated and because these active isotopes will start disintegrating at a certain rate (given by the decay-constant, λ), the number of activated metal nuclei at a certain moment of irradiation can be written as:

$$dN/dt = m_{mon}N_a\theta\sigma\varphi/M - \lambda N \qquad 3.2$$

In this equation σ represents the cross-section (definition see section 1.5) of the activation reaction. Solving this differential equation for the total duration of the irradiation involves, first integrating N between a value of 0 (no active isotopes at the start of irradiation) and N_o (the amount of active isotopes at the end of irradiation) and, second integrating time (t) between 0 at the start of irradiation and t_i, which is the total irradiation time (figure 3.3). Considering these constraints and assuming the flux is constant, we can write down the number of activated metal monitor nuclei at the end of the irradiation as:

$$N_o = \lambda^{-1}(m_{mon}N_a\theta\sigma\varphi/M)(1-e^{-\lambda t_i}) \qquad 3.3$$

In this equation the factor $(1-e^{-\lambda t_i})$ is called the *saturation factor* (S).

The activity (A) is defined as the number of active isotopes times the disintegration constant of that isotope or:

$$A = -dN/dt = \lambda N_o \qquad 3.4$$

So, the activity of the fluence monitor at the end of the irradiation is given by:

$$A_o = \lambda N_o = (m_{mon}N_a\theta\sigma\varphi/M)(1-e^{-\lambda t_i}) \qquad 3.5$$

If the (γ) activity of the fluence monitor at the end of irradiation is measured precisely, the relationship above can be solved for φ and the neutron flux can be calculated. However, measurement of the activity is performed a certain time after irradiation. The time period between the end of irradiation and the start of activity measurement is called the *decay time* (t_d).

For example, after a particular decay time, at time t_1, the activity of the monitor will already have dropped to a value A_1 (figure 3.3). Furthermore, the measurement in itself takes a certain period of time, the *measuring time* (t_m), during which the activity continues to decrease. The relationship between the measured activity (A_m) and the original activity (A_o) is illustrated in figure 3.3 and can be written as:

$$A_m = t_m^{-1} \int_{t_d}^{t_d+t_m} A_o e^{-\lambda t} dt \qquad 3.6$$

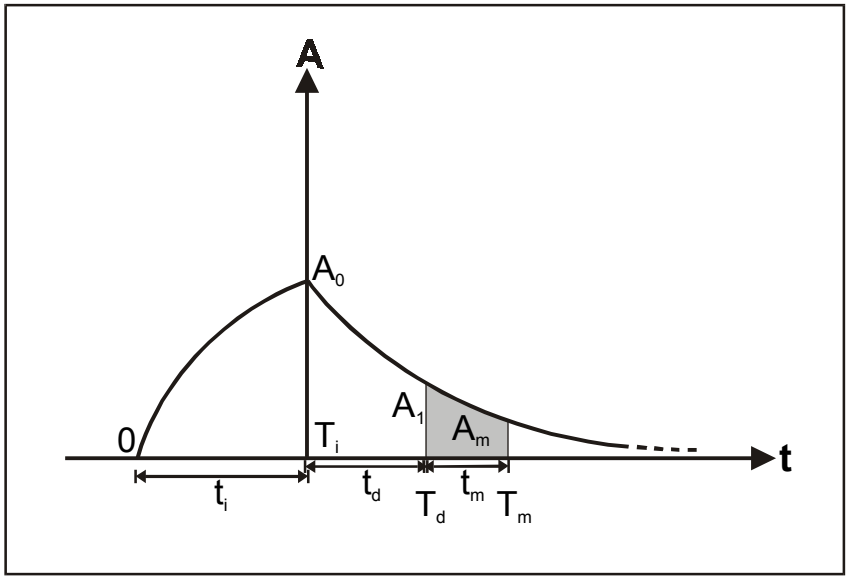

Figure 3.3: The γ-activity (A) of a metal activation monitor as a function of time (t). At the start of the irradiation (point 0) the activity is 0, after a total irradiation time of t_i, the activity reaches a maximum of A_o, after which it decreases due to decay of the active isotopes. After a delay time, t_d, and during a certain measure time, t_m, a time-integrated activity of A_m is measured by means of γ-spectrometry.

After integration, equation (3.6) becomes:

$$A_m = \frac{A_o e^{-\lambda t_d}}{\lambda t_m}(1 - e^{-\lambda t_m}) \qquad 3.7$$

or:

$$A_o = e^{\lambda t_d} \frac{\lambda t_m}{1 - e^{-\lambda t_m}} A_m \qquad 3.8$$

In this manner we can define two factors for correcting the measured activity to its original value right after irradiation: $e^{-\lambda t_d}$ as the *decay factor* (D) and $\frac{1 - e^{-\lambda t_m}}{\lambda t_m}$ as the *counting factor* (C).

Determining the value of A_m involves measurement of peak areas (N_p) in a γ-spectrum recorded with a γ-spectrometer through a Ge(Li) detector. This peak area is determined with appropriate software. Parameters specific for the detector and the measurement system used influence the shape of the peak and thus should be taken into account. The relationship between N_p and A_m is defined as:

$$A_m = \frac{N_p}{\varepsilon_p (1-\delta) I_\gamma t_m} \qquad 3.9$$

In which ε_p represents the so-called *peak detection efficiency*. The value of ε_p depends on the energy and intensity of the γ-radiation (E_γ and I_γ) and on the particular set-up of the detector (the shape of the activated monitor and the measuring distance from the detector to the monitor). For each possible set-up, the value of the detection efficiency is determined by calibration on the basis of analysis of standard γ-sources with known energy. When registering γ-pulses, the detector and connected measuring system need a certain time to analyze and process the pulse. During this time, the so-called *dead time*, no other pulses can be recorded. A detector and measuring system is therefore equipped with a so-called dead time stabilizer, an electronic correction circuit that ensures that the measuring time is corrected and dead time is added to the measurement. Depending on the activity of the measured isotope, a *dead time stabilization factor* (δ) can be imposed on the detector and measuring system. The δ-factor is expressed as a fraction of the measuring time t_m, so $0 \leq \delta \leq 1$. For the measurement of low to moderately active samples δ can be set to 0 and measurement can be performed in *live time*.

Summarizing the above, we can write down following expression for the γ-peak area for the given isotope measured with a γ-spectrometer in function of the neutron flux during irradiation:

$$N_p = \frac{m_{mon} N_a \theta}{M} \sigma\varphi (1 - e^{-\lambda t_i}) e^{-\lambda t_d} \frac{(1 - e^{-\lambda t_m})}{\lambda t_m} \left[\varepsilon_p (1-\delta) I_\gamma t_m\right] \qquad 3.10$$

An additional correction should be applied however. As stated in section 1.6, thermal, epithermal and fast neutrons contribute to the total neutron flux in a reactor. The epithermal neutrons are also capable of activating the metal monitors, so a correction for the contribution of epithermal neutrons has to be worked out. Even in a well-thermalized irradiation channel an epithermal neutron flux contribution has to be taken into account. We can split up the factor σφ in the last equation into a thermal part and an epithermal part:

$$(\sigma\varphi)_{tot} = (\sigma\varphi)_{th} + (\sigma\varphi)_{epi} \qquad 3.11$$

or:

$$(\sigma\varphi)_{tot} = \sigma_o \varphi_{th} + I_o \varphi_{epi} \qquad 3.12$$

In the latter equation we rely on the so-called *Høgdahl* convention for calculating the neutron fluence (see Bellemans, 1996 for a recent and detailed account). The σ_o-factor is the cross-section for the specific isotope for reaction with neutrons having a velocity of 2200 m s^{-1}. The 2200 m s^{-1} value corresponds to the velocity of thermal neutrons at their most probable energy (0.0253 eV) in the Maxwell-Boltzman distribution (see section 1.6; figure 1.9). I_o is the resonance integral for epithermal neutrons (see section 1.6). The thermal and epithermal neutron flux are represented by φ_{th} and φ_{epi} respectively. In the Høgdahl convention they actually represent the so-called subcadmium and epicadmium fluxes. Because of the specific absorption properties for low-energy neutrons of Cd, the metal is used to define the flux of thermal and epithermal neutrons. Neutrons with energies smaller than ~0.55 eV are almost completely absorbed by Cd. This is the so-called *effective Cd cut-off energy* (E_{Cd}). By convention the thermal neutron flux corresponds to the flux of neutrons with an energy < E_{Cd}, while the neutrons with energies > E_{Cd} constitute the epithermal neutron flux.

Reorganizing equation 3.12 in order to calculate the thermal neutron flux yields:

$$\left(\sigma\varphi\right)_{tot} = \sigma_o\varphi_{th}\left(1+\frac{I_o}{\sigma_o}\frac{\varphi_{epi}}{\varphi_{th}}\right) \qquad 3.13$$

Including this factor in the expression for N_p gives:

$$N_p = \frac{m_{mon}N_a\theta}{M}(1-e^{-\lambda t_i})e^{-\lambda t_d}\frac{(1-e^{-\lambda t_m})}{\lambda t_m}\left[\varepsilon_p(1-\delta)I_\gamma t_m\right]\sigma_o\varphi_{th}\left(1+\frac{I_o}{\sigma_o}\frac{\varphi_{epi}}{\varphi_{th}}\right) \qquad 3.14$$

Rewriting this expression finally yields following equation that allows calculating the thermal neutron flux:

$$\varphi_{th} = \frac{M}{m_{mon}N_a\theta}\frac{1}{\left(1-e^{-\lambda t_i}\right)}e^{\lambda t_d}\frac{\lambda t_m}{\left(1-e^{-\lambda t_m}\right)}\frac{N_p}{\left[\varepsilon_p(1-\delta)I_\gamma t_m\right]}\frac{1}{\sigma_o\left(1+\frac{I_o}{\sigma_o}\frac{\varphi_{epi}}{\varphi_{th}}\right)} \qquad 3.15$$

This apparently complicated equation actually comes down to the measurement of the peak area, N_p, by simpely placing the metal activation monitor at a specific distance above a γ-detector and processing the γ-spectrum on one hand, and weighing the monitor in order to derive the mass , m_{mon}, of specific metal (Au or Co) on the other hand. All other factors are (i) specific nuclear constants for the metal under investigation (see table 3.3 for values for M, θ, λ, I_γ, σ_o and I_o for Au and Co), (ii) general constants (Avogadro's number N_a), (iii) time factors (t_i, t_d, t_m) which can be monitored very precisely, (iv) parameters specific to the detector and measuring system (ε_p and δ which can also be determined accurately), and (v) parameters specific to the nuclear reactor and irradiation channel used ($\varphi_{epi}/\varphi_{th}$, which are monitored at the reactor facility).

To calculate an FT age from the fundamental FT age equation (section 1.5) we need the thermal neutron fluence (ϕ_{th}):

$$\phi_{th} = \varphi_{th}\, t_i \qquad 3.16$$

Table 3.3: Relevant nuclear constants used in this work for the calculation of neutron induced γ-activity on the basis of Au and Co metal activation monitors (after De Corte et al., 1991; Rosman and Taylor, 1998; Chun et al., 1999; Holden, 1999; Holden and Hoffman, 2000; Mughabghab, 2003). See text for definitions and explanation of the tabulated parameters.

			^{197}Au (n,γ)^{198}Au	^{59}Co (n,γ)^{60}Co	
θ		isotopic abundance	1	1	
σ_o	(barn)	thermal neutron cross-section	98.7	37.2	
I_o	(barn)	resonance integral	1550	74.0	
M	(g.mol^{-1})	atomic weight	196.97	58.93	
$T_{1/2}$	(a)	half-life time	7.3813×10^{-3}	5.2714	
λ	(s^{-1})	decay-constant	2.976×10^{-6}	4.170×10^{-9}	
E_γ	(keV)	energy of specific γ-radiation	411.8	1173.2	1332.5
I_γ		fractional absolute intensity of γ-radiation	0.9556	0.9985	0.9998

The γ-spectrometry for the neutron dosimetry measurements presented in this study was performed at the INW, the institute where the Thetis nuclear reactor is situated. This has the great advantage that the time parameters (t_i, t_d, t_m) can be attuned precisely to one another. Soon after each irradiation the Au- and Co-monitors were removed from the irradiated package and cleaned. The γ-activity of each of the monitors was measured with a single open-ended coaxial Phillips® Ge(Li)-detector connected to a 4000-channel Canberra® (MCA40) analyzer (more details are presented in the papers by Van den haute et al., 1988 and De Corte et al., 1991). All measurements were carried out at a source-detector distance of 15 cm and detection efficiencies were calculated on the basis of this distance and the metal monitor sizes. At least 60,000 counts or γ-photons were collected for each monitor. The γ-spectra were then transferred to files on a VAX3000 computer and the peak area (N_p) was calculated with purpose designed software developed at the institute (*Angela*-program; Op de Beeck, 1976). The mass of each measured metal activation monitor was then determined with a high precision (± 10^{-3} mg) balance (Mettler MTS).

3.2.2. Results

The results of the absolute ϕ_{th} determinations for the individual metal activation monitors are presented in table 3.4. Averages for the monitor type and overall averages of the ϕ_{th} value are calculated. The overall averaged value (the irradiation average) is the value adopted for ϕ_{th} and is used for further FT age calculations.

Table 3.4: Thermal neutron fluence (ϕ_{th}) values obtained for individual metal activation monitors for each of the five (I to V) irradiations of apatite samples from the Altai and Tien Shan mountains. All fluence values are given in 10^{15} neutrons/cm^2. Average values for individual Co-monitors, average values for monitor type and overall averages or irradiation averages are calculated.

Irriadiation	Monitor	E_γ (keV)	ϕ_{th} (in 10^{15} neutrons/cm)	Individual Co-monitor average	Monitortype average	Irradiation average
I	Au_1	411.8	2.725			
	Au_2	411.8	2.808			
	Au_3	411.8	2.743		2.759	
	Co_1	1173.2	2.774			
		1332.5	2.806	2.790		
	Co_2	1173.2	2.833			
		1332.5	2.862	2.848		
	Co_3	1173.2	2.778			
		1332.5	2.773	2.776	2.805	***2.782***
II	Au_1	411.8	1.542			
	Au_2	411.8	1.711		1.627	
	Co_1	1173.2	1.594			
		1332.5	1.574	1.584		
	Co_2	1173.2	1.750			
		1332.5	1.750	1.750	1.667	***1.647***
III	Au_1	411.8	1.907			
	Au_2	411.8	2.083			
	Au_3	411.8	2.006		1.999	
	Co_1	1173.2	1.906			
		1332.5	1.889	1.898		
	Co_2	1173.2	2.016			
		1332.5	2.004	2.010	1.954	***1.977***
IV	Au_1	411.8	1.981			
	Au_2	411.8	2.217			
	Au_3	411.8	2.109		2.102	
	Co_1	1173.2	1.958			
		1332.5	1.971	1.965		
	Co_2	1173.2	2.183			
		1332.5	2.177	2.180	2.073	***2.088***
V	Au_1	411.8	2.216			
	Au_2	411.8	2.325		2.271	
	Co_1	1173.2	2.165			
		1332.5	2.176	2.171		
	Co_2	1173.2	2.234			
		1332.5	2.291	2.263	2.217	***2.244***

For each irradiation ϕ_{th} values obtained with Au and Co monitors can be compared and a thermal neutron fluence ratio (ϕ_{Co}/ϕ_{Au}) can be attained. This ratio gives information on the consistency of the absolute thermal neutron determinations (Van den haute et al., 1988). For the five irradiations in this study these ratios are the following:

Irradiation	I	$\phi_{Co}/\phi_{Au} = 1.017 \pm 0.036$
	II	$\phi_{Co}/\phi_{Au} = 1.025 \pm 0.036$
	III	$\phi_{Co}/\phi_{Au} = 0.977 \pm 0.034$
	IV	$\phi_{Co}/\phi_{Au} = 0.986 \pm 0.035$
	V	$\phi_{Co}/\phi_{Au} = 0.976 \pm 0.034$

The average value for these rates is calculated as 0.996 ± 0.035. These rates imply that the absolute thermal neutron fluence determination by means of γ-spectroscopy of neutron irradiation induced activity in Au and Co metal activation monitors in this study shows a consistency within 1.4 to 2.5% of unity, and within 0.4% of unity when considering the average value. This is well in agreement with values cited by e.g. Van den haute et al., 1988 and Vercoutere and Van den haute, 1993.

3.3. Fission track counting and the use of glass dosimeters and apatite age standards

3.3.1. Track counting procedure

Track counting was performed with an Olympus BH2 microscope equipped with transmitted and reflected light. A nominal magnification of 1250 × was reached using 10 × eyepieces, a 100 × dry objective and a supplementary 1.25 × magnification factor due to a drawing tube module attached to the microscope. Transmitted light is used to identify the characteristic shape of the fission tracks in the interior of the crystals, while reflected light clearly shows the surface features of the crystals and thus enables the confirmation that a specific fission track effectively intersects the surface.

Counting was done using an eyepiece grid with numbered squares calibrated against a stage graticule (0.1 mm with 50 × 2μm divisions). A counting unit area was chosen that matched the average grain size in a specific sample (figure 3.4). Fission tracks falling within the counting unit area in a single grain were then counted. The counting area was chosen away from the grain edges to discount possible tracks derived from disintegration of ^{238}U isotopes in adjacent grains and to assure 4π-geometry. Grains with numerous dislocations or inclusions were not counted, nor was this the case for grains showing a clear heterogeneous distribution of the tracks. For statistical reasons, and whenever possible, several grains were counted until a total amount of 1000 spontaneous tracks per sample was reached, however several samples did not have enough suitable grains or a too low spontaneous FT density to reach this number.

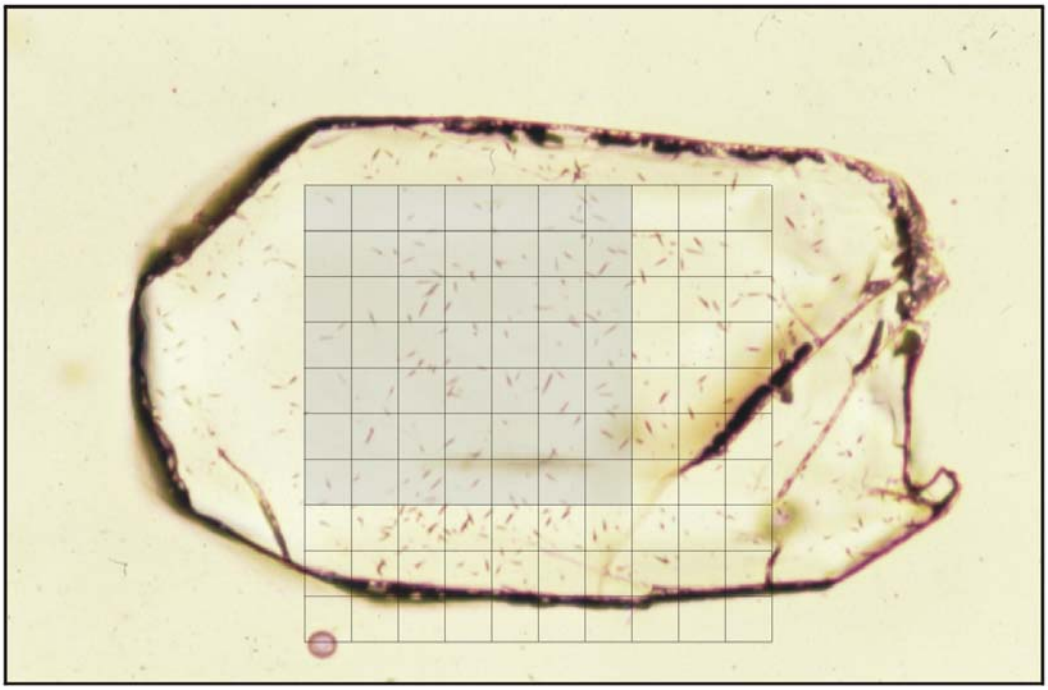

Figure 3.4: Fission tracks in an apatite crystal at 1250 × magnification. A unit area of a counting grid in a microscope eyepiece lens is chosen to fall within the centre of the crystal. The unit area is calibrated against a stage graticule.

All samples and standards in this study were analyzed with the external detector (ED) method (see section 1.8.2). This involves counting the spontaneous fission tracks in the apatite crystal and the induced tracks in the mica ED at exact the same position. The most widely used technique to achieve this is by fixing the apatite mount and the ED -track side up- next to each other, forming mirror images (figure 3.5). Counting of the spontaneous and induced tracks then involves switching back and forth (with a computer-controlled motorized stage) between apatite and ED. This requires making reference points in the apatite mount and the ED and applying a complicated co-ordinate transformation to find the exact imprint of the induced tracks in the ED corresponding to the apatite grain, and more specifically to the counted area of spontaneous tracks. An obvious and simple alternative is described by Jonckheere and Wagner (2000). Their procedure simply entails replacing the ED after etching exactly in the same position on the apatite mount as during irradiation (figure 3.5). This is easily done under the microscope with manipulation by cotton-tipped swabs for example and takes no time at all. The attainable positioning precision is very high and even allows for track-to-track matching between induced tracks in apatite and the ED. Counting the spontaneous tracks is achieved by focussing on the apatite surface through the ED; refocusing on the trackside of the ED then enables the researcher to view and count the induced tracks. At the large magnifications used for FT counting, there is no interference between both images. In this study, this procedure has been used.

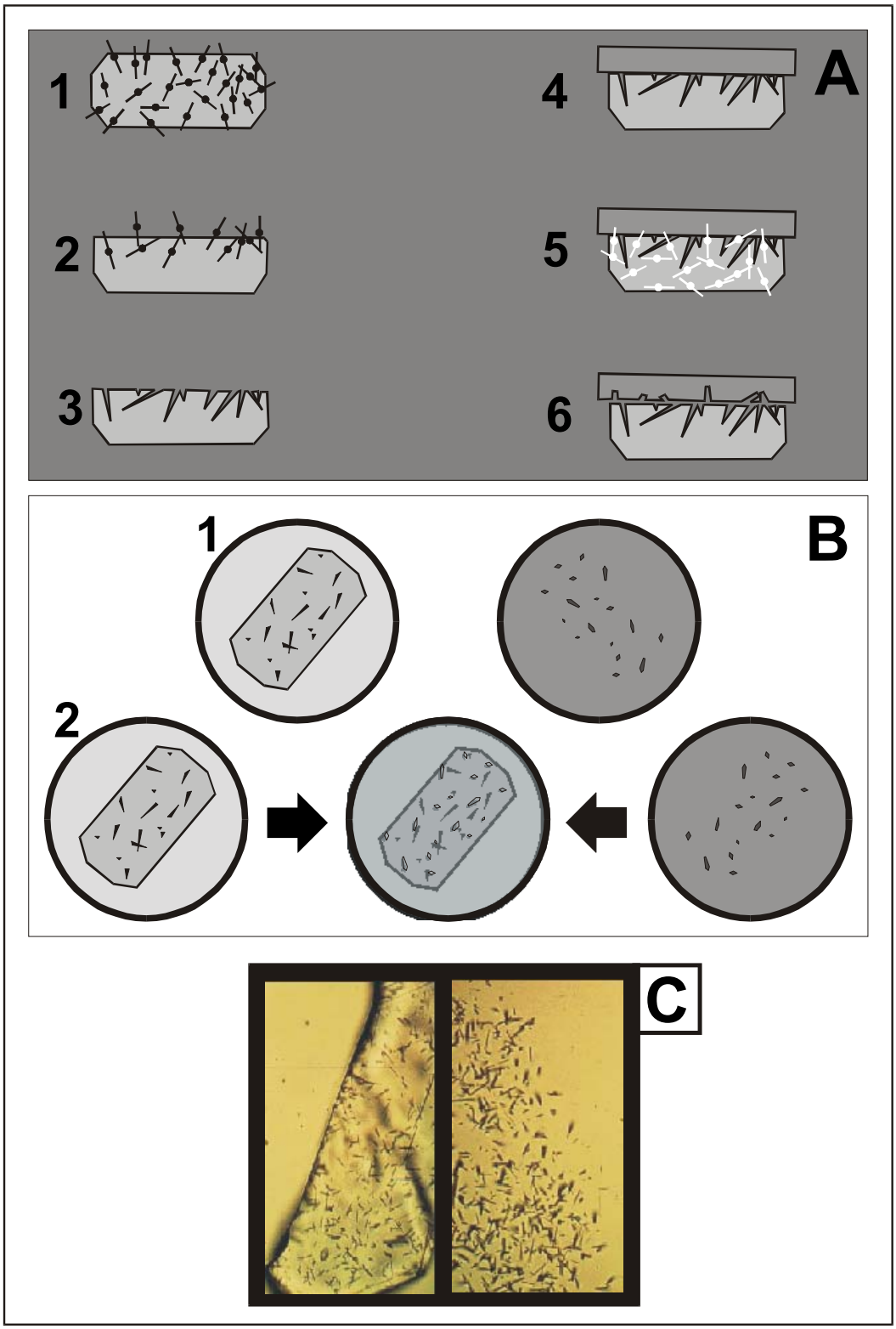

Figure 3.5: A. Latent spontaneous ^{238}U fission tracks in an apatite crystal (1). An internal surface of the apatite crystal is polished (2) and etched (3). A muscovite external detector (ED) is attached (4). During irradiation latent induced ^{235}U fission tracks are created (5) and subsequently etched in the ED (6). B. (1) Generally apatite and ED are placed next to each other, track side up, on a glass slide and an automated microscope stage switches from spontaneous tracks in the apatite to induced tracks in the ED. (2) An alternative is to place the ED, track side down, exactly in its original position and to count spontaneous and induced tracks by simply refocusing of the microscope. C. Example of spontaneous fission tracks in an apatite crystal and its mirror induced track image in the ED.

3.3.2. Irradiations and glass dosimeters

Table 3.5: Fission track counting results for the induced tracks from the glass dosimeters (IRMM-540) included in each of the five (I to V) irradiation packages. DUR and FCT glasses represent glass shards embedded with Durango or Fish Canyon Tuff apatite age standards, "GL" glasses are separately embedded shards. The relative position of the glass mounts within each irradiation package is given in mm from the package centre, which was chosen as an arbitrary reference point at position 0 mm (see figure 3.2 for a graphic representation). N_d is the number of tracks counted in an attached muscovite external detector, and ρ_d is the induced track density at the position of the dosimeter glass.

Irradiation	Glass dosimeter	Position (mm)	N_d	$\rho_d \pm 1\sigma$ (10^5 tracks/cm^2)
I	FCT2I gl	-13.0	1904	5.87 ± 0.16
	DUR7I gl	-11.5	1878	5.79 ± 0.13
	DUR4I gl	-1.0	1870	5.76 ± 0.14
	DUR6I gl	1.0	2131	5.84 ± 0.16
	FCT1I gl	10.25	2349	5.79 ± 0.12
	DUR5I gl	11.25	1836	5.66 ± 0.13
II	GL 1	28.0	1597	3.26 ± 0.08
	GL 2	20.5	1625	3.32 ± 0.08
	GL 3	4.0	1618	3.30 ± 0.08
	GL 4	-3.5	1643	3.35 ± 0.08
	GL 5	-19.25	1689	3.45 ± 0.09
	GL 6	-27.0	1677	3.42 ± 0.08
III	FCT2II gl	-28.25	3080	3.89 ± 0.08
	DUR4II gl	-19.5	1261	3.94 ± 0.11
	DUR7II gl	-10.5	1244	3.89 ± 0.12
	DUR6II gl	0.0	1245	3.89 ± 0.11
	DUR5II gl	11.5	3046	3.85 ± 0.09
	FCT1II gl	30.0	1173	3.67 ± 0.10
IV	DUR9II gl	-13.75	3103	3.92 ± 0.07
	DUR12II gl	1.0	1201	3.75 ± 0.11
	DUR19II gl	13.75	2405	3.82 ± 0.07
	GL8	27.0	1218	3.81 ± 0.10
V	FCT1III gl	-27.0	1332	4.16 ± 0.11
	DUR4III gl	-15.0	2654	4.15 ± 0.09
	DUR5III gl	-4.5	2565	4.01 ± 0.11
	DUR6III gl	6.0	2669	4.17 ± 0.11
	DUR7III gl	16.5	2618	4.09 ± 0.08
	FCT2III gl	27.0	1253	3.92 ± 0.10

The thermal neutron fluence of the irradiations performed in this work was also monitored by using U-doped glass dosimeters. For this purpose the IRMM-540 (De Corte et al., 1998) reference glass was used (section 1.7.1.3). The glass discs were broken into pieces and were embedded with the apatite age standards or separately in epoxy resin. The mounts containing the glass shards were provided with a muscovite ED in the same fashion as for the apatite mounts. Irradiation of the glass with thermal neutrons induces nuclear fission of the ^{235}U nuclei in the glass and hence produces induced fission tracks in the adjacent ED. Etching of the ED will reveal these tracks. The density of these induced tracks (ρ_d) obviously depends on the absolute value of the thermal neutron fluence and the U-content of the glass.

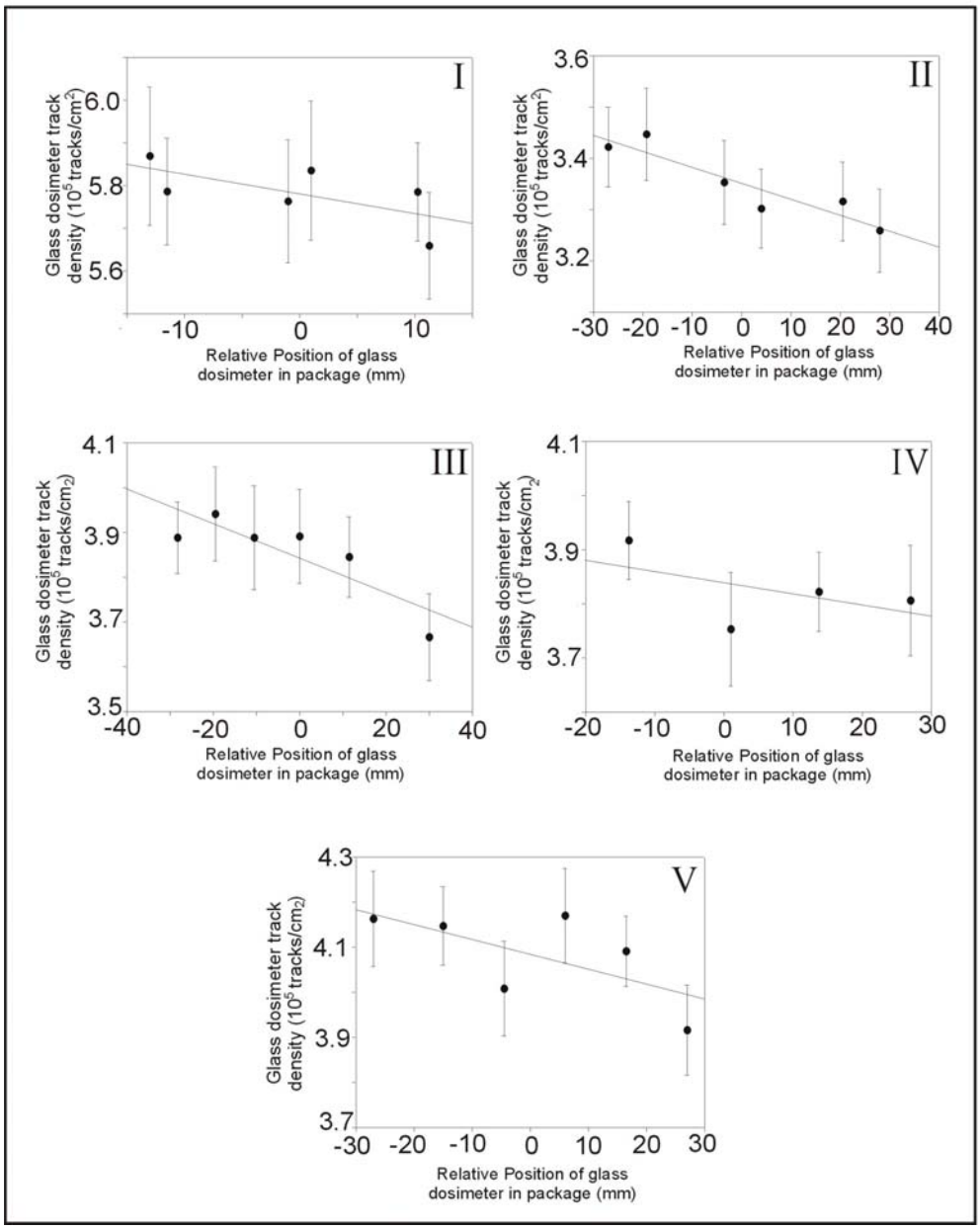

Figure 3.6: Interpolation curves on the basis of induced track densities of the glass dosimeters and their positions in each of the irradiation packages as shown in figure 3.2.

The relative positions of the glass dosimeters in each of the five irradiation packages is illustrated in figure 3.2. These positions were chosen at regular intervals within the packages in order to have an estimate on the axial gradient of the thermal neutron fluence. The regularly spaced positions also allowed the construction of an interpolation curve by plotting the induced track density (ρ_d) against the position of the glass dosimeter in the irradiation package. An equation for each curve is obtained by linear regression. The slope of the curve will depend on the axial gradient of the absolute thermal neutron fluence.

In this way, and knowing the relative positions of each irradiated mount, it is possible to calculate a ρ_d-value for each sample and age standard individually. These values were used to determine ζ-calibration factors and ζ-ages (equations 1.30 and 1.31). The ρ_d-values used for the age calculations further on in this study are the interpolated values as outlined in this section. The ρ_d-data for the glasses of the five irradiations are listed in table 3.5 and the construction of the interpolation curves through linear regression is presented in figure 3.6.

If x represents the position (in mm) of the glass dosimeter along the axis of the irradiation package and y the track density ρ_d, then for each of the five (I to V) irradiations the regression equations of the interpolation curves are given by (r is the correlation coefficient):

I:	$y = 5.78042 - (4.52200 \times 10^{-3})x$	$r^2 = 0.4367$
II:	$y = 3.35073 - (3.10071 \times 10^{-3})x$	$r^2 = 0.8580$
III:	$y = 3.84250 - (3.81250 \times 10^{-3})x$	$r^2 = 0.7249$
IV:	$y = 3.83851 - (2.00000 \times 10^{-3})x$	$r^2 = 0.2756$
V:	$y = 4.08306 - (3.27683 \times 10^{-3})x$	$r^2 = 0.4242$

Substitution of the known relative position of the samples as the parameter x will yield their ρ_d-values.

3.4. ζ-calibration

The theoretical aspects of this calibration method based on analysis of apatite age standards, have been described in section 1.7.2. Here the results of the determination of the ζ-calibration factor are presented. As outlined in the theoretical section, the ζ-calibration factor is a personal factor determined by each FT researcher individually, and is given by (equation 1.30):

$$\zeta = \frac{e^{\lambda_\alpha t_S} - 1}{\lambda_\alpha (\rho_s/\rho_i)_S G(\rho_d)_S}$$

The expression contains the α-decay constant of ^{238}U (λ_α = 1.55125 × $10^{-10}a^{-1}$) that closely approximates the total decay constant of ^{238}U (λ_{tot}). Because in practice ζ-calibration involves the use of the ED method, the geometry ratio G = 0.5 (sections 1.7.2.1 and 1.8.2). In this study more than 30 mounts of Durango (DUR) and Fish Canyon Tuff (FCT) apatite were analyzed. Their ages (t_S) are precisely known, and are 31.4 ± 0.5 Ma for DUR and 27.9 ± 0.5 Ma for FCT apatite (section 1.7.2.2). The corresponding induced FT density in the glass dosimeter, ρ_d, was directly known for shards that were embedded in the same mount as the age standard, or the value was calculated using the interpolation curves presented in section 3.3. Counting of the spontaneous and induced FT densities for each of the age standard mounts gives the final parameter (ρ_s/ρ_i) needed for the ζ-calculation. Hence, if we assume that the reference ages for the age standards are correct, a ζ-determination is solely based on observation of fission tracks (spontaneous, induced and originating from the glass dosimeter). Table 3.6 lists the data relevant to the FT analysis of all age standards and the calculated ζ-factors. The table also contains some data relating to the procedure or Q-factor on which more details shall be given in section 3.5.

Taking into account that radioactive decay is a stochastic process described by Poissonian statistics, and following the so-called conventional method for uncertainty calculation in FT dating (Green, 1981) we can write the simplified equation for the statistical uncertainty of the ζ-values (σ_ζ) as:

$$\sigma_\zeta = \zeta\sqrt{\left(\frac{\sigma_{t_S}}{t_S}\right)^2 + \frac{1}{N_s} + \frac{1}{N_i} + \frac{1}{N_d}} \qquad 3.17$$

Where t_S is the reference age of the standard and σ_{t_S} the error of that reference age (see above: 31.4 ± 0.5 Ma for DUR and 27.9 ± 0.5 Ma for FCT apatite), N_s, N_i and N_d are the number of counted spontaneous tracks, induced tracks from the sample and the glass dosimeter respectively. Analogous to the interpolation of the ρ_d values, N_d is also interpolated using the same regression equations.

With the ζ-data from table 3.6 we calculated a *sample weighted mean zeta* (SWMZ) value for each of the two apatite age standards (DUR and FCT) used (e.g. Hurford & Green, 1983; Green, 1985). The weighing factor for the calculation of the SWMZ must assign a more important role or "weight" to more precise estimates of ζ, which is a fact that a simple arithmetical mean does not take into account. This implies that results that bear a smaller statistical error have more weight in the calculation of the mean value. The weighing factor used is the reciprocal value of the squared absolute uncertainties of that specific ζ-value. With this in mind the expression for SWMZ is:

$$SWMZ = \frac{\sum_j \frac{\zeta_j}{\sigma_j^2}}{\sum_j \frac{1}{\sigma_j^2}} \qquad 3.18$$

And the weighted uncertainty is given by:

$$\sigma_{SWMZ} = \sqrt{\frac{1}{\sum_j \frac{1}{\sigma_j^2}}} \qquad 3.19$$

Doing so with the date from table 3.6, we determine following SWMZ values (in a cm^2):

$SWMZ_{DUR} = 267.7 \pm 2.8$
$SWMZ_{FCT} = 236.6 \pm 4.5$

Combining these two values in an analogous manner, we can now determine an *overall weighted mean zeta* (OWMZ) (also in a cm^2) that finally gives the single calibration factor we set out to determine (e.g. Hurford & Green, 1983; Green, 1985). Our OWMZ value is:

$OWMZ = 253.1 \pm 2.4$

This final OWMZ calibration factor, or just ζ-factor for short, is a personal factor for use only by a single FT researcher under specific preparational and observational circumstances. As mentioned before, the OWMZ depends on the material used (in this case apatite) and also on the glass dosimeter (IRMM-540). Although there is a significant difference between the SWMZ value for Durango and Fish Canyon Tuff apatite, the conventional, recommended OWMZ value was calculated. This apatite OWMZ value for IRMM-540 dosimeter glass of 253.1 ± 2.4 will be used later on to calculate the apatite FT ζ-ages of the Altai and Tien Shan samples. Figure 3.7 shows plots of the different ζ-values obtained over several irradiations as presented in table 3.6. The values for Durango apatite are shown in comparison to the $SWMZ_{DUR}$ (figure 3.7.a) and those for Fish Canyon Tuff in comparison to $SWMZ_{FCT}$ (figure 3.7.b). All values are plotted combined in comparison to the OWMZ (figure 3.7.c).

The SWMZ values for both apatite age standards differ 13%. As a comparison, published SWMZ values by Hurford and Green (1983) obtained for zircon standards and putative zircon standards (e.g. Bishop Tuff zircon, Kimberlite zircon and others) and SRM612 glass differ by 32%, for zircon and CN-1 glass by 14%, for zircon and CN-2 glass by 19%. Green (1985) obtained a difference of 11% using zircons and the U3 glass dosimeter, and 24% using apatites (Fish Canyon Tuff, Durango, Mount Dromedary and Lake Mountain Rhyodacite) with SRM612 glass. However, this author reported a less than 1% discrepancy between Fish Canyon Tuff apatite and Durango apatite (using SRM612 glass). The standard mounts used by Green (1985) were stacked in single irradiation packages and irradiated together. Our SWMZ values were obtained using several apatite age standard mounts irradiated in 5 different irradiations, using different fluences and two different irradiation channels. Hurford (1998) on the other hand reports a 50% difference in separate ζ determinations from one analyst using the same apatite age standard mounts and CN-5 glass repeatedly over time, and a 23% difference between OWMZ's by 13 analysts on the same apatite age standard mounts.

Table 3.6: FT analysis of Durango (DUR) and Fish Canyon Tuff (FCT) apatite age standards. Irr is the irradiation number, $n_{s,i}$ the number of counted grains for spontaneous (s) and induced (i) FTs, $N_{s,i}$ is the amount of counted spontaneous and induced tracks. Track densities for spontaneous and induced tracks is given by $\rho_{s,i}$ and ρ_s/ρ_i is their ratio (average of individual grain by grain analysis with ED). N_d is the amount of tracks counted in the glass dosimeter (IRMM-540) and ρ_d is the corresponding track density. ζ- and Q-factors and their standard deviations (σ) are also given. All calculations are made using a ^{238}U decay constant $\lambda_\alpha = 1.55125 \times 10^{-10} a^{-1}$ and geometry ratio G = 0.5. Track densities are in 10^5 tracks/cm^2.

Irr	Standard	n_s	N_s	ρ_s (± 1σ)	n_i	N_i	ρ_i (± 1σ)	ρ_s/ρ_i	N_d	ρ_d (± 1σ)	ζ	σ(ζ)	Q	σ(Q)
I	DUR1 I	100	920	1.813 (0.075)	100	2196	3.338 (0.101)	0.419	1891	5.835 (0.134)	257.5	12.4	1.10	0.05
	DUR4 I	100	881	1.675 (0.072)	100	2465	3.838 (0.108)	0.357	1870	5.763 (0.144)	306.0	14.8	1.30	0.06
	DUR5 I	100	1308	2.153 (0.082)	100	1324	5.113 (0.125)	0.401	1836	5.659 (0.124)	277.4	13.4	1.15	0.06
	DUR6 I	100	1345	2.194 (0.083)	100	1419	5.056 (0.123)	0.395	2131	5.835 (0.126)	273.1	12.7	1.17	0.06
	DUR7 I	100	1279	2.625 (0.091)	100	1321	5.154 (0.126)	0.394	1878	5.786 (0.125)	276.2	13.3	1.17	0.06
	FCT1 I	100	1472	2.591 (0.090)	100	1761	6.131 (0.146)	0.339	2349	5.785 (0.112)	285.2	12.7	1.22	0.06
	FCT2 I	100	1152	2.453 (0.088)	100	2242	6.175 (0.134)	0.325	1904	5.869 (0.162)	293.2	13.6	1.26	0.06
II	DUR9 I	100	511	2.086 (0.092)	100	871	3.555 (0.102)	0.606	1625	3.281 (0.081)	316.6	20.0	1.29	0.08
	DUR10 I	100	500	2.041 (0.091)	100	801	3.269 (0.116)	0.648	1618	3.345 (0.083)	290.4	18.6	1.21	0.08
	DUR11 I	100	469	1.914 (0.088)	100	944	3.853 (0.125)	0.514	1643	3.357 (0.083)	364.8	23.2	1.52	0.10
	DUR12 I	250	1070	2.140 (0.044)	250	1718	3.436 (0.090)	0.623	1631	3.351 (0.083)	301.6	14.7	1.25	0.06
	DUR19 I	80	389	1.985 (0.101)	80	766	3.908 (0.141)	0.518	1689	3.417 (0.083)	355.7	24.4	1.51	0.10
	DUR20 I	250	825	1.650 (0.030)	250	1173	2.346 (0.049)	0.703	1611	3.275 (0.082)	273.4	14.8	1.11	0.06
	DUR21 I	250	882	1.764 (0.031)	250	1422	2.844 (0.069)	0.620	1683	3.423 (0.083)	296.6	15.4	1.26	0.07
	FCT3 I	55	584	2.167 (0.127)	55	952	3.532 (0.162)	0.634	1597	3.269 (0.082)	269.8	21.7	1.09	0.06
	FCT4 I	40	482	2.459 (0.158)	40	814	4.153 (0.206)	0.597	1677	3.428 (0.074)	273.3	23.7	1.16	0.07
III	DUR4 II	80	1062	1.676 (0.051)	80	1613	2.545 (0.063)	0.711	1261	3.941 (0.111)	224.7	11.5	0.92	0.05
	DUR5 II	60	993	2.089 (0.066)	60	1568	3.299 (0.083)	0.659	3046	3.845 (0.070)	248.5	11.7	0.99	0.05
	DUR6 II	60	923	1.942 (0.064)	60	1555	3.272 (0.083)	0.610	1245	3.891 (0.110)	265.2	14.0	1.07	0.05
	DUR7 II	60	929	1.955 (0.064)	60	1488	3.131 (0.081)	0.642	1244	3.888 (0.110)	252.2	13.4	1.01	0.05
	FCT1 II	60	1017	2.350 (0.070)	60	1591	3.348 (0.084)	0.645	1173	3.666 (0.107)	204.5	10.6	0.89	0.05
	FCT2 II	60	975	2.052 (0.066)	60	1582	3.329 (0.084)	0.637	3080	3.888 (0.070)	225.8	10.8	0.92	0.05
IV	DUR9 II	60	875	1.841 (0.062)	60	1530	3.219 (0.082)	0.583	3103	3.917 (0.070)	275.7	13.4	1.06	0.05
	DUR11 II	60	904	1.902 (0.063)	60	1437	3.024 (0.080)	0.651	2152	3.821 (0.082)	253.1	12.7	0.95	0.05
	DUR20 II	100	1081	1.365 (0.042)	100	1686	2.129 (0.052)	0.695	1218	3.884 (0.111)	233.2	11.9	0.89	0.04
	DUR21 II	100	1060	1.338 (0.041)	100	1782	2.250 (0.053)	0.624	2405	3.749 (0.076)	269.1	12.6	0.99	0.05
V	DUR4 III	50	523	1.634 (0.071)	50	848	2.650 (0.091)	0.645	2654	4.147 (0.087)	235.4	14.4	0.89	0.06
	DUR5 III	80	973	1.900 (0.061)	80	1753	3.424 (0.082)	0.567	2565	4.008 (0.075)	277.0	13.1	1.01	0.05
	DUR6 III	60	704	1.833 (0.069)	60	1258	3.276 (0.092)	0.582	2669	4.170 (0.083)	259.4	13.8	0.99	0.05
	DUR7 III	70	816	1.821 (0.064)	70	1394	3.112 (0.083)	0.604	2618	4.091 (0.077)	254.8	12.9	0.95	0.05
	FCT1 III	60	983	2.560 (0.082)	60	1584	4.125 (0.104)	0.630	1332	4.163 (0.106)	210.9	11.0	0.81	0.05
	FCT2 III	60	867	2.258 (0.077)	60	1389	3.617 (0.097)	0.640	1253	3.916 (0.100)	215.4	11.8	0.81	0.05

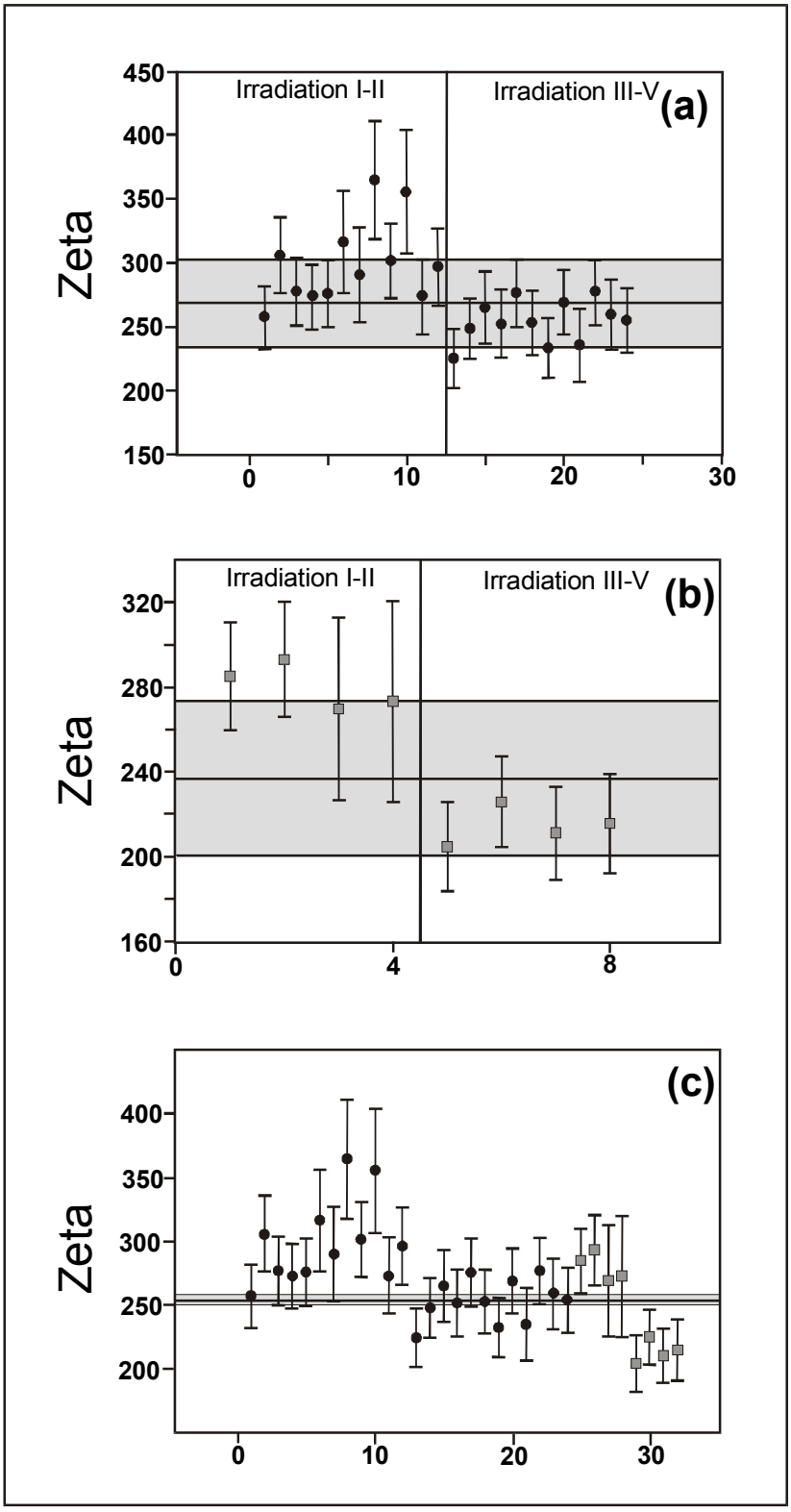

Figure 3.7: ζ-calibration factors for Durango (DUR) apatite with IRMM-540 dosimeter glass (a) and Fish Canyon Tuff (FCT) apatite (b) determined on the basis of co-irradiated mounts of these age standards in the several irradiation packages. Error bars are 2σ. SWMZ values for both DUR and FCT are indicated by the shaded area. (c) Composite of both DUR and FCT ζ-values in respect to the OWMZ value (see text for further details).

The OWMZ presented here is calculated for IRMM-540 glass as mentioned before. The characteristics of this glass were described by De Corte et al. (1998) (section 1.7.1.3). An overview of specific characteristics of other U-doped glass monitors used in FT dating is presented by Hurford (1998). Of particular interest is the ^{235}U concentration in these glasses. On the basis of this parameter, ζ-factors obtained with different glass dosimeters can be compared. A relationship between ζ-factors calculated from ρ_d-values from different glass dosimeters and the ^{235}U concentrations of these respective glass dosimeters was established by Green (1985) and can be written as:

$$\zeta_1\left[^{235}U_1\right] = \zeta_2\left[^{235}U_2\right] \qquad 3.20$$

or:

$$\zeta_1 = \zeta_2 \frac{\left[^{235}U_2\right]}{\left[^{235}U_1\right]} \qquad 3.21$$

Subscripts 1 and 2 denote two different U-doped glass dosimeters, and $[^{235}U]$ is the concentration (ppm) of this isotope in the particular glass. Using equation 3.19 and our OWMZ value of 253.1 ± 2.4 (using IRMM-540 glass), corresponding ζ-values for the SRM612, CN-1, CN-2 and CN-5 glasses (section 1.7.1.3) were calculated and compared to some published values (table 3.7). Shin and Nishimura (1991) performed an extensive study of ζ-values for apatite using the SRM612, CN-1, and CN-2 glasses irradiated at several irradiation facilities.

Table 3.7: Comparison of corresponding ζ values (ζ_{cor}) calculated on the basis of an OWMZ of 253.1 ± 2.4 obtained for the IRMM-540 glass dosimeter, and the ^{235}U concentration (in 10^{-2}ppm) in four other (SRM612, CN-1, CN-2 and CN-5) glass dosimeters. These values are compared to published ζ factors (ζ_{comp}) for these glass dosimeters. All ζ factors are expressed as (a cm^2) and uncertainties are reported on the basis of 2σ.

Glas dosimeter	**$[^{235}U]$**	**ζ_{cor}**	**ζ_{comp}**	**Reference**
IRMM-540	10.0080	253.1 ± 4.8	---	---
SRM 612	8.9413	283.3 ± 5.4	305.9 ± 41.2	Shin and Nishimura (1991)
CN-1	28.6632	88.4 ± 1.7	101.1 ± 14.6	Shin and Nishimura (1991)
CN-2	26.2800	96.4 ± 1.8	109.6 ± 15.8	Shin and Nishimura (1991)
CN-5	8.7624	291.2 ± 5.5	350 ± 40	Hurford (1998)

3.5. The Q-factor

3.5.1. Determination of Q from age standards analysis

The Q-factor or procedure factor (Wagner and Van den haute, 1992) is a parameter used in the absolute FT age equation (see section 1.4) that, like the ζ-factor, incorporates uncertain quantities linked to personal, procedural, revelation and observational aspects as explained earlier. The difference with ζ is that Q does not include nuclear parameters such as the ^{238}U fission decay-constant (λ_f) and the thermal neutron cross section (σ) and that Q is used in the age equation together with the absolute thermal neutron fluence (ϕ) determined with metal activation monitors. In this way, the Q-factor can also be viewed as a calibration factor, as a deconvoluted ζ-factor where nuclear parameters are considered as known constants and subsequently lifted out of the ζ-factor.

As explained, when the spontaneous and induced tracks are revealed and observed with exactly the same efficiency, this Q-factor should equal 1. This should theoretically be the case for apatite if a population method of FT analysis is followed. However, for obvious reasons, there always are substantial differences in preparational and observational conditions when different materials are used to obtain the ρ_s and ρ_i values, so we expect a Q-factor ≠ 1 in the ED method (also see section 1.8.2 for more details).

If we consider the fundamental FT age equation as it was deduced in section 1.4 (for explantion of the symbols see the mentioned section), we find for an apatite age standard with reference age t_S:

$$t_S = \lambda_\alpha^{-1} \ln[(\lambda_\alpha/\lambda_f)(\rho_s/\rho_i)QGI\sigma\phi + 1] \qquad 3.22$$

Or rewriting the equation for Q yields:

$$Q = \frac{\lambda_f}{\lambda_\alpha} \frac{\left(e^{t_S\lambda_\alpha} - 1\right)}{\frac{\rho_s}{\rho_i} GI\sigma\phi} = \frac{R_{e,i}\eta_i q_i}{R_{e,s}\eta_s q_s} \qquad 3.23$$

So, when an apatite age standard (e.g. Durango, $t_S = 31.4 \pm 0.5$ Ma), with a muscovite ED attached ($G = 0.5$) is irradiated with an absolute thermal neutron fluence ϕ (determined by use of metal activation monitors for example) and considering all nuclear parameter known, a Q- factor can be calculated for that particular age standard by simply counting the spontaneous and induced tracks as is done for the ζ-factor.

Following Poissonian statistics and the same reasoning as was done for the ζ-calibration in the previous section, the error on the Q-factor can be calculated from:

$$\sigma_Q = Q\sqrt{\left(\frac{\sigma_{t_S}}{t_S}\right)^2 + \frac{1}{N_s} + \frac{1}{N_i} + \left(\frac{\sigma\phi}{\phi}\right)^2} \qquad 3.24$$

The relative error for the absolute thermal neutron fluence (ϕ) determinations carried out with γ-spectrometry for the irradiation facility and detectors used in this work, is typically 2.5% (e.g. Van den haute et al., 1988).

Q-data for Durango and Fish Canyon Tuff apatite are listed in table 3.6. In the same fashion as SWMZ in the previous section, we define a *sample weighted mean Q-factor* (SWMQ) for these apatite age standards:

$$SWMQ = \frac{\sum_j \frac{Q_j}{\sigma_j^2}}{\sum_j \frac{1}{\sigma_j^2}} \qquad 3.25$$

With an error given by:

$$\sigma_{SWMQ} = \sqrt{\frac{1}{\sum_j \frac{1}{\sigma_j^2}}} \qquad 3.26$$

Calculation for both apatite age standards yields following result:

$SWMQ_{DUR} = 1.061 \pm 0.011$

$SWMQ_{FCT} = 1.020 \pm 0.023$

Combining both values, we determined an *overall weighted mean Q-factor*, OWMQ = 1.054 ± 0.010.

In comparison with the SWMZ values of both apatite age standards, the OWMQ values exhibit a smaller difference (4% compared to 13%). The main reason for this smaller discrepancy in our opinion is that in the ζ-factor calculation the FT density from glass dosimeters (ρ_d) is used (equation 1.30). This ρ_d value is an extra source of uncertainty. If a more systematic investigation of this issue would confirm these findings, it would provide an additional point of advantage for the use of Q-factors instead of ζ-factors in the calibration of FT dating with the ED method.

Using this OWMQ, or Q-factor, the relevant nuclear parameters and an absolutely determined thermal neutron fluence, we are able to use the fundamental FT age equation formulated by Wagner and Van den haute (1992) and we can obtain absolute FT ages next to ζ-ages as is conventional (Hurford, 1990). The Durango Q-data are presented in figure 3.8 in relation to the SWMQ.

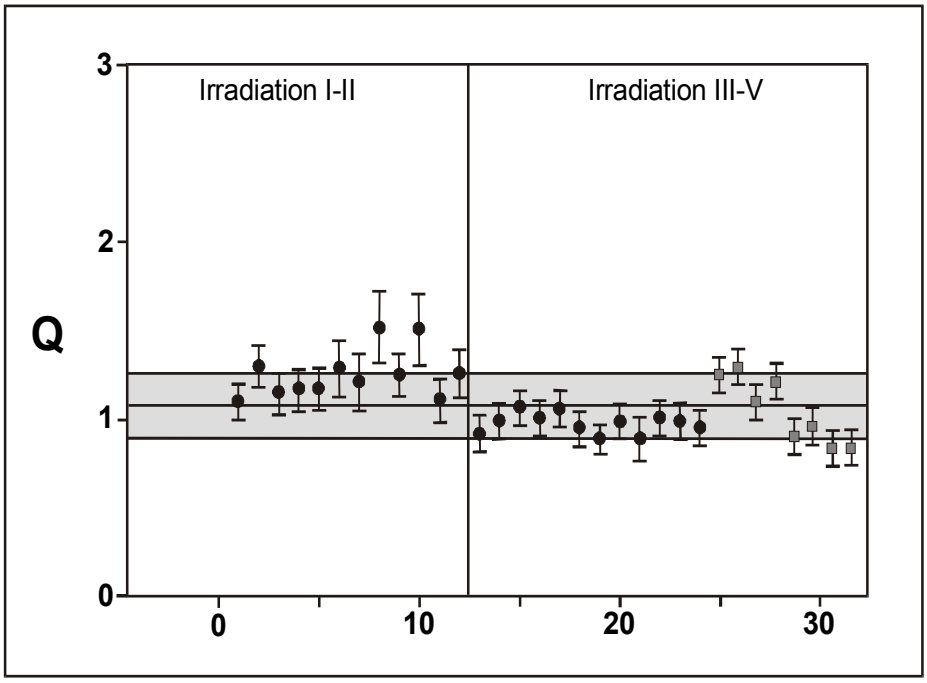

Figure 3.8: Q-calibration factors for Durango (black dots) and Fish Canyon Tuff (gray squares) apatite on the basis of co-irradiated mounts of the age standards in several irradiation packages. The OWMQ value is indicated by the shaded area.

The determination of the Q-factor in this way involves a 4π-geometry or internal polished and etched surface of the spontaneous tracks in the apatite and a 2π-geometry for the external surface of the ED for the induced tracks.

3.5.2. Experimental determination of the Q-factor

In order to evaluate the Q-factor for apatite dating with a muscovite ED we irradiated a pre-annealed apatite sample with an attached ED. If it is considered that Q = 1, the induced FT density in the apatite (ρ_{ap}) should be equal to the induced FT density in the attached muscovite ED (ρ_{ED}). Deviation from unity for the ρ_{ap}/ρ_{ED} values can only be attributed to differences in registration, revelation and observation between the materials apatite and muscovite. The following experiments were based on work by Jonckheere and Van den haute (2002); Jonckheere (2003a) and Enkelmann and Jonckheere (2003) on the efficiency of FT counts in internal and external surfaces in Durango apatite and a muscovite ED.

In chapter 1 (section 1.3, equation 1.7) we derived an expression for the areal fission track density as (for symbols see the appropriate section):

$$\rho_e = gNR_e\eta q$$

If we write this expression for the cases of ρ_{ap} and ρ_{ED} and if we the ratio we obtain:

$$\frac{\rho_{ap}}{\rho_{ED}} = \frac{g_{ap}\,{}^{235}NR_{e,ap}\eta_{ap}q_{ap}}{g_{ED}\,{}^{235}NR_{e,ED}\eta_{ED}q_{ED}} \qquad 3.27$$

Because the tracks in the apatite and the ED both originate from the ^{235}U present in the apatite, the spatial concentration of the ^{235}U (^{235}N) can be omitted from the equation. Considering the definitions for the geometry ratio (G) and the procedure factor (Q) as given in section 1.5 (equations 1.16, 1.17 and 1.18), we can write:

$$\frac{\rho_{ap}}{\rho_{ED}} = \frac{g_{ap}}{g_{ED}}\,\frac{1}{Q} \qquad 3.28$$

The geometry ratio here, $G = g_{ap}/g_{ED}$ equals 1 (0.5/0.5) if a 2π geometry is used (external surface of an apatite crystal is etched), or $G = 2$ (1.0/0.5) if a 4π geometry is used (internal surface).

In irradiation V of this work, two pre-annealed apatite mounts with muscovite ED were irradiated (DUR-AN-1 and DUR-AN-2). Prismatic sections, parallel to the c-axis, of a single Durango apatite crystal were used. The apatite was annealed in a furnace at 450°C for 10 hours. After irradiation ($\phi = 2.244 \times 10^{15}$ neutrons/cm^2, see table 3.2) the apatite and muscovite ED were etched according to the characteristics described in table 3.1.

$2\pi/2\pi$ geometry

In a first experiment the $2\pi/2\pi$ geometry ratio was used ($G = 1$), so the reciprocal value of the $\frac{\rho_{ap}}{\rho_{ED}}$ ratio directly gives the Q-factor. In this experiment the ED and the Durango apatite crystals were directly etched after irradiation. For the apatite the etched surface is an external surface as tracks only originated from under the originally polished and etched surface. Results of the counting of the induced tracks in both the apatite and the ED muscovite are presented in table 3.8.

Based on the average $\frac{\rho_{ap}}{\rho_{ED}}$ ratio, calculation of the Q-factor yielded following results:

DUR-AN-1: $Q = 0.91 \pm 0.04$

DUR-AN-2: $Q = 0.96 \pm 0.03$

This yields a $SWMQ_{DUR}$ of 0.94 ± 0.02, which is in agreement with results for Durango apatite published by Iwano and Danhara (1998). These researchers obtained a value of 0.98 ± 0.04 for Durango apatite in a 2π/2π geometry. The small deviation from unity, if significant, implies that more tracks are counted in the apatite in comparison to the mica.

Table 3.8: FT analysis of Durango apatite age standards for the experimental determination of the Q-factor for both 2π/2π and 4π/2π geometry. The number of counted grains in the apatite (ap) and the external detector (ED) is represented by $n_{ap,ED}$, $N_{ap,ED}$ is the number of counted tracks. The track densities for the apatite and the ED are given by $\rho_{ap,ED}$ and ρ_{ap}/ρ_{ED} is their ratio (average of individual apatite grain by grain analysis with ED). Track densities are given in 10^5 tracks/cm^2.

Geometry	Standard	n_{ap}	N_{ap}	ρ_{ap} (± 1σ)	n_{ED}	N_{ED}	ρ_{ED} (± 1σ)	ρ_{ap}/ρ_{ED}
2π/2π	DUR-AN-1	100	1825	2.852 (0.067)	100	1695	2.648 (0.064)	1.077 ± 0.037
2π/2π	DUR-AN-2	100	1999	3.123 (0.070)	100	1936	3.025 (0.069)	1.032 ± 0.033
4π/2π	DUR-AN-1	50	1751	5.472 (0.131)	50	910	2.844 (0.094)	1.924 ± 0.081
4π/2π	DUR-AN-2	50	1844	5.763 (0.134)	50	919	2.872 (0.097)	2.007 ± 0.086

Conversely, Iwano and Danhara (1998) obtained a value of 1.16 ± 0.05 for Fish Canyon Tuff apatite. This gives an OWMQ = 1.06 ± 0.03 for their apatite data. Also for zircon (OWMQ = 1.34) and sphene (OWMQ = 1.13) age standards they find values considerably higher than 1. Hence, in contrast to our experiments and those by Iwano and Danhara (1998) for Durango apatite, track revelation and observation for all other experiments of these authors are higher in the mica. One of the main differences between the Durango apatite and the other apatites and minerals used in the Iwano and Danhara (1998) experiments is the fact that Durango forms excellent euhedral crystals from which centimeter scale prismatic slices perfectly parallel to the crystallographic c-axis can easily be obtained. This is not the case for Fish Canyon Tuff apatite and the zircon and sphene samples used by Iwano and Danhara (1998). Although these authors stress they took great care in selecting only the prismatic crystal faces in these other samples, the counting was done on several grains, with possibly different crystallographic orientations. Moreover, there might exist an etching efficiency difference between Durango and Fish Canyon Tuff apatite due to their different chemical composition. Whatever the case, it appears that more tracks are registered and counted in Durango apatite with respect to the mica ED attached. This seems strange as the etchable range (R) of an induced track by a single fission fragment in apatite is lower (~8 μm) than in muscovite (~10 μm) (see figure 3.9). While the effect for apatite to mica (8 to 10 μm) can be considered as modest, it is

more outspoken for sphene (6.5 to 10 μm) and zircon (5 to 10 μm), which is indeed reflected by the high Q-factors obtained by Iwano and Danhara (1998) for these minerals. In our opinion the paradox in the case of Durango apatite could be explained by the fact that the small deficiency in track registration of the apatite with respect to the mica is overcompensated by bulk etching of the apatite surface. In this scenario the bulk etching removes material from the apatite surface at μm scale and reaches track ends within the interior of the apatite crystal; track ends that did not originally intersect the polished surface. In this way, during etching, an amount of tracks is added apparently at such a rate that it overcompensates the fission fragment range difference between Durango apatite and muscovite mica. This hypothesis is only provisional and deserves a more elaborate systematic research. However, Jonckheere (1995) found etch velocities perpendicular to several types of crystal surfaces of Durango apatite ranging from 0.1 to 0.6 μm per minute.

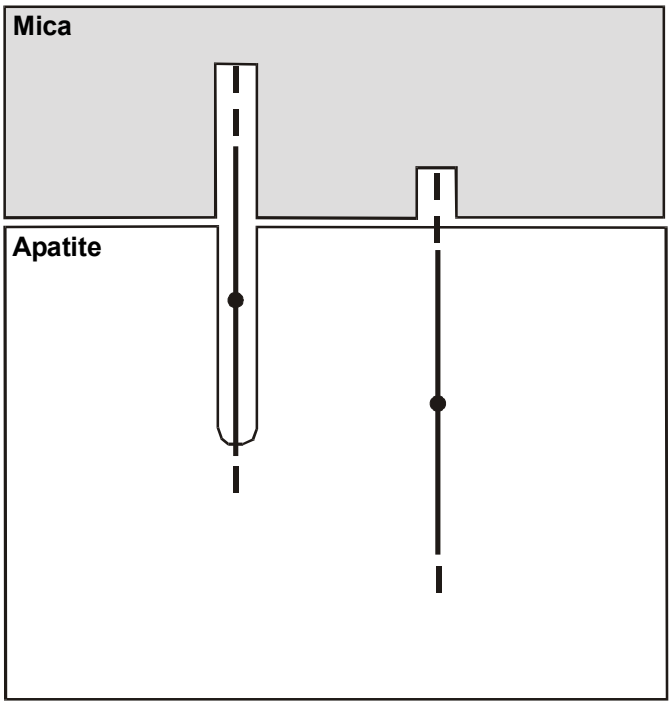

Figure 3.9: A ^{235}U nuclide (black dot) fissions in the interior of an apatite crystal and produces a latent FT with a specific registration threshold for apatite (black solid lines) and the attached mica external detector (black broken lines). When the ^{235}U nuclide is close enough to the etched apatite surface (i.e. less than ~8 μm, which is the etchable range of the latent track in apatite), etching reveals the track in both the apatite and the mica (left side of drawing). When the fissioned nuclide was located more than ~8 μm, but less than ~10 μm (the etchable range of the track in mica) below the etched surface, the track is not revealed in the apatite, but it still is revealed in the mica (right side of drawing). When the nuclide was even further down (more than ~10 μm) in the interior of the crystal, it is not revealed at all (after Iwano and Danhara, 1998).

4π/2π geometry

A second experiment involved determination of the Q-factor in a 4π/2π geometry ratio (G = 2). This is the same geometry used for our age standard Q-factor determination (section 3.5.1) and used in conventional FT dating with the ED method. In this case, nothing changed for the ED in respect to the previous experiment, but the apatite was repolished and then re-etched under the same conditions, exposing in this way an internal etched apatite surface intersected by fission tracks originating from both under and above the polished and etched surface. Counting results are presented in table 3.8. Given the 4π/2π geometry and considering equation 3.26, the Q-factor in this case is given by the reciprocal value of $\frac{1}{2}\frac{\rho_{ap}}{\rho_{ED}}$. This produced following results:

DUR-AN-1: $Q = 1.04 \pm 0.04$

DUR-AN-2: $Q = 1.00 \pm 0.04$

In this case a $SWMQ_{DUR}$ value of 1.02 ± 0.03 is obtained (within 1σ). Within errors, this value corresponds with the value of 1.01 ± 0.02 published by Iwano and Danhara (1998) for this geometry ratio. Our value does however differ somewhat from the OWMQ of 1.054 ± 0.010 we obtained by means of age standard analysis that also exhibit the 4π/2π geometry ratio (section 3.5.1). Our value of 1.054 ± 0.010 was obtained after several analyses of both Durango and Fish Canyon Tuff apatite, while in these experiments only Durango was used. Iwano and Danhara (1998) obtain an experimentally derived OWMQ for both apatite age standards (Durango and Fish Canyon Tuff) of 1.098 ± 0.030. For zircon they find 1.37 and for sphene 1.20. The 4π/2π Q-factor we derived on experimental basis is rather low when compared to the Iwano and Danhara (1998) data and the OWMQ from our age standard analyses. We therefore opt to solely use our 1.054 ± 0.010 OWMQ value to calculate absolute FT Q-ages (see chapter 6).

CHAPTER 4

THE ALTAI AND TIEN SHAN MOUNTAIN RANGES: GEOLOGICAL AND GEODYNAMICAL SETTING IN THE CENTRAL ASIAN DEFORMATION ZONE

In this chapter a detailed overview is given of the geological and geodynamical history of the study areas in the Altai and Tien Shan Mountains. Both mountain ranges are situated in the Central Asian Deformation Zone. Our overview concentrates mainly on the several units composing this Central Asian Deformation Zone, but also bordering regions such as the West Siberian Basin, the Tibetan Plateau and the Himalayan orogen are discussed. The geological evolution of these adjacent regions influenced our study areas at various moments in geological history. Our AFT results can clearly be linked to some of these events. Moreover, other AFT studies conducted within the Central Asian Deformation Zone and within these adjacent areas will be compared to our results (chapter 6). Therefore we decided to present a broad geological and geodynamical setting as a framework in which we can more easily inegrate our AFT data interpretation.

4.1. Location and general setting

4.1.1. The Central Asian Deformation Zone

The *Central Asian Deformation Zone* (CADZ) is the largest intracontinental orogenic system in the world. It runs over a distance of more than 5000 km, from the Pamir-Tien Shan region northwest of the Himalayan orgenic front to the Stanovoy range near the Okhotsk Sea (figure 4.1). It is composed of many larger and smaller tectonic and geodynamic units in a basin and range configuration, making up a characteristical blocky mosaic structure as e.g. described by Şengör et al. (1993). Two components, the Altai Mountains and the Tien Shan Mountains will be discussed in greater detail as they represent the study areas for this work.

The CADZ can be regarded as the suture zone between the Archean and Early Proterozoic Siberian cratons and an assemblage of North Chinese and Central Asian terranes. All these different blocks were accreted onto the Eurasian plate during the Palaeozoic and Mesozoic. The accretion also continued in the Cenozoic, with the India-Eurasia collision as a final and marked example.

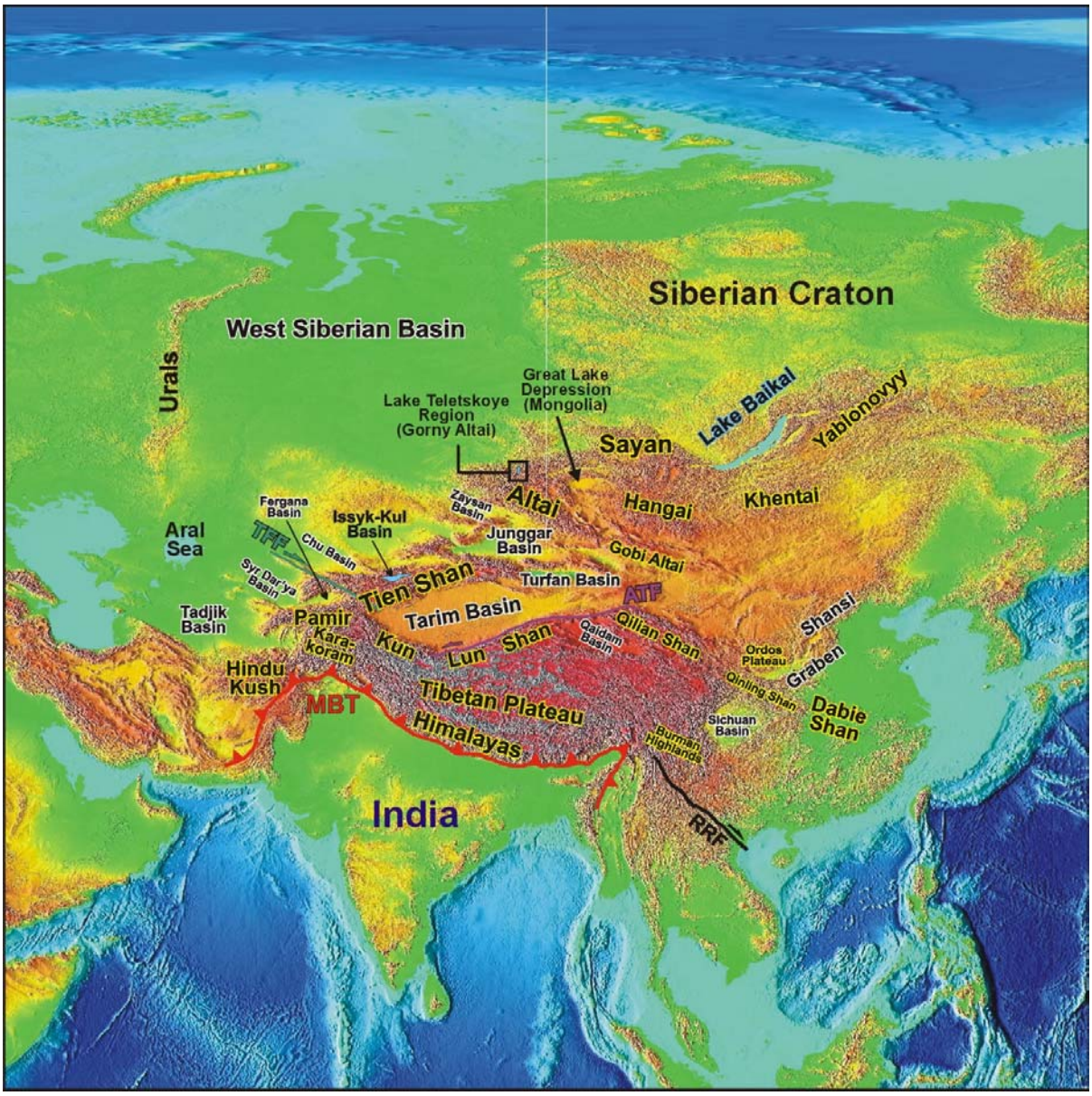

Figure 4.1: Relief map of Asia. The main units composing the Central Asian Deformation Zone (CADZ) between the West Siberian Basin, India and the Siberian craton are indicated. The areas studied in this work are highlighted: The Russian Altai Mountains, in particular the Lake Teletskoye Region, and the Kyrgyz Tien Shan Mountains, in particular the Lake Issyk Kul Region. Important structures are also shown: MBT = Main Boundary Thrust of the Himalayas, RRF = Red River Fault zone (strike-slip), ATF = Altyn Tagh Fault zone (strik-slip), TFF = Talas-Fergana Fault zone (strike-slip).

This major continent-continent collision is seen as the main driving force for the present tectonic reactivation throughout many parts of the CADZ (e.g. Molnar and Tapponier, 1975 and 1977 and Tapponier and Molnar, 1979). Other authors have indicated that mantle plume activity could also play a role in the development of the CADZ (e.g. Khain, 1990; Ufimtsev, 1990; Dobretsov et al., 1996). Still others see the evolution of the CADZ in a broader lithospheric folding with a characteristic wavelength that encompasses the entire lithosphere (Nikishin et al., 1993; Burov et al., 1993; Cloetingh et al., 1999). The lithospheric folding is seen as an effect of intraplate compressive stresses induced by the ongoing convergence between India and Eurasia and causing its typical basin and range geometry. In this perspective, basins represent whole-lithospheric synclines and mountain ranges whole-lithospheric anticlines.

In any case, active crustal deformation is taking place today over a vast region between the Himalayas and Siberia, resulting in the so-called eastward stepping en-echelon configuration of the composing mountain belts (e.g. Pamir, Hindu Kush, Tien Shan, Altai, Sayan and others) (figure 4.1). In the literature, the CADZ is also termed the *Central Asian Mountain Belt* (e.g. Khain, 1990; Ufimtsev, 1990; Dobretsov et al., 1996), *Central Asian Fold Belt* (e.g. Khain et al., 2002), *Central Asian Mobile Belt*, *Central Asian Orogenic Belt* and so forth, or the *Central Asian Triangle* (e.g. Cobbold and Davy, 1988). In this work, parallel with the work by Dehandschutter (2001) who deals with the same study areas in a structural geological framework, CADZ is used to denote the entire actively deforming region in Central Asia.

4.1.2. The Altai-Sayan Mountains

The *Altai-Sayan* Mountains form the northern-central part of the CADZ (figure 4.1). They represent a Late Cenozoic reactivated mountain belt located at the junction of Russia, Mongolia, China and Kazakhstan. The present Altai mountains are composed of several smaller tectonic units. Our study focuses mainly on one such unit, the *Gorny Altai*, in the northern Altai ranges in Siberia. The E-W

Figure 4.1: Relief map of Asia. The main units of the Central Asian Deformation Zone (CADZ) between the Urals, India and the Siberian craton are indicated. MBT is the Main Boundary Thrust of the Himalayas, RRF, is de Red River Fault zone, ATF is the Altyn Tagh Fault zone, and TTF is de Talas-Fergana Fault zone.

considered as a single unit in Russian geomorphological and orographical literature. It comprises the Russian (northern Altai) *Rudny Altai* and Gorny Altai, *Tuva*, *West and East Sayan*. This division is indeed acceptable in physiographical terms and geologically reasonable to some extent, but it should be stressed that the tectonic and geodynamic evolution has been completely different in all these regions.

To the north, the Altai Mountains fan out in E-W striking ranges in their western part and in N-S striking ranges to the east. They are bounded by the *West Siberian Basin*, in particular by the *Biya-Barnaul* depression to the west (figure 4.1 and further, figure 4.16).

The Biya-Barnaul depression is separated from the *Kuznetsk* basin to its east by the *Salair* and *Alatau* Mountains, which can be considered as the northern foothills of the Altai. In the northern part of Gorny Altai, just south of the Salair-Alatau mountains, lies the N-S trending *Teletskoye Lake*, occupying a young graben. To the southwest the Altai is bounded by the *Irtysh-Zaisan* depression, forming part of the vast Kazakh plains. This boundary is clearly defined by the so-called *Irtysh* shear zone and the *Junggar* basin, which covers most parts of the Junggar microplate. To the southeast the Altai passes into the *Gobi-Altai* mountains. To the east the Sayan is bordered by the *Baikal* rift zone. South of Sayan and east of Altai, the *Depression of the Great Lakes of Mongolia* composes a plateau of lower elevation, passing eastward into the *Hangai* dome (see e.g. figure 4.1 and 4.16).

4.1.3. The Tien Shan Mountains

The *Tien Shan*, "the Heavenly Mountains" are a long (2500 km), seismically very active E-W trending intracontinental mountain range of high elevation (up to more than 7000 m). They are situated along the northern rim of the lens-shaped *Tarim* microplate, largely overlain by the present Tarim basin (figure 4.1 and 4.2).

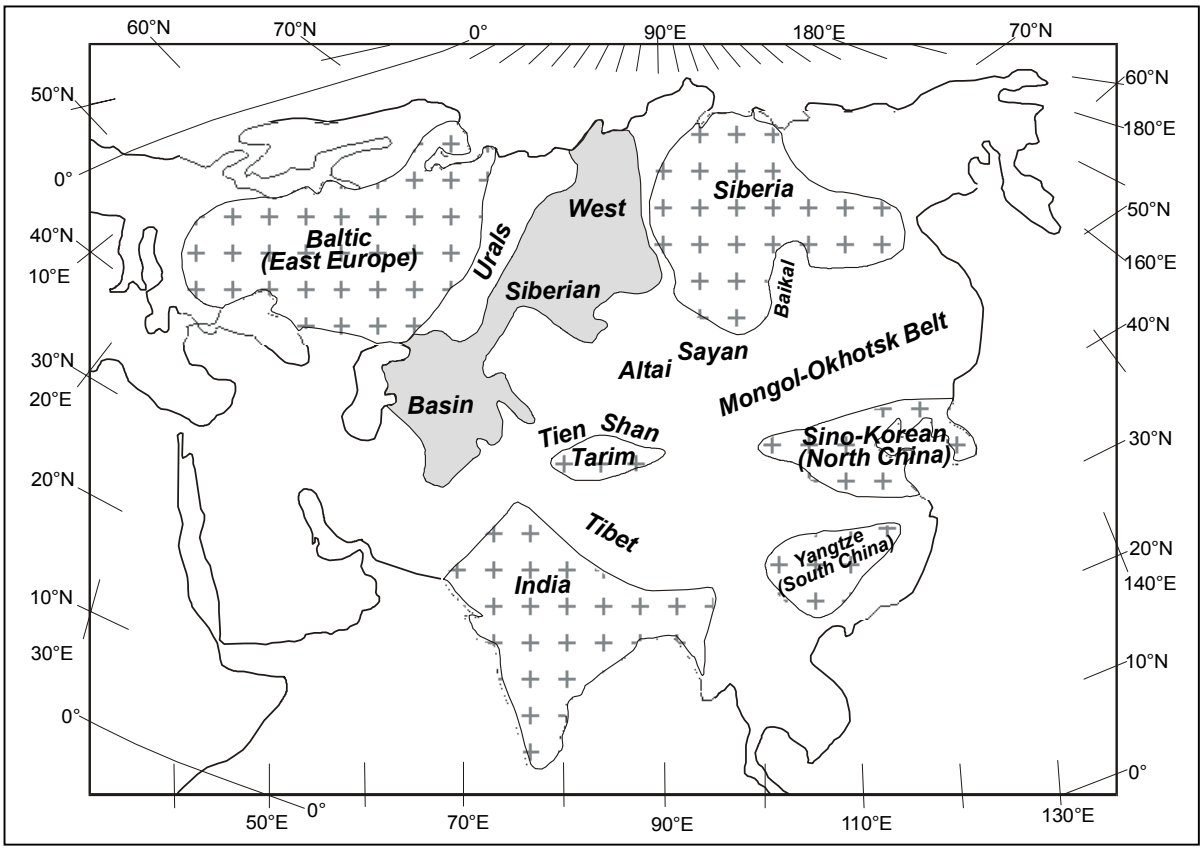

Figure 4.2: Sketch map of the positions of major cratonic cores, basins and fold belts within the Eurasian continent.

The eastern Tien Shan mountains are located in China, while the western part mainly extends within the republics of Kyrgyzstan, Tadjikistan and Uzbekistan. To the northwest, the Tien Shan are bounded by the Kazakh plains, to the northeast by the Junggar basin, north of which we find the Altai mountains as mentioned before. The southwestern tips of the Tien Shan join the *Pamir* and *Karakoram* mountains, which in their turn link up with the *Tibetan Plateau*. In the northern, Kyrgyz part of the Tien Shan, the *Issyk Kul Lake* occupies a large intramontane pull-apart basin. On the northeastern tip, the Tien Shan ranges are structurally linked to the southern parts of the Gobi Altai mountains (figure 4.1).

4.2. Precambrian evolution of the CADZ

The geological history of the CADZ can be traced back to the Late Proterozoic (Riphean) and Early Palaeozoic with the formation of the so-called *Palaeo-Asian Ocean* (PAO) at the current southern margins of the Archean-Early Proterozoic Siberian craton. The Siberian craton consists of two stable cores, the *Anabar* in the northern part and the *Aldan* Shield in the south (e.g. Khramov et al., 1985; Aftalion et al., 1991; Melnikov et al., 1994; Frost et al., 1998; Smethurst et al., 1998; Griffin et al., 1999) (figure 4.2 and 4.3). The East European or Baltic shield (*Baltica*), the North American cratons (*Laurentia*), and Siberia were connected by an world-wide orogenic event, the *Grenvillian* orogeny. In this way the aforementioned continents composed a Late Proterozoic supercontinent, *Rodinia*, distinct from most of *Gondwana*, the southern supercontinent at that time (Ilyin, 1990; Condie and Rosen, 1994; Frost et al, 1998; Pelechaty, 1998). The combined Siberia-Baltica continent is sometimes termed *Laurasia*. According to Palaeomagnetic data, Siberia resided most of its early history at equatorial latitudes with a manifest northward migration starting in Mid-Palaeozoic times and resulting in its present northerly position (Torsvik et al., 1995; Smethurst et al., 1998; Kravchinsky et al., 2001).

To the west and southwest, the Siberian basement is covered by a thick and deformed (meta)sedimentary cover, prominent on the so-called Anabar-Lena plate (figure 4.3) in the southern part of the craton, which is seen by some authors as a third distinctive component of the Siberian craton (Kravchinsky et al., 2001). The sediments represent Late Proterozoic passive margin sequences associated with the initial stages of the PAO evolution after the break-up of Rodinia (e.g. Zonenshain et al., 1990, Dobretsov et al., 1995a; Khomentovsky and Gibsher, 1996; Lindsay et al., 1996; Pelechaty et al., 1996). Relics of the PAO crust are preserved in ophiolite belts fringing the southern margin of the Siberian craton. Some of these ophiolites have been interpreted as obducted slabs of oceanic crust, thrust upon the southern Siberian margin during the the final stages of the PAO evolution at the Proterozoic-Phanerozoic transition (Vendian-Cambrian; see figure 4.4) (e.g. Dobretsov et al., 1992; Zorin et al., 1993; Melnikov et al., 1994; Dobretsov et al, 1995a).

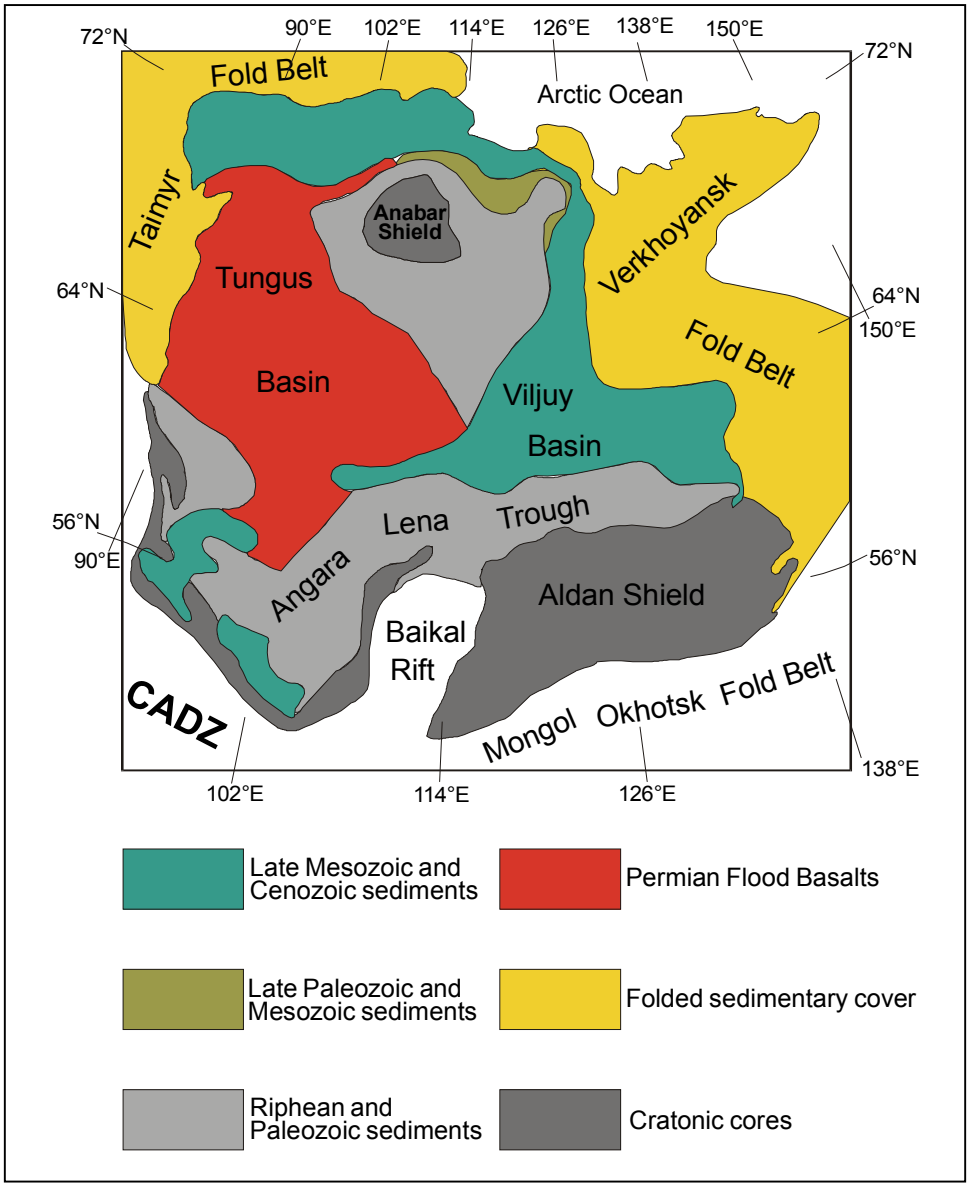

Figure 4.3: Sketch map of the Siberian craton, composed of the Anabar and Aldan shields and the Angara-Lena platform, with its deformed Phanerozoic cover.
CADZ = Central Asian Deformation Zone (redrawn after Smethurst et al., 1998).

On the other hand, Khain et al. (2002) proposed that far older ophiolites are exposed along the southern rims of the Siberian craton. These authors obtained a U-Pb zircon age of ~1Ga for the Dunzhugur ophiolite complex in eastern Sayan. This is the oldest known ophiolite suite within the CADZ and gives evidence of a Mesoproterozoic Siberian margin/oceanic basin interface that might be linked to the opening and spreading phase of the PAO or represent the development of another oceanic basin altogether. This hypothesis would cast considerable doubt on the supposed configuration of Siberia within the Rodinian supercontinent. However, it can be reconciled with the hypothesis of Dobretsov et al. (1995a), who constrain the initial stages of POA evolution between 1.0 and 0.9 Ga, directly succeeding the Grenvillian orogeny.

The eastern part of the CADZ is squeezed between the Siberian craton to the north and the *North China* or *Sino-Korean* craton to the south (figure 4.2). The North China craton is also mainly of Archean age and is composed of a western and eastern unit separated by a reworked central zone (Zhao et al., 1993; Zhao, 2001). To the west, the CADZ disappears under Mesozoic deposits of the West Siberian Basin. The vast West Siberian Basin is in turn separated from the East European craton by the *Ural* Mountain Belt.

4.3. Palaeozoic evolution of the CADZ

The Palaeozoic evolution of the northern parts of the CADZ is largely dominated by the evolution of the Palaeo-Asian Ocean (PAO) south of the Siberian craton. This evolution already started in the late stages of the Precambrian and possibly earlier as mentioned above. The PAO represented a vast oceanic domain resulting from the fragmentation of the Rodinia supercontinent and separating Siberia from Gondwana to the south. During the closure of the PAO in Latest Precambrian to Early Palaeozoic times, various peri-Gondwanian fragments and oceanic domains (island arcs, seamounts e.g.) were accreted onto the Siberian craton. The Palaeozoic era is strongly characterized by this large-scale accretion and growth of Eurasia. During this time the ancestral characteristic blocky mosaic structure of the present CADZ was formed (e.g. Coleman, 1989; Zonenshain et al., 1990; Şengör et al., 1993; Zorin et al., 1993). The several composing units, of what is called the tectonic collage, are mainly separated by large strike-slip fault zones, reactivated during several successive tectonic events (e.g. Dobretsov, 1993 and 1995b; Şengör et al., 1993; Delvaux et al., 1995a; Laurent-Charvet et al., 2002; Buslov et al., 2003). Şengör et al. (1993) label the Late-Precambrian-Early Mesozoic orogenic rim of southern Siberia as the *Altaids* (section 4.3.3).

Most of the collisional events described below are followed by episodes of large-scale syn- and post-collisional plutonism, again adding to the crustal growth of Eurasia (e.g. Dobretsov et al, 1995a; Han et al., 1997; Vladimirov et al., 1997; Chen et al., 2000; Distanova, 2000; Hu et al., 2000). Also widespread evidence of regional metamorphism is abundant in these Central Asian zones. Metamorphic events in some cases were of high-grade character as shown by UHP (eclogites) rocks and blueschists in various regions. The diamond-bearing Kokchetav UHP massif of Northern Kazakhstan is one obvious example (Theunissen et al., 2000).

4.3.1. The Early Palaeozoic

The *Altai-Mongol* (AM), *Tuva-Mongolia* (TM) and *Kazakhstan* microplates are examples of possible Gondwanian terranes (figure 4.4) accreted directly onto the Siberian craton. On the other hand, terranes such as *Gorny Altai* and *Rudny Altai* (in the Russian Altai Mountains), represent PAO island arc and seamount sequences (Dobretsov, 1993 and 1995b; Berzin et al., 1994; Berzin and Kungurtsev, 1996; Buslov et al., 2001b).

The microplates typically consist of Precambrian basement rocks (e.g. Salnikova et al., 2001) with mainly continental affinities, overlain by their specific Palaeozoic cover. It has been proposed that the TM plate came into contact with Siberia by Vendian-Cambrian times (Melnikov et al., 1994; Pecherskii et al., 1994; Kravchinsky et al., 2001), and that it was an integral part of Siberia in Early Silurian times (Bachtadse et al., 2000).

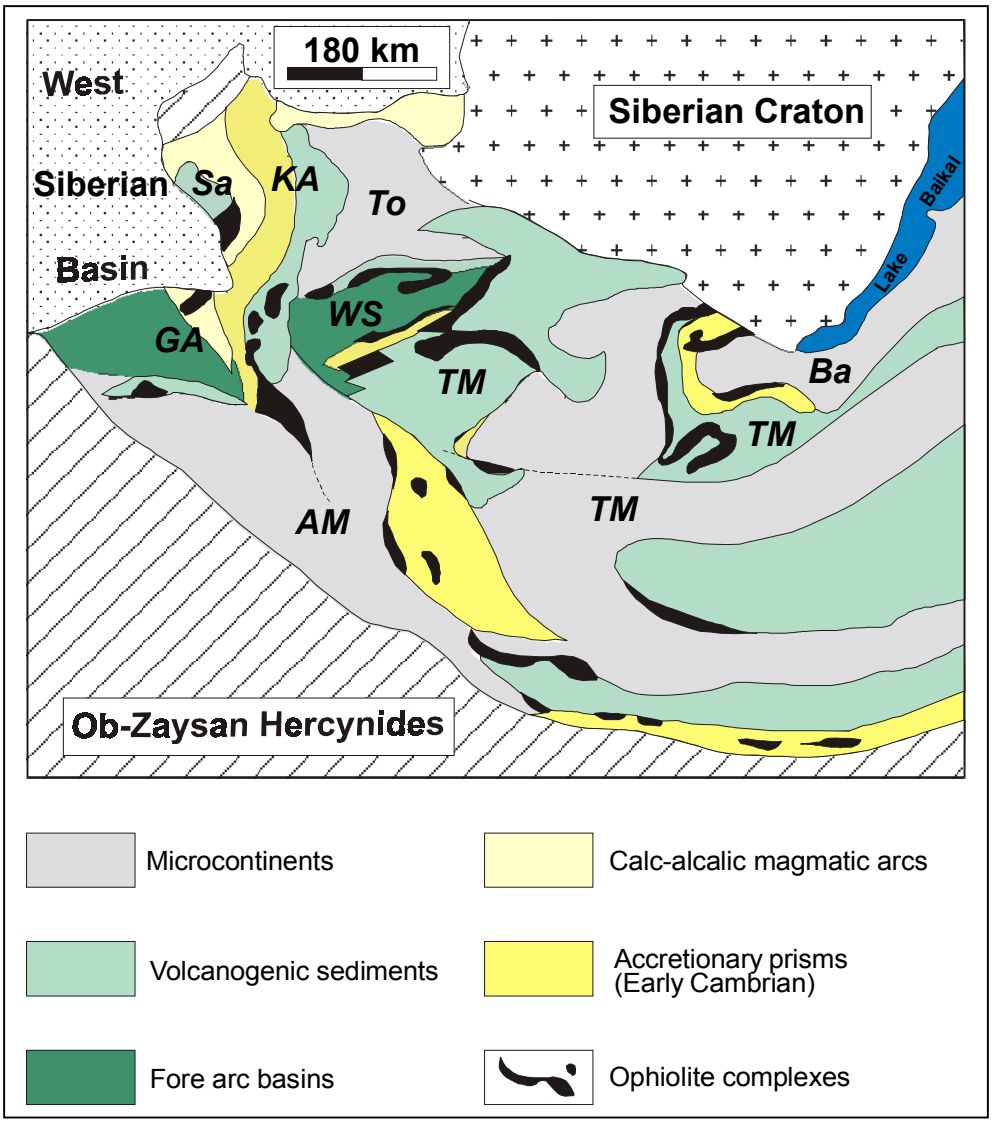

Figure 4.4: Caledonian and Hercynian orogenic rim of the Siberian craton. Subsequent collisions of microplates (To = Tomsk, Ba = Barguzin, TM = Tuva-Mongolia, AM = Altai-Mongolia) with Siberia during the Caledonian orogeny, wedged several Paleo-Asian Oceanic domains (Sa = Salair, KA = Kuznetsk-Alatau, GA = Gorny Altai, WS = West Sayan, TM = Tuva-Mongolia island arc complex) in the orogenic edifice. Various ophiolite complexes occur along the sutures. As Kazakhstan collided with the Siberian orogenic rim, closure of the Ob-Zaysan part of the Palaeo-Asian Ocean during the Hercynian orogeny completed the accretion of Eurasia (after Dobretsov et al., 1996).

The island arc systems such as Gorny Altai (figure 4.4) were accreted onto Siberia either as separate units or as an amalgamated part of a larger unit, as a composite with a microplate for example (e.g. Coleman, 1989; Berzin et al., 1994). In the latter case this gave rise to early collision events (Late Sinian-Vendian) within the microplates and arcs themselves. Still older events can be either related to the Grenvillian orogeny or to collision events of island arc systems with seamount arrays (Dobretsov et al., 1995a). The evolution of the Gorny Altai island arc system is a clear example of the latter case and will be discussed in somewhat more detail in the next chapter.

In analogy with Western literature, these Early Palaeozoic collisions are sometimes grouped as the *Caledonian* orogeny (e.g. Dergunov and Kheraskova, 1982; Mossakovsky and Dergunov, 1985; Dergunov, 1988; Delvaux et al., 1995a). Collision of the TM microplate with the Angara-Lena platform of Siberia was such an Early Caledonian event. In a first stage the Siberian passive margin and TM were still separated by an oceanic branch, with an active south-dipping subduction zone beneath TM further consuming the PAO crust. In the Late Cambrian-Early Ordovician TM collided with the southern margin of Siberia with subduction migrating southwards (Zorin et al., 1993). By the Early Silurian, TM was an integral part of the Siberian continent (Bachtadse et al., 2000). TM formed an accreted wedge on South Siberia and effectively divided the original continuous oceanic basin of the PAO (sometimes termed the proto-PAO) into a western (West Palaeo-Asian Ocean, WPAO) and an eastern (Palaeo-*Mongol Okhotsk Ocean*, PMOO) section. The latter evolved as a vast gulf of the already existing and spreading Palaeo-Pacific Ocean, resulting in fragmentation of the Rodinia supercontinent. Other smaller tectonic units collided with Siberia during that time. To the west, collision with the *Tomsk* microplate and to the east, near the present position of Lake Baikal, collision with the Barguzin microplate occurred (Delvaux et al., 1995a) (figure 4.4). Many of these collisions are associated with obduction of ophiolite complexes (e.g. Dobretsov et al., 1991; Simonov et al., 1999; Buchan et al., 2001; Buslov et al., 2001b).

Late-Silurian to Devonian tectonic events are known to have occurred along Siberia's southern margin and are grouped in a Late Caledonian stage. A Late Devonian-Early Carboniferous collision is distinguished in the WPAO domain and interpreted as an oblique collision of the AM microplate with the amalgamated Siberian margin (Berzin et al., 1994; Dobretsov et al., 1995b; Buslov, 1998; Buslov et al., 2000; Buslov et al., 2001b). In this way several oceanic units were wedged in between (e.g. the Gorny Altai and Rudny Altai unit) and important dextral strike-slip faults such as the *Teletsk, Kuznetsk-Kurai* and *Charysh-Terekta* were created. The AM microplate was by that time already a composite of several smaller terranes of which the so-called *Chulyshman* terrane is an example. Hence a western Siberian active margin developed between the accreted AM terrane and the Kazakhstan microplate to the southwest. Both terranes were at that time separated by a branch of the WPAO, the so-called *Ob-Zaysan* or *Irtysh-Zaysan* basin.

Evolution of the eastern CADZ involved the extension and subsequent closure of the Mongol-Okhotsk Ocean (MOO) between the amalgamated southeastern rim of Siberia and the North China craton with associated smaller (Mongolian) units (Mueller et al., 1991; Zhao et al.; 1993; Gordienko, 1994; Robinson et al., 1999). The Uralian Ocean separated the Siberian and East European cratons.

The Tien Shan area

The Tarim basin is underlain by a vast core of continental crust in the interior of the CADZ (see figure 4.2). The Tien Shan Mountains form its northern boundary suture with the Central Asian terranes discussed so far.

Along its northern margin two Palaeozoic collisional events have been inferred by most authors, although Chen et al. (1999) argue that the ancestral Tien Shan developed as the result of a single Palaeozoic closure of an oceanic domain in an oblique and hence diachronous fashion. During the Palaeozoic and even earlier, ophiolite and accretionary complexes were obducted along the sutures onto the continental crust (e.g. Gao et al., 1995; Volkova and Budanov, 1999; Chen et al., 1999). A first, Middle Palaeozoic collision occurred in Late Devonian-Early Carboniferous times. It involved thrusting of a small continental fragment, the central part of the present Tien Shan (the *Ili* or *Yili* block) onto the northern Tarim margin. An oceanic basin, the South Tien Shan Ocean extending between the colliding landmasses was actively subducted under the Central Tien Shan terrane, producing a magmatic arc in the Central Tien Shan. The collision occurred along the Southern Tien Shan suture, called the *Nikolaev* line or the *Qinbulak-Qawabulak* suture. A jump in subduction occurred and shifted to the current northern edge of the combined Tarim/Central Tien Shan block as the so-called *Turkestan* Ocean or North Tien Shan Ocean was being consumed. These events took place unrelated to the assembling Asian continent more to the north (Windley et al., 1990; Allen et al., 1991b; Allen et al., 1992; Zhang et al., 1993; Carroll et al., 1995; Gao et al., 1998; Chen et al., 1999; Brookfield, 2000).

4.3.2. The Late Palaeozoic

Again, in analogy with Western literature, the Late Palaeozoic geodynamical evolution of the CADZ is grouped as the *Variscan* or *Hercynian* orogenic cycle. Effects of the AM-Siberia collision persisted throughout much of the Carboniferous, reactivating Caledonian structures (e.g. Delvaux et al., 1995a; Dobretsov et al., 1995b; Buslov, 1998; Buslov et al., 2003). In the Permian the PAO (including the Ob-Zaysan branch) is closed completely, resulting in collision of Kazakhstan with Siberia and inducing large sinistral strike slip displacements of the blocky mosaic orogenic rim of Siberia (e.g. Buslov et al., 2000) (see figure 4.4). These events all contributed to the formation of the Pangea supercontinent. The newly formed as well as the older, reactivated shear zones carved up the juvenile supercontinent. Strike-slip deformation and displacement rearranged the complex assemblage of terranes. The Hercynian period is further characterized by a counter-clockwise rotation of the Siberian craton together with its entire stabilized Caledonian rim, and by a progressing evolution of the MOO in the eastern part of the CADZ (Mueller et al., 1991; Xu et al., 1997; Robinson et al., 1999; Zorin, 1999) where magmatic events were related to the convergence of Siberia with North China and associated blocks (Zhu et al., 2001). Northward subduction of the MOO underneath Siberia gave rise to an active Andean type margin. In the early stages of convergence a southward dipping subduction zone existed underneath the North Chinese terranes.

Middle and Late Palaeozoic collisional events are clearly recognized at both converging margins and are thought to be caused by smaller blocks or intenders as precursors to the main, complete closure of the MOO during the Mesozoic (Parfenov and Natal'in, 1986), that gave rise to the Mongol-Okhotsk fold belt (see next section).

The Tien Shan area

During Hercyian times continued closure of the so-called Turkestan or North Tien Shan Ocean, further to the south resulted in the accretion of the combined Tarim/Central Tien Shan terrane to the North Tien Shan/Bogda Shan island arc. This collision occurred in Late-Carboniferous-Early Permian times along the *Borohoro*-Northern Tien Shan suture (e.g. Kwon et al., 1989; Windley et al., 1990; Allen et al., 1991; Allen et al., 1992; Carroll et al., 1995; Allen and Vincent, 1997; Gao et al., 1998; Chen et al., 1999; Brookfield, 2000). The so-called *Junggar* Ocean between the combined Tarim, Kazakhstan and Siberian plates also closed during this time, although a small fragment of the Junggar Ocean was still present between the Tien Shan/Tarim block and the assembling Siberian continent (e.g. Li et al., 1989; Carroll et al., 1990). Later in the Permian, frontal collision of both landmasses resulted in complete amalgamation and assembly of Eurasia, trapping part of the Junggar plate between the collision zones. To the southwest the Tien Shan/Tarim collided with the *Turan* plate due to closure of the Turkestan Ocean between them. The Turan terrane is situated between the present Aral and Caspian Seas and the modern Tien Shan (Lemaire et al., 1997; Thomas et al., 1999a and 1999b). In the final stages of closure of the WPAO and amalgamation of the Altai, Kazakhstan, Junggar, Tien Shan and Tarim terranes in the Late Permian, older Hercynian and Caledonian structures were reactivated and large-scale counter-clockwise rotation and sinistral strike-slip fault movements characterize this deformational episode in most parts of the CADZ (Şengör et al., 1993; Allen et al., 1995; Dobretsov et al., 1995a; Bazhenov et al., 1999; Buslov et al., 2003). Major sinistral displacement of over more than 1000 km is recorded along the major *Irtysh* shear zone, following a somewhat older dextral shearing along the structure due to translation of Siberia with respect to Baltica. The Irtysh shear zone is a major structural boundary in the CADZ. It separates Siberian, Mongolian and Altai units to the north from Kazakhstan, Tien Shan, and Tarim to the south.

The Ural area

In the late stages of the Hercynian orogeny and Pangea assembly, closure of the Uralian Ocean between the East European craton and Siberia with its Caledonian and Hercynian rims was finalized, and the Uralian orogen was created (e.g. Scarrow et al., 2002). Today the Ural Mountains still outline the boundary between the European and Asian parts of the Eurasian plates.

4.3.3. The Altaid evolution

Şengör et al. (1993) present a somewhat different view on the Palaeozoic evolution of the CADZ from the one outlined above. Instead of several, distinct subsequent collisional and subduction events building the south Siberian orogenic rim, these authors propose a single long-lasting and large-scale subduction zone, the *Kipchak* arc. In their view, the Altaids evolved along this single zone during the Palaeozoic as a subduction-accretion complex with arc-magmatism migrating through the complex with time. Earlier events along the southern Siberian margin are suggested to originate from a separate tectonic episode, the *Baikalide* orogeny, correlated with a so-called *pre-Uralide* orogeny along the eastern margin of the Baltica continent. Vendian rifting would have split of parts of the orogenic rim and opened an oceanic basin, the *Khanty-Mansi* Ocean which would more or less correspond to the WPAO (e.g. Dobretsov et al., 1996). An eastern oceanic basin, the *Khangai-Khantey* Ocean would represent the proto-MOO as described earlier. The rifted part of the orogenic rim is the Kipchak arc, linking Baltica and Siberia in an analogous fashion as the Aleutian arc today links Siberia with North America. Oroclinical bending of the subduction-accretionary complexes along the Kipchak arc due to convergent and lateral movements of Baltica with respect to Siberia is thought to be responsible for the complex blocky mosaic structure of the Altaids, for the large-scale strike slip tectonics and for the orogenic events during Devonian-Early Carboniferous and Permo-Triassic times. During these events, the Khanty-Mansi Ocean was being consumed by subduction under the Kipchak units. However, in the model of Şengör et al. (1993), the Khangai-Khantey Ocean would have closed during the Early Mesozoic, which is contradicted by recent tectonic reconstructions and stratigraphic work of Zorin (1999). Şengör and Natal'in (1996) use the *Altaids* terminology by Şengör et al (1993) for the Palaeozoic orogens from Central Asia. Following the same terminology, the Mesozoic closure of the Tethys Ocean resulted in the development of the *Tethysides* to the South (Tibet e.g.). The terranes extending between the Altaids and Thetysides are called the *Intermediates* by these authors. They were accreted onto the southern Eurasian margin during the Palaeozoic-Mesozoic transition. The Turan plate (presently underlying North Iran, North Afghanistan, Uzbekistan, Turkmenistan and Southwest Kazakhstan) is thought to be an example of such a unit.

4.4. Mesozoic evolution

After the Hercynian orogeny, most of the orogenic southern Siberian rim remained a mountainous, uplifted terrane during the Triassic period. Within the continental interior, break-up of Pangea by mantle-plume activity was initiated as is testified by Permo-Triassic magmatism (flood basalts) and rifting processes (Nikishin et al., 2002). The Jurassic and Early Cretaceous are characterized by more localized events leading to formation of a number of tectonic intramontane depressions, filled with typical continental molasse deposits, volcanics and lacustrine coal bearing sediments. In general, these events started earlier in the western part of the orogenic belt.

In the Baikal region these basins have been associated with the initial stages of extension and opening of the Baikal Rift Zone (BRZ) after collapse of the uplifted area following the exclusively compressional tectonics during the Mongol-Okhotsk orogeny (Ermikov, 1994; Delvaux et al., 1995a; Zorin, 1999). During this continental extension various metamorphic core complexes were exhumed as a result of tectonic unroofing. During the Late-Cretaceous-Early Palaeogene, a period of regional tectonic quiescence and a warm, humid climate led to the development of an ubiquitous lateritic peneplain in many parts of Central Asia. It is recognized from the Baikal area to the current Tien Shan and Tarim areas (Ermikov, 1994; Deev et al., 1995; Delvaux et al., 1995a; Dobretsov et al; 1996). Dobretsov et al. (1996) also suggest the existence of a Triassic peneplain that is also found reworked in coal-bearing Jurassic intramontane basins in the Altai-Sayan area of the CADZ.

To the west of the current CADZ the Mesozoic development of the West Siberian Basin began. Its rifting can be associated with the incipient break-up of Pangea. To the east closure of the MOO continued and finally resulted in the Mongol-Okhotsk orogeny as mentioned earlier. At the southern Eurasian margin, accretion was a still ongoing process due to subduction of the Palaeo-Tethys oceanic lithosphere between Gondwana and Eurasia. Tectonic units forming the present Tibetan Plateau and adjacent regions collided with the amalgamated Eurasian continent as precursors of the collision with India during the Cenozoic. During the Mesozoic a less-active tectonic regime prevailed in the Tarim/Tien Shan region. Nevertheless during the Triassic to Middle Jurassic important episodic fault movements appear to have taken place throughout the region (e.g. Burtman, 1980; Hendrix, 2000).

4.4.1. The Mongol-Okhotsk Fold Belt

Sustained subduction of the MOO finally led to complete closure of the oceanic basin in the Late Jurassic-Early Cretaceous. Plutons from the Siberian active margin typically yield K-Ar ages from the Triassic to the Late-Jurassic. Subduction only occurred at the Siberian active margin as the North Chinese margin evolved into a passive margin during Permo-Triassic plate reorganization, marking the incipient break-up of the Pangea supercontinent. Remnants of the subducted oceanic lithospheric slab can still be recognized by seismic tomography as zones of high seismic velocity west of the present Lake Baikal (Van der Voo et al., 1999). North China was associated with Central Mongolian terranes during Early-Late Permian collisions that led to a composite Mongolian-North China continent. Collision between this North Chinese continent with the assembled Siberian orogenic rim resulted in the construction of the Mongol-Okhotsk Fold Belt, which is thought to have been similar in style and dimensions to the modern Himalayan orogen (e.g. Xu et al., 1997; Zorin, 1999). The main collision is constrained to the Middle Jurassic by Zorin (1999). During this collision several oceanic domains and island arcs (the *Onon* arc for example) were incorporated in the orogenic edifice. The collision has been documented by AFT dates that indicate an important Early Cretaceous denudation of the orogen in the Baikal area (van der Beek et al., 1996).

Deformation was not only confined to the collision zone itself, but affected many parts of the Caledonian and Hercynian hinterland, reaching even the Siberian cratonic border in the Transbaikal area (Ermikov, 1994; Zorin, 1999). The Mongol-Okhotsk orogeny therefore dominates (in most part) the Mesozoic history of the eastern areas of the CADZ. Stresses were mainly transmitted through reactivation of pre-existing Caledonian and Hercynian structures within the crust. Further to the east, accretion of Siberia led to another contemperaneous Mesozoic fold belt bordering the Siberian cratonic core: the *Verkhoyansk* Fold Belt (figure 4.3) (e.g. Faure et al., 1995; Parfenov et al., 1995; Bazhenov et al, 1999a) which is in fact a continuous suture with the Mongol-Okhotsk Fold Belt running from the Lake Baikal region to the present Sea of Okhotsk. Today the Mongol-Okhotsk fold belt can be followed along mountain ranges south of the Siberian craton (Hangai and Khentai for example) (figure 4.1).

4.4.2. The West Siberian Basin

The West Siberian Basin is a large sedimentary basin accommodating thick, mainly continental, Mesozoic and Cenozoic sequences but with evidence of marine incursions. The basin is located between the East European and Siberian cratons (figure 4.1 and 4.2). It is bounded by the Urals in the west, by parts of the CADZ (Kazakh and Altai orogens) to the south and southeast, and by the Siberian craton to the east. To the north it is limited by the so-called *Taymyr* fold belt (figure 4.3), which is a Late Palaeozoic-Early Mesozoic fold belt forming the northern margin of Siberia. The continental sediments were supplied by rivers draining the Siberian Hercynian orogenic rim (Surkov et al., 1994). The Mesozoic sediments of the basin form an important hydrocarbon reservoir (e.g. Sahagian et al., 1996; Shurygin et al., 1999).

The basement of the West Siberian Basin is composed of typical units that also make up the Caledonian and Hercynian basement of the CADZ, and in that sense it is an integral part of these Palaeozoic fold belts suturing the East European and Siberian cratons in the Pangea assembly. The basement is thus a continuation of the Caledonian and Hercynian orogens related to the evolution of the Uralian and Palaeo-Asian oceans, with island arcs and collisional systems (the Novosibirsk area e.g.), microcontinents (the Kokchetav microcontinent of Kazakhstan e.g.), relict ocean basins and rifts (Aplonov, 1995). During Permo-Triassic times, a rift system developed in the West Siberian basin as a consequence of the early break-up of Pangea due to mantle plume activity (Surkov et al., 1994; Dobretsov et al., 1996; Nikishin et al., 2002). The Irtysh rift that is related to the vast Irtysh shear zone, bounding the southwestern Altai Mountains, is an example of a main rift within the West Siberian Basin. Rifting occurred during most of the Early Mesozoic. In the early phases (~250 Ma ago) it was associated with a vast province of rift basalts which recently have been correlated with the enormous area of Siberian flood basalts (Siberian Traps, Tungus basin; see figure 4.3) on the Siberian craton, making it the largest known flood basalt province on Earth (Nikishin et al., 2002; Reichow et al., 2002). The majority of the West Siberian rifts evolved and became extinct entirely in a continental setting. However, parts developed into a new, small oceanic basin with active sea-floor spreading, called the *Obsky* Ocean (Aplonov, 1988 and 1995).

Sediments in the West Siberian Basin bare witness to several marine, trangressive incursions. After active rifting, the West Siberian Basin experienced subsidence in a passive tectonic regime, and in Late Cretaceous-Early Tertiary times, the basin was largely filled with sediments (Aplonov, 1995). From the Middle Cenozoic onwards, basins of the Arctic Ocean opened, shifting depocenters further northwards (Surkov et al., 1997).

In summary, it appears that the first stages of West Siberian Basin evolution and Early Mesozoic sedimentation are clearly linked with continental rifting and tectonic processes affecting the Palaeozoic basement, while a second episode, from Upper Jurassic until Middle Eocene sedimentation is characterized by transgressive and regressive cycles (Surkov et al., 1994; Sahagian et al., 1996; Surkov et al., 1997; Baraboshkin, 1999; Pinous et al., 1999; Shurygin, et al., 1999). After this episode, and persisting until the present, West Siberia became a tectonically stable platform, residing near sea level with small oscillations possibly linked to Arctic ocean spreading.

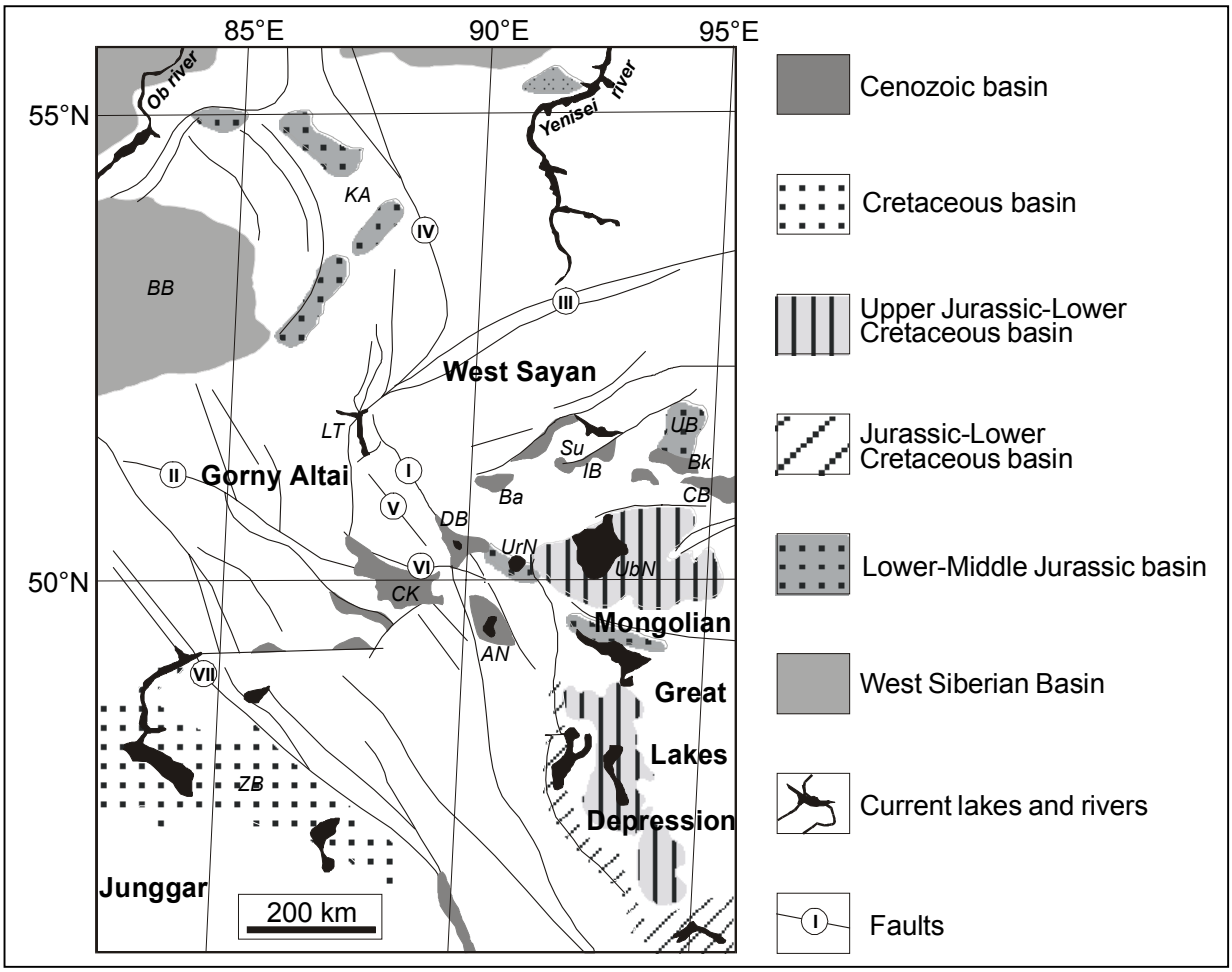

Figure 4.5: Mesozoic and Cenozoic basins in the western Altai-Sayan (after Dobretsov et al., 1996 and Dehandschutter, 2001). Basins: AN = Achit-Nuur, Ba = Barlik, BB = Biya-Barnaul, Bk = Baikhak, CB = Chagyshai basin, CK = Chuya-Kurai depression, DB = Dzhulukul basin, IB = Initial basin, KA = Kuznetsk-Alatau, LT = Lake Teletskoye, Su = Sutkol, UB = Uluchkhem basin, UbN = Ubsu-Nuur, UrN = Ureg-Nuur, ZB = Zaisan basin. Faults: I = Shapshal, II = Charysh-Terekta, III = West-Sayan, IV = Kuznetsk-Alatau, V = Chulyshman, VI = Kurai, VII = Irtysh.

4.4.3. The Altai region

As like many parts of the CADZ, the Altai region was subjected to peneplanation in Triassic times, after the cessation of tectonic movements associated with the closure of the Ob-Zaysan branch of the WPAO in the Permian. This period of tectonic quiescence was disturbed in the Jurassic. Two pulses of a Jurassic tectonic reactivation of the orogen are evident from coarse, often coal-bearing molasse infill in Mesozoic intramontane basins in the Altai region. These fault-controlled basins are scarce in the Russian Altai region. However, they are more abundant in the Mongolian and Gobi Altai (figure 4.5). In some of these basins, an Early Jurassic molasse unconformably overlies the Hercynian basement. In other places this molasse rests on remnants of Triassic red beds. This first Jurassic pulse seems to have been followed by a less active period, characterized by lacustrine deposits in the Mesozoic Altaian basins.

A Late Jurassic-Early Cretaceous tectonic event is witnessed in the stratigraphy by another horizon of coarse molasse deposits. The Jurassic molasse deposits reach 1 to 2 km in thickness in some of the basins (Dobretsov et al., 1996). Later in the Cretaceous and the Palaeogene, the newly developed Jurassic orogen was subjected to peneplanation and finer clastics were deposited. The sedimentary evidence of Jurassic mountain building in the Altai is also supported by sedimentary suites in the large basins bordering the Altai, i.e. the Biya-Barnaul and Kuznetsk depressions of the West Siberian basin to the north, the Zaisan and Junggar basin to the southwest and the Mongolian Depression of the Great Lakes to the east (e.g. Cunningham et al, 1996a and 1996b; Dobretsov et al., 1996; Novikov, 2002; Buslov et al., 2003). These basins accumulated most of the eroded material originating from the denudation of the Mesozoic Altai. Burial history analyses in hydrocarbon exploration studies on the northern Junggar margin confirm this Late Jurassic-Early Cretaceous event (Parnell et al., 1993). The Mesozoic Kuznetsk basin was affected at that time by oblique thrust movements along the northern limit of the Altai Mountains and is thought to have been situated directly north of the Mesozoic Altai orogenic deformation front (Novikov, 2002; Buslov, pers. comm.). At present, the reactivated deformation front of the Altai Mountains does not extend that far to the north.

Jurassic tectonic activity in the Altai region is also demonstrated by the development of thrusts (as in the Kuznetsk area) and other fault movements, by plutonic activity (e.g. Ilyin et al., 1994; Vladimirov et al., 1997) and metamorphism (e.g Novikov, 2002). The Jurassic and Early Cretaceous activity occurred along older Palaeozoic structures. In our study area in the Altai, the *Shapshal*, *Kurai* and Irtysh fault zones were sites of major strike-slip movements during this period (e.g. Chikov and Zinoviev, 1996; Dobretsov et al., 1995b and 1996; Laurent-Charvet et al., 2002; Buslov et al., 2003).

The Mesozoic reactivation is evident, but not well understood. The timing coincides clearly with the evolution of the West Siberian Basin and the Mongol-Okhotsk orogen, but it is not clear how and to what extent tectonic activity in the Altai is related to these events.

It should also be noted that there has been a considerable post-Permian internal reorganisation of the various tectonic units by rotation and strike slip (e.g. Li, et al., 1989; Sharps et al., 1989; Cogné et al., 1995; Gilder et al., 1996; Buslov, 1998; Bazhenov et al., 1999; Buslov et al., 2003) that might be linked to both Mesozoic events mentioned above, as well as to continuing accretion at the southern margin of Eurasia.

4.4.4. The Tien Shan region

Collision of Tibetan and adjacent blocks resulted in polyphase reactivation of the Palaeozoic Tien Shan structures. A clear illustration of this is given by the Mesozoic reactivation of the *Talas-Fergana* fault zone and the development of the associated *Fergana* basin (e.g. Bazhenov, 1993; Sobel and Arnaud, 2000) (figure 4.6).

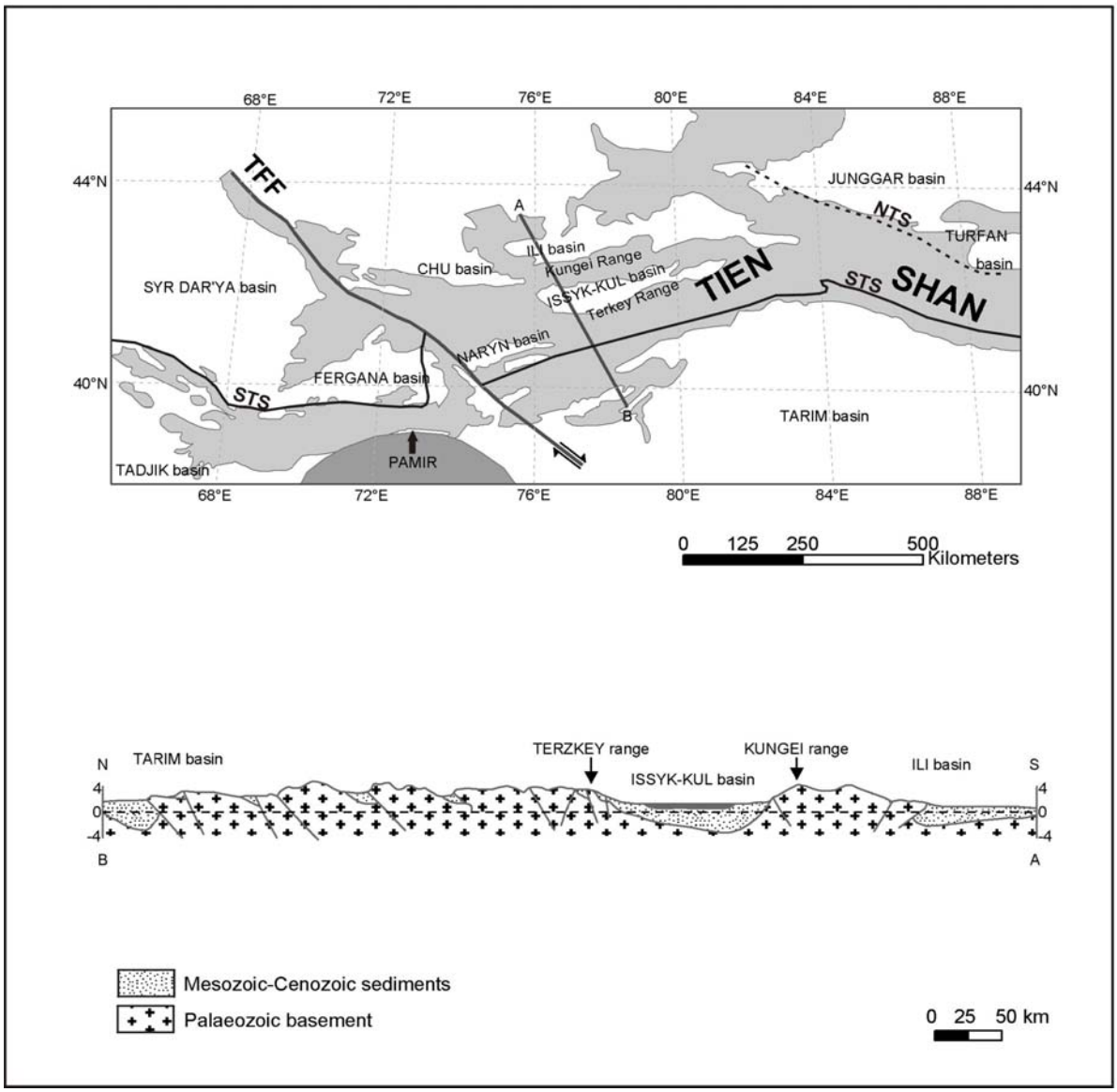

Figure 4.6: Sketch map and cross section of the western Tien Shan with intramontane and adjacent foreland basins with Mesozoic and Cenozoic sediments. TFF = Talas-Fergana Fault, NTS = North Tien Shan Suture (or Borohoro suture), STS = South Tien Shan Suture (or Nikolaev line or Qinbulak-Qawabulak suture).

As in many places within the CADZ, the Permian is a period of clastic, continental sedimentation, interrupted by pulses of magmatism, linked to Pangea disassembly and extension within the Junggar plate. In the Triassic, tectonic reactivation (reverse faulting and thrusting) can be associated with collisions within Tibet along the Kunlun and Altyn Tagh sutures. In this manner an ancestral Tien Shan orogen was created, acting as a physiographical boundary between the Junggar and Tarim basins. Subsequent tectonic pulses related to Tibetan evolution are also recorded in the Jurassic after an episode of Early Jurassic stability. Intramontane basins accumulated significant amounts of lacustrine and alluvial deposits that are often coal bearing, and the Junggar and Tarim basins acted as foreland basins accumulating thick, mostly coarse clastics derived from the orogen (e.g. Allen et al., 1991; Chen et al., 1991; Hendrix et al., 1992; Allen and Vincent, 1997; Hendrix, 2000). During the Cretaceous, a new episode of tectonic quiescence commenced as the terranes composing the present-day Tibet had amalgamated onto the Eurasian margin. The Cretaceous and Early Palaeogene is consequently a period of peneplanation and formation of red beds which are called the *Kokturpak* suite in the Kyrgyz Tien Shan. Small amounts of basaltic and diabasic rocks (dated with the $^{40}Ar/^{39}Ar$ method) were emplaced (Sobel and Arnaud, 2000) and could be the result of a small plume beneath the Tien Shan. The $^{40}Ar/^{39}Ar$ dates for the basaltic rocks range roughly between 20 and 80 Ma, with most dates clustering between 40 and 50 Ma. According to these authors, this magmatism may be a far-field effect of the MOO closure. Yin (2003) argues that partially molten Mesozoic slabs of subducted Tethyan lithosphere might be the source of these magma's.

The Cenozoic collision of India with Eurasia initiated a new and ongoing era of tectonic reactivation and active mountain building in the Tien Shan region (section 4.5.5.1). This younger neotectonic overprint of the same inherited structures impedes the identification and interpretation of the Mesozoic tectonics.

4.4.5. Tibet and adjacent regions

Tibet as it appears today is built up by continental fragments broken off from Gondwana during Late Palaeozoic and Early Mesozoic (figure 4.7). The *Qiangtang* block broke off during Late Carboniferious-Early Permian times, while the *Lhasa* block drifted away in the Late Triassic (Garzanti et al., 1999). By the Cretaceous, Gondwana was disintegrating rapidly, resulting in the break-off of the Indian subcontinent that started its northward movement behind the smaller fragments towards the Siberian/Eurasian continent (Acharyya, 1998). This caused the progressive closure of the *Palaeo-Tethys* and *Neo-Tethys* Oceans (figure 4.7) existing between both continents (e.g. Dewey et al., 1988; Enkin et al., 1992; Ricou, 1994; Yin and Harrison, 2000). In the Latest Triassic, the smaller Peri-Gondwanian fragments started colliding with the southern Eurasian Thetyan margin. From west to east, the *Farah* or *Afghan* block, the *Central Pamir* block and the Qiangtang block docked with Eurasia along the so-called *Jinsha* suture (e.g. Tapponier et al., 1981; Bazhenov, 1996; Thomas et al., 1999a).

Deformation associated with these events can be traced throughout the Eurasian margin into the continental interior where it caused fault movements in the Junggar, Tarim and Tien Shan regions (Allen et al.; 1991b; Hendrix et al., 1992; Otto, 1997) as mentioned in the previous section.

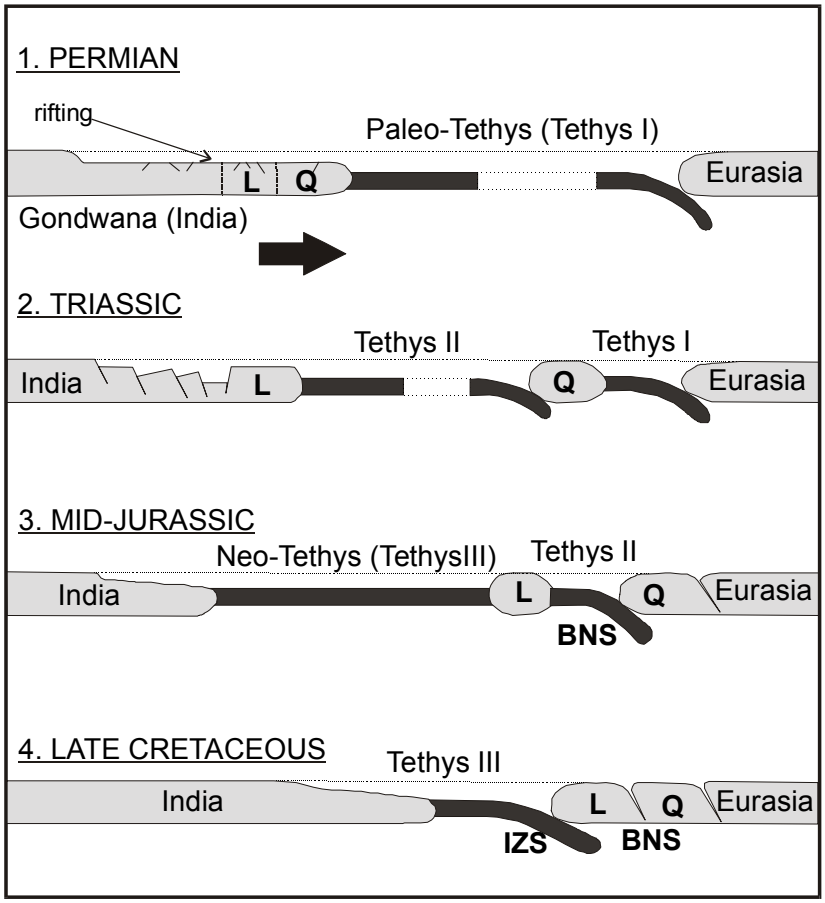

Figure 4.7: Mesozoic break-off of the Qiangtang and Lhasa blocks from Gondwana and subduction of the Paleo- and Neo-Thetys Oceans under the active southern Eurasian rim. Mesozoic accretion of these blocks onto Eurasia formed the basement of the current Tibetan Plateau and acted as a precursor to the major India/Eurasia continent-continent collision in the Cenozoic.

During the Early and Middle Jurassic, a volcanic arc developed along the new southern orogenic rim of Eurasia, related to the northward subduction of Neo-Tethyan oceanic crust (Liu and Einsele, 1994; Ricou, 1994), while the northern Indian margin remained a passive margin. In the Late Jurassic to Early Cretaceous the Lhasa block collided with Eurasia along the *Banggong-Nujiang* suture (Mattern et al., 1998) (figure 4.7 and 4.10). Subduction shifted towards the southern Lhasa margin, where a large batholith, the *Transhimalayan* or *Gangdese* batholith, developed (Weinberg and Dunlap, 2000) (figures 4.8 and 4.9). Both the volcanic arc and the batholith evolution point towards the existence of an Andean type orogeny at that time. At that time the Lhasa block was part of a larger merged microplate, called *Mega Lhasa* (Ricou, 1994), joining Lhasa with parts of present Iran, Afghanistan and Burma (Acharyya, 1998). The collision started somewhat earlier in the west (Iran) and progressively migrated eastward in a scissor-like movement. All the aforementioned collisions together constitute the *Cimmerian* or *Cimmeride* orogeny.

Within the Junggar and Tarim/Tien Shan region, some tectonic activity at that time can be linked to distal effects of this collision (Liu, 1986; Coleman, 1989; Enkin et al., 1992; Hendrix et al., 1992; Allen et al., 1995; Otto, 1997; Allen et al., 2001). For example, thrusting at the margins of the Tarim and Junggar basins induced the development of a flexural foreland basin in that region (Allen et al., 1993). In the Mid-Cretaceous, subduction of the Neo-Tethys ocean lithosphere continued in the western part of the Eurasian margin, while to the east the Burmese part of Mega Lhasa was accreted completely. An island arc system, the *Dras-Kohistan-Ladakh Arc* (e.g. figure 4.8) collided with the Pamir and Lhasa blocks in the Early Cretaceous, forming the northern suture along which the Himalayas started to develop around the Cretaceous-Palaeogene transition, and causing deformation within the Pamirs (Bard, 1983; Treolar et al., 1996; Yamamoto and Nakamura, 1996; Searle et al., 1999a).

A smaller crustal block, the *Karakoram*, was squeezed between the Pamir block and the Kohistan-Ladakh Arc, along the so-called *Shyok* suture (Gaetani et al., 1996; Gaetani, 1997). The boundary between the Tarim and Karakoram is formed by the western *Kunlun* Mountain Belt (e.g. Mattern et al, 1996; Yang et al., 1996). Another smaller block trapped between Tibet (Qiangtang) and Tarim is the *Qaidam* block, forming the basement of the present Qaidam basin (Chen, W. et al., 1999) (figure 4.10). The boundary between the Qaidam basin and Tibet is formed by the eastern Kunlun Mountains, along which a major sinistral strike slip fault is exposed, the Kunlun fault (e.g. Mock et al., 1999). The boundary between Qaidam and Tarim is delineated by another major sinistral strike slip fault zone, the *Altyn Tagh* fault (e.g. see figures 4.1 and 4.10), which is one of the most prominent faults in the CADZ (Şengör and Natal'in, 1996; Bedrosian et al., 2001). The northeastern boundary of the Qaidam basin is formed by the *Qilian Shan* Mountains. To its southwestern part the Altyn Tagh fault cuts the Kunlun Mountain Belt, dividing it in the eastern and western section mentioned above. The Kunlun Mountains are terranes belonging to the southern margin of Tarim and some smaller allochtone terranes accreted onto this margin during several events (e.g. Yang et al., 1996; Xiao et al., 2002). During the evolution of the Tibetan Plateau, the Kunlun and the Qinling ranges were reactivated and consist of actively forming mountain fronts today (Xue et al., 1996).

During the Mesozoic and continuing in the Cenozoic, the basins located in present Central Asia and Western China are characterized by compressional tectonics during the Mongol-Okhotsk, Cimmeride and Himalayan orogenies (e.g. Tarim, Junggar, Qaidam), while more to the east, the basins are characterized by extensional tectonics (e.g. Baikal, Shansi, Bohai) associated with incipient rifting within and behind the subduction zone of the Pacific Ocean (Chen and Dickinson, 1986; Delvaux et al., 1995a).

4.5. Cenozoic evolution of the CADZ and adjacent regions

The Cenozoic evolution of Central Asia is clearly dominated by the collision and ongoing convergence and indentation of India into Eurasia. The partitioning of the strain throughout this entire region resulted in the formation of the Himalayan mountain range, uplift of the Tibetan Plateau, extrusion tectonics along major strike slip faults and rejuvenation of older structures far in the interior of the Eurasian plate.

4.5.1. The India/Eurasia collision

There has been some debate on the exact timing of the continent-continent collision of India with Eurasia. In the last years, some compromise has been reached, constraining the collision to the Palaeocene-Eocene transition some 45 to 55 Ma ago (e.g. Yin and Harrison, 2000). Because the collision zone is over 2000 km long, collision was likely diachronous and can hardly be confined to a sharply defined point in time for the entire zone. Incipient collision was accompanied by a marked velocity reduction in the northward movement of the Indian plate as can be observed in Palaeomagnetic seafloor data (Patriat and Achache, 1984; Klootwijk et al., 1992). The collision was caused by the complete closure of the Tethyan Ocean between the converging Gondwanian continents of India, Arabia and Africa with Eurasia, resulting in a vast orogenic zone at the southern Eurasian margins (Ricou, 1994). This orogenic zone was called the Thetysides by Şengör and Natal'in (1996) and comprises the Alpine orogen in southern Europe and the Himalayan orogen in South-Central Asia.

India rifted away from Gondwana in the Middle Cretaceous, during the incipient opening of the Indian Ocean. There is evidence of an early contact between India and Eurasia, around the Cretaceous-Palaeocene transition ~65 Ma ago (e.g. Patriat and Achache, 1984; Klootwijk et al., 1985; Klootwijk et al., 1992). The hypothesis is that this earlier contact indicates a *Greater India* (Veevers et al., 1975). The huge subducting Thetyan oceanic slab would have pulled the northern zones of the Indian lithosphere under Eurasia where it would still reside today (e.g. Patzelt et al., 1996; Mattauer et al., 1999). In this way, part of India is underthrust or underplated under Tibet. Break-off of the dense and cold slab as it sunk deeper into the mantle would have released the less dense Indian plate and buoyancy effects could then have played a role in the rise of the Tibetan Plateau. The effects of this massive collision are not solely accommodated by crustal thickening under the Himalayas and Tibet. Penetration of India (probably 2600 ± 900 km according to Patriat and Achache, 1984) also caused the extrusion of Southeast Asia along strike slip faults, and reactivation and active tectonics in the CADZ as is dealt with in the next sections. There is also evidence that the interior of the Indian plate is being deformed as convergence continues (Neprochnov et al., 1988; Curray and Munasinghe, 1989).

In recent years, geodetic techniques such as GPS measurements have extensively been used to study the rates of active deformation within the collision zone itself and in Central and East Asia as a whole (Larson et al., 1999; Chen et al., 2000; Holt et al., 2000; Reigber et al., 2001; Wang et al., 2001; Thompson et al., 2002). These measurements clearly improve our understanding of the effects associated with a major continent-continent collision.

4.5.2. The Himalayan orogeny

One of the most obvious results of the India/Eurasia collision is the Himalaya mountain belt (figures 4.8 and 4.9) that developed on the southern Tibetan and northern Indian margins. The timing of the collision is constrained to the Early Eocene. The suture zone of the collision is marked by several ophiolitic complexes (e.g. Wang et al., 2000; Corfield et al., 2001; Pedersen et al., 2001) and is called the *Indus-Zangbo* (or Indus-Yarlung) suture zone (IZSZ) (e.g. Aitchison et al., 2000). To the north of this suture, in southern Lhasa, lies the *Transhimalayan* or *Gangdese* batholith (see section 4.4.5). In the western part of the orogen, the Dras-Kohistan Island Arc was accreted to the Pamir-Karakoram block in the Middle Cretaceous along the Shyok suture. Development of the Himalayas to the south of Kohistan occurred through thrusting of the Kohistan sequences onto the Indian plate along the Main Mantle Thrust (MMT) (e.g. Anczkiewicz et al., 2000). The Kohistan Arc is separated from the so-called *Ladakh Arc* by the wedging *Nanga-Parbat* syntaxis of the Himalayas (e.g. Butler et al., 1989; Vince and Treolar, 1996). The Nanga Parbat promontory was probably the first part of India to collide with Eurasia. Both arc sequences may well have belonged to the same Tethyan volcanic arc that accreted to southwestern Tibet during the Mesozoic.

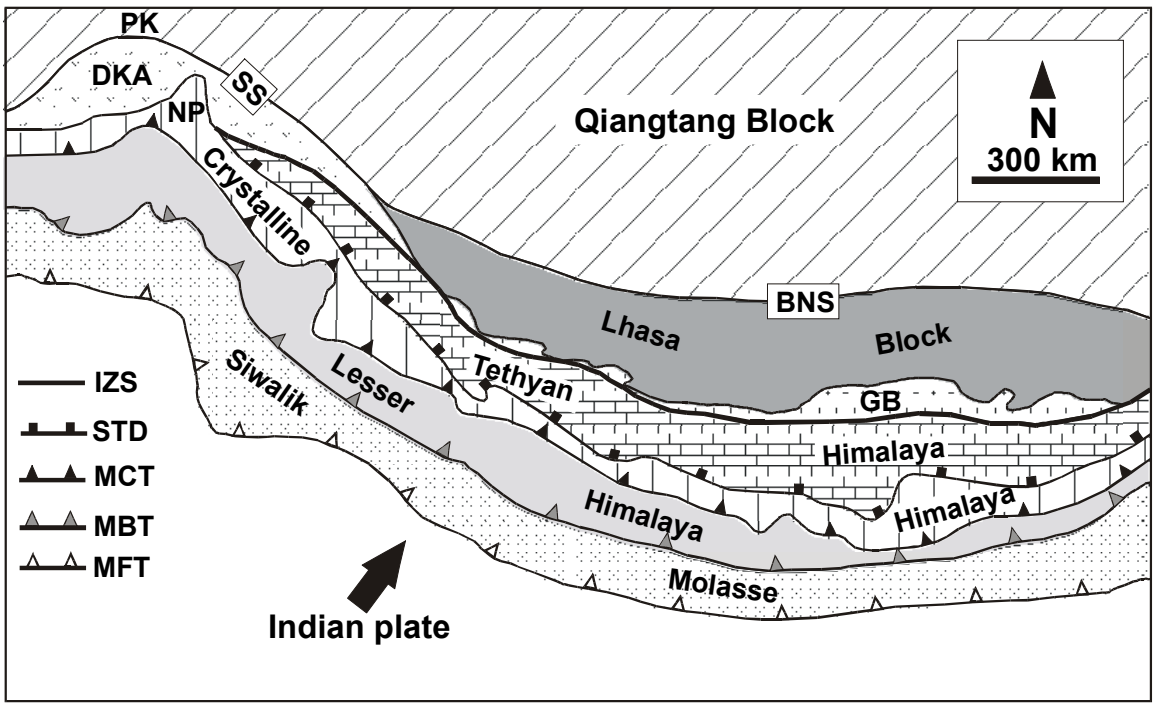

Figure 4.8: Sketch map of the Himalayan orogen. The several tectonic units of the orogen are discussed in the text. BNS = Bangong-Nujiang suture, DKA = Dras-Kohistan Arc, GB = Gangdese Batholith, IZS = Indus-Zangbo suture, MBT = Main Boundary Thrust, MCT = Main Central Thrust, MFT = Main Frontal Thrust, NP = Nanga Parbat syntaxis, PK = Pamir-Karakoram, SS = Shyok suture, STD, Southern Tibetan Detachment.

The region is at present a site of extensive exhumation and tectonic and isostatic uplift, exposing high-grade metamorphic rocks and migmatites (e.g. George et al., 1995; Searle, 1996a; Dunlap et al., 1998; Leland, 1998; Hubbard et al., 1999; Schneider et al., 2001). The movements are related to the dextral Karakoram fault zone, running along the eastern edge of the Pamir-Karakoram-Ladakh region, where it adjoins the IZSZ.

South of the IZSZ the *Tethyan Himalayas* or *Tibetan Tethys Zone* is exposed (Liu and Einsele, 1994; Patzelt et al., 1996; Willems et al., 1996). They are inverted Indian Tethyan passive margin sequences (Mesozoic-Early Tertiary) forming the former northern edge of the Indian plate and bound by the *South Tibetan Detachment* (STD). The STD branches off into an array of low angle normal faults, the *North Himalayan Normal Fault System* (NHNF) along which the northern part of the Himalayan orogen developed (Henry et al.; 1997; Lee et al., 2000). Directly south of the STD is the domain of the *High Himalayas* or *Crystalline Himalayas*, thrust southward upon the *Lesser Himalayas* (DeCelles et al., 2000; Huyghe et al., 2001) along the *Main Central Thrust* (MCT). The High Himalayas are assumed to represent Indian basement rocks and are composed mainly of high-grade metasedimentary rocks (Marquer et al., 2000), intruded by granitoids of Early Palaeozoic and of Miocene age (e.g. Miller et al., 2001; Noble et al., 2001). The Early Palaeozoic granitoids represent an old event that is not related to the evolution of the Himalayan orogen. Mount Everest is part of the Crystalline Himalayas. The high-grade rocks are tectonically exhumed by a coeval combined movement of thrust nappes along the MCT and synorogenic extension related to the NHNF (Beaumont et al., 2001; Vannay and Grasemann, 2001). The active fold belt of the *Siwaliks* forms the southern limitation of the Himalayan mountain belt (Harrison et al., 1993; Hurtrez et al., 1999). The Siwaliks are separated from the Lesser Himalayas by the *Main Boundary Thrust* (MBT) and from the undeformed Indian plate by the *Main Frontal Thrust* (MFT). The Siwaliks are largely made up of Miocene and Pleistocene molasse sediments derived from the uplifted Himalayan thrust belts and deposited in the evolving Himalayan foreland basin.

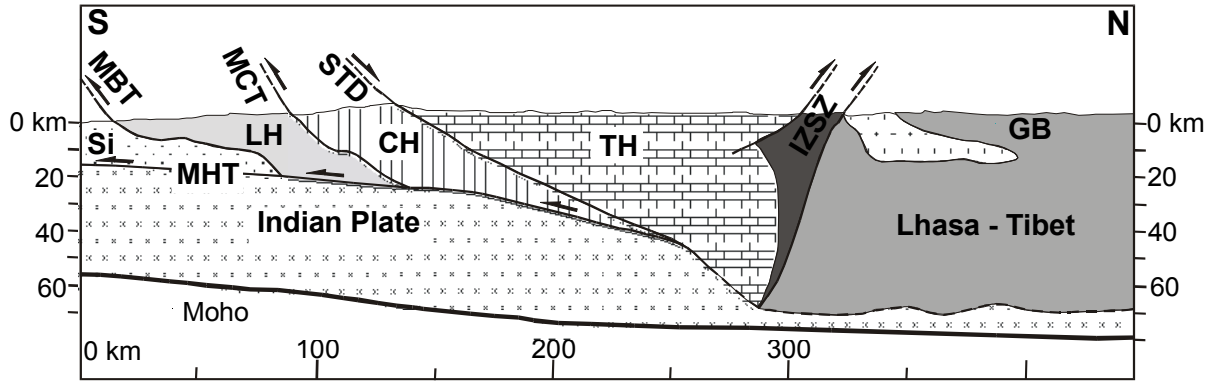

Figure 4.9: Cross-section of the Himalayan orogen. CH = Crystalline Himalaya, GB = Gangdese Batholith, IZSZ = Indus-Zangbo suture zone, LH = Lesser Himalaya, MBT = Main Boundary Thrust, MCT = Main Central Thrust, MFT = Main Frontal Thrust, MHT = Main Himalayan Thrust, Si = Siwaliks, STD = Southern Tibetan Detachment, TH = Tethyan Himalaya.

Timing, rate and amount of growth (uplift) of the several Himalayan ranges is associated with the activity of the different major Himalayan thrust systems. The oldest continental sediments in the Himalayan foreland basins are thought to be of Late Eocene age (Najman et al., 2001). The Himalayan thrusts form main structures along which crustal stacking resulted in the significant thickening of the Indian crust and the formation of the Himalayan orogenic wedge. After initial contact along the IZSZ in the Eocene, the Gangdese batholith was thrust over the IZSZ probably during the Oligocene along the Gangdese thrust system (GTS) (Harrison et al., 1992; Yin and Harrison, 2000). Underthrusting of the Indian plate shifted southward to the MCT in Early Miocene times (~20 Ma ago), subsequently to the MBT and finally to the presently active MFT of the southern Siwaliks (Johnson and Rogers, 1997; Johnson et al., 2001; Vannay and Grasemann, 2001). More or less synchronously with the MCT activity extension along the STD tectonically exhumed large parts of the Crystalline Himalayas (Burchfiel et al., 1992). The Himalayan thrust and extensional structures seem to converge at depth to a "Main Himalayan Thrust", which might be interpreted as the zone along which the Indian lithosphere is underthrusting Eurasia (Hauck et al., 1998).

The main thrusting and formation of the Himalayan orogen is probably of Miocene age, while several studies have indicated an intensifying active Himalayan and Tibetan tectonic and isostatic uplift since the Pliocene and have linked this evolution to a dynamic interaction with changing climate (Burbank, 1992; Harrison et al., 1993; Peizhen et al., 2001). In particular, the development of the Asian monsoon is seen to be an effect of the Himalayan and Tibetan uplift as the large uplifted area disturbed pre-existing atmospherical circulation, while the monsoonal climate has an impact in its turn on the erosion, isostatic uplift and landscape development of the entire area. The climatic markers are mainly vegetation shifts and stable isotope composition of Himalayan gastropod shells for example.

4.5.3. The Tibetan Plateau

The assembly of Tibet mainly occurred in the Middle and Late Mesozoic as discussed in section 4.4.5. The southern part of Tibet, the Lhasa block, was part of the Eurasian active margin as India collided with Eurasia in the Eocene. The southern part of Lhasa (South Tibet) is characterized by the large Transhimalayan or Gangdese batholith. Directly south of the batholith is the IZSZ, marking the northern boundary of the Himalayan mountain belt and the suture between Eurasian and Indian basement (figures 4.8, 4.9 and 4.10). North of the suture lies the Tibetan Plateau. In the southwest Tibet is bound by the dextral *Karakoram* strike slip fault zone (KKF). The KKF separates Tibet from the Pamir-Karakoram block. In the southeast the *Jiali* dextral fault zone (JF) forms the boundary of the Plateau. Between the KKF and Jiali, smaller dextral faults seem to form transfer zones between both larger structures (figure 4.10). In this zone several E-W extensional structures (grabens) are forming since about Pliocene times (e.g. Armijo et al., 1986; Yin, 2000). The amount of extension in its own right however is quite small compared to the scale of the collision induced tectonic movements on a broader scale. The extensional features are present in southern Tibet as well as in the northern part of the Himalayan orogen (Tapponnier et al., 2001).

These structures, here and elsewhere in the CADZ, directly postdate associated volcanic activity. Following these structures further to the east, through eastern Tibet, Yunnan (China) and to the South China Sea, the JF seems to pass into the important dextral *Red River* fault zone (RRF). The South China Sea is actually interpreted as a pull-apart basin at the southern extremity of the RRF (see e.g. figures 4.10 and 4.11).

The northern limit of Tibet is delineated largely by the major sinistral *Altyn Tagh* fault (ATF, see earlier); in the northeast, the boundary is formed by the sinistral *Kunlun* fault (KLF) (figure 4.10 e.g.). Along the ATF and KLF, the Kunlun orogen has developed along the Tibet-Tarim border as a consequence of crustal shortening and fault movements associated with the India/Eurasia collision. The smaller *Altyn Tagh* orogen along the ATF is a transpressional feature linked to the large left lateral displacement of the ATF acting simultaneously with thrusts in the N-S compressional regime induced by the India/Eurasia collision (Wittlinger et al., 1998). The Qaidam basin is situated in the northeastern corner of the Tibetan Plateau, between the ATF and KLF gap. The basin is bound to the north by smaller thrust belts (*Nan Shan* and *Qilian Shan*). The combination of sinistral movements in the north and dextral movements in the south of Tibet, resulted in an eastward extrusion of the entire Tibetan Plateau with respect to the indenting Indian plate (Dewey et al., 1988; Armijo et al., 1989; Yin et al.; 1999; Yin and Harrison, 2000).

The Tibetan strike-slip movements along the ATF, KKF and KLF seem to have been the most intense in the last 5 Ma and especially in the Holocene (e.g. Searle, 1996b; Bedrosian et al., 2001; Washburn et al., 2001). Recent (Pliocene-Quaternary) tectonic activity is also evident in the Qaidam basin, in the bordering Qilian Shan ranges (Chen, W., 1999; Bedrosioan et al., 2001; Wang et al., 2001) and in the Kunlun Mountains (Wu et al., 2001) (figure 4.10). The movements are coeval with active thrusting of the Pamir onto the southern Tarim margin, which can also be linked to the dextral slip along the KKF.

Strike-slip along the ATF is thought to be responsible for a large amount of accommodation of the northward convergence of India during the present. However, Bendick et al. (2000) find no evidence of large-scale activity along the ATF. Movements along the RRF are responsible for the extrusion of Southeast Asia (see next section), and are older, mainly of Oligocene to Early Miocene age, directly preceding the major Miocene thrust movements in the Himalayan orogen (Fielding, 1996). The Miocene change (around 20 Ma ago) in tectonic regime is quite marked and prominent in a variety of geological records. In general, the Late Palaeogene deformation is mainly expressed by extrusion tectonics (mainly along the RRF), but in general, Palaeogene deformation in the region and in the entire CADZ is far less understood. In some areas there is evidence of Eocene and Oligocene red beds in Tibet, suggesting some episode of quiescence.

It is clear that a large portion of the India/Eurasia convergence is taken up by crustal thickening and underplating in the Himalayas, Tibet, and adjacent regions. The average Moho-depth under Tibet is at least 65 km, and reaches 75 km under the Himalayas (figure 4.9).

Large-scale strike-slip movements accommodate another significant portion of the India/Eurasia convergence, resulting in extrusion tectonics (see next section). The mechanism of uplift of the Tibetan Plateau has been the subject of debate since long and several hypotheses have been put forward. A much cited explanation is that it is an effect of the underthrusting and buoyancy induced rebound of the Indian crust under Tibet (Owens and Zandt, 1997). Another hypothesis is that ongoing convergence and compression resulted in the shortening of the entire Asian crustal column, including both the Himalayas as well as Tibet. A third line of reasoning follows the underplating theory of southern Eurasia, involving the stripping of parts of the lithospheric mantle (lithospheric delamination) of Tibet by the subducting Indian slab, and replacement by hotter, less dense asthenospheric material (e.g. England and Houseman, 1988). Willett and Beaumont (1994) suggested that subduction of the Asian lithospheric mantle beneath Tibet could account for the uplift of the Plateau. Yet another possibility is injection of parts of the Indian crust in the ductile lower crust of Tibet, raising the Tibetan Plateau hydraulically (Zhao and Morgan, 1987). Le Pichon et al. (1997) present an interesting alternative and argue that metamorphic transitions from eclogite to granulite facies within the lower Tibetan crust may account for an overall crustal density decrease, leading to an isostatic adjustment and uplift of the Plateau.

Another subject of debate involves the time when the maximal elevation of the Plateau was attained. Most authors nowadays think that Tibet reached its present altitude about 8 Ma ago (Harrison et al., 1992 and 1995; Fielding, 1996; Yin and Harrison, 2000), while others presume that it has been at its present elevation for more than 14 Ma. Still others attribute a very young age of 3.5 Ma and less to the uplift of Tibet (Wu et al., 2001). Wu and co-workers base their hypothesis mainly on the climatic record. Whatever the exact cause and timing may be, it is thought that at a certain point the Tibetan Plateau reached a maximum elevation, after which the constraining stresses at its margins were not sufficient any more to resist the high gravitational potential of the Plateau, causing it to collapse and inducing the aforementioned extensional features, the strike-slip movements and resulting eastward extrusion along its margins (Fielding, 1996). However, Tapponnier et al. (2001) argue that the extension must not necessarily be explained in this way and that simple kinematics related to slip-partitioning and divergent thrusting are sufficient. It is at this time of maximal elevation that climatic effects start to be manifest. Qiang et al. (2001) and Zhisheng et al. (2001) made correlations between tectonics and climate and link the vast Chinese loess deposits around 8 Ma ago to the onset of the Asian monsoon and the Tibetan uplift. An intensifying monsoon regime has been observed around 3.5 Ma. This coincides with and would explain the data of Wu et al. (2001) mentioned above.

Recently Tapponnier et al. (2001) presented a comprehensive review of the formation and growth of the Tibetan Plateau, postulating a new, but still conjectural model. These authors suggest an oblique stepwise rise and growth of the Tibetan Plateau (figure 4.10).

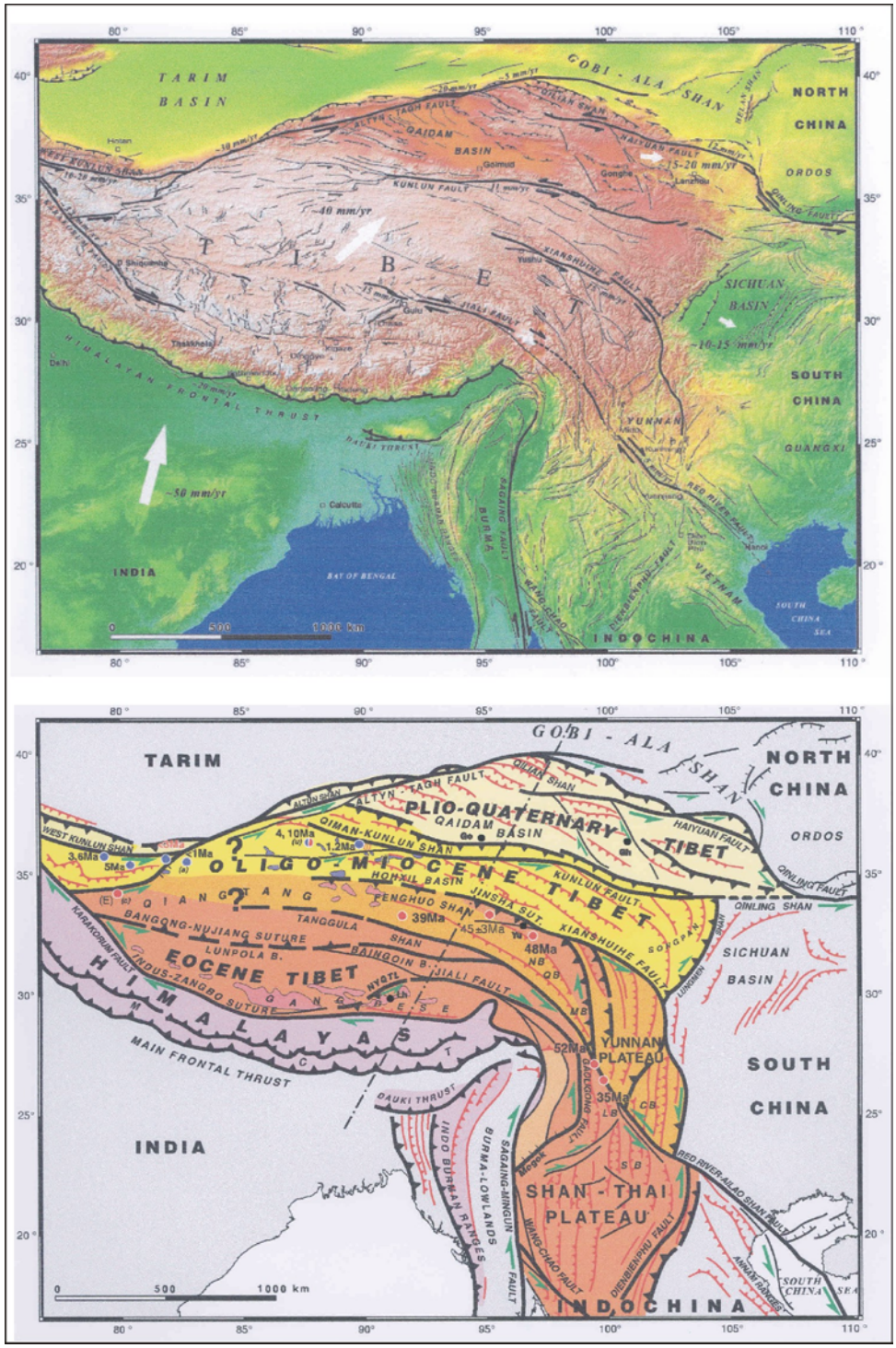

Figure 4.10: Relief map and tectonic sketch map of Tibet (after Tapponnier et al., 2001). See text for explanation.

They propose that the strike-slip faulting and thrusting are not deformation events related to the collision, but rather act coevally in a sort of accretionary wedge setting. In this way the Tibetan Plateau would have been formed in successive diachronous steps, starting at its southern rim (Lhasa and southern Qiangtang) during the Eocene. During Oligocene-Miocene times, the rise of the northern Qiangtang (central Plateau) would have occurred as the growth of the Plateau continued in northeastern direction. Finally, active (since Pliocene) uplift of the immature Qaidam-Qilian Shan part would reflect continuing active growth of the Plateau in that direction. The boundaries along which these different phases acted are deep-rooted pre-existing zones of weakness in the lithosphere, e.g. the Mesozoic sutures within Tibet (e.g. Wittlinger et al., 1998). The underlying mechanism is thought to be an oblique southwestward subduction of Eurasian lithospheric mantle along these zones of weakness. The crust is then decoupled from the lithospheric mantle and is shaped into an accretionary prism in which the Tibetan crust is thickened. Ongoing indentation of the Indian plate into Asia shifts the subduction zone northeastward and accounts for the three different steps in the plateau building process as there is a sequential rejuvenation of sutures in this direction. It also explains volcanic events taking place above these supposed subduction zones. Moreover the different stages of plateau growth could have contributed to trigger or enhance the climatic effects associated with the Himalayan and Tibetan uplift.

4.5.4. Indentation and extrusion tectonics

The northward indentation of India with respect to Eurasia is an active process yielding a N-S compressive tectonic regime in the collision zone itself. As explained, important crustal thickening via thrust movements has occurred in the mountain belts directly north of the India/Eurasia suture zone. The indentation is however also compensated by widespread major strike slip movements in the Eurasian hinterland (figures 4.11 and 4.13). These movements have an outspoken E-W orientation. To the west, the interior of the Eurasian plate forms a rigid restraint on the lateral movement of blocks along these strike slip faults. To the east and southeast however, the constriction by the Pacific subduction margin is far less rigid (a so-called “free” plate boundary), resulting in large displacements of crustal blocks to the (south)east as India advanced further into the Eurasian plate. The squeezing out of these blocks is referred to as extrusion or escape tectonics. As explained, westward extrusion is rather limited, but has been observed in areas west of the Pamir Mountains (Tapponnier et al., 1981; Pozzi and Feinberg, 1991). Eastward extrusion is by far more widely recognized along the prominent Altyn Tagh, Kunlun and Red River strike slip faults (Molnar and Tapponnier, 1977; Gilder et al., 1993; Zhang et al., 1998; Morley, 2001) as mentioned before. Because of obvious geometric reasons, the extruded blocks (e.g. Tibetan, South Chinese and Indochinese blocks) are subjected to a clockwise rotation. Analogue models using plasticine and a rigid intender for example have been developed and experimentally confirm this hypothesis (Tapponnier et al., 1982; Cobbold and Davy, 1988; Peltzer and Tapponnier, 1988). The eastward extrusion has been linked to lithospheric thinning and the development of rift basins in the eastern parts of the CADZ (Baikal rift) and Southeast Asia (Bohai basin) (Yin, 2000) (figure 4.12).

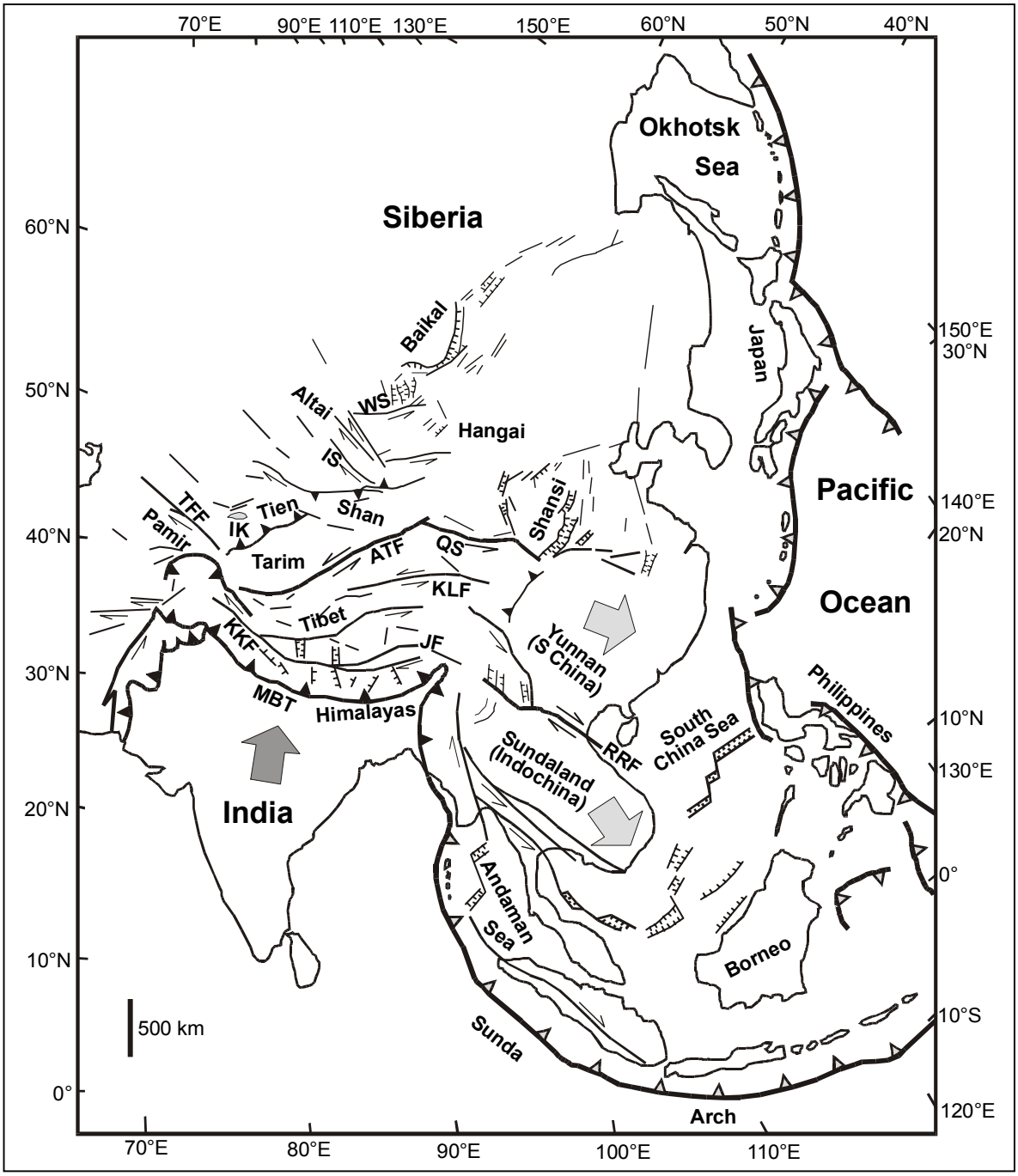

Figure 4.11: Schematic map of large scale Cenozoic structures in the Central Asian Deformation Zone (CADZ) as a result of Indian/Eurasian continent-continent collision and subduction (gray, open barbed lines) of the Pacific Ocean (after Peltzer and Tapponnier, 1988). Crustal thickening and thrusting (black barbed lines) is evident in the Himalayas and Tibet. Strike-slip movements characterize the deformation in Tibet, Southeast Asia and Central Asia all the way to the Baikal Rift Zone (BRZ). The BRZ, Tibet, Shansi and Yunnan regions and the South China Sea are characterized by extension. This extension can be linked to extrusion or escape tectonics as Sundaland (Indochina) Tibet and South China are laterally extruded eastward to the "free" Pacific subduction boundary along major strike-slip faults. Strike slip faults are solid lines with lateral direction of movement indicated by the arrows. Extensional structures are indicated by striped lines. ATF = Altyn Tagh Fault, IK = Issyk Kul basin, IS = Irtysh Shearzone, JF = Jaili Fault, KKF = Karakoram Fault, KLF = Kunlun Fault, QS = Qilian Shan, RRF = Red River Fault, TFF = Talas-Fergana Fault, WS = West-Sayan fault

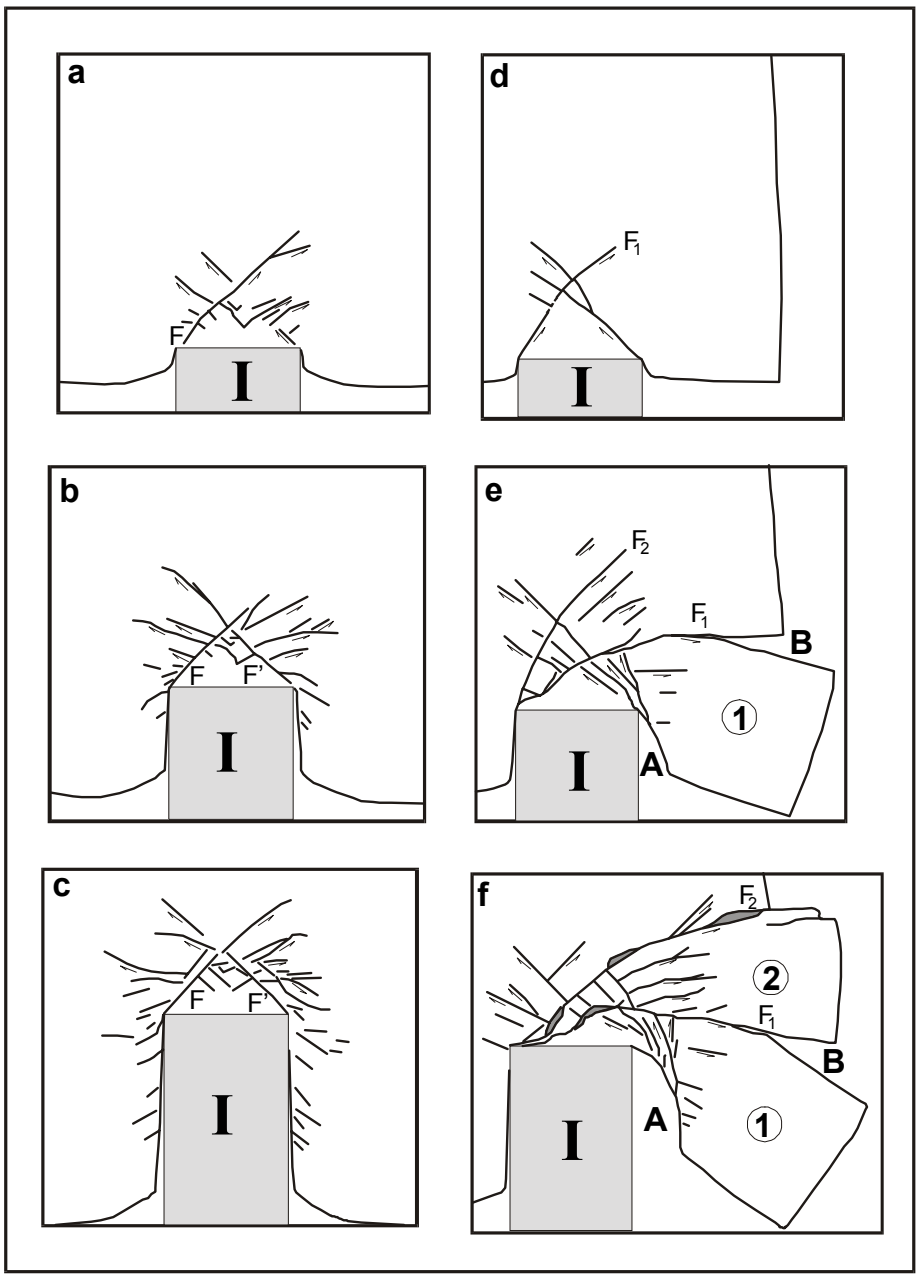

Figure 4.12: Analogue modelling of extrusion tectonics related to the Indian/Eurasian continent-continent collision (after Tapponnier et al., 1982). A rigid intender (I) of about 5 cm is penetrated in plasticine, representing India intending into Eurasia. A, B and C are the results of plasticine constrained rigidly to the west and east. D, E, F, have a "free" eastern boundary, which represents the Pacific subduction zone. The latter series shows remarkable similarities with the geology in Tibet and Southeast Asia. Faults (F_1 and F_2) subsequently form in the plasticine, and blocks 1 and 2 are extruded eastward along these major faults. They can be linked to the Sundaland and Tibetan-South China block as they are being extruded along the Jaili-Red River faults and the Altyn Tagh-Kunlun faults (figure 4.11). Gaps (shaded areas in f) are formed as extensional and transtensional structures in the plasticine and can readily be associated with their geological analogues in Southern Tibet and Yunnan. This is also the case for large basins (A and B) appearing south of the extruded plasticine bodies. They are interpreted as the Andaman Sea and South China Sea analogues (compare with figure 4.11).

4.5.5. Intracontinental reactivation within Central Asia

It has long been recognized that Cenozoic deformation throughout the CADZ, from the Himalayan orogen to deep within the Eurasian interior (e.g. the Baikal rift) can be associated with the India/Eurasia collision (Molnar and Tapponnier, 1975; Tapponnier and Molnar, 1979; Le Pichon et al., 1992). Even more distant far-field effects are acknowledged as far as the Sea of Okhotsk (Worrall et al., 1996). In addition to the processes of crustal thickening and extrusion, the stresses at the southern margin of Eurasia are being transported through the Eurasian lithosphere into the plate's interior. The stress transfer is directed by pre-existing zones of lithospheric weakness and in particular follows sutures and structures that developed during the earlier intricate accretionary history of Central Asia. These sutures are predominantly subduction-accretion complexes, amalgamated to Eurasia in Caledonian and Hercynian times. These zones were reactivated and active deformation is spread throughout Central Asia with the development of the huge intracontinental orogenic system, the Central Asian Deformation Zone (CADZ) as we called it. The deformation is of progressively younger age toward the north(east). In this way, a significant amount of the convergence between India and Eurasia is being accommodated (figure 4.13). The active deformation is taking place in the Palaeozoic and Mesozoic accreted terranes between the converging rigid intender, being the Indian plate, and the rigid continental core of Siberia. Smaller rigid (cold) blocks in the tectonic mosaic collage of Central Asia resisted the stresses and stayed relatively undeformed. The Tarim plate is the most marked example. In this respect the Tien Shan Mountains on the northern Tarim margin can be viewed as the northern extension of Tibet around and beyond Tarim. This is more or less analogous with the developing Qilian Shan and Nan Shan thrust belts northeast of the more or less stable Qaidam basin. The onset of reactivation of the Tien Shan is thought to be of Middle to Late Miocene age, following the major Miocene thrust movements in Tibet and the Himalaya. Reactivation further north in the Altai and Baikal regions started in the Late Miocene to Pliocene (Dobretsov et al., 1996; Delvaux et al., 1997).

4.5.5.1. The Tien Shan Mountains

The northward indentation of India thrusted the northern parts of Tibet onto the stable Tarim crust along the ATF and the KKF, while the Pamir was directly thrusted onto the southwest of the Tien Shan, onto the southern margin of the Tadjik depression (Burtman, 2000) (figure 4.6). After Palaeocene and Eocene continental red bed formation, tectonic movements seem to have begun in the Oligocene and Miocene (Allen et al., 1993 and 1994). They clearly intensified during the last 5 Ma (Cobbold et al., 1994; Searle, 1996; Reigber et al., 2001), causing the Pamir-Hindu Kush region to evolve into one of the most seismically active regions in the world (Pavlis and Das, 2000). Ongoing activity is evident from a variety of geological information (Molnar et al., 1994; Abdrakhmatov et al., 1996; Tibaldi et al., 1997; Tibaldi, 1998; Burbank et al., 1999; Bullen et al., 2001; Abdrakhmatov et al., 2002; Thompson et al., 2002).

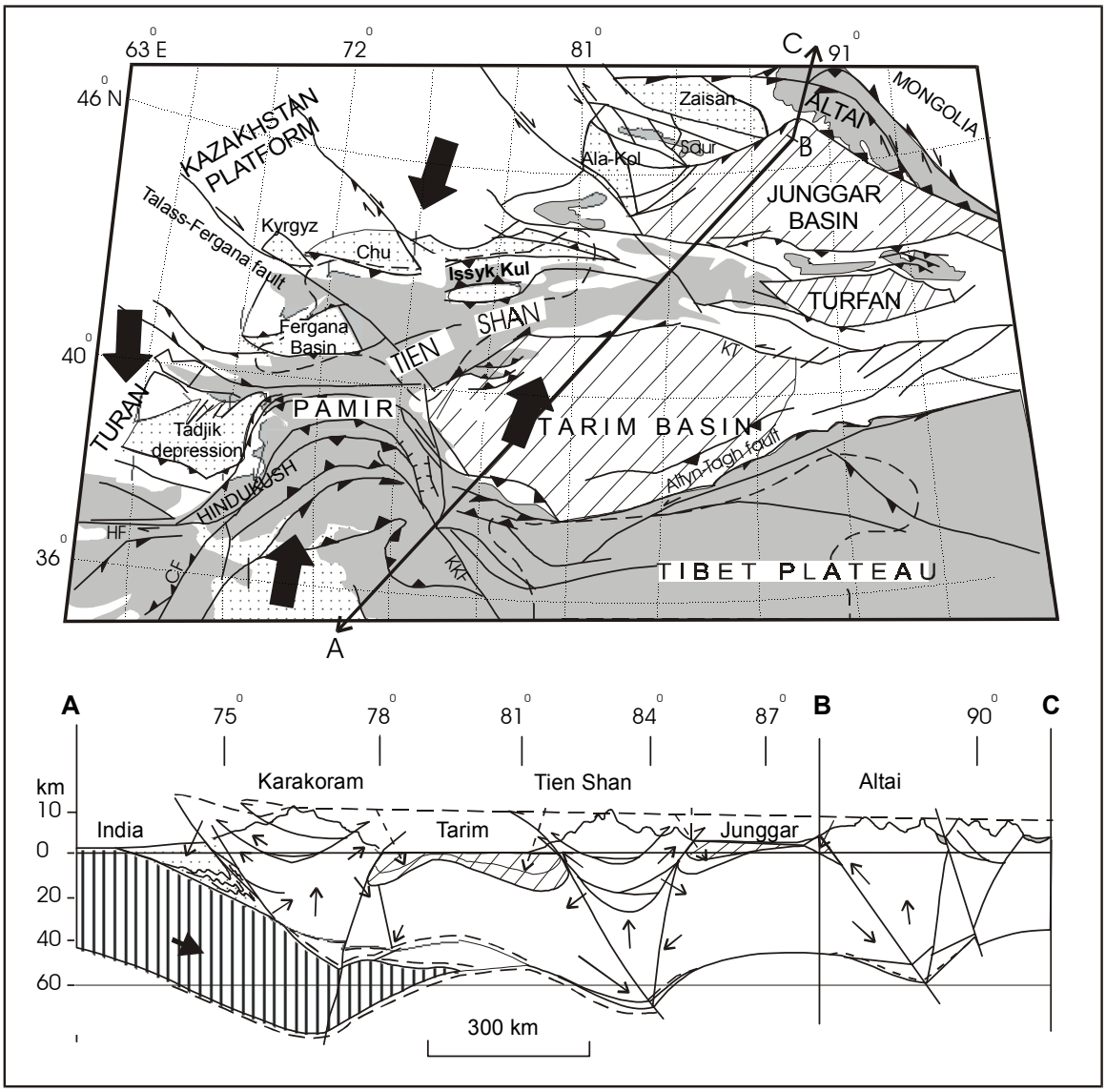

Figure 4.13: General map and cross section (ABC) of the Central Asian Deformation Zone (CADZ). Ongoing indentation of India into Eurasia is also accommodated by reactivation of the inheritant structures within the CADZ. The deformation front is migrating northward and hence reactivation is younger toward the northern parts of the CADZ.

Along its northern margin, Tarim is thrust under the Tien Shan in a sort of domino-style reaction to the compressive forces at its southern edge (Dobretsov et al., 1996) (figure 4.13). Along with the Cenozoic clockwise rotation of the Tarim block and the rejuvenated dextral displacement along one of the most important fault zones in the orogen - the Early-Palaeozoic *Talas-Fergana* fault (TFF) - the Tien Shan are actively being deformed in a dextral transpressional regime (e.g. Chen et al., 1992; Cobbold et al., 1994; Khudoley, 1993; Thomas et al., 1999b; Allen et al., 2001). This tectonic regime is responsible for considerable crustal thickening of the Tien Shan region, where the Moho reaches depths of 50 km (e.g. Burov et al., 1990).

To the north, the Tien Shan are bounded by the rigid basement of the Junggar basin in the east and the Kazakh microplate in the west. Pinched between these stable blocks, the Tien Shan forms an E-W striking pop-up or flower structure with southward dipping thrusts in the northern part and northward dipping thrusts in the southern part (figure 4.13). In this way, the Junggar basin in the north and Tarim basin in the south act as flexural Neogene foreland basins in relation to the orogen and in the orogenic edifice itself, E-W striking ranges are actively being thrust onto adjacent, elongate parallel basins (e.g. Tadjik basin, Fergana basin, Naryn basin, Ili basin, Chu Basin, Issyk Kul basin, Korla basin, Turfan basin etc.) (Allen et al., 1991a, 1993 and 1994; Cobbold et al., 1994) (figures 4.6 and 4.13). A significant amount of shortening caused by the northward movement of India is in this way accommodated (Avouac et al., 1993; Avouac and Tapponnier, 1993; Thompson et al., 2002). Deformation of the Tien Shan, in particular its northern part, seems to have been facilitated by a clear tectonic layering of the crust, originating from an abnormal hot mantle underneath (Buslov et al., submitted). Partially molten zones in the shallow crust act as a detachment and lubricant for thin skin tectonic movements. The movements occur along older, Palaeozoic reactivated structures, characteristic for the reactivation in the entire CADZ. At present the Tien Shan has developed into a high, active mountain range, subject to denudation under arid conditions.

4.5.5.2. The Altai Mountains

More or less according to the same domino-principle (Dobretsov et al., 1996), the Altai Mountains represent a reactivated deformation zone between the rigid Junggar and Tuva-Mongolian (TM) microplates (see figures 4.13 and 4.14). Strike-slip along major shear zones in the Altai -e.g. for Gorny Altai, mainly sinistral movements along the *Irtysh*, *West Sayan*, *Kurai, Teletsk-Bashkauss, Kuznetsk-Alatau* fault zones and oblique dextral movement and thrusting along the *Shapshal* fault zone (see figure 4.14)- installed a presently active, mainly transpressional tectonic regime in the Altai and Gobi Altai mountains (Cunningham et al., 1996a, 1996b and 1997; Owen et al., 1999b; Novikov, 2001). Both sinistral (mainly in Gobi Altai) and dextral (mainly in Altai) structures have been identified. Although the Altai and the Gobi Altai evolved contemperaneously as intracontinental transpressional mountain belts, their kinematic histories are different. The structural fabric and trends of the Gobi Altai show similarities with the Altyn Tagh and Tien Shan and may form a chief connection between the Tien Shan and Altai deformation zones within the CADZ (Cunningham et al., 1996a). The *Hangai Dome* is separated from the Altai and Gobi Altai by the Depression of the Great Lakes in Mongolia. The rigid Hangai is part of the TM microplate and is underlain by Precambrian basement. Smaller Mesozoic basins are found in the area. Cenozoic tectonic and magmatic activity mostly occurred in Mid Tertiary to Quaternary times. Uplift of the Hangai dome since the formation of the Central Asian Late Cretaceous-Palaeogene peneplanation surface is evident. Remnants of this surface are found at elevation of 3 to 3.5 km in the Hangai area. Several mechanisms for uplift of the Hangai Dome, including the existence of a mantle plume, have been put forward (Windley and Allen, 1993; Dobretsov et al., 1996; Cunningham, 2001; Petit et al., 2002).

The deformed area situated between the more rigid blocks (figure 4.14) is composed of several smaller tectonic units, accreted onto the margins of the rigid blocks during the PAO evolution in the Palaeozoic. As in the Hangai area, Cenozoic deformation in the Altai is evident in the Oligocene and Miocene, but some minor activity is already recorded in Late Eocene sediments. Nevertheless the main, still active deformation is clearly constrained to the Pliocene and Quaternary, mostly along Caledonian and Hercynian inherited structures (Dergunov, 1972; Dobretsov et al., 1995b and 1996; Lukina, 1996; Cunningham et al., 1997; Buslov et al., 1999; Chlachula, 2001; Dehandschutter et al., 2002; Novikov, 2002). Locally however, the recent tectonic reactivation has induced transtensional and extensional structures such as basins and fault zones, which occur in a parallel (more or less N-S) alignment (figure 4.15). These fault zones are often associated with recent, Quaternary unconsolidated tectonic breccias. The Pleistocene *Lake Teletskoye* in Gorny Altai, forming a textbook example of a graben-like basin is a marked illustration of this tectonic activity (Dehandschutter et al., 2002).

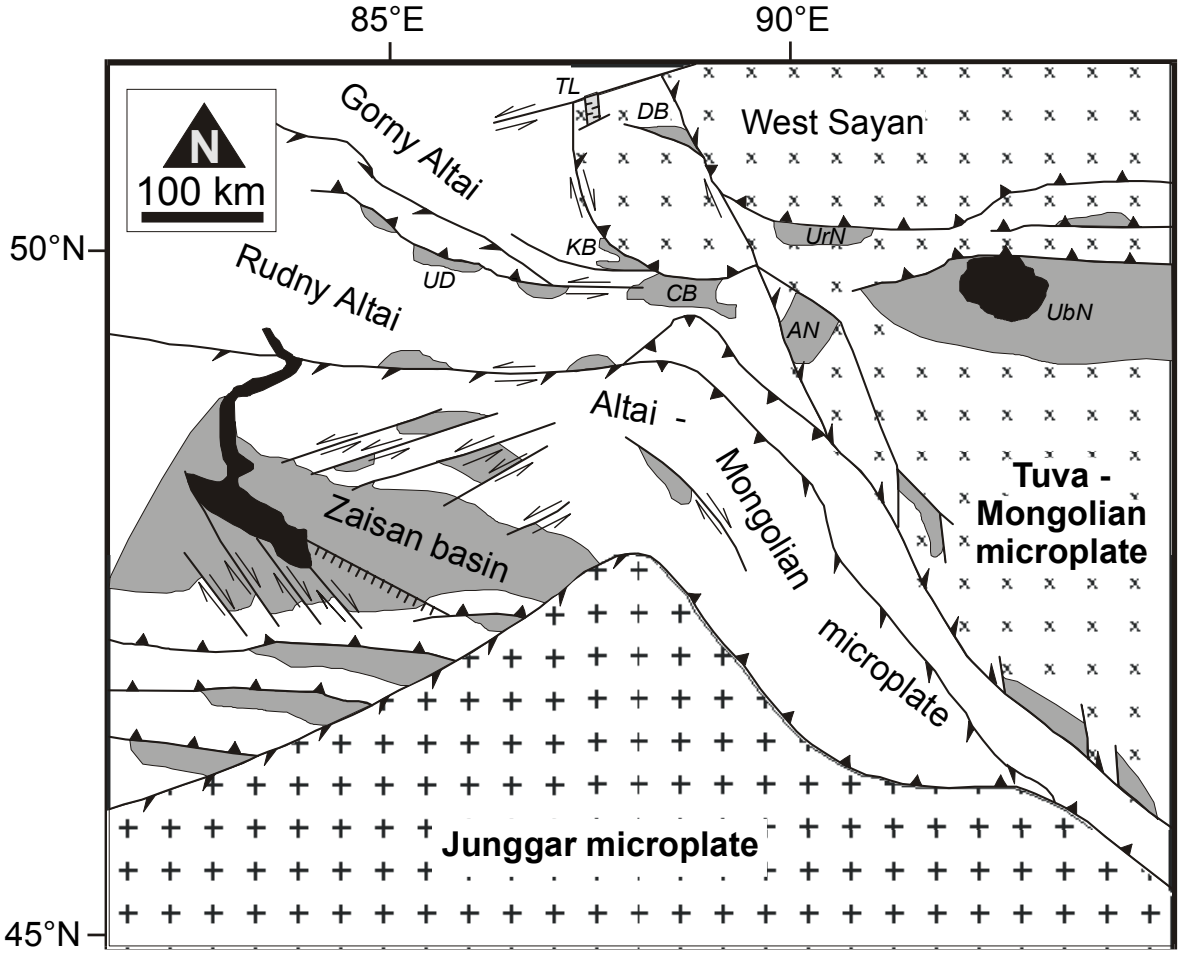

Figure 4.14: Cenozoic tectonic framework of the Altai region (after Buslov et al., 1999). Directions on strike slip faults are indicated by arrows, thrusts are indicated by normal solid barbed lines, oblique thrusts by oblique barbed lines. Extensional structures are represented by striped lines. The less deformed Junggar and Tuva-Mongolian microplates are shown. Cenozoic sediments are located in the shaded areas. AN = Achit-Nuur, CB = Chuya basin, DB = Dzhulukul Basin, KB = Kurai Basin, TL = Teletskoye Lake, UD = Uimon Depression, UbN = Ubsu-Nuur, UrN = Ureg-Nuur basin.

The Cretaceous-Palaeogene peneplenation surface in the Altai region was fragmented in the Oligocene and differential fault movements uplifted the terrane in a complex blocky configuration (Dergunov, 1972; Novikov, 1996; Cunningham et al., 1996a and 1997; Buslov et al., 1999). Coarse sediments were deposited during this time and confirm the timing of reactivation. During an apparent, short interruption in tectonic activity in the Neogene, basins within and adjacent to the developing Altai orogen recorded fine clastic infill (figures 4.5 and 4.15). Intensification of neotectonic reactivation occurred in the Late Neogene. The fact that the activity is still continuing is corroborated by geological and geomorphological evidence (seismicity and associated geomorphological features such as landslides, forebergs, displaced rivers and morraines) (Lukina, 1996; Chipizubov and Smekalin, 1999; Owen et al., 1999a; Philip and Ritz, 1999; Novikov, 2001 and 2002) (figure 4.16).

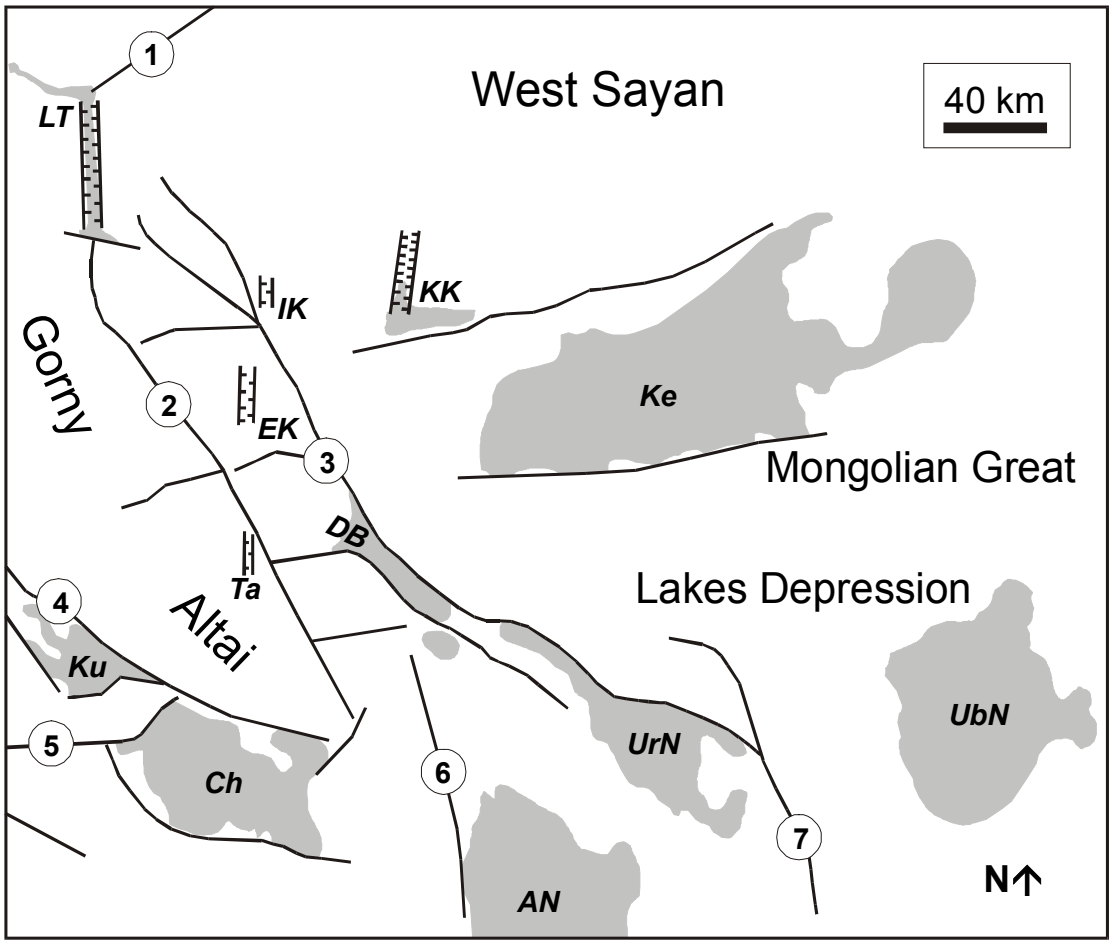

Figure 4.15: Major Quaternary basins and structures in the Russian Altai mountains (after Dehandschutter et al., 2002). Quaternary sediments are indicated by the shaded regions. Extensional structures are shown by striped lines. AN = Achit-Nuur, Ch = Chuya basin, DB = Dzhulukul Basin, EK = Eri-Kol, IK = Ity-Kul, Ke = Kemchuk basin, Ku = Kurai basin, LT = Lake Teletskoye, Ta = Tartagai, UbN = Ubsu-Nuur, UrN = Ureg-Nuur basin. Faults: 1 = West-Sayan, 2 = Chulyshman, 3 = Shapshal, 4 = Kurai, 5 = Charysh-Terekta, 6 = Tolbonursky, 7 = Tsagan.

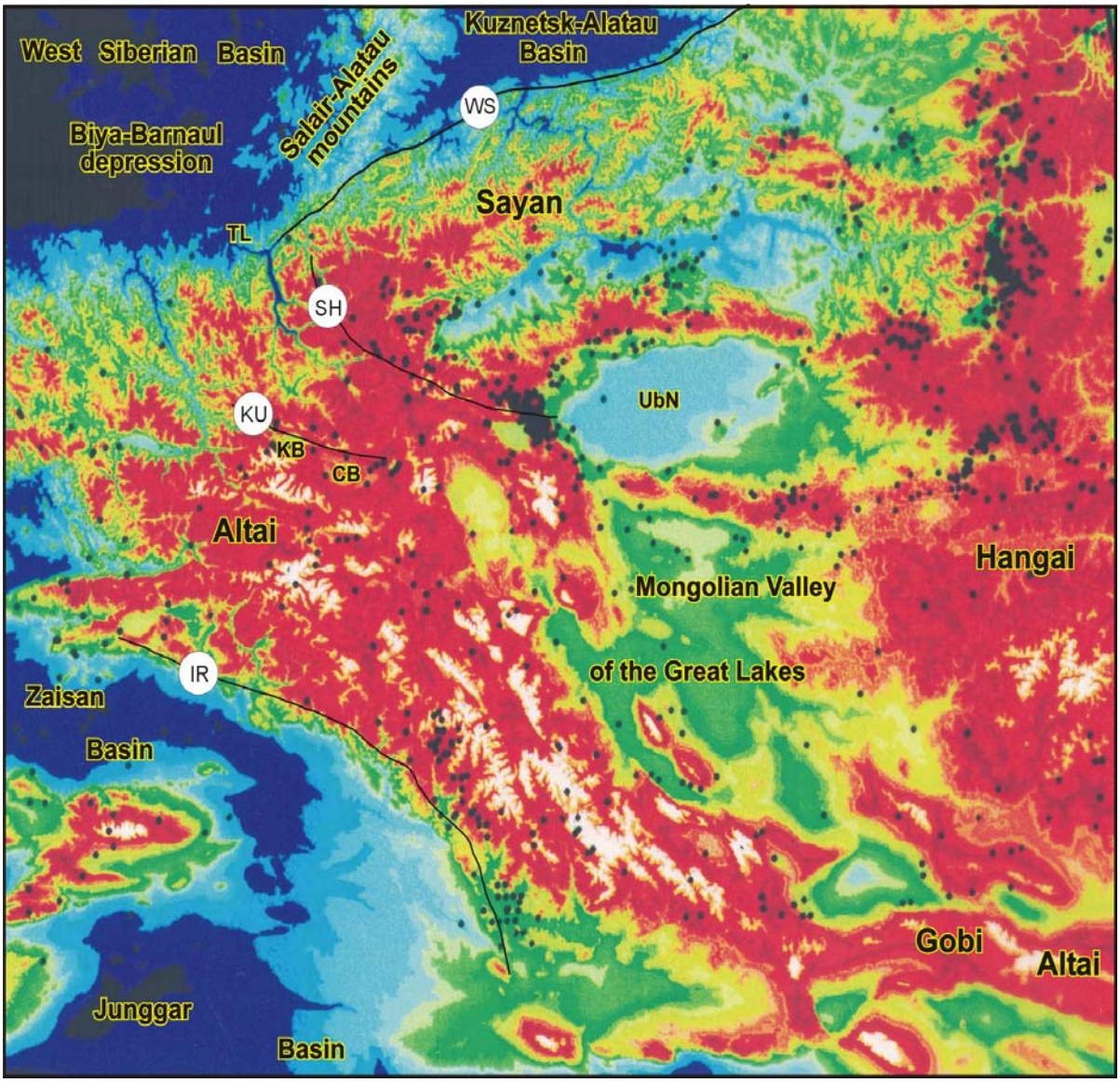

Figure 4.16: Relief of the Altai Mountains and adjacent regions. Historical seismic events are indicated by the dots. Important basins and faults are indicated: CB = Chuya Basin, IR = Irtysh fault, KB = Kurai Basin, KU = Kurai fault, SH = Shapshal fault, TL = Teletskoye Lake, UbN = Ubsu-Nuur, WS = West-Sayan fault.

The geomorphology of the region was shaped in Quaternary times by interactions of active tectonics and climate. The area was subjected to major glaciations, as is evident from many landforms (Novikov, 1996; Chlachula, 2001). Pleistocene ice-dammed lake failures and resulting outbursts and floods have produced some of the world's largest known freshwater floods, causing the development of spectacular landforms (like giant current ripples) (e.g. Baker et al., 1993; Carling, 1996). During this time, intense tectonic activity is thought to have uplifted the area up to 2000 m, according to geomorphological markers (Deev, et al., 1995; Novikov, 1996; Chlachula, 2001). The southern Altai is clearly of significant higher elevation compared to the northern areas. This type of topography was probably already established by Late Pliocene times.

The Cenozoic era in the Altai is registered in a complete sedimentary succession filling the Chuya basin, in southern Gorny Altai (Delvaux et al., 1995c; Buslov et al., 1999). It is therefore an important study area for constraining the Cenozoic history of the entire Altai region. Other Altai basins only contain Neogene and/or Quaternary deposits. This is the case for the Dzhulukul basin in southern Gorny Altai, at the boundary with West-Sayan (Mongolian border). The Cenozoic sediments are mainly alluvial and lacustrine. In some areas however glacial climate related thick aeolian deposits (loess) are found. At present, the climate in the Altai region is typically of continental signature with extreme, cold winters and warm, wet summers.

4.5.5.3. The Baikal Rift Zone

Reactivation of Palaeozoic and Mesozoic structures (Melnikov et al., 1994; Delvaux et al., 1995b) as a far-field effect of the India/Eurasia collision has been proposed as a passive rifting model for the Baikal Rift zone (BRZ) and adjacent areas (so-called Transbaikal mountains). Other authors favour an active rifting model, whereby a rising asthenospheric diapir under the BRZ would, at least to some extent, be responsible for lithospheric thinning and rifting (Kiselev and Popov, 1992; Logatchev and Zorin, 1992; Gao et al., 1994). Recently, Lesne et al. (1998) showed that the passive model is more plausible, while Poort et al. (1998) infer that a possible asthenospheric upwarp would not be centered under the BRZ itself.

The BRZ developed in two rifting phases. Incipient rifting occurred in Late Oligocene to Pliocene times, while the Late-Pliocene (3-4 Ma ago) and Quaternary are the time of major rifting (Logatchev, 1993; Mats et al., 1993; Delvaux et al., 1997 and 2000; Petit, 1998). Rifting is associated with volcanic activity (e.g. Rasskazov, 1994). During the latest and ongoing phase, the rift is evolving in a transtensional to purely extensional tectonic setting (Sherman, 1992; Agar and Klitgord, 1995; Petit et al., 1996; Delvaux et al., 1997), between the Siberian Craton and Mongolia and the so-called *Amur* (North Chinese) block. The rift zone is bounded by transpressional orogens (Sayan, Stanovoy) and the BRZ is confined to a recess within the so-called *Vitim* Embayment within the Siberian craton.

It can therefore be regarded as a crustal strain shadow, protected by the Angara Promontory of the Siberian craton (Cunningham, 2001). The neotectonic activity is apparently induced by stress propagation and extrusional effects from the India/Eurasia collision. As has been mentioned before, retreating subduction zones along the Pacific margin provide room for an eastwardly extruding lithosphere and may be an additional factor in the BRZ development.

CHAPTER 5

STUDY AREAS AND SAMPLING: GORNY ALTAI (SIBERIA) AND THE ISSYK KUL REGION, NORTHERN TIEN SHAN (KYRGYZSTAN)

5.1. The Lake Teletskoye region in Gorny Altai

5.1.1. General aspects and location

Lake Teletskoye occupies the narrow, recent *Teletsk graben* located in the northwestern sector of the Altai Mountains (see figures 5.1, 5.2 and also figures 4.1, 4.5, and 4.14). It is situated at the geological boundary between the Gorny Altai (GA) and West Sayan (WS) structural blocks in southern central Siberia. The lake is 77 km long by 4 km wide and water depth attains a maximum of 325 m. It forms the second largest freshwater reservoir in Russia, after Lake Baikal. The lake is composed of a 50 km long north-south oriented part filling the main Teletsk graben as such (figures 5.3 and 5.4), and a narrow, 27 km long east-west trending part. The Teletsk graben is bordered by steep slopes, rising up to 500 m above the lake level in its northern part, and to more than 2000 m in the southern part. In addition, the sediment infilling of the lake reaches more than 800 m (Seleznev et al., 1995).

The recent formation of the Teletsk graben is thought to be a distant result of the ongoing convergence between the Indian and Eurasian continents. As a matter of fact, this convergence is responsible for the tectonic reactivation of the entire CADZ. The Teletsk graben formed in a local extensional regime, and is the largest of a series of north-south oriented graben structures (figure 4.15). At its northeastern extremity, the graben splays off in the *Kamga* graben (figure 5.3) that runs along the large *West Sayan* fault zone. The southeastern edge of the Teletsk graben, near Chiri is formed by the *Kyga* graben (figure 5.4). The West Sayan fault zone divides the Gorny Altai (GA) and West Sayan (WS) terranes in the north of the Lake Teletskoye basement. The West Sayan fault zone runs through the northern part of the basin and separates the mountainous region of the Altai in the south from its lower, hilly foreland (figure 5.5 and 4.16). Of the 50 AFT samples from the Altai Mountains, the majority (29) come from the Lake Teletskoye basement and surrounding region (table 5.1, figure 5.2).

Table 5.1: Apatite samples from the Altai and Tien Shan mountains used for AFT analyses in this study.

Sample	Latitude	Longitude	Altitude (m a.s.l.)	Locality	Lithology
AFT Samples from Gorny Altai					
A. Teletskoye Region					
TEL 101	51°23'49"N	87°41'31"E	2210	Altyntauss massif	granite
TEL 105	51°26'10"N	87°41'22"E	2000	Altyntauss massif	granite
TEL 107	51°27'37"N	87°41'23"E	1585	Altyntauss massif	granite
TEL 108	51°27'39"N	87°41'23"E	1390	Altyntauss massif	granite
TEL 109	51°28'19"N	87°41'29"E	1155	Altyntauss massif	granite
TEL 110	51°28'22"N	87°41'41"E	940	Altyntauss massif	granite
TEL 111	51°28'27"N	87°41'52"E	820	Altyntauss massif	granite
TEL 112	51°28'39"N	87°42'00"E	610	Altyntauss massif	granite
AL 262	51°07'43"N	87°47'55"E	480	Chulyshman valley	granite
AL 272	51°21'56"N	87°44'50"E	435	Altyntauss massif	granite
SH 1	51°45'13"N	87°55'40"E	1850	Katayatsk massif	diorite
SH 2	51°44'42"N	87°55'44"E	1950	Katayatsk massif	diorite
SH 3	51°44'32"N	87°55'44"E	2010	Katayatsk massif	diorite
SH 4	51°44'58"N	87°55'55"E	2100	Katayatsk massif	diorite
SH 5	51°45'31"N	87°55'11"E	1720	Katayatsk massif	granodiorite
SH 6	51°20'56"N	87°56'56"E	650	Kyga valley	granite (sheared)
SH 9	51°24'11"N	88°08'21"E	2250	Kojildukir massif	red sandstone
SH 11	51°23'07"N	88°11'38"E	1700	Kosbashi massif	gray sandstone
SH 15a	51°20'30"N	88°15'30"E	2150	Karakol Creek	gneiss
SH 15b	51°18'16"N	88°20'09"E	1950	Tugunluarchikkil lake	gneiss
SH 16	51°17'37"N	88°17'45"E	1900	Tugunluarchikkil lake	granite
SH 18	51°16'51"N	87°58'46"E	2050	Ljukjil lake	gneiss
SH 19	52°01'08"N	87°51'51"E	470	Blyka village	granite
GA 30	51°27'00"N	87°46'32"E	440	Bele terrace	gneiss
GA 31	51°23'22"N	87°55'24"E	2300	Baskon massif	granodiorite
GA 32	51°21'00"N	87°49'30"E	440	Kyga valley/Chiri outpost	diorite
GA 33	51°48'53"N	87°10'36"E	420	Artybash village	diorite
GA 34	51°55'13"N	87°05'42"E	400	Kebezen village	diabase
CHU 01	51°07'30"N	87°49'50"E	1500	Chulyshman valley	granite
B. South Chulyshman Plateau					
GA 06	50°32'21"N	88°09'23"E	1365	Saratan village/Bashkauss valley	gneiss
GA 07	50°36'21"N	88°49'11"E	1630	Yazula village	gabbro
GA 08	50°35'25"N	89°02'52"E	1870	Mushtuair valley	gneiss
GA 15	50°35'57"N	88°51'10"E	1585	Yazula village (Cardon camp)	gneiss
GA 16	50°35'30"N	88°51'04"E	1720	Yazula village (Cardon camp)	amphibolite
GA 18	50°35'26"N	88°47'50"E	1635	Yazula village (Cardon camp)	gneiss
GA 19	50°36'49"N	88°45'03"E	1300	Yazula village	gneiss
GA 21	50°33'48"N	88°33'32"E	2325	Karatesh pass	diabase
GA 23	50°32'57"N	87°47'30"E	1580	Kubadru river (Ust Ulagan)	granite
C. Dzhulukul Basin					
GA 09	50°43'00"N	89°15'17"E	2240	Mayrikbazhi massif	gneiss
GA 12	50°45'50"N	89°18'10"E	2785	Trechglavaya massif	granodiorite
GA 13	50°45'11"N	89°19'28"E	2500	Trechglavaya massif	granodiorite
GA 20	50°37'54"N	89°14'18"E	2015	Uzun Uyok river	granitic aplite

Table 5.1: continued.

Sample	Latitude	Longitude	Altitude (m a.s.l.)	Locality	Lithology
AFT Samples from Gorny Altai					
D. Kurai - Chuya					
AL 235	49°44'06"N	88°05'50"E	3490	Dzankiol pass	pegmatite
AL 239	50°16'31"N	88°04'25"E	2720	Ildugemsky pass	mylonite
AL 240	50°16'00"N	88°04'00"E	2440	Ildugemsky pass	granodiorite
E. West Gorny Altai Transect					
Be 1	51°56'24"N	84°45'24"E	290	Belokuriha massif (Chernovaya)	granite
GA 01	51°55'16"N	85°51'15"E	295	Rybalka massif (Sausga village)	granodiorite
GA 03	50°38'59"N	86°17'54"E	1100	Chiquetaman pass	granodiorite
GA 24	51°19'48"N	85°40'14"E	840	Shebalino village	rhyolite
Novosibirsk					
No 1	54°59'15"N	82°59'12"E	90	Borok quarry, Priobsky complex	monzodiorite
AFT Samples from Tien Shan, Issyk Kul basement					
A. Kungei Range					
TS 04	42°51'19"N	76°34'39"E	2360	Chon Kemin valley	gneiss
TS 06	42°43'35"N	76°49'51"E	3950	Kungei, Almaty road transect	granite (pink)
TS 07	42°43'23"N	76°50'37"E	3700	Kungei, Almaty road transect	diorite
TS 08	42°43'05"N	76°50'38"E	3515	Kungei, Almaty road transect	granite (pink)
TS 10	42°43'14"N	76°51'31"E	3085	Kungei, Almaty road transect	granite (pink)
TS 11	42°42'17"N	76°51'51"E	2860	Kungei, Almaty road transect	quartz porphire
TS 12	42°40'40"N	76°51'03"E	2420	Kungei, Almaty road transect	granite (pink)
TS 13	42°46'09"N	77°31'25"E	1850	Aksu valley (Cemenovska)	granite (pink)
TS 14	42°48'07"N	77°31'50"E	2080	Aksu valley (Cemenovska)	granite (pink)
TS 18	42°27'51"N	76°00'52"E	1630	Rybachye	red sandstone
B. Terzkey Range					
TS 19	42°07'11"N	77°08'30"E	2020	Agat camp	granite (pink)
TS 20	42°05'03"N	77°22'04"E	2150	Tioch Sor valley	granite
TS 22	42°03'00"N	77°09'55"E	3500	Tashtarata massif	granite (pink)
TS 23	42°03'12"N	77°09'31"E	3310	Tashtarata massif	granite (pink)
TS 24	42°03'16"N	77°09'07"E	3080	Tashtarata massif	granite (pink)
TS 26	42°04'14"N	77°08'46"E	2700	Tashtarata massif	granite (pink)
C. Kindel Las Range					
KAZ 01	43°21'00"N	74°57'00"E	1250	Kur-Dai pass	quartz porphire
KAZ 03	43°14'00"N	74°45'00"E	760	Sjugete (Volga) village	plagiogranite
D. Boom Canyon					
TS 02	42°41'03"N	75°53'21"E	1370	Djel Arik	pegmatite
TS 15	42°26'57"N	75°51'39"E	2150	Rybachye	granite (pink)
TS 16	42°27'06"N	75°51'23"E	1960	Rybachye	granite (pink)
TS 17	42°27'13"N	75°51'25"E	1830	Rybachye	granite (pink)

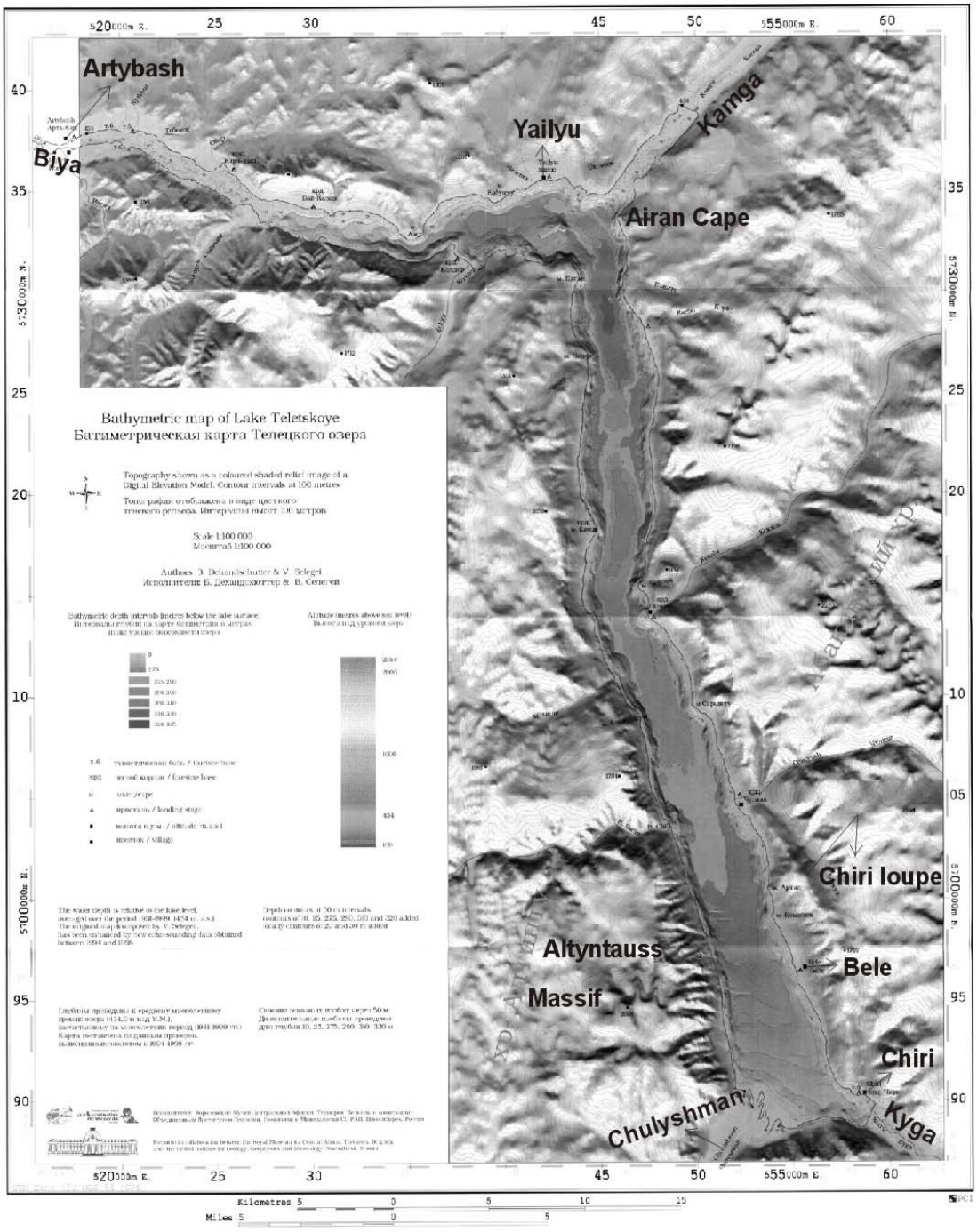

Figure 5.1: Bathymetric map of Lake Teletskoye and topography of the surrounding basement (from Selegei et al., 2001). Indication of locality names for orientation.

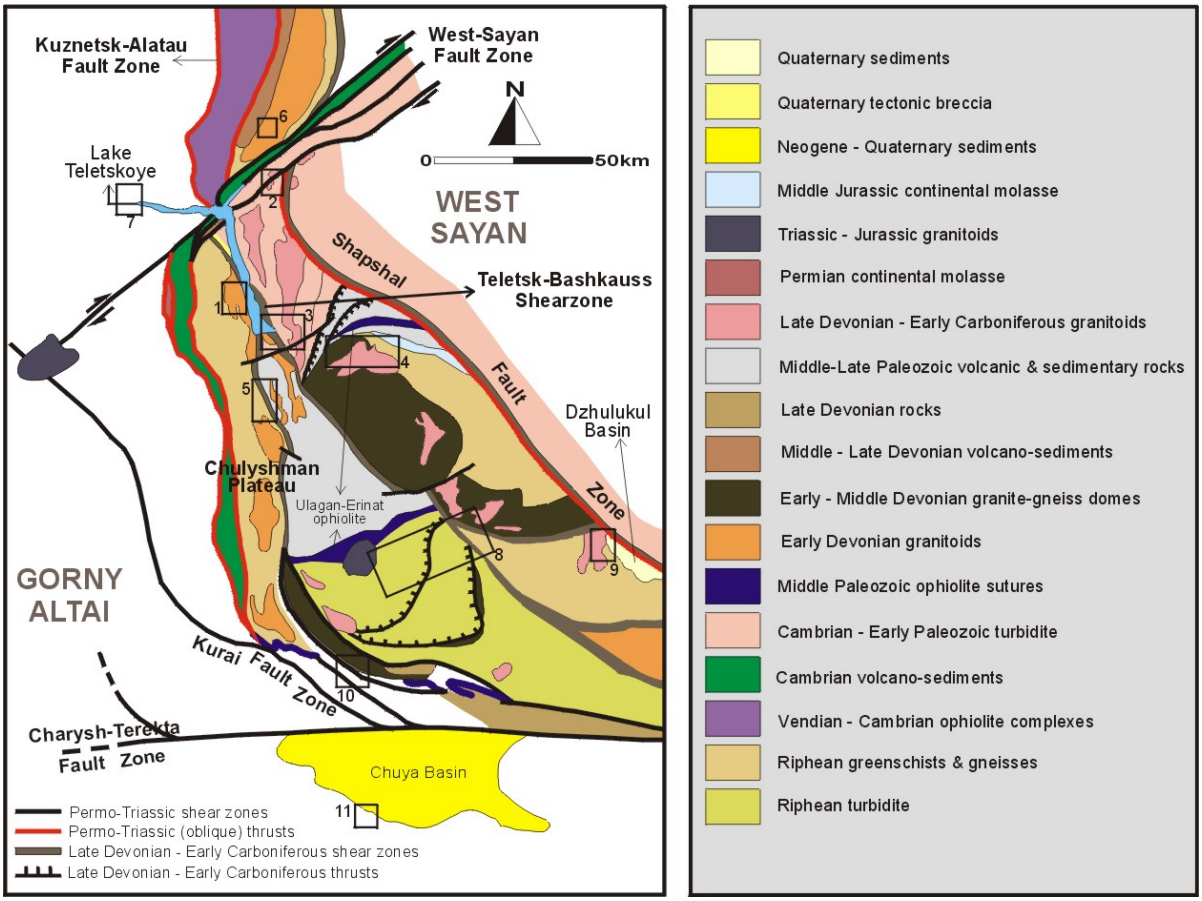

Figure 5.2: Geological map of Gorny Altai, Russian Altai Mountains, South Siberia (after Buslov, 1998). General AFT sample locations are indicated by the numbered boxes: 1 = Altyntauss massif (TEL-samples and AL272); 2 = Katayatsk massif (samples SH1-SH5); 3 = Kyga valley region (samples SH6, SH18, GA30-GA32); 4 = samples SH9-SH16; 5 = lower Chulyshman valley (samples CHU-01 and AL262); 6 = Blyka massif (sample SH19); 7 = Artybash area (samples GA33-34); 8 = South Chulyshman Plateau samples (samples GA 06, 07, 08, 15, 16, 18, 19, 21, 23); 9 = Dzhulukul Basin (samples GA 09, 12, 13, 20); 10 = Kurai Range (samples AL239-240); 11 = South Chuya Basin (sample AL235). See table 5.1 for sample details.

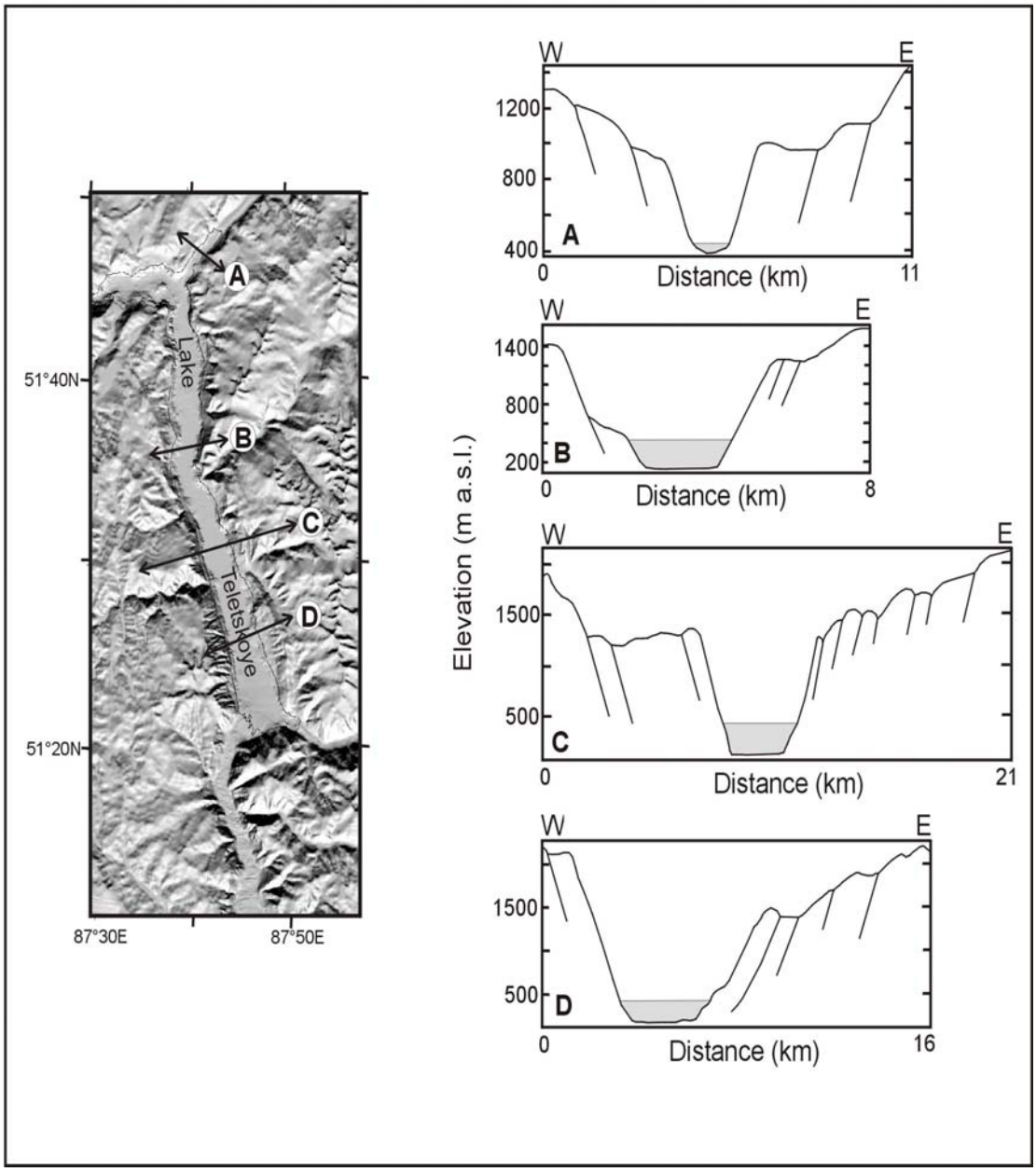

Figure 5.3: Profiles across the Teletsk graben, locations indicated on the digital terrane model (after Dehandschutter et al., 2002). Vertical exaggeration is 3.5 for A, 2 for B, 4 for C, and 3 for D.

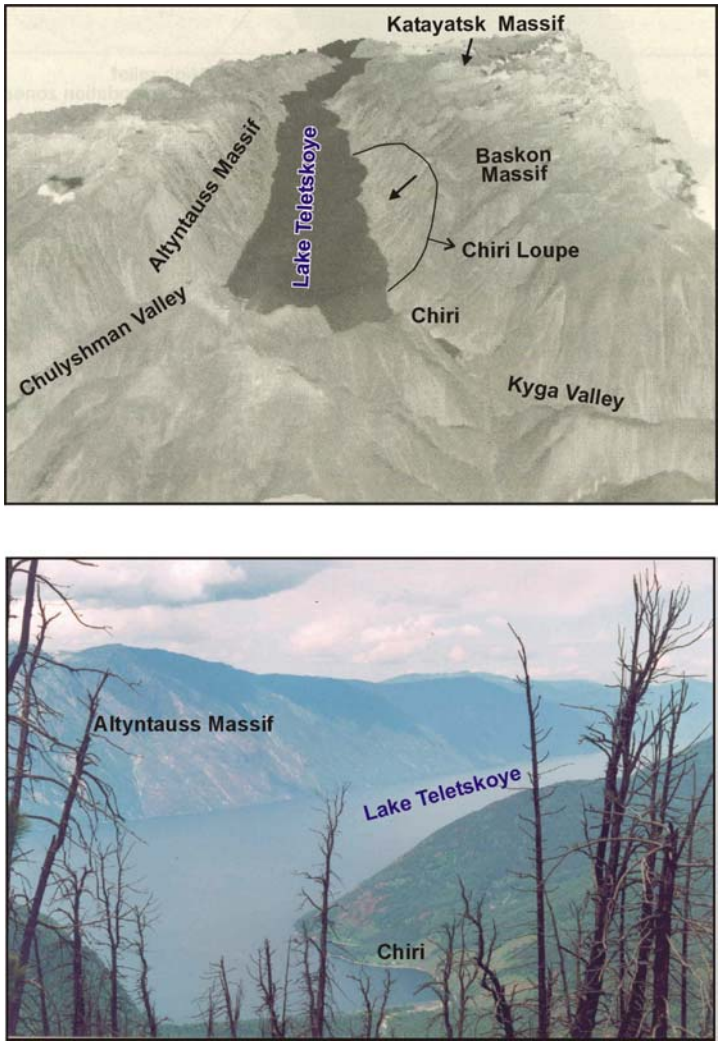

Figure 5.4: Morphology of the Teletsk graben. Top: Three dimensional view of the graben (south to north), constructed after a SPOT satellite image (from Dehandschutter et al., 2002), with indication of important structures and sampled areas. Bottom: Picture of the Teletsk graben from the southern flank of the Kyga valley (field work 1999).

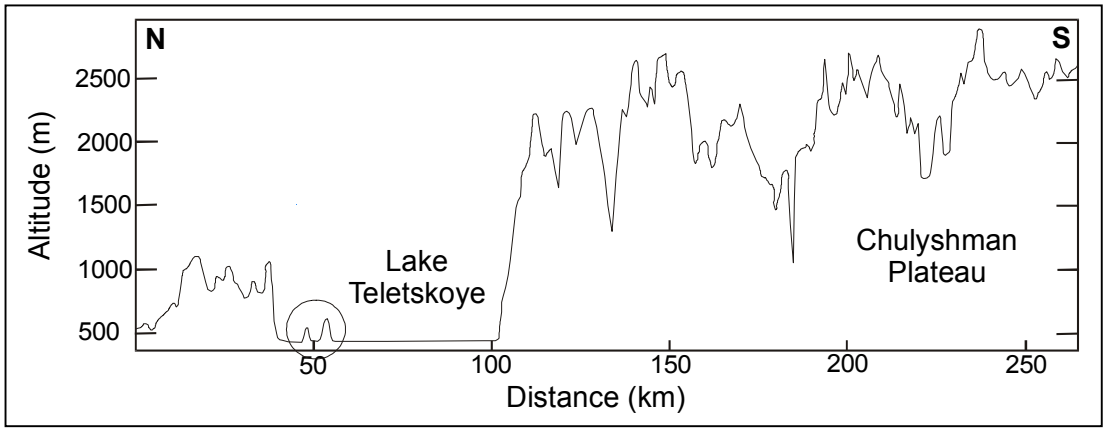

Figure 5.5: N-S profile across Lake Teletskoye and the Chulyshman Plateau (redrawn after Dehandschutter, 2001). The area north of Teletskoye is clearly of lower elevation than the Chulyshman region. The Chulyshman Plateau is dissected by deep E-W trending valleys, which are interpreted as strike-slip faults, carving up the plateau into several distinct rotating blocks. The Lepnova ridge separating the Teletsk graben into several sub-basins (see text for discussion) is also clearly visible.

5.1.2. Geological history

5.1.2.1. The Late Proterozoic – Palaeozoic basement

The Teletsk graben developed at the geological boundary between the Gorny Altai (GA) and West Sayan (WS) Palaeozoic structural blocks (figure 5.2). The geological history of these blocks reflects the typical Siberian accretionary Palaeozoic evolution as outlined in chapter 4. The geology of the Teletsk basement has been extensively studied e.g. by Buslov et al. (1993) and (2001a), Buslov and Sintubin (1995), Sintubin et al. (1995), Buslov (1998) and Smirnova et al. (2002).

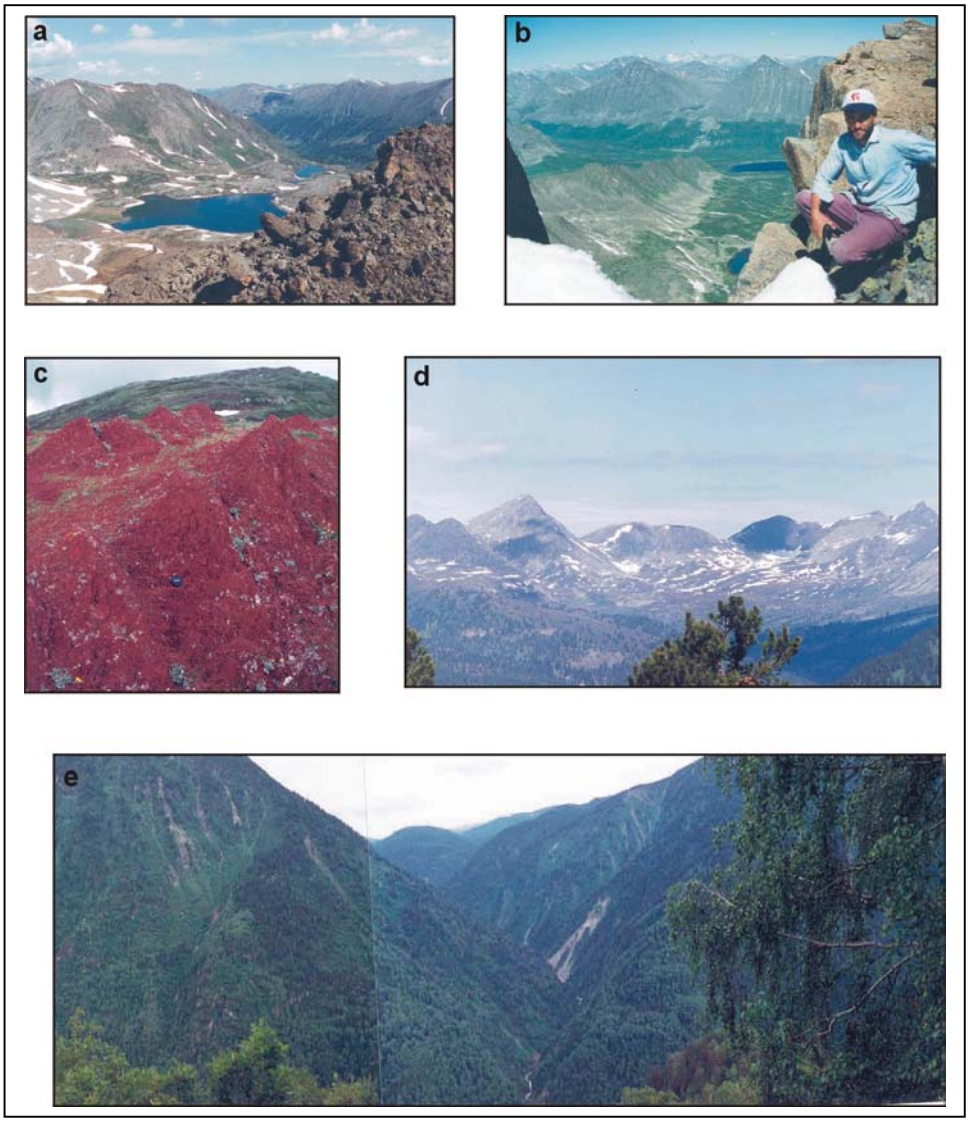

Figure 5.6: Structures and morphology of Gorny Altai. (a) Northern segment of the Ulagan-Erinat ophiolite in the background (see figure 5.2 for location). (b) Segment of the transpressional, reactivated Shapshal fault from Trechglavaya peak, Dzhulukul area. (c) Remnants of the red Cretaceous-Paleogene peneplanation surface, Kojildukir area. (d) Glacial geomorphology: cirques and glacial horns dominate the Altai landscape. (e) The Kyga valley, southeast Teletskoye basement.

The GA terrane mainly consists of Late Proterozoic and Early Palaeozoic rocks (figure 5.2) that were formed and deposited in an island arc and accretionary prism environment with seamount-guyot sequences such as the *Biya-Katun* sequence (Buslov et al., 1993; Buslov and Watanabe, 1996; Buslov, 1998; Buslov et al., 2001b). Several island arcs similar to the GA fringed the Siberian continent during that time. The rocks of the GA island arc include ophiolites (figure 5.2 and 5.6), boninites, blueschists, eclogites, metasediments and (pillow)lavas (mostly tholeiitic in composition and often metamorphosed to greenschists), tuffites, sheeted dyke complexes and carbonates. Geodynamically these rocks represent remnants of a Late-Riphean oceanic crust (the so-called *Manzherok* suite), a Vendian-Early Cambrian primitive PAO island arc, a Vendian-Early Cambrian back-arc basin and accretionary prism (aforementioned seamount-guyot arrays collided with and closed the subduction zone at that time), and a younger Early-Middle Cambrian normal island arc (the *Kaimsk* suite).

In the Middle Palaeozoic, Gorny Altai was the setting of a passive margin and during the Ordovician an extended carbonate platform formed and grey and red terrigeneous sediments accummulated in lagoonal and tidal basins (e.g. Buslov et al., 1993; Berzin et al., 1994; Kozlov and Dubatolev, 1994; Yolkin et al., 1994; Berzin and Kungurtsev, 1996). They unconformably overlie the Vendian-Cambrian island arc rocks via a basal conglomerate. The passive margin rocks are followed by Early and Middle Devonian (Emsian-Givetian) active margin assemblages, reflecting the onset of the collision between the amalgamated Altai-Mongolian microplate, including Gorny Altai, with the Siberian orogenic rim (e.g. Buslov et al., 2001b). These Devonian rocks are mainly composed of acid as well as basic volcanics and of back-arc terrigeneous and volcanogenic sediments (Buslov et al., 1993; Berzin et al., 1994; Kozlov and Dubatolev, 1994; Yolkin et al., 1994; Berzin and Kungurtsev, 1996). In the Teletskoye area, these latter sediments are represented by red and gray medium-grained sandstones. A large Devonian granitoid intrusion, the *Blyka* granitoids (sample SH19), outcrops, just north of the Teletskoye basin, and builds the foothills of the present-day Altai Mountains. The intrusion is thought to be related to the abovementioned active margin that was installed in Devonian times.

The western section of the basement of Lake Teletskoye is situated in the GA terrane. It is characterized by the occurrence of Vendian-Cambrian volcano-sedimentary rocks of island arc and oceanic crust affinity. Ordovician passive margin sediments and Devonian active margin sediments are exposed as well (figures 5.7 and 5.8). Locally in this zone, the rocks are cut by gabbro-diabase dykes and sills, and also by small granodioritic plutons (samples GA 33 and GA 34). These igneous rocks are probably related with the Devonian active margin (e.g. Yolkin et al., 1994; Dobretsov and Vladimirov, 2001).

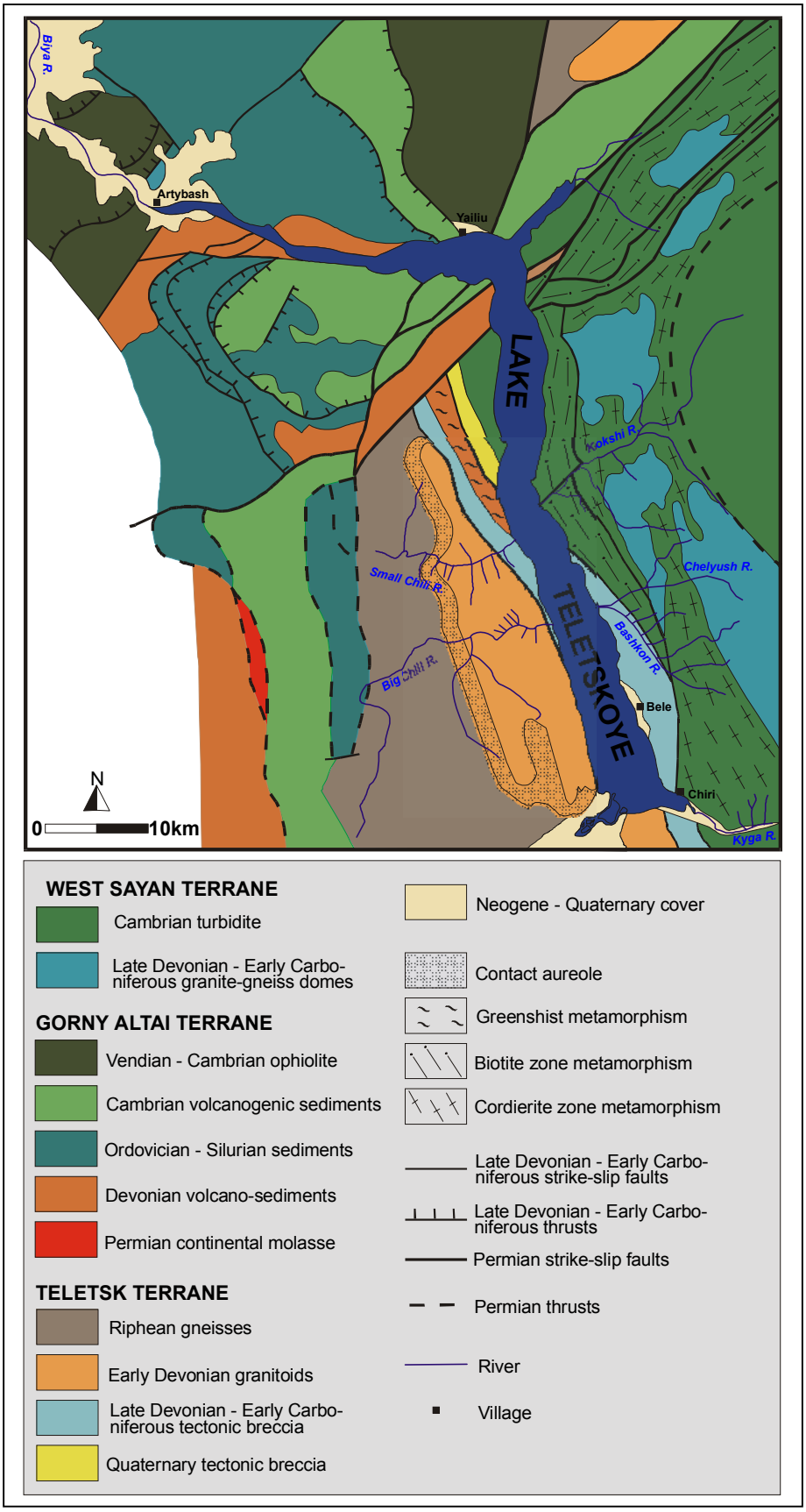

Figure 5.7: Geological and tectonic sketch map of the Teletskoye basement (after Buslov, 1998 and Smirnova et al., 2002).

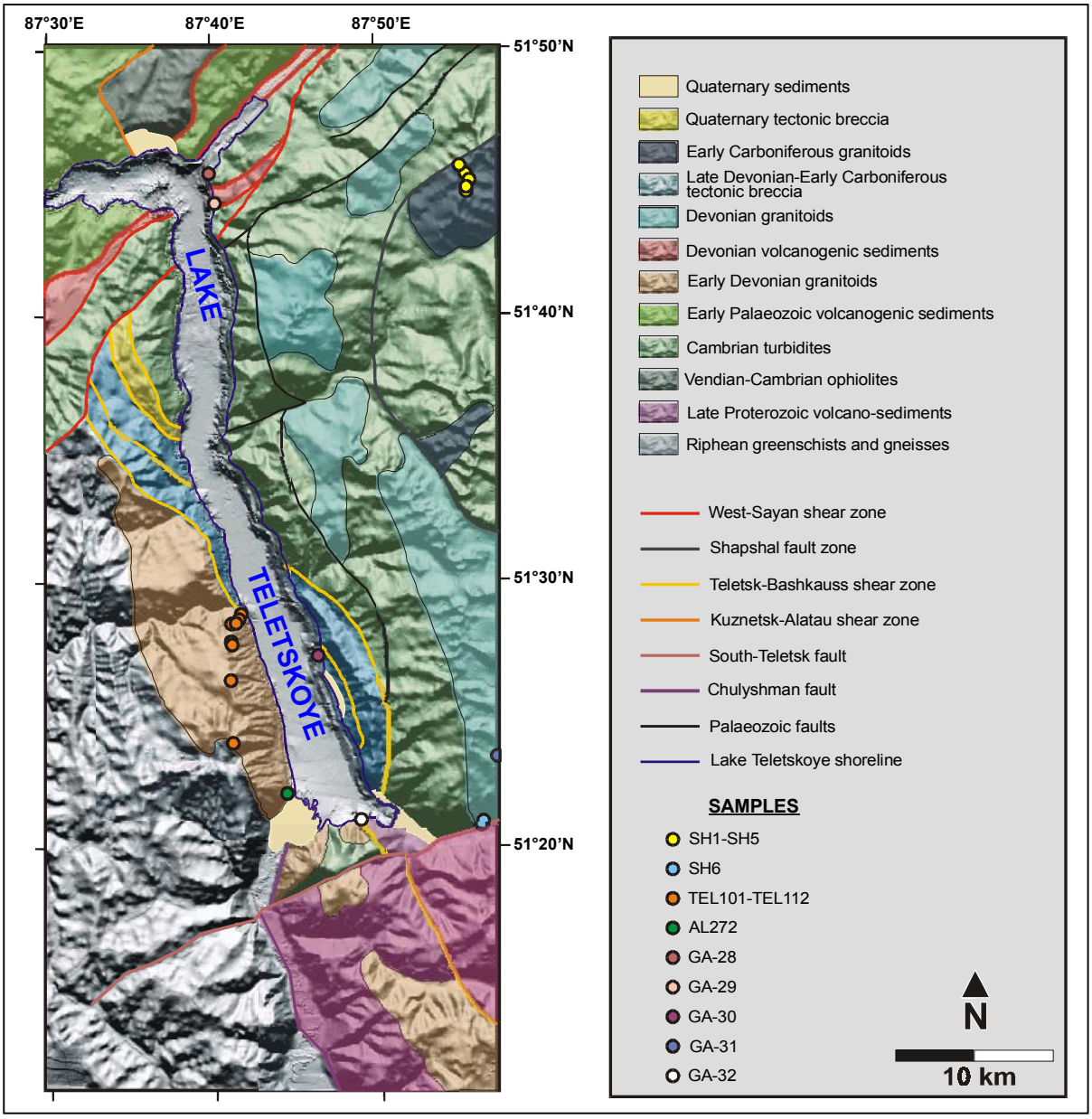

Figure 5.8: Superposition of geological and tectonic features on a digital terrane model of the Teletskoye basement. AFT sample locations in the area are indicated.

The WS terrane evolved independently from the GA in a marginal sea and fore-arc setting as indicated by the Late Riphean to Ordovician metasediments that are predominantly turbidites (Kazanskii et al., 1999). In the Teletskoye region the WS terrane consists of two units: the *Teletsk* Unit in the southwest and a northeastern unit, separated by the Late Devonian-Early Carboniferous *Teletsk-Bashkauss* (TB) fault zone, which converges in the south with the *Kurai* fault zone. A tectonic breccia along the TB fault in the Teletsk Unit is associated with its activity. Turbidites from the northeastern WS unit are abundantly exposed on the eastern shores of Lake Teletskoye. They form the so-called *Kokshi* series of Cambrian to Ordovician age (figure 5.7 and 5.8). They are correlated with the widespread *Manchurek* Formation in the interior section of the WS terrane, as described in detail by Sennikov et al. (2000). The Teletsk Unit is mainly composed of Riphean gneisses. The WS terrane is widely intruded by several granitoid complexes. They are in part of Early Devonian age, reflecting plutonism associated with the initial stages of collision of the Siberian margin with the Altai-Mongolian microplate. The *Altyntauss* massif (samples TEL 101 to 112, GA 32 and AL 272, figure 5.8), forms the southwestern flank of the Teletsk graben and is a good example of this type of pluton. Associated outcrops occur in the Chulyshman valley, south of Lake Teletskoye (samples AL 262 and CHU 01). The Altyntauss Massif is bordered by a well-developed hornfelsic contact aureole. Other granitoids and granite-gneiss domes are of Late Devonian-Early Carboniferous age and represent post-collisional plutonism associated with the collision (e.g. Vladimirov et al., 1997). The *Baskon* or *Chelyush-Abakan* (sample GA 31) and *Katayatsk* (samples SH1 to SH5) complexes within the Cambrian-Ordovician turbidites flanking the east of Lake Teletskoye (figure 5.7 and 5.8) are examples of these plutons. During this collision, large NW-SE trending sinistral strike-slip and thrust faults developed in the WS unit. The TB and *Shapshal* fault zones are prime examples of these Late Devonian-Early Carboniferous structures (figure 5.2 and 5.6). Both parallel structures and associated thrusts form the contact between both terranes in this area. The Pleistocene Teletsk graben developed mainly along the TB fault zone, while the Shapshal zone links with the basin via the Kyga valley-lineament (sample SH6 from the lower Abakan massif) (figure 5.6 and 5.8). Dehandschutter et al., (2002) called this transfer fault the *South Teletsk* fault. The Shapshal fault can be traced far to the south were is separates the Altai mountain ranges from the Mongolian Depression of the Great Lakes. Late Devonian-Early Carboniferous thrusts have been recognized along this zone (figure 5.2). The amphibolite facies metamorphism of the WS rocks dates from this period as well. The metasediments on the eastern Teletskoye flank are mainly biotite schists with blasts of garnet or cordierite (figure 5.7). Amog these metasediments, the *Chiri* series is widely exposed along the southeastern shores of Lake Teletskoye, south of the turbiditic Kokshi series. Locally, gneiss outcrops occur as well (sample GA 30, figure 5.8). Rocks similar to the Late Devonian-Early Carboniferous granite-gneiss domes that compose the southeastern margin of the Teletskoye basement were also found and sampled (SH15a and b, SH16 and SH18) further to the southeast, near a rare and small Jurassic deposit, and the fragment of the so-called *Ulagan-Erinat* ophiolite (figure 5.2 and 5.6). Devonian sandstones from the *Koshbashi* and *Kojildukir* massifs (samples SH9 and SH11) in the same area, were also sampled for AFT analysis.

The Middle-Palaeozoic Ulagan-Erinat ophiolite marks the southern suture between the WS terrane and units from the Altai-Mongolian microplate sensu stricto. It is displaced by the Late Devonian-Early Carboniferous TB and Shapshal fault zones (figure 5.2).

In the Chiri series, at the base of a lens-shaped fault, the so-called Chiri "loupe" (figure 5.4) pseudotachylites have been discovered (Sintubin et al., 1995; Theunissen et al., 2002). The Chiri loupe is a curvilinear fault segment of the TB shear zone. It is hitherto not clear whether or not these pseudotachylites are related to the evolution of the Teletsk basin. They might represent cataclastic downfaulting along the Chiri loupe during the opening of the graben. The Chiri loupe forms the southeastern border of the Teletsk basin and seems to render the basin a half-graben morphology with the Chiri loupe representing a listric fault along which the bordering basement block is downfaulted and tilted towards the lake (profile "D" in figure 5.3 and figure 5.4). Seismic reflection data from the lake, however, reveal a typical full-graben morphology with two converging bordering normal faults and symmetrical sediment distribution (figure 5.9) (Seleznev et al., 1995 and 2001; Dehandschutter et al., 2002).

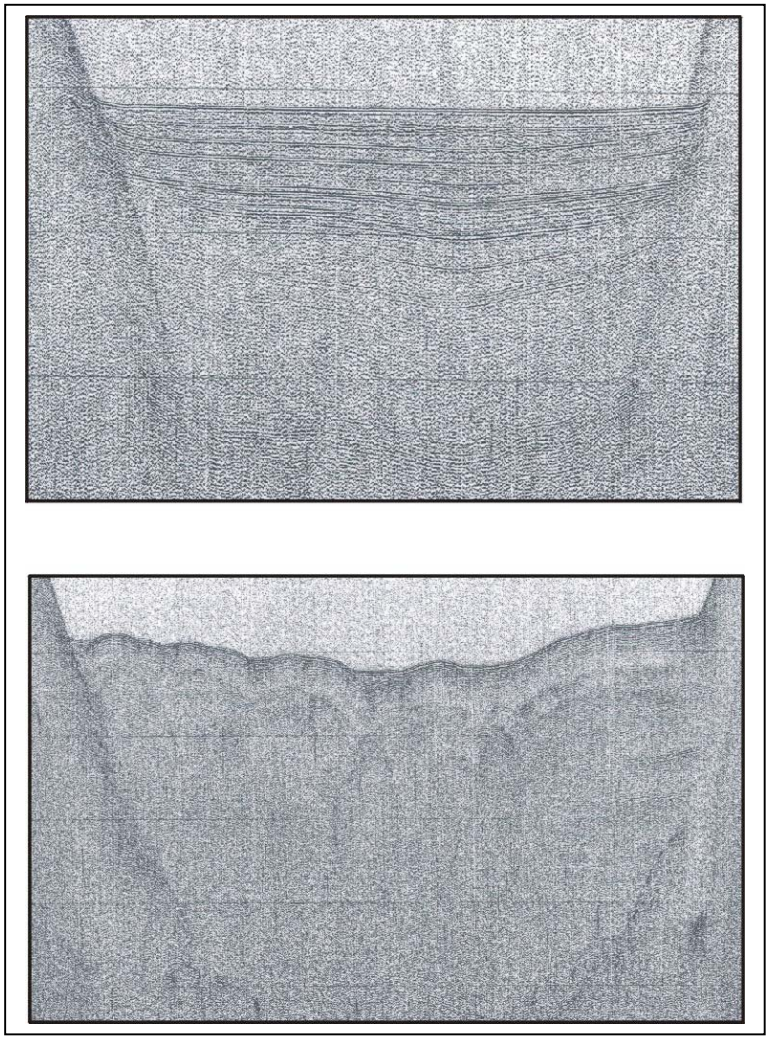

Figure 5.9: E-W seismic sections showing the full-graben morphology of two converging border faults and symmetrical basin infill of the Teletsk graben (from Dehandschutter et al., 2002). Top: section from the southern basin of the Teletsk graben, top sediments are undeformed. Bottom: section from the northern basin of the Teletsk graben, top sediments are clearly deformed.

The final closure of the Western Palaeo-Asian Ocean (WPAO) in the Permo-Triassic as a result of the collision of the Siberian orogenic rim with a combined Kazakhstan plate (chapter 4), induced dextral strike-slip and thrust displacement along the vast West-Sayan (WS) fault zone and associated structures. These movements led to the GA-WS juxtaposition as it appears nowadays (Buslov et al., 2003). Thrusting of the WS terrane along the Teletsk Unit triggered the formation of small thrust-related intramontane basins and subsequent Permian molasse infill (figure 5.7). The presently reactivated sinistral WS fault zone forms the boundary between the GA and WS terranes in the northern part of Teletskoye basement. It is one of the most important structures of the northern Altai and even of the entire CADZ (Şengör et al., 1993). The shear zone is traceable over a distance of more than 1000 km, linking up with the Baikal Rift Zone in the east. It is exposed as a 6 to 8 km wide active fault zone. As it cuts the TB and Shapshal fault zones in the northern Teletskoye basement, it is clearly of younger age. In the same area where the WS fault zone cuts the TB and Shapshal structures, the WS fault also intersects the Kuznetsk-Alatau (KA) fault zone (figure 5.2). These vast shear zones are long-lived, multiphase reactivated structures of major importance to the tectonic evolution of the area. They represent major Palaeozoic sutures and may crosscut the entire crust and even parts of the lithospheric mantle. Dehandschutter et al. (2002) demonstrated their importance for the development of the Teletsk graben.

5.1.2.2. The Mesozoic

In general, the Teletskoye region is thought to have been tectonically inactive during the Mesozoic. Mesozoic tectonism was limited to adjacent regions as was outlined in the previous chapter. Nevertheless, the presence of a small Jurassic intramontane basin about 25 km southeast of Lake Teletskoye indicates that at least some activity was taking place during that time. Also, several Triassic-Jurassic granitoid intrusions occur in the direct vicinity (figure 5.2). In addition significant thrust movements may have occurred along the KA fault zone, in the Kuznetsk basin, north of the present-day Altai deformation front (figure 4.16). The broader tectonic framework in which these events took place is not exactly understood, but they could represent a complex interplay between active continental rifting in the West Siberian Basin and major compression induced by the Mongol-Okhotsk orogeny (as thought by Buslov and Sintubin, 1995). Moreover, active Cenozoic deformation could have erased any existing geological record from the Mesozoic reactivation episode. A widespread Cretaceous-Palaeogene peneplanation surface is however clearly recognized in the Teletskoye area as well (figure 5.6 and 5.10) (Deev et al., 1995).

5.1.2.3. Cenozoic reactivation

During the Cenozoic, at the beginning of the India/Eurasia continent-continent collision, the Altai mountains were reactivated, as the stress and deformation propagated through the crust of the CADZ. This reactivation preferentially occurred along older inherited structures. The Pliocene and Quaternary are particularly characterized by an intensified tectonic activity (see chapter 4).

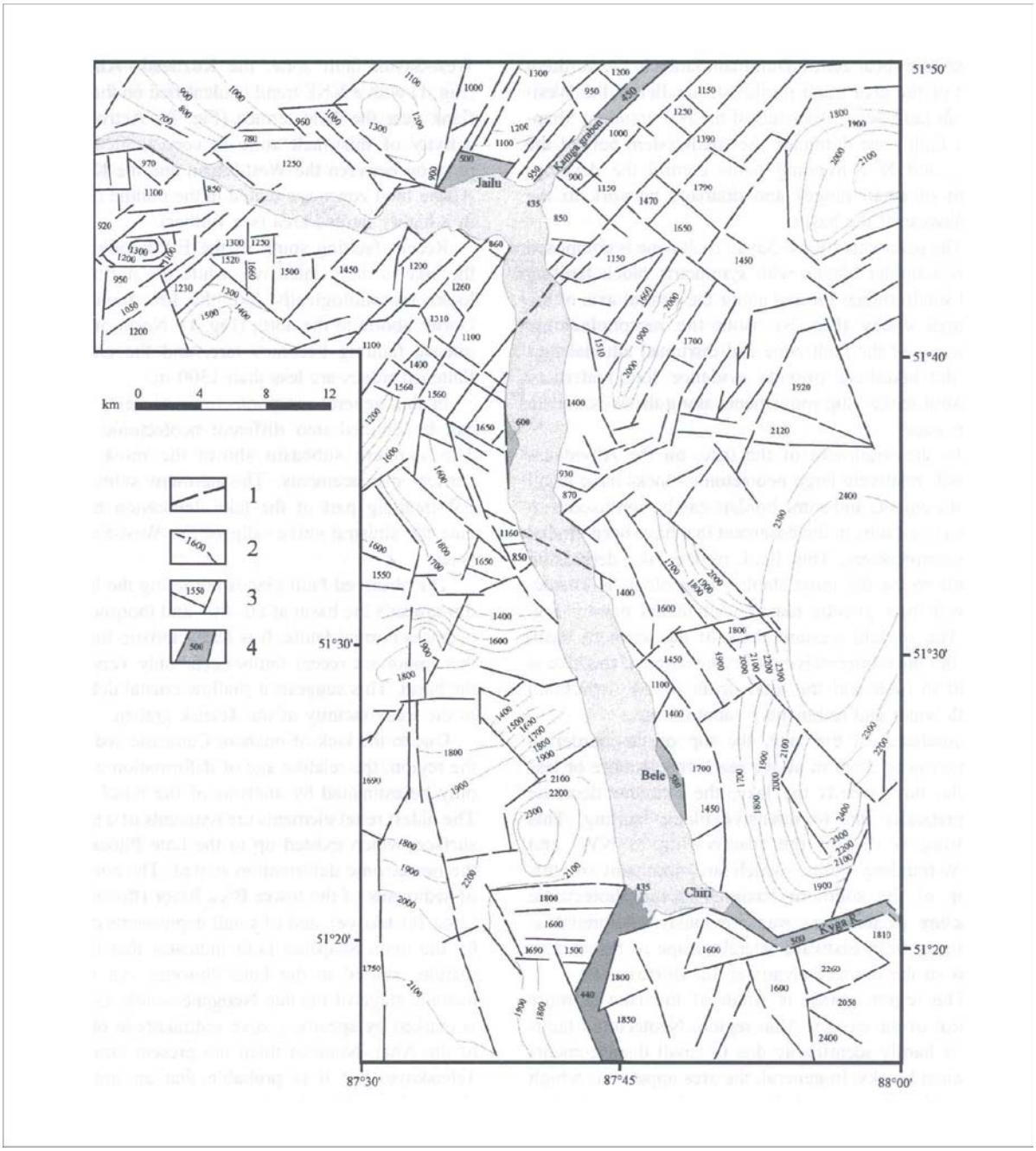

Figure 5.10: Neotectonic features of the Lake Teletskoye basement (from Dehandschutter et al., 2002). 1: recent faults; 2: isohypses of the Cretaceous-Paleogene peneplanation surface; 3: fault bounded blocks with nearly flat summits; 4: sediment accumulative surfaces of downfaulted blocks.

Probably during the Middle Pleistocene and up to recent times fragmentation and vertical displacement of a widespread pre-Cenozoic planation surface reached 600 m in the northern part of the Teletskoye region and up to 3000 m in the south (e.g. Deev et al., 1995). Remnants of the planation surface still exist (figures 5.6 and 5.10) indicating that the Pliocene to Recent uplift has not been accompanied by extensive Pliocene or Quaternary denudation. The active tectonics of the Altai, and specifically the Teletskoye region, were studied in detail by Delvaux et al. (1995a), Dehandschutter et al. (1997), (2001), and (2002), and Dehandschutter (2001). From these studies, it is clear that inherited basement structures play an important role in the neotectonic activity in the Teletskoye region.

In general, the present day mountainous relief in the Altai region began to form in the Late Pliocene as a distant result of the India/Eurasia collision (Delvaux et al., 1995c; Dobretsov et al., 1996). In the Teletskoye area, the recent reactivation of the TB shear zone is evident from the occurrence of a Quaternary, unconsolidated tectonic breccia (figures 5.7 and 5.8). The breccia contains rock fragments from the adjacent Altyntauss Massif, as well as from the bordering turbidites. Also reworked Devonian rocks from the TB shear zone (mylonites, migmatites e.g.) are found. Another marked example of a Quaternary unconsolidated breccia is found at *Cape Airan* of Lake Teletskoye, were it was formed syn-kinematically with movements along the WS fault zone in the early stages of the tectonic formation of the basin (figure 5.11). The recent tectonic activity is thus also expressed as a sinistral reactivation of the WS fault zone and as a dextral and reverse reactivation of the Shapshal zone. Dehandschutter et al. (2002) have shown that the area is subjected to an overall transpressional stress regime, which is in agreement with observations elsewhere in the Altai and adjacent regions (Cunningham et al., 1996a and 1996b). The fault zones are highly fractured melange zones, consisting of a heterogeneous aggregate of various rock types, originating from adjacent formations. Hus et al. (1999) and Dehandschutter (2001) showed that active faults around Lake Teletskoye can be identified from radon emanation profiles taken across the fault traces. The WS fault zone seems to delineate the active tectonic zone. North of this fault zone no major tectonic activity is recorded, and the area consists of low hilly foreland (Kuznetsk, Salair, Gorny Shoria areas) progressesing into the flat West Siberian Basin.

The Teletsk basin (figure 5.1) is composed of three sub-basins, a southern and northern part within the Teletsk graben proper, and an E-W trending northern zone which is separated from the N-S oriented graben by the submerged so-called *Lepnova* ridge, running parallel to the WS fault on shore (figure 5.5). Hence the Kuznetsk-Alatau fault intersects with the WS fault. The southern basin is almost completely filled with sediments deposited by the Chulyshman river. The northern Teletsk basin exhibits a markedly deformed basin floor morphology, effectively producing a set of smaller sub-basins in the northern section, while the E-W basin is characterized by a complex horst-graben structure. The Teletsk basin has a full-graben morphology, but seems to evolve into an incipient half-graben along the listric Chiri loupe fault. Sediments in the northern sub-basin are clearly deformed even in the upper section, while in the south the youngest sediments remain undisturbed. This indicates that an older deformation phase occurred in the southern sub-basin while a younger, still active phase affects the northern sub-basin.

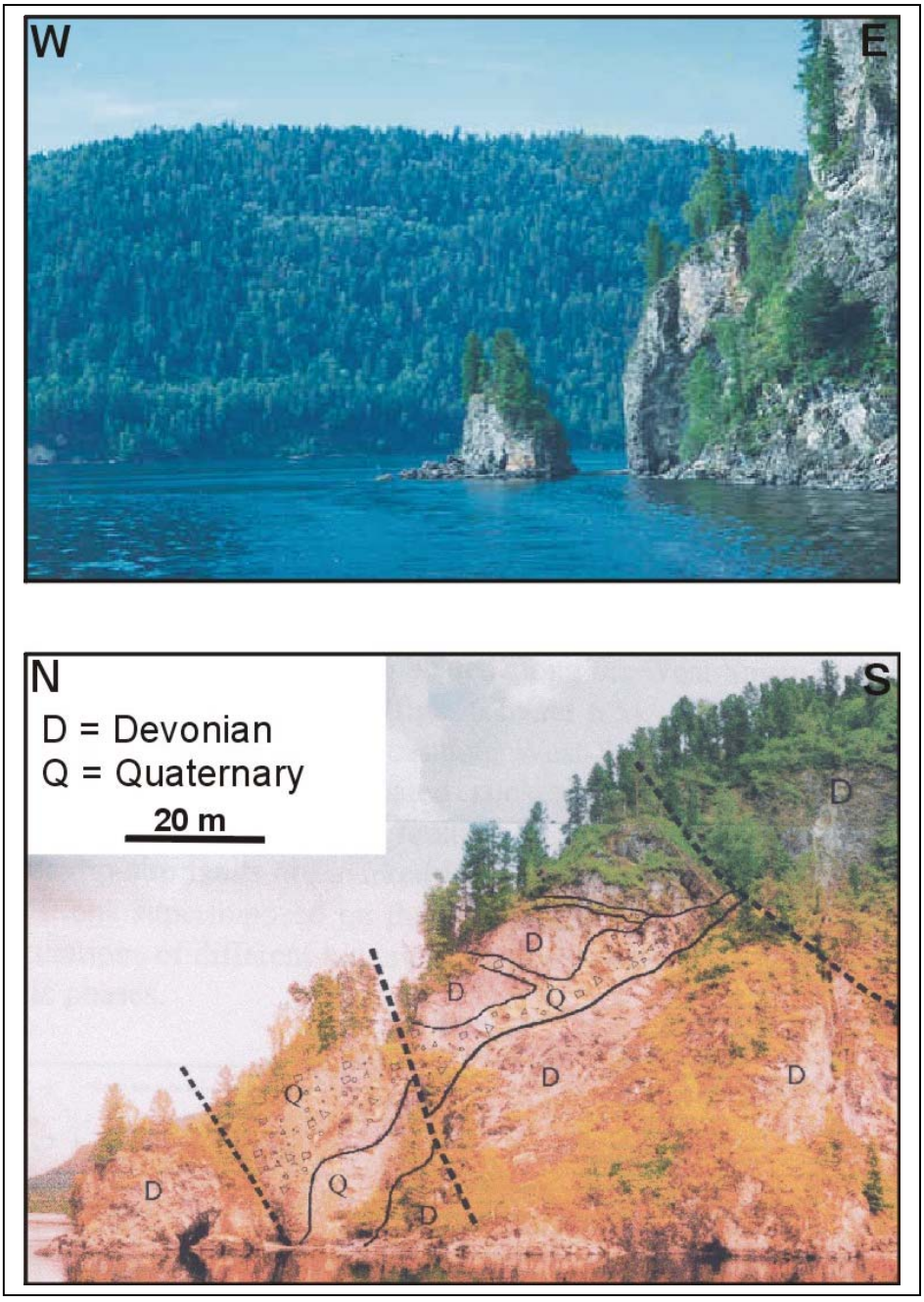

Figure 5.11: Recent tectonic fault breccia at Airan Cape, Lake Teletskoye. Top: view of Airan Cape from South to North. Bottom: view of Airan Cape from West to East, with indication of the Devonian basement and its fragments within the Quaternary loose breccia.

Dehandschutter et al. (2002) propose a two-stage formation history of the Teletsk graben (figure 5.12). In a first Quaternary stage (Q1), lateral slip along the transpressionally reactivated (Shapshal and Teletsk related) faults in the Kyga area and along the WS and TB shear zones induced the initial opening of the southern and northern Teletsk basins respectively. As mentioned before, the graben of the southern basin developed within the TB zone itself. The WS fault controlled the opening of the northern basin. The second phase (Q2) is of Holocene age and is characterized by a pure extensional tectonic regime as the WS and GA terranes are moving in opposite sense due to sinistral movements along the WS zone and dextral movements along the Shapshal fault zone. The latter fault zone is one of the most seismically active zones in the Altai Mountains today (Zhalkovskii et al., 1995; Dobretsov et al., 1996; Lukina, 1996).

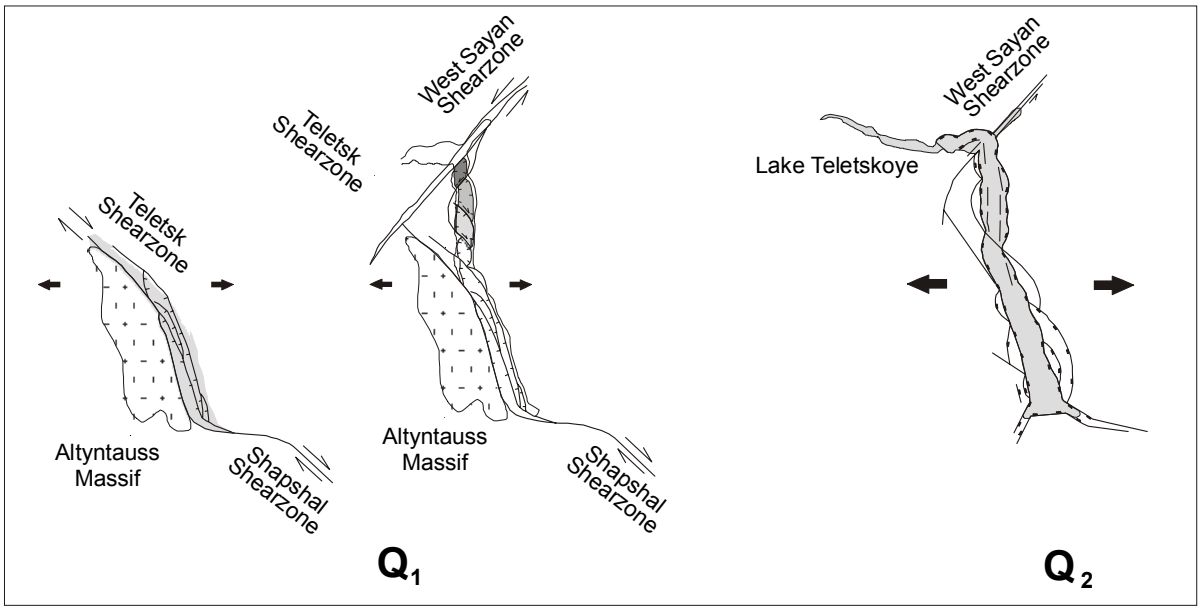

Figure 5.12: Formation model of the Quaternary Teletsk basin (after Dehandschutter et al., 2002). In a first phase, Q1, opening of the southern basin occurred due to reactivation of the Shapshal and Teletsk-Bashkauss shear zones with extension within an accordingly created pull-apart structure. Northern sub-basins opened by contemperaneous reactivation of the West-Sayan shear zone, also with extension in a pull-apart setting. A second phase, Q2, saw the final opening of the Teletsk basin by rapid E-W extension.

The present-day geomorphology of the Altai Mountains in general and the Teletskoye region in particular is clearly shaped by the Pleistocene glacial climate (figure 5.6) (e.g. Vysotsky, 2001). Recent tectonic activity is demonstrated by the fact that associated structures crosscut and displace several glacial landforms such as glacial cirques and morraines. Bobrov et al. (1999) and Kalugin (2001) constrained the modern sedimentation rate by means of ^{137}Cs markers in the sediments from the 1950's nuclear tests in the region to ~2 mm/a in the northern Teletsk basin and ~8 mm/a in the south. Extrapolation of these rates gives a rough estimate of the onset of sedimentation in the basin. This would have happened around 400 ka, while undisturbed sediments in the southern basin constrain the age of deformation of the southern basin to 50-75 ka. Pleistocene climate oscillations in the Teletskoye region have been recorded in the lake sediments by Goldberg et al. (2001) and by

geomorphological analysis (Deev et al., 1995; Vysotsky, 2001). Nowadays the continental climate in the Teletskoye region is greatly influenced by the presence of the lake and is termed a limnoclimate (Selegei, 2001a and b) with mean summer temperatures between 15 and 16°C and mean winter temperatures around –8°C. Mean precipitation values amount to more than 850 mm/a. Duchkov et al. (1995) and (2001) investigated the heat flow beneath Lake Teletskoye and concluded that the low values are within the range normally found in undisturbed basement and do not correspond to an actively developing rift.

5.1.3. Available geochronological information

K-Ar and Ar-Ar ages obtained on biotite and amphibole from the Altyntauss granite (AFT samples TEL 101 to 112, GA 32 and AL 272) range from 352 to 390 Ma. They are interpreted as reflecting the emplacement and cooling of the plutons in the Early to Middle Devonian. This probably occurred in the active Siberian margin setting (Buslov and Sintubin; Buslov, 1998; Smirnova et al., 2002).

Biotite and muscovite K-Ar and Ar-Ar ages from the Chiri series schists fall between 352 and 318 Ma and reflect Early Carboniferous post-metamorphic cooling and exhumation of that part of the Teletskoye basement (Dehandschutter et al., 1997; Buslov, 1998; Smirnova et al., 2002). A young age from an actinolite sample from the Chiri series of 260 Ma was interpreted by the authors to represent a Permian thermal overprint due to the tectonic activity induced by the complete closure of the Ob-Zaysan branch of the Palaeo-Asian Ocean.

Biotite and muscovite K-Ar and Ar-Ar analyses from samples within the Devonian tectonic breccia of the TB shear zone yield ages between 325 and 350 Ma, and are representative of the period when the shear zone was active (Buslov and Sintubin, 1995; Dehandschutter et al., 1997; Buslov, 1998; Smirnova et al., 2002).

5.2. The South Chulyshman Plateau

The Chulyshman river flows into the southern Teletsk basin. The river originates in the Dzhulukul basin (section 5.3). In between, the river cuts the so-*called Chulyshman Plateau* or *Chulyshman Highlands* (figure 5.2 and 5.13). This part of the Russian Altai Mountains formed a part of the Altai-Mongolian microcontinent when it collided with GA and the Siberian active margin in late Devonian-Early Carboniferous times. It is situated to the south of the GA terrane, south of the Ulagan-Erinat ophiolite complex, together with which it was displaced by Hercynian strike-slip movements (figure 5.2). It is mainly composed of Riphean turbidites, greenschists and gneisses and is intruded by Middle Palaeozoic granite-gneiss domes (figure 5.2). Both the strike-slip motions and the intrusional magmatism are correlated with the collision. In the Late Cenozoic, probably since the Pliocene, the region, along with the Dzhulukul area has been reactivated by wrench deformation, contractional uplift and extensional basin formation (Dehandschutter, 2001).

Dehandschutter (2001) characterizes the recent deformation in
zones of local extension at pull-apart and releasing bend du
region, the recent deformation clearly follows older, inh
the deformation south of the South Teletsk fault z
tectonic regime acting between the more rigid
(figure 5.14). Clockwise rotation of the bloc
sinistral strike-slip that occurred in the C
local contractional reactivation. The fa
of the regional Cretaceous-Palaeo
uplift has not been compensate

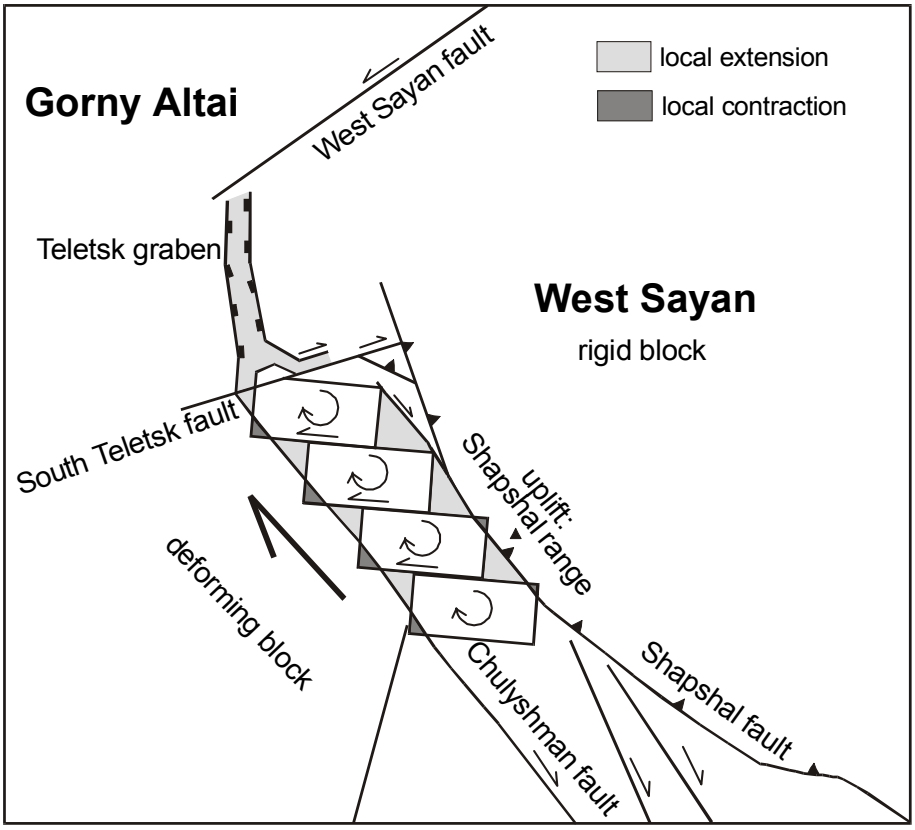

Figure 5.14: Inferred deformation model for southern Gorny Altai by Dehandschutter (2001). The West Sayan acts as a rigid block along which dextral wrenching occurs along the Shapshal fault. Fault bounded blocks within the wrench zone are displaced along strike-slip faults and are subjected to vertical axis rotation. This geometry explains extension zones and uplifted ranges in the region.

From the southern part of this zone, mainly from around Ust-Ulagan, Saratan, and the infamous *Yazula* village, 9 samples were successfully prepared for AFT analysis (table 5.1: GA06-08, GA15-16, GA18-19, GA21 and GA23). This area is more or less situated at the junction of the TB shear zone and the Chulyshman shear zone (figure 5.13).

5.3. The Dzhulukul basin and the Shapshal Range

The Dzhulukul basin is a Cenozoic basin that developed along the transpressionally reactivated Shapshal fault zone (figure 5.2; also figures 4.5, 4.14, and 4.15). At present the basin floor resides at around 2000 m of elevation and consequently glacial erosion and sedimentation influenced its morphology considerably (figure 5.15). Dzhulukul basin is mainly filled with sandy and silty glacial deposits, locally intercalated with peat horizons. Novikov (2002) presents evidence that in some locations the basin contains Jurassic deposits as well, on which the Cenozoic sediments rest unconformably.

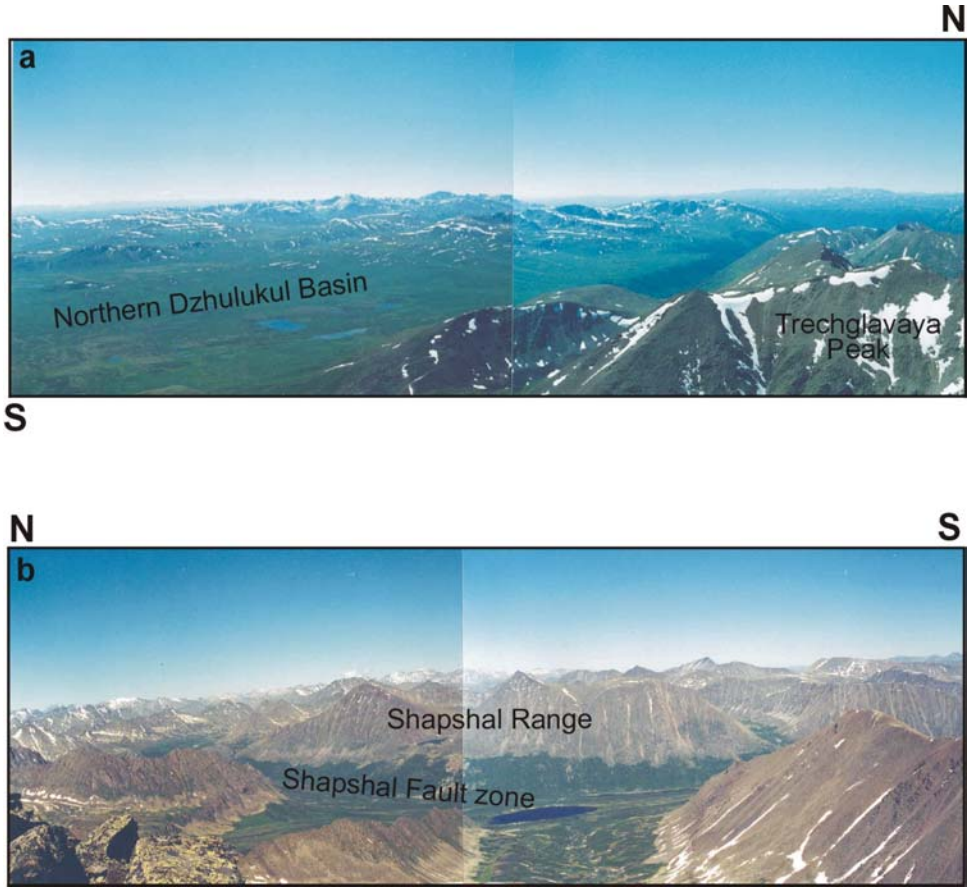

Figure 5.15: Top: view of the northern Dzhulukul basin from the Trechglavaya peak in the Shapshal range. Bottom: southern Shapshal fault segment along the Shapshal range in the northern Dzhulukul basin, seen to the east from Trechglavaya peak.

To the east the basin is flanked by the Shapshal range (figure 5.15), which is being actively uplifted against the more rigid WS terrane, as a direct consequence of the transpressional regime acting along the Shapshal fault zone. Four samples from the northern part of the basin were used for this AFT study (see table 5.1: samples GA09, GA12, GA13, GA20). In the sampled area, the Shapshal fault forms the contact between the Proterozoic greenschists and gneisses from the Chulyshman complex, intruded by Devonian granite-gneiss domes, and the Ordovician granitoids of the Shapshal range. The Quaternary sediments cover the contact and outcrop between both zones (figure 5.16). The Shapshal fault segment is clearly reactivated here as a reverse and oblique-contractional structure (Dehandschutter, 2001). The movements are manifest in the sampled area, at the base of the so-called *Trechglavaya* peak (three headed peak) of the Shapshal range. At its base, a Vendian volcanic sequence (basalts) is obliquely thrust upon the granitoid core of the mountain. This entire mass in its turn is thrust upon the sediments of the Dzhulukul basin (figure 5.15 and 5.16). The Dzhulukul basin can therefore be described as a half-ramp structure. Around the contact zones of the various units, the sedimentary sequences are strongly deformed.

Several recent earthquakes occurred during thrusting along the Shapshal fault in the Dzhulukul basin area (Bayasgalan et al., 1999a and 1999b). Analogous information has been derived from the Ureg-Nuur basin, to the east of Dzhulukul, at the Mongolian border (figures 4.5, 4.14, 4.15 and 4.16).

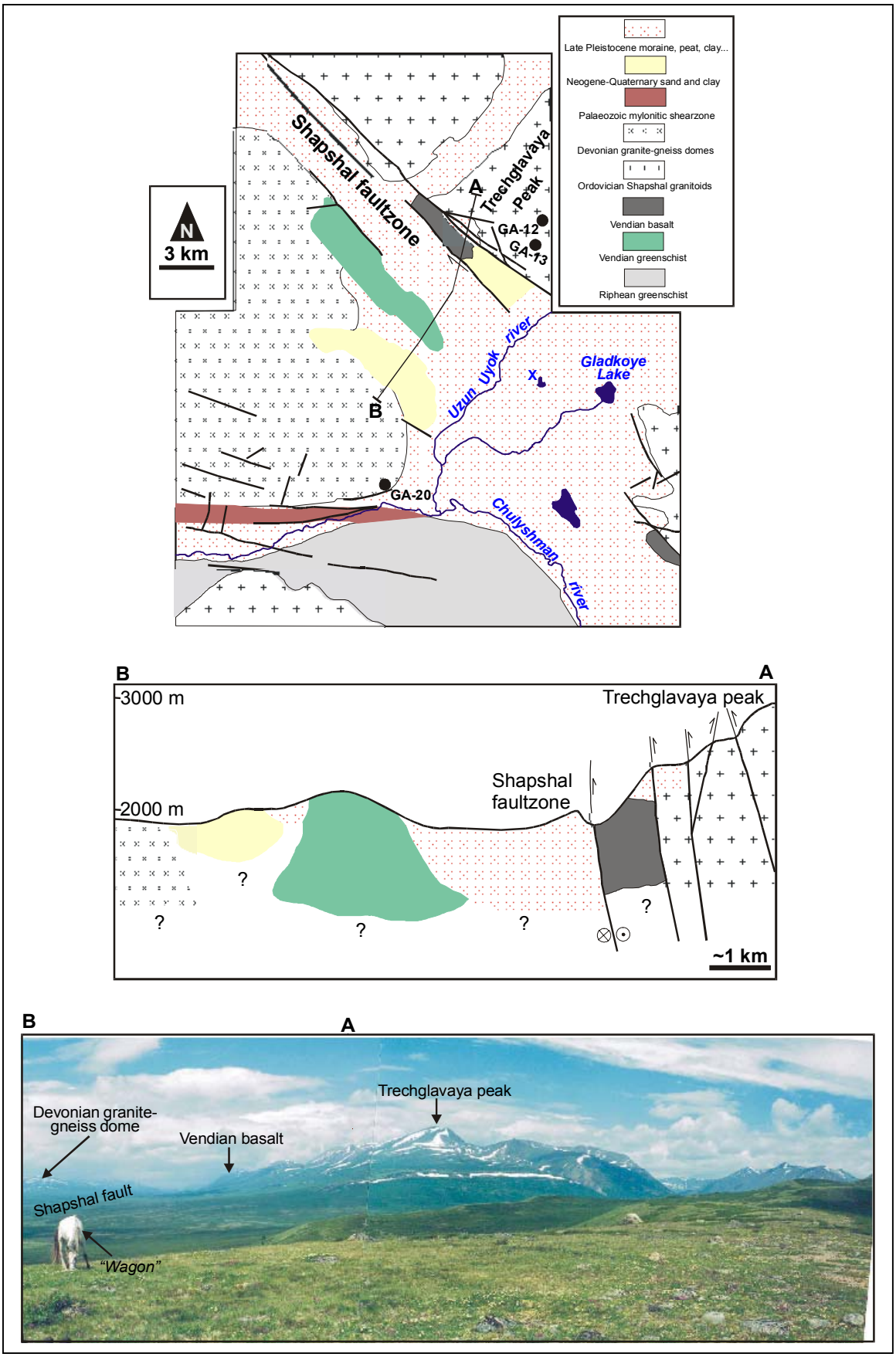

Figure 5.16: Geological sketch map and cross section (AB) of the northern Dzhulukul basin with indication of some sample locations. X, near a small glacial lake west of Lake Gladkoye, marks the locality from where the cross section and the accompanying photograph were taken towards the northwest.

5.4. The Chuya and Kurai basins and the Kurai range

5.4.1. General outline

The Chuya basin is an important continental Cenozoic depression in the southeastern Russian Altai Mountains, at the junction zone between the West Sayan terrane and the Altai-Mongolian microcontinent (figure 5.17 and figures 4.5, 4.14, 4.15, and 4.16). The Gorny Altai terrane is situated to the northwest of the basin (figure 5.2). The Chuya basin is actually part of the larger Kurai-Chuya depression with the Kurai and Chuya basins divided by the Chagan Uzun horst-like massif, which contains ophiolites, interpreted as Palaeo-Asian oceanic floor remnants (Buslov and Watanabe, 1996). The basin is bordered by the highest of the Altai ranges, the Chuya and Kurai ranges. Three samples (AL235, AL239 and AL 240), from the Dzankiol and Ildugemsky passes in the Kurai range, were collected and prepared for AFT analysis (table 5.1 and figure 5.17).

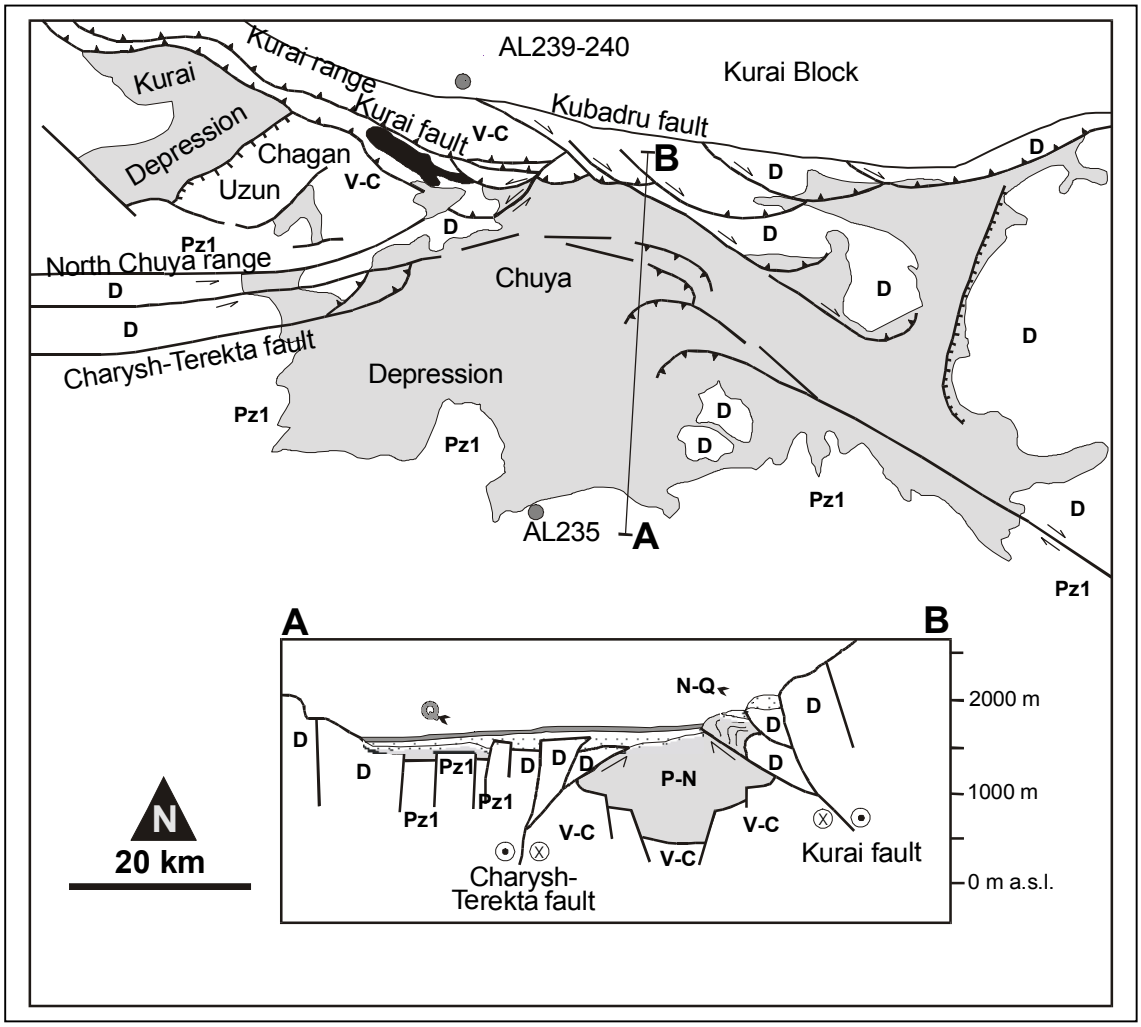

Figure 5.17: Tectonic sketch map and cross section (AB) of the Kurai-Chuya basin in southern Gorny Altai. AFT sample localities are indicated. V-C = Vendian-Cambrian, D = Devonian, Pz_1 = undivided Upper Palaeozoic; N-Q = Neogene-Quaternary, and Q = Quaternary.

5.4.2. Geological history

Infilling of the Kurai-Chuya basin took place during the entire Cenozoic era, although Early Cenozoic sequences are rare. The sediments, averaging 1200 m in thickness, unconformably overlie Palaeozoic basement along erosional contacts, or rest on the Late Cretaceous-Early Palaeogene peneplanation surface. The Palaeozoic basement bears witness to the complex accretionary history of the Siberian orogenic rim.

In general, a Vendian-Cambrian volcanic arc and an accretionary prism are typical, as well as Cambrian turbidites. Devonian active continental margin deposits are also abundant in the area (e.g. Buslov and Watanabe, 1996; figure 5.17). At present these Devonian rocks are thrust onto the basin margins. The Devonian is further characterized by the development of the Charysh-Terekta shear zone. Overlying Early Cenozoic sediments occur in a patchy fashion, but the Early Oligocene *Karachum* Formation is observed throughout the basin, and has been correlated with the Early Oligocene units in nearby Mongolian basins and in the Dzhulukul basin. The basal conglomerate of the Karachum Formation suggests an incipient stage of orogeny in the Altai region. The sediments point to a shallow lacustrine basin as depositional environment. This setting prevailed for much of the Miocene, while in the Late Miocene new coarse-grained intercalations with angular fragments indicate the onset of thrusting and mountain building along the Kurai ridge. A low-elevation (~ 1000 m a.s.l.) mountain lake was formed in the Kurai-Chuya basin during the Early Pliocene. From the Pliocene to the present, the sediments (e.g. the Late-Pliocene *Beken* Formation) recorded the progressive uplift of the bordering mountain ridges, i.e. the Kurai range north of the basin and the North and South Chuya ridges to the south of the Kurai and Chuya basin respectively. In the Pliocene and Early Pleistocene, the basin clearly evolved in a compressional regime, from a half-ramp into a full-ramp basin, as the basement blocks along the flanks is obliquely thrust onto the basin edges (e.g. Buslov et al., 1999). Oblique thrusting along the Kurai fault is an ongoing process and accounts for the active transpressional tectonic regime that has been observed in several places in the Altai Mountains (Cunningham et al., 1996a and 1996b; Bayasgalan et al., 1999a and 1999b; Dehandschutter, 2001). Further deformation of the basin during the Quaternary is caused by strike-slip movements along the reactivated Charysh-Terekta fault. This strike-slip is presumably responsible for the uplift of the Chagan-Uzun horst in the Middle Pliocene (Delvaux et al., 1995c; Buslov et al., 1999), during which time the Kurai and Chuya depressions were separated and attained their present-day configuration (figure 5.17). This model for the reactivation of the Chuya area fits well in the overall framework for the Altai as a Pliocene neotectonic feature of active deformation of the Altai-Mongolian (AM) terrane (including the Chulyshman block) in between the rigid Junggar and Tuva-Mongolian (TM) microplates (figure 4.14). It is also corroborated by Palaeomagnetic data in the Chuya and the Zaisan region to the southwest (Thomas et al., 2002).

Thomas and co-workers attribute a significant counter-clockwise rotation of the Chuya basin with respect to the TM microplate since the Pliocene. This also supports the wrenching and induced block rotation model proposed by Dehandschutter (2001) (figure 5.14).

It should be noted, that as elsewhere in the region, the Pleistocene glaciations had a marked effect on the sedimentology and morphology of the basin. Catastrophic ice-dammed lake outbursts originated from lakes residing in the Chuya basin as was described in section 4.5.5.2 (Baker et al., 1993; Novikov and Parnachev, 2000).

5.4.3. Available geochronological information

K-Ar ages have been obtained from amphiboles, muscovite and chlorite minerals from metamorphic rocks from the Chagan-Uzun ophiolite. They range from about 480 Ma to 570 Ma (Buslov and Watanabe, 1996). The younger ages were obtained on amphibolitic rocks, while the older ones were found on greenschists. The results are interpreted to date the Cambrian and Early Ordovician metamorphism in the Palaeo-Asian Ocean subduction zone in the Kurai area. The older age is related to onset of subduction and growth of the accretionary complex, while the younger age would reflect the collision with the amalgamating Siberian continent and its related metamorphism. Ar-Ar amphibole ages on eclogites of about 630 Ma have also been reported and are probably related to an early stage of metamorphism within the PAO subduction zone in Vendian times (Buslov et al., 2001b).

K-Ar and Ar-Ar ages on amphiboles and biotite from granite-gneiss domes and shear zone mylonites from the Kurai ridge range roughly between 325 and 380 Ma and reflect the Late Devonian-Early Carboniferous collision of the Altai-Mongolian microplate with the Siberian orogenic rim (Buslov et al., 2001b).

5.5. Gorny Altai western transect and the Novosibirsk area

5.5.1. General outline

Additional AFT samples in Gorny Altai were collected along the main road from the city of Gornyaltaisk to the south (the Chuisky highway), to Tashanta at the Mongolian border. This road transects the Chulyshman and Kurai areas in the south and the lower, hilly areas in the northwest of Gorny Altai.

Samples from the latter area are grouped as the “Western Gorny Altai Transect” (table 5.1). Their location and setting will briefly be discussed. Also in this section, we will deal with sample No-1, which comes from a granite quarry close to the city of Novosibirsk (table 5.1). This region forms part of the low lying, flat and stable platform of the West Siberian Basin and has not been tectonically reactivated in the Cenozoic. No-1 acts therefore as reference sample from the stable, unaffected area northwest of the CADZ.

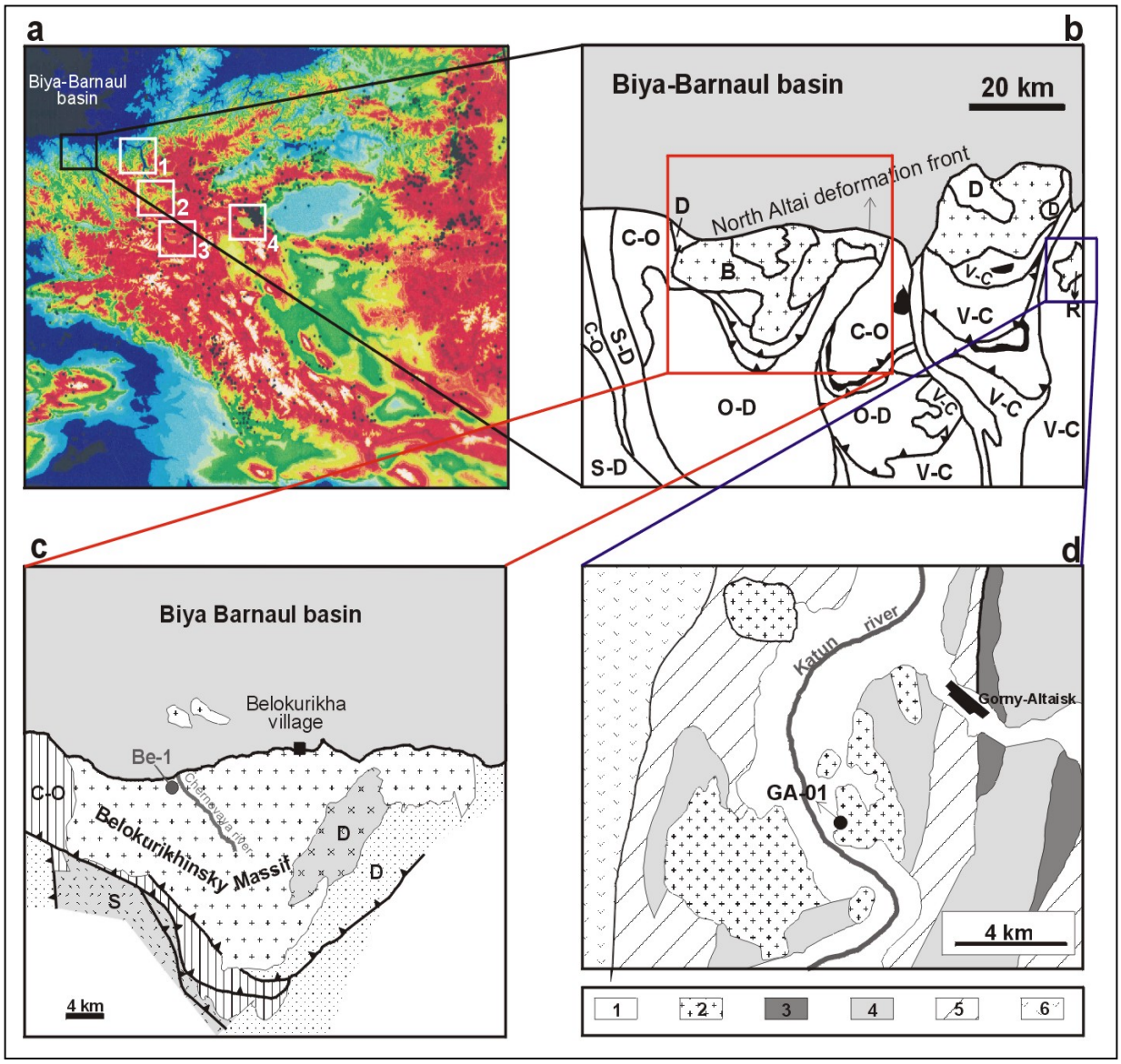

Figure 5.18: (a) General setting of the AFT study areas in Gorny Altai: (1) the Teletskoye region, (2) the South Chulyshman Plateau, (3) The Chuya-Kurai Basin area, and (4) the Dzhulukul Basin area. The northern part of the 'Western Transect" samples is also indicated and shown in more detail in the following panels. (b) Tectonic sketch map of northern Gorny Altai, at the transition with the Biya-Barnaul part of the West Siberian Basin (redrawn after Dobretsov and Vladimirov, 2001). The Early Palaeozoic basement of Paleo-Asian Oceanic and Siberian margin units (V-C = Vendian-Cambrian, C-O = Cambrian-Ordovician, O-D = Ordovician-Devonian, S-D = Silurian-Devonian, D = Devonian) is intruded by various Late Devonian-Early Carboniferous and Permo-Triassic granitoid massifs (crossed zones): B = the Belokurikhinsky massif, R = the Rybalka massif. (c) Location of AFT sample site Be-1 in the Permo-Triassic Belokurikhinsky massif at the northern extremity of the Altai deformation front, at the boundary with the Biya-Barnaul depression (C-O = Cambrian-Ordovician, S = Silurian, D = Devonian). (d) Location of AFT sample site GA-01 in the Late Devonian Rybalka massif. 1 = Quaternary alluvial deposits of the Katun river, 2 = Late Devonian Rybalka massif, 3 = Cambrian dolerite sills, 4 = Cambrian terrigenous and carbonate sediments, 5 = Cambrian volcanogenic sediments, 6 = Vendian-Cambrian volcanogenic and sedimentary rocks.

5.5.2. The Belokurikhinsky granitoid massif

The Belokurikhinsky massif has a laccolithic structure, and is situated in the northwest of the Russian Altai Mountains, close to the stable hinterland of the Biya-Barnaul basin (figure 5.18). The massif is a Permo-Triassic postcollisional granitoid, intruded in a basement of Riphean and Vendian-Cambrian ophiolitic melange units and Ordovician-Devonian passive and active margin sediments (Dobretsov and Vladimirov et al., 1997). Sample Be-1 was taken from a leucogranite outcrop along the Chernovaya river (figure 5.18). The Rb-Sr whole-rock age of the Belokurikhinsky granitoids was constrained to 232 ± 5 Ma by Vladimirov et al. (1997). The Cenozoic reactivation of the Altai has thrust this area on the stable Biya-Barnaul depression, along a marked 300 to 600 m high scarp, which delineates the boundary of active Altai deformation.

5.5.3. The Rybalka granitoid and gabbroid massif

The Rybalka massif is located between the city of Gornyaltaisk and the Belokurikhinsky massif (figure 5.18). Sample GA-01 was taken near the village of Sausga, on the eastern banks of the Katun river, where granodiorites are exposed (figure 5.18). Rb-Sr analysis of the massif by Titov et al. (1997) yielded an age of 365 ± 13 Ma and date the Late Devonian-Early Carboniferous collision of the Altai-Mongolian microplate with Siberia. The Rybalka pluton has intruded volcanogenic sedimentary units with Vendian-Cambrian arc affinity.

5.5.4. The Chiquetaman granitoid massif

The Chiquetaman massif is a large pluton in the southeast of the Russian Altai mountains and was built up in four distinct intrusive phases (figure 5.19): an early medium to fine grained dioritic phase, a second, medium to coarse grained quartz dioritic and tonalitic sequence, a third medium to coarse grained granodiorite phase, and finally, a medium to coarse grained biotite-rich granite. The pluton has a distinct amphibole-hornfels contact aureole. It was emplaced in Cambrian and Ordovician terrigeneous sedimentary units of Siberian marginal sea and passive margin setting, and in Devonian active margin units. Dobretsov and Vladimirov (2001) found a zircon U-Pb crystallization age of 370 Ma, related to the Late Devonian-Early Carboniferous events, as is the case for the Rybalka massif. Our sample, GA-03 was taken at the roadside on the Chiquetaman pass, in the granodiorites of the third intrusive phase.

5.5.5. The Shebalino rhyolite

Directly south of the Belokurikhinsky and Rybalka massifs various outcrops of Devonian active margin units are exposed near the Chuisky road. An altered sequence of rhyolite lavas and tuffs near the village of Shebalino was sampled (sample GA-24, table 5.1) and found to contain sufficient apatite for AFT analysis.

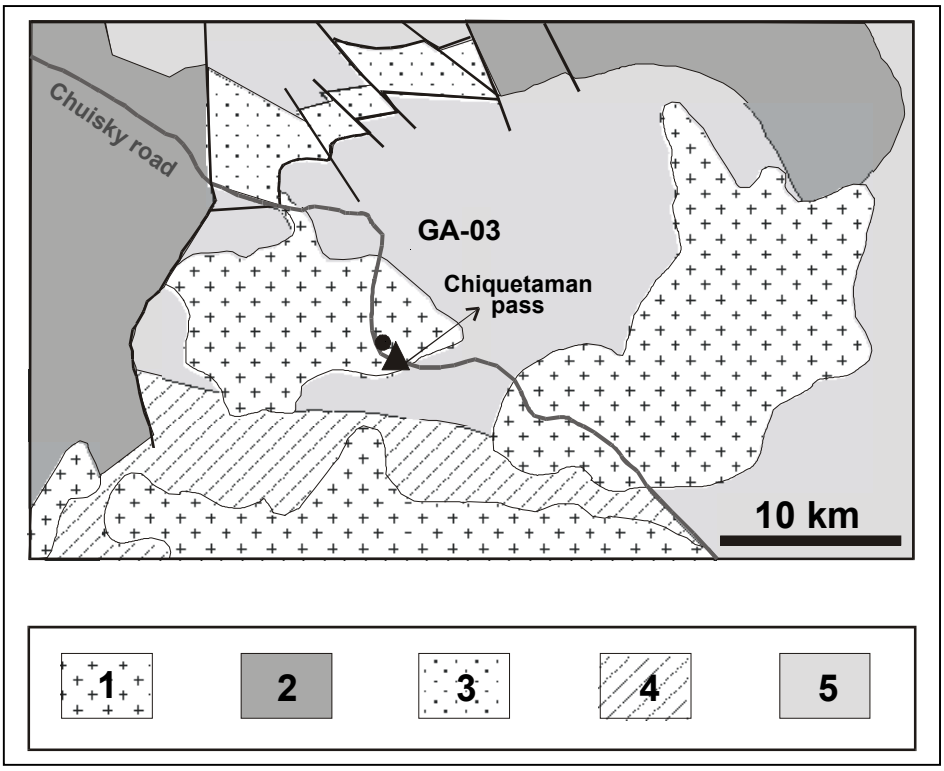

Figure 5.19: Location of AFT sample site GA-03 in the Late Devonian Chiquetaman massif (1 in figure), 2 = Devonian volcanics (e.g. rhyolites similar to the Devonian Shebalino rhyolite, sample GA-24), 3 = Devonian volcanogenic and sedimentary rocks, 4 = Ordovician sedimentary rocks, 5 = Cambrian-Ordovician sedimentary rocks (redrawn after Dobretsov and Vladimirov, 2001).

5.5.6. The Novosibirsk Priobsky complex

The basement of the West Siberian Basin consists of tectonic units that were involved in the Palaeozoic accretionary history of the Siberian continent as has been discussed in chapter 4. The Novosibirsk area is situated in the eastern part of the West Siberian Basin. This part of Siberia has not been affected by the Cenozoic reactivation caused by the India/Eurasia collision.

In Novosibirsk, a granite (No-1, table 5.1) from the Borok quarry in the Priobsky batholith granitoids has been sampled as a reference sample for the stable Siberian platform. Sotnikov et al. (2000) dated the batholith by means of Ar-Ar on biotite and obtained an age of 250 Ma. Dobretsov and Vladimirov (2001) relate this batholith, in analogy with the Belokurikhinsky massif, to a postcollisional intrusion after the complete closure of the Palaeo-Asian Ocean and amalgamation of Pangea. In the Borok quarry, monzodiorites and granosyenites of the Priobsky complex are in contact with thermally metamorphosed continental sandstones and shales of Late Devonian-Early Carboniferous age (figure 5.20).

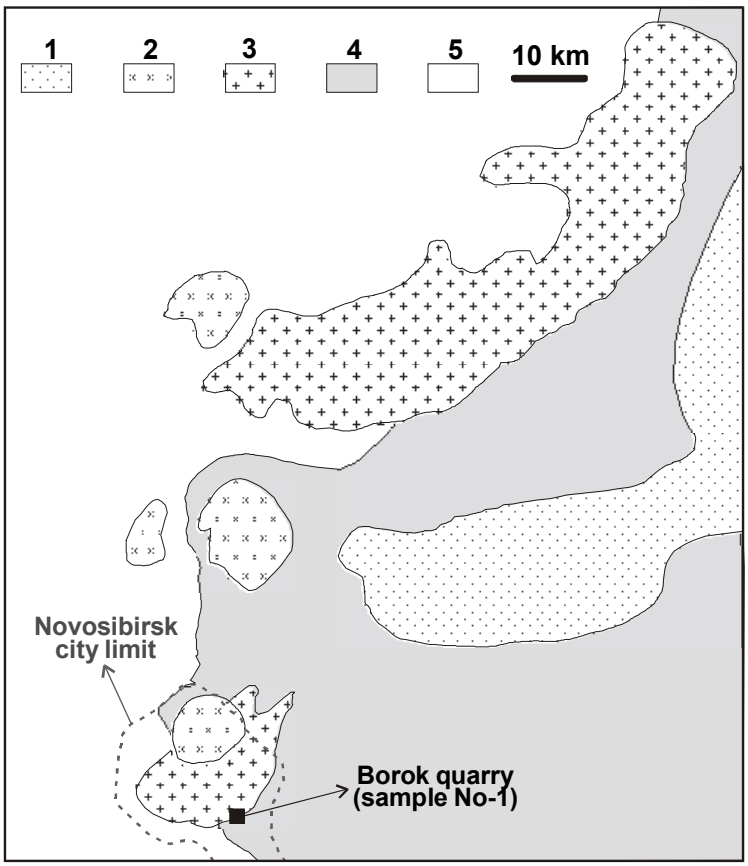

Figure 5.20: Location of AFT sample No-1 in the monzodiorte Borok quarry (Novosibirsk) in the Priobsky massif (redrawn after Dobretsov and Vladimirov, 2001). 1 = Miocene sandstones and clays, 2 = leucogranites of the Triassic Barlak complex, 3 = Permo-Triassic Priobsky granitoid massif, 4 = Late-Devonian-Early Carboniferous sedimentary rocks, 5 = undivided Palaeozoic basement of the West Siberian Basin.

5.6. The Issyk Kul basin in the Kyrgyz Tien Shan mountains

5.6.1. General aspects and location

The samples from the Kyrgyz Tien Shan Mountains were all collected in the basement of the *Issyk Kul* intramontane basin (table 5.1 and figure 5.21). The basin accommodates Lake Issyk Kul (figure 5.22). Two elevation profiles in pink Ordovician granites of the Issyk Kul basement were sampled: to the north of the basin, this is the *Kungei* range (samples TS04-TS14 and TS18), and to the south, the *Terzkey* range (samples TS19-26). A third set of samples comes from the *Boom* canyon area (samples TS02 and TS15-17), where the compressional character of the deformation of the Tien Shan is strikingly observed. Additionally, two samples were analyzed from the lower foreland of the northern Tien Shan. These samples (KAZ01 and KAZ 03) were collected in the *Kindil Las* range, in the republic of Kazakhstan (figure 5.21 and 5.23).

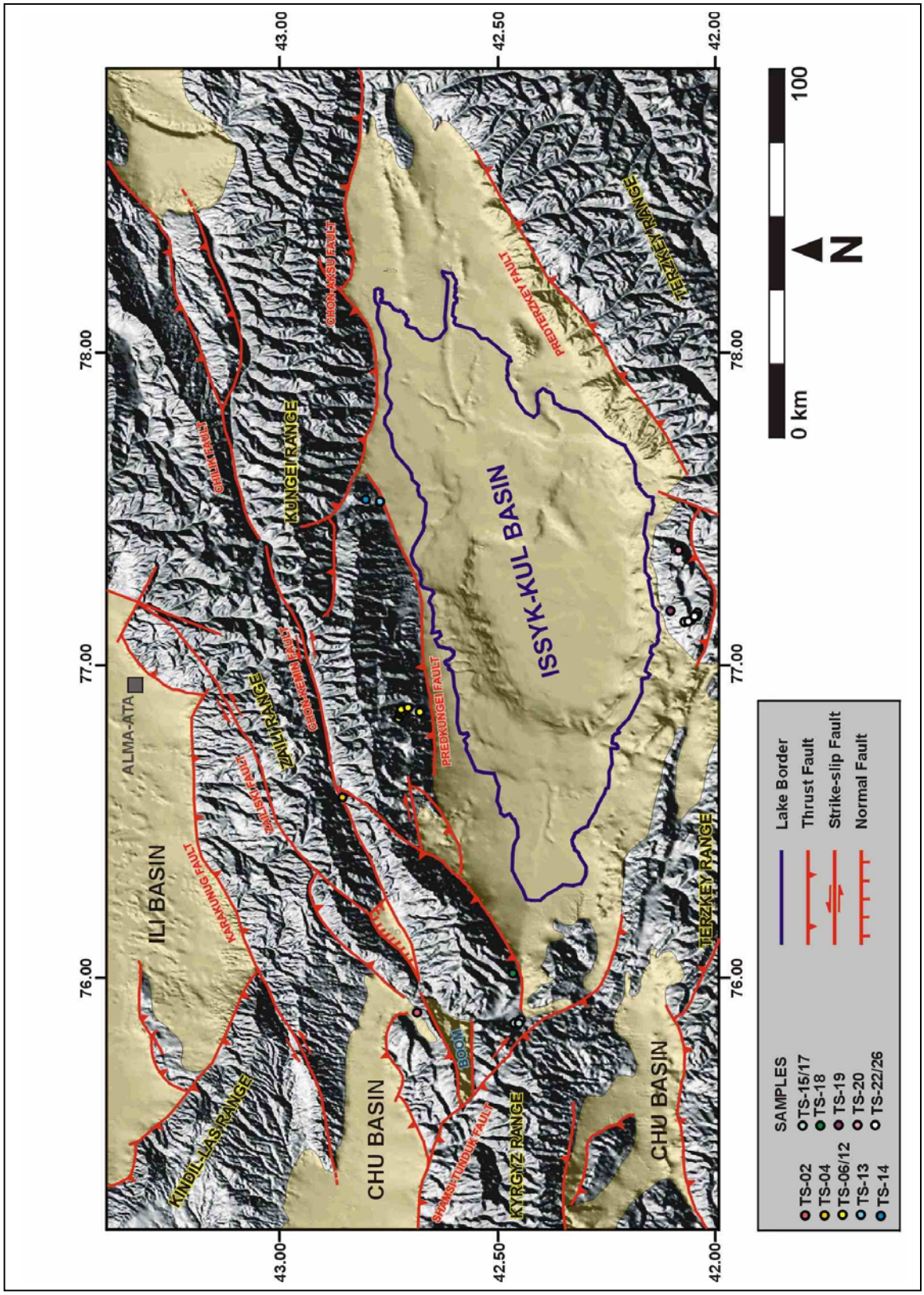

Figure 5.21: Digital terrane model of the Issyk Kul basin and surrounding area in the northern Kyrgyz Tien Shan (courtesy of the KMMA, Tervuren, Belgium). Cenozoic basins are shaded in yellow. Reactivated ranges, thrusts, normal faults and strike-slip faults are indicated. AFT sample locations are shown as colored dots.

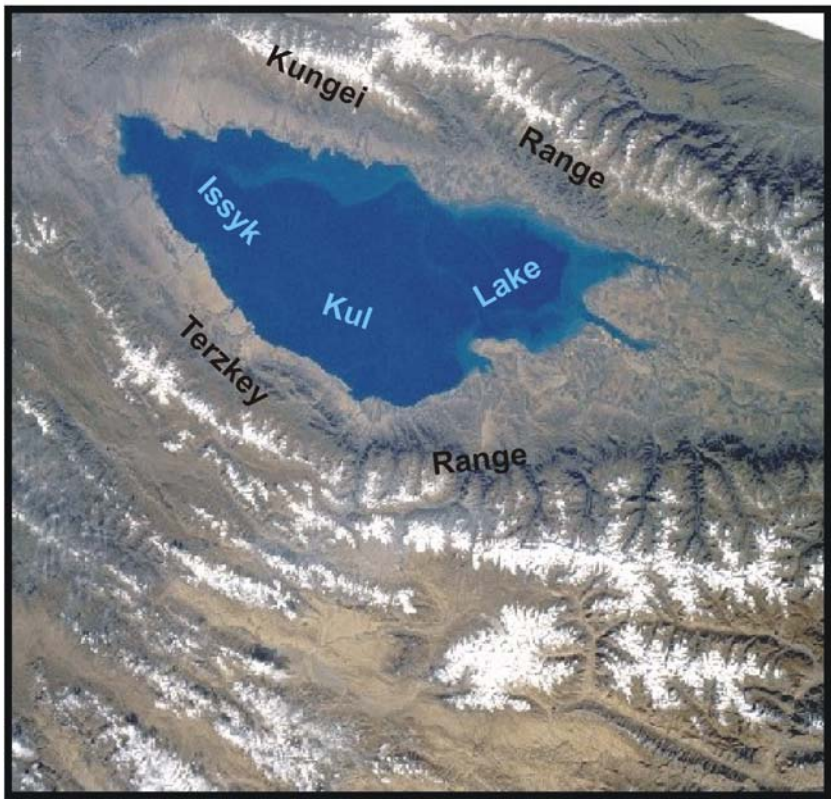

Figure 5.22: NASA satellite image of Issyk Kul Lake basin and bordering ranges.

The overall morphology of the Tien Shan mountain belt is characterized by an alternation of high ranges and large intramontane basins, divided by major active faults. A marked example of such an intramontane basin in the northern Tien Shan, is the Issyk Kul basin in northern Kyrgyzstan (figure 5.23 and figure 4.6). The basin is bordered by 5000 m high ranges, the Kungei range in the north and the Terzkey in the south, while the level of the modern lake itself lies at an elevation of 1607 m. Sediments testify to the fact that a larger Palaeo-lake filled the Issyk Kul basin in Tertiary times. The Issyk Kul basin has an E-W trending elongated lens shape; the lake is 178 km long in E-W direction and 60 km wide on average. The mean water depth is 278 m, with a maximum of about 668 m (De Batist et al., 2002). De Batist et al. (2002) estimate the basin infill at 3.5 to 4 km of Tertiary and Quaternary continental sediments (with minor basal Mesozoic sequences). These sediments are proximal and distal deltaic deposits on the more shallow eastern and western platforms, while turbidites and hemipelagites were deposited in the deep and flat central part of the basin.

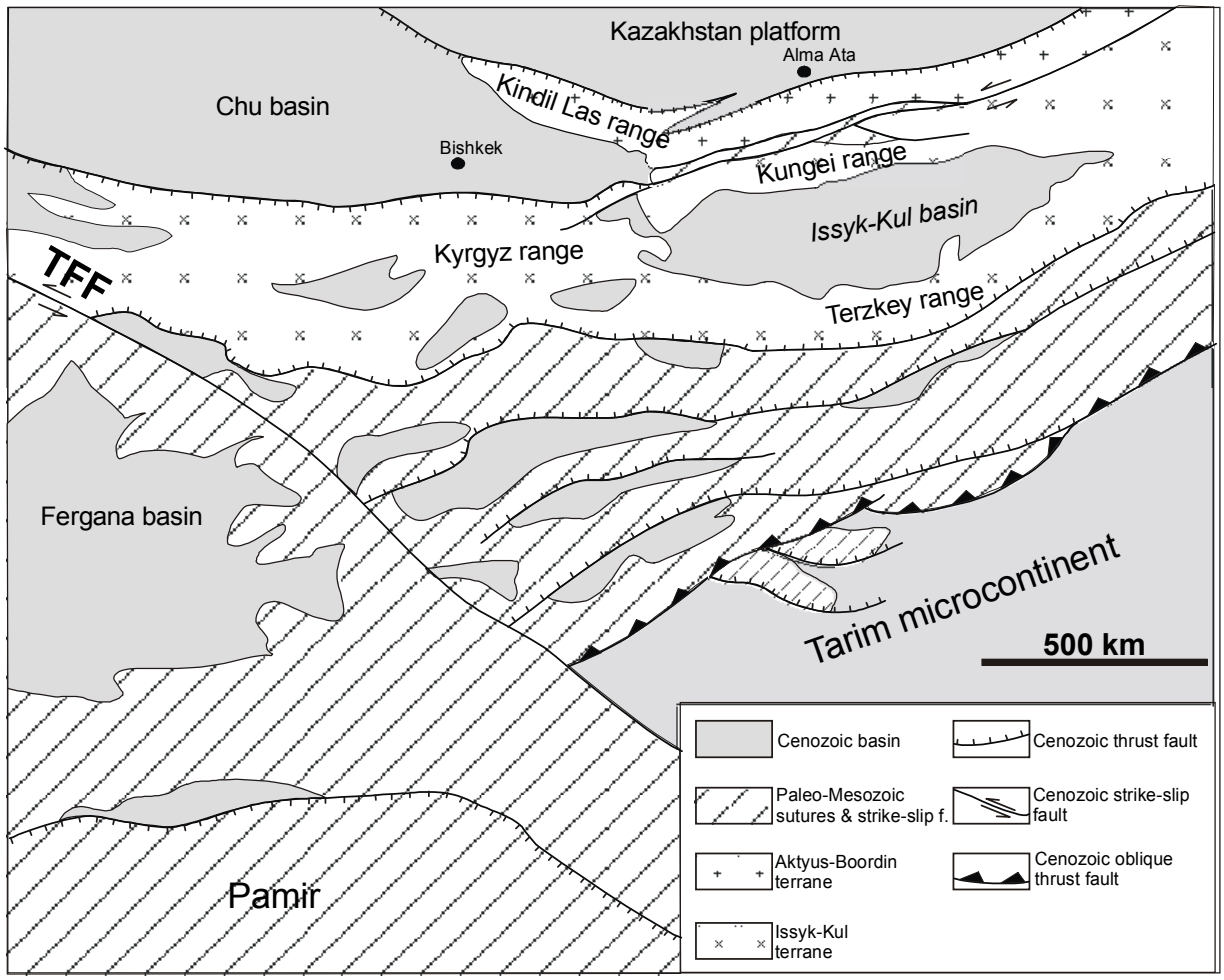

Figure 5.23: Tectonic sketch map of the Kyrgyz Tien Shan: basement terranes, reactivated structures, and Cenozoic basins. TFF = Talas-Fergana Fault.

The India/Eurasia continent-continent collision has reactivated the Proterozoic-Palaeozoic basement of the Tien Shan in a N-S compressional regime. In our study area, this active tectonism is evident in the geomorphology. It is expressed in the bordering ranges, especially the Kungei range, which have a long record of major earthquakes in historical times. One of the most important and most seismically active structures is the *Chon-Kemin* fault zone (figure 5.21 and 5.24) (Abdrakhmatov et al., 2002). Further north of our study area lie the vast, stable Kazakh plains, that remained unaffected by the Cenozoic deformation. Although Fin'ko (1992) showed that slight Quaternary movements are noticeable. This might be a sign that ongoing convergence of India and Eurasia is affecting even these stable areas at present.

Figure 5.24: Structures, geological and geomorphological features of the northern Tien Shan in Kyrgyzstan.
(a) Western Chon-Kemin valley
(b) Eastern Chon-Kemin valley, along which the major Chon-Kemin fault is traceable.
(c) Snowy peaks of the Kungei range, seen from the southern shores of Lake Issyk Kul.
(d) The basal Early Paleogene Kokturpak Formation of Issyk Kul basin sediments.
(e) Arid climatic conditions are very obvious, especially south of Lake Issyk Kul.

5.6.2. Geological and tectonic history

5.6.2.1. Basement characteristics

The Tien Shan are characterized by two Palaeozoic collision events during the growth of the Eurasian continent (see chapter 4). A first event occurred in Late Devonian-Early Carboniferous at the southern margin of the Tien Shan, when the Central Tien Shan block collided with the Tarim plate during the closure of the Turkestan Ocean (Allen et al., 1992; Carroll et al., 1995; Brookfield, 2000). In our study area, the Central Tien Shan block is represented by the *Chu-Terzkey* terrane. The second collision involved the so-called North Tien Shan island arc, which came into frontal contact with the combined Tarim/Central Tien Shan block in the Early Permian. During the Permian, all oceanic basins dividing the several Central Asian terranes were closed and the continent was assembled within the Pangea. In the Triassic and Jurassic, tectonic activity was reduced significantly, although episodic tectonic events during those periods are recognized and are possibly linked to the evolution of Tibet, south of the Tarim plate, on the Thetyan Asian margin. The Cretaceous and Palaeogene is seen as a period of tectonic quiescence and peneplanation, abruptly disrupted by late Oligocene-Early Miocene tectonic reactivation as a response to the Cenozoic collision and indentation of India with the Asian continent. The deformation continued during the Miocene and Pliocene, and even at present, intense tectonic activity is ongoing (Allen et al., 1993 and 1994; Cobbold et al., 1994; Abdrakhmatov et al 1996 and 2002). The modern Tien Shan Mountains extending between the stable Tarim and Junggar/Kazakhstan plates are a direct result of the northwardly propagated deformation stresses originating from the India/Eurasia indentation zone. It is thought that a considerable portion of the convergence between India and Eurasia is absorbed by the present-day deformation within the Tien Shan (Abdrakhmatov et al., 1996).

The Kyrgyz Tien Shan mountains is composed of two stable Palaeozoic cores, the Issyk-Kul (IK) and *Aktyuz-Boordin* (AB) terranes in the north and of Palaeo-Mesozoic suture zones, shear zones and other deformed areas in the south (figure 5.23). These zones are covered by various Cenozoic basins. The stable IK and AB terranes are underlain by Archean and Early-Proterozoic metamorphic rocks that are covered by Late Riphean and Cambrian-Ordovician volcanogenic-sedimentary sequences. The basement rocks are further intruded by Late Riphean to Middle Palaeozoic plutons (figure 5.25). The sampled granites of the Kungei and Terzkey ranges bordering the Issyk Kul basin are prime examples of these Ordovician plutons. This is also the case for the Kindil Las and Kyrgyz ranges at the rims of the *Chu* basin further to the west (figure 5.21). Devonian-Carboniferous volcanogenic and sedimentary rocks overlie the older crystalline basement. They are abundantly exposed south of the Terzkey range (figure 5.25), and are related to the active Turkestan margin that existed between this area of the Central Tien Shan (Chu-Terzkey) and the Tarim plate. The Issyk Kul basin is located in the centre of the IK terrane. The Palaeozoic shear zones bordering the IK terrane are the site of present-day reactivated strike-slip faults, notably, the relayed array of the *Chon-Kemin*, *Chon-Aksu* and *Chilik* faults to the north and the *Pred-Terzkey* fault to the south (figure 5.21). The latter fault forms the boundary between the Issyk Kul basin and the Terzkey range, while the so-called Pred-Kungei fault separates the basin from the Kungei range.

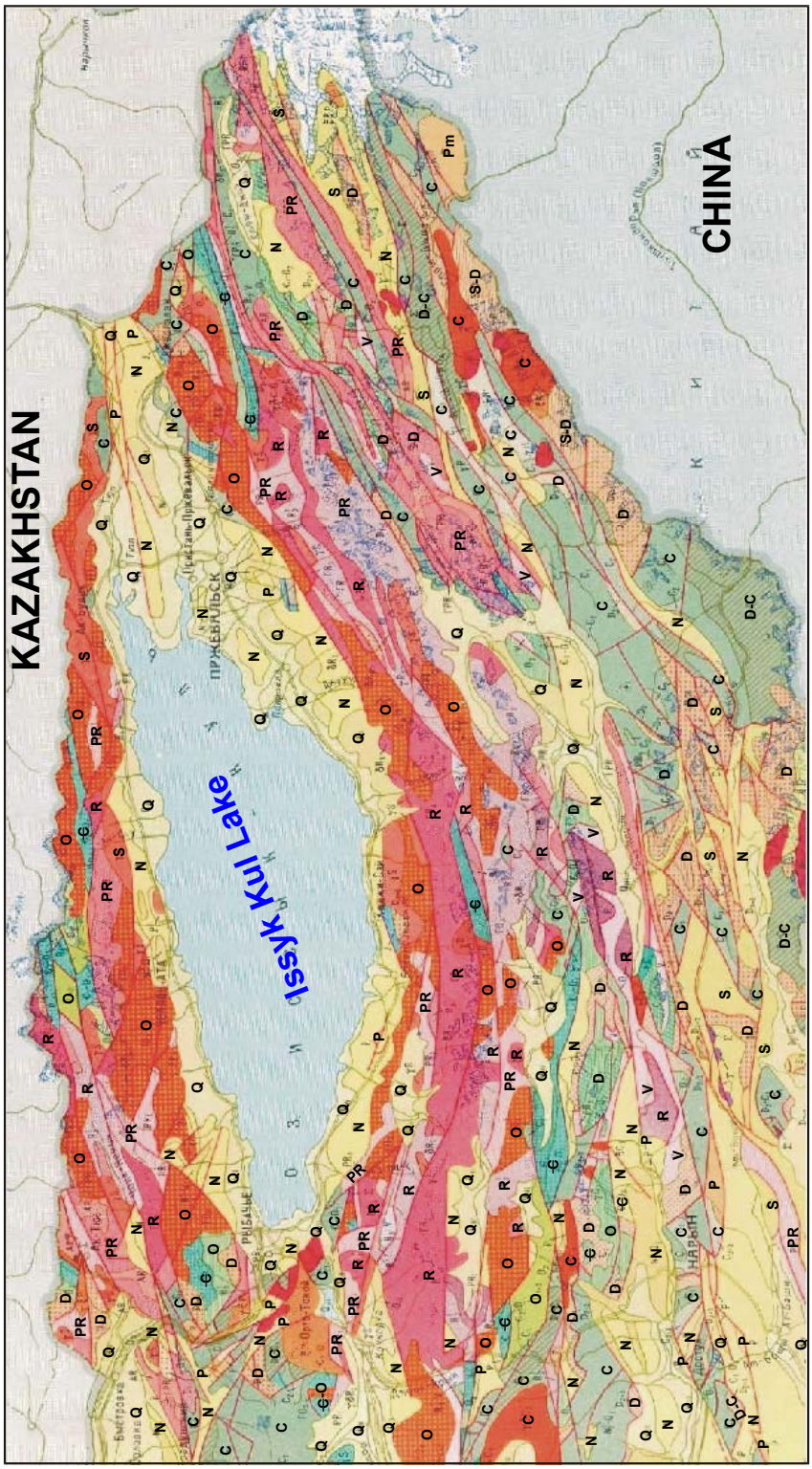

Figure 5.25: Geological map of the Issyk Kul region (Atlas Kyrgyzkaya, 1987). Simplified legend: Q = Quaternary, N = Neogene, P = Paleogene, Pm = Permian, C = Carboniferous, D = Devonian, S = Silurian, O = Ordovician, C = Cambrian, V = Vendian, R = Riphean, PR = undivided Proterozoic.

5.6.2.2. The Cenozoic reactivation

Besides small pockets of Jurassic sediments (quartzitic sandstones and coal-bearing shales), the Palaeocene-Eocene *Kokturpak* suite forms the base of the Issyk Kul basin sediments. They unconformably overlie the older, mainly Palaeozoic, basement rocks of the basin (Cobbold et al., 1994). The Kokturpak suite is composed of a red, calcerous breccia and clay sequence with evaporitic minerals, reflecting a slowly subsiding, continental, lacustrine basin under subtropical conditions (figure 5.24). The suite also contains intercalations of basaltic rocks (Sobel and Arnaud, 2000). It is followed by the Oligocene-Miocene *Kyrgyz* suite, which contains lacustrine and alluvial gravels, sands and clay. The general coarsening upward character of the suite is caused by the intensifying orogeny that caused an unconformity between the Kyrgyz and the Pliocene *Issyk-Kul* or *Chreyskaya* suite. The Issyk-Kul suite consists of pale yellow clays, grading upwards into a conglomerate, which is evidence of an intense pulse of tectonic activity. This activity culminated in a second unconformity and in the deposition of the mollassic *Chapeldak* suite in the latest Pliocene and Pleistocene. Late Pleistocene and Holocene deposits are an alternation of typical glacial and interglacial deposits of aeolian, lacustrine, alluvial-fan or fluvio-glacial facies. The present lake occupies a much smaller part of the basin compared to Middle Tertiary times. More arid climatic conditions (figure 5.24), and tectonic causes (deepening of the lake, redirection of major streams like the Chu river) can be invoked as plausible explanations. A small antropogenous effect may also have contributed to the lowered water level.

Neogene to recent reactivation of the Tien Shan has been confirmed by sedimentary evidence (Hendrix et al., 1992; Metivier and Gaudemer, 1997). Geomorphological evidence such as displaced Pleistocene glacial landforms and recent landslides (Tibaldi et al., 1997; Abrakhmatov et al., 2002), and geodetic and seismic evidence (Abrakhmatov et al., 1996; Reigber et al., 2001). In summary, we can state that the modern Tien Shan showed signs of reactivation in the Oligocene, that the orogen clearly started to form in the Middle Miocene, and that orogeny is an ongoing process.

The structure of the present-day Issyk Kul basin is still a matter of debate. Several models, including a half-ramp, a full-ramp and a pull-apart structure have been put forward (Cobbold et al., 1994; Korzhenkov, 2000; Mikolaichuk, 2000; Abdrakhmatov et al., 2002). Buslov et al. (submitted) propose a combination of these models, with a full-ramp structure developed at the western and eastern edges of the basin where the basement is thrust both on the northern and southern margins of the Tertiary basin. A half-ramp structure exists in the wider central section at the location of the modern lake, where the Terzkey ridge underthrusts the basin, resulting in recent rapid uplift of the southern Issyk Kul basin and tectonic subsidence in the interior zones. The northward dipp of sediment beds in the Terzkey range supports this suggestion. Finally, a pull-apart structure is proposed for the deep, innermost part of the basin (figures 5.26 and 5.27). The model would explain both the compressional and strike-slip features observed in the vicinity of lake Issyk Kul, and seems to be confirmed by preliminary geodetic data. For example a clear pop-up or flower structure in the Boom Canyon in the west of the on-shore part of the basin obviously demonstrates the overall N-S compressional character of the deformation.

While dextral strike slip in the Pred-Kungei fault zone, north of the lake would account for the central pull-apart basin. Strike-slip and compression are combined in the movements along the important Chon-Kemin fault. Delvaux et al. (2000) attribute a sinistral transpressional regime to the structure, which is in agreement with Tibaldi et al. (1997), who interpreted a similar regime acting on the Chilik fault.

An additional matter of debate is the mode of formation of the deep pull-apart centre of the basin. Buslov et al. (submitted) retain the classic idea of a catastrophic Holocene collapse of the central basin, while De Batist et al. (2002) argue that the sedimentary record of the basin does not supports this hypothesis. Pull-apart structures are also observed further to the north: e.g. the Alma-Ata lake basin in southernmost Kazakhstan (Tibaldi et al., 1997). This pull-apart basin formed due to movements along the eastern segment of the *Zailiski* fault (figure 5.21).

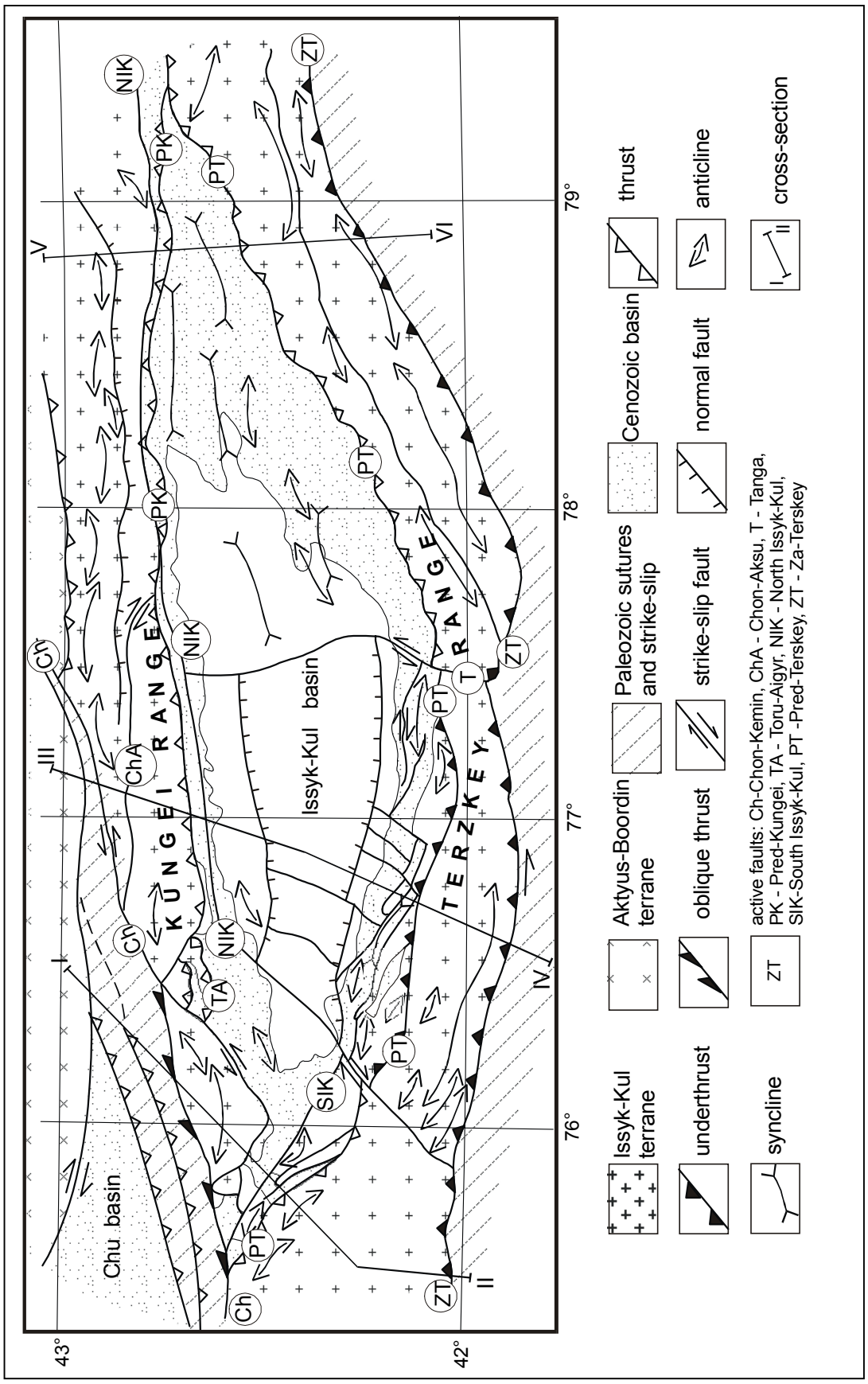

Figure 5.26: Structural sketch map of the Issyk Kul Basin and its basement (after Buslov et al., submitted).

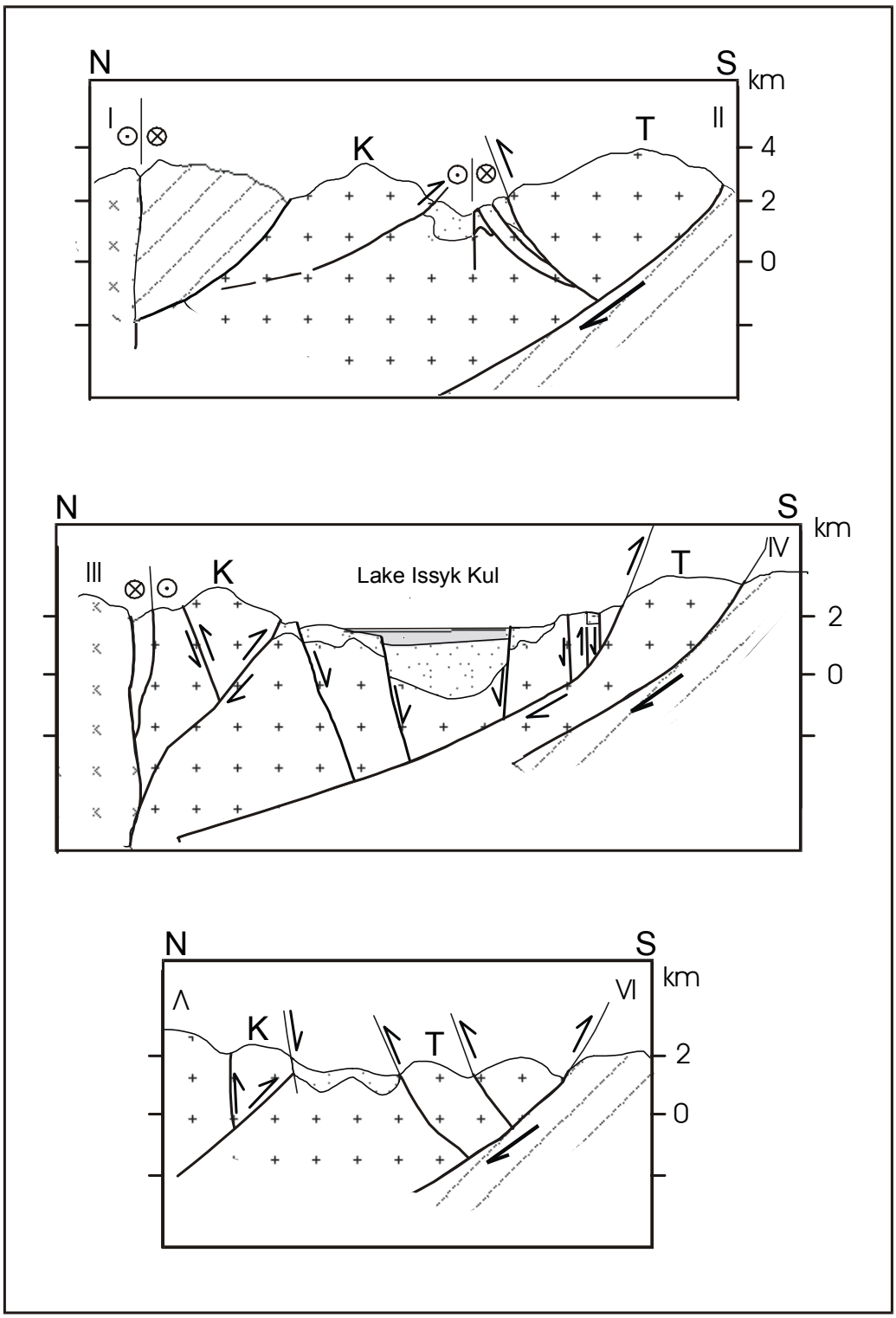

Figure 5.27: Cross-sections through the Issyk Kul basement (locations see figure 5.26). I-II: western Issyk-Kul basin with full-ramp structure (e.g. Boom structure). III-IV: central part of the basin, at the lake's locality, exhibiting a half-ramp structure with an underthrusting Terzkey range, and a pull-apart extension in the overriding structure in the middle of the basin. V-VI: eastern part of the basin, again with full-ramp structure (redrawn after Buslov et al., submitted). K = Kungei range, T = Terzkey range.

CHAPTER 6

APATITE FISSION-TRACK THERMOCHRONOLOGY: RESULTS, MODELLING AND INTERPRETATION

6.1. Mineral separation and sample preparation

Rock samples from Altai and Tien Shan include sedimentary rocks (3 Devonian sandstones), metamorphic rocks (gneisses) and igneous rocks (granitoids). The vast majority of the rock samples (blocks of about 1 kg) is of granitoid composition. They were collected during field campaigns in the summers of 1998, 1999 and 2000. Their position and elevation were recorded by use of the Global Positioning System (GPS) in combination with detailed topographic maps. The 3 sandstone samples yielded AFT ages consistent with the granitoids and gneisses and are significantly younger than their Devonian depositional ages. Hence, we consider the apatites from these sandstones as bedrock apatites.

The rock samples were crushed in a jaw crusher and subsequently ground with a cone-grinder in order to retrieve a fraction between 80 and 200 μm. The samples were then washed on a 50 μm sieve and decantated to remove fine dust. During the drying process care was taken not to warm the samples above ~50°C. Apatite is a diamagnetic mineral and has a density of 3.1 to 3.2 $g.cm^{-3}$. Hence, first the magnetic minerals were removed from the sample using a Franz Isodynamic magnetic separator. The non-magnetic fraction was subsequently treated with heavy liquids, bromoform (d = 2.82 $g.cm^{-3}$) and methylene iodide (d = 3.31 $g.cm^{-3}$). From the resulting separate, several hundred suitable apatite grains for each sample were selected by handpicking under a stereo-microscope. When possible, only euhedral or subhedral clear and transparent crystals were chosen. Samples yielding insufficient amounts of apatite or having apatite of poor quality, were not retained for further analysis.

The apatite separates were mounted for apatite fission track (AFT) analysis. In a first step, the selected grains were embedded in epoxy resin. Araldit® resin (AY 103) and hardner (HY 956) were mixed in a 5/1 ratio at room temperature to make the epoxy liquid. A few drops were poured in small, round plastic moulds (diameter 2.0 or 2.5 cm) and the apatite grains were strewn on top and allowed to sink to the bottom, where after some more epoxy liquid was added to reach a thickness of a few millimeters. Hardening of the epoxy in a drying furnace at 40 to 50°C generally took 24 to 48 hours. When hard the uneven, reverse side of the epoxy disc was ground until an even and flat disc of one to two millimeter thickness was obtained.

The front, containing the apatite grains was then carefully ground on fine (#500, #800, #1000 and #2000 mesh size) SiC-paper until flat internal surfaces of most of the grains were exposed. Next the discs were polished with a Struers polishing machine (DP-U4) using 6 µm, 3 µm, 1 µm and finally 0.25 µm Struers diamond pastes. Considering the size of the irradiation containers (diameter 2.0 cm and height 7.0 cm) the small discs (∅ 2.0 cm) were irradiated as such, but the larger ones (∅ 2.5 cm) were cut into rectangular shapes of 1.0 by 1.5 cm.

The polished apatite mounts were etched in a 2.5% HNO_3 solution (~0.4N) at room temperature for 70 seconds in order to reveal the spontaneous fission tracks in the crystal surfaces. For the external detector (ED), muscovite mica (low U-content) was cut from large sheets to appropriate dimensions for the specific sample. For one irradiation (Irradiation I, section 3.1.2) Jahre® mica was used, but due to a significant amount of background tracks, all later irradiations were carried out with Goodfellow® "clear ruby" mica as an ED. The mica EDs were firmly attached to the apatite mounts with tape. A number of apatite age standards (Durango and Fish Canyon Tuff apatite, section 1.7.2.2) were prepared in the same manner and under the same conditions. Most of the age standard mounts also contain shards of dosimeter glass (IRMM-540, section 1.7.1.2).

Track counting was done using the same procedure as outlined in section 3.3.1. Track length measurements were carried out using a semi-automatic measuring system (KONTRON-MOP-AMO3) consisting of a high-resolution digitizing tablet and cursor with central LED linked to a microprocessor, which translates the XY-coordinates of the track end-points into length, after pre-calibration against a stage graticule. The LED light spot on the cursor is superimposed on the microscopic image via the mirror of the drawing tube attachment of the BH2 microscope. The light spot of the cursor is positioned at each end of a track and by clicking the cursor both positions on the tablet are transmitted and a length calculated and displayed. Only horizontal confined tracks (section 1.2.4) were measured without making distinction between TINTs and TINCLEs, nor was the track orientation taken into account. Horizontal confined tracks are easily identified with reflected light because these tracks do not intersect the surface and show a bright internal reflection. When both track ends are in focus simultaneously, the track is horizontal or parallel to the crystal surface and thus the track is seen over its total length. In this manner a length distribution is constructed. Where possible, 100 tracks were measured, but in samples with few grains or low track densities this was not attainable. Some track length distributions are thus composed using less than 100 measurements, other samples yielded totally insufficient amounts of confined tracks for further use in modelling.

Before analysis of the Altai and Tien Shan samples, these track counting and measuring procedures were carried out on apatite age standards (Durango and Fish Canyon Tuff apatite) in order to get skilled in the preparation and analyzing methods. Later on these standards were used to calculate appropriate calibration factors for the method under the described conditions (sections 3.4 and 3.5).

6.2. Analytical results

The results obtained on the apatite samples from the Altai and Tien Shan mountains are presented in table 6.1. The samples are grouped according to the region of sampling in analogy with table 5.1. Table 6.1 lists all analytical data, both with respect to track counting and track length measurements. Parameters specific to the particular irradiation of an individual sample can be found in chapter 3; the irradiation numbers in table 6.1 refer to the corresponding values in tables 3.2 and 3.4. The AFT ages presented here are reported as Q-ages (with absolute thermal neutron fluence calibration) and as conventional ζ-ages. The Q-ages are further divided into Q-ages calculated on the basis of apatite age standard analyses (Q_s) and on the basis of an experimentally derived Q-value (Q_{exp}). Details on these approaches are given in section 3.5. Table 6.1 also lists the FT mean lengths. The uncertainties of values presented in table 6.1 are calculated according to the details outlined in chapter 3 and are essentially based on the work of Green (1981). For the 50 samples which yielded track length data, a track length distribution was constructed (see figure 6.1). Finally, on the basis of the conventional ζ-ages and the track length data and distributions, AFT modelling for thermal history reconstruction was carried out using the AFTSolve program (Ketcham et al., 1999 and 2000). The annealing equations used in the modelling were those of Laslett et al. (1987). Details on the software and annealing equations used here can be found in sections 2.5.2 and 2.5.8.4. The AFT age and length data for all samples is shown on the maps of the specific study areas (figure 6.2 for the Russian Altai, figure 6.3 for a detail of the Lake Teletskoye area in the Russian Altai and figure 6.4 for the Lake Issyk Kul region in the Kyrgyz Tien Shan).

6.3. Q-ages versus ζ-ages: a discussion

The theoretical aspects concerning the Q-factor or procedure factor were discussed is section 3.5. The Q factor was calculated firstly on the basis of apatite age standard analyses, for which Durango and Fish Canyon Tuff apatite was used (totalling 24 Durango analyses and 8 Fish Canyon Tuff analyses, over 5 different irradiations, see figure 3.8). We call the procedure factor determined in this way Q_s. The fundamental FT age equation (1.19) was used to calculate the Q_s factor as 1.05 ± 0.01 (section 3.5.1). AFT ages for apatite samples were subsequently determined by means of the fundamental age equation (1.19) and use of this Q_s factor. These values are presented in table 6.1 as $t(Q_s)$.

A second way of determining the procedure factor was carried out by annealing the spontaneous fission tracks in Durango apatite and irradiating it with a muscovite ED. We call the procedure factor determined in this experimental way (in the $4\pi/2\pi$ geometry, section 3.5.2) Q_{exp} and it was calculated for Durango as $Q_{exp} = 1.02 \pm 0.03$. Within the limits of the uncertainties, Q_s and Q_{exp} can be considered equal. Again applying the fundamental FT age equation (1.19) but now substituted with the Q_{exp} value gave AFT ages for the apatite samples from Central Asia. These are presented as $t(Q_{exp})$ in table 6.1.

Table 6.1: AFT age and length data for the Altai and Tien Shan samples. Irradiation characteristics are described by IN, the irradiation number (tables 3.2 and 3.4 for details). ρ_s, ρ_i, and ρ_d are respectively, the density of spontaneous, induced tracks and induced tracks in an ED irradiated against a dosimeter glass. The ρ_d-values are interpolated values obtained from regularly spaced glass dosimeters in each of the irradiation packages (section 3.3.2), expressed as 10^5 tracks/cm^2. Values for ρ_s and ρ_i are expressed as 10^6 tracks/cm^2. N_s, N_i, and N_d are respectively, the number of counted spontaneous, induced tracks and induced tracks in an ED irradiated against a dosimeter glass. N_d is also an interpolated value. $P(\chi^2)$ is the chi-squared probability that the dated grains have a constant ρ_s/ρ_i-ratio, it is given on a 0 to 1 scale. AFT ages, t(Qs), t(Qexp) and t(ζ) are respectively calculated with Q_s (section 3.5.1), Q_{exp} (section 3.5.2) and ζ (section 3.4). Q_s has an OWMQ value of 1.05 ± 0.01 (section 3.5.1) and Q_{exp} of 1.02 ± 0.03 (section 3.5.2). The Q-ages were calculated on the basis of an absolute metal-activation monitor controlled thermal neutron fluence (ϕ_{th}) characteristic of the particular irradiation (IN; tables 3.1 and 3.3 for exact values). Further constants, besides conventional and overall accepted parameters, used for Q-age determination were 8.46×10^{-17} a^{-1} for the ^{238}U fission decay constant (λ_f) and 570.8 barn for the thermal neutron cross-section (σ) (section 1.6). An OWMZ value of 253.1 ± 2.4 a.cm^2 (section 3.4) was used for the calculation of t(ζ). AFT length data are reported as a mean track length (l_m) with standard deviation, σ, obtained from the measurement of a number (n) of confined tracks. Ages are expressed in Ma, lengths in µm. Samples are grouped as in table 5.1.

Sample	IN	ρ_s (± 1σ)	N_s	ρ_I (± 1σ)	N_i	ρ_d (± 1σ)	N_d	ρ_s/ρ_i	$P(\chi^2)$	t(Q_s)	t(Q_{exp})	t(ζ)	l_m	n	σ
AFT samples from Gorny Altai															
A. Teletskoye Region															
TEL 101	I	3.047 (0.073)	1732	2.199 (0.060)	1332	5.789 (0.134)	1879	1.377 ± 0.050	<0.01	98.0 ± 4.5	94.9 ± 5.1	100.1 ± 4.4	12.2	70	1.9
TEL 105	I	2.799 (0.054)	2676	2.167 (0.048)	2039	5.794 (0.134)	1881	1.312 ± 0.039	0.31	93.4 ± 3.7	90.5 ± 4.3	95.5 ± 3.7	12.4	100	1.7
TEL 107	I	4.336 (0.088)	2444	2.999 (0.072)	1721	5.800 (0.134)	1882	1.507 ± 0.047	0.26	107.2 ± 4.5	103.8 ± 5.1	109.7 ± 4.4	12.5	100	1.7
TEL 108	I	4.319 (0.184)	549	3.901 (0.171)	520	5.804 (0.134)	1884	1.104 ± 0.068	0.88	78.7 ± 5.2	76.2 ± 5.5	80.6 ± 5.4	---	---	---
TEL 109	I	2.663 (0.057)	2189	2.599 (0.056)	2130	5.809 (0.134)	1885	1.066 ± 0.032	0.09	76.0 ± 3.0	73.6 ± 3.6	77.9 ± 3.0	12.3	100	1.7
TEL 110	I	6.084 (0.112)	2956	5.958 (0.111)	2905	5.814 (0.134)	1887	1.027 ± 0.027	0.75	73.3 ± 2.8	70.9 ± 3.2	75.1 ± 2.7	12.3	100	1.8
TEL 111	I	5.296 (0.099)	2879	4.978 (0.095)	2758	5.819 (0.134)	1889	1.067 ± 0.028	0.97	76.1 ± 2.9	73.6 ± 3.4	78.1 ± 2.8	12.4	100	1.5
TEL 112	I	4.115 (0.083)	2480	4.942 (0.092)	2899	5.826 (0.134)	1891	0.889 ± 0.024	0.01	63.5 ± 2.3	61.4 ± 2.8	65.2 ± 2.4	11.2	100	1.6
AL 272	II	3.306 (0.058)	3305	2.171 (0.047)	2170	3.304 (0.082)	1611	1.567 ± 0.043	0.43	66.2 ± 2.5	64.1 ± 3.0	65.2 ± 2.5	11.9	100	2.0
AL 262	III	0.699 (0.035)	1150	0.350 (0.014)	591	3.944 (0.111)	1262	2.144 ± 0.108	0.94	108.4 ± 6.0	104.9 ± 6.6	106.1 ± 6.2	---	---	---
SH 1	I	2.551 (0.049)	2718	2.033 (0.044)	2177	5.747 (0.133)	1865	1.269 ± 0.036	0.95	90.4 ± 3.5	87.5 ± 4.0	91.6 ± 3.5	12.8	100	1.8
SH 2	I	4.013 (0.062)	4148	3.089 (0.055)	3167	5.751 (0.133)	1867	1.324 ± 0.031	0.39	94.3 ± 3.4	91.3 ± 4.1	95.7 ± 3.3	13.3	100	1.5
SH 3	I	1.618 (0.030)	2961	1.293 (0.027)	2350	5.756 (0.133)	1868	1.287 ± 0.036	0.7	91.7 ± 3.4	88.7 ± 4.2	93.1 ± 3.5	13.2	100	1.3
SH 4	I	6.291 (0.109)	3304	4.542 (0.094)	2324	5.760 (0.133)	1870	1.429 ± 0.039	0.80	101.7 ± 3.8	98.5 ± 4.6	103.4 ± 3.8	12.8	100	1.8

Table 6.1 continued

SH 5	I	1.442 (0.028)	2746	1.160 (0.025)	2200	5.765 (0.133)	1871	1.296 ± 0.037	0.81	92.3 ± 3.6	89.4 ± 4.3	93.9 ± 3.6	13.1	62	1.6
SH 6	II	1.299 (0.036)	1322	0.993 (0.031)	1011	3.320 (0.083)	1616	1.429 ± 0.060	1.00	60.4 ± 3.0	58.8 ± 3.3	59.8 ± 3.0	---	---	---
SH 9	III	1.728 (0.057)	929	1.133 (0.046)	609	3.374 (0.083)	1642	1.704 ± 0.089	1.00	72.0 ± 4.1	70.2 ± 4.6	72.4 ± 4.2	11.3	24	1.9
SH 11	II	1.409 (0.060)	546	0.703 (0.043)	269	3.379 (0.083)	1645	2.239 ± 0.167	0.31	94.4 ± 7.5	91.4 ± 7.6	95.0 ± 7.5	---	---	---
SH 15a	II	0.837 (0.026)	1020	0.314 (0.016)	383	3.383 (0.083)	1647	2.904 ± 0.174	0.80	122.2 ± 8.0	118.3 ± 8.5	123.1 ± 8.1	12.8	95	1.4
SH 15b	II	1.670 (0.074)	513	1.081 (0.059)	332	3.387 (0.083)	1649	1.613 ± 0.114	1.0	68.1 ± 5.1	66.0 ± 5.3	68.8 ± 5.2	---	---	---
SH 16	V	5.454 (0.144)	1430	2.871 (0.104)	759	4.083 (0.080)	2613	1.947 ± 0.087	0.98	111.7 ± 5.9	108.1 ± 6.3	99.8 ± 5.0	14.4	100	1.4
SH 18	II	0.913 (0.044)	427	0.492 (0.033)	224	3.399 (0.084)	1654	1.926 ± 0.159	0.99	81.3 ± 7.1	78.7 ± 7.1	82.3 ± 7.1	---	---	---
SH 19	II	0.511 (0.023)	501	0.227 (0.015)	222	3.405 (0.084)	1657	2.452 ± 0.198	1.00	103.3 ± 8.7	100.0 ± 9.0	104.8 ± 8.9	11.2	80	2.0
GA 30	IV	1.185 (0.039)	924	0.844 (0.033)	658	3.822 (0.083)	2153	1.488 ± 0.076	1.00	79.6 ± 4.5	77.1 ± 5.0	71.6 ± 4.0	13.8	100	1.4
GA 31	IV	0.989 (0.033)	890	0.532 (0.024)	479	3.818 (0.082)	2150	1.910 ± 0.108	0.98	102.0 ± 6.4	98.8 ± 6.7	91.6 ± 5.6	13.8	73	1.6
GA 32	IV	0.916 (0.026)	1237	0.618 (0.021)	834	3.815 (0.082)	2149	1.587 ± 0.071	0.82	84.9 ± 4.6	82.2 ± 4.6	76.2 ± 3.9	13.6	100	1.3
GA 33	IV	1.119 (0.031)	1320	0.620 (0.023)	705	3.807 (0.082)	2144	1.811 ± 0.084	0.97	96.8 ± 5.2	93.7 ± 5.6	86.7 ± 4.5	---	---	---
GA 34	V	4.650 (0.153)	926	2.170 (0.106)	420	3.804 (0.082)	2142	2.210 ± 0.130	1.00	126.6 ± 8.3	122.6 ± 8.7	105.5 ± 6.7	---	---	---
CHU 01	II	1.841 (0.075)	601	1.216 (0.061)	397	3.293 (0.082)	1603	1.989 ± 0.129	0.52	83.9 ± 5.9	81.2 ± 6.1	82.4 ± 5.8	11.8	28	2.3
B. South Chulyshman Plateau															
GA 06	V	0.800 (0.029)	768	0.310 (0.018)	298	4.068 (0.080)	2604	2.566 ± 0.175	1.00	146.8 ± 10.6	142.1 ± 11.1	130.8 ± 9.3	13.9	65	2.0
GA 07	IV	1.283 (0.041)	1001	0.550 (0.027)	429	3.854 (0.083)	2171	2.375 ± 0.137	1.00	126.6 ± 8.0	122.6 ± 8.6	114.8 ± 7.2	14.0	100	1.4
GA 08	V	3.904 (0.109)	1296	2.084 (0.079)	691	4.058 (0.080)	2597	1.911 ± 0.090	0.99	109.7 ± 6.0	106.1 ± 6.4	97.4 ± 5.1	13.3	65	1.8
GA 15	V	0.918 (0.038)	582	0.309 (0.023)	179	4.044 (0.079)	2588	3.019 ± 0.258	0.99	172.4 ± 15.5	166.9 ± 15.6	152.7 ± 13.5	---	---	---
GA 16	V	0.873 (0.035)	619	0.352 (0.022)	262	4.039 (0.079)	2585	2.441 ± 0.180	1.00	139.7 ± 11.0	135.3 ± 11.2	123.6 ± 9.5	---	---	---
GA 18	IV	4.899 0.085)	3307	2.609 (0.062)	1761	3.844 (0.083)	2165	1.893 ± 0.056	1.00	101.1 ± 4.0	97.9 ± 4.8	91.4 ± 3.5	13.6	100	1.4
GA 19	V	2.698 (0.062)	1865	1.463 (0.046)	1011	4.034 (0.079)	2582	1.982 ± 0.078	0.98	113.7 ± 5.4	110.1 ± 6.0	100.4 ± 4.5	14.0	100	1.5
GA 21	V	1.338 (0.047)	795	0.706 (0.034)	429	4.019 (0.079)	2572	1.927 ± 0.115	1.00	110.6 ± 7.2	107.0 ± 7.5	97.3 ± 6.2	13.0	29	1.7
GA 23	IV	0.964 (0.028)	1157	0.463 (0.020)	555	3.833 (0.082)	2159	2.169 ± 0.112	0.99	115.7 ± 6.6	112.0 ± 7.3	104.4 ± 5.9	14.2	100	1.5

Table 6.1 continued

C. Dzhulukul Basin														
GA 09	V	2.009 (0.068)	862	0.992 (0.046)	457	4.054 (0.080)	2595	1.915 ± 0.111	0.99	109.9 ± 7.1	106.4 ± 7.4	97.5 ± 6.0	---	---	---
GA 12	V	3.433 (0.100)	1188	1.407 (0.063)	503	4.049 (0.079)	2592	2.614 ± 0.139	0.30	149.5 ± 9.0	144.8 ± 9.5	132.6 ± 7.6	---	---	---
GA 13	IV	2.846 0.078)	1332	0.872 (0.043)	408	3.851 (0.083)	2169	3.265 ± 0.185	0.99	173.5 ± 11.0	167.9 ± 11.4	157.2 ± 9.6	13.4	100	1.4
GA 20	V	1.197 (0.031)	1532	0.588 (0.021)	753	4.024 (0.079)	2576	2.091 ± 0.093	0.76	119.9 ± 6.1	116.1 ± 6.9	105.6 ± 5.2	14.1	100	1.4
D. Kurai – Chuya														
AL 235	V	2.175 (0.055)	1580	1.263 (0.042)	912	4.113 (0.080)	2633	1.929 ± 0.080	0.36	110.7 ± 5.4	107.1 ± 6.0	99.6 ± 4.7	13.8	100	1.7
AL 239	II	1.219 (0.032)	1486	0.683 (0.024)	832	3.315 (0.083)	1614	1.869 ± 0.081	1.00	78.9 ± 4.0	76.4 ± 4.5	77.9 ± 4.0	11.2	51	2.2
AL 240	III	1.657 (0.026)	3937	0.950 (0.020)	2257	3.934 (0.111)	1259	1.777 ± 0.047	0.01	90.0 ± 3.4	87.1 ± 4.0	87.9 ± 3.5	13.5	100	1.3
E. West Gorny Altai Transect and Novosibirsk sample														
Be 1	V	0.951 (0.030)	979	0.525 (0.022)	551	4.108 (0.080)	2629	1.921 ± 0.102	0.99	110.2 ± 6.4	106.7 ± 7.0	99.1 ± 5.7	13.7	32	1.6
No 1	V	4.246 (0.082)	2682	1.296 (0.046)	788	4.078 (0.080)	2610	3.509 ± 0.142	0.54	199.9 ± 9.6	193.6 ± 10.5	178.6 ± 8.2	---	---	---
GA 01	V	1.739 (0.051)	1144	0.777 (0.034)	510	4.073 (0.080)	2607	2.358 ± 0.125	1.00	135.0 ± 8.1	130.7 ± 8.5	120.4 ± 6.9	13.3	60	2.0
GA 03	IV	0.899 0.032)	809	0.447 (0.022)	402	3.858 (0.083)	2173	2.039 ± 0.124	1.00	108.9 ± 7.1	105.4 ± 7.5	98.8 ± 6.5	13.6	58	1.9
GA 24	V	3.551 (0.110)	1044	1.131 (0.062)	338	4.014 (0.079)	2569	3.300 ± 0.207	0.81	188.2 ± 12.8	182.2 ± 13.3	165.5 ± 11.0	---	---	---
AFT samples from Tien Shan, Issyk Kul basement														
A. Kungei Range														
TS 04	III	1.091 (0.023)	2281	0.393 (0.014)	820	3.751 (0.108)	1200	2.815 ± 0.115	0.99	141.9 ± 7.0	137.4 ± 7.7	132.3 ± 6.7	---	---	---
TS 06	III	2.927 (0.058)	2504	1.018 (0.034)	871	3.759 (0.108)	1203	2.919 ± 0.115	1.00	147.1 ± 7.0	142.4 ± 7.9	137.4 ± 6.8	12.4	100	1.5
TS 07	V	2.281 (0.059)	1518	0.829 (0.035)	547	4.157 (0.081)	2661	2.826 ± 0.141	0.96	161.5 ± 9.2	156.4 ± 9.8	147.0 ± 8.0	13.1	100	1.6
TS 08	III	2.059 (0.029)	4892	0.673 (0.017)	1599	3.771 (0.108)	1207	3.123 ± 0.090	0.95	157.3 ± 6.2	152.3 ± 7.2	147.3 ± 6.2	12.5	100	1.5

Table 6.1 continued

TS 10	III	2.492 (0.032)	5922	0.896 (0.019)	2130	3.785 (0.108)	1211	2.827 ± 0.072	0.89	142.5 ± 5.2	138.0 ± 6.4	134.0 ± 5.3	12.6	100	1.4
TS 11	III	1.965 (0.042)	2148	0.695 (0.025)	749	3.793 (0.108)	1214	2.910 ± 0.123	0.99	146.7 ± 7.4	142.0 ± 8.0	138.2 ± 7.2	12.3	73	1.5
TS 12	V	1.435 (0.044)	1058	0.586 (0.029)	418	4.152 (0.081)	2657	2.493 ± 0.144	1.00	142.7 ± 9.1	138.1 ± 9.6	129.7 ± 8.0	---	---	---
TS 13	III	3.736 (0.079)	2219	1.133 (0.044)	673	3.812 (0.109)	1220	3.418 ± 0.150	0.93	171.9 ± 8.7	166.5 ± 9.6	162.8 ± 8.7	12.4	100	1.3
TS 14	III	6.177 (0.128)	2348	1.957 (0.072)	744	3.818 (0.109)	1222	3.206 ± 0.135	0.97	161.4 ± 8.0	156.3 ± 9.0	153.1 ± 7.9	12.6	100	1.6
TS 18	III	2.273 (0.062)	1350	0.879 (0.038)	522	3.854 (0.110)	1233	2.609 ± 0.134	0.86	131.7 ± 7.5	127.5 ± 8.2	126.0 ± 7.5	13.0	96	1.7
B. Terzkey Range															
TS 19	V	1.515 (0.130)	135	0.719 (0.090)	64	4.147 (0.081)	2654	2.065 ± 0.313	0.96	118.4 ± 18.4	114.6 ± 18.0	107.5 ± 16.5	---	---	---
TS 20	III	0.939 (0.035)	714	0.779 (0.032)	592	3.869 (0.110)	1238	1.270 ± .071	1.00	64.4 ± 4.0	62.4 ± 4.2	61.9 ± 3.9	12.8	54	1.8
TS 22	III	0.754 (0.048)	250	0.576 (0.044)	173	3.887 (0.110)	1244	1.417 ± 0.140	0.97	71.8 ± 7.3	69.5 ± 7.4	69.3 ± 7.2	---	---	---
TS 23	III	0.901 (0.037)	600	0.637 (0.031)	433	3.893 (0.110)	1246	1.480 ± 0.093	0.98	75.0 ± 5.1	72.6 ± 5.2	72.0 ± 5.0	---	---	---
TS 24	V	1.218 (0.058)	445	0.614 (0.040)	232	4.137 (0.080)	2648	1.976 ± 0.160	1.00	113.3 ± 9.7	109.7 ± 9.7	102.6 ± 8.6	---	---	---
TS 26	V	0.129 (0.007)	371	0.088 (0.006)	254	4.127 (0.080)	2641	1.510 ± 0.123	1.00	86.8 ± 7.4	84.0 ± 7.6	78.4 ± 6.6	---	---	---
C. Boom Canyon															
TS 02	III	0.146 (0.008)	348	0.058 (0.005)	139	3.738 (0.108)	1196	2.734 ± 0.274	1.00	137.9 ± 14.3	133.5 ± 14.4	128.1 ± 13.4	---	---	---
TS 15	III	2.685 (0.056)	2297	0.881 (0.032)	754	3.823 (0.109)	1223	3.107 ± 0.130	0.94	156.5 ± 7.8	151.5 ± 8.7	148.6 ± 7.7	13.2	100	1.8
TS 16	III	1.585 (0.043)	1356	0.709 (0.029)	607	3.833 (0.109)	1226	2.299 ± 0.112	0.93	116.2 ± 6.5	112.4 ± 7.0	110.6 ± 6.3	12.9	100	1.4
TS 17	III	2.103 (0.050)	1799	0.875 (0.032)	749	3.848 (0.110)	1231	2.492 ± 0.108	0.91	125.8 ± 6.4	121.8 ± 7.0	120.2 ± 6.4	13.0	100	1.5
D. Kindil Las Range															
KAZ 01	IV	3.793 (0.080)	2253	1.303 (0.047)	774	3.873 (0.083)	2181	3.034 ± 0.127	0.92	161.3 ± 8.1	156.2 ± 8.8	147.0 ± 7.0	12.4	100	1.6
KAZ03	IV	2.764 (0.068)	1642	0.840 (0.038)	499	3.870 (0.083)	2180	3.353 ± 0.171	1.00	178.1 ± 10.2	172.4 ± 11.0	162.2 ± 9.1	13.1	100	1.2

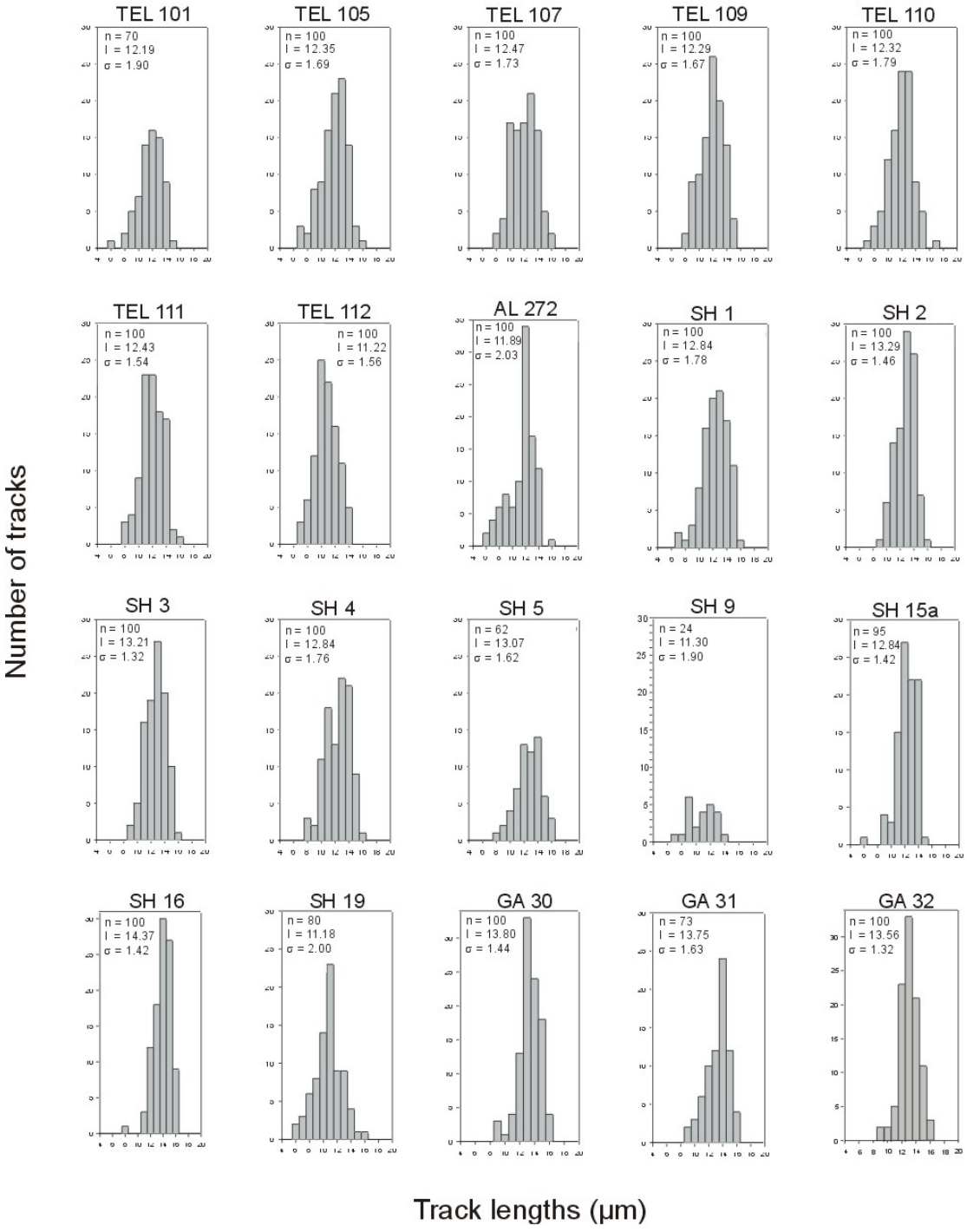

Figure 6.1: AFT length distributions of confined tracks from the Altai and Tien Shan samples, n is the number of measured tracks, l is the mean track length and σ the standard deviation of the distribution.

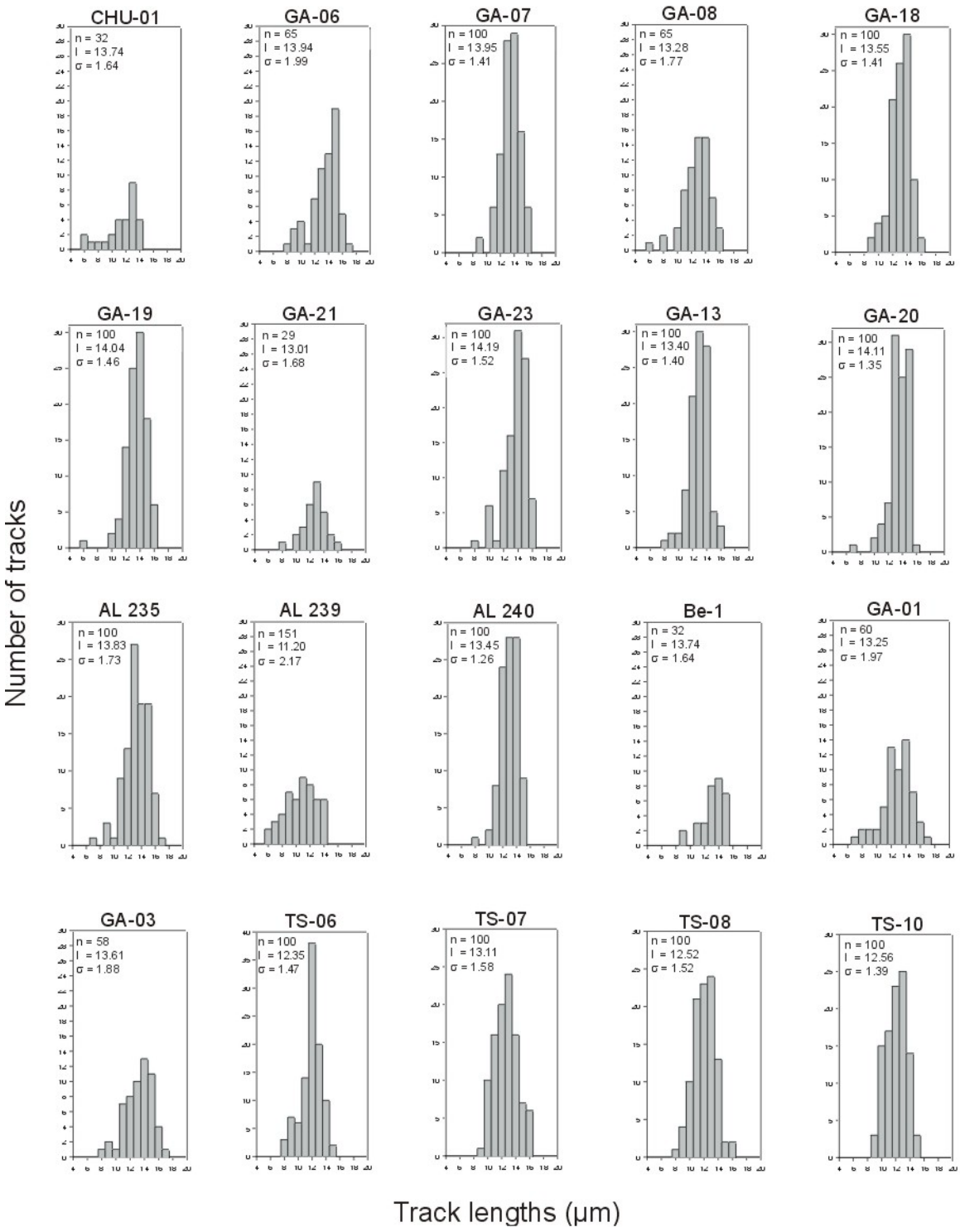

Figure 6.1: Continued.

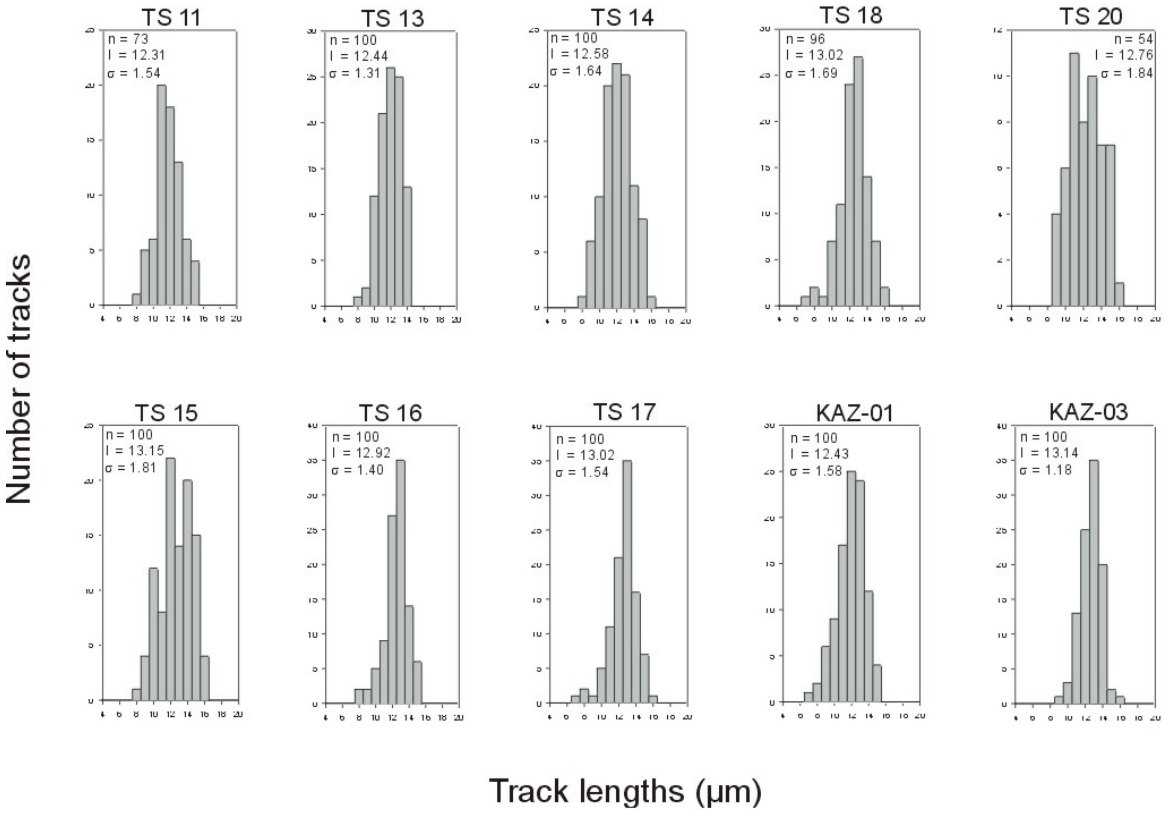

Figure 6.1: Continued.

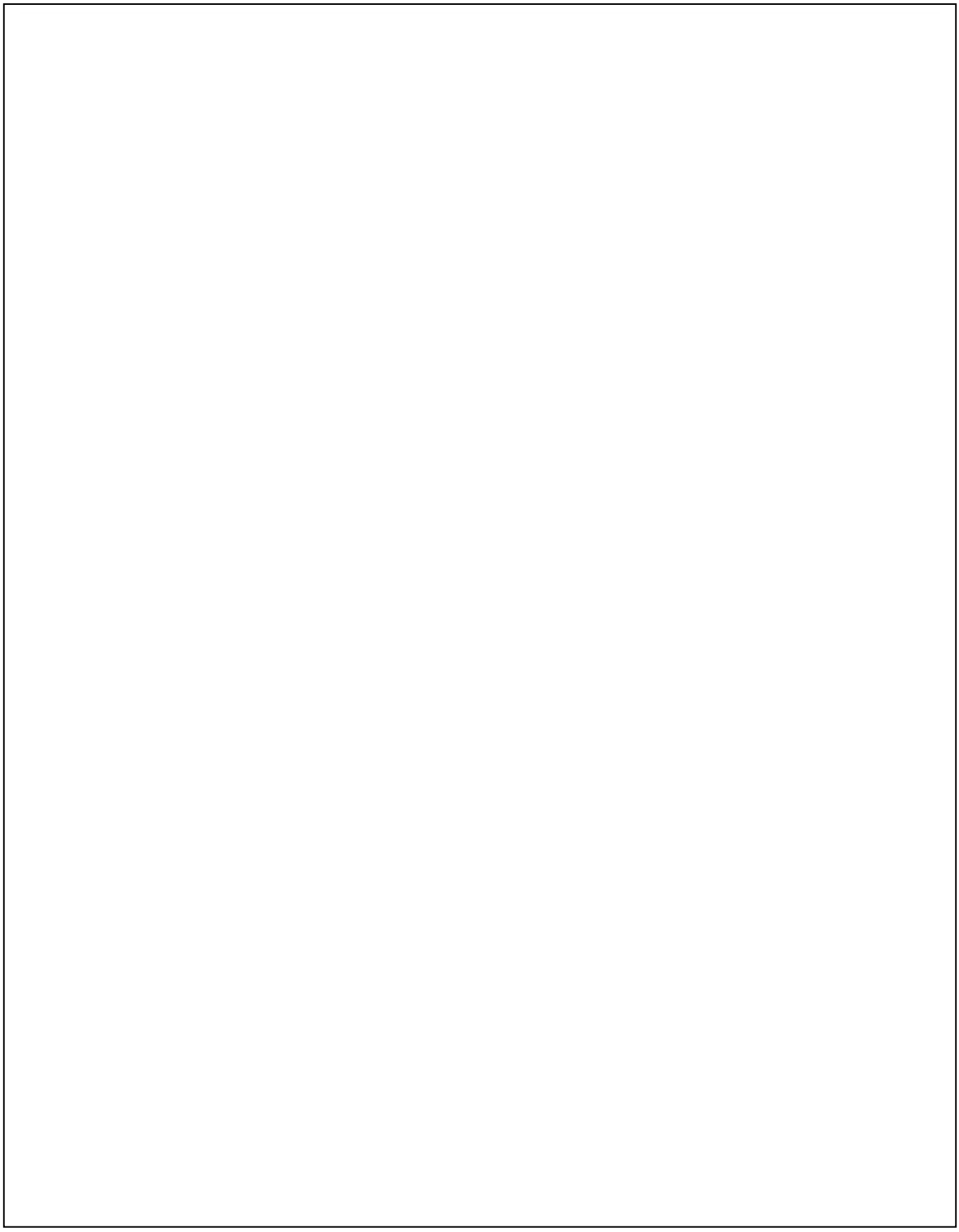

Figure 6.2 : Tectonic and structural sketch map of the Russian Altai Mountains with indication of sample locations and AFT age and length data. A detail of the Teletskoye area (blue box) is presented in figure 6.3.

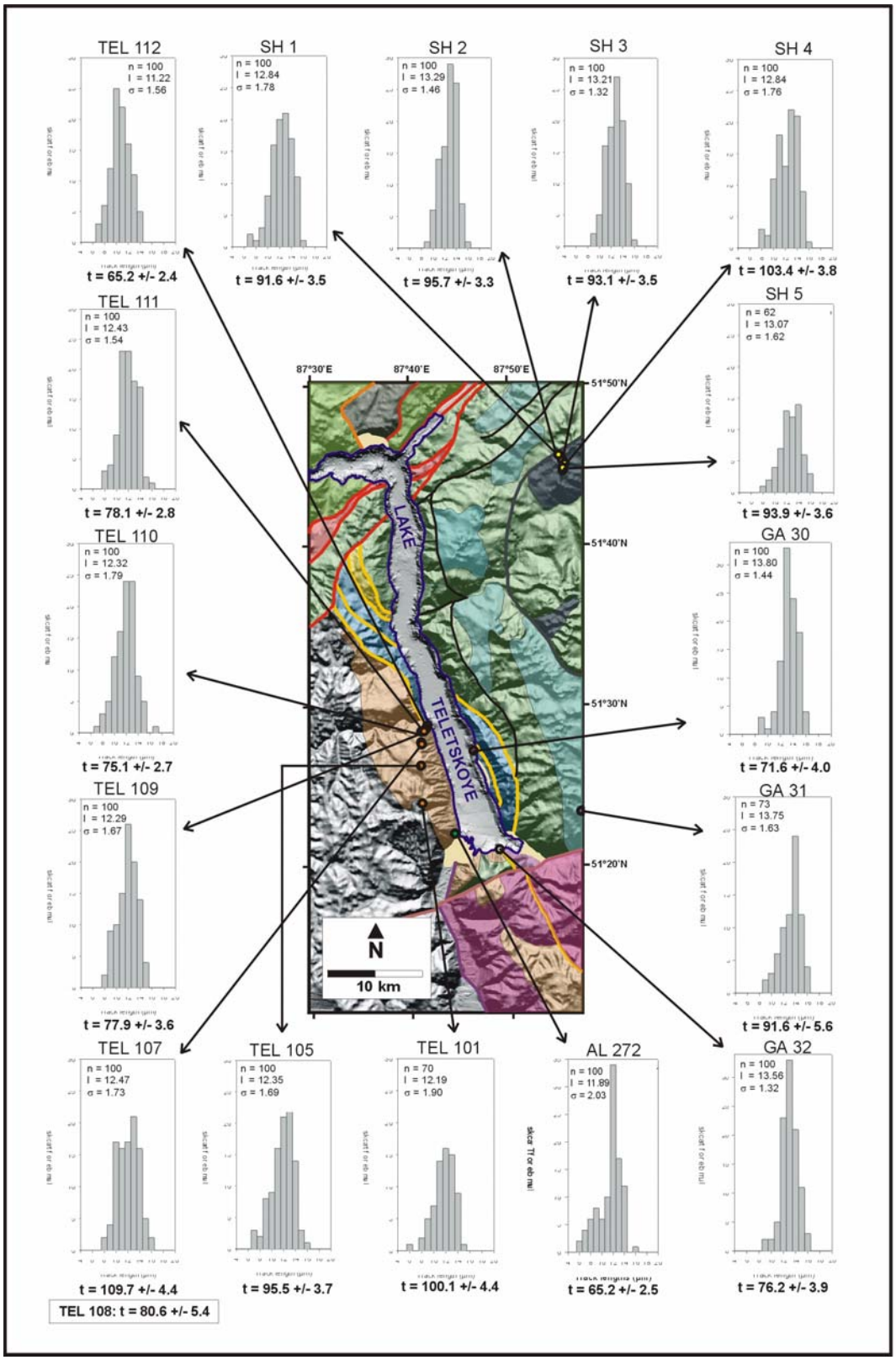

Figure 6.3 : Digital terrane model of the Teletskoye area with superimposed geological map. Sample locations are shown with their AFT age and length data.

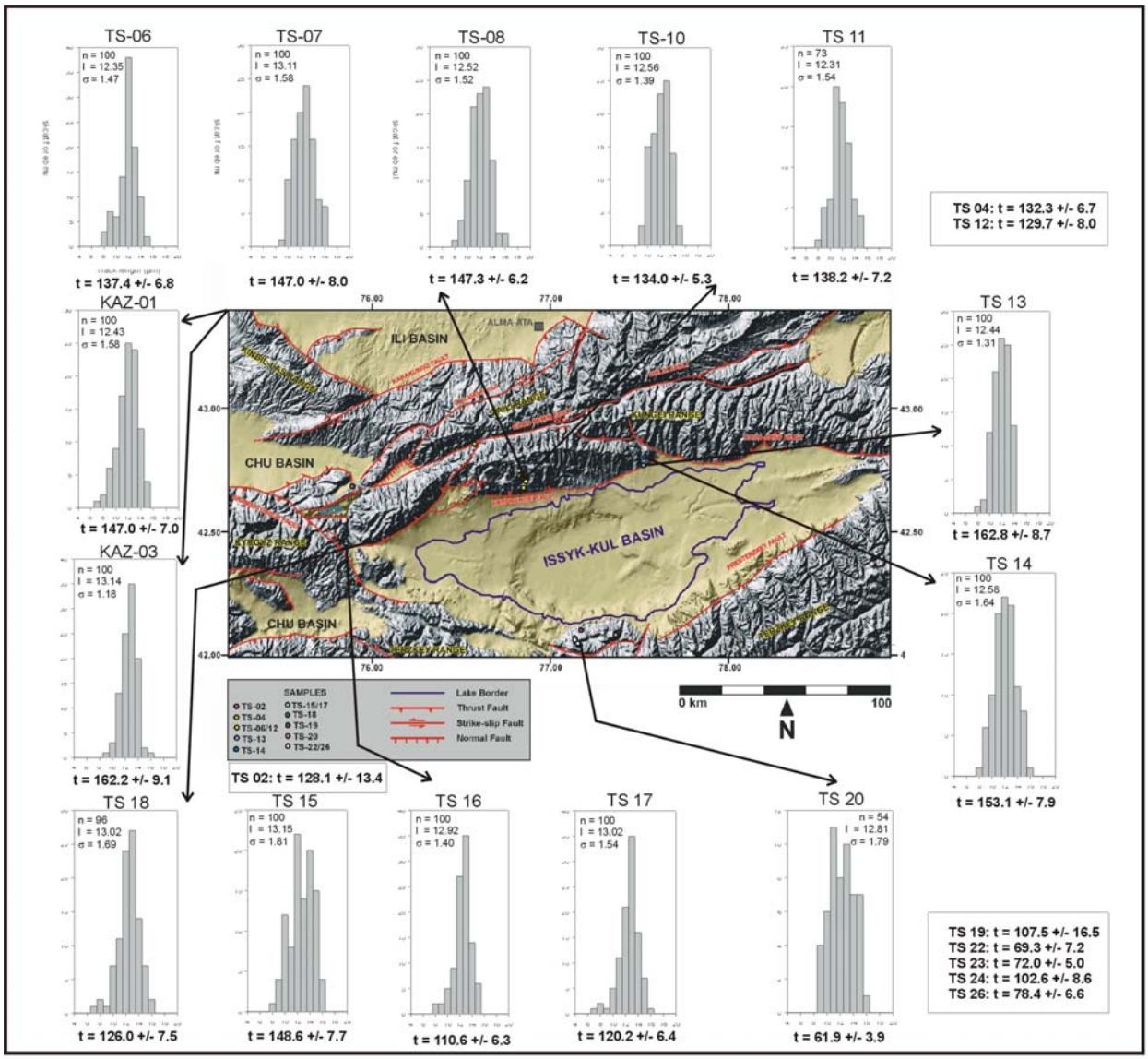

Figure 6.4 : Digital terrane model of the Lake Issyk Kul area. Cenozoic basins are indicated as yellow shaded areas. Sample locations are shown with their AFT age and length data.

Figure 6.2 shows plots of both the Q_s- and Q_{exp}-ages versus the ζ-ages and of the Q_{exp}-ages versus the Q_s-ages. Both Q-ζ plots are in very good agreement with each other, but in comparison to the ζ-ages, the Q-ages seem to register a higher value, especially when considering older ages. This results in a small departure from the 1:1-line. Similar observations were made by Grimmer et al. (2002). The Q_{exp}-ages and Q_s-age are in good agreement as can be expected from the values.

The considerations concerning ζ- and Q-ages presented here demonstrate in our opinion clearly that absolute calibration of the FT method by use of metal activation monitors works well when nuclear parameters are accurately known and when thermal neutron fluence monitoring is carried out as in Van den haute et al. (1988). These findings support our preliminary data on this subject published earlier (De Grave and Van den haute, 2002). This work demonstrates that the use of the absolute calibration and the Q-factor yield reliable AFT ages even when applying the ED method. The procedure factor hence represents a deconvoluted ζ-factor and contrary to the latter is interpretable in function of etching and track registration characteristics. It thus can be regarded as an improvement of the ζ-calibration that has always been considered an interim measure by the proponents of this calibration factor (Hurford, 1998). The results of this work in our opinion clearly show that the Q-approach merits a more systematic and experimental investigation. For further discussion and modelling of the AFT results on the samples from Siberia and Central Asia it was however opted to use the conventional ζ-ages to be in agreement with the international recommendations concerning AFT reporting (Hurford, 1990a and 1990b).

6.4. AFT-results of the Altai and Tien Shan samples

6.4.1. The Teletskoye region

In general, apparent AFT ages (ζ-ages) from the Teletskoye region in Gorny Altai fall between about 60 Ma and 105 Ma (table 6.1), and are thus Late Cretaceous. One sample, SH 15a, a gneiss sample taken at a high altitude of 2150 m some 30 km southeast of Lake Teletskoye (Karakol Creek) shows a higher age of ~123 Ma (Early Aptian, i.e. Middle Cretaceous). These apparent AFT ages correspond to the period directly pre-dating onset of widespread Late Cretaceous-Paleogene peneplanation in the area as outlined in section 4.5.5.2. Except for sample SH 16, mean lengths for all samples indicate a clear shortening of the tracks with values ranging between 11.5 and 13.5 µm. Furthermore the length distributions (figure 6.1) are rather broad with 1.3 µm < standard deviation < 2.3 µm, have a distinct negative skewness and mostly show a relatively small number of tracks with length above 14 µm.

No clear picture can be derived from the age-elevation, length-elevation and age-mean track length plots for the samples from the Russian Altai region (figure 6.6). Too much scatter from too broad of a region obviously blurs possible trends. When filtering out the Teletskoye Region data a somewhat clearer picture can be seen (figure 6.7). The AFT age is more distinctly correlated with elevation, with older samples at higher altitudes.

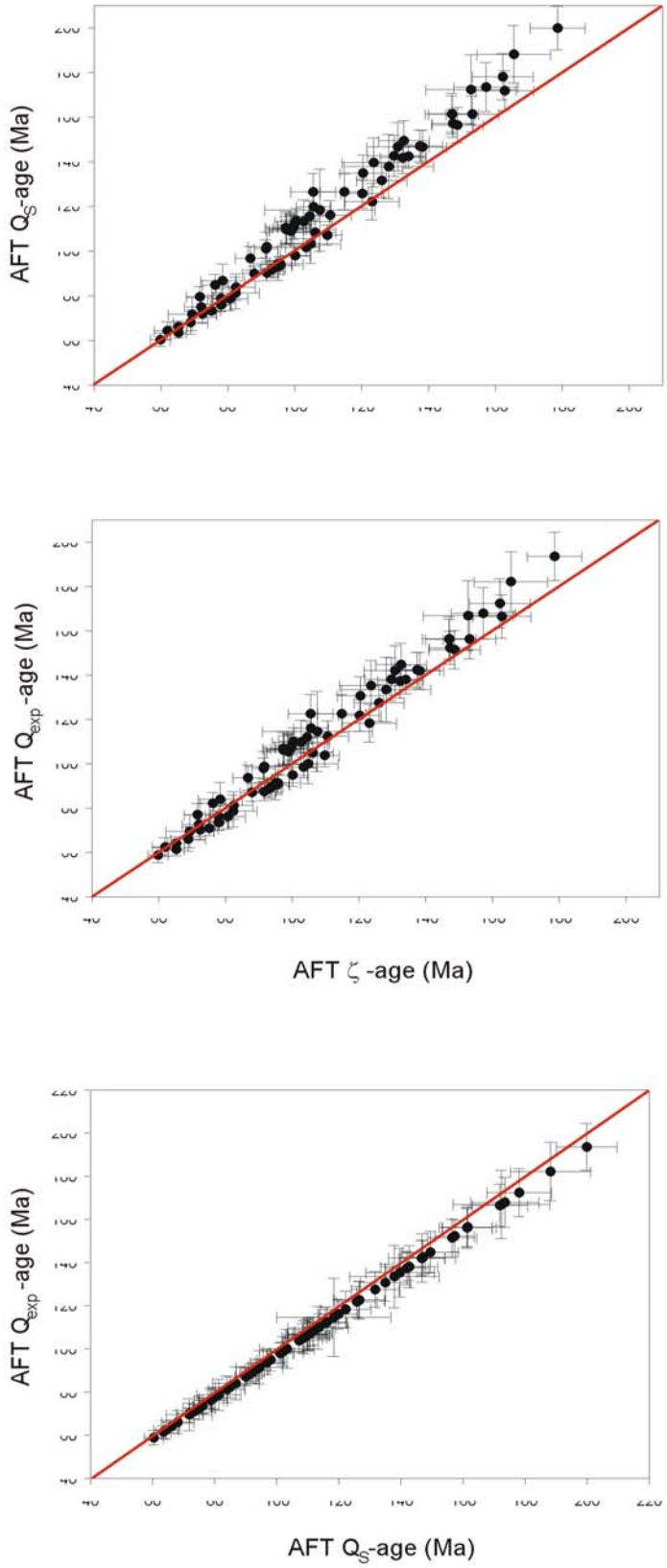

Figure 6.5: Plots of the AFT ζ-ages vs. Q-ages. Q_s was calculated from age standard analyses (section 3.5.1), and Q_{exp} from the ratio of induced track densities in apatite and a muscovite external detector (section 3.5.2).

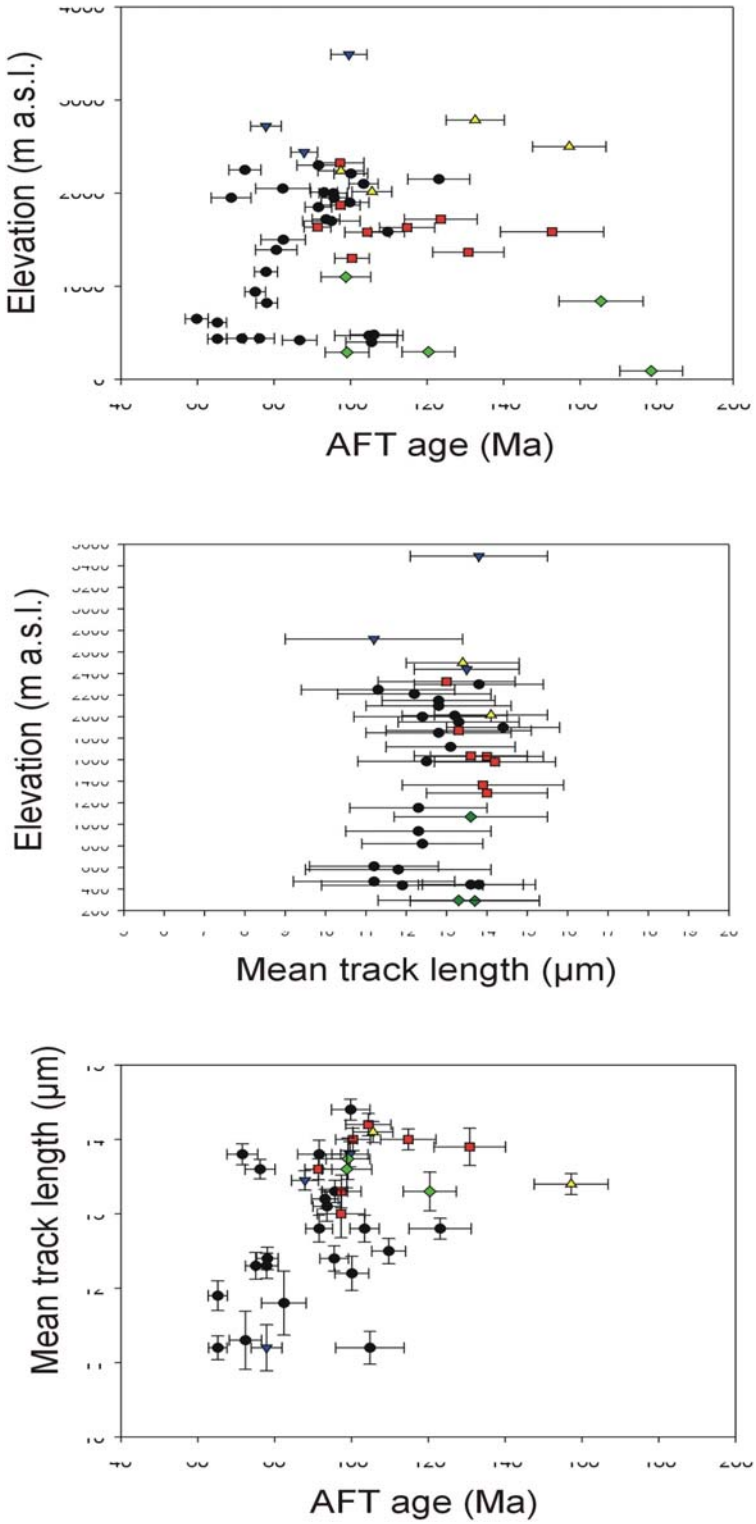

Figure 6.6: AFT age-elevation, AFT mean track length-elevation and AFT age-mean track length plots for the Altai samples. Black circles: Teletskoye samples, red squares: South Chulyshman Plateau samples, yellow triangles (up): Dzhulukul samples, blue triangles (down): Chuya-Kurai samples, green diamonds: Western transect samples.

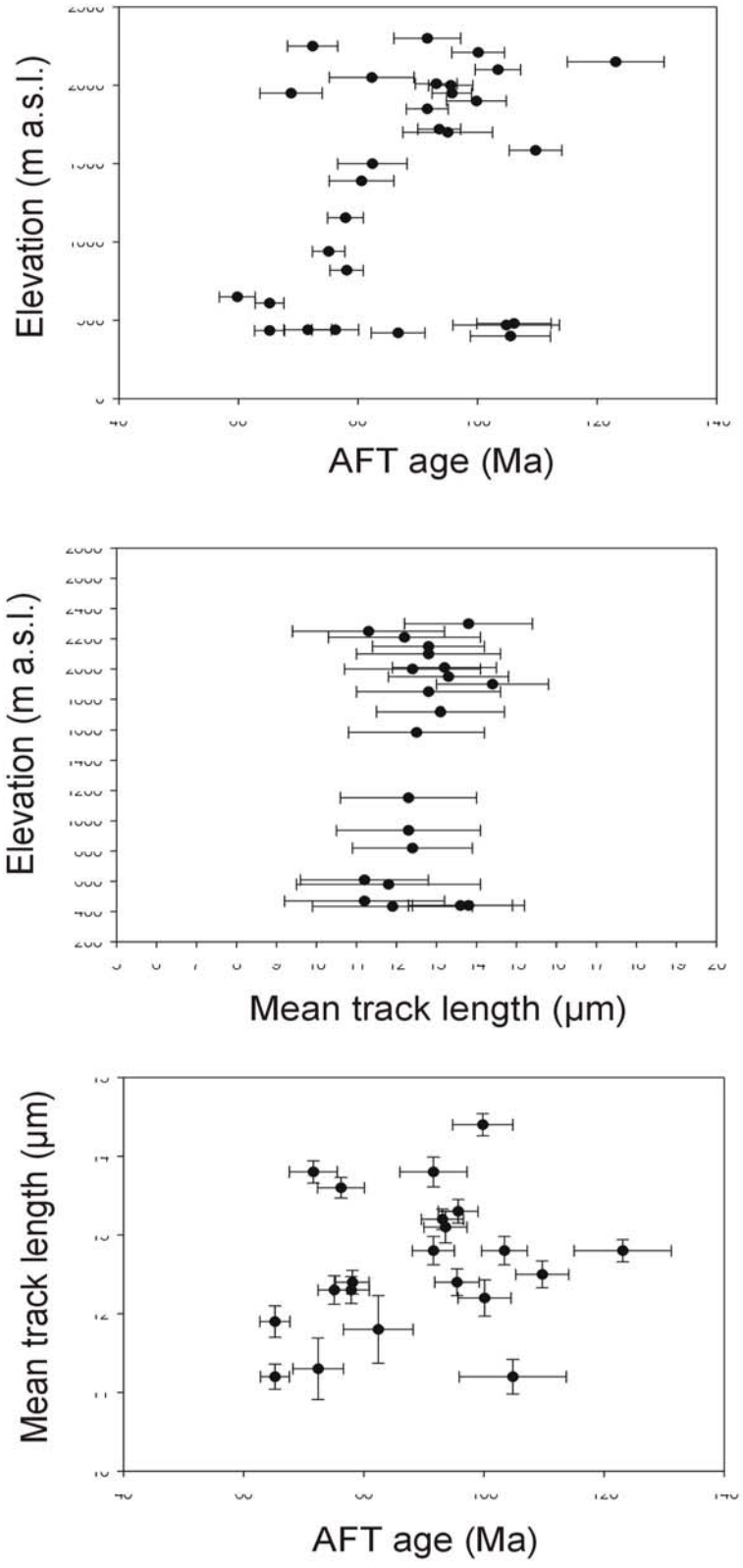

Figure 6.7: AFT age-elevation, AFT mean track length-elevation and AFT age-mean track length plots for the samples from the Teletskoye Region, Russian Altai Mountains.

Nevertheless some scatter still occurs and is possibly related to local differential movements or variations in geothermal gradient and/or apatite chemical composition. At least some of the scatter at low altitudes (SH 19, GA 34...) can be explained by the fact that these samples are from the low lying, inactive northern foreland (north of the West Sayan fault zone, e.g. figure 5.2) of this part of the Altai Mountains. They are clearly from a distinct geodynamic unit.

Two elevation profiles were sampled in the basement flanking the Teletskoye graben. A first profile was sampled in the Devonian Altyntauss granitoids, with an elevation difference of about 1800 m (TEL samples and sample AL 272). The second profile was sampled in a small diorite-granodiorite complex near the Katayatsk river about 15 km to the northeast of the lake (samples SH1-SH5) between 1700 and 2100 m elevation. The Altyntauss profile is located to the west of the Teletsk-Bashkauss (TB) fault zone, while the Katayatsk profile lies to its east. The latter profile lies west of the Shapshal fault, close to its junction with the West Sayan (WS) fault zone. Results concerning these profiles were presented earlier (De Grave and Van den haute, 2002). Some adjustments however are made here concerning the ζ-ages because the OWMZ has been determined more precisely now on the basis of larger number of age standard analyses. It is clear from figure 6.8 that the age-elevation plot of these profiles exhibits a linear trend without break-in-slope. Taking into account our AFT length data and considering the elevation profile data with break-in-slope by Gleadow and Fitzgerald (1987) from the Transantarctic Mountains (section 2.7.4), the Teletskoye Region profiles would correspond to their more gently sloping upper profile section.

In the Teletskoye region, AFT evidence from both length data and age versus elevation data show that the region might have resided in the APAZ in the crust for a considerable time prior to its cooling to the present ambient temperatures. Interpretation of the apparent AFT ages in this case is not straightforward. Qualitatively speaking, we can say that during the Cretaceous (~105-60 Ma according to the apparent AFT ages), preceding large-scale regional peneplanation in the Late Cretaceous-Paleogene as indicated by various lines of geological evidence (Deev et al., 1995), the rocks in the study area possibly attained upper APAZ temperatures. Denudation and consequent cooling must have brought the rocks to that position in the crust at that time. Denudation and cooling must then have occurred prior to the time recorded by the apparent AFT ages, but later than the Permo-Triassic cooling (from ~300°C at ~260 Ma) as recorded by the $^{40}Ar/^{39}Ar$ data from the Teletskoye basement rocks in the Chiri area (Dehandschutter et al., 1997). Some time after the Cretaceous-Palaeogene peneplanation, the rocks must have cooled from the APAZ temperatures to surface temperatures due to at least one denudational event, most probably related to the active tectonic phase occurring in the region at present. AFT modelling is necessary to elaborate this qualitative hypothesis in a quantitative fashion.

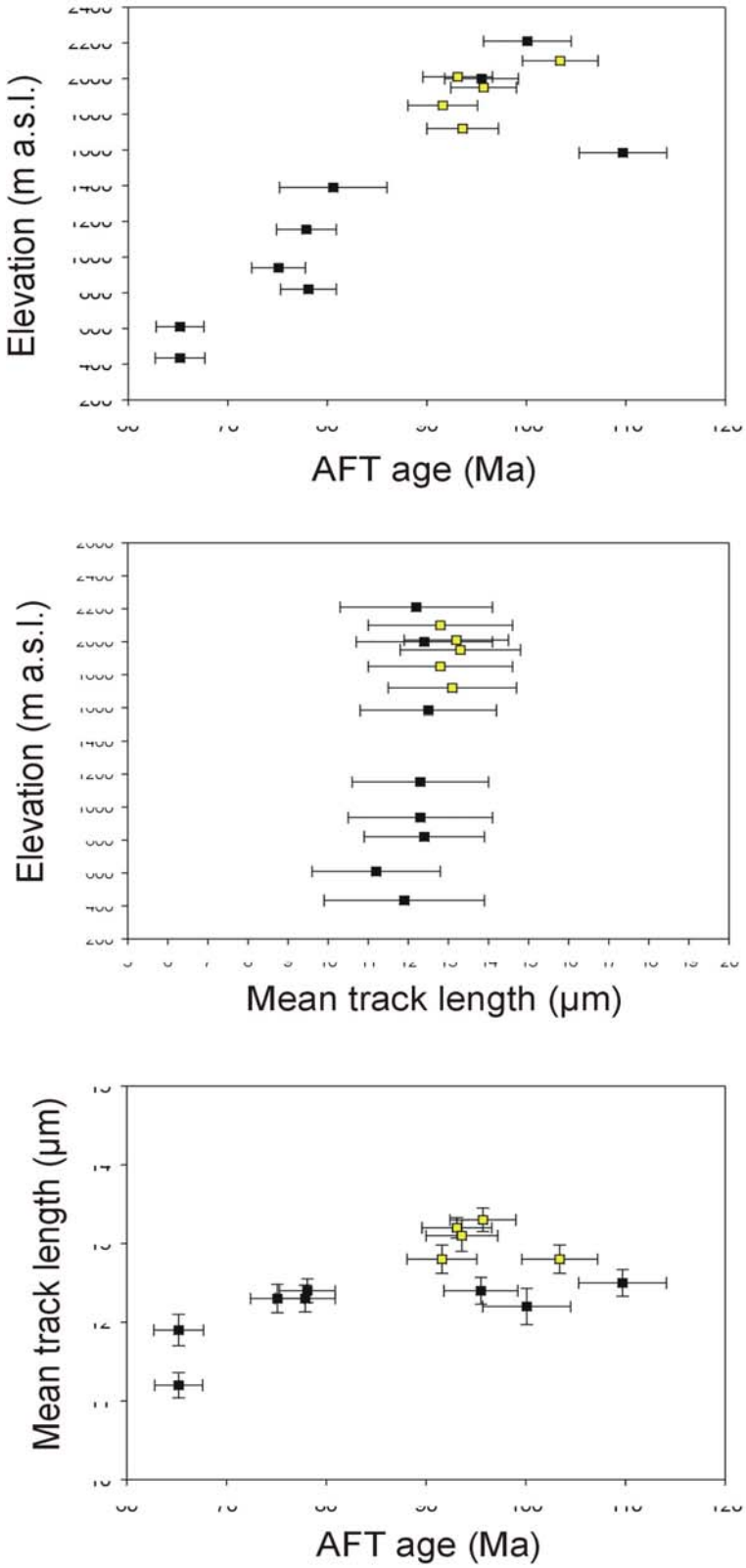

Figure 6.8: AFT age-elevation, AFT mean track length-elevation and AFT age-mean track length plots for the Altyntauss (black) and Katayatsk (yellow) profile samples near Lake Teletskoye.

6.4.2. Other regions in the Russian Altai mountains

In this section the AFT results from the other sample areas in Gorny Altai and adjacent areas (South Chulyshman Plateau, Dzhulukul Basin, Chuya-Kurai area, the Western transect and the Novosibirsk sample) will be discussed. For sample locations see figure 5.2 or 5.18.

Apparent AFT ages (ζ-ages) from these regions approximately fall between 150 Ma and 80 Ma, covering the Latest Jurassic and most of the Cretaceous. These ages correspond well with the Teletskoye samples. Nevertheless many of them are higher. These higher ages were in part obtained for regions in the south that were on average at significant higher altitude (especially in the South Chulyshman Plateau, Dzhulukul Basin, and Chuya-Kurai area), while high ages were also found in the low-lying, not to moderately tectonically reactivated zone of the present Altai Mountains (most pronounced along the Western transect). In the former case, higher AFT ages can be the result of the fact that the high altitude areas passed through the APAZ in the crust in an earlier, Mesozoic stage in the denudational history of the region. In the case of the inactive lowlands, an early Mesozoic cooling can be expected to be the only effect these rocks experienced as there are no indications for neotectonic activity.

Track length information shows an unmistakably smaller thermal influence with respect to the samples from the Teletskoye Region. With the exception of sample AL 239, mean track lengths for this study area fall between 13.0 μm and 14.2 μm. Track length distributions appear more symmetrical and do not exhibit an outspoken negative skewness. In comparison to the Teletskoye region, the rocks must have been exhumed through the APAZ isotherms faster. The inferred Mesozoic event would have brought the rocks to the upper part of the APAZ and even to within the Total Stability Zone for FTs in apatite, limiting any subsequent thermal annealing in these samples.

Sample No-1 from Novosibirsk city within the stable basement of the West Siberian Basin, yielded the highest AFT age of 179 ± 8 Ma. Sample GA 24 from the low lying, inactive northern foreland of the Russian Altai Mountains yielded a closely resembling AFT age of 166 ± 10 Ma. These Middle Jurassic ages (Late Lias-Dogger) probably represent the age of the stabilization surface after a Jurassic pulse of tectonic activity and accompanying denudational cooling of the crust. Unfortunately the small number of dateable apatite grains in both samples did not contain sufficient confined tracks and hence it was impossible to establish a length distribution and AFT cooling model for them.

Some samples from the South Chulyshman Plateau and from the Shapshal range in the Dzhulukul basin area also yielded high AFT ages of 120 Ma to 160 Ma in comparison with the Teletskoye region and with other samples from the southern part of the Russian Altai Mountains. This suggests significant differential vertical movements in the area along the Shapshal fault zone as well as in the internal part of the South Chulyshman Plateau. The latter supports the present structure and deformational pattern within the Plateau as suggested by Dehandschutter (2001) (section 5.2). Apart from the exception of the Chuya-Kurai samples, no clear correlation is observed in the AFT age-elevation plot of the region (figure 6.9).

The age-mean track length and age-standard deviation plots (figure 6.9) also do not show a clear correlation, yet an apparent clustering of the data can be observed. Again, this qualitative discussion should be refined by AFT modelling of the data (section 6.5).

6.4.3. The Kyrgyz Tien Shan Mountains

The AFT results from the Kyrgyz Tien Shan, around Lake Issyk Kul reflect a clear distinction between the several tectonic domains. Apparent AFT ages from the Kungei Range, the northern boundary range of the Issyk Kul basin, fall between about 130 Ma and 160 Ma (the Malm-Neocomian epochs of the Late Jurassic-Early Cretaceous). The two samples from the Kindil Las Range, to the northwest of the Kungei Range, within the Kazakhstan territory yield 147 Ma and 162 Ma with overlapping error bars. This coincides with the Dogger-Malm transition (Late Jurassic). These samples are hence slightly older than the Kungei samples. Samples from the Boom Canyon region, in the northwestern zone of the Issyk Kul basement are, on average, slightly younger and range from 113 Ma to 152 Ma. For the southern Issyk Kul basin boundary range, the Terzkey Range, AFT ages of about 60 Ma to 110 Ma were obtained. These are evidently younger than the ages from the basement to the north of the basin and point to a different thermal history for the northern and southern Issyk Kul basin flanks.

All Tien Shan samples show a manifest thermal influence and APAZ signature in their length data. Mean track lengths vary between 12.4 μm and 13.2 μm with most of the distributions being asymmetric and negatively skewed. This gives evidence for a complex thermal history. These observations corroborate those presented by Bullen (1999) and Bullen et al. (2001) and (2003) who studied the Kyrgyz Range, stretching out to the west of the Issyk Kul basin area. In contrast to these studies, no Late Cenozoic AFT ages were found in our samples. The active tectonic phase experienced by the Tien Shan since the Late Miocene must undoubtedly have uplifted the investigated area to its present high elevation, but it has not been accompanied by significant denudation in order to be registered by the AFT system. The younger ages for the Terzkey Range reflect a more important denudation of this range with respect to the northern Issyk Kul basement. AFT modelling in the next section will shed more light on this issue.

The age elevation plot of the study area (figure 6.10) exhibits a relatively distinct correlation, with decreasing ages for samples from lower altitudes. No break-in-slope can be recognized in the age elevation profiles. However some scatter in the Kungei and Boom Canyon samples is observed, particularly at lower elevations. Rock types and sample localities were on the other hand quite different and could account for possible variations in apatite composition. Yet an additional amount of scatter is present in the Terzkey profile with two outliers of higher apparent AFT age. It should be noted here that the apatite quality of all Terzkey samples was poor and track densities were low (table 6.1). Consequently this resulted in quite large uncertainties on the apparent AFT ages. This fact also influenced track length measurements as only one of the samples (TS-20) yielded sufficient confined tracks and was able to be modelled with the AFTSolve software.

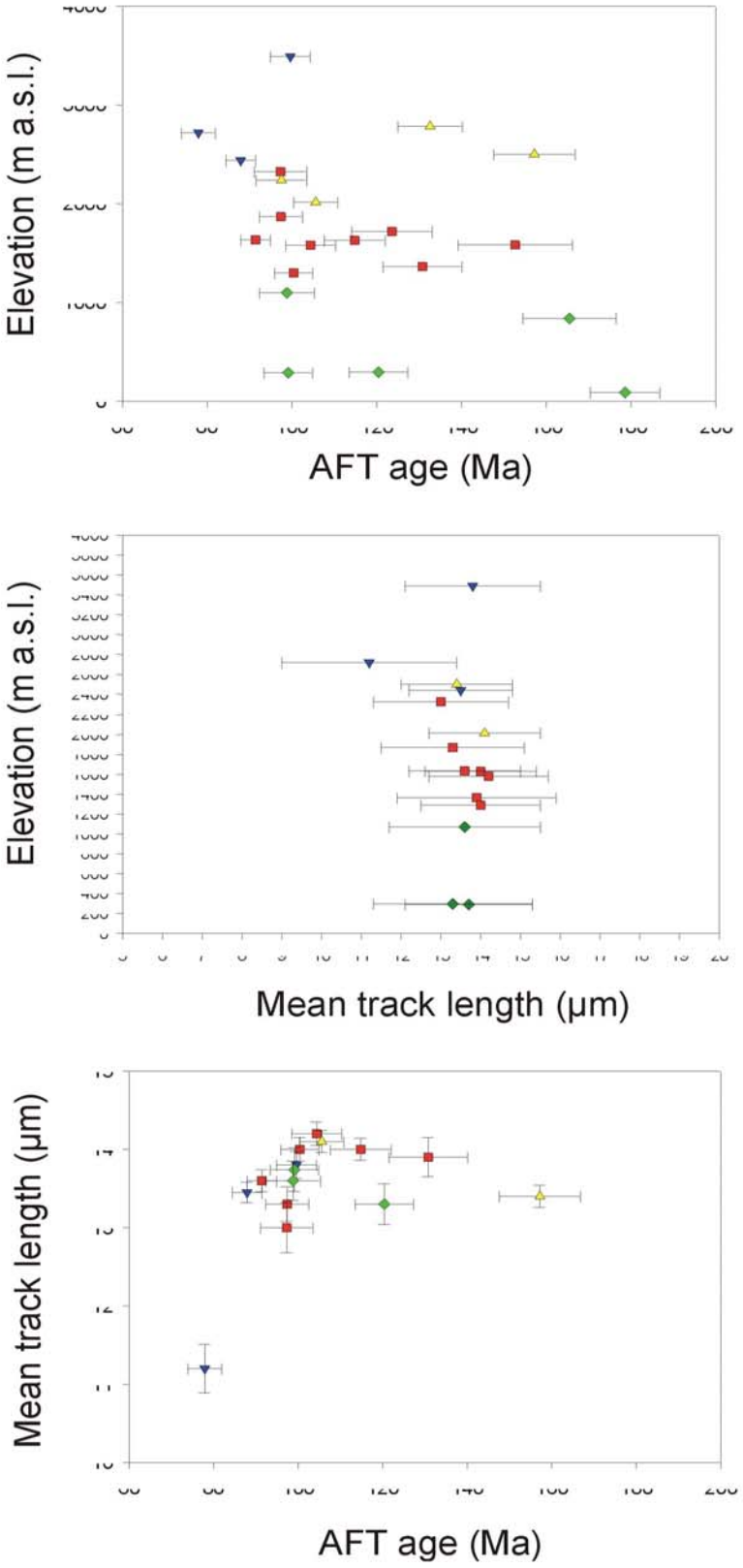

Figure 6.9: AFT age-elevation, AFT mean track length-elevation and AFT age-mean track length plots for the Altai samples, excluding the Teletskoye data. Legend as in figure 6.3.

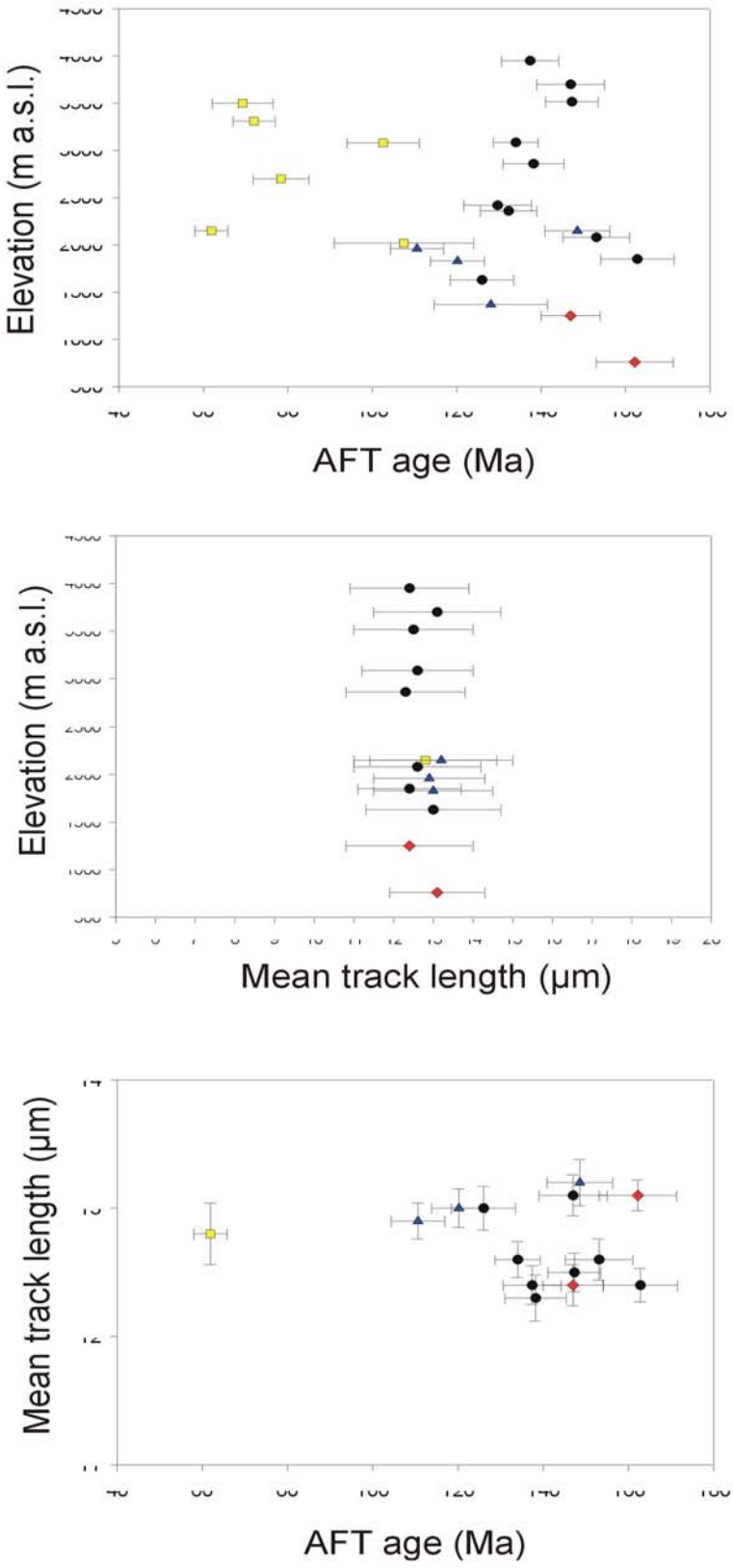

Figure 6.10: AFT age-elevation, AFT mean track length-elevation and AFT age-mean track length plots for the Tien Shan samples. Black circles: Kungei profile samples, yellow squares: Terzkey profile samples, blue triangles: Boom Canyon samples, red diamonds: Kindil Las samples.

The age-mean track length and age-standard deviation plots show clustering of the Kungei, Kindil Las and Boom data (representing the northern part of the Issyk Kul basement) and a marked isolation of the TS-20 (Terzkey Range, southern area) plot from these clusters. Of course, because of a lack of length data for the Terzkey samples, we can not say to what extent the isolation of this single sample represents the whole of the Terzkey sample set.

6.5. AFT thermochronology and modelling

6.5.1 General notes

On the basis of the AFT ages and the length data (table 6.1) a total of 50 samples were found to be suitable for AFT thermal history modelling. As discussed in section 2.5.7.4, the AFTSolve software (Ketcham et al., 2000) was used. This program allows the user to define the specific FT annealing model he or she prefers. The software was especially developed for use of a multi-kinetic annealing model based on D_{par} values or Cl-contents of the investigated apatites (Carlson et al., 1999; Donelick et al., 1999 and Ketcham et al., 1999). Because of lack of compositional data for our samples, we opted to apply the widely used Laslett et al. (1987) annealing model. This model is based on experimental annealing of Durango apatite, which has a Cl/(Cl + F) ratio of ~ 0.1. All samples were inversely modelled, i.e. the software generated thermal histories that produce a modelled AFT age and length distribution that are tested against the actual data. On the basis of the so-called Constrained Random Search (CRS) numerical technique by Willet (1997) cooling histories are iteratively generated and a particular misfit function is calculated between input and fitted data. On these grounds, the model is refined until a good fit between both modelled and observed data is attained. The misfit functions for age and length data are inspired by the so-called Kolmogorov-Smirnov (K-S) test. The thus obtained discrete good fits in the (t, T)-model space are presented as a good fit envelope and represent possible cooling histories that would produce the specific observed AFT data. From these discrete cooling paths the best fit solution is also highlighted.

In a first run the model was constrained by a present-day surface temperature of15°C, and by a high temperature starting interval, well above the 120°C isotherm (for the lower APAZ boundary) far enough back in time, i.e. predating the apparent AFT ages, and chosen around the Permo-Triassic (Altai) or Permian (Tien Shan). Geological evidence suggests the study areas have been affected by intense tectonic activity prior to that time. After the initial run, a general trend of the thermal history was usually observed, although age and length data were in most cases statistically badly fit. The general trend, however allowed defining additional (t, T)-constraints. These were uploaded in the model as broad temperature (T) intervals at a certain time (t) along which the model was still allowed to fluctuate. By adding constraints, and hence nodal points between the constraints, the model was refined until a good fit envelope was obtained. This trial-and-error strategy was repeated until the best fit model showed at least a 95% good fit between the observed and modelled AFT age as well as between the observed and modelled AFT length distribution. In the great majority of the cases, these thresholds were reached and even better fits were recorded.

Only in a small number of runs a 95% fit was not reached. Even in these cases we tried to model at least one of the data sets (age or length) with >95% probability. The results of all 50 individual models are presented in figure 6.11. In the following sections these models are discussed and interpreted within the regional geological framework.

6.5.2. AFT thermal history models from the Russian Altai Mountain samples

6.5.2.1. The Teletskoye region

The thermal history models for the Teletskoye region are depicted along with the models for the other study areas in the Russian Altai Mountains in figure 6.12. The models for the Teletskoye region are divided in a panel dealing with samples from the Altyntauss profile (TEL samples and AL 272), a panel for the Katayatsk profile (samples SH1-SH5) and one for the remaining Teletskoye samples.

Altyntauss profile

AFT modelling of the Altyntauss and Katayatsk profiles has been published earlier (De Grave and Van den haute, 2002), but as mentioned, refinement of the ζ-calibration factor led to corrected ζ-ages, on the basis of which new thermal history models have been generated. The Altyntauss models exhibit a fair deal of scatter, but still all show an adequately similar three-stage cooling history. The existing scatter can be interpreted as the uncertainty of the model. Still it does not obscure the underlying trend. If one considers the envelope of best fit solutions versus the good fit envelope of each individual sample (figure 6.11), not much difference can be seen. The three-stage cooling history started with a Late Mesozoic cooling event that brought the rocks quite rapidly into the APAZ. This first event is followed by a period of relative thermal stability, keeping the rocks within the APAZ temperature range. The modelled (t, T)-history is concluded with a young phase of rapid cooling during the Late-Neogene and Pleistogene. This agrees with the qualitative interpretation of the AFT data in the previous section. In the Late Mesozoic, the rocks were within the APAZ where they must have resided until relatively recently according to their low mean track lengths, the asymmetrical, negatively skewed distributions (figure 6.1) and the low frequency of long (> 14 μm) confined tracks. Taking into account the geological setting of the study area and the absence of geothermal activity in its Mesozoic and Cenozoic history, the two cooling events identified here are interpreted as denudation induced cooling.

For the Altyntauss profile, (t, T)-models from samples from higher altitudes pass through the APAZ sooner than the samples from lower altitudes (e.g. the passing of the 120°C isotherm at ~130 Ma for TEL 101 vs. ~95 Ma for TEL 112). The general cooling trend of the Altyntauss profile (figure 6.12a) shows an obvious Late Mesozoic cooling event that seems to have been active since at least 160 Ma ago (Late Jurassic Dogger-Malm transition). Between this time and about 100 Ma ago (Early Cretaceous Albian age) rocks from the Altyntauss granitoid massif were cooled down below 120°C.

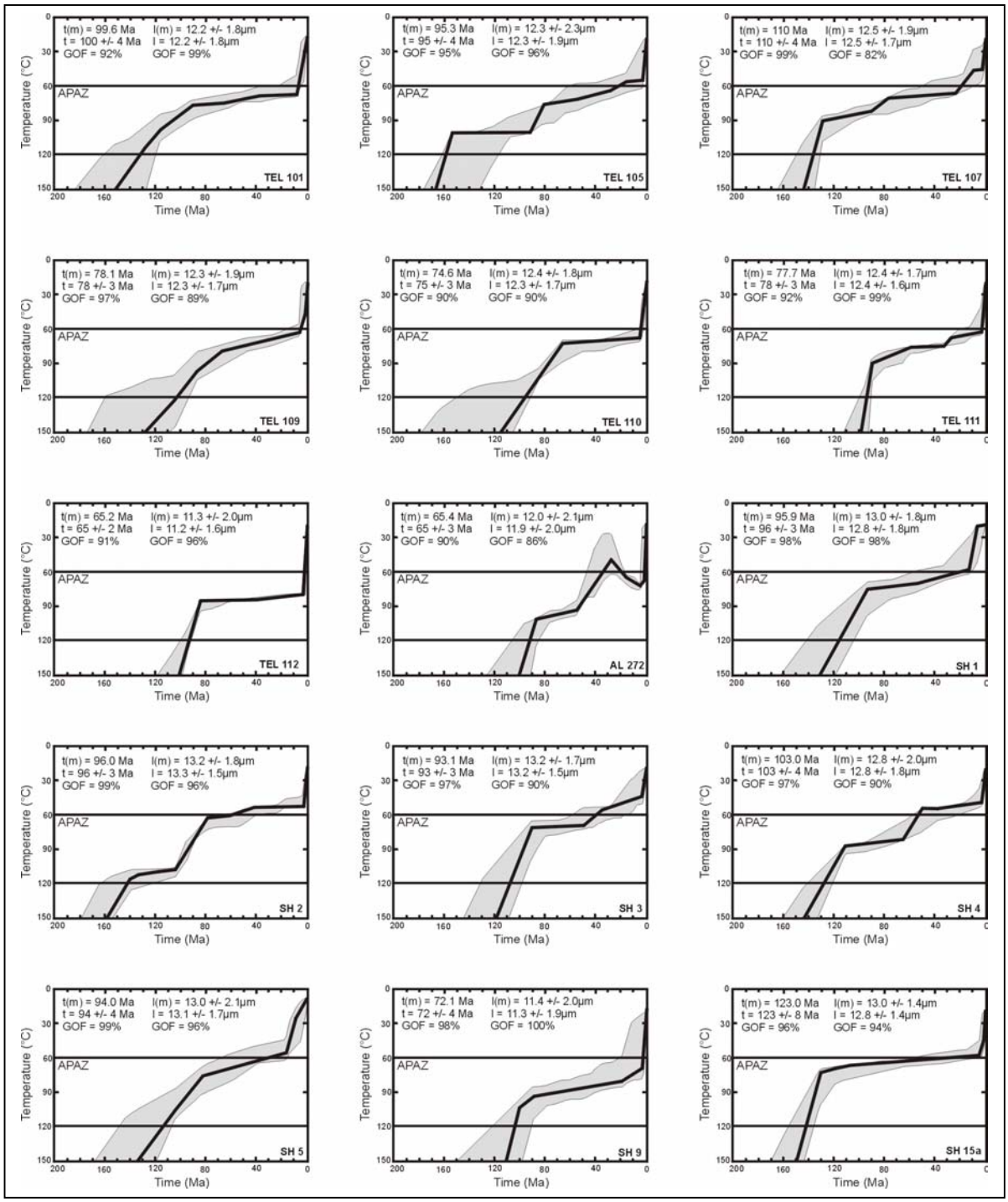

Figure 6.11: AFT (t, T)-paths for the Altai and Tien Shan samples. The models were obtained with the AFTSolve program (Ketcham et al., 2000) using the Laslett et al. (1987) annealing equations. Solid black lines represent best fit solutions, the gray envelope depicts good fit solutions. The fit (GOF = Goodness of fit) between modelled (subscript 'm') and observed AFT data is indicated.

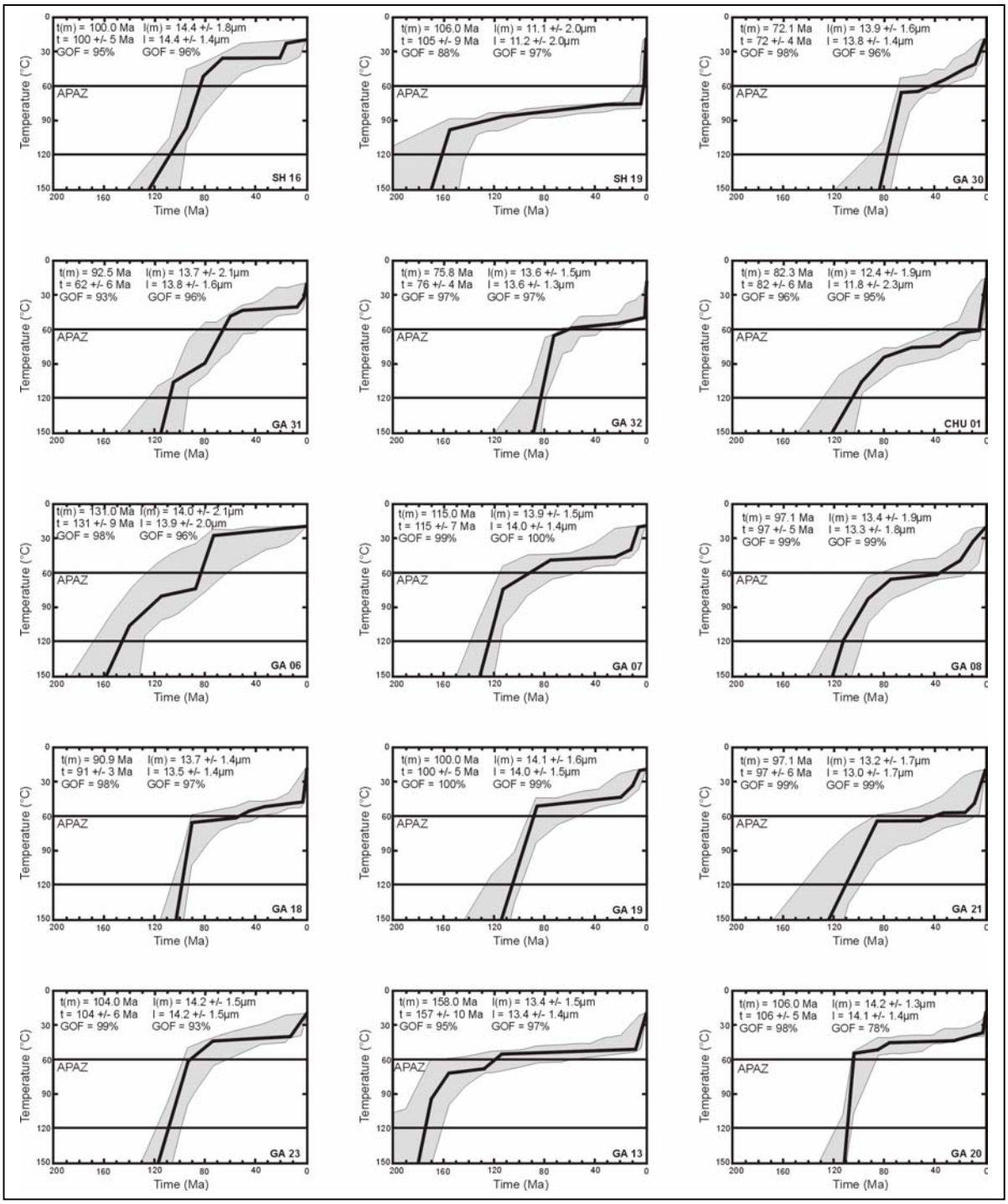

Figure 6.11 : Continued

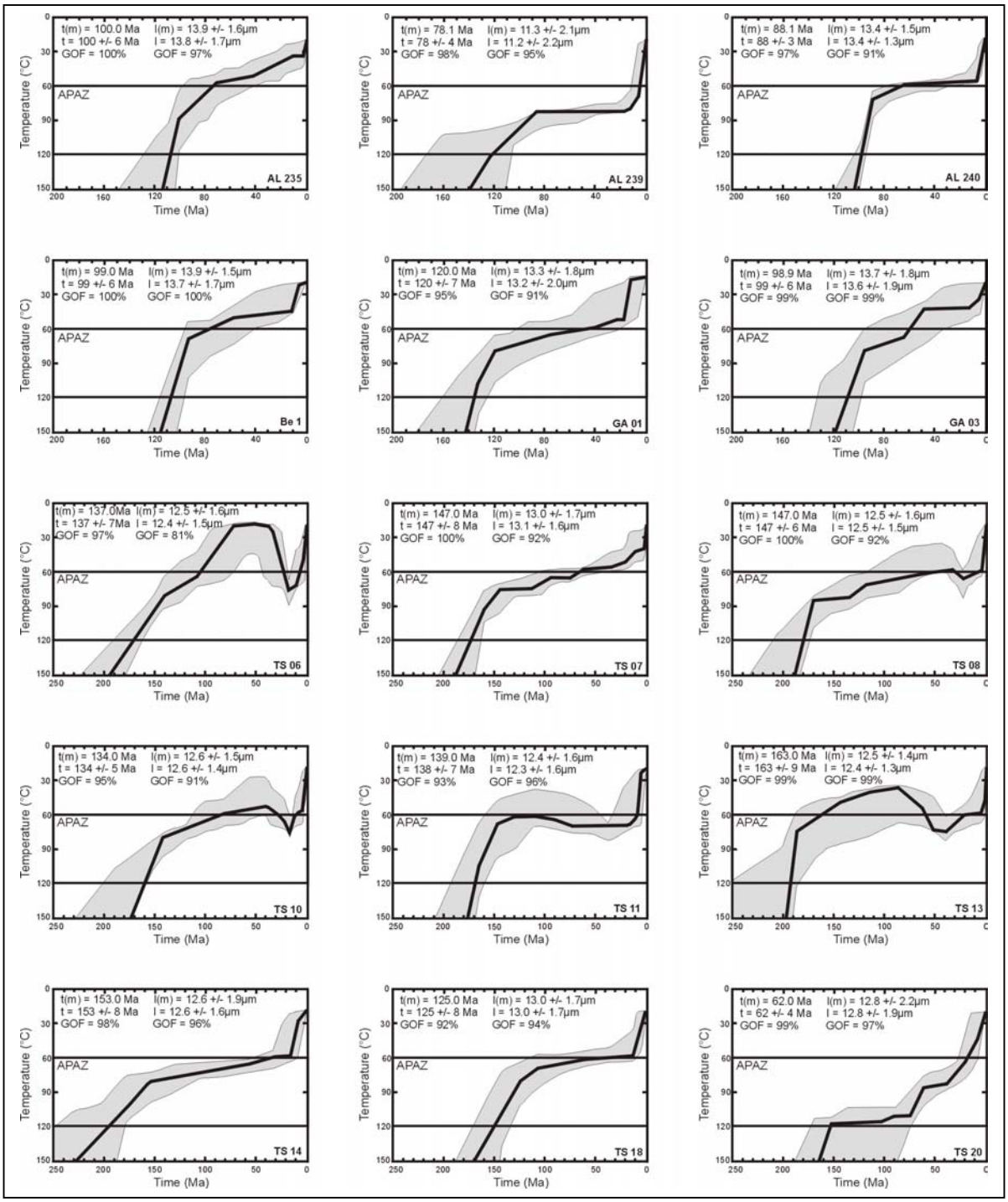

Figure 6.11 : Continued

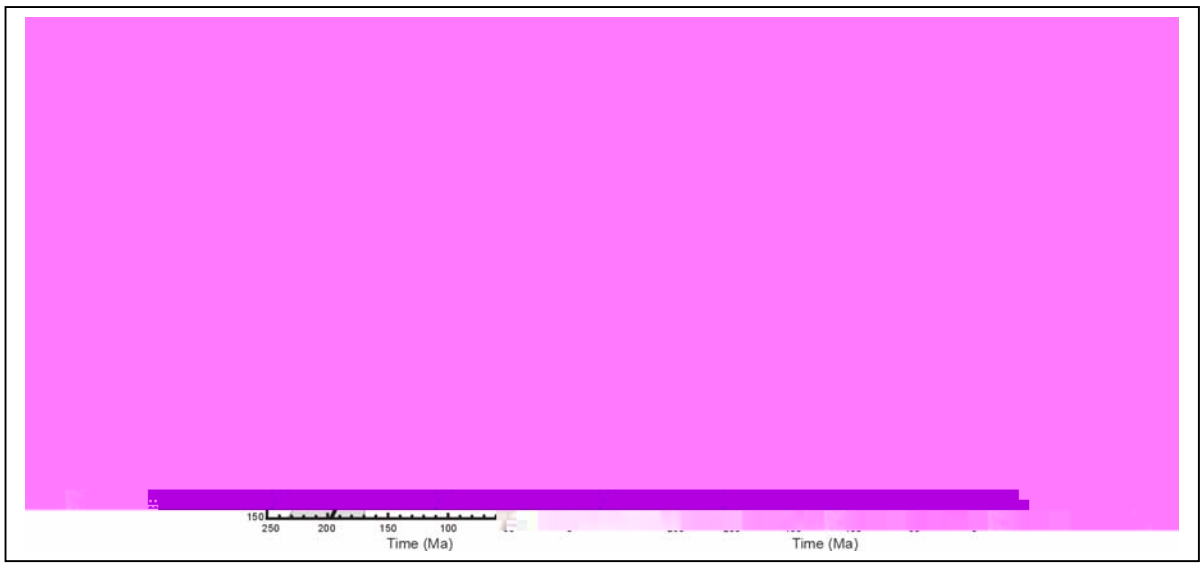

Figure 6.11 : Continued

The Late Mesozoic cooling event ended at around 85 to 90 Ma ago (early Late Cretaceous) and brought the rocks to temperatures of about 75°C to 100°C. Assuming a geothermal gradient of 25 to 30 °C/km, the Altyntauss granitoids were situated at a depth of 4.0 to 2.5 km. The Late Jurassic-Cretaceous cooling is followed by a period of relative quiescence with only a small amount of cooling taking place until onset of the second rapid cooling event at about 5 Ma (Pliocene). At the onset of the Pliocene cooling the Altyntauss rocks had reached an upper APAZ position around 50°C to 80°C, corresponding with a depth of 2 to 3 km. During the Pliocene to recent cooling event, the rocks were brought to ambient surface temperatures. When the latter event is investigated in detail (figure 6.13) it is observed that the most rapid cooling occurred in the last 2 Ma (Quaternary Period). The only exception to this cooling history is exhibited by the lowermost sample of the profile, AL 272. Its cooling history suggests it was cooled below APAZ temperatures by about 35 to 40 Ma ago and subsequently reheated to upper APAZ temperatures before onset of the Pliocene to Recent cooling (figure 6.13). Whether this reflects geological reality is doubtful. Nevertheless this cooling path gives a statistically better fit between observed and modelled data. When constraining the AL 272 cooling path to the overall trend as expressed by the other Altyntauss samples, the fit is worse (80%) but still acceptable. Therefore AL 272 does not contradict the general cooling history.

Katayatsk profile

The modelled (t, T)-paths for the Katayatsk profile (figure 6.12b) exhibit a smaller scatter and a similar general cooling trend as for the Altyntauss samples. In the Late Jurassic-Early Cretaceous (~140 Ma to 120 Ma), the Katayatsk rocks cooled down to APAZ temperatures. The Mesozoic cooling halted around 80 Ma to 90 Ma ago (early Late Cretaceous) at upper APAZ temperatures of 65°C to 85°C. For a geothermal gradient of 25-30°C/km, this would correspond to a depth of 3.4 to 2.2 km. During a subsequent long period of relative stability, the rocks slowly cooled to within the AFT Total Stability Zone (ATSZ) between 70 and 20 Ma ago.

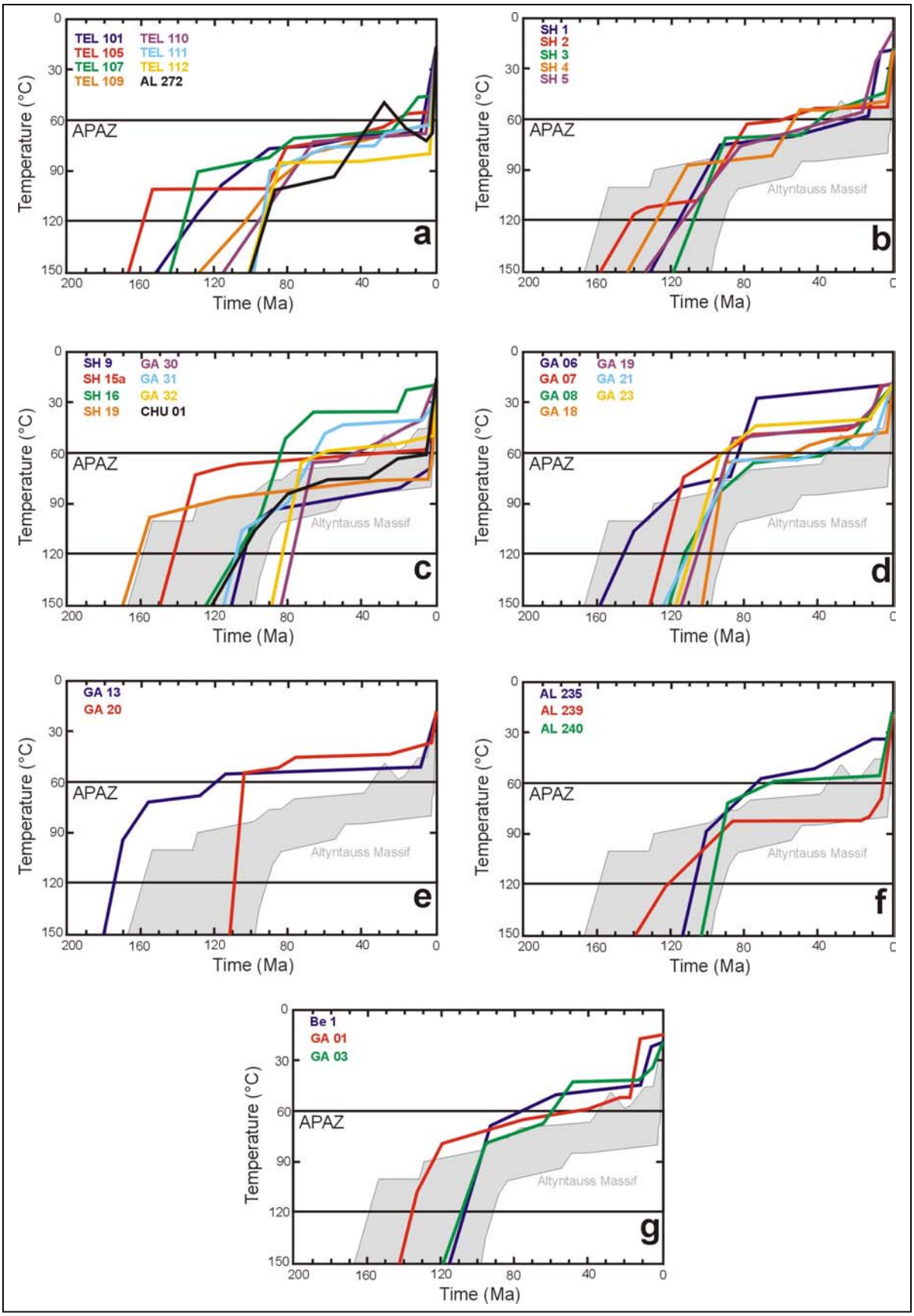

Figure 6.12: Best fit (t, T)-paths for the Altai samples. a: Altyntauss profile samples, b: Katayatsk profile samples, c: remaining Teletskoye Region samples, d: South Chulyshman Plateau samples, e: Dzhulukul samples, f: Chuya-Kurai samples, g: Western transect samples. The Altyntauss best fit envelope is shown in gray for reference.

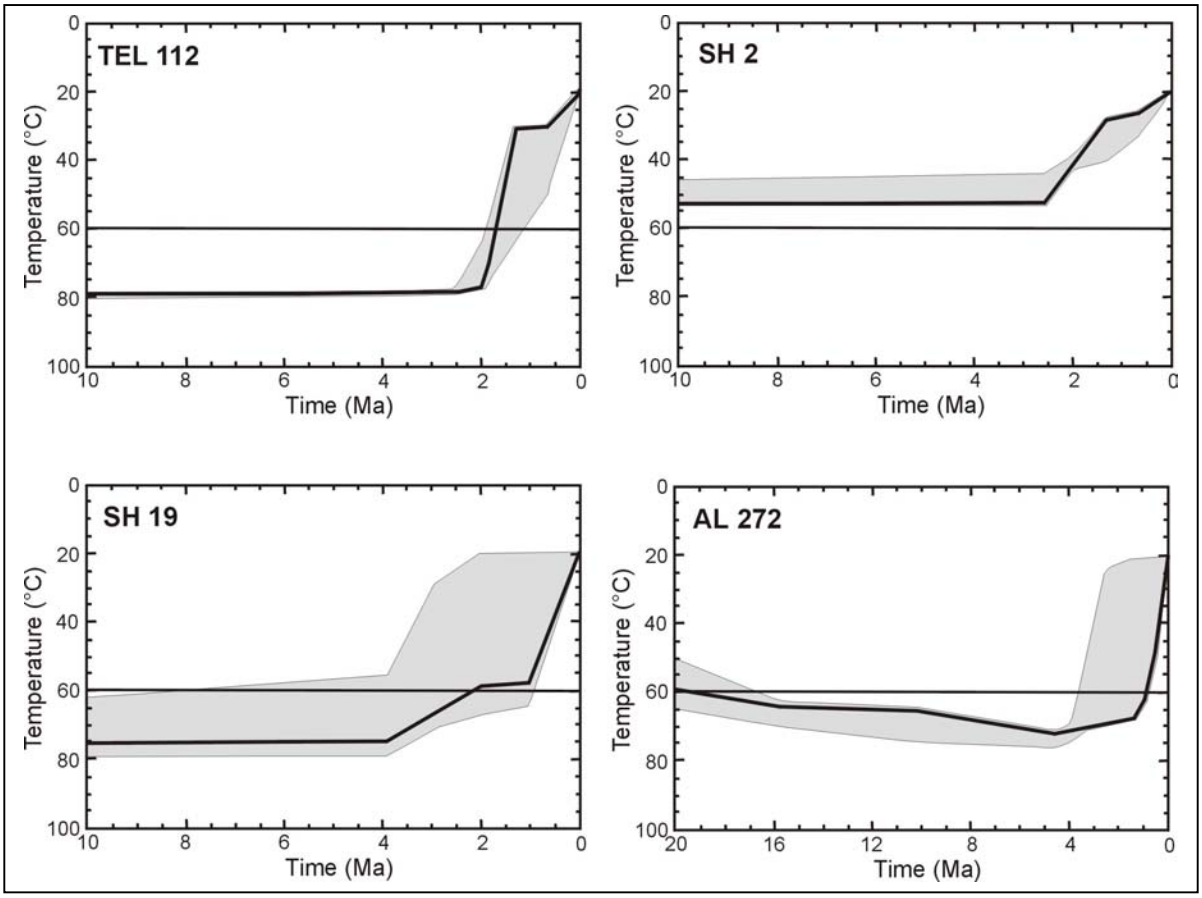

Figure 6.13: Detail of the Late Cenozoic thermal history of samples from the Russian Altai Mountains.

Finally, a Late Neogene to Recent rapid cooling brought the rocks from between ~60°C and 45°C (1.5 to 2.5 km depth) to their present ambient surface temperature. For SH 1 and SH 5 (the lowermost two samples of the profile) the young cooling event seems to have set in earlier, around 12 Ma ago (Late Miocene), while for the remaining samples the recent cooling is largely confined to the last 2 Ma (Quaternary).

The three stages in the cooling model of the Katayatsk profile are in good agreement with that of the Altyntauss profile, but compared to the latter, the Late Mesozoic event cooled the Katayatsk samples to lower temperatures. Hence, disregarding possible regional variation of the geothermal gradient and possible variation in apatite composition, the Mesozoic event brought the Katayatsk massif to shallower crustal depths. As a result, the Late Neogene-Quaternary cooling was less intense in this area in comparison to the Altyntauss samples.

Other Teletskoye Region samples

The thermal history models of the remaining samples from the basement exposed in the vicinity of the Teletskoye graben again show a significant scatter (figure 6.12c). SH 15a and SH 19 appear to define a common trend. SH 19 comes from a different structural domain as the other samples discussed in this section.

It was sampled from the Blyka granite complex in the inactive northern Altai foreland, north of the West Sayan fault zone (figure 5.2). Moreover, the departure of SH15a and SH19 from the common trend of the remaining samples seems to be limited to the Mesozoic event. For the young rapid cooling and the preceding slow cooling period they follow the general trend of the other samples. The Mesozoic cooling part of the curves does not differ much from the Altyntauss best fits envelope (figure 6.9). For SH 15a and SH 19, the Late Mesozoic cooling is evident in the models at about 145 Ma to 160 Ma ago when the modelled (t, T)-paths enter the APAZ. The cooling ended between 130 and 155 Ma ago and had cooled SH 19 to about 95°C and SH 15a to about 70°C. The rest of the samples in this group (chiefly from intermediate or low altitudes) seem to have been affected later by the Late Mesozoic cooling event. They reached the APAZ temperature limit of 120°C between 85 and 110 Ma ago (Middle to Late Cretaceous), roughly at the same time as the lower Altyntauss samples (figure 6.12a). At 70 to 75 Ma (Maastrichtian, Late Cretaceous), the cooling halted and the following period of stability or slow cooling kept this set of samples, as well as SH 15a and SH 19, at upper APAZ - lower ATSZ temperatures of 40°C to 80°C (1.3 to 3.2 km) until cooling in Late Neogene to Quaternary times. Except for sample SH 16, which seems to have been at low temperatures (~ 35°C) since the Late Mesozoic, the young rapid cooling is restricted to the Late Miocene-Pliocene to Recent with accelerated cooling taking place in the Quaternary, in the last 2 Ma (figure 6.13).

On the whole and bearing in mind possible regional variation of the geothermal gradient, apatite composition, differential structural patterns and its influence on denudation patterns, the modelled cooling paths for the Teletskoye Region show a similar general trend in timing and intensity of the cooling. An overview is given in table 6.2.

6.5.2.2. The South Chulyshman Plateau

The AFT thermal history models obtained for the samples from the South Chulyshman Plateau (figure 6.12d) also exhibit the three-stage cooling history as obtained for the Teletskoye samples. Excluding the somewhat deviating (t,T)-path of sample GA 06, the South Chulyshman samples display an analogous cooling history as the Katayatsk profile samples. Between 110 Ma and 130 Ma (Early Cretaceous) the Late Mesozoic event brought the rocks below 120°C. Rapid cooling persisted up to around 90 Ma when temperatures between 60°C and 80°C were reached at depths of about 2 to 3 km. Slow cooling lasted until the Late Neogene, at which time temperatures of 40°C to 50°C were reached. In contrast to the Teletskoye region in the north, the Late Neogene cooling in this area seems to have been active since 10 to 15 Ma (Late Miocene). A more intense pulse is noticeable during the last 2 to 4 Ma in samples GA 18 and GA 21.

In general it is also clear that at the end of the Mesozoic event, most samples were already at lower ATSZ temperatures in comparison to the samples from the Teletskoye area, which stayed within the APAZ longer. This implies that the Mesozoic event is more outspoken to the south of the Teletskoye Region and that hence the Neogene event is of relatively lesser importance.

Table 6.2: Overview and comparison of in the modelled thermal histories for the Russian Altai Mountains. T°C indicates sample temperatures within the crust.

Study Area	**Start Mesozoic cooling event**	**End Mesozoic cooling event**	**T°C at end of Mesozoic event**	**Start recent cooling event**	**Mesozoic cooling rate**	**Rate during slow cooling**	**Recent cooling rate**	**Mesozoic denudation**	**Recent denudation**
Altyntauss profile	100 – 160 Ma	85 – 95 Ma	75 – 100°C	2 – 5 Ma	1 – 4 °C/Ma	~ 0.25 °C/Ma	~ 10 °C/Ma	700-1800m	1300-2400m
Katayatsk profile	120 – 140 Ma	80 – 90 Ma	65 – 85°C	2 – 12 Ma	~ 2.5 °C/Ma	~ 0.3 °C/Ma	5–10 °C/Ma	1200-2400m	1000-1200m
Rest of Teletskoye	85 – 160 Ma	70 – 75 Ma	40 – 80°C	~ 2 Ma	~ 2.5 °C/Ma	< 0.1 °C/Ma	5–15 °C/Ma	1000-3200m	700-2400m
South Chulyshman	110 – 130 Ma	~ 90 Ma	60 – 80°C	15 – 5 Ma	~ 2 °C/Ma	~ 0.3 °C/Ma	3–10 °C/Ma	1300-2400m	1000-1200m
Dzhulukul Basin	175 – 115 Ma	~ 110 Ma	50 – 55°C	10 – 2 Ma	~2.5 - 7 °C/Ma	~ 0.1 °C/Ma	3–10 °C/Ma	~2500m	~ 1000 m
Chuya-Kurai area	100 – 120 Ma	80 – 90 Ma	60 – 80°C	10 – 5 Ma	~2.5 - 5 °C/Ma	~0.1-0.3°C/Ma	~ 5 °C/Ma	1500-2400m	800–2500m
Western transect	110 – 135 Ma	~ 95 Ma	70 – 80°C	~ 15 Ma	~ 2 °C/Ma	~0.2-0.4°C/Ma	~ 2.5 °C/Ma	~ 1500m	1000-1500m

As mentioned, GA 06, the lowermost of the South Chulyshman samples, shows a different (t, T)-path. Although a Late Mesozoic cooling event is prominent in the (t, T)-path, this event cooled the sample down from lower APAZ temperatures since 150 Ma ago (latest Jurassic) to near-surface temperatures around 70 Ma ago (latest Cretaceous). After the Late Mesozoic event, the sample only experienced slow cooling until the present. A young rapid cooling event is therefore not recorded.

6.5.2.3. The Dzhulukul Basin

Only two samples, GA 13 and GA 20, from the northern Dzhulukul Basin area (in the eastern part of the Russian Altai Mountains) were suitable for AFT thermal history modelling (figure 6.12e). The (t,T)-path of sample GA 13 from the Shapshal range, east of the important Shapshal fault, shows rapid Late Mesozoic cooling, passing the 120°C isotherm at about 175 Ma ago (the Early Dogger), and attaining upper APAZ temperatures 155 Ma ago (Dogger-Malm transition). GA 13 then experienced some additional cooling until ~115 Ma ago (Early Cretaceous) which finally brought the sample out of the APAZ to temperatures of 50 to 55°C. GA 20 on the other hand (west of the Shapshal fault) experienced an even more rapid Mesozoic cooling, which moved it through the entire APAZ to 50 to 55°C from 110 to 105 Ma ago (Early Cretaceous, Albian age). From that time on, both modelled (t, T)-paths show a period of thermal stability with slow cooling, lasting to about 8 Ma ago (Late Miocene) for GA 13 and to about 2 Ma ago for GA 20. Then a Late Neogene-Quaternary cooling event affected the area and brought the rocks to the surface. Thus the general trend of the modelled thermal histories in other parts of the Altai is also observed in the Dzhulukul Basin area. See table 6.2 for comparison.

6.5.2.4. The Chuya-Kurai area

Also the (t, T)-paths for the Chuya-Kurai samples exhibit the same general trend (figure 6.12f). Between 100 Ma and 120 Ma ago (Early Cretaceous) they entered the APAZ. This Late Mesozoic cooling terminated between 80 and 90 Ma at which time the samples were at temperatures of 60 to 80 °C, corresponding to a depth of 2 to 3 km when a geothermal gradient of 25 to 30 °C/km is assumed. Until about 10 Ma ago (Late Miocene) the samples were thermally more or less stable with AL 239 at ~80°C, AL 240 at ~55°C, and AL 235 cooling more from around 60°C to 40°C. Since ~ 10 Ma ago the region experienced rapid cooling, intensifying around 5 Ma (Pliocene), until present surface temperatures were reached.

6.5.2.5. The Western Transect samples

The three (t, T)-paths from the Western transect through Gorny Altai support the general thermal history derived from the other areas (figure 6.12g). Late Mesozoic cooling affected the samples as they cooled below 120°C at about 110 Ma to 135 Ma ago (Early Cretaceous). This cooling continued until about 95 Ma ago, at which time upper APAZ temperatures of 70 to 80°C were attained (2.3 to 3.2 km depth). Slow cooling during a subsequent episode of relative thermal stability brought the samples to temperatures just above the APAZ at depths of ~1.5 to 2 km. In the Late Miocene and Pliocene to recent times (starting 10 to 15 Ma ago), a new rapid cooling event to ambient surface temperatures was set in. Again, this recent cooling is seen to affect the area earlier than in the Teletskoye region.

6.5.2.6. The Altai cooling models: overview and conclusions

From this discussion and the overview presented in table 6.2, it appears that the Late Mesozoic and Cenozoic evolution of the upper crust in the Russian Altai region can be described by a three-stage cooling history. This confirms the conclusions of De Grave and Van den haute (2002) and extends them to a broader area. The three-stage cooling history starts with a Late Mesozoic rapid cooling, followed by a Late Cretaceous-Paleogene period of relative thermal stability, and concludes with a Late Neogene-Quaternary phase of renewed rapid cooling. The latter event is thought to be still active.

The Late Mesozoic event

Although some modelled (t, T)-paths deviate somewhat, the onset of the Late Mesozoic cooling event is recorded by the AFT thermochronometer between 160 Ma and 100 Ma ago, i.e. in the Late Jurassic-Early Cretaceous, when the temperature of the rocks from the investigated area dropped below the 120°C isotherm. Considering a geothermal gradient of 25 to 30 °C/km, this corresponds to the time at which the rocks attained a depth of about 4 km in the cust. The weak constraints on the timing of this event might be caused by differences in apatite composition, affecting annealing properties of the apatites, by regional variations of the Late Mesozoic palaeo-geothermal gradient, or by differential vertical movements occurring along inherited Palaeozoic faults. To some extent, the broad interval can also be caused by differences in elevation between the samples. Samples from higher elevations would have crossed the 120°C isotherm before those from lower elevations. The lowermost samples, Be-1 and GA-01 (table 5.1), are from the northern zone of the western transect through Gorny Altai, just where the active deformation front separates the Russian Altai Mountains from the Biya-Barnaul depression of the West Siberian Basin (figure 5.18). Their elevations are around 290 m a.s.l. The highest sample, AL 235 (table 5.1), is from the high Kurai range in the south of the Russian Altai Mountains, with an elevation of 3490 m a.s.l. Mostly, but not exclusively, the samples from higher altitudes show (t, T)-paths passing the 120°C isotherm earlier in geological time.

The earliest record of the Late Mesozoic event is registered by sample GA 13 that is from 2500 m altitude in the high Shapshal range near the Dzhulukul basin. It is also the most eastwardly located sample, and the only modelled sample east of the important Shapshal fault zone. It started cooling down to APAZ temperatures around 175 Ma (Lias-Dogger transition) (figure 6.12). The latest registration of the cooling is seen in the lowest basement areas (~ 430 m a.s.l.) directly bounding the Teletskoye graben. The (t, T)-paths of samples GA 30 and GA 32 (table 5.1) pass the 120°C isotherm around 85 Ma (early Late Cretaceous). Almost directly after that, between about 80 and 90 Ma, the Late Mesozoic cooling terminates according to the models. At that time rocks from the different study areas reached upper APAZ or lower ATSZ temperatures (table 6.2) with variations attributed to either local variation of the geothermal gradient, or to differential denudation rates in the various studied fault-bounded terranes. The ATSZ temperatures (~60°C) are reached at the end of the Late Mesozoic event for several samples to the south of the Teletskoye Region, in the more interior parts of the modern Altai orogen. The cooling rates associated with this event vary between ~1 °C/Ma and 7 °C/Ma, a value of 2.5 °C/Ma is most frequently registered.

The pre-120°C thermal history of the modelled samples is shown up to about 150°C but considering the annealing characteristics of apatite (total FT annealing above 120°C), this is merely a speculation. However, there are some constraints on the pre-Mesozoic thermal history of the rocks. In particular, $^{40}Ar/^{39}Ar$ data are available from the Teletskoye basement. Dehandschutter et al. (1997) presented biotite and hornblende $^{40}Ar/^{39}Ar$ ages from amphibolitic paragneisses of the Chiri series, which constitute the southeastern basement of the Teletskoye graben (section 5.1.2.1 and figure 5.7). This is also the apatite sample location of GA 30 and GA 32 that yield consistent (t, T)-paths (figure 6.12). Dehandschutter et al. (1997) obtained biotite $^{40}Ar/^{39}Ar$ ages of 380 ± 5 Ma (Middle Devonian) which they interpreted as post-metamorphic cooling of the gneisses after the Devonian collision event recognized in the whole of the Altai orogen and the emplacement of the Altyntauss granitoids which flank the Chiri gneisses (chapter 4 and 5). The closure temperature (T_C) for the biotite $^{40}Ar/^{39}Ar$ thermochronometer is 373 ± 21°C for grain sizes >500 µm (Berger and York, 1981) and at 310 ± 30°C for smaller grain sizes (McDougall and Harrison, 1988). Also a hornblende $^{40}Ar/^{39}Ar$ age of 260 ± 7 Ma (Late Rotliegendes Epoch, Late Permian) was found for the same rock sample from Chiri (Dehandschutter et al., 1997). The T_C for the hornblende $^{40}Ar/^{39}Ar$ system is about 490°C for a grain size of around 80 µm (Harrison, 1981) and up to 685 ± 53°C (Berger and York, 1981) for larger grains (> 210 µm). The Permian hornblende age was interpreted by the authors as a sign of tectonic reactivation and accompanying metamorphism in the area due to collision of Siberia and Kazakhstan and final closure of the Palaeo-Asian Ocean. This Permian event is widely recognized in the Altai Mountains and is discussed in chapter 4 and 5. It is worth noting here that this Permian tectonic and thermal event at about 260 Ma ago was used as an upper (t, T)-constraint for constructing the thermal history models of the Russian Altai Mountains. Figure 6.14 sketches the Late Palaeozoic to Recent thermal history of rocks in the Teletskoye basement. Considering the large-scale influence of the Middle-Devonian and Permian tectonic events, and the similar tectonic, lithological and structural indicators over the whole area, we are in favour of adopting this thermal model (figure 6.14) for the entire Russian Altai Mountains.

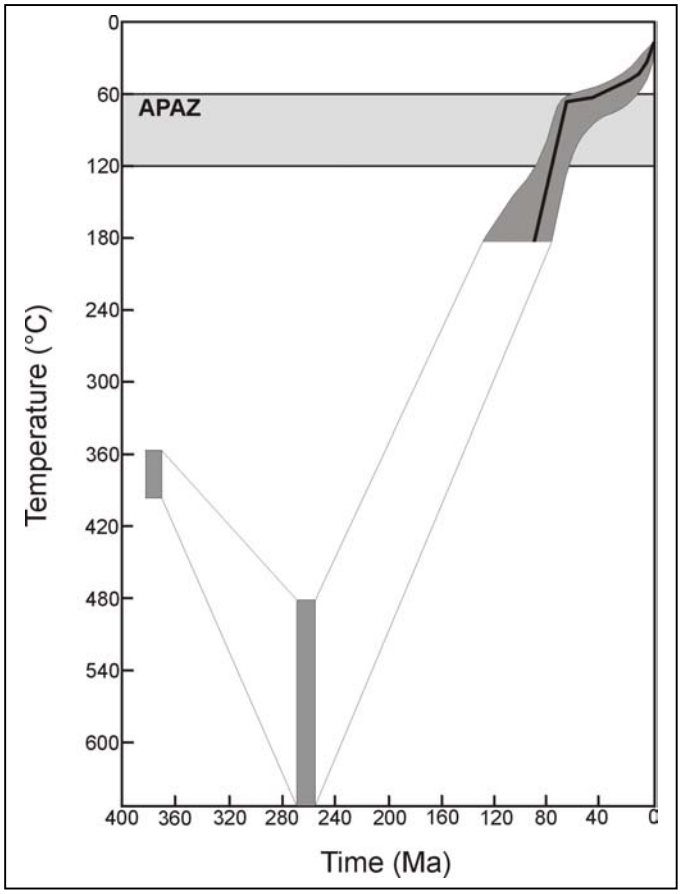

Figure 6.14: Thermal history model for the Teletskoye Region (Russian Altai Mountains) combining AFT and $^{40}Ar/^{39}Ar$ data.

The Late Cretaceous-Palaeogene slow cooling

Following the cessation of the Late Jurassic-Early Cretaceous cooling event, all the thermal history models in the Russian Altai reconstruct a period of relative thermal stability and slow cooling starting between 80 Ma and 90 Ma ago, and lasting until the onset of the Late Neogene-Pleistogene cooling. During this Late Cretaceous-Paleogene slow cooling period, the rocks from the studied areas cooled from upper APAZ temperatures (table 6.2) to upper APAZ or lower ATSZ temperatures of roughly 40 to 80°C at rates of about 0.1 to 0.3 °C/Ma, depending on the sample position within the rock column (higher elevation versus lower elevation at present).

The Late Neogene-Quaternary event

All samples with the exception of GA 06, record a Late Neogene-Pleistocene rapid cooling event. In the Teletskoye region, the event starts about 5 Ma ago (Pliocene), but it is most distinct, and in some cases only detectable for the last 2 Ma (Quaternary). In the other areas in the Russian Altai the event seems to set in earlier, between 10 Ma and 15 Ma ago (Late Miocene), but also here, some samples show an accelerated cooling during the Quaternary. The cooling event seems to have been quite rapid, with cooling rates generally between 5 and 10 °C/Ma (table 6.2).

In the Teletskoye Region this value is even exceeded, while for samples more to the south the event is less important and even absent in sample GA 06.

6.5.3. AFT Models from the Kyrgyz Tien Shan Mountain samples

6.5.3.1. The Kungei profile

The thermal histories for the Kyrgyz Tien Shan Mountains are depicted in figure 6.15. In the first panel the modelled cooling path for the samples from the Kungei profile are shown. Despite the scatter largely due to samples TS 06 and TS 13, a general four-stage model for the thermal history emerges. When we exclude the two aforementioned samples for the general discussion, the Kungei Range (t, T)-path envelope reveals a Mesozoic cooling, followed by a period of thermal stability, and a modest reheating event in the Late Cenozoic, immediately followed by a new young rapid cooling event (figure 6.15a).

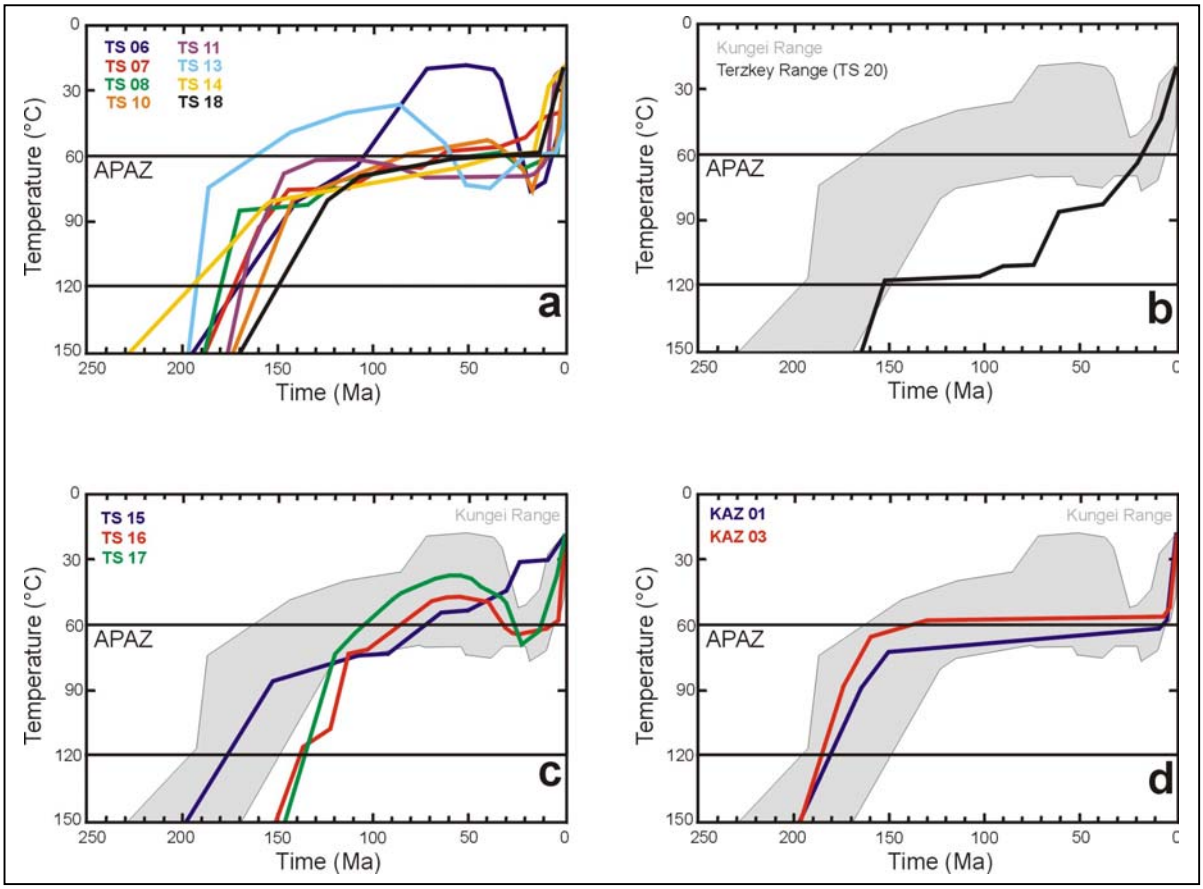

Figure 6.15: Best fit (t, T)-paths for the Tien Shan samples. a: Kungei profile samples, b: Terkey profile sample, c: Boom Canyon samples, d: Kindil Las samples. The Kungei best fit envelope is shown in gray for reference)

The Mesozoic cooling as registered by the AFT data, starts in the Early-Middle Jurassic between 150 Ma and 195 Ma ago (Lias-Dogger), when the modelled (t, T)-paths cross the 120°C isotherm and ended about 125 Ma ago (Early Cretaceous). It brought the samples to upper APAZ temperatures of 60 to 75 °C. Assuming a geothermal gradient of 25-30°C/km, this implies that the rocks resided at depths of 2 to 3 km. The rocks remained more or less at these temperatures and depths during a stable period, when only slow cooling occurred. This slow cooling lasted until about 40 Ma ago (Middle Eocene) when uppermost APAZ and lower ATSZ temperatures were reached and a modest reheating of the Kungei rocks seems to have taken place. This reheating, that lasted until about 20 Ma ago (Early Miocene) exposed the samples again to temperatures of about 75°C. Given the nature of this event and the geological setting of the sample area, we do not interpret this reheating event as the result of reburial, but of advection of heat. Finally, between 10 and 20 Ma ago the rocks were brought from upper APAZ to ambient surface temperatures by a Miocene to recent rapid cooling. A more detailed analysis (figure 6.16) shows that this event started about at 7 Ma (Late Miocene), and lasted until the present.

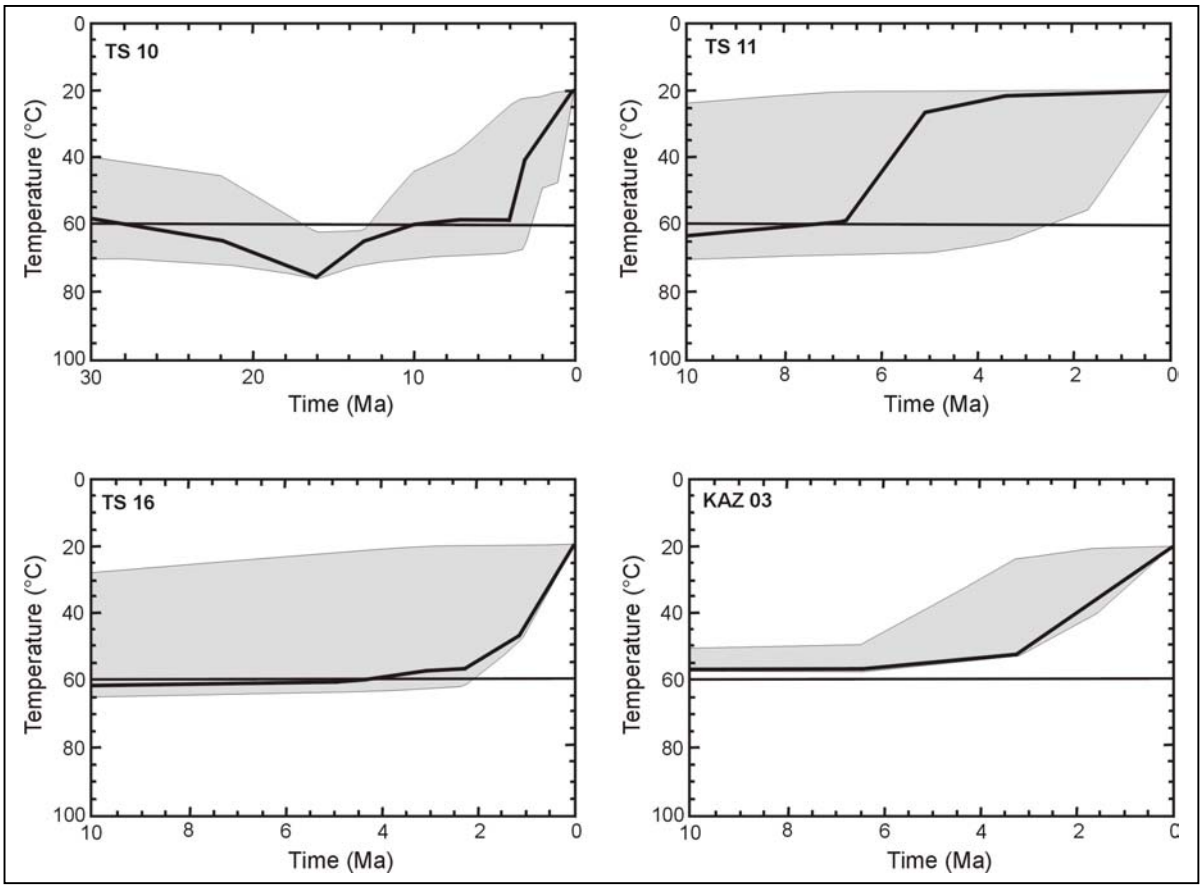

Figure 6.16: Detail of the Late Cenozoic thermal history of samples from the Kyrgyz Tien Shan Mountains.

Not all best-fitting (t, T)-paths register the reheating event clearly (e.g. TS 07, TS 14, TS 18). In some cases it is only when considering the good-fit envelopes (figure 6.11) that the event is recognized. Samples TS 06 and TS 13 represent the upper- and lowermost samples of the Kungei profile respectively. TS 06 from the top of the 'new Almaty road'-pass through the Kungei Range (near 4000 m altitude) is more affected by Mesozoic cooling and reached near-surface temperatures by the end of the Mesozoic (Cretaceous), 70 to 80 Ma ago (figure 6.15a). Before the reheating event from 40 to 20 Ma ago, the samples remained at near-surface temperatures during a stable period. Reheating was strong in comparison to the other Kungei samples, and TS 06 also attained temperatures of ~75°C before the onset of the Late Miocene cooling event. TS 13 reached lower temperatures after the Mesozoic cooling event. However, TS 13 (along with TS 14) was sampled in the Cemenovska region of the Kungei Range, several tens of kilometres eastward from the other Kungei profile samples (figure 5.21). Regional variation of the geothermal gradient, differential vertical movements along intervening faults or the apatite composition could have caused the deviating trend. The reheating event also seems to have affected TS 13 earlier in the other samples (figure 6.15a). This could be due to a time lag associated with regional variations of the geothermal gradient.

6.5.3.2. The Terzkey profile

Only sample TS-20 from the Terzkey Range contained sufficient confined tracks (54) for (t, T)-path modelling. Its thermal history differs significantly from the ones obtained from the Kungei Range (figure 6.15b). Because only TS 20 from the Terzkey Range was able to be modelled, we base this discussion on the good fit envelope of sample TS 20 as shown in figure 6.11. From this good fit envelope a general trend points toward a continuous cooling of sample TS 20, bringing the sample below 120°C between ~80 Ma to 90 Ma ago and lasting until the present. Between 10 and 20 Ma ago, the cooling accelerated somewhat. On the other hand, the best fit (t, T)-path (figure 6.15b) shows that ~150 Ma ago, the sample already entered the APAZ, but stayed close to the 120°C isotherm until ~70Ma ago, implying that the sample remained at around 3.5 to 4 km in the crust. If significant, the (t, T)-path barely reveals a Mesozoic cooling around 150 Ma ago (Early Malm; Late Jurassic), which is in agreement with the overall regional thermal history reconstructed by our models. According to the best fit (t, T)-path, TS 20 experienced a more or less stable thermal regime between 150 Ma and 70 Ma ago (Cretaceous). This is also to a large extent coeval with the slow cooling episode recognized in the Kungei (t, T)-paths. From about 70 Ma onwards, the best fit TS 20 cooling curve exhibits a trend of gradually increasing cooling rates lasting until the present, with, as mentioned, an accelerated cooling starting between 10 and 20 Ma ago. Contrary to the Kungei Range, the TS 20 sample from the Terzkey Range does not exhibit a Cenozoic reheating event. Although caution is required when interpreting just the single best fit (t, T)-path, the TS 20 best fit shows some similarities with the overall trend in the Kungei model, especially concerning the Mesozoic and Early Cenozoic. Nevertheless, it is evident that both ranges bordering the Issyk Kul Basin display quite a different cooling behaviour, as was already concluded from a qualitative description of the AFT data (section 6.4.3).

6.5.3.3. The Boom Canyon area

The samples from the Boom Canyon area, to the soutwest of the Kungei Range and northwest of the Terzkey Range, yield modelled (t, T)-paths closely resembling those of the Kungei samples (figure 6.15c). A Mesozoic cooling event is evident from the fact that the samples pass the 120°C isotherm between 150 Ma and 175 Ma ago (Dogger). Rapid Mesozoic cooling prevails until about 115 Ma ago (Aptian-Albian transition in the Early Cretaceous). The slow cooling recognized in the Kungei and Terzkey samples is less obvious for the Boom Canyon samples. Between about 115 Ma and 40 Ma, cooling is still distinct, but the rate drops in respect to the period between 175 Ma and 115 Ma ago. This constitutes an intermediate evolution between the forthright thermal quiescence seen in the Kungei (t, T)-paths (and the Kindil Las (t, T)-paths; section 6.5.3.4), and the quasi-constant cooling rate of the Terzkey Range during the Late Mesozoic-Early Cenozoic. Between passing the 120°C isotherm and the 115 Ma break-in-slope in the (t, T)-paths, the samples would have been exhumed from 4 km to about 3 km. Comparison of the cooling rates for the different episodes and regions is made in table 6.3.

After the less rapid cooling phase, the Boom Canyon samples show the same reheating event between 20 Ma – 40 Ma (Late Eocene-Early Miocene), as the Kungei Range. At the onset of the reheating the samples resided between the 40°C and 50°C isotherms. They were reheated to upper APAZ temperatures between 60 and 70°C. However, contrary to the others, the (t, T)-path for TS 15 does not indicate reheating. The modelled (t, T)-history of the Boom Canyon area is terminated by a young rapid cooling event, which immediately succeeds reheating. The cooling event starts around 10 to 15 Ma ago (Middle Miocene) and accelerates during the last 5 Ma (Pliocene and Quaternary) as seen in a detailed (t, T)-path section presented in figure 6.16.

6.5.3.4. The Kindil Las Range

Both (t, T)-paths of the Kindil Las samples are in excellent agreement with each other. Moreover, they are comparable to the general trend found for the Kungei samples (figure 6.15d).Their thermal histories consist out of three distinct phases. A Late Eocene-Early Miocene reheating event is absent.

As a result of Jurassic cooling event, the Kindil Las (t, T)-paths cross the 120°C isotherm between 180 Ma and 185 Ma ago (Toarcian, Late Lias). The event cooled the sampled rocks down to uppermost APAZ temperatures (65 – 75 °C) when it ended about 150 Ma ago (Tithonian, Early Malm), corresponding to depths of about 3 km. Subsequently a long phase of stability kept the rocks more or less at the same depth. It lasted until about 4 Ma to 6 Ma ago (Early Pliocene), when a new and still active episode of rapid cooling carried the Kindil Las rocks from about 60 °C to ambient surface temperatures.

Table 6.3: Overview and comparison of the modelled thermal histories of the Kyrgyz Tien Shan Mountains. T°C indicates sample temperatures within the crust.

Study Area	**Start Mesozoic cooling event**	**End Mesozoic cooling event**	**T°C at end of Mesoz.oic**	**Reheating event**	**Heating T°C**	**Start recent cooling event**	**Mesozoic cooling rate**	**Rate during slow cooling**	**Reheating rate**	**Recent cooling rate**	**Mesozoic denudation**	**Recent denudation**
Kungei	150-195 Ma	~125 Ma	60-75	20-40 Ma	~75 °C	10-20 Ma	1-2°C/Ma	0.1-0.2°C/Ma	~1°C/Ma	2-3°C/Ma	1500-2400m	2000-2500m
Terzkey	~150 Ma	~150 Ma	110-120	---	---	~35 Ma	---	0.1-0.2°C/Ma	---	~2°C/Ma	---	2200-2600m
Boom	150-175 Ma	~115 Ma	~75	20-40 Ma	~70°C	10-20 Ma	~1°C/Ma	~0.4°C/Ma	~1.5°C/Ma	2-3°C/Ma	1500-1800m	2200-1800m
Kindil Las	180-185 Ma	~150 Ma	65-75	---	---	4 – 6 Ma	1.5-2°C/Ma	~0.1°C/Ma	---	5-10°C/Ma	1500-2200m	1300-1800m

6.5.3.5. The Tien Shan cooling models: overview and conclusions

From the above discussion and the overview presented in table 6.3 and figure 6.15, it is evident that the Mesozoic and Cenozoic thermal evolution of the upper crust of the Issyk Kul basement in the Kyrgyz Tien Shan Mountains can be described by a three- or four stage (t, T)-path. It starts with a Jurassic-Early Cretaceous rapid cooling event, followed by a Cretaceous-Early Palaeogene period of relative thermal stability. The thermal history concludes with a Late Miocene-Quaternary and still active phase of renewed rapid cooling. A fourth feature, a Late Eocene-Early Miocene reheating event, is not expressed in all (t, T)-paths and seems to be confined to the northwestern Issyk Kul basement (Kungei Range and Boom Canyon area). Furthermore we can clearly distinguish a differential thermal history for the Kungei and Terzkey ranges that form the northern and southern border range of the Issyk Kul intramontane basin respectively.

The Jurassic-Early Cretaceous event

The Jurassic-Early Cretaceous cooling event is registered in all (t, T)-paths of the Issyk Kul basement samples. For the single modelled Terzkey Range sample (TS 20), the event, if significant at all (see earlier), might just have brought the rocks within the deeper APAZ (to 110-120°C). This occurred ~150 Ma ago (Lower Malm). For the other samples, the Jurassic event is recognized earlier, from 150 Ma to 195 Ma, thus spanning almost the entire Jurassic period. The exact timing depends on the specific sample location and elevation. Differential vertical displacements, variations of the geothermal gradient and apatite composition can in part account for differences between the (t, T)-paths. This cooling event seems to have terminated between 115 Ma and 150 Ma ago (Late Jurassic-Early Cretaceous). Except for the TS 20 sample, and the TS-06 sample, which attained ATSZ temperatures early in its thermal history, the Jurassic-Early Cretaceous cooling brought the samples to upper APAZ temperatures of 60 to 75°C, corresponding to a depth of 2 to 3 km in the crust if we assume a geothermal gradient of 25 to 30 °C/km.

The Cretaceous-Early Palaeogene stage of slow cooling

The Jurassic-Early Cretaceous cooling event is followed by a period of quasi-constant temperatures lasting from 150 Ma ago until about 40 Ma ago (Bartonian, Late Eocene). The slow cooling is expressed by nearly horizontal (t,T)-paths for most Kungei samples and the Kindil Las samples. Also the early part of the best fit (t, T)-path of the Terzkey sample (TS 20) conforms to this overall trend, while the later part is interrupted by rapid cooling starting between 60 and 70 Ma ago (Late Cretaceous). For the TS 06 sample from the Kungei profile (taken at the highest elevation of nearly 4000 m a.s.l.), the initial Jurassic-Early Cretaceous rapid cooling event lasted until 60 to 70 Ma ago, after which only a short period of stability is noticeable. In the Boom Canyon area, the Cretaceous-Early Palaeogene period actually corresponds to an episode of moderate cooling. It is delineated in figure 6.15c by a shoulder in the (t, T)-paths around 115 Ma ago (Late Aptian, Middle Cretaceous). The period of stability or moderate cooling abruptly ends ~40 Ma ago for most of the Kungei Range and Boom Canyon samples when they appear to have been exposed to a reheating pulse.

However, for some of these samples and the Kindil Las samples, the period of moderate cooling continued until the onset of a young episode of rapid cooling in the Late Miocene to Quaternary. At the end of the moderate cooling process the rocks were left at uppermost APAZ or lower ATSZ temperatures (with the exception of TS 06 which near-surface temperatures).

The Late Eocene-Early Miocene reheating event

As outlined, not all of the Kyrgyz Tien Shan samples contain evidence for this thermal feature in their modelled thermal histories, but for most of the Kungei and Boom Canyon samples, a modest reheating between 20 Ma and 40 Ma ago can be observed. It increased the temperature to shallow APAZ values (70 to 75°C). Three Kungei samples and one Boom Canyon sample do not clearly show evidence of the reheating. This is also the case for the Kindil Las samples that remained around the upper APAZ boundary for ~150 Ma. The Terzkey sample (TS 20) shows a different behaviour altogether. Instead of being reheated between 20 to 40 Ma ago, the TS 20 (t, T)-path shows a Cretaceous-Early Palaeogene stage of gradually increasing cooling.

The Late Miocene-Quaternary cooling event

Late Cenozoic cooling for the Terzkey Range hence seems to have started quite early. In the (t, T)-paths from all other samples from the Issyk Kul Basin region, Late Cenozoic rapid cooling is distinguishable from about 20 Ma (Early Miocene) onwards. In more detail (figures 6.13 and 6.16), most samples constrain the onset of the event between 10 and 20 Ma (Middle Miocene), directly following a reheating event that affected only the western Kungei Range and the Boom Canyon area. The late cooling becomes more outspoken between 5 and 10 Ma ago, and in some cases an increasing cooling rate can be seen during the last 5 Ma (Pliocene). The Kindil Las cooling paths exhibit the more rapid cooling only during the last 5 Ma. This could indicate that the Late Miocene-Quaternary cooling consisted out of several discrete steps and seemingly affected the region in a differentil fashion.

6.6. Geological interpretation of the AFT thermochronologic results

6.6.1. The Meso-Cenozoic thermotectonic history of the Russian Altai Mountains

6.6.1.1. The Late Jurassic-Early Cretaceous cooling event

Given the regional geological context, we interpret the Late Jurassic-Early Cretaceous cooling observed in the modelled thermal histories of the Russian Altai samples as the effect of a denudational event. The order of magnitude of the denudation ranges between about 1 and 3 km if we assume a geothermal gradient of 25-30°C/km (table 6.2). If we further consider the geothermal gradient to be constant throughout the region, local differences in denudation must be attributed to differential vertical block movements along bordering faults.

However, the denudation revealed by the AFT models, affected the whole of the studied region in more or less similar fashion. Hence a regional tectonic pulse must have occurred during the Late Jurassic-Early Cretaceous. This contradicts the traditional views of the Mesozoic inactive period in the Russian Altai Mountains (e.g. Buslov, 1998). After the Permo-Triassic Pangea assembly, resulting in a complete closure of the Palaeo-Asian Ocean, a Triassic tectonic quiescent episode is thought to have followed. Nevertheless, the Russian Altai Mountains at that time were bordered by two active regions: the rifting West Siberian Basin to the west and the developing Mongol-Okhotsk orogen to the east. In our opinion, a complex interaction of both the extensional tectonic regime to the west and the compressive tectonics in the east, resulted in a distal tectonic effect within the Russian Altai. The timing of this tectonically driven denudation is constrained by the AFT thermochronometer to the Late Jurassic-Early Cretaceous. However, since the AFT clock is only triggered when the rocks pass through the 120°C isotherm in the crust, the tectonic event may have been active before the Late Jurassic. This is suggested by the $^{40}Ar/^{39}Ar$ data of Dehandschutter et al. (1997) (figure 6.14).

The Late Jurassic-Early Cretaceous denudation is contemperaneous with the final stage of closure of the Mongol-Okhotsk Ocean that existed between the Siberian craton and a composite of the North China (Sino-Korean) craton with amalgamated Mongolian terranes (section 4.4.1). The Mongol-Okhotsk oceanic lithosphere was subducted underneath the southern Siberian orogenic rim during the Late Palaeozoic and Mesozoic. This is evidenced by the presence of large batholithic plutons (Zorin, 1999), exposed in the Khentai mountains (figure 4.1), and by the presence of cold subducted lithospheric slab segments (Van der Voo et al., 1999) in the area, ranging west of Lake Baikal all the way to the Sea of Okhotsk. Zorin (1999) argues that complete closure and ensuing collision of Siberia and North China was initiated at the Early-Middle Jurassic transition (Lias-Dogger, ~175-180 Ma ago). The collisional episode is thought to have lasted throughout the remainder of the Jurassic period until it ceased in the Early Cretaceous (~110-140 Ma ago). During this continent-continent collision, the Mongol-Okhotsk orogeny gave rise to an enormous mountain belt thought to have been similar in style and dimensions to the Himalayas (Xu et al., 1997; Zorin, 1999). Many authors argue that the consequent deformation associated with the orogeny was not confined to the collision zone proper, but also affected regions as far as the boundary of the Siberian cratonic core far in the hinterland (Ermikov, 1994; Zorin, 1999). Van der Beek et al. (1996) found that their AFT data and (t, T)-paths for the Transbaikal area reflected a clear signature of Late Jurassic-Early Cretaceous denudation, associated with the Mongol-Okhotsk orogeny (section 6.6.1.4).

The western edges of the Mongol-Okhotsk subduction and collision zone reach the eastern parts of the modern Altai Mountains in Mongolia and the Depression of the Great Lakes in Mongolia (figure 4.1). Considering the magnitude of the collision, and the fact that the deformation has affected an area far in the northern hinterland, we conclude that the denudation in the Russian part of the Altai Mountains is related to this event. Therefore, in our opinion the deformation associated with the collision affected an area to the west of the collision zone proper, reaching the present-day Russian Altai Mountains, where it induced considerable denudation of the area. This denudation corresponds with the Late Jurassic-Early Cretaceous cooling we observe in our AFT thermal history models.

This conclusion is supported by sedimentary evidence. The Altai Mountains are fringed by Late Mesozoic basins containing km-scale thick Jurassic clastic deposits (figure 4.5). The most important basins are situated to the south of the Altai orogen in the Zaisan-Junggar area, to the east in the Mongolian Great Lakes Depression, and to the north in the Biya-Barnaul part of the West Siberian Basin. In the latter area, basins formed in front of Kuznetsk-Alatau thrust that was active during the Jurassic. This also indicates that Mesozoic tectonic processes were active in the Altai region. Additionally, within the Altai Mountains Jurassic-Early Cretaceous fault-controlled intramontane basins developed. They were filled with continental (often lacustrine and coal bearing) sediments. These intramontane basins are quite abundant in the Mongolian part of the Altai (Dobretsov et al., 1996; Novikov, 2002), but are quite scarce in the Russian part (see the Jurassic basin close to the northern Erinat-Ulagan segment, figure 6.2).

The Jurassic sediments unconformably overlie Palaeozoic basement or remnants of a Triassic peneplain that developed during a period of quiescence following the assembly of Pangea. The Jurassic sedimentary sequence, up to 2 km thick in some of the intramontane depressions, contains two horizons of coarse molasse-type sediments (Dobretsov et al., 1996) indicating tectonically induced denudation of the orogen. The second of these pulses has been constrained to the Late Jurassic and to the Early Cretaceous. These pulses have also been distinguished in the larger adjacent basins, e.g. in the Zaisan-Junggar basins (Parnell et al., 1993).

Another piece of information that has to be taken into account is the fact that the Altai region was bordered by a system of continental rifts in the interior of the Mesozoic West Siberian Basin (section 4.4.2). During the entire Mesozoic and Early Cenozoic, the West Siberian Basin subsided and became infilled with kilometer thick deposits supplied by rivers draining the Palaeozoic orogenic rim of Siberia, including the Altai region. The rift system developed during incipient break-up of the Pangean supercontinent in Permo-Triassic times, almost directly succeeding the assembly of Pangea. In this phase the rift system was associated with the Siberian flood basalt province. The development of the basin implied a significant base level drop northwest of the Altai region; thus a part of the Late Jurassic-Early Cretaceous denudation could be accounted for in this manner. Nevertheless, in our opinion, the denudation was tectonically induced as indicated by the fault-controlled intramontane depressions, thrust related basins and molasse-type sediments. The Mongol-Okhotsk orogeny is the most plausible driving force of this tectonic reactivation.

6.6.1.2. The Late Cretaceous-Palaeogene episode of stability

In all AFT thermal history models obtained for the Altai samples, a distinct Late Cretaceous-Tertiary (onset ~80-90 Ma ago) period of stability (quasi constant temperature) is prominent, keeping most samples at upper APAZ-lower ATSZ temperatures. It coincides with a ubiquitous erosional lateritic Late Cretaceous-Palaeogene peneplain observed in many parts of Siberia and Central Asia (Ermikov, 1994; Deev, 1995; Delvaux et al., 1995a; Dobretsov et al., 1996; Vysotsky, 2001). The peneplain formed in a regime of long-lasting tectonic quiescence.

The temperatures reached by our modelled (t, T)-paths at the end of the Late Mesozoic tectonic activity were maintained during the peneplanation period during which thermal relaxation of the isotherms is assumed to have occurred. The slow cooling observed in the (t, T)-paths could have been associated with minor denudation of the exposed rocks, effectively keeping the investigated samples more or less at the position in the crust that they had reached after the Late Jurassic-Early Cretaceous denudation. Hence it is straightforward to interpret the period of stability or slow cooling as reflecting the stable and quiet tectonic regime during which the Siberian-Central Asian Late Cretaceous-Palaeogene peneplain developed.

6.6.1.3. The Late Neogene-Quaternary cooling

The (t, T)-paths of the Altai samples suggests a rapid cooling from Late Neogene-Quaternary age for the entire region. Given the evidence for recent tectonic reactivation of the Altai Mountains related to the ongoing convergence between India and Eurasia (sections 4.5.5.2 and 5.1.2.3), it is obvious to interpret the young cooling in terms of a Late Neogene-Quaternary denudation associated with this tectonic reactivation. Because most samples resided at lower ATSZ or upper APAZ temperatures at the end of the episode of thermal stability, a denudation of ~ 2 km has been estimated (table 6.2). Denudation of the growing orogen would consequently result in the upward movement and cooling of the rocks in the upper crust, as is seen in the AFT models. This interpretation corresponds well with the fact that reactivation in the Altai Mountains was initiated in the Late Neogene and intensified due to the transpressional tectonic movements in the Pliocene and Quaternary (Delvaux et al., 1995c; Cunningham et al., 1996a and 1996b; Dobretsov et al., 1996; Chlachula, 2001; Dehandschutter et al., 2002). Active tectonic indicators have been described for our entire area of study within the Russian Altai territory. Moreover, denudation as a result of this still active tectonism can also be inferred from the presence of several Late Cenozoic basins in the Altai region (figures 4.5, 4.14 and 4.15). The sediments filling these basins show several horizons of coarse clastics dating from the Late Neogene-Quaternary period.

The Late Neogene-Quaternary cooling event is more pronounced for samples from the Teletskoye area and samples from the northern part of the Russian Altai Mountains than for samples from regions more to the south (e.g. the South Chulyshman Plateau). Hence, the denudation of this area was of lesser proportions with respect to e.g. the Teletskoye area. A possible explanation for this observation is that the north of the present-day Altai Mountains (Teletskoye region) is the site of more intense denudation than the south. This can be expected as major rivers are shaping the present geomorphology of the northern part of the Altai Mountains. This northern part is widely dissected by these rivers. In particular for the Teletskoye region, the Teletskoye basin acts as an important local depression in which many smaller rivers are able to deposit their sediment load. The regions more to the south, like the South Chulyshman Plateau, have a plateau-morphology and dissection by rivers is much more limited.

The Cenozoic reactivation of the Altai Mountains is also demonstrated by the uplift, break-up, and displacement of remnants of the Late Cretaceous-Palaeogene peneplanation surface. In comparison to the low-lying inactive hinterland, remnants of the peneplain are vertically displaced by 2 km or more in some parts of the Russian Altai Mountains. Within the mountains, adjacent blocks capped with remnants of the lateritic peneplain show vertical offsets of several hundreds of meters relative to each other (figure 5.11). However, the fact that remnants of the Late Cretaceous-Palaeogene peneplanation surface are preserved puts an upper limit to the extent of denudation that can have taken place and on the magnitude of concomitant cooling. However, the preservation of the peneplanation surface is local and not regional (figure 5.10). This indicates that some of the uplifted blocks were indeed subjected to denudation. In addition, all samples were collected at the surface and along vertical profiles situated well below the estimated position of the planation surface.

To conclude, tectonic as well as sedimentary evidence indicates a Late Neogene-Quaternary episode of intense tectonic activity with rapid uplift and sedimentation. Although to some extent the AFT evidence may overestimate the amount of denudation associated with this event (section 2.5.2.2), the Late Neogene-Quaternary event itself and its timing are accurately reflected in the modelled (t, T)-paths. We hence interpret the young rapid cooling event as observed in the thermal history models of the Altai Mountains to be related to Late Neogene-Quaternary denudation in a transpressional tectonic regime that is still active today (Abdrakhmatov et al., 2002).

6.6.1.4. Related thermochronology studies

Except for our own preliminary data (De Grave and Van den haute, 2000 and 2002), no thermochronologic studies have been performed on samples from the Russian Altai region. However, some data from adjacent or related study areas are available.

The Baikal Region

The data and models by Van der Beek et al. (1996) and Van der Beek (1995) and (1997) suggest an Early Cretaceous (~120-140 Ma ago) rapid cooling of the regions northwest (Primorsky Range) and southeast (Khamar-Daban) of Lake Baikal as well as around the lake itself through the APAZ, followed by an episode of slow cooling that brought the samples from lower ATSZ temperatures to ambient surface temperatures. The (t, T)-model is interpreted as reflecting Early Cretaceous denudation associated with the Mongol-Okhotsk orogeny, followed by a period of stability corresponding to the development of a regional Late Cretaceous-Palaeogene peneplanation surface. This scenario corresponds well with the conclusions presented in our work. Yet there are differences concerning the intensity and exact timing of the Late Mesozoic cooling, and concerning the abscence of a young cooling event. In our (t, T)-paths the Mongol-Okhotsk orogenic event is seen to affect the Altai region earlier (in the Late Jurassic-Early Cretaceous ~100-160 Ma ago).

This can be understood as the result of the oblique Siberia-North China collision model, which involves a scissors-like closure of the Mongol-Okhotsk Ocean, starting in the west (closer to our study areas), and later on progressing eastwards, towards the Baikal region (Xu et al., 1997; Zorin, 1999). The AFT data by Van der Beek and co-workers indicate a stronger denudation, taking the samples through the entire APAZ during this single event, whereas in our models, most samples remain at upper APAZ temperatures up until the onset of the Late Neogene-Quaternary cooling event. This is clearly reflected by the AFT length data. In our work we found significantly shorter mean lengths, and hence a stronger thermal influence. This can be explained by the fact that the Baikal area is located closer to the collision zone and experienced a stronger tectonic effect of the orogeny. Consequently, denudation in the Baikal region would have been more intense and the rocks would have attained a more shallow position in the crust than in the Altai Mountain basement. In contrast to our results, Van der Beek et al. (1996) did not identify a Neogene-Quaternary cooling event. Although the authors used different annealing equations (Crowley et al., 1991) than in the present study (Laslett et al., 1987), it is unlikely that this would be responsible for the observed differences (Jonckheere, pers. comm.). We therefore conclude that the domino-reactivation of the CADZ (section 4.5.5 and Dobretsov et al., 1996) due to the continuing India-Eurasia convergence has reached the more northerly Baikal region later than the Altai region. The movements associated with this reactivation are younger and mainly limited to the Pliocene (Delvaux et al, 1997) whereas some of the reactivation in the Altai Mountains is recorded as early as in the Late Oligocene and Miocene. Probably the reactivation in the Baikal region is too young to be recorded by the AFT thermochronometer. Moreover, the young Cenozoic tectonic regime is completely different in that area. Where it is transpressional in the Altai Mountains, it is extensional in the Baikal Rift Zone.

The Urals

The Ural orogen bounds the West Siberian Basin to the west and marks the Pangean suture between the Siberian and East European cratons. The area experienced a strong collision during the Late Palaeozoic assembly of Pangea, involving them in the Variscan orogenic cycle that also affected many parts of Siberia, including the Altai region. AFT data and models from the Urals suggest that the orogen was subjected to denudation during the Late Devonian-Carboniferous (~300-350 Ma) and during the Permo-Triassic (~250 Ma) (Seward et al., 1997; Leech and Stockli, 2000; Glasmacher et al., 2002). The latter denudation phase represents the final stage of assembly of the Pangean supercontinent. The AFT data are supported by other thermochronological information obtained with the ZFT method (Seward et al., 1997) and the $^{40}Ar/^{39}Ar$ method (Beane and Connelly, 2000). The Hercynian evolution of the Urals corresponds quite well with the pre-Mesozoic history of the Altai region. However, in contrast to the Altai Mountains, the Urals were not reactivated during the Mesozoic or Cenozoic.

6.6.2. The Meso-Cenozoic thermotectonic history of the Kyrgyz Tien Shan Mountains

6.6.2.1. The Jurassic-Early Cretaceous cooling

Taking into account the regional geological and geodynamical setting of the Tien Shan Mountains, we interpret the Jurassic-Early Cretaceous cooling observed in the modelled AFT thermal histories for our Issyk-Kul region samples, to reflect a denudational event. If we assume a geothermal gradient of 25-30°C/km, the amount of denudation would be in the order of 1 to 3 km. The Late Mesozoic denudation (~150-195 Ma ago) in the Kyrgyz Tien Shan area predates the Late Mesozoic event (~100-160 Ma ago) that we registered in the Russian Altai region. This timing, together with the distance between the Tien Shan and the Mongol-Okhotsk orogen, makes it doubtful that both events are related. A more plausible tectonic driving force for the Late Mesozoic denudation of the Kyrgyz Tien Shan are the Mesozoic tectonics associated with the accretion of the Tibetan blocks onto the southern Eurasian continent, south of the Tarim microplate (sections 4.4.4 and 4.4.5). These blocks (the Qiangtang and Lhasa blocks) separated from Gondwana during an active rifting phase in the Permo-Triassic. Their northward drift progressively closed parts of the Tethyan oceanic basin (Tethys I and Tethys II) that existed between Gondwana and Eurasia (Liu and Einsele, 1994; Ricou, 1994; Acharyya, 1998; Mattern et al., 1998; Garzanti et al., 1999; Yin and Harrison, 2000). By the Middle Jurassic, Qiangtang had docked with the Eurasian active margin along the Jinsha suture. This was followed in the Late-Jurassic-Earlt Cretaceous by the collision of the Lhasa block (or mega-Lhasa) with Qiangtang and the southern Eurasian active margin along the Bangong-Nujiang suture zone (figure 4.7). These collisions, grouped as the Cimmeride orogeny, can be seen as a continuation of the Eurasian accretion tectonics, responsible for the Palaeozoic formation of the continent or as precursors to the major India-Eurasia collision in the Cenozoic. The main phase of the orogeny is constrained to the Dogger-Malm (Middle-Late Jurassic) transition (~150-160 Ma ago).

Deformation associated with the Qiangtang and Lhasa collisions affected the Eurasian hinterland to the north of the Tarim microplate, inducing fault movements in the Tien Shan region and even as far as the Junggar Basin (Allen et al., 1991b; Enkin et al., 1992; Hendrix et al., 1992; Allen et al., 1995; Otto, 1997; Allen et al., 2001) (figure 4.1). Thrusting at the Tarim and Junggar Basin edges caused the formation of a flexural foreland basin in those regions. Both basins were separated by the reactivated Tien Shan orogen, and km-thick, often coarse clastic deposits derived from the orogen accumulated in both basins (Chen et al., 1991; Allen and Vincent, 1997; Hendrix, 2000). During reactivation several intramontane basins filled with related sediments developed within the Tien Shan, such as the Turfan, Korla, and Fergana basins for example. Also the modern Issyk Kul basin seems to have a Jurassic precursor, as witnessed by pockets of preserved Jurassic deposits unconformably overlying the Palaeozoic Issyk Kul basement rocks (Cobbold et al., 1994).

In this context, we interpret the Jurassic-Early Cretaceous cooling observed in the AFT (t, T)-paths to reflect a phase of uplift and denudation of the Issyk Kul basement. We furthermore interpret this uplift and denudation to be a distant response to the Cimmeride orogeny and associated with the

collision of Qiangtang and Lhasa terranes, forming the present-day Tibetan Plateau, with the active southern Eurasian margin.

6.6.2.2. The Cretaceous-Early Palaeogene phase of thermal stability

After the Jurassic-Early Cretaceous event of rapid cooling, most modelled AFT (t, T)-paths from the Issyk Kul region samples exhibit a period of quasi-constant temperature or slow cooling lasting from about 115-150 Ma ago (Early-Middle Cretaceous) until about 40 Ma ago (Bartonian, Late Eocene). During this period, most of the samples resided at upper APAZ or ATSZ temperatures or at about 2 km depth. The slow cooling episode seen in the models corresponds with the timing of formation of a Cretaceous-Early Palaeogene red bed peneplanation surface. This surface is more or less contemperaneous with similar red beds found all over Central Asia and Siberia, including the Altai area (section 6.6.1.2). In the Kyrgyz Tien Shan, these red beds are known as the Kokturpak suite (e.g. Bazhenov, 1993; Cobbold et al., 1994; Sobel and Arnaud, 2000) (section 4.4.4). Except in some places where Jurassic pockets overlie the basement, the Kokturpak suite forms the base of the Issyk Kul Basin sediments. Like the Jurassic sediments, the Kokturpak red beds unconformably overlie the Palaeozoic basement. We therefore interpret the slow cooling stage as an episode of tectonic stability during which a regional peneplain developed and the basement rocks maintained there position within the crust at upper APAZ-lower ATSZ temperatures.

6.6.2.3. The Late Eocene-Early Miocene thermal event

A puzzling feature in the AFT thermal history models from the Issyk Kul area is the presence of a reheating event affecting only a part of the samples (Kungei Range and Boom Canyon area samples) from about 40 Ma until about 20 Ma (table 6.3). This reheating event brought the samples back to temperatures within the upper APAZ (70-75°C). Because the reheating only affected part of the samples, the cause is probably local and regional. Furthermore, because samples from the same tectonic or structural terrane (e.g. Kungei Range), show both affected and unaffected (t, T)-paths, we interpret this reheating phase as due to a thermal event of non-tectonic origin.

In several parts of the Chinese and the Kyrgyz Tien Shan, small volumes of basaltic rocks, primarily emplaced within Upper Mesozoic and Palaeogene sedimentary units, have been observed (Sobel and Arnaud, 2000). In the Issyk Kul Basin area, these rocks occur almost exclusively in the western Kungei and Boom Canyon area, where our models suggest the occurrence of a reheating event. The igneous rocks are intercalated in Palaeocene-Eocene sediments. Both stratigraphical and $^{40}Ar/^{39}Ar$ ages in the northern Issyk Kul area constrain their emplacement between ~ 20 Ma and 50 Ma (Sobel and Arnaud, 2000). This is in agreement with our modelled reheating event. Sobel and Arnaud (2000) interpret the occurrence of these rocks as evidence of a small thermal anomaly in the mantle beneath the Tien Shan. In their opinion, it is a trace of a small short-lived mantle-plume. Dobretsov et al. (1996) also addressed this issue, but they favoured a large, long-lived mantle plume, which does

not seem to agree with the small quantities of igneous rocks nor with the local thermal effect recorded by the AFT thermochronometer. An anomalous thermal structure of the Kyrgyz Tien Shan crust and mantle also fits with the model of Cenozoic deformation by the Indian indentation of the area proposed by Buslov et al. (submitted). Yin (2003) attributes these magmas to the existence of partially molten remnants of Mesozoic subducted slabs under the region that constituted the southern Eurasian active margin at that time.

Considering the arguments above, we interpret the Late Eocene-Early Miocene reheating event observed in the AFT (t, T)-paths for the Kungei and Boom Canyon samples as real and associated with the emplacement of basaltic and diabasic rocks at that time. Apparently a Late Eocene-Early Miocene increased geothermal gradient locally disturbed the isotherms and reheated the rocks sufficiently to be recorded in the AFT length data.

6.6.2.4. Late Miocene-Quaternary reactivation

The final stage in the thermal history of the Issyk Kul samples is a Late Cenozoic rapid cooling event, displayed by all individual (t, T)-paths, albeit with a different timing. The Terzkey (t, T)-path (only sample TS 20) shows accelerated cooling from the Early Oligocene onwards (~35 Ma), while most other (t, T)-paths exhibit a rapid cooling phase starting between 20 and 10 Ma ago. Still other models (e.g. the Kindil Las samples for example) detect the event from ~5 Ma (Pliocene) onwards, which is coeval with an intensified cooling discernable in most other models. Given the regional geological history (sections 4.5.5.1 and 5.6.2.2) we interpret this cooling as due to renewed uplift and denudation of the reactivated Tien Shan mountain belt.

The reactivation occurred in a mostly dextral transpressional tectonic regime induced by the ongoing convergence between India and Eurasia (Allen et al., 2001; Abdrakhmatov et al., 2002). The strain and resulting deformation produced by the collision changed dramatically around 20 Ma ago, marking a transition from extrusion (strike-slip) dominated deformation to crustal thickening (thrust) dominated deformation, immediately after large-scale strike-slip movements and eastward extrusion of Southeast Asian lithospheric segments. In the Early and Middle Miocene intense thrusting in the Himalyas and Tibet occurred. It is generally thought that in the Middle and Late Miocene also thrusting and reactivation commenced in the Tien Shan region (Allen et al., 1993 and 1994). The reactivation intensified in the Pliocene and is still active today (Cobbold et al., 1994; Searle, 1996; Reigber et al., 2001). In particular, the rigid and stable Tarim microplate transfers the strain and stresses, originating from the ongoing convergence of India and Eurasia, to the north towards the Tien Shan area (Burtman, 2000; Buslov et al., submitted). Further reactivation within the interior of the Eurasian plate may also be caused by this domino-effect. The rigid Junggar microplate north of the Tien Shan would in this scenario transfer the stresses further northward toward the Altai region (figure 4.13). This model explains the fact that the reactivation of intracontinental Eurasia becomes progressively younger when moving to the north. This is confirmed by our (t, T)-paths for the Altai

and Tien Shan region: while uplift and denudation occurs in the Tien Shan in the Middle Miocene, it is only evident in the Altai Mountains from the Pliocene onwards.

The present-day Tien Shan forms an effective physiographical boundary between the stable Tarim and Junggar plates, underlying the Tarim and Junggar Basins. The Tien Shan is thrust onto the northern margin of the Tarim Basin and onto the southern margin of the Junggar Basin. These basins act as Neogene flexural foreland basins, and, together with the intramontane Tien Shan basins (Fergana, Turfan, Korla, Issyk Kul basins etc.) outline the location where detrital material from the orogen is deposited. In particular, in the Issyk Kul basin, the Cretaceous-Paleogene red beds of the Kokturpak Suite are unconformably overlain by Oligocene-Miocene (Kyrgyz Suite), Pliocene (Issyk Kul Suite) and Plio-Pleistocene (Chapeldak Suite) sediments. Between and within these suites, erosional contacts and coarse molasse horizons bear witness to active mountain building processes during this period of time.

Besides by sedimentary evidence (Hendrix et al., 1992; Metivier and Gaudemer, 1997), geomorphological evidence (such as displaced Pleistocene glacial landforms and recent landslides; Tibaldi et al., 1997; Abdrakhmatov et al., 2002), and geodetic and seismic constraints (Abrakhmatov et al., 1996; Reigber et al., 2001), the Neogene to Quaternary reactivation of the Tien Shan has also been confirmed by other FT studies (Hendrix et al., 1994; Sobel and Dumitru, 1997; Bullen, 1999; Bullen et al., 2001 and 2003; section 6.6.2.5). We therefore conclude that themorphological expression of the Tien Shan started in the Oligocene, in particular since the Middle Miocene and continuing at present, as reflected by a phase of rapid cooling at the end of all the (t, T)-paths. We consequently interpreted this cooling as a denudational event related to the active mountain building in the region.

6.6.2.5. Related thermochronology studies

The Tien Shan area

Hendrix et al. (1994) performed an AFT study on 5 apatite samples from Mesozoic sandstones from the northern Tien Shan-Junggar Basin border in China. All the samples show evidence of thermal influence and have short mean track lengths between about 12 and 13 μm. A single sample showed an AFT provenance age of ~186 Ma (Early Jurassic), a little older than our Jurassic AFT ages. The other samples yielded ages of 20 to 25 Ma. The authors interpret these ages as reflecting the onset of Late Oligocene-Early Miocene unroofing of the reactivated Tien Shan orogen. This corresponds with the Miocene cooling that we observed in our modeled (t, T)-paths from the Issyk Kul area. These authors however did not calculate a thermal history model from their data.

Sobel and Dumitru (1997) investigated samples from sedimentary sections along the southern Tien Shan-Tarim boundary and in the Western Kunlun Mountains, southwest of the Tarim Basin. From their AFT data, especially for the Kunlun sections, the authors infer a denudation event occurring

150-200 Ma ago, in agreement with the Jurassic-Early Cretaceous cooling and denudation that we observed in the Kyrgyz Tien Shan. These authors also interpret these ages as evidence for a tectonic reactivation and denudation of the region due the docking of the Tibetan block, in particular the accretion of the Qiangtang block. Together with our data, this demonstrates that a large region was affected by these collisions (Cimmeride orogeny), including the Western Kunlun Mountains, the Tarim Basin, the southern Chinese Tien Shan and the Kyrgyz Tien Shan. The 186 Ma AFT provenance age obtained by Hendrix et al. (1994) indicates that the northern part of the Chinese Tien Shan was also affected. Sobel and Dumitru (1997) also concluded that the unroofing of the modern Tien Shan started ~20 Ma ago, marking a transition of deformation style in Central Asia from extrusion to thrust fault tectonics. These observations also correspond to the Miocene rapid cooling associated with denudation of the Kyrgyz Tien Shan inferred from our data. Recent $^{40}Ar/^{39}Ar$ data of Lee et al. (2003) show however that the eastward extrusion of Tibet along the Jiali strike-slip fault zone continued until Middle Miocene times (~ 18 to 12 Ma.

Sobel (2000) presented preliminary AFT data for sediments and basement rocks from the Kyrgyz and Chinese Tien Shan Mountains (Kyrgyz and Atbashi Range). His data exhibit three main AFT age clusters: one Jurassic (no details), one around 60-65 Ma (Late Cretaceous) and a last AFT age cluster between about 15 and 20 Ma (Miocene). Length data are scarce but show clear APAZ signatures with low mean track lengths. The Jurassic ages probably correspond with our AFT data obtained from the Kindil Las Range, Kungei Range and Boom Canyon area, while the Late Cretaceous ages correspond with the results we obtained for the Terzkey Range. But the Miocene ages reported by Sobel (2000) were not found in our samples. This timing does however correspond to the onset of uplift and denudation discernable in our (t, T)-paths. Therefore, on the whole, the AFT thermal histories we constructed for the Kyrgyz Tien Shan are in agreement with the data of Sobel (2000).

The Kyrgyz Range and adjoining Chu Basin, west of our study area in the Issyk Kul Basin region, were also studied by Bullen (1999) and Bullen et al. (2001) and (2003) by means of AFT (sedimentary and bedrock AFT data) and apatite (U/Th)-He thermochronology and magnetostratigraphy, although no AFT thermal history modelling was performed. From their data these authors inferred a Permian cooling event around ~260-270 Ma ago that is not registered by our samples. A Jurassic cooling event (~150-165 Ma) fits well with the Jurassic-Early Cretaceous denudation deduced from our Issyk Kul (t, T)-paths, although the authors do not ascribe the cooling they observed to a particular tectonic event. Between the Jurassic and the recent reactivation of the Tien Shan Mountains (between 165 and 11 Ma ago according to their data) Bullen et al. (2001) assume a period of slow cooling, corresponding to the Cretaceous-Early Palaeogene phase of peneplanation and red bed formation. However, the authors also find an apparent AFT age cluster between 50 and 80 Ma, which we also obtained for the Terzkey Range. By combining the use of the more sensitive apatite (U/Th)-He method with AFT data, the authors were able to constrain the onset of recent cooling of the Kyrgyz Tien Shan more precisely than is possible with the AFT thermochronometer alone. They found that exhumation of the Kyrgyz Range commenced around 11 Ma ago (Late Miocene), which is in agreement with our AFT (t, T)-paths.

Bullen (1999) present AFT length data from vertical profiles that are in good agreement with those presented in this work (figure 6.1 and 6.7). However, in their later article (Bullen et al., 2001) they omit the length data from their discussion. It is indeed not clear how their AFT age and length data relate to each other. Short mean track lengths of ~12 to 13 µm are seen for all samples regardless of their elevation, both in our work and in the work of Bullen (1999) and Bullen et al. (2001). An elevation profile spanning at least 2 km, might be expected to yield an uplifted APAZ signature with a break in slope in the AFT age-elevation plot. This is however not the case. A possible explanation is that the differences in topographic elevation are more due to block tilting or step-faulting than to denudation. This implies that a vertical sampling profile is not perpendicular, and may even stand at low angles to the palaeo-isotherms. Our (t, T)-paths show that a reheating event between 20 and 40 Ma can also explain the AFT data. Moreover, reheating (both in terms of space and time) is geologically well-documented. In our opinion, the AFT data of Bullen (1999) are in agreement with a Cenozoic reheating event if they had been modelled. In that case the AFT data set of Bullen (1999) and Bullen et al. (2001) for the Kyrgyz Tien Shan would be similar to the one presented in this work (Jurassic cooling, Cretaceous-Palaeogene peneplanation, local reheating and Miocene rapid cooling).

Preliminary FT data by Schwab et al. (2000) from the Pamir-Tien Shan connection, shows very rapid Late Miocene cooling, corresponding to fast exhumation supported by geological evidence (Searle et al., 1999a).

The Tibetan Plateau and adjacent regions

Several AFT studies have been carried out in Tibet and the adjacent mountain belts. Copeland et al. (1987) studied the granodiorites from the Gangdese batholith, north of the Indus-Zangbo suture zone (IZSZ) in the Lhasa tectonic terrane by means of AFT and $^{40}Ar/^{39}Ar$ thermochronology. As mentioned before (section 4.5.2), the Gangdese or Transhimalayan batholith is a remnant of the southern Eurasian active margin during Tethyan subduction and Indian collision at the Meso-Cenozoic transition. The Ar-ages cluster around 40 Ma and are interpreted as crystallization ages of the batholith, while an apparent AFT age of about 10 Ma was obtained. Copeland et al. (1987) suggest rapid exhumation of the batholith between 17 and 20 Ma ago. This was confirmed by Pan et al. (1993) who studied the same area by means of $^{40}Ar/^{39}Ar$ and AFT analyses. These authors obtained young apparent AFT ages of ~3 to 5 Ma that give evidence of a recent rapid cooling that started in the Late Miocene according to their $^{40}Ar/^{39}Ar$ data. These results were also supported by Copeland et al. (1995). Yang et al. (1999) also obtained Ar, ZFT and AFT data from the Lhasa area. They found that the <20 Ma event only affected the southern part of the batholith. More to the north they found that the most important Cenozoic cooling occurred between 40 Ma and 15 Ma ago. Even more to the south of this region, just across the IZSZ, metamorphic core complexes (domes) are exposed and are linked to rapid tectonic exhumation that occurred during Late Miocene-Pliocene extension, possibly related to gravitational collapse of the Tibetan Plateau (section 4.5.3). Lee et al. (2000) determined Ar- and AFT ages for the Kangmar dome. Their data indicate a rapid tectonic unroofing of the area between 11 and 5.5 Ma ago.

Lewis (1990) studied the Kunlun batholith in northern Tibet with various isotopic techniques, including AFT analysis. She concluded that the area was subjected to Late Mesozoic cooling around ~120 Ma (Early Cretaceous), which in our opinion, is related to denudation associated with Late Mesozoic accretion tectonics. Furthermore her AFT data point to a Late Cenozoic cooling between 8 and 20 Ma. These ages are interpreted to date the uplift of the Tibetan Plateau, and are in agreement with $^{40}Ar/^{39}Ar$ ages obtained by Mock et al. (1999).

The same thermotectonic history is found for the eastern part of the Tibetan Plateau, near the Longmen Shan Mountains, east of the Qaidam Basin. Arne et al. (1997), using $^{40}Ar/^{39}Ar$, ZFT and AFT analyses, found that significant Mid-Tertiary cooling affected the area between ~38 and 10 Ma ago. AFT modelling suggests slow cooling during the Late Mesozoic-Early Cenozoic, and rapid cooling starting ~20 Ma ago. The same region was studied (ZFT and AFT) more extensively by Xu and Kamp (2000). Their data confirm those of Arne et al. (1997) and give more detail about the < 20 Ma cooling phase. Xu and Kamp (2000) divide the Late Cenozoic cooling in three distinct phases, occurring respectively 22 Ma, 7 Ma and 2 Ma ago. Jolivet et al. (1999) studied the Altun Shan or Altyn Shan Mountains, on the eastern Tibetan Plateau, north of the Qaidam Basin. They found slow cooling between about 120 Ma and 10 Ma ago. Subsequently a rapid cooling event brought their samples from upper APAZ temperatures to ambient surface temperatures. Later, Jolivet et al. (2001) identified an Early Mesozoic phase of rapid cooling by applying the ZFT technique. Late Oligocene-Early Miocene rapid cooling was recorded by their AFT data and again confirm the ~20 Ma phase of rapid cooling and denudation across most parts of the Tibetan Plateau.

These FT results define an overall trend that is observed in the entire Central Asian region. Early Mesozoic cooling is interpreted as the consequence of Tibetan accretion onto the Eurasian continent, while Late Mesozoic-Early Cenozoic slow cooling can be interpreted to reflect lateral movements induced by the Indian indentation into Eurasia: this is the period of large-scale strike-slip movements and escape tectonics. Around 20 Ma ago the deformation regime changed drastically. Thrust tectonics dominate after this period and vertical movements become more important. Denudation and consequent cooling of the crust is associated with these movements and is recorded by the AFT system. The deformation propagated northwards and affected the Tien Shan between 10 and 20 Ma ago, while it reached the Altai only later.

The Himalayan orogen

Zeitler et al. (1982) presented one of the first FT studies performed in the Himalayas (Main Mantle Thrust), including apatite, zircon and sphene analyses. Their data suggests differential Cenozoic cooling on both sides of the thrust prior to 15 Ma ago, while from 15 Ma onward the entire region experienced rapid cooling. These results were later confirmed by Zeitler (1985). The latter paper also reports on FT data from the Himalayan Nanga Parbat syntaxis. These data confirm the very recent (Pliocene-Quaternary) uplift and exhumation of this part of the Himalayan orogen. This is also confirmed by Chamberlain et al. (1991) and by a limited dataset published by Carpéna and

Rutkiewicz (1989). The latter paper concentrates mainly on ZFT data, which, like the ZFT data of Cerveney et al. (1989), yield Late Mesozoic-Early Cenozoic ages. These reflect the higher temperature history of India-Eurasia collision. Sorkhabi (1993) reviews these data and reconstructs the thermal history of the northwestern Himalaya and the Kohistan-Karakoram region. The author infers a rapid cooling from the Early Miocene onwards, with an increase of the cooling rate during the last ~ 5 Ma (Pliocene). This very rapid Pliocene cooling is supported by later FT publications (Foster et al., 1994) and is interpreted to reflect rapid uplift-induced denudation of the area. Leland et al. (1998) have shown that this process is still continuing in recent times. Recently, the Late Oligocene-Early Miocene ZFT ages in the area were confirmed in a study of Khattak et al. (2001).

Miocene and Pliocene cooling and denudation have been found for other parts of the Himalayan orogen as well. For example, Guillot et al. (1994) reported on $^{40}Ar/^{39}Ar$ cooling ages of 16 to 19 Ma of a leucogranitic pluton from the Crystalline Himalayan Sequence, close to the South Tibetan Detachment Zone. Burg et al. (1998) use several isotopic techniques, including AFT analysis, to establish a Pliocene rapid cooling and denudation of the Namche Barwa syntaxis (the eastern Himalayan syntaxis). Searle et al. (1996a and 1999b) obtained Late Miocene ZFT ages and Pliocene AFT ages from the western Himalayas (Garhwal Himalayas). They infer an extremely rapid exhumation and cooling in the area between 21 and 23 Ma ago (Early Miocene), bringing the rocks to temperatures of ~300°C. The ZFT and AFT data suggest a stage of less rapid cooling for the remainder of the Miocene. For the last 1 Ma they deduce a stage of rapid erosion. Stüwe and Foster (2001) report $^{40}Ar/^{39}Ar$ and AFT data from the Bhutan Himalaya and also find Late Miocene and Pliocene cooling.

CHAPTER 7

GENERAL CONCLUSIONS

7.1. Method and calibration

In this work the low-temperature thermochronologic history of the Russian Altai Mountains (South Siberia, Russia) and the Tien Shan Mountains (Kyrgyzstan, Central Asia) was reconstructed on the basis of apatite fission-track (AFT) analysis. This analysis included fission track (FT) age determinations with the external detector (ED) method and FT length measurements of horizontal confined tracks. The FT age and length data were combined to model the thermal histories of the samples using the modelling software (AFTSolve) of Ketcham et al. (2000). Calibration of the FT ages was based on apatite age standards (Durango and Fish Canyon Tuff apatite) and co-irradiated U-doped dosimeter glasses following the conventional ζ-calibration approach. In addition, metal activation monitors (Au and Co) for absolute calibration of the thermal neutron fluence were used to calculate a procedure factor (Q). The Q-factor was determined based on 40 analyses of apatite age standards (Q_s) as well as through a direct experiment (Q_{exp}). AFT ages calculated with the conventional ζ-approach and the Q-factor approach are in good agreement. Therefore it has been demonstrated in this work that absolute calibration of AFT dating with the ED method is possible and works well when the relevant nuclear parameters and parameters depending on the reactor facility are precisely known and thermal neutron fluence measurements are carried out with the state of the art equipment and techniques. It has hence been shown that reliable AFT ages can be obtained when applying the Q-factor calibration. The Q-factor represents a deconvoluted ζ-factor with direct physical significance in terms of etching and observation conditions. The use of this Q-factor is therefore recommended to FT researchers. At the very least, the methodical results in this work provide a rationale for further systematic and experimental investigation of FT age calibration aimed at the introduction of Q-calibration in FT dating.

7.2. The thermotectonic history of the Russian Altai Mountains

AFT dating and (t, T)-path modelling of samples from the Russian Altai Mountains reconstruct a three-stage cooling history for the region. First, a Late Mesozoic cooling event interpreted as an episode of uplift and denudation in the Altai Mountains, affected the region between ~160 and 100 Ma ago. Most of the samples were brought to shallow crustal levels (~2 km depth) during this event. The Mesozoic tectonic history of the Russian Altai Mountains has hitherto been thought of as a

period of tectonic stability. Our results contradict this. We interpret this Late Mesozoic denudation as the combined effect of two important tectonic events in adjacent regions. To the west of the Altai Mountains, the Mesozoic is characterized by active rifting in the West Siberian Basin and to the east by the development of the vast Mongol-Okhotsk orogen. Far-field effects produced by these processes resulted in denudation of the Altai region and the development of fault-controlled intramontane basins. The Late Mesozoic denudation of the Altai region produced Jurassic and Cretaceous sediments that, in part accumulated in these basins but, for the most part, were deposited in the surrounding foreland basins (e.g. Junggar Basin). The Late Mesozoic denudation is followed in the models by a period of stability that persisted throughout the Late Cretaceous and Palaeogene. Only slow cooling occurred in the Altai crust during this period. We relate this phase of stability to the development of a ubiquitous, contemperaneous peneplanation surface. Finally, the AFT results led us to distinguish a Late Neogene-Quaternary rapid cooling event that brought the samples to ambient surface temperatures. We interpret this cooling event as the result of denudation of the modern Altai Mountain Belt that has been transpressionally reactivated in the Neogene and Quaternary due to the ongoing convergence between the Indian and Eurasian continents.

Furthermore, a difference in Late Cenozoic cooling and consequently denudation between the northern Altai area and the central parts of the orogen is observed in our models. In the north, the Late Neogene-Quaternary denudation is more important. We interpret this by the fact that the northern areas in the Russian Altai Mountains are characterized by widespread, deep river incision, while the central parts, south of the Teletskoye Basin area, have a plateau-like morphology. Rivers are not deeply incised into the plateau, accounting for a lesser amount of Late Cenozoic denudation with respect to the more northerly situated areas.

From a methodical point of view we have to take into account that the AFT thermal annealing equations on which our thermal history models are based, perhaps overestimate the extent of the late cooling. If this is the case here, the amount of Late Neogene-Quaternary denudation we observe in our models may also be an overestimation. Notwithstanding this, we can be confident that the tectonic processes active in the Altai Mountains in the Late Cenozoic are responsible for denudation induced cooling inferred from our modelled (t, T)-paths.

7.3. The thermotectonic history of the Kyrgyz Tien Shan Mountains

We obtained similar three-stage thermal histories for the samples from the Issyk Kul Basin area in the Kyrgyz Tien Shan Mountains. Locally, some of the models exhibit a four-stage thermal history. First, a Mesozoic cooling induced by denudation is also present in all our Tien Shan models. With respect to the Mesozoic cooling in the Altai Mountains, the event is registered earlier for the Tien Shan, where it lasted throughout the Jurassic until the Early Cretaceous (~195-115 Ma ago). This denudation brought most of the samples through the APAZ, to shallow crustal depths. We interpret this denudation as a response to tectonic reactivation of the Mesozoic Tien Shan orogen. The tectonic driving force was provided by the so-called Cimmeride orogeny related to the Mesozoic collision of

several blocks, such as the Qiangtang and Lhasa blocks composing the present-day Tibetan Plateau, with the southern active margin of Eurasia. Distal effects of this orogeny resulted in denudation within the Tien Shan region. Sediments associated with this denudation were deposited Mesozoic intramontane basins and in the vast Junggar and Tarim Basins. Both these basins acted as flexural foreland basins to the north and south of the ancestral Tien Shan respectively. Following the Jurassic-Early Cretaceous cooling, a period of stability and slow cooling is also observed in our Tien Shan thermal history models between about 150 and 40 Ma. This period is interpreted as an episode of peneplanation and red bed formation. Remnants of these red beds are distributed throughout many parts of Central Asia, including the Kyrgyz Tien Shan region. Some of the models exhibit a reheating event between ~ 40 and 20 Ma ago. The reheating brought the rocks back to upper APAZ temperatures. This is only the case for samples collected west of the Issyk Kul Basin and in the western part of the Kungei Range (which is the mountain range bordering of the Issyk Kul Basin to the north). We interpret this local reheating as the result of a locally increased geothermal gradient associated with the emplacement of basalts and diabase bodies in the western and nortwestern sector of the Issyk Kul Basin during the Eocene and Oligocene. The emplacement of these igneous rocks may result from the presence of partially molten remnant subducted slabs under the Mesozoic active margin of Eurasia. Finally, all our Tien Shan models identified Late Miocene-Quaternary cooling. We interpret this cooling as denudation of the actively forming modern Tien Shan orogen. The tectonic reactivation of the Tien Shan occurred in several steps from the Late Miocene to the present (from ~20 Ma ago onwards). It is the result of the ongoing indentation of the Indian plate in the Eurasian continent. Although the possibility of methodical artifacts have to be considered, there is abundant field evidence in support of our interpretation.

7.4. Tectonic and geodynamical significance of the thermochronological results

The Late Palaeozoic assembly of Pangea was the climax of continuing multi-phase Palaeozoic accretion of the Siberian craton that lies at the origin of formation of the Eurasian continent. It is formed by the East European and Siberian cratonic cores with their vast orogenic-accretionary rims. After Early Mesozoic disintegration of the Pangean supercontinent, Eurasia remained a single, solid continent. Moreover, ongoing accretion was responsible for sustaining growth of Eurasia during the Mesozoic. The Mid-Mesozoic collision of Siberia and North China-Mongolia caused the development of the Mongol-Okhotsk orogen. The collision of the tectonic blocks now constituting Tibet with the southern active (Tethyan) Eurasian margin was responsible for the Cimmeride orogeny during that time. Both events bear witness to the enduring Mesozoic accretion and amalgamation of Eurasia. Furthermore, these events triggered distal tectonic effects within the complex accretionary structure of the present-day CADZ in the interior of the Eurasian continent. The events caused denudation and cooling of the affected areas that was recorded by the AFT thermochronometer. We have established that far-field effects of the Mongol Okhotsk orogeny and the Tibetan Cimmeride orogeny affected the Russian Altai and the Kyrgyz Tien Shan Mountains respectively in the Middle to Late Mesozoic.

In general, most low-temperature thermochronological data from the Himalayan orogen, at the boundary between the converging Indian and Eurasian plates, point to a Miocene-Pliocene (from ~20 Ma onwards) onset of denudation of the orogen. This is in agreement with data obtained from the Tibetan Plateau and indicates that, from the Miocene on, thrust tectonics and associated uplift, denudation and cooling dominated deformation within the India-Eurasia collision zone. It is thought that the style of deformation changed drastically from lateral extrusion dominated to thrust dominated tectonics around ~ 20 Ma ago. This deformation consequently seems to have propagated northwards to intracontinental Central Asia via zones of lithospheric weakness. Our AFT data and published data show incipient Mid-Miocene denudation and cooling occurring in the Tien Shan Mountains. Furthermore we have demonstrated that the AFT system recorded cooling and denudation in the Altai Mountains (further north in the interior of Eurasia) later, during the Late Miocene and Pliocene. Published AFT models for the Baikal area, northeast of the Altai Mountains, do not register the recent tectonic reactivation and ensuing denudation and cooling at all. Nor is this the case for the unaffected stable West Siberian Platform, north of the Russian Altai Mountains in this study. Our AFT data thus confirm the hypothesis that reactivation of the Central Asian intracontinental mountain belt is younger further north of the India-Eurasia collision zone proper.

Before onset of this Late Cenozoic reactivation of the Central Asian Deformation Zone (CADZ), the area experienced a period of Late Mesozoic-Early Cenozoic peneplanation. The period is characterized by a stable thermal regime. It is registered in AFT models, including the ones presented in this work, for the entire CADZ as an episode of slow cooling.

NEDERLANDSE SAMENVATTING

1. Inleiding

Sedert de introductie van de theorie van de platentektoniek in de aardwetenschappen in de jaren ‘70 wordt de tektoniek van de Aarde vanuit een totaal andere dynamische context benaderd. In het licht van de nieuwe ideeën werd erkend dat de actieve intracontinentale gebergtenketens in Centraal-Azië zich vormden als gevolg van aanhoudende convergentie van de Indische en de Euraziatische lithosferische platen. Beide continentale massa’s kwamen in het Vroeg-Cenozoïcum tot botsing na de sluiting van het tussenliggend bekken van de Tethys Oceaan. Deze grootschalige continentale collisie en de aanhoudende penetratie van India in Eurazië heeft verscheidene implicaties voor de Aziatische lithosfeer. In eerste instantie treedt crustale verdikking op ter hoogte van de collisiezone zelf. Dit gaf aanleiding tot de ontwikkeling van het Himalaya orogeen als resultaat van een intense plooiings- en overschuivingstektoniek. Subductie van de Indische lithosfeer onder de zuidrand van Eurazië resulteerde verder in de opheffing van het Tibetaans Plateau. Gebergten werden ook gevormd aan de noordrand van Tibet (b.v. Kun Lun Shan, Qilian Shan, Altyn Tagh) als gevolg van de crustale verdikking resulterend uit de convergentie van Tibet met het stabiele Tarim Bekken.

Horizontale verschuivingen en strike-slip deformatie vormen een tweede belangrijk tektonisch effect van de aanhoudende convergentie tussen India en Eurazië. Langs grootschalige strike-slip breuksystemen (b.v. Red River fault, Altyn Tagh fault, Jiali fault) gebeurden substantiële laterale verplaatsingen van segmenten van de Zuid- en Zuidoost-Aziatische lithosfeer. Men spreekt in dit geval van extrusietektoniek. De laterale extrusie van deze segmenten is voornamelijk oostwaarts gericht. Deze laterale bewegingen ondervonden immers een geringere weerstand van de Pacifische subductiezone van Oost-Azië in vergelijking met de weerstand geleverd door het rigide Euraziatische continent in het westen.

Tot slot wordt een deel van de spanning die in de collisiezone wordt opgebouwd, ontlast door reactivatie van oudere orogenen in intracontinentaal Centraal-Azië en Siberië. De spanningen werden vaak via overgeërfde lithosferische zwaktezones noordwaarts gepropageerd en bereiken aldus deze oudere structuren. Afhankelijk van de regionale geologische context, werden transpressieve (b.v. de Tien Shan en Altai gebergten) tot zelfs extensionele (b.v. de Baikal Riftzone) vervormingen geïnduceerd in de intracontinentale omgeving van Centraal-Azië en Siberië. In het Laat-Cenozoïcum werd op deze wijze een reusachtig gebied, tussen

het Tibetaans Plateau en de Okhotsk Zee (Oost-Siberië) aan reactivatie en deformatie blootgesteld.

Deze studie heeft tot doel de verticale tektonische bewegingen die hebben plaatsgevonden in de intracontinentale omgeving van Centraal-Azië en Siberië, meer bepaald van het Altai en Tien Shan gebergte, te bestuderen. Lage-temperatuurs thermochronologische technieken vormen de meest gebruikte methoden om deze problematiek te onderzoeken. Deze technieken combineren chronologische en thermische informatie vervat in een mineraal-specifiek isotopisch systeem om de thermo-tektonische geschiedenis van het onderzoeksgebied te reconstrueren. In deze studie wordt de apatiet-fissiesporen methode gebruikt. Deze methode is in het laatste decennium uitgegroeid tot een van de meest succesvolle en daardoor meest aangewende methoden om dergelijke thermo-tektonische reconstructies uit te voeren.

2. De apatiet-fissiesporen dateringsmethode

De fissiesporenmethode is een radiometrische dateringsmethode die steunt op de spontane fissie van het isotoop ^{238}U in uranium-houdende mineralen zoals bijvoorbeeld apatiet. Spontane fissie is een vorm van nucleair verval dat optreedt bij zware, onstabiele nucliden. In de natuur is enkel de fissie van ^{238}U van belang. De fissie van een ^{238}U kern resulteert in twee sterk positief geladen fissiefragmenten die met hoge energie van elkaar weggeslingerd worden en een lineair traject beschrijven in de vaste stof waarin de ^{238}U moedernuclide voorkomt. In mineralen, zoals apatiet, zullen de beide fissiefragmenten een blijvend lineair beschadegingsspoor in het kristalrooster veroorzaken: het fissiespoor.

Thermisch onaangetaste fissiesporen in apatiet hebben een lengte van ongeveer 16 µm en zijn slechts enkele nm in doorsnede. Om dergelijke latente sporen zichtbaar te maken onder een optische microscoop -men spreekt van revelatie- wordt het kristaloppervlak chemisch geëtst met HNO_3. Het aantal spontane geëtste fissiesporen geteld per eenheid van oppervlakte (de spontane fissiesporen dichtheid ρ_s) vormt een maat voor de schijnbare fissiesporenouderdom van het onderzochte apatiet. Dit op voorwaarde dat het uraniumgehalte van het monster gekend is.

Het uraniumgehalte van het apatiet wordt bepaald door het met thermische neutronen te bestralen in een gethermaliseerd kanaal van een nucleaire reactor. Een dergelijke bestraling induceert fissie van het isotoop ^{235}U dat in de natuur in constante verhouding tot ^{238}U voorkomt. Op deze wijze worden geïnduceerde fissiesporen bekomen en hun aantal per eenheid van oppervlakte (de geïnduceerde fissiesporen dichtheid ρ_i) is functie van het uraniumgehalte en de fluentie van thermische neutronen (ϕ_{th}) waaraan het monster gedurende de bestraling werd blootgesteld.

Er bestaan verschillende manieren om geïnduceerde fissiesporen te registreren. In dit werk werd de zogenaamde externe detectormethode gebruikt. Een externe detector (ED) is een U-vrij materiaal dat in nauw contact met het monster samen wordt bestraald en dat zo de geïnduceerde fissiesporen registreert. Voor geologische toepassingen wordt doorgaans een micablaadje (muscoviet) als ED gebruikt. Het mica wordt na de bestraling geëtst met HF om de sporen voor optische microscopie zichtbaar te maken.

De gemeten fissiesporenouderdom van het apatiet wordt berekend uit de verhouding van de spontane tot de geïnduceerde sporendichtheid (ρ_s/ρ_i) en de nauwkeurig bepaalde waarde van ϕ_{th}. Dit laatste wordt gedaan door fluentiemonitoren samen met de te onderzoeken monsters te bestralen. In dit werk werden metaal-monitoren gebruikt (Au en Co) onder de vorm van verdunde Al-Au en Al-Co folies. Gedurende de bestraling wordt het Au en Co geactiveerd in een mate die afhankelijk is van de waarde van ϕ_{th}. Het geactiveerde Au en Co in de monitoren vervalt vervolgens met het uitzenden van een kenmerkende γ-straling. De activiteit van deze straling wordt met een γ-spectrometer gemeten en is een maat voor de waarde van ϕ_{th}. Deze werkwijze wordt de absolute benadering genoemd. In principe wordt zij zelden toegepast in combinatie met de ED techniek. Om de absolute benadering in combinatie met de ED techniek te gebruiken moet er immers een bijkomende factor, de procedurefactor (Q) worden bepaald. Deze is afhankelijk van het verschil in spoorregistratie, etskarakteristieken en fissiespoor observatiecriteria tussen het apatiet en de muscoviet ED.

Om dit te omzeilen en (vroeger) ook om de bepaling van ϕ_{th} uit de weg te gaan, bestaat er een kalibratietechniek die de zeta (ζ) methode wordt genoemd. Deze bestaat er in dat apatiet ouderdomsstandaarden in contact met een ED bestraald en geanalyseerd worden. Zo kunnen ρ_s/ρ_i-verhoudingen voor de ouderdomsstandaarden bepaald worden. Bovendien worden U-gedopeerde glazen met een ED samen met de standaarden bestraald. Op deze wijze worden ook ^{235}U geïnduceerde sporen afkomstig van de glas dosimeter in de ED geregistreerd. Hun aantal per eenheid van oppervlakte of hun dichtheid (ρ_d) vormt dan onrechtstreeks een maat voor de ϕ_{th} waarde. Aangezien de exacte ouderdom van de standaarden gekend is, kunnen de ongekende en de te bepalen parameters in de fissiesporen ouderdomsvergelijking ingevuld worden in functie van de ouderdom van de standaard en de ρ_s/ρ_i en ρ_d waarden. Aldus wordt de ζ-kalibratiefactor bekomen. De waarde ervan wordt verfijnd door analyse van verschillende monsters van meerdere standaarden. De waarde van ζ is onder meer afhankelijk van het onderzochte mineraal, van het type glasdosimeter en van de gebruikte etscondities. De waarde fungeert enkel als een persoonlijke kalibratiefactor die kan varieëren van onderzoeker tot onderzoeker. Analyse van onbekende monsters komt vervolgens neer op het bepalen van de ρ_s/ρ_i en ρ_d waarden voor de monsters. Samen met de ζ-factor laten zij toe de fissiesporenouderdom van onbekende apatiet monsters te berekenen.

In deze studie werd zowel de absolute benadering als de ζ-kalibratie toegepast. Als apatiet ouderdomsstandaarden werd het traditionele Durango apatiet en Fish Canyon Tuff apatiet

gebruikt. Als glasdosimeter werd er van het gecertifieerde IRMM-540 glas gebruik gemaakt. Het IRMM-540 glas is een dosimeter die speciaal voor de fissiesporen dateringsmethode werd ontwikkeld door het Institute for Reference Materials and Measurements van de Europese Commissie in samenwerking met het Instituut voor Nucleaire Wetenschappen (INW) van de Universiteit Gent en onze onderzoekseenheid.

3. De thermische stabiliteit van fissiesporen en thermochronologische reconstructies

Fissiesporen bezitten slechts een beperkte thermische stabiliteit. Bij verhoogde temperatuur verdwijnen zij door herstel van het kristalrooster. Dit fenomeen werd reeds in het begin van de ontwikkeling van de fissiesporen dateringsmethode experimenteel vastgesteld in laboratoriumcondities. Ook voor verhittingstijden in geologische context (~1 Ma en meer) werd er vastgesteld dat in apatiet sporenverlies begint op te treden vanaf 60°C en dat de uitgloeiing compleet is bij 120°C. Bij temperaturen lager dan 60°C worden de sporen in apatiet als quasi stabiel beschouwd, terwijl in het temperatuursinterval 60-120°C de sporen partieel worden uitgegloeid. Dit stemt overeen met een zone in de aarkorst die de Apatite Partial Annealing Zone (APAZ) wordt genoemd. De uitgloeiing resulteert in eerste instantie in de verkorting van de spoorlengtes. Het meten van deze lengtes en het opstellen van een lengtedistributie van de spontane fissiesporen geeft bijgevolg bijkomende informatie inzake de thermische geschiedenis van het onderzochte apatiet. De lengtemetingen geschieden meestal op zogenaamde horizontale confined tracks. Deze sporen liggen in het inwendige van het apatietkristal en worden over hun volledige lengte aangeëtst doordat het etsmiddel via een barst of een oppervlaktespoor het inwendige van het kristal kan binnendringen.

Het uitgloeiingsproces van fissiesporen in apatiet is uitvoerig bestudeerd met laboratoriumproeven. Verschillende modellen en vergelijkingen werden naar voor gebracht om dit fenomeen mathematisch te beschrijven. Deze modellen laten toe om via combinatie van de apatiet fissiesporenouderdommen en lengte-informatie de thermochronologische evolutie van het gesteente beneden de 120°C te reconstrueren. In de praktijk impliceert dit dat de apatiet-fissiesporenmethode de thermische geschiedenis van gesteenten tot ongeveer 4 km diep in de aardkorst kan reconstrueren. Het is bijgevolg een zeer geschikte techniek voor de studie van gebergtevorming. Een van de meest gebruikte modellen, dat ook in deze studie werd aangewend, is het model van Laslett et al. (1987). Het AFTSolve softwarepakket (Ketcham et al., 2000) werd gebruikt om thermische geschiedenissen te modelleren.

De apatiet-fissiesporenmethode registreert de afkoeling (of verhitting) van gesteenten in een absoluut tijdskader. De thermische geschiedenis van een gesteente hangt samen met de relatieve verplaatsing van dat gesteente in de korst ten opzichte van de positie van de geo-isothermen. In sommige gevallen reflecteert deze geschiedenis een thermisch event veroorzaakt door veranderingen in de geothermische gradient als gevolg van de intrusie van een magma of de circulatie van warme fluïda bijvoorbeeld. Deze gebeurtenissen zijn echter

meestal van lokale aard. Op regionale schaal worden afkoeling of verhitting gezien als het directe resultaat van respectievelijk denudatie of begraving. Denudatie zal vaak, doch niet altijd, samengaan met opheffing, reliëfs- en gebergtevorming. Begraving is dan weer gekoppeld aan bekkenvorming en sedimentatie. Kennis van de regionale geologie van het onderzoeksgebied is bijgevolg een belangrijke factor bij de interpretatie van apatiet-fissiesporendata en de thermische geschiedenissen die er uit gemodelleerd worden.

4. Het onderzoeksgebied: lokatie en geologische en geodynamische evolutie

4.1. Het Altai-Sayan gebergte

Het Altai-Sayan gebergte situeert zich op het grensgebied tussen Rusland (Zuid-Siberië), Kazakhstan, China en Mongolië. Voor onze studie werden meerdere gesteentemonsters uit het Russische gedeelte van het Altai-Sayan gebergte verzameld en werd de apatietfractie afgescheiden. De onderzochte gesteenten zijn voor het merendeel afkomstig van de regio rondom het Teletskoye meer dat zich situeert in de jonge Teletsk graben in het noorden van het gebergte. In andere regio's (het Zuid-Chulyshman Plateau, de Chuya-Kurai regio, de Dzhulukul regio en de Westelijke Altai) werden eveneens monsters verzameld. In totaal werd een 50-tal monsters geschikt bevonden en geanalyseerd.

Het Paleozoïcum

Het Altai-Sayan gebergte vormt een deel van de uitgestrekte orogene gordel ten zuiden van het Siberische craton. Deze gordel werd grotendeels gevormd gedurende het Paleozoïcum. Het Paleozoïcum wordt gekenmerkt door grootschalige crustale accretie en vorming van het Euraziatische continent. Verschillende tektonische eenheden amalgameerden aan de huidige zuidrand van het Siberische craton. Belangrijk hierbij was de evolutie van de zogeheten Paleo-Aziatische Oceaan die zich uitstrekte tussen Siberië en het zuidelijke supercontinent Gondwana. Verschillende Paleo-Aziatische oceanische eenheden (zoals bijvoorbeeld eilandbogen, accretieprisma's, seamounts e.d.) en peri-Gondwana continentale fragmenten (de Tuva-Mongolië, Altai-Mongolië en Kazakhstan microcontinenten bijvoorbeeld) werden gedurende het Paleozoïcum door progressieve sluiting van dit oceanisch bekken aan Siberië toegevoegd. In het Altai-Sayan gebergte was er grootschalige tektonische activiteit tijdens twee belangrijke collisies. In het Laat-Devoon tot Vroeg-Carboon botste Altai-Mongolië met de actieve rand van Zuid-Siberië en in het Permo-Trias kwam Kazakhstan in frontale botsing met de Siberische orogene gordel. Deze laatste gebeurtenis markeert de volledige sluiting van de Paleo-Aziatische Oceaan, en in een breder plaattektonisch kader stemt dit overeen met de samensmelting van Eurazië en Gondwana en met de vorming van het supercontinent Pangea.

Het Mesozoïcum

Over het algemeen wordt het Mesozoïcum in de Altai-Sayan regio gezien als een periode van tektonische stabiliteit. De regio werd toen echter begrensd door twee actieve gebieden. In het westen vormde zich het West-Siberisch Bekken en in het oosten speelde zich de Mongol-Okhotsk orogenese af. Het West-Siberische Bekken vormde zich reeds in het Trias kort na het ontstaan van Pangea. Actieve riftvorming en lokaal zelfs oceanisatie in dit bekken luidde de desintegratie van Pangea in. Deze gebeurtenissen hielden aan gedurende het grootste deel van het Jura, maar het Euraziatische continent bleef in essentie één grote landmassa. Vanaf het Laat-Jura en gedurende het Krijt werd het bekken volledig opgevuld met sedimenten o.a. afkomstig van de aan erosie blootgestelde Siberische orogene gordel. Ten oosten van het studiegebied wordt het Mesozoïcum gekarakteriseerd door de sluiting van de Mongol-Okhotsk Oceaan in het Jura en Vroeg-Krijt. Deze sluiting resulteerde in de botsing van Siberië met Noord-China (Sino-Korea) dat in feite reeds een amalgaam was van Noord-Chinese en Mongoolse tektonische eenheden. Deze grootschalige collisie luidde de vorming in van het Mongol-Okhotsk orogeen en wijst op de verdere groei van Eurazië in het Mesozoïcum. De invloedssfeer van deze orogense reikte zeker tot in het Mongoolse gedeelte van het Altai-Sayan gebergte en ook in het Russische deel zijn er sporen van tektonische reactivatie.

Het Cenozoïcum

Zoals reeds in de inleiding werd vermeld, wordt de Cenozoïsche evolutie van intracontinentaal Centraal-Azië gedomineerd door de distale effecten van de botsing van de Indische met de Euraziatische plaat en hun voordurende convergentie. In de Altai-Sayan regio worden het Laat-Krijt en Paleogeen gekenmerkt door stabiliteit en de vorming van een regionale peneplaine. Pas in de loop van het Mioceen en uitgesproken vanaf het Plioceen zorgt de tektonische reactivatie van het gebied voor de vorming van het moderne gebergte en voor de hoofdzakelijk transpressionele bewegingen. Gedurende de laatste 2 Ma is de tektonische activiteit er wijdverspreid en deze duurt voort tot op de dag van vandaag. De Teletsk graben van waar het merendeel van de aptietmonsters uit deze studie afkomstig zijn, is een mooi voorbeeld van deze recente tektonische activiteit. De graben is een Quartaire structuur die zich vormt in een locaal extensioneel regime tussen twee Paleozoische tektonische blokken: het Gorny-Altai blok en het West Sayan blok.

4.2. Het Tien Shan gebergte

Het Tien Shan gebergte is één van de meest actieve intracontinentale gebergteketens ter wereld. Het gebergte strekt zich uit langs de noordrand van het rigide en stabiele Tarim Bekken ten noorden van het Tibetaans Plateau. Het oostelijk gedeelte van de Tien Shan ligt in het noordwesten van China. Het westelijk gedeelte, dat in dit proefschrift werd bestudeerd,

situeert zich grotendeels in de voormalige Sovjet-republieken Kyrgyzstan, Tadjikistan en Uzbekistan. Het Tien Shan gebergte heeft een uitgesproken oost-west strekking en is opgebouwd uit een serie parallelle bergketens, onderling gescheiden door intramontane bekkens. Het Issyk-Kul bekken in het noorden van Kyrgyzstan is een mooi voorbeeld van dergelijk intramontaan bekken. Het bekken, met centraal het Issyk-Kul meer, wordt aan haar noordrand begrensd door de Kungei-keten, terwijl de Terzkey-keten de zuidelijke grens definieert. Beide bergketens werden samen met enkele aangrenzende structuren, uitvoerig bemonsterd voor apatiet-fissiesporen onderzoek. In totaal wordt een 20-tal monsters in deze studie besproken.

Het Paleozoïcum

De Paleozoïsche geschiedenis van het Tien Shan gebergte toont grote gelijkenissen met deze van het Altai-Sayan gebergte en weerspiegelt eveneens de complexe Paleozoïsche accretie van het Euraziatische continent. Ook hier worden twee belangrijke Paleozoïsche collisies onderscheiden: een eerste in het Laat-Devoon tot Vroeg-Carboon, en een tweede in het Perm. Beide collisies worden gezien in het raam van de evolutie en sluiting van de Turkestan of Tien Shan Oceaan. De eerste collisie slaat op de botsing van een microcontinentaal fragment, het zogeheten Ili blok of de centrale Tien Shan met de zuidelijke Tien Shan. De zuidelijke Tien Shan omvat in feite de noordrand van de Tarim plaat die de sokkel vormt van het huidige Tarim Bekken. De tweede collisie vond plaats tussen deze orogene noordrand van Tarim en de noordelijke Tien Shan. Deze laatste bestond uit een vulkanische eilandenboog die tot stand gekomen was in de noordelijke Tien Shan Oceaan. Tussen deze Laat-Paleozoïsche orogene gordel en de Paleo-Aziatische domeinen (inclusief de Altai-Sayan regio) verder ten noorden, bleek een klein, (relict) oceanisch bekken te bestaan: de Junggar Oceaan. Dit geheel werd samengevoegd gedurende het Permo-Trias en werd integraal opgenomen in het supercontinent Pangea.

Het Mesozoïcum

Na de desintegratie van Pangea vormde het Tarim Bekken, met ten noorden hiervan de ancestrale Tien Shan, de zuidrand van Eurazië. Tussen Eurazië en het zuidelijk gelegen Gondwana continent ontwikkelde zich de Tethys Oceaan. Fragmenten van het uiteenvallende Gondwana continent waren in het Mesozoïcum onderworpen aan een noordwaartse drift door sluiting van de (Proto-)Tethys Oceaan. Progressieve subductie van deze oceanische lithosfeer onder de actieve zuidrand van Eurazië resulteerde uiteindelijk in de collisie van deze fragmenten (o.a. het Qiangtang en het Lhasa blok) met de actieve Euraziatische rand. Deze botsingen voltrokken zich respectievelijk in het Laat-Trias tot Vroeg-Jura en in het Laat-Jura tot Vroeg-Krijt gedurende de zogeheten Cimmeriaan orogenese. Deze orogenese had duidelijk een tektonische reactivatie van structuren in de Tien Shan tot gevolg.

Vanaf het Laat-Krijt was het ancestrale Tien Shan orogeen bllotgesteld aan erosie en peneplanatie. In het Laat-Krijt was de Zuid-Euraziatische subductiezone in dit gebied verschoven naar de zuidrand van het aangelaste Lhasa blok. Voortdurende subductie van de Tethys lithosfeer resulteerde in de ontwikkeling van een reusachtige batholiet, de Transhimalaya of Gangdese batholiet. Uiteindelijk, ongeveer tijdens de Meso-Cenozoïsche transitie, was de Tethys volledig geconsumeerd en kwam India, als reusachtig Gondwana fragment, in frontale botsing met de actieve Euraziatische rand.

Het Cenozoïcum

Analoog met wat reeds werd vermeld, wordt de Cenozoïsche geschiedenis van de Tien Shan regio tot op heden sterk beïnvloed door de grootschalige continent-continent collisie van India en Eurazië. De vervormingen verantwoordelijk voor de vorming van de Himalaya en de opheffing van het Tibetaans Plateau omzeilden de rigide sokkel van het Tarim Bekken en bereikten de Tien Shan in het Laat-Paleogeen met een transpressionele reactivatie van het gebergte tot gevolg. In het algemeen ziet men het Laat-Oligoceen en Mioceen als de tijdvakken waarin de vorming van de moderne Tien Shan begon. Vooral in het Laat-Mioceen en Plioceen waren de vervormingen en bewegingen intens. In deze periode greeep ook de vorming plaats van het Issyk-Kul bekken als mogelijke pull-apart structuur.

5. Apatiet-Fissiesporen thermochronologie: resultaten, modellering en interpretatie

5.1. Het Altai-Sayan gebergte

De gemeten apatiet-fissiesporenouderdommen bekomen op de Altai-Sayan monsters situeren zich allen in het Jura en het Krijt, en de meeste ouderdommen zelfs in het Laat-Jura en Vroeg-Krijt. Dit geldt voor zowel de berekende Q- als ζ-ouderdommen. Hierbij kon aangetoond worden dat er een goede correlatie bestaat tussen beide kalibratietechnieken en dat dus de weinig gebruikte absolute benadering (Q-factor) voor de ED methode een volwaardig alternatief vormt. Niettegenstaande werden de conventionele ζ-ouderdommen gebruikt om de thermische geschiedenissen te modelleren.

Nagenoeg alle apatietmonsters van de Altai-Sayan regio dragen een significante APAZ-signatuur. De gemiddelde lengtes zijn vrij laag (~12 a 13 μm) en de meeste distributies zijn asymmetrisch met negatieve scheefheid. Op basis van deze data kunnen we reeds kwalitatief afleiden dat de Altai-Sayan gesteenten in het Midden- tot Laat-Mesozoïcum de 120°C isotherm in de aardkorst bereikten, maar dat zij nadien gedurende lange tijd in de APAZ verbleven. Pas relatief recent moet de 60°C isotherm zijn gepasseerd waarmee apatiet-fissiesporen accummulatie volledig werd en de sporen stabiel bleven.

Modellering van deze data resulteerde in een consistent drie-fasig afkoelingsmodel voor de Altai-Sayan. Wanneer we de algemene trend in de gemodelleerde tijds-temperatuurs (t, T)-paden beschouwen, zien we: (1) een Laat-Jura tot Krijt fase met snelle afkoeling waarbij de gesteenten afkoelen beneden de 120°C isotherm en in de hogere korst gebracht worden tot in de APAZ, (2) een Laat-Krijt en Paleogeen periode van relatieve thermische stabiliteit waarbij hoogstens zeer trage afkoeling te noteren valt, en (3) een Laat-Neogene en Quartaire snelle afkoeling die aanhoudt tot op heden, met specifiek een intensificatie gedurende de laatste 2 Ma.

Wij interpreteren deze drie fasige thermische geschiedenis als het gevolg van: (1) Laat-Jura tot Krijt denudatie van het Altai-Sayan gebergte, (2) Laat-Krijt en Paleogeen tektonische stabiliteit met vorming van een wijdverspreide peneplaine, en (3) een Laat-Neogene en Quartaire denudatie.

De eerste fase van denudatie, de Laat-Jura tot Krijt denudatie van het Altai-Sayan gebergte was een gevolg van een tektonische reactivatie van de regio. Deze reactivatie is waarschijnlijk een distaal effect van de Mongol-Okhotsk orogenese die zich ten oosten van het studiegebied afspeelde gedurende de botsing van Siberië met het geassembleerd Noord-China-Mongolië continent. Deze resultaten tonen dus aan dat de invloedssfeer van deze orogenese verder westwaarts reikte dan tot nog toe gedacht werd. Verder dient er opgemerkt te worden dat mogelijk een deel van deze Mesozoïsche denudatie te verklaren is door een bijkomend effect van de tektonische activiteit in het West Siberisch Bekken.

De tweede fase van denudatie in het Laat-Neogeen en Quartair interpreteren we als direct gevolg van de neotektonische reactivatie en vorming van het moderne Altai-Sayan gebergte. Ons model plaatst de moderne gebergtevorming voornamelijk in het Plioceen, met een belangrijke Quartaire componente.

We kunnen nog opmerken, dat wanneer we de gemodelleerde (t, T)-paden onderling vergelijken, de jonge denudatiefase kwantitatief belangrijker is voor monsters uit het noordelijk deel van het Altai-Sayan gebergte (meer bepaald in de Teletskoye regio). Dit komt overeen met een in het oog springend geomorfologisch-topografisch kenmerk van de regio. De noordelijk zone is immers duidelijk meer ingesneden door rivieren, terwijl de meer zuidelijke gebieden (het Chulyshman Plateau bijvoorbeeld) een meer uitgesproken plateau-morfologie vertonen. Dit bevestigt het recente karakter van de opheffingsbewegingen, waarbij de zuidelijke hoogplateau's in vergelijking met de noordelijke zone, nog slechts nauwelijks zijn geërodeerd.

5.2. Het Tien Shan gebergte

De gemeten apatiet-fissiesporenouderdommen bekomen op de Tien Shan monsters situeren zich allen in het Jura en het Krijt. In het algemeen zijn deze ouderdommen hoger dan deze bekomen voor het Altai-Sayan gebergte. Over het algemeen valt ook op dat de ouderdommen van de noordelijke sokkel (Kungei-keten) van het Issyk-Kul bekken aanzienlijk ouder zijn (Laat-Jura) dan deze van de zuidelijke sokkel (Laat-Krijt voor de Terzkey-keten). Ook in dit geval werd een goede correlatie gevonden tussen de Q- en de ζ-ouderdommen. Een thermische invloed (o.a. korte gemiddelde spoorlengtes) is eveneens voor de Tien Shan apatieten duidelijk merkbaar.

Modellering van deze data resulteerde in een consistent drie- tot vier-fasig afkoelingsmodel. Wanneer we de algemene trend in de gemodelleerde (t, T)-paden beschouwen, zien we: (1) een Jura tot Vroeg-Krijt fase van snelle afkoeling waarbij de gesteenten in de korst gebracht worden tot lagere APAZ temperaturen en zelfs stabiliteitstemperaturen (~50-80°C), (2) een Laat-Krijt en Vroeg-Paleogeen periode van relatieve thermische stabiliteit waarbij hoogstens een zeer trage afkoeling te noteren valt, (3) sommige monsters (uitsluitend afkomstig van de noordwestelijke sokkel van het Issyk-Kul bekken) tonen een verhittingsfase tussen 40 en 20 Ma (Laat-Eoceen tot Vroeg-Mioceen), en (4) een Neogeen tot Quartaire snelle afkoeling die aanhoudt tot op heden.

Wij interpreteren deze fasen als volgt: (1) Jura tot Vroeg-Krijt denudatie van de ancestrale Tien Shan in een episode van tektonische reactivatie, (2) een Laat-Krijt tot Vroeg-Paleogeen fase van tektonische inactiviteit en peneplanatie, (3) een puls van verhitting in het Laat-Eoceen tot Vroeg-Mioceen met verhoogde geothermische gradiënt in het noordwesten van de Issyk-Kul sokkel, en (4) een Neogeen en Quartaire denudatie ten gevolge van de jonge reactivatie van het Tien Shan gebergte.

De fase van Jura tot Vroeg-Krijt denudatie van de ancestrale Tien Shan interpreteren we als een gevolg van een episode van tektonische reactivatie ten gevolge van de Cimmeriaan orogenese. Deze orogenese ging gepaard met de botsing van tektonische blokken, Qiangtang en Lhasa, die het huidige Tibet opbouwen enerzijds, met de actieve zuidrand van Eurazië (Tarim) anderzijds. Effecten, onder meer opheffing en denudatie, die gepaard gingen met deze orogenese zijn duidelijk aan te wijzen in de hele Tien Shan regio. Zo accumuleerden er zich dikke Midden-Mesozoïsche sedimentpakketten in het Junggar en Tarim Bekken die toen fungeerden als flexuur voorlandbekkens respectievelijk ten noorden en ten zuiden van de Tien Shan.

De Laat-Eoceen tot Vroeg-Mioceen verhittingspuls waargenomen in de modellen voor het noordwesten van de Issyk-Kul sokkel associëren we met een verhoogde thermische gradiënt tijdens een korte en lokale magmatische fase onder de vorm van diabaas dykes en sills. Het gelokaliseerde magmatisme is een algemeen verschijnsel in verscheidene gebieden in de Tien

Shan. De onderliggende reden kan misschien gezocht worden in het voorkomen van partieel gesmolten relicten van gesubduceerde fragmenten van de Tethys plaat.

De denudatiefase in het Neogeen en Quartair interpreteren we als het resultaat van de neotektonische, transpressionele reactivatie en vorming van het moderne Tien Shan gebergte. Ons model plaatst het begin van de moderne gebergtevorming in de Tien Shan in het Mioceen, tussen de 10 en 20 Ma, met een intensificatie in het Plioceen en Quartair.

De voorgaande bespreking heeft voornamelijk betrekking tot de noordelijke sector van de Issyk-Kul sokkel (o.a. de Kungei bergketen). Onze dataset voor de zuidelijke zone (Terzkey) is beperkter, maar wijst op een andere thermische geschiedenis van dit gebied. Het thermotektonisch model dat wij vonden voor de Terzkey-keten toont een continue, graduele afkoeling sinds het Laat-Krijt en Vroeg-Tertiair met een intensificatie vanaf het Mioceen.

Tot slot kunnen we opmerken dat onze thermotektonische modellen voor de Altai-Sayan en de Tien Shan regio onderling grote gelijkenissen vertonen in algemene allure, hoewel de timing van de verschillende fasen enigszins anders is. Beide studiegebieden vertonen een fase van Mesozoïsche tektonische reactivatie. Voor de Altai-Sayan regio is dit in het Laat-Jura tot Laat-Krijt, terwijl dit voor de Tien Shan reeds het geval is vanaf het Vroeg-Jura. In beide gevallen gaat het om een reactivatie ten gevolge van distale effecten van orogenesen die geassocieerd zijn met de sluiting van oceanische bekkens ten zuiden van het toenmalig Euraziatisch continent. Dit wijst op de voortdurende groei van dit continent, ook gedurende het grootste deel van het Mesozoïcum. Na een tussenliggende, regionaal wijdverspreide pauze in tektonische activiteit tijdens het Laat-Krijt en het Paleogeen, zien we een Laat-Cenozoïsche neotektonische reactivatie van beide gebieden in intracontinentaal Centraal-Azië en Siberië. Voor de Tien Shan begint deze reeds in het Mioceen, terwijl de bewegingen in de Altai-Sayan regio duidelijk jonger zijn en pas vanaf het Plioceen een aanvang nemen. Dit past in het algemeen geodynamisch model van de noordwaarts propagerende vervorming in Centraal-Azië als distaal effect van de voortdurende convergentie tussen het Indische en het Euraziatische continent.

REFERENCES

Abbott, L.D., Silver, E.A., Anderson, E.A., Smith, R., Ingle, J.C., Kling, S.A., Haig, D., Small, E., Galewsky, J., Sliter, W. (1997). Measurement of tectonic surface uplift rate in a young collisional mountain belt. *Nature*, 385, 501-507.

Abdrakhmatov, K. Ye., Aldazhanov, S.A., Hager, B.H., Hamburger, M.W., Herring, T.A., Kalabaev, K.B., Makarov, V.I., Molnar, P., Panasyuk, S.V., Prilepin, M.T., Reilinger, R.E., Sadybakasov, I.S., Souter, B.J., Trapeznikov, Yu. A., Tsurkov, V. Ye., Zubovich, A.V. (1996). Relatively recent construction of the Tien Shan inferred from GPS measurements of present-day crustal deformation. *Nature*, 384, 450-453.

Abdrakhmatov, K.Y., Djanuzakov, K.D., Delvaux, D. (2002). Active tectonics and seizmic hazard of the Issyk-Kul basin in the Kyrgyz Tian-Shan. *In*: Klerkx, J., Imanackunov, B. (Eds). *Lake Issyk-Kul: its natural environment*. Kluwer Academic Publishers, Dordrecht, pp. 147-160.

Acharyya, S.K. (1998). Break-up of the greater Indo-Australian continent and accretion of blocks framing South and East Asia. *Journal of Geodynamics*, 26 (1), 149-170.

Aftalion, M., Bibikova, E.V., Bowes, D.R., Hopgood, A.M., Perchuk, L.L. (1991). Timing of Early Proterozoic collisional and extensional events in the granulite-gneiss-charnockite-granite complex, Lake Baikal, U.S.S.R.: a U-Pb, Rb-Sr and Sm-Nd isotopic study. *Journal of Geology*, 99, 851-862.

Agar, S.M., Klitgord, K.D. (1995). Rift flank segmentation, basin initiation and propagation: a neotectonic example from Lake Baikal. *Journal of the Geological Society, London*, 152, 849-860.

Aitchison, J.C., Badengzhu, Davis, A.M., Liu, J., Luo, H., Malpas, J.G., McDermid, I.R.C., Wu, H., Ziabrev, S.G., Zhou, M. (2000). Remnants of a Cretaceous intra-oceanic subduction system within the Yarlung-Zangbo suture (southern Tibet). *Earth and Planetary Science Letters*, 183, 231-244.

Allen, M.B., Vincent, S.J. (1997). Fault reactivation in the Junggar region, northwest China: the role of basement structures during Mesozoic-Cenozoic compression. *Journal of the Geological Society, London*, 154, 151-155.

Allen, M.B., Windley, B.F., Zhang Chi (1991a). Active alluvial systems in the Korla basin, Tien Shan, northwest China: sedimentation in a complex foreland basin. *Geological Magazine*, 128 (6), 661-666.

Allen, M.B., Windley, B.F., Zhang Chi, Zhao, Z.-Y., Wang, G.-R. (1991b). Basin evolution within and adjacent to the Tien Shan range, NW China. *Journal of the Geological Society, London*, 148, 369-378.

Allen, M.B., Windley, B.F., Zhang Chi (1992). Palaeozoic collisional tectonics and magmatism of the Chinese Tien Shan, Central Asia. *Tectonophysics*, 220, 89-115.

Allen, M.B., Windley, B.F., Zhang Chi, Guo, J. (1993). Evolution of the Turfan Basin, Chinese Central Asia. *Tectonics*, 12 (4), 889-896.

Allen, M.B., Windley, B.F., Zhang Chi (1994). Cenozoic tectonics in the Urumqi-Korla region of the Chinese Tien Shan. *Geologische Rundschau*, 83, 406-416.

Allen, M.B., Şengör, A.M.C., Natal'in, B.A. (1995). Junggar, Turfan and Alakol basins as Late Permian to ?Early Triassic extensional structures in a sinistral shear zone in the Altaid orogenic collage, Central Asia. *Journal of the Geological Society, London*, 152, 327-338.

Allen, M.B., Alsop, G.I., Zhemchuzhnikov, V.G. (2001). Dome and basin refolding and transpressive inversion along the Karatau fault System, southern Kazakstan. *Journal of the Geological Society, London*, 158, 83-95.

Anczkiewicz, R., Burg, J.P., Villa, I.M., Meier, M. (2000). Late Cretaceous blueschist metamorphism in the Indus suture zone, Shangla region, Pakistan Himalaya. *Tectonophysics*, 324, 111-134.

Aplonov, S.V. (1988). An aborted Triassic ocean in West Siberia. *Tectonics*, 7, 1103-1122.

Aplonov, S.V. (1995). The tectonic evolution of West Siberia: an attempt at a geophysical analysis. *Tectonophysics*, 245, 61-84.

Armijo, R., Tapponnier, P., Mercier, J.P., Han, T. (1986). Quaternary extension in southern Tibet. *Journal of Geophysical Research*, 91, 13803-13872.

Armijo, R., Tapponnier, P., Han, T. (1989). Late Cenozoic right-lateral strike-slip faulting in southern Tibet. *Journal of Geophysical Research*, 94, B3, 2787-2838.

Arne, D., Worley, B., Wilson, C., Chen, S.F., Foster, D., Luo, Z.L., Liu, S.G., Dirks, P. (1997). Differential exhumation in response to episodic thrusting along the eastern margin of the Tibetan Plateau. *Tectonophysics*, 280, 239-256.

Atlas Kyrgyzkaya (1987). Moscow, Academia Nauka, 157 pp.

Avouac, J.P., Tapponnier, P. (1993). Kinematic model of active deformation in Central Asia. *Geophysical Research Letters*, 20, 895-898.

Avouac, J.P., Tapponnier, P., Bai, P., You, H., Wang, G. (1993). Active thrusting and folding along the northern Tien Shan, and Late Cenozoic rotation of the Tarim relative to the Junggar and Kazakhstan. *Journal of Geophysical Research*, 98, 6755-6804.

Bachtadse, V., Pavlov, V.E., Kazansky, A.Y., Tait, J.A. (2000). Siluro-Devonian paleomagnetic results from the Tuva terrane (southern Siberia, Russia): implications for the paleogeography of Siberia. *Journal of Geophysical Research*, 105, B6, 13509-13-518.

Back, S., Strecker, M.R. (1998). Asymmetric late Pleistocene glaciations in the North Basin of the Baikal rift, Russia. *Journal of the Geological Society, London*, 155, 61-69.

Back, S., De Batist, M., Strecker, M.R., Vanhauwaert, P. (1999). Quaternary depositional systems in northern Lake Baikal. *Journal of Geology*, 107, 1-12.

Baker, V.R., Benito, G., Rudoy, A.N. (1993). Paleohydrology of Late Pleistocene superflooding, Altay Mountains, Siberia. *Science*, 259, 348-350.

Baraboshkin, E.J. (1999). Berriasian-Valanginian (Early Cretaceous) seaways of the Russian Platform Basin and the problem of Boreal/Tethyan correlations. *Geologica Carpathica*, 50 (1) 5-20.

Bard, J.P. (1983). Metamorphism of an obducted island arc: example of the Kohistan sequence (Pakistan) in the Himalayan collided range. *Earth and Planetary Science Letters*, 65, 133-144.

Bayasgalan, A., Jackson, J., Ritz, J.-F., Carretier, S. (1999a). Forebergs, flower structures, and the development of large intracontinental strike-slip faults: the Gurvan Bogd fault system in Mongolia. *Journal of Structural Geology*, 21, 1285-1302.

Bayasgalan, A., Jackson, J., Ritz, J.-F., Carretier, S. (1999b). Field examples of strike-slip fault terminations in Mongolia and their tectonic significance. *Tectonics*, 18 (3), 394-411.

Bazhenov, M.L. (1993). Cretaceous paleomagnetism of the Fergana Basin and adjacent ranges, Central Asia: tectonic implications. *Tectonophysics*, 221, 251-267.

Bazhenov, M.L., Perroud, H., Chauvin, A., Burtman, V.S., Thomas, J.-C. (1994). Paleomagnetism of Cretaceous red beds from Tadzhikistan and Cenozoic deformation due to India-Eurasia collision. *Earth and Planetary Science Letters*, 124, 1-18.

Bazhenov, M.L., Alexutin, M.V., Bondarenko, G.E., Sokolov, S.D. (1999a). Mesozoic paleomagnetism of the Taigonos peninsula, the Sea of Okhotsk: implications to kinematics of continental and oceanic plates. *Earth and Planetary Science Letters*, 173, 113-127.

Bazhenov, M.L., Burtman, V.S., Dvorova, A.V. (1999b). Permian paleomagnetism of the Tien Shan fold belt, Central Asia: post-commisional rotations and deformation. *Tectonophysics*, 312, 303-329.

Beane, R.J., Connelly, J.N. (2000). $^{40}Ar/^{39}Ar$, U-Pb, and Sm-Nd constraints on the timing of metamorphic events in the Maksyutov Complex, southern Ural Mountains. *Journal of the Geological Society of London*, 157, 811-822.

Bedrosian, P.A., Unsworth, M.J., Wang, F. (2001). Structure of the Altyn Tagh fault and Daxue Shan from magnetotelluric surveys: Implications for faulting associated with the rise of the Tibetan Plateau. *Tectonics*, 20 (4), 474-486.

Begemann, F., Ludwig, K.R., Lugmair, G.W., Min, K., Nyquist, L.E., Patchett, P.J., Renne, P.R., Shih, C.-Y., Villa, I.M., Walker, R.J. (2001). Call for an improved set of decay constants for geochronological use. *Geochimica et Cosmochimica Acta*, 65 (1), 111-121.

Bellemans, F. (1996). A nuclear-analytical contribution to the absolute calibration of the fission track dating method (in Dutch). Phd thesis, University of Gent, Analytical Chemistry Department, 177 pp.

Bellemans, F., De Corte, F., Van den haute, P. (1995a). Corning CN glasses for the evaluation of the neutron spectrum in fission track dating. *Applied Radiation and Isotopes*, 46 (12), 1351-1354.

Bellemans, F., De Corte, F., Van den haute, P., Ingelbrecht, C. (1995b). Towards a new glass monitor for the determination of the neutron fluence in fission-track dating. *Radiation Measurements*, 25, 527-530.

Bendick, R., Bilham, R., Freymueller, J., Larson, K., Yin, G. (2000). Geodetic evidence for a low slip rate in the Altyn Tagh fault system. *Nature*, 404, 69-72.

Berger, G.W., York, D. (1981). Geothermometry from $^{40}Ar/^{39}Ar$ dating experiments. *Geochimica et Cosmochimica Acta*, 45, 795-811.

Bertel, E., Märk, T.D. (1983). Fission tracks in minerals: annealing kinetics, track structure and age correction. *Physics and Chemistry of Minerals*, 9, 197-204.

Berzin, N.A., Kungurtsev, L.V. (1996). Geodynamic interpretation of Altai-Sayan geological complexes. *Russian Geology and Geophysics*, 37 (1), 56-73.

Berzin, N.A., Coleman, R.G., Dobretsov, N.L., Zonenshain, L.P., Xiao Xuchang, Chang, E.Z. (1994). Geodynamic map of the western part of the paleoasian Ocean. *Russian Geology and Geophysics*, 35 (7-8), 5-22.

Bhandari, N., Bhat, S.G., Lal, D., Rajagopalan, G., Tamhane, A.S.J., Venkatavaradan, V.S. (1971). Fission fragment tracks in apatite: recordable track lengths. *Earth and Planetary Science Letters*, 13, 191-199.

Bigazzi, G. (1981). The problem of the decay constant λ_f of ^{238}U. *Nuclear Tracks*, 5 (1/2), 35-44.

Bigazzi, G., Hadler N., J.C., Iunes, P.J., Oddone, M., Paulo, S.R., Poupeau, G. (1990). On neutron dosimetry: comparison between different dosimeters: preliminary results. *Nuclear Tracks and Radiation Measurements*, 17 (3), 217-221.

Bigazzi, G., Hadler N., J.C., Iunes, P.J., Oddone, M., Paulo, S.R., Zuñiga, A. (1995). Absolute thermal neutron fluence determination by thin film of natural uranium. *Nuclear Instruments and Methods in Physics Research*, A 352, 588-591.

Bigazzi, G., Guedes, S., Hadler N., J.C., Iunes, P.J., Paulo, S.R., Oddone, M., Osorio A., A.M., Zuñiga, A. (1999). Potentialities and practical limitations of absolute neutron dosimetry using thin films of uranium and thorium applied to the fission track dating. *Radiation Measurements*, 31, 651-656.

Bobrov,V.A., Kalugin, I.A., Klerkx, J., Duchkov, A.D., Shcherbov, B.L., Stepin, A.S. (1999). The rate of recent sedimentation in Lake Teletskoe according to gamma-spectrometry (137Cs) data. *Russian Geology and Geophysics*, 40 (4), 530-536.

Braun, J. (2002). Quantifying the effect of recent relief changes on age-elevation relationships. *Earth and Planetary Science Letters*, 200, 331-343.

Brookfield, M.E. (2000). Geological development and Phanerozoic crustal accretion in the western segment of the southern Tien Shan (Kyrgyzstan, Uzbekistan and Tajikistan). *Tectonophysics*, 328, 1-14.

Brown, R.W. (1991). Backstacking apatite fission-track "stratigraphy": a method for resolving the erosional and isostatic rebound components of tectonic uplift histories. *Geology*, 19, 74-77.

Brown, R.D., Summerfield, M.A. (1997). Some uncertainties in the derivation of rates of denudation from thermochronological data. *Earth Surface Processes and Landforms*, 22, 239-248.

Buchan, C., Cunningham, D., Windley, B.F., Tomurhuu, D. (2001). Structural and lithological characteristics of the Bayankhongor ophiolite zone, Central Mongolia. *Journal of the Geological Society, London*, 158, 445-460.

Bullen, M.E. (1999). Late Cenozoic tectonic evolution of the Kyrgyz range and adjoining Chu Basin: new age constraints from fission-track, (U-Th)/He, and magnetostratigraphy. Master Thesis, Pennsylvania State University, USA, 74 pp.

Bullen, M.E., Burbank, D.W., Garver, J.I., Abdrakhmatov, K,Ye. (2001). Late Cenozoic tectonic evolution of the northwestern Tien Shan: New age estimates for the initiation of mountain building *Geological Society of America Bulletin*, 113/12, 1544-1559.

Bullen, M.E., Burbank, D.W., Garver, J.I. (2003). Building the Northern Tien Shan: integrated thermal, structural and topographic constraints. *Journal of Geology*, 111, 149-165.

Burbank, D.W. (1992). Causes of recent Himalayan uplift deduced from deposited patterns in the Ganges basin. Nature, 357, 680-683.

Burbank, D., Anderson, R. (2000). *Tectonic Geomorphology*. Blackwell Science, Oxford, 288 pp.

Burbank, D.W., McLean, J.K., Bullen, M., Abdrakhmatov, K.Y., Miller, M.M. (1999). Partitioning of intramontane basins by thrust related folding, Tien Shan, Kyrgyzstan. *Basin Research*, 11, 75-92.

Burchfiel, B.C., C. Zhiliang, K.V. Hodges, L. Yuping, L.H. Royden, D. Changrong, and X. Jiene (1992). The South Tibetan Detachment System, Himalayan Orogen; extension contemporaneous with and parallel to shorteningin a collisional mountain belt. *Geological Society of America Special Paper,* 269, 41 pp.

Burg, J.-P., Nievergelt, P., Oberli, F., Seward, D., Davy, P., Maurin, J.-C., Diao, Z., Meier, M. (1998). The Namche Barwa syntaxis: evidence for exhumation related to compressional crustal folding. *Journal of Asian Earth Sciences*, 16 (2-3), 239-252.

Burov, E., Kogan, M.G., Lyon-Caen, H., Molnar, P. (1990). Gravity anomalies, the deep structure, and dynamic processes beneath the Tien Shan. *Earth and Planetary Science Letters*, 96, 367-383.

Burov, E.B., Lobkovsky, L.I., Cloetingh, S., Nikishin, A.M. (1993). Continental lithosphere folding in Central Asia (Part II): constraints from gravity and topography. *Tectonophysics*, 226, 1-14.

Burtman, V.S. (1980). Faults of Middle Asia. *American Journal of Science*, 280, 725-744.

Burtman, V.S. (2000). Cenozoic crustal shortening between the Pamir and Tien Shan and a reconstruction of the Pamir-Tien Shan transition zone for the Cretaceous and Palaeogene. *Tectonophysics*, 319, 69-92.

Burtner, R.L., Nigrini, A., Donelick, R.A. (1994). Thermochronology of Lower Cretaceous source rocks in the Idaho-Wyoming thrust belt. *AAPG Bulletin*, 78, 10, 1613-1636.

Buslov, M.M. (1998). Terrain tectonics and geodynamics of mossaic-block type folded areas – an example from Altai-Sayan and East Kazakhstan regions. PhD. Thesis, UIGGM Press, Novosibirsk, Russia, 300 pp.

Buslov, M.M., Sintubin, M. (1995). Structural evolution of the Lake Teletskoe zone, Altai-Sayan folded area. *Russian Geology and Geophysics*, 36 (10), 81-87.

Buslov, M.M., Watanabe, T. (1996). Intrasubduction collision and its role in the evolution of an accretionary wedge: the Kurai zone of Gorny Altai (Central Asia). *Russian Geology and Geophysics*, 37 (1), 74-84.

Buslov, M.M., Bersin, N.A., Dobretsov, N.L., Simonov, S.A. (1993). Geology and tectonics of Gorny Altai. IGCP-283, 4th International Symposium, Field excursion guidebook. Novosibirsk, pp. 122.

Buslov, M.M., Zykin, V.S., Novikov, I.S., Delvaux, D. (1999). Cenozoic history of the Chuya depression (Gorny Altai): Structure and Geodynamics. *Russian Geology and Geophysics*, 40 (12), 1687-1701.

Buslov, M.M., Fujiwara, Y., Safonova, I. Yu., Okada, S., Semakov, N.N. (2000). The junction zone of the Gorny Altai and Rudny Altai terranes: Structure and evolution. *Russian Geology and Geophysics*, 41 (3), 377-390.

Buslov, M.M., Smirnova, L.V., Theunissen, K. (2001a). Geological structure and basement evolution of the region of Lake Teletskoye. *Geological Sciences Annals of the Royal Museum for Central Africa, Tervuren, Belgium*, 105, 183-204.

Buslov, M.M., Saphonova, I.Yu., Watanabe, T., Obut, O.T., Fujiwara, Y., Iwata, K., Semakov, N.N., Sugai, Y., Smirnova, L.V., Kazansky, A.Yu. (2001b). Evolution of the Paleo-Asian Ocean (Altai-Sayan region, Central Asia) and collision of possible Gondwana-derived terranes with the southern marginal part of the Siberian continent. *Geosciences Journal*, 5 (3), 203-224.

Buslov M.M., Watanabe, T., Smirnova, L.V., Fujiwara I., Iwata, K., De Grave, J., Semakov N.N., Travin, A.V., Kiryanova, A.P., Kokh, D.A. (2003). Role of strike-slip faults in Late Paleozoic-Early Mesozoic tectonics and geodynamics of the Altai-Sayan and East Kazakhstan folded zone. *Russian Geology and Geophysics*, 44, 1-2, 49-75.

Buslov, M.M., Klerkx, J., Abdrakhmatov, K., Delvaux, D., Kuchai, O.A., Muraliev, A. (submitted to Tectonophysics). Recent geodynamics of northern Tien Shan.

Butler, R.W.H., Prior, D.J., Knipe, R.J. (1989). Neotectonics of the Nanga Parbat syntaxis, Pakistan, and crustal stacking in the northwest Himalayas. *Earth and Planetary Science Letters*, 94, 329-343.

Carling, P.A. (1996). Morphology, sedimentology and palaeohydraulic significance of large gravel dunes, Altai Mountains, Siberia. Sedimentology, 43, 647-664.

Carlson, W.D. (1990). Mechanisms and kinetics of apatite fission-track annealing. *American Mineralogist*, 75, 1120-1139.

Carlson, W.D. (1993). Mechanisms and kinetics of apatite fission-track annealing – Reply to Green et al. *American Mineralogist*, 78, 446-449.

Carlson, W.D., Donelick, R.A., Ketcham, R.A. (1999). Variability of apatite fission-track annealing kinetics: I. Experimental results. *American Mineralogist*, 84, 1213-1223.

Carpéna, J., Mailhé, D. (1987). Fission-track dating calibration of the Fish Canyon Tuff standard in French reactors. *Chemical Geology (Isotope Geoscience Section)*, 66, 53-59.

Carpéna, P.J., Rutkiewicz, W. (1989). Ages traces des fission des apatites et des zircons du sommet du K2 (8611 m), Pakistan. *Eclogae Geologicae Helvetiae*, 82, 735-742.

Carpenter, S.B. (1984). Standard reference materials: calibrated glass standards for fission track use. *Natural Bureau of Standards Special Publications*, 206-92.

Carpenter, S.B., Reimer, G.M. (1974). Standard reference materials: calibrated glass standards for fission track use. *Natural Bureau of Standards Special Publications*, 206-49.

Carroll, A.R., Liang, Y., Graham, S.A., Xiao, X., Hendrix, M.S., Chu, J., McKnight, C.L. (1990). Junggar Basin, northwest China: trapped Late Paleozoic ocean. *Tectonophysics*, 181, 1-14.

Carroll, A.R., Graham, S.A., Hendrix, M.S., Ying, D., Zhou, D. (1995). Late Paleozoic tectonic amalgamation of northwestern China: sedimentary record of the northern Tarim, northwestern Turpan and southern Junggar basins. *Geological Society of America Bulletin*, 107 (5), 571-594.

Cerveney, P.F., Naeser, C.W., Keleman, P.B., Lieberman, J.E., Zeitler, P.K. (1989). Zircon fission-track ages from the Gasherbrum diorite, Karakorum range, northern Pakistan. *Geology*, 17, 1044-1048.

Chaillou, D., Chambaudet, A., Zidler, B. (1981). Sur la retention des traces de fission de l'uranium dans les minéraux. *Journal Physique*, 42, 343-345.

Chamberlain, C.P., Zeitler, P.K., Erickson, E. (1991). Constraints on the tectonic evolution of the northwestern Himalaya from geochronologic and petrologic studies of Babusar Pass, Pakistan. *Journal of Geology*, 99, 829-849.

Champel, B., van der Beek, P., Mugnier, J.L., Leturmy, P. (2002). Growth and lateral propagation of fault-related folds in the Siwaliks of western Nepal: rates, mechanisms and geomorphic signature. *Journal of Geophysical Research*, 107, B6, 10.1029/2001JB000578, 18pp..

Chen, C., Lu, H., Jia, D., Cai, D., Wu, S. (1999). Closing history of the southern Tianshan oceanic basin, western China: an oblique collisional orogeny. *Tectonophysics*, 302, 23-40.

Chen, J., Zhou, T., Xie, Z., Zhang, X., Guo, X. (2000). Formation of positive $\varepsilon_{Nd}(T)$ granitoids from the Alataw mountains, Xinjiang, China, by mixing and fractional crystallization: implication for Phanerozoic crustal growth. *Tectonophysics*, 328, 53-67.

Chen, Q., Dickinson, W.R. (1986). Contrasting nature of petroliferous Mesozoic-Cenozoic basins in eastern and western China. *American Association of Petroleum Geologists Bulletin*, 70 (3), 263-275.

Chen, W.-P., Chen, C.-Y., Nábelek, J.L. (1999). Present-day deformation of the Qaidam basin with implications for intra-continental tectonics. *Tectonophysics*, 305, 165-181.

Chen, Y., Cogné, J.-P., Courtillot, V., Avouac, J.-P., Tapponnier, P., Wang, G., Bai, M., You, H., Li, M., Wei, C., Buffetaut, E. (1991). Paleomagnetic study of Mesozoic continental sediments along the northern Tien Shan (China) and heterogeneous strain in Central Asia. *Journal of Geophysical Research*, 96, B3, 4065-4082.

Chen, Y., Cogné, J.-P., Courtillot, V. (1992). New Cretaceous paleomagnetic poles from the Tarim Basin, northwestern China. *Earth and Planetary Science Letters*, 114, 17-38.

Chen, Z., Burchfiel, B.C., Liu, Y., King, R.W., Royden, L.H., Tang, W., Wang, E., Zhao, J., Zhang, X. (2000). Global positioning system measurements from eastern Tibet and their implications for India/Eurasia intercontinental deformation. *Journal of Geophysical Research*, 105, B7, 16215-16227.

Chikov, B.M., Zinoviev, S.V. (1996). Post-Hercynian collisional structures of western Altai. *Russian Geology and Geophysics*, 37 (11), 59-67.

Chipizubov, A.V., Smekalin, O.P. (1999). Fault scarps and the causative prehistoric earthquakes in the main Sayan fault zone. *Russian Geology and Geophysics*, 40 (6), 921-931.

Chlachula, J. (2001). Pleistocene climate change, natural environments and palaeolithic occupation of the Altai area, west-central Siberia. *Quaternary International*, 80-81, 131-167.

Chun, S.Y., Nordberg, H., Firestone, R.B., Ekstrøm, L.P. (1999). *Isotope Explorer*, version 2.23).

Cloetingh, S., Burov, E., Poliakov, A. (1999). Lithospheric folding: primary response to compression? (from central Asia to Paris basin). *Tectonics*, 18 (6), 1064-1083.

Cobbold, P.R., Davy, P. (1988). Indentation tectonics in nature and experiment. 2. Central Asia. *Bulletin of the Geological Institutions of Uppsala* N.S., 14, 143-162.

Cobbold, P.R., Sadybakasov, E., Thomas, J.C. (1994). Cenozoic transpression and basin development, Kyrghyz Tienshan, Central Asia. *In*: Roure, F., Ellouz, N., Shein, V.S., Skvortsov, I (Eds) Geodynamic evolution of sedimentary basins, International Symposium. Moscow, 181-202.

Cogné, J.-P., Chen, Y., Courtillot, V., Rocher, F., Wang, G., Bai, M., You, H. (1995). A paleomagnetic study of Mesozoic sediments from the Junggar and Turfan basins, northwestern China. *Earth and Planetary Science Letters*, 133, 353-366.

Coleman, R.G. (1989). Continental growth of nortwest China. *Tectonics*, 8 (3), 621-635.

Copeland, P., Harrison, T.M., Kidd, W.S.F, Xu, R., Zhang, Y. (1987). Rapid early Miocene acceleration of uplift in the Gangdese Belt, Xizang (southern Tibet) and its bearing on accommodation mechanisms of the India-Asia collision. *EPSL*, 86, 240-252.

Copeland, P., Harrison, T.M., Yun, P., Kidd, W.S.F., Roden, M., Zhang Yuquan (1995). Thermal evolution of the Gangdese batholith, southern Tibet: A history of episodic unroofing. *Tectonics*, 14 (2), 223-236.

Condie, K.C., Rosen, O.M. (1994). Laurentia-Siberia connection revisited. *Geology*, 22, 168-170.

Corrigan, J. (1991). Inversion of apatite fission track data for thermal history information. *Journal of Geophysical Research*, 96, B6, 10347-10360.

Corrigan, J. (1993). Apatite fission-track analysis of Oligocene strata in South Texas, U.S.A.: Testing annealing models. *Chemical Geology (Isotopes Geoscience Section)*, 104, 227-249.

Coyle, D.A., Wagner, G.A., Hejl, E., Brown, R., Van den haute, P. (1997). The Cretaceous and younger thermal history of the KTB site (Germany): apatite fission-track data from the Vorbohrung. *Geologische Rundschau*, 86, 203-209.

Cowan, G.A., Adler, H.H. (1976). The variability of the natural abundance of ^{235}U. *Geochimica et Cosmochimica Acta*, 40, 1487-1490.

Crowley, K.D. (1985). Thermal significance of fission-track length distributions. *Nuclear Tracks*, 10 (3), 311-322.

Crowley, K.D. (1986). Neutron dosimetry in fission-track analysis. *Nuclear Tracks and Radiation Measurements*, 11 (4/5), 237-243.

Crowley, K.D. (1993). Lenmodel: a forward model for calculating length distributions and fission-track ages in apatite. *Computers and Geosciences*, 19 (5), 619-626.

Crowley, K.D., Cameron, M., Schaefer, R.L. (1991). Experimental studies of annealing of etched fission tracks in fluorapatite. *Geochimica et Cosmochimica Acta*, 55, 1449-1465.

Cunningham, W.D. (2001). Cenozoic normal faulting and regional doming in the southern Hangay region, Central Mongolia: implications for the origin of the Baikal rift province. *Tectonophysics*, 331, 389-411.

Cunningham, W.D., Windley, B.F., Dorjnamjaa, D., Badamgarov, J., Saandar, M. (1996a). Late Cenozoic transpression in southwestern Mongolia and the Gobi Altai – Tien Shan connection. *Earth and Planetary Science Letters*, 140, 67-81.

Cunningham, W.D., Windley, B.F., Dorjnamjaa, D., Badamgarov, J., Saandar, M. (1996b). A structural transect across the Mongolian western Altai: active transpressional mountain building in Central Asia. *Tectonics*, 15 (1), 142-156.

Cunningham, W.D., Windley, B.F., Owen, L.A., Barry, T., Dorjnamjaa, D., Badamgarav, J. (1997). Geometry and style of partitioned deformation within a Late Cenozoic transpressional zone in eastern Gobi Altai Mountains, Mongolia. *Tectonophysics*, 277, 285-306.

Curray, J.R., Munasinghe, T. (1989). Timing of intraplate deformation, northeastern Indian Ocean. *Earth and Planetary Science Letters*, 94, 71-77.

Dahl, P.S. (1995). The crystal-chemical basis for Ar retention in micas: inferences from interlayer partitioning and implications for geochronology. *Contributions to Mineralogy and Petrology*, 123, 22-39.

Dakowski, M., Burchart, J., Gałązka, J. (1974). Experimental formula for thermal fading of fission tracks in minerals and natural glasses. *Bulletin de l'Académie Polonaise des Sciences, Série des Sciences de la Terre*, 22 (1), 11-17.

Dartyge, E., Duraud, J.P., Langevin, Y., Maurette, M. (1981). New model of nuclear particle tracks in dielectric minerals. *Physical Review*, B23, 5213-5229.

De Batist, M., Imbo, Y., Vermeersch, P., Klerkx, J., Giralt, S., Delvaux, D., Lignier, V., Beck, C., Kalugin, I., Abdrakhmatov, K.Y. (2002). Bathymetry and sedimentary environments of Lake Issyk-Kul, Kyrgyz Republic (Central Asia): a large, high-altitude, tectonic lake. *In*: Klerkx, J., Imanackunov, B. (Eds.). *Lake Issyk-Kul: its natural environment*. Kluwer Academic Publishers, Dordrecht, 101-123.

De Carvalho, H.G., Martins, J.B., Medeiros, E.L., Tavares, O.A.P. (1982). Decay constant for the spontaneous-fission process in ^{238}U. *Nuclear Instruments and Methods*, 197, 417-426.

De Corte, F., Van den haute, P., De Wispelaere, A., Jonckheere, R., (1991). Calibration of the fission-track dating method: is Cu useful as an absolute thermal neutron fluence monitor? *Chemical Geology (Isotope Geoscience Section)*, 86, 187-194.

De Corte, F., Van den haute, P., Bellemans, F. (1995a). The use of uranium doped glasses in fission-track dating. *Radiation Measurements*, 25, 511-516.

De Corte, F., Masumoto, K., De Wispelaere, A., Bellemans, F. (1995b). A Dedicated NAA Method to Determine the Neutron Spectrum Monitor Elements Co, Au and Lu with High Accuracy in Alloyed Wires and Foils. *Journal of Radioanalytical and Nuclear Chemistry*, 192 (1), 91.

De Corte, F., Bellemans, F., Van den haute P., Ingelbrecht, C., Nicholl, C. (1998). A new U doped glass certified by the European Commission for the calibration of fission-track dating. In: Van den haute, P. and De Corte, F. (Editors) *Advances in fission-track geochronology,* Kluwer Academic Publishers, Dordrecht, pp. 67-78.

Deer, W.A., Howie, R.A., Zussman, J. (1962). *Rock forming minerals, Volume 5, Non-silicates*. Longmans, London, 371 pp.

Deev, E.V., Vysotsky, E.M., Novikov, I.S., Mistryukov, A.A. (1995). Geomorphological analysis of the Lake Teletskoe Region. *Russian Geology and Geophysics*, 36 (10), 122-131.

De Grave, J., Van den haute, P. (2000). Apatite fission-track thermochronology of the Altai Mountains, Lake Teletskoye Region, South Siberia: Preliminary results. *In*: W.P. Noble, P.B. O'Sullivan, R.W. Brown (eds) 9th International Conference on fission track dating and thermochronology, Lorne 2000. *Geological Society of Australia Abstracts* No. 58, 63-65.

De Grave, J., Van den haute, P. (2002). Denudation and cooling of the Lake Teletskoye region in the Altai Mountains (South Siberia) as revealed by apatite fission-track thermochronology. Tectonophysics, 349, 145-159.

Dehandschutter, B. (2001). Study of the recent structural evolution of continental basins in Altai-Sayan (Central Asia). PhD. Thesis, Vrije Universiteit Brussel, Belgium, pp. 212.

Dehandschutter, B., Delvaux, D., Boven, A. (1997). The Lake Teletsk tectonic depression (Altai): new kinematic data and chronological relations. *Annual Report of the Department of Geology and Mineralogy, Royal Museum for Central Africa, Tervuren, Belgium*, 1995-1996, 147-167.

Dehandschutter, B., Buslov, M.M., Vysotsky, E.M., Klerkx, J., Delvaux, D. (2001). Active tectonics of the Teletsk basin. *Geological Sciences Annals of the Royal Museum for Central Africa, Tervuren, Belgium*, 105, 205-237.

Dehandschutter, B., Vysotsky, E., Delvaux, D., Klerkx, J., Buslov, M.M., Seleznev, V.S., De Batist, M. (2002). Structural evolution of the Teletsk graben (Russian Altai). *Tectonophysics*, 351, 139-167.

Delvaux, D., Fernandez-Alonso, M., Klerkx, J., Kuzmin, A., Matton, C., Selegei, V., Theunissen, K., Vysotsky, E. (1995a). Evidence for active tectonics in Lake Teletskoe (Gorny Altai). *Russian Geology and Geophysics*, 36 (10), 100-112.

Delvaux, D., Moeys, R., Stapel, G., Melnikov, A., Ermikov, V. (1995b). Paleostress reconstructions and geodynamics of the Baikal region, Central Asia, Part 1. Palaeozoic and Mesozoic pre-rift evolution. *Tectonophysics*, 252, 61-101.

Delvaux, D., Theunissen, K., Van der Meer, R., Berzin, N. (1995c). Dynamics and paleostress of the Cenozoic Kurai-Chuya depression of Gorny Altai (South Siberia): tectonic and climatic control. *Russian Geology and Geophysics*, 36 (10), 26-45.

Delvaux, D., Moeys, R., Stapel, G., Petit, C., Levi, K., Miroshnichenko, A., Ruzhich, V., San'kov, V. (1997). Paleostress reconstructions and geodynamics of the Baikal region, Central Asia, Part 2. Cenozoic rifting. *Tectonophysics*, 282, 1-38.

Delvaux, D., Fronhoffs, A., Hus, R., Poort, J. (1998). Normal fault splays, relay ramps and transfer zones in the central part of the Baikal rift basin: Insights from digital topography and bathymetry. *Bulletin des Centres Reserches, Explorations-Productions, Elf Aquitaine*, 22, 341-357.

Delvaux, D., Abdrakhmatov, K., Strom, A., Havenith, H.-B., Trefois, P. (2000). Active sinistral transpression along the Chon Kemin-Chilik fault zone on North Tien Shan: paleoseismic and neotectonic significance. *In*: Geodynamics of Tien Shan, International Workshop (abstracts and papers), Bishkek, 19.

Derbyshire, M., Ingelbrecht, C., De Corte, F., Van den haute, P., Van Ham, J. (2001). Preparation of two uranium glass reference materials for fission-track dating of geological samples. *Radiation Measurements*, 30, 419-422.

Dergunov, A.B. (1972). Quaternary compression and extension structures in the easern Altai. *Geotectonica*, 3, 99-110.

Dergunov, A.B. (1988). Zones of tectonic shortening in Central Asian Caledonides. *Geotectonics*, 22 (3), 243-252.

Dergunov, A.B., Kheraskova, T.N. (1982). Composition of volcanics of the early phase of development of the caledonides in Central Asia (Central Kazakhstan, Altay-Sayan region, and western Mongolia). *International Geology Review*, 24 (10), 1117-1132.

Dewey, J.F., Shackleton, R.M., Chengfa, C., Yiyin, S (1988). The tectonic evolution of the Tibetan Plateau. *Philosophical Transactions of the Royal Society, London*, A327, 379-413.

Distanova, A.N. (2000). Early Paleozoic granitoid associations of the Altai-Sayan folded area: their types and role in paleogeodynamic reconstructions. *Russian Geology and Geophysics*, 41 (9), 1202-1213.

Dobretsov, N.L., Vladimirov, A.G. (Eds.) (2001). Continental growth in the Phanerozoic: Evidence from Central Asia. Geology, magmatism and metamorphism of the western part of Altai-Sayan Fold Region. IGCP-420, 3rd Workshop, Field Excursion Guide. Novosibirsk, pp. 139.

Dobretsov, N.L., Buslov, M.M., Simonov, V.A. (1991). Associated ophiolites, glaucophane schists and eclogites of the Gornyy Altai. *Doklady, Earth Science*, 319 (5), 123-128.

Dobretsov, N.L., Simonov, V.A., Buslov, M.M., Kurenkov, S.A. (1992). Oceanic and island arc ophiolites of Gorny Altai. *Russian Geology and Geophysics*, 12, 3-14.

Dobretsov, N.L., Berzin, N.A., Buslov, M.M. (1995a). Opening and tectonic evolution of the Paleo-Asian Ocean. *International Geology Review*, 37, 335-360.

Dobretsov, N.L., Berzin, N.A., Buslov, M.M., Ermikov, V.D. (1995b). General aspects of the evolution of the Altai region and the interrelationships between its basement pattern and the neotectonic structural development. *Russian Geology and Geophysics*, 36 (10), 3-15.

Dobretsov, N.L., Buslov, M.M., Delvaux, D., Berzin, N.A., Ermikov, V.D. (1996). Meso- and Cenozoic tectonics of the Central Asian mountain belt: effects of lithospheric plate interaction and mantle plumes. *International Geology Review*, 38, 430-466.

Dodson, M.H. (1973). Closure temperature in cooling geochronological and petrological systems. *Contributions to Mineralogy and Petrology*, 40, 259-274.

Dodson, M.H. (1979). Theory of cooling ages. In: Jäger, E., Hunziker, J.C. (Eds.). Lectures on isotope geology. Springer-Verlag, Berlin, 194-202.

Donelick, R.A. (1991). Crystallographic orientation dependence of mean etchable fission track length in apatite: An empirical model and experimental observations. *American Mineralogist*, 76, 83-91.

Donelick, R.A., Miller, D.S. (1991). Enhanced TINT fission track densities in low spontaneous track density apatites using ^{252}Cf-derived fission fragment tracks: a model and experimental observations. *Nuclear Tracks and Radiation Measurements*, 18, 3, 301-307.

Donelick, R.A., Roden, M.K., Mooers, J.D., Carpenter, B.S., Miller, D.S. (1990). Etchable length reduction of induced fission tracks in apatite at room temperature (~23°C): crystallographic orientation effects and "initial" mean lengths. *Nuclear Tracks and Radiation Measurements*, 17, 3, 261-265.

Donelick, R.A., Ketcham, R.A., Carlson, W.D. (1999). Variability of apatite fission-track annealing kinetics: II. Crystallographic orientation effects. *American Mineralogist*, 84, 1224-1234.

Duchkov, A.D., Klerkx, J., Kazantsev, S.A.. (1995). Heat flow in Lake Teletskoe. *Russian Geology and Geophysics*, 36 (10), 132-142.

Duchkov, A.D., Kazantsev, S.A., Klerkx, J., Duchkov, A.A. (2001). Heat flow and temperature field of the bottom fill of Lake Teletskoye. *Geological Sciences Annals of the Royal Museum for Central Africa, Tervuren, Belgium*, 105, 283-301.

Duddy, I.R., P.F. Green, Laslett, G.M. (1988). Thermal annealing of fission tracks in apatite. 3. Variable temperature behaviour. *Chemical Geology (Isotopes Geoscience Section)*, 73, 25-38.

England, P.C., Houseman, G.A. (1988). The mechanics of the Tibetan Plateau. *Philosophical Transactions of the Royal Society, London*, A326, 301-320.

England, P., Molnar, P. (1990). Surface uplift, uplift of rocks, and exhumation of rocks. *Geology*, 18, 1173-1177.

Enkelmann, E., Jonckheere, R. (2003). Correction factors for systematic errors related to the track counts in fission-track dating with the external detector method. *Radiation Measurements*. In press.

Enkin, R.J., Yang, Z., Chen, Y., Courtillot, V. (1992). Paleomagnetic constraints on the geodynamic history of the major blocks of China, from the Permian to the present. *Journal of Geophysical Research*, 97, B10, 13953-13989.

Ermikov, V.D. (1994). Mesozoic precursors of the Cenozoic rift structures of Central Asia. *Bulletin des Centres Recherches, Explorations-Productions, Elf Aquitaine*, 18 (1), 123-134.

Faure, M., Natal'in, B.A., Monié, P., Vrublevsky, A.A., Borukaiev, C., Prikhodko, V. (1995). Tectonic evolution of the Anuy metamorphic rocks (Sikhote Alin, Russia) and their place in the Mesozoic geodynamic framework of East Asia. *Tectonophysics*, 241, 279-301.

Fielding, E.J. (1996). Tibet uplift and erosion. *Tectonophysics*, 260, 55-84.

Fin'ko, E.A. (1992). The relationship of recent vertical movements to the morphostructural pattern of the Kazakh shield. *Journal of Geodynamics*, 15 (3/4), 209-214.

Fitzgerald, P.G., Gleadow, A.J.W. (1990). New approaches in fission track geochronology as a tectonic tool: examples from the Transantarctic Mountains. *Nuclear Tracks and Radiation Measurements*, 17, 3, 351-357.

Fitzgerald, P.G., Sorkhabi, R.B., Redfield, T.F., Stump, E. (1995). Uplift and denudation of the central Alaska Range: A case study in the use of apatite fission track thermochronology to determine absolute uplift parameters. *Journal of Geophysical Research*, 100, B10, 20175-20191.

Fitzgerald, P.G., Muñoz, J.A., Coney, P.J., Baldwin, S.L. (1999). Asymmetric exhumation across the Pyrenean orogen: implications for the tectonic evolution of a collisional orogen. *Earth and Planetary Science Letters*, 173, 157-170.

Fleischer, R.L., Hart, H.R., Jr. (1972). Fission track dating: techniques and problems. In: Bishop, W.W., Miller, D.A., Cole, S. (Eds). *Proceedings of the Burg Wartenstein Conference on Hominoid Evolution*. Scottish Academy Press, Edinburgh, 135-170.

Fleischer, R.L., Price, P.B. (1964). Techniques for geological dating of minerals by chemical etching of fission fragment tracks. *Geochimica et Cosmochimica Acta*, 28, 1705-1714.

Fleischer, R.L., Price, P.B., Walker, R.M. (1965). Effects of temperature, pressure and ionization on the formation and stability of fission tracks in minerals and glasses. *Journal of Geophysical Research*, 70, 1497-1502.

Fleischer, R.L., Price, P.B., Walker, R.M. (1975). *Nuclear tracks in solids: principles and applications*. University of California Press, Berkeley, 605 pp.

Flerov, G.N., Petrzhak, K.A. (1940). Spontaneous fission of uranium. *Journal of Physics*, 3, 275-280.

Foster, D.A., Gleadow, A.J.W., Mortimer, G. (1994). Rapid Pliocene exhumation in the Karakoram (Pakistan), revealed by fission-track thermochronology of the K2 gneiss. *Geology*, 22, 19-22.

Frost, B.R., Avchenko, O.V., Chamberlain, K.R., Frost, C.D. (1998). Evidence for extensive Proterozoic remobilization of the Aldan shield and implications for Proterozoic plate tectonic reconstructions of Siberia and Laurentia. *Precambrian Research*, 89, 1-23.

Gaetani, M. (1997). The Karakorum block in Central Asia, from Ordovician to Cretaceous. *Sedimentary Geology*, 109, 339-359.

Gaetani, M., Le Fort, P., Tanoli, S., Angiolini, L., Nicora, A., Sciunnach, D., Khan, A. (1996). Reconnaissance geology in Upper Chitral, Baroghil and Karambar districts (northern Karakorum, Pakistan). *Geologische Rundschau*, 85, 683-704.

Galbraith, R.F. (1990). The radial plot: graphical assessment of spread in ages. *Nuclear Tracks and Radiation Measurements*, 17, 3, 207-214.

Gallagher, K. (1995). Evolving temperature histories from apatite fission-track data. *Earth and Planetary Science Letters*, 136, 421-435.

Gallagher, K., Sambridge, M. (1994). Genetic algorithms: a powerful method for large scale non-linear optimisation problems. *Computers and Geosciences*, 20, 1229-1236.

Galliker, D., Hugentobler, E., Hahn, B. (1970). Spontane kernspaltung von ^{238}U und ^{241}Am. *Helveticae Physicae Acta*, 43, 593-606.

Gao Jun, He Guoqi, Li Maosong, Xiao Xuchang, Tang Yaoqing, Wang, J., Zhao, M. (1995). The mineralogy, petrology, metamorphic PTDt trajectory and exhumation mechanism of blueschists, south Tienshan, northwestern China. *Tectonophysics*, 250, 151-168.

Gao Jun, Li Maosong, Xiao Xuchang, Tang Yaoqing, He Guoqi (1998). Paleozoic tectonic evolution of the Tienshan orogen, northwestern China. *Tectonophysics*, 287, 213-231.

Gao, S., Davis, P.M., Liu, H., Slack, P.D., Zorin, Y.A., Logatchev, N.A., Kogan, M., Burkholder, P.D., Meyer, R.P. (1994). Asymmetric upwarp of the asthenosphere beneath the Baikal rift zone, Siberia. *Journal of Geophysical Research*, 99, B8, 15319-15330.

Garwin, L. (1985). Fission track dating and tectonics in the Eastern Pyrenees. Unpublished doctoral thesis, University of Cambridge.

Garzanti, E., Le Fort, P., Sciunnach, D. (1999). First report of Lower Permian basalts in south Tibet: tholeiitic magmatism during break-up and incipient opening of Neothetys. *Journal of Asian Earth Sciences*, 17, 533-546.

George, M., Reddy, S., Harris, N. (1995). Isotopic constraints on the cooling history of the Nanga Parbat-Harramosh Massif and Kohistan Arc, western Himalaya. *Tectonics*, 14 (2), 237-252.

Gilder, S.A., Coe, R.S., Wu, H., Kuang, G., Zhao, X., Wu, Q., Tang, X. (1993). Cretaceous and Tertiary paleomagnetic results from Southeast China and their tectonic implications. *Earth and Planetary Science Letters*, 117, 637-652.

Gilder, S., Zhao, X., Coe, R., Meng, Z., Courtillot, V., Besse, J. (1996). Paleomagnetism and tectonics of the southern Tarim basin, northwestern China. *Journal of Geophysical Research*, 101, B10, 22015-22031.

Glasmacher, U.A., Wagner, G.A., Puchkov, V.N. (2002). Thermotectonic evolution of the western fold-and-thrust belt, southern Uralides, Russia, as revealed by apatite fission track data. *Tectonophysics*, 354, 25-48.

Gleadow, A.J.W. (1981). Fission-track dating methods: what are the real alternatives? *Nuclear Tracks*, 5 (1/2), 3-14.

Gleadow, A.J.W., Duddy, I.R. (1981). A natural long-term track annealing experiment for apatite. *Nuclear Tracks*, 5, 169-174.

Gleadow, A.J.W., Fitzgerald, P.G. (1987). Uplift history and structure of the Transantarctic Mountains: new evidence from fission track dating of basement apatites in the Dry Valley area, southern Victoria Land. *Earth and Planetary Science Letters*, 82, 1-14.

Gleadow, A.J.W., Lovering, J.F. (1977). Geometry factor for external detectors in fission track dating. *Nuclear Track Detection*, 1 (2), 99-106.

Gleadow, A.J.W., Duddy, I.R., Lovering, J.F. (1983). Fission track analysis: a new tool for the evaluation of thermal histories and hydrocarbon potential. *Australian Petroleum Exploration Association Journal*, 23, 93-102.

Gleadow, A.J.W., Duddy, I.R., Green, P.F., Lovering, J.F. (1986a). Confined fission track lengths in apatite: a diagnostic tool for thermal history analysis. *Contributions to Mineralogy and Petrology*, 94, 405-415.

Gleadow, A.J.W., Duddy, I.R., Green, P.F., Hegarty, K.A. (1986b). Fission track lengths in the apatite annealing zone and the interpretation of mixed ages. *Earth and Planetary Science Letters*, 78, 245-254.

Goldberg, E.L., Grachev, M.A., Phedorin, M.A., Kalugin, I.A., Khlystov, O.M., Mezentsev, S.N., Azarova, I.N., Vorobyeva, S.S., Zheleznyakova, T.O., Kulipanov, G.N., Kondratyev, V.I., Miginsky, E.G., Tsukanov, V.M., Zolotarev, K.V., Trunova, V.A., Kolmogorov, Yu., P., Bobrov, V.A. (2001). Application of synchrotron X-ray fluorescent analysis to studies of the records of paleoclimates of Eurasia stored in the sediments of Lake Baikal and Lake Teletskoye. *Nuclear Instruments and Methods in Physics Research*, A 470, 388-395.

Gordienko, I.V. (1994). Paleozoic geodynamic evolution of the Mongol-Okhotsk fold belt. *Journal of Southeast Asian Earth Sciences*, 9 (4), 429-433.

Goswami, J.N., Jha, R., Lal, D. (1984). Quantitative treatment of annealing of charged particle tracks in common minerals. *Earth and Planetary Science Letters*, 71, 120-128.

Green, P.F. (1980). On the cause of the shortening of spontaneous fission tracks in certain minerals. *Nuclear Tracks*, 4, 91-100.

Green, P.F. (1981). A new look at statistics in fission-track dating. *Nuclear Tracks*, 5, 77-86.

Green, P.F. (1985). Comparison of zeta calibration baselines for fission-track dating of apatite, zircon and sphene. *Chemical Geology (Isoptope Geosciece Section),* 58, 1-22.

Green, P.F. (1986). On the thermo-tectonic evolution of Northern England: evidence from fission track analysis. *Geological Magazine*, 123, 5, 493-506.

Green, P.F. (1988). The relationship between track shortening and fission track age reduction in apatite: combined influences of inherent instability, annealing anisotropy, length bias and system calibration. *Earth and Planetary Science Letters*, 89, 335-352.

Green, P.F., Durrani, S.A. (1977) Annealing studies of tracks in crystals. *Nuclear Tracks*, 1, 33-39.

Green, P.F.; Durrani, S.A. (1978). A quantitative assessment of geometry factors for use in fission track studies. *Nuclear Tracks*, 2, 207-213.

Green, P.F., Hurford, A.J. (1984). Thermal neutron dosimetry for fission track dating. *Nuclear Tracks*, 9 (3/4), 231-241.

Green, P.F., Duddy, I.R., Gleadow, A.J.W., Tingate, P.R., Laslett, G.M. (1985). Fission-track annealing in apatite: track length measurements and the form of the Arrhenius plot. *Nuclear Tracks*, 10, 323-328.

Green, P.F., Duddy, I.R., Gleadow, A.J.W., Tingate, P.R., Laslett, G.M. (1986). Thermal annealing of fission tracks in apatite.1. A qualitative description. *Chemical Geology (Isotopes Geoscience Section)*, 59, 237-253.

Green, P.F., Duddy, I.R., Laslett, G.M. (1988). Can fission track annealing in apatite be described by first-order kinetics? *Earth and Planetary Science Letters*, 87, 216-228.

Green, P.F., Duddy, I.R., Laslett, G.M., Hegarty, K.A., Gleadow, A.J.W., Lovering, J.F. (1989a). Thermal annealing of fission tracks in apatite. 4. Quantitative modelling techniques and extension to geological timescales. *Chemical Geology (Isotopes Geoscience Section)*, 79, 155-182.

Green, P.F., Duddy, I.R., Gleadow, A.J.W., Lovering, J.F. (1989b). Apatite fission-track analysis as a paleotemperature indicator for hydrocarbon exploration. *In*: Naeser, N.D., McCulloh, T.H. (Eds). Thermal histories of sedimentary basins: Methods and Case histories. Springer-Verlag, New York, 181-195.

Green, P.F., Laslett, G.M., Duddy, I.R. (1993). Mechanisms and kinetics of apatite fission-track annealing – Discussion. *American Mineralogist*, 78, 441-445.

Griffin, W.L., Ryan, C.G., Kaminsky, F.V., O'Reilly, S.Y., Natapov, L.M., Win, T.T., Kinny, P.D., Ilupin, I.P. (1999). The Siberian lithosphere traverse: mantle terranes and the assembly of the Siberian craton. *Tectonophysics*, 310, 1-35.

Grimmer, J.C., Jonckheere, R., Enkelmann, E., Ratschbacher, L., Hacker, B.R., Blythe, A.E., Wagner, G.A., Wu, Q., Liu, S., Dong, S. (2002). Cretaceous-Cenozoic history of the southern Tan-Lu fault zone: apatite fission-track and structural constraints from the Dabie Shan (eastern China). *Tectonophysics*, 359, 225-253.

Guedes, S., Hadler Neto, J.C., Iunes, P.J., Paulo, S.R., Zuñiga, A. (2000). Measurement of the spontaneous fission decay constant of 238U using SSNTD. *Journal of Radioanalytical and Nuclear Chemistry*, 245, 441-442.

Guedes, S., Hadler Neto, J.C., Iunes P.J., Burke, A.K., Kakazu, M.H., Sarkis, J.E.S., Paulo, S.R., Tello, C.A. (2002). Determination of the ^{238}U spontaneous fission decay constant without neutron irradiation. *Journal of Radioanalytical and Nuclear Chemistry*, 253, 73-76.

Guedes, S., Hadler Neto, J.C., Iunes P.J., Zuñega, A., Tello, C.A., Paulo, S.R. (2003). The use of the U(n,f) reaction dosimetry in the determination of the λ_f value through fission-track techniques. *Nuclear Instruments and Methods in Physics Research A*, 496, 215-221.

Guillot, S., Hodges, K., Le Fort, P., Pêcher, A. (1994). New constraints on the age of the Manslu leucogranite: evidence for episodic tectonic denudation in the Central Himalayas. *Geology*, 22, 559-562.

Hadler, J.C., Bigazzi, G., Guedes, S., Iunes, P.J., Oddone, M., Tello, C.A., Paulo, S.R. (2003) Spontaneous ^{238}U fission half-life measurements based on fission-track techniques. *Journal of Radioanalytical and Nuclear Chemistry*, 256, 155-157.

Hahn, O., Strassmann, F. (1939). Über den nachweis und das verhalten der bei der bestrahlung des urans mittels neutronen entstehenden erdalkalimetalle. *Die Naturwissenschaften*, 27, 11-15.

Han, B., Wang, S., Jahn, B., Hong, D., Kagami, H., Sun, Y. (1997). Depleted-mantle source for the Ulungur River A-type granites from North Xinjiang, China: geochemistry and Nd-Sr isotopic evidence, and implications for Phanerozoic crustal growth. *Chemical Geology*, 138, 135-159.

Harrison, T.M. (1981). Diffusion of ^{40}Ar in hornblende. *Contributions to Mineralogy and Petrology*, 78, 324-331.

Harrison, C.G.A. (1994). Rates of continental erosion and mountain building. *Geologische Rundschau*, 83, 431-447.

Harrison, T.M., Copeland, P., Kidd, W.S.F., Yin, A. (1992). Raising Tibet. *Science*, 255, 1663-1670.

Harrison, T.M., Copeland, P., Hall, S.A., Quade, J., Burner, S., Ojha, T.P., Kidd, W.S.F. (1993). Isotopic preservation of Himalayan/Tibetan uplift, denudation, and climatic histories of two molasse deposits. *Journal of Geology*, 101, 157-175.

Harrison, T.M., Copeland, P., Kidd, W.S.F., Lovera, O. (1995). Activation of the Nyainqentanghla shear zone: implications for uplift of the southern Tinetan Plateau. *Tectonics*, 14, 658-676.

Hartshorn, K., Hovius, N., Dade, W.B., Slingerland, R.L. (2002). Climate-driven bedrock incision in an active mountain belt. *Science*, 297, 2036-2038.

Hauck, M.L., Nelson, K.D., Brown, L.D., Zhao, W.J., Ross, A.R. (1998). Crustal structure of the Himalayan orogen at 90° east longitude from Project INDEPTH deep reflection profiles. *Tectonics*, 17, 481-500.

Hejl, E. (1995). Evidence for unetchable gaps in apatite fission tracks. *Chemical Geology (Isotope Geoscience Section)*, 122, 259-269.

Hendrix, M.S. (2000). Evolution of Mesozoic sandstone compositions, southern Junggar, northern Tarim, and western Turpan basins, northwest China: a detrital record of the ancestral Tian Shan. *Journal of Sedimentary Research*, 70 (3), 520-532.

Hendrix, M.S., Graham, S.A., Carroll, A.R., Sobel, E.R., McKnight, C.L., Schulein, B.J., Wang, Z. (1992). Sedimentary record and climatic implications of recurrent deformation in the Tien Shan: evidence from the Mesozoic strata of the north Tarim, south Junggar, and Turpan basins, northwest China. *Geological Society of America Bulletin*, 104, 53-79.

Hendrix, M.S., Dumitru, T.A., Graham, S.A. (1994). Late Oligocene – Early Miocene unroofing in the Chinese Tien Shan: an early effect of the India-Asia collision. *Geology*, 22, 487-490.

Henry, P., Le Pichon, X., Goffé, B. (1997). Kinematic, thermal and petrological model of the Himalayas: constraints related to metamorphism within the underthrust Indian crust and topographic elevation. *Tectonophysics*, 273, 31-56.

Holden, N.E. (1989). Total and spontaneous fission half-lives for uranium, plutonium, americium and curium nuclides. *Pure and Applied Chemistry*, 61, 104-112.

Holden, N.E. (1999). Neutron scattering and absorption properties. In: Lide, D.R. (Ed.) *Handbook of chemistry and physics*, CRC Press LLC.

Holden, N.E., Hoffman, D.C. (2000). Spontaneous fission half-lives for ground-state nuclides. *Pure and Applied Chemistry*, 72, 1525-1562.

Holden, N.E. and Holden, K.A. (1989). Re-examination of 2200 meter/second cross section experiments for neutron capture and fission standards. *Pure and Applied Chemistry*, 61, 1505-1510.

Holt, W.E., Chamot-Rooke, N., Le Pichon, X., Haines, A.J., Shen-tu, B., Ren, J. (2000). Velocity field in Asia inferred from Quaternary fault slip rates and Global Positioning System observations. *Journal of Geophysical Research*, 105, B8, 19185-19209.

Hu, A., Jahn, B., Zhang, G., Chen, Y., Zhang, Q. (2000). Crustal evolution and Phanerozoic crustal growth in northern Xinjiang: Nd isotopic evidence. Part I. Isotopic characterization of basement rocks. *Tectonophysics*, 328, 15-51.

Hubbard, M.S., Grew, E.S., Hodges, K.V., Yates, M.G., Pertsev, N.N. (1999). Neogene cooling and exhumation of upper amphibolite-facies 'whiteschists' in the southwest Pamir Mountains, Tajikistan. *Tectonophysics*, 305, 325-337.

Hurford, A.J. (1990a). International Union of Geological Sciences subcommission on geochronology recommendation for the standardization of fission track dating calibration and data reporting. *Nuclear Tracks and Radiation Measurements*, 17 (3), 233-236.

Hurford, A.J. (1990b). Standardization of fission track dating calibration: Recommendation by the Fission Track Working Group of the I.U.G.S. Subcommission on Geochronology. *Chemical Geology (Isotope Geoscience Section)*, 80, 171-178.

Hurford, A.J. (1998). Zeta: the ultimate solution to fission-track analysis calibration or just an interim measure? In: Van den haute, P. and De Corte, F. (Editors) *Advances in fission-track geochronology,* Kluwer Academic Publishers, Dordrecht, pp. 19-32.

Hurford, A.J. and Gleadow, A.J.W. (1977). Calibration of fission track dating parameters. *Nuclear Track Detection*, 1 (1), 41-48.

Hurford, A.J., Green, P.F. (1981). A reappraisal of neutron dosimetry and uranium-238 λ_f values in fission-track dating. *Nuclear Tracks*, 5 (1/2), 53-61.

Hurford, A.J., Green, P.F. (1982). A users' guide to fission track dating calibration. *Earth and Planetary Science Letters,* 59, 343-354.

Hurford, A.J., Green, P.F. (1983). The zeta age calibration of fission-track dating. *Geoscience,* 1, 285-317.

Hurford, A.J., Hammerschmidt, K. (1985). $^{40}Ar/^{39}Ar$ and K-Ar dating of the Bishop and Fish Canyon Tuffs: calibration ages for fission-track dating standards. *Chemical Geology (Isotope Geoscience Section)*, 58, 23-32.

Hurtrez, J.-E., Lucazeau, F., Lavé, J., Avouac, J.-P. (1999). Investigation of the relationships between basin morphology, tectonic uplift, and denudation from the study of an active fold belt in the Siwalik Hills, central Nepal. *Journal of Geophysical Research*, 104, B6, 12779-12796.

Hus, R., Dehandschutter, B., Bobrov, V.A., Acopachov, N.E. (1999). Active fault identification using Radon measurements around Lake Teletskoye (Altai, Russia). *Annual Report of the Department of Geology and Mineralogy, Royal Museum for Central Africa, Tervuren, Belgium*, 1997-1998, 177-201.

Huyghe, P., Galy, A., Mugnier, J.-L., France-Lanord, C. (2001). Propagation of the thrust system and erosion in the Lesser Himalaya: geochemical and sedimentological evidence. *Geology*, 29 (11), 1007-1010.

Ilyin, A.V. (1990). Proterozoic supercontinent, its latest Precambrian rifting, breakup, dispersal into smaller continents, and subsidence of their margins: Evidence from Asia. *Geology*, 18, 1231-1234.

Ilyin, A.V., Khalilov, V.A., Kozlov, M.S., Maslov, V.I., Timkin, V.I. (1994). The age of the Alakhinskii stock in Gorny Altai according to U-Pb and Rb-Sr dating. *Russian Geology and Geophysics*, 35 (1), 66-68.

Ingelbrecht, C., Peetermans, F., De Corte, F., De Wispelaere, A., Vandecasteele, C., Courtijn, E., D'Hondt, P. (1991). Aluminium-gold reference material for the k_o-standardisation of neutron activation analysis. *Nuclear Instruments and Methods in Physics Research*, A303, 119-122.

Issler, D.R. (1996). Optimizing time step size for apatite fission track annealing models. *Computers and Geosciences*, 22 (1), 67-74.

Iwano, H., Danhara, T. (1998). A re-investigation of the geometry factors for fission-track dating of apatite, sphene and zircon. In: Van den haute, P. and De Corte, F. (Editors) *Advances in fission-track geochronology,* Kluwer Academic Publishers, Dordrecht, pp. 47-66.

Iwano, H., Kasuya, M., Yamashita, T., Danhara, T. (1992). One-to-one correlation of fission tracks between zircon and mica detectors. *Nuclear Tracks and Radiation Measurements*, 20 (2), 341-347.

Iwano, H., Kasuya, M., Danhara, T., Yamashita, T., Tagami, T. (1993). Track counting efficiency and unetchable track range in apatite. *Nuclear Tracks and Radiation Measurements*, 21 (4), 513-517.

Jaffey, A.H., Flynn, K.F., Glendenin, L.E., Bentley, W.C., Essling, A.M. (1971). Precission measurements of half-lives and specific activities of ^{325}U and ^{238}U. *Physical Review*, C4, 1889-1906.

James, K., Durrani, S.A. (1986). Fission track closure temperatures. *Nuclear Tracks*, 12, 921-925.

Johnson, M.R.W., Rogers, G. (1997). Rb-Sr ages of micas from the Kathmandu complex, Central Nepalese Himalaya: implications for the evolution of the Main Central Thrust. *Journal of the Geological Society, London*, 154, 863-869.

Johnson, M.R.W., Oliver, G.J.H., Parrish, R.R., Johnson, S.P. (2001). Synthrusting metamorphism, cooling, and erosion of the Himalayan Kathmandu Complex, Nepal. *Tectonics*, 20 (3), 394-415.

Jolivet, M., Roger, F., Arnaud, N., Brunel, M., Tapponnier, P., Seward, D. (1999). Exhumation history of the Altun Shan with evidence for the timing of the subduction of the Tarim block beneath the Altyn Tagh system, North Tibet. *CR de l'Académie des Sciences, Paris, Earth and Planetary Sciences*, 329, 749-755.

Jolivet, M., Brunel, M., Seward, D., Xu, Z., Yang, J., Roger, F., Tapponnier, P., Malavieille, J., Arnaud, N., Wu, C. (2001). Mesozoic and Cenozoic tectonics of the northern edge of the Tibetan Plateau: fission-track constraints. *Tectonophysics*, 343, 111-134.

Jonckheere, R. (1992). Traces de fission de l'uranium et matériaux géologiques. *Rapport final ADED*, pp. 117.

Jonckheere, R. (1995). De absolute ouderdomsbepaling van apatiet gebaseerd op uranium-fissiesporen: een methodologisch onderzoek (in Dutch). PhD. Thesis, University of Gent, Belgium, 504 pp.

Jonckheere, R. (2003a). On the densities of etchable fission tracks in a mineral and co-irradiated external detector with reference to fission-track dating of minerals. *Chemical Geology*. In press.

Jonckheere, R. (2003b). On methodical problems in estimating geological temperature and time from measurements of fission tracks in apatite. *Radiations Measurements*. In press.

Jonckheere, R., Van den haute, P. (1996). Observations on the geometry of etched fission tracks in apatite: implications for models of track revelation. *American Mineralogist*, 81, 1476-1493.

Jonckheere, R., Van den haute, P. (1998). On the frequency distributions per unit area of the dimensions of fission tracks revealed in an internal and external mineral surface and in the surface of an external detector. *Radiation Measurements*, 29, 135-143.

Jonckheere, R., Van den haute, P. (1999). On the frequency distributions per unit area of the projected and etchable lengths of surface-intersecting fission tracks: influences of track revelation, observation and measurement. *Radiation Measurements*, 30, 155-179.

Jonckheere, R., Van den haute, P. (2002). On the efficiency of fission-track counts in an internal and external apatite surface and in a muscovite external detector. *Radiation Measurements*, 35, 29-40.

Jonckheere, R., Wagner, G. (2000). A non-standard procedure for the analysis of external detector samples introduced at the Heidelberg fission-track lab. In: Noble, W.P., O'Sullivan P.B., Brown, R.W. (Eds). 9th *International conference on fission track dating and thermochronology, Lorne, 2000*. Geological Society of Australia Abstracts, 58, 191-192.

Jonckheere, R., Mars, M., Van den haute, P., Rebetez, M., Chambaudet, A. (1993). L'apatite de Durango (Mexique): Analyse d'un minéral standard pour la datation par traces de fission. *Chemical Geology*, 103, 141-154.

Jonckheere, R., Van den haute, P., De Corte, F., Wagner, G. (2000). Fission track age calibration – the next generation. In: Noble, W.P., O'Sullivan, P.B., Brown, R.D. (Eds). 9th International Conference on Fission Track dating and thermochronology, Lorne, 2000. *Geological Society of Australia Abstracts*, 58, 187-188.

Kalugin, I.A. (2001). Recent bottom fill of the Teletsk Basin. *Geological Sciences Annals of the Royal Museum for Central Africa, Tervuren, Belgium*, 105, 263-282.

Kazanskii, A.Yu., Metelkin, D.V., Kungurtsev, L.V., Lavrenchuk, A.V. (1999). New paleomagnetic data on the early Cambrian of West Sayan. *Russian Geology and Geophysics*, 40 (4), 526-545.

Ketcham, R.A., Donelick, R.A., Carlson, W.D. (1999). Variability of apatite fission-track annealing kinetics: III. Extrapolation to geologic time scales. *American Mineralogist*, 84, 1235-1255.

Ketcham, R.A., Donelick, R.A., Donelick, M.B. (2000). AFTSolve: A program for multi-kinetic modeling of apatite fission-track data. *Geological Materials Research*, 2 (1), 1-32.

Khain, V.E. (1990). Origin of the central Asian mountain belt: collision or mantle diapirism. *Journal of Geodynamics*, 11, 389-394.

Khain, V.E., Bibikova, E.V., Kröner, A., Zhuravlev, D.Z., Sklyarov, E.V., Fedotova, A.A., Kravchenko-Berezhnoy, I.R. (2002). The most ancient ophiolite of the Central Asian fold belt: U-Pb and Pb-Pb zircon ages

for the Dunzhugur Complex, eastern Sayan, Siberia, and geodynamic implications. *Earth and Planetary Science Letters*, 199, 311-325.

Khattak, N.U., Qureshi, A.A., Hussain, S.S., Akram M., Mateen, A., Khan, H.A. (2001). Study of the tectonic uplift history of the Sillai Patti granitic gneiss, Pakistan: constraints from zircon fission-track dating. *Journal of Asian Earth Sciences*, 20, 1-8.

Khomentovsky, V.V., Gibsher, A.S. (1996). The Neoproterozoic-Lower Cambrian in northern Govi-Altay, western Mongolia: regional setting, lithostratigraphy and biostratigraphy. *Geological Magazine*, 133 (4), 371-390.

Khramov, A.N., Gurevich, E.L., Komissarova, R.A., Osipova, E.P, Pisarevsky, S.A., Rodionov, V.P., Slautsitais, I.P. (1985). Paleomagnetism, microplates and Siberian plate consolidation. *Journal of Geodynamics*, 2, 127-139.

Khudoley, A.K. (1993). Structural and strain analysis of the middle part of the Talassian Alatau ridge (Middle Asia, Kirgizstan). *Journal of Structural Geology*, 15 (6), 693-706.

Kirkpatrick, S., Gelatt Jr., C.D., Vecchi, M.P. (1983). Optimization by simulated annealing. *Science*, 220, 671-680.

Kiselev, A.I., Popov, A.M. (1992). Asthenospheric diapir beneath the Baikal rift: petrological constraints. *Tectonophysics*, 208, 287-295.

Klootwijk, C.T., Conaghan, P.J., Powell, C.M. (1985). The Himalayan arc: large-scale continental subduction, oroclinal bending and back-arc spreading. *Earth and Planetary Science Letters*, 75, 167-183.

Klootwijk, C.T., Gee, J.S., Peirce, J.W., Smith, G.M., McFadden, P.L. (1992). An early India-Asia contact: paleomagnetic constraints from Ninetyeast Ridge, ODP leg 121. *Geology*, 20, 395-398.

Korzhenkov, A.M. (2000). Cenozoic tectonics and seismicity of the northwestern part of the Issyk-Kul basin (Tian Shan). *Russian Geology and Geophysics*, 41 (7), 971-982.

Kozlov, M.S., Dubatolov, V.N. (1994). Middle Paleozoic stratigraphy of southwestern Altai. *Russian Geology and Geophysics*, 35 (12), 14-29.

Kraml, M., Keller, J., Henjes-Kunst F. (1996). Spot fusion and incremental heating of single crystals from Kaiserstuhl volcanic rocks with the BGR $^{40}Ar/^{39}Ar$ laser probe. *V.M. Goldschmidt Conference 1996*, Heidelberg, Germany. Conference Abstracts, 332.

Kravchinsky, V.A., Konstantinov, K.M., Cogné, J.-P. (2001). Palaeomagnetic study of Vendian and Early Cambrian rocks of South Siberia and Central Mongolia: was the Siberian Platform assembled at this time? *Precambrian Research*, 110, 61-92.

Kwon, S.-T., Tilton, G.R., Coleman, R.G., Feng, Y. (1989). Isotopic studies bearing on the tectonics of the West Junggar Region, Xinjiang, China. *Tectonics*, 8 (4), 719-727.

Lal, D., Rajan, R.S., Tamhane, A.S. (1969). Chemical composition of $Z \geq 22$ in cosmic rays using meteoric minerals as detectors. *Nature*, 221, 33-37.

Larson, K.M., Bürgmann, R., Bilham, R., Freymueller, J.T. (1999). Kinematics of the India-Eurasia collision zone from GPS measurements. *Journal of Geophysical Research*, 104, B1, 1077-1093.

Laslett, G.M., & Galbraith, R.F. (1996a) Statistical properties of semi-tracks in fission track analysis. *Radiation Measurements*, 26, 565-576.

Laslett, G.M., Galbraith, G.M. (1996b). Statistical modelling of thermal annealing of fission tracks in apatite. *Geochimica et Cosmochimica Acta*, 60 (24), 5117-5131.

Laslett, G.M., Kendall, W.S., Gleadow, A.J.W., Duddy, I.R. (1982). Bias in measurement of fission-track length ditributions. *Nuclear Tracks*, 6, 2/3, 79-85.

Laslett, G.M., Green, P.F., Duddy, I.R., Gleadow, A.J.W. (1987). Thermal annealing of fission tracks in apatite. 2. A quantitative analysis. *Chemical Geology (Isotopes Geoscience Section)*, 65, 1-13.

Laslett, G.M., Galbraith, R.F., & Green, P.F. (1993) The analysis of projected fission track lengths. *Radiation Measurements,* 23, 103-123.

Laurent-Charvet, S., Charvet, J., Shu, L., Ma, R., Lu, H. (2002). Palaeozoic late collisional strike-slip deformations in Tianshan and Altay, Eastern Xinjiang, NW China. *Terra Nova*, 14, 249-256.

Lee, H.-Y., Chung, S.-L., Wang, J.-R., Wen, D.-J., Lo, C.-H., Yang, T.F., Zhang, Y., Xie, Y., Lee, T.-Y., Wu, G., Ji, J. (2003). Miocene Jiali faulting and its implications for Tibetan tectonic evolution. *Earth and Planetary Science Letters,* 205, 185-194.

Lee, J., Hacker, B.R., Dinklage, W.S., Wang, Y., Gans, P., Calvert, A., Wan, J., Chen, W., Blythe, A.E., McClelland, W. (2000). Evolution of the Kangmar Dome, southern Tibet: structural, petrologic, and thermochronologic constraints. *Tectonics*, 19 (5), 872-895.

Leech, M.L., Stockli, D.F. (2000). The late exhumation history of the ultrahigh-pressure Maksyutov Complex, south Ural Mountains, from new apatite fission track data. *Tectonics*, 19 (1), 153-167.

Leland, J., Reid, M.R., Burbank, D.W., Finkel, R., Caffee, M. (1998). Incision and differential bedrock uplift along the Indus River near Nanga Parbat, Pakistan Himalaya, from 10Be and 26Al exposure age dating of bedrock straths. *Earth and Planetary Science Letters*, 154, 93-107.

Lemaire, M.M., Westphal, M., Gurevitch, E.L., Nazarov, K., Feinberg, H., Pozzi, J.P. (1997). How far between Iran and Eurasia was the Turan plate during Triassic-Jurassic times? *Geologie en Mijnbouw*, 76, 73-82.

Le Pichon, X., Fournier, M., Jolivet, L. (1992). Kinematics, topography, shortening and extrusion in the India-Eurasia collision. *Tectonics*, 11 (6), 1085-1098.

Le Pichon, X., Henry, P., Goffé, B. (1997). Uplift of Tibet: from eclogites to granulites – implications for the Andean Plateau and the Variscan Belt. *Tectonophysics*, 273, 57-76.

Lesne, O., Calais, E., Deverchère, J. (1998). Finite element modelling of crustal deformation in the Baikal rift zone: new insight into the active-passive rifting dabate. *Tectonophysics*, 289, 327-340.
Li, Y., Sharps, R., McWilliams, M., Nur, A., Li, Y., Li, Q., Zhang, W. (1989). Paleomagnetic results from Late Paleozoic dykes from the northwestern Junggar block, northwestern China. *Earth and Planetary Science Letters*, 94, 123-130.

Lewis, C.L.E. (1990). Thermal history of the Kunlun batholith, N. Tibet, and implications for uplift of the Tibetan Plateau. *Nuclear Tracks and Radiation Measurements*, 17 (3), 301-307.

Lindsay, J.F., Brasier, M.D., Shields, G., Khomentovsky, V.V., Bat-Ireedui, Y.A. (1996). Glacial facies associations in a Neoproterozoic back-arc setting, Zavkhan Basin, western Mongolia. *Geological Magazine*, 133 (4), 391-402.

Link, K., Rahn, M., Keller, J. (2003). Thermo-tectonic evolution of the Upper Rhine Graben rift shoulders. *EGS-AGU-EUG Joint Assembly, Nice, France, 06-11 April 2003,* Abstract Volume, EAE03-A-11729, TS7-1FR1P-0237.

Liu, G., Einsele, G. (1994). Sedimentary history of the Tethyan basin in the Tibetan Himalayas. *Geologische Rundschau*, 83, 32-61.

Liu, H. (1986). Geodynamic scenario and structural styles of Mesozoic and Cenozoic basins in China. *American Association of Petroleum Geologists Bulletin*, 70 (4), 377-395.

Logatchev, N.A. (1993). History and geodynamics of the Lake Baikal rift in the context of the eastern Siberia riftsystem: a review. *Bulletin des Centres Reserches, Explorations-Productions, Elf Aquitaine*, 17 (2), 353-370.

Logatchev, N.A., Zorin, Yu. A. (1992). Baikal rift zone: structure and geodynamics. *Tectonophysics*, 208, 273-286.

Loss, R.D., De Laeter, J.R., Rosman, K.J.R., Benjamin, T.M., Curtis, D.B., Gancarz, A.J., Delmore, J.E., Maeck, W.J. (1988). The Oklo natural reactors: cumulative fission yields and nuclear characteristics of Reactor Zone 9. *Earth and Planetary Science Letters*, 89, 193-206.

Lukina, N.V. (1996). Active faults and seismicity in Altai. *Russian Geology and Geophysics*, 37 (11), 68-71.

Lutz, T.M., Omar, G. (1991). An inverse method of modeling thermal histories from apatite fission-track data. *Earth and Planetary Science Letters*, 104, 181-195.

Märk, E., Pahl, M., Purtscheller, F., Märk, T.D. (1973). Thermische ausheilung von uran-spaltspuren in apatiten, alterkorrekturen und beiträge zur geothermochronologie. *Tschermaks Mineralogische und Petrologische Mitteilungen*, 20, 131-154.

Marquer, D., Chawla, H.S., Challandes, N. (2000). Pre-alpine high-grade metamorphism in High Himalaya crystalline sequences: Evidence from Lower Palaeozoic Kinnaur Kailas granite and surrounding rocks in the Sutlej Valley (Himachal Pradesh, India). *Eclogae Geologicae Helvetiae,* 93, 207-220.

Mats, V.D. (1993). The structure and development of the Baikal rift depression. *Earth Science Reviews,* 34, 81-118.

Mattauer, M., Matte, P., Olivet, J.-L. (1999). A 3D model of the India-Asia collision at plate scale. *CR de l'Académie de Science,* 328, 499-508.

Mattern, F., Schneider, W., Li, Y., Li, X. (1996). A traverse through the western Kunlun (Xinjiang, China): tentative geodynamic implications for the Paleozoic and Mesozoic. *Geologische Rundschau*, 85, 705-722.

Mattern, F., Schneider, W., Wang, P., Li, C. (1998). Continental strike-slip rifts and their stratigraphic signature: application to the Bangong/Nujiang zone (Tibet) and the South Penninic Zone (Alps). *Geologische Rundschau*, 87, 206-224.

McConnell, D. (1973). *Apatite*. Springer-Verlag. Wien, 111 pp.

McDougall, I., Harrison, T.M. (1988). Geochronology and thermochronology by the $^{40}Ar/^{39}Ar$ method. *Oxford Monographs on Geology and Geophysics*, 9, Oxford University Press, New York, 212 pp.

McDowell, F.W., Keizer, R.P. (1977). Timing of mid-Tertiary volcanism in the Sierra Madre Occidental between Durango City and Mazatlan, Mexico. *GSA Bulletin*, 88, 1479-1487.

Melnikov, A.I., Mazukabzov, A.M., Sklyarov, E.V., Vasiljev, E.P. (1994). Baikal rift basement: structure and tectonic evolution. *Bulletin des Centres Reserches, Explorations-Productions, Elf Aquitaine*, 18 (1), 99-122.

Metivier, F., Gaudemer, Y. (1997). Mass transfer between eastern Tien Shan and adjacent basins (Central Asia). *Geophysical Journal International*, 128, 1-17.

Metner, L., Frisch, O.R. (1939). Disintegration of Uranium by neutrons: a new type of nuclear reaction. *Nature*, 143, 239-240.

Mikolaichuk, A.V. (2000). The structural position of thrusts in the recent orogen of the central Tian Shan. *Russian Geology and Geophysics*, 41 (7), 961-970.

Miller, D.S., Duddy, I.R., Green, P.F., Hurford, A.J., Naeser, C.W. (1985). Results of interlaboratory comparison of fission-track age standards: fission-track workshop – 1984. *Nuclear Tracks*, 10 (3), 383-391.

Miller, D.S., Eby, N., McCorkell, R., Rosenberg, P.E., Suzuki, M. (1990). Results of interlaboratory comparison of fission track ages for the 1988 Fission Track Workshop. *Nuclear Tracks and Radiation Measurements*, 17, 237-245.

Miller, D.S., Crowley, K.D., Dokka, R.K., Galbraith, R.F., Kowallis, B.J., Naeser, C.W. (1993). Results of interlaboratory comparison of fission track ages for the 1992 fission track workshop. *Nuclear Tracks and Radiation Measurements*, 21, 565-573.

Miller, C., Thöni, M., Frank, W., Grasemann, B., Klötzli, U., Guntli, P., Draganits, E. (2001). The early Palaeozoic magmatic event in the northwest Himalaya, India: source, tectonic setting, and age of emplacement. *Geological Magazine*, 138 (3), 237-251.

Mock, C., Arnaud, N.O., Cantagrel, J.-M. (1999). An early unroofing in northeastern Tibet? Constraints from $^{40}Ar/^{39}Ar$ thermochronology on granitoids from the eastern Kunlun range (Qianghai, NW China). *Earth and Planetary Science Letters*, 171, 107-122.

Moens, L. (1981), De K_0 comparatormethode als nieuwe standaardisatietechniek in reactorneutronenactiveringsanalyse (in Dutch). Unpublished PhD thesis, University of Gent, 354 pp.

Molnar, P., Tapponnier, P. (1975). Cenozoic tectonics of Asia: Effects of a continental collision. *Science*, 189, 4201, 419-426.

Molnar, P., Tapponnier, P. (1977). Relation of the tectonics of eastern China to the India-Eurasia collision: Application of slip-line field theory to large-scale continental tectonics. *Geology*, 5, 212-216.

Molnar, P., Thorson Brown, E., Burchfiel, B.C., Deng, Q., Feng, X., Li, J., Raisbeck, G.M., Shi, J., Wu, Z., Yiou, F., You, H. (1994). Quaternary climate change and the formation of river terraces across growing anticlines on the north flank of the Tien Shan, China. *Journal of Geology*, 102, 583-602.

Montgomery, D.R. (1994). Valley incision and the uplift of mountain peaks. *Journal of Geophysical Research*, 99, 13913-13921.

Moore, M.A., England, P.C. (2001). On the inference of denudation rates from cooling ages of minerals. *Earth and Planetary Science Letters*, 185, 265-284.

Morley, C.K. (2001). Combined escape tectonics and subduction rollback-back arc extension: a model for the evolution of Tertiary rift basins in Thailand, Malaysia and Laos. *Journal of the Geological Society, London*, 158, 461-474.

Mossakovsky, A.A., Dergunov, A.B. (1985). The Caledonides of Kazakhstan, Siberia and Mongolia: a review of structure, development history, and palaeotectonic environments. *In*: Gee, D.G., Sturt, B.A. (Eds). The Caledonide Orogen – Scandinavia and related areas. John Wiley & Sons Ltd, Chichester, UK, 1201-1215.

Mueller, J.F., Rogers, J.J.W., Jin, Y., Wang, H., Li, W., Chronic, J., Mueller, J.F. (1991). Late Carboniferous to Permian sedimentation in Inner Mongolia, China, and tectonic relationships between North China and Siberia. *Journal of Geology*, 99, 251-263.

Mughabghab, S.F. (2003). Thermal neutron capture cross sections, resonance integrals and g-factors. *Report International Nuclear Data Committee (Nuclear Data Section)*, 440, 32 pp.

Naeser, C.W. (1967). The use of apatite and sphene for fission track age determinations. *Bulletin of the Geological Society of America*, 78, 1523-1526.

Naeser, C.W. (1979). Fission track dating and geologic annealing of fission tracks. *In*: Jäger, E., Hunziker, J.C. (Eds). Lectures in isotope geology. Springer-Verlag, Heidelberg, 154-169.

Naeser, C.W. (1981). The fading of fission tracks in the geologic environment. Data from deep drill holes. *Nuclear Tracks*, 5, 248-250.

Naeser, C.W., Fleischer, R.L. (1975). Age of the apatite at Cerro de Mercado, Mexico: a problem for fission-track annealing corrections. *Geophysical Research Letters*, 2 (2), 67-70.

Naeser, C.W., Forbes, R.B. (1976). Variation of fission track ages with depth in two deep drill holes. *Transactions of the American Geophysical Union*, 57, 353.

Naeser, C.W., Zimmermann, R.A., Cebula, G.T. (1981). Fission-track dating of apatite and zircon: an interlaboratory comparison. *Nuclear Tracks*, 5 (1/2), 65-72.

Najman, Y., Pringle, M., Godin, L., Oliver, G. (2001). Dating of the oldest continental sediments from the Himalayan foreland basin. *Nature*, 410, 194-197.

Neprochnov, Y.P., Levchenko, O.V., Merklin, L.R., Sedov, V.V. (1988). The structure and tectonics of the intraplate deformation area in the Indian Ocean. *Tectonophysics*, 156, 89-106.

Nikishin, A.M., Cloetingh, S., Lobkovsky, L.I., Burov, E.B., Lankreijer, A.C. (1993). Continental lithosphere folding in Central Asia (Part I): constraints from geological observations. *Tectonophysics*, 226, 59-72.

Nikishin, A.M., Ziegler, P.A., Abbott, D., Brunet, M.-F., Cloetingh, S. (2002). Permo-Triassic intraplate magmatism and rifting in Eurasia: implications for mantle plumes and mantle dynamics. *Tectonophysics*, 351, 3-39.

Noble, S.R., Searle, M.P., Walker, C.B. (2001). Age and tectonic significance of permian granites in western Zanskar, High Himalaya. *Journal of Geology*, 109, 127-135.

Novikov, I.S. (1996). Geomorphological effects of intracontinental collision on the example of Gorny Altai. *Russian Geology and Geophysics*, 37 (11), 51-58.

Novikov, I.S. (2001). Cenozoic strike-slip tectonics in Altai. *Russian Geology and Geophysics*, 42 (9), 1377-1388.

Novikov, I.S. (2002). Late Paleozoic, Middle Mesozoic, and Late Cenozoic stages of the Altai orogeny. *Russian Geology and Geophysics*, 43 (5), 432-443.

Novikov, I.S., Parnachev, S.V. (2000). Morphotectonics of Late Quaternary lakes in river valleys and intramontane troughs of southeastern Altai. *Russian Geology and Geophysics*, 41 (2), 228-240.
Op de Beeck, J. (1976). Description and structure of the programs GELIAN and MULTIP. Internal Report of the Institute of Nuclear Sciences, University of Gent, Gent, 61pp.

O'Sullivan, P.B., Brown, R.W. (1998). Effects of surface cooling on apatite fission-track data: evidence for Miocene climatic change, North Slope, Alaska. *In*: Van den haute, P. and De Corte, F. (Editors) *Advances in fission-track geochronology,* Kluwer Academic Publishers, Dordrecht, pp. 255-267.

O'Sullivan, P.B., Parrish, R.R. (1995). The importance of apatite composition and single-grain ages when interpreting fission track data from plutonic rocks: a case study from the Coast Ranges, British Columbia. *Earth and Planetary Science Letters*, 132, 213-224.

Otto, S.C. (1997). Mesozoic-Cenozoic history of deformation and petroleum systems in sedimentary basins of Central Asia: implications of collisions on the Eurasian margin. *Petroleum Geoscience*, 3, 327-341.

Owen, L.A., Cunningham, W.D., Richards, B.W.M., Rhodes, E., Windley, B.F., Dorjnamjaa, D., Badamgarav, J. (1999a). Timing of formation of forebergs in the northeasern Gobi Altai, Mongolia: implications for estimating mountain uplift rates and earthquake recurrence intervals. *Journal of the Geological Society*, London, 156, 457-464.

Owen, L.A., Cunningham, W.D., Windley, B.F., Badamgarov, J., Dorjnamjaa, D. (1999b). The landscape evolution of Nemegt Uul: a late Cenozoic transpressional uplift in the Gobi Altai, southern Mongolia. *In*: Smith, B.J., Whalley, W.B., Warke, P.A. (Eds). Uplift, erosian and stability: perspectives on longterm landscape development. *Geological Society, London, Special Publications*, 162, 201-218.

Owens, T.J., Zandt, G. (1997). Implications of crustal property variations for models of Tibetan plateau evolution. *Nature*, 387, 37-43.

Pan, Y., Copeland, P., Roden, M.K., Kidd, W.S.F., Harrison, T.M. (1993). Thermal and unroofing history of the Lhasa area, southern Tibet – evidence from apatite fission track thermochronology. *Nuclear Tracks and Radiation Measurements*, 21 (4), 543-554.

Parfenov, L.M., Natal'in, B.A. (1986). Mesozoic tectonic evolution of northeastern Asia. *Tectonophysics*, 127, 291-304.

Parfenov, L.M., Prokopiev, A.V., Gaiduk, V.V. (1995). Cretaceous frontal thrusts of the Verkhoyansk fold belt, eastern Siberia. *Tectonics*, 14 (2), 342-358.

Parnell, J., Geng, A., Fu, J., Sheng, G. (1994). Geology and geochemistry of bitumen vein deposits at Ghost City, Junggar Basin, northwest China. *Geological Magazine*, 131 (2), 181-190.

Patriat, P., Achache, J. (1984). India-Eurasia collision chronology has implications for crustal shortening and driving mechanisms of plates. *Nature*, 311, 615-621.

Patzelt, A., Li, H., Wang, J., Appel, E. (1996). Paleomagnetism of Cretaceous to Tertiary sediments from southern Tibet: evidence for the extent of the northern margin of India prior to the collision with Eurasia. *Tectonophysics*, 259, 259-284.

Paul, T.A. (1993). Transmission electron microscopic investigation of unetched fission tracks in fluorapatite – physical processes of annealing. *Nuclear Tracks and Radiation Measurements*, 21, 507-511.

Paul, T.A., Fitzgerald, P.G. (1992). Transmission electron microscopic investigation of fission tracks in fluorapatite. *American Mineralogist*, 77, 336-344.

Pavlis, G.L., Das, S. (2000). The Pamir-Hindu Kush seismic zone as a strain marker for flow in the upper mantle. *Tectonics*, 19 (1), 103-115.

Pecherskii, D.M., Didenko, A.N., Kazanskii, A.Y., Buslov, M.M., Kurenkov, S.A., Simonov, V.A., Bragin, S.S. (1994). Paleomagnetic characteristics of terranes from the Early Paleozoic accretion-collision structure of paleoasian Ocean, southern Siberia. *Russian Geology and Geophysics*, 35 (7-8), 62-72.

Pedersen, R.B., Searle, M.P., Corfield, R.I. (2001). U-Pb zircon ages from the Spontang ophiolite, Ladakh Himalaya. *Journal of the Geological Society, London*, 158, 513-520.

Peizhen, Z., Molnar, P., Downs, W.R. (2001). Increased sedimentation rates and grain sizes 2-4 Myr ago due to the influence of climate change on erosion rates. *Nature*, 410, 891-897.

Pelechaty, S.H. (1998). Intigrated chronostratigraphy of the Vendian system of Siberia: implications for a global stratigraphy. *Journal of the Geological Society, London*, 155, 957-973.

Pelechaty, S.H., Grotzinger, J.P., Kashirtsev, V.A., Zhernovsky, V.P. (1996). Chemostratigraphic and sequence stratigraphic constraints on Vendian-Cambrian basin dynamics, northeast Siberian craton. *Journal of Geology*, 104, 543-563.

Peltzer, G., Tapponnier, P. (1988). Formation and evolution of strike-slip faults, rifts, and basins during the India-Asia collision: an experimental approach. *Journal of Geophysical Research*, 93, B12, 15085-15117.

Petit, C. (1998). Style of active intraplate deformation from gravity and seismicity data: the Baikal Rift, Asia. *Terra Nova*, 10, 160-169.

Petit, C., Déverchère, J, Houdry, F., Sankov, V.A., Melnikova, V.I., Delvaux, D., 1996. Present-day stress field changes along the Baikal rift and tectonic implications. *Tectonics*, 15 (6), 1171-1191.

Petit, C., Déverchère, J, Calais, E., San'kov, V., Fairhead, D., 2002. Deep structure and mechanical behavior of the lithosphere in the Hangai-Hövsgöl region, Mongolia: new constraints from gravity modeling. *Earth and Planetary Science Letters*, 197, 133-149.

Philip, H., Ritz, J.-F. (1999). Gigantic paleolandslides associated with active faulting along the Bogd fault (Gobi-Altay, Mongolia). *Geology*, 27 (3), 211-214.

Pinous, O.V., Sahagian, D.L., Shurygin, B.N., Nikitenko, B.L. (1999). High-resolution sequence stratigraphic analysis and sea-level interpretation of the middle and upper Jurassic strata of the Nyurolskaya depression and vicinity (southeastern West Siberia, Russia). *Marine and Petroleum Geology*, 16, 245-257.

Poort, J., van der Beek, P., ter Voorde, M. (1998). An integrated modelling study of the central and northern Baikal rift: evidence for non-uniform lithospheric thinning? *Tectonophysics*, 291, 101-122.

Pozzi, J.-P., Feinberg, H. (1991). Paleomagnetism in the Tajikistan: continental shortening of European margin in the pamirs during Indian Eurasian collision. *Earth and Planetary Science Letters*, 103, 365-378.

Price, P.B., Walker, R.M. (1963). Fossil tracks of charged particles in mica and the age of minerals. *Journal of Geophysical Research*, 68, 4847-4862.

Qiang, X.K., Li, Z.X., Powell, C.M., Zheng, H.B. (2001). Magnetostratigraphic record of the Late Miocene onset of the East Asian monsoon, and Pliocene uplift of northern Tibet. *Earth and Planetary Science Letters*, 187, 83-93.

Rasskazov, S.V. (1994). Magmatism related to the eastern Siberia rift system and the geodynamics. *Bulletin des Centres Reserches, Explorations-Productions, Elf Aquitaine*, 18 (2), 437-452.

Reichow, M.K., Saunders, A.D., White, R.V., Pringle, M.S., Al'Mukhamedov, A.I., Medvedev, A.I., Kirda, N.P. (2002). $^{40}Ar/^{39}Ar$ dates from the West Siberian Basin: Siberian flood basalt province doubled. *Science*, 296, 1846-1849.

Reigber, C., Michel, G.W., Galas, R., Angermann, D., Klotz, J., Chen, J.Y., Papschev, A., Arslanov, R., Tzurkov, V.E., Ishanov, M.C. (2001). New space geodetic constraints on the distribution of deformation in Central Asia. *Earth and Planetary Science Letters*, 191, 157-165.

Ricou, L.-E. (1994). Teyhys reconstructed: plates, continental fragments and their boundaries since 260Ma from Central America to South-eastern Asia. *Geodinamica Acta,* 7 (4), 169-218.

Roberts, J.H., Gold, R., Armani, R.J. (1968). Spontaneous-fission decay constant of 238U. *Physical Review*, 174 (4), 1482-1484.

Robinson, P.T., Zhou, M.-F., Hu, X.-F., Reynolds, P., Wenji, B., Yang, J. (1999). Geochemical constraints on the origin of the Hegenshan ophiolite, Inner Mongolia, China. *Journal of Asian Earth Sciences*, 17, 423-442.

Rosman, K.J.R., Taylor, P.D.P. (1998). Isotopic compositions of the elements 1997. *Pure and Applied Chemistry*, 70, 217-235.

Sahagian, D., Pinous, O., Olferiev, A., Zakharov, V. (1996). Eustatic curve for the Middle Jurassic-Cretaceous based on Russian Platform and Siberian stratigraphy: Zonal resolution. *American Association of Petroleum Geologists Bulletin*, 80 (9), 1433-1458.

Salnikova, E.B., Kozakov, I.K., Kotov, A.B., Kröner, A., Todt, W., Bibikova, E.V., Nutman, A., Yakovleva, S.Z., Kovach, V.P. (2001). Age of Palaeozoic granites and metamorphism in the Tuvino-Mongolian Massif of the Central Asian mobile belt: loss of a Precambrian microcontinent. *Precambrian Research*, 110, 143-164.

Scarrow, J.H., Ayala, C., Kimbell, G.S. (2002). Insights into orogenesis: getting to the root of a continent-ocean-continent collision, southern Urals, Russia. *Journal of the Geological Society of London*, 159, 659-671.

Schneider, D.A., Zeitler, P.K., Kidd, W.S.F., Edwards, M.A. (2001). Geochronologic constraints on the tectonic evolution and exhumation of Nanga Parbat, Western Himalaya syntaxis, revisited. *Journal of Geology*, 109, 563-583.

Schreurs, J.W.H., Friedman, A.M., Rokop, D.J., Hair, W.H., Walker, R.M. (1971). Calibrated U-Th glasses for neutron dosimetry and determination of uranium and thorium concentration by the fission track method. *Radiation Effects*, 7, 231-233.

Schwab, M., Ratschbacher, L., Kuhlemann, A., Dunkl, I., Frisch, W. (2000). Evolution of an active orogen within a continental interior position: examples from the Tien Shan and NE- and Central Pamirs in Central Asia. *In*: W.P. Noble, P.B. O'Sullivan, R.W. Brown (Eds.) 9th International Conference on fission track dating and thermochronology, Lorne 2000. *Geological Society of Australia Abstracts* No. 58, 287-288.

Searle, M.P. (1996a). Cooling history, erosion, exhumation, and kinematics of the Himalaya-Karakoram-Tibet orogenic belt. . *In*: Yin, A., Harrison, T.M. (Eds). *The tectonic evolution of Asia*. Cambridge University Press, Cambridge, 486-640.

Searle, M.P. (1996b). Geological evidence against large-scale pre-Holocene offsets along the Karakoram Fault: Implications for the limited extrusion of the Tibetan Plateau. *Tectonics*, 15/1, 171-186.

Searle, M.P., Khan, M.A., Fraser, J.E., Gough, S.J., Jan, M.Q. (1999a). The tectonic evolution of the Kohistan-Karakoram collision belt along the Karakoram highway transect, North Pakistan. *Tectonics*, 18 (6), 929-949.

Searle, M.P., Noble, S.R., Hurford, A.J., Rex, D.C. (1999b). Age of crustal melting, emplacement and exhumation history of the Shivling leucogranite, Garhwal Himalaya. *Geological Magazine*, 136 (5), 513-525.

Şengör, A.M.C., Natal'in, B.A. (1996). Paleotectonics of Asia: fragments of a synthesis. *In*: Yin, A., Harrison, T.M. (Eds). The tectonic evolution of Asia. Cambridge University Press, Cambridge, 486-640.

Şengör, A.M.C., Natal'in, B.A., Burtman, V.S. (1993). Evolution of the Altaid tectonic collage and Palaeozoic crustal growth in Eurasia. *Nature*, 364, 299-307.

Selegei, V.V. (2001a). Limnoclimate of the Teletsk Basin. *Geological Sciences Annals of the Royal Museum for Central Africa, Tervuren, Belgium*, 105, 95-135.

Selegei, V.V. (2001b). Climate of Lake Teletskoye and its surroundings (from observations through 1931-1999). *Geological Sciences Annals of the Royal Museum for Central Africa, Tervuren, Belgium*, 105, 137-162.

Selegei, V.V. (2001c). Mapping on Lake Teletskoye: a historic overview. *Geological Sciences Annals of the Royal Museum for Central Africa, Tervuren, Belgium*, 105, 1-52.

Selegei, V.V., Dehandschutter, B., Klerkx, J. (2001). New bathymetric map of Lake Teletskoye. *Geological Sciences Annals of the Royal Museum for Central Africa, Tervuren, Belgium*, 105, 61-94.

Seleznev, V.S., Nikolaev, V.G., Buslov, M.M., Babushkin, S.M., Larkin, G.V., Evdokimov, A.A. (1995). The structure of sedimentary deposits of Lake Teletskoe according to the data of continuous one-channel seismic profiling. *Russian Geology and Geophysics*, 36 (10), 113-121.

Seleznev, V.S., Dehandschutter, B., Buslov, M.M., Soloviev, V.M., De Batist, M. (2001). The sediment load of Lake Teletskoye: a seismic study. *Geological Sciences Annals of the Royal Museum for Central Africa, Tervuren, Belgium*, 105, 239-262.

Sennikov, N.V., Yolkin, E.A., Izokh, N.G., Klets, A.G. (2000). The Ordovician molasse complex of the southwestern part of West Sayan (Manchurek Formation). *Russian Geology and Geophysics*, 41 (1), 30-43.

Seward, D., Pérez-Estaún, A., Puchkov, V. (1997). Preliminary fission-track results from the southern Urals – Sterlitamak to Magnitogorsk. *Tectonophysics*, 276, 281-290.

Sharps, R., McWilliams, M., Li, Yi., Cox, A., Zhang, Z., Zhai, Y., Gao, Z., Li, Yo., Li, Q. (1989). Lower Permian paleomagnetism of the Tarim block, northwestern China. *Earth and Planetary Science Letters*, 92, 275-291.

Sherman, S.I. (1992). Faults and tectonic stresses of the Baikal rift zone. *Tectonophysics*, 208, 297-307.

Shin, S.-C., Nishimura, S. (1991). Direct comparison of zeta calibration constants for fission-track dating by double-checking of two irradiation facilities with different degrees of neutron flux thermalization. *Chemical Geology (Isotope Geoscience Section),* 87, 147-166.

Shurygin, B.N., Pinous, O.V., Nikitenko, B.L. (1999). Sequence-stratigraphy interpretation of the Callovian and Upper Jurassic (Vasyugan horizon) of southeastern West Siberia. *Russian Geology and Geophysics*, 40 (6), 827-845.

Simonov, V.A., Stupakov, S.I., Loskutov, I., Yu., Kovyazin, S.V. (1999). Paleogeodynamic setting for ophiolite formation in Kuznetsk Alatau. Russian *Geology and Geophysics*, 40 (12), 1725-1738.

Sintubin, M., Buslov, M.M., Trappeniers, G., Dasmasceno de Oliveira, D. (1995). Structural characteristics of the basement along Lake Teletskoe (Gorny Altai). *Russian Geology and Geophysics*, 36 (10), 88-99.

Smethurst, M.A., Khramov, A.N., Torsvik, T.H. (1998). The Neoproterozoic and Palaeozoic paleomagnetism data for the Siberian Platform: from Rodinia to Pangea. *Earth Science Reviews,* 43, 1-24.

Smirnova, L.V., Theunissen, K., Buslov, M.M. (2002). Formation of the Late Palaeozoic structure of the Teletsk region: kinematics and dynamics (Gorny Altai – West Sayan junction). *Russian Geology and Geophysics*, 43 (2), 100-113.

Sobel, E.R. (2000). Cenozoic exhumation of the Kyrgyz Tian Shan. *In*: W.P. Noble, P.B. O'Sullivan, R.W. Brown (Eds.) 9th International Conference on fission track dating and thermochronology, Lorne 2000. *Geological Society of Australia Abstracts* No. 58, 291-293.

Sobel, E.R., Arnaud, N. (2000). Cretaceous-Paleogene basaltic rocks of the Tuyon basin, NW China and the Kyrgyz Tian Shan: the trace of a small plume. *Lithos*, 50, 191-215.

Sobel, E.R., Dumitru, T.A. (1997). Thrusting and exhumation around the margins of the western Tarim Basin during the India-Asia collision. *Journal of Geophysical Research*, 102, 5043-5064.

Sorkhabi, R.B. (1993). Time-temperature pathways of Himalayan and Trans-Himalayan crystalline rocks: a comparison of fission-track ages. *Nuclear Tracks and Radiation Measurements*, 21 (4), 535-542.

Sotnikov, V.I., Fedoseev, G.S., Ponomarchuk, V.A. (2000). Granitoid complexes of the Kolyvan-Tomsk folded zone (West Siberia). *Russian Geology and Geophysics*, 41 (1), 120-125.

Steiger, R.H., Jäger, E. (1977). Subcommission on Geochronology: convention on the use of decay constants in geo- and cosmochronology. *Earth and Planetary Science Letters*, 36, 359-362.

Stüwe, K., Foster, D. (2001). $^{40}Ar/^{39}Ar$, pressure, temperature and fission track constraints on the age and nature of metamorphism around the Main Central Thrust in the eastern Bhutan Himalaya. *Journal of Asian Earth Sciences*, 19, 85-95.

Stüwe, K., White, L., Brown, R. (1994). The influence of eroding topography on steady-state isotherms. Application to fission track analysis. *Earth and Planetary Science Letters*, 124, 63-74.

Sugai, T., Ohmori, H. (1999). A model of relief forming by tectonic uplift and valley incision in orogenesis. *Basin Research*, 11, 43-57.

Summerfield, M.A., and Brown, R.W. (1998). Geomorphic factors in the interpretation of fission-track data. *In*: Van den haute, P. and De Corte, F. (Editors) *Advances in fission-track geochronology,* Kluwer Academic Publishers, Dordrecht, pp. 269-284.

Surkov, V.S., Smirnov, L.V., Zhero, O.G. (1994). Early Mesozoic rifting and evolution of the West Siberian Basin. *In*: Roure, F., Ellouz, N., Shein, V.S., Skvortsov, I. (Eds). Geodynamic evolution of sedimentary basins, International Symposium, Moscow, 135-143.

Surkov, V.S., Smirnov, L.V., Gurari, F.G., Devyatov, V.P., Kazakov, A.M. (1997). Dynamics of the accumulation of the Mesozoic-Cenozoic sedimentary layer in the West-Siberian Basin. *Russian Geology and Geophysics*, 38 (5), 957-964.

Tagami, T. (1987). Determination of zeta calibration constant for fission track dating. *Nuclear Tracks and Radiation Measurements*, 13 (2/3), 127-130.

Tagami, T., Nishimura, S. (1989). Intercalibration of thermal neutron dosimeter glasses NBS-SRM612 and Corning 1 in some irradiation facilities: a comparison. *Nuclear Tracks and Radiation Measurements*, 16 (1), 11-14.

Tagami, T., Nishimura, S. (1992). Neutron dosimetry and fission-track age calibration: insights from intercalibration of uranium and thorium glass dosimeters. *Chemical Geology (Isotope Geoscience Section)*, 102, 277-296.

Tapponnier, P., Molnar, P. (1979). Active faulting and Cenozoic tectonics of the Tien Shan, Mongolia, and Baykal regions. *Journal of Geophysical Research*, 84, B7, 3425-3459.

Tapponnier, P., Mattauer, M., Proust, F., Cassaigneau, C. (1981). Mesozoic ophiolites, sutures, and large-scale tectonic movements in Afghanistan. *Earth and Planetary Science Letters*, 52, 355-371.

Tapponnier, P., Peltzer, G., Le Dain, A.Y., Armijo, R., Cobbold, P. (1982). Propagating extrusion tectonics in Asia: new insights from simple experiments with plasticine. *Geology*, 10, 611-616.

Tapponnier, P., Zhiqin, X., Roger, F., Meyer, B., Arnaud, N., Wittlinger, G., Jingsui, Y. (2001). Oblique stepwise rise and growth of the Tibet Plateau. *Science*, 294, 1671-1677.

Theunissen, K., Dobretsov, N.L., Shatsky, V.S., Smirnova, L., Korsakov, A. (2000a). The diamond-bearing Kokchetav UHP massif in Northern Kazakhstan: exhumation structure. *Terra Nova*, 12, 181-187.

Theunissen, K., Smirnova, L., Dehandschutter, B. (2002). Pseudotachylytes in the southern border fault of the cenozoic intracontinental Teletsk basin (Altai, Russia). Tectonophysics, 351, 169-180.

Thomas, J.C., Cobbold, P.R., Shein, V.S., Le Douaran, S. (1999a). Sedimentary record of late Paleozoic to Recent tectonism in Central Asia – analysis of subsurface data from the Turan and Kazak domains. *Tectonophysics*, 313, 243-263.

Thomas, J.C., Grasso, J.R., Bossu, R., Martinod, J., Nurtaev, B. (1999b). Recent deformation in the Turan and South Kazakh platforms, western Central Asia, and its relation to Arabia-Asia and India-Asia collisions. *Tectonics*, 18 (2), 201-214.

Thomas, J.C., Lanza, R., Kazansky, A., Zykin, V., Semakov, N., Mitrokhin, D., Delvaux, D. (2002). Paleomagnetic study of Cenozoic sediments from the Zaisan basin (SE Kazakhstan) and the Chuya depression (Siberian Altai): tectonic implications for central Asia. *Tectonophysics*, 351, 119-137.

Thompson, S.C., Weldon, R.J., Rubin, C.M., Abdrakhmatov, K., Molnar, P., Berger, G.W. (2002). Late Quaternary slip rates across the central Tien Shan, Kyrgyzstan, Central Asia. *Journal of Geophysical Research*, 107, B09, 2203, doi10.1029/2001JB000596,2002, 32 pp.

Tibaldi, A. (1998). Effects of topography on surface fault geometry and kinematics: examples from the Alps, Italy and Tien Shan, Kazakstan. *Geomorphology*, 24, 225-243.

Tibaldi, A., Graziotto, E., Forcella, F., Gapich, V.H. (1997). Morphotectonic indicators of Holocene faulting in Central Tien Shan, Kazakstan, and geodynamic interpretations. *Journal of Geodynamics*, 23 (1), 23-45.

Titov, A.V., Kruk, N.N., Pospelova, L.N. (1997). Crystallization conditions and origin of magmas of the Rybalkinsky gabbro-diorite-tonalite intrusion (Gorny Altai). *Russian Geology and Geophysics*, 38 (12), 1921-1931.

Torsvik, T.H., Tait, J., Moralev, V.M, McKerrow, W.S., Sturt, B.A., Roberts, D. (1995). Ordovician paleogeography of Siberia and adjacent continents. *Journal of the Geological Society, London*, 152, 279-287.

Toulemonde, M., Dufour, Ch., Meftah, A., Paumier, E. (2000). Transient thermal processes in heavy ion irradiation of crystalline inorganic insulators. *Nuclear Mrthods in Physics Research B*, 166-167, 903-912.

Treolar, P.J., Petterson, M.G., Jan, M.Q., Sullivan, M.A. (1996). A re-evaluation of the stratigraphy and evolution of the Kohistan Arc sequence, Pakistan Himalaya: implications for magmatic and tectonic arc-building processes. *Journal of the Geological Society, London*, 153, 681-693.

Ufimtsev, G.F. (1990). The recent Central Asian orogenic belt. *Zeitschrift Geomorphologie NF*, 34 (2), 199-211.

Van der Beek, P. (1995). Tectonic evolution of continental rifts. Inferences from numerical modelling and fission track thermochronology. PhD thesis, Vrije Universiteit Amsterdam, The Netherlands, pp. 232.

Van der Beek, P. (1997). Flank uplift and topography at the central Baikal Rift (SE Siberia): A test of kinematic models for continental extension. *Tectonics*, 16 (1), 122-136.

Van der Beek, P., Delvaux, D., Andriessen, P.A.M., Levi, K.G. (1996). Early Cretaceous denudation related to convergent tectonics in the Baikal region, SE Siberia. *Journal of the Geological Society*, London, 153, 515-523.

Van der Voo, R., Spakman, W., Bijwaard, H. (1999). Mesozoic subducted slabs under Siberia. *Nature*, 397, 246-249.

Van den haute, P., Chambaudet, A. (1990). Results of an interlaboratory experimentfor the 1988 fission track workshop on a putative apatite standard for internal calibration. *Nuclear Tracks and Radiation Measurements*, 17, 247-252.

Van den haute, P., Jonckheere, R., De Corte F. (1988). Thermal neutron fluence determination for fission-track dating with metal activation monitors: a re-investigation. *Chemical Geology (Isotope Geoscience Section),* 73, 233-244.

Van den haute, P., De Corte, F., Jonckheere, R., Bellemans, F. (1998). The parameters that govern the accuracy of fission-track age determinations: a re-appraisal. In: Van den haute, P. and De Corte, F. (Editors) *Advances in fission-track geochronology,* Kluwer Academic Publishers, Dordrecht, pp. 33-46.

Vannay, J.-C., Grasemann, B. (2001). Himalayan inverted metamorphism and syn-convergence extension as a consequence of a general shear extrusion. *Geological Magazine,* 138 (3), 253-276.

Veevers, J.J., Powell, C.Mc.A., Johnson, B.D. (1975). Greater India's place in Gondwanaland and Asia. *Earth and Planetary Science Letters*, 27, 383-387.

Vercoutere, C., Van den haute, P. (1993). Post-Palaeozoic cooling and uplift of the Brabant Massif as revealed by apatite fission track analysis. Geological Magazine, 130 (5), 639-646.

Vladimirov, A.G., Ponomareva, A.P., Shokalskii, S.P., Khalilov, V.A., Kostitsyn, Y.A., Ponomarchuk, V.A., Rudnev, S.N., Vystavnoi, S.A., Kruk, N.N., Titov, A.V. (1997). Late Paleozoic-Early Mesozoic granitoid magmatism in Altai. *Russian Geology and Geophysics*, 38 (4), 755-770.

Vince, K.J., Treolar, P.J. (1996). Miocene, north-vergent extensional displacements along the Main Mantle Thrust, NW Himalaya, Pakistan. *Journal of the Geological Society, London*, 153, 677-680.

Volkova, N.I., Budanov, V.I. (1999). Geochemical discrimination of metabasalt rocks of the Fan-Karategin transitional blueschist/greenschist belt, south Tianshan, Tajikistan: seamount volcanism and accretionary tectonics. *Lithos*, 47, 201-216.

Vrolijk, P., Donelick, R.A., Queng, J., Cloos, M. (1992). Testing models of fission track annealing in apatite in a simple thermal setting: Site 800, Leg 129. *In*: Larson, R.L., Lancelot, Y. (Eds). *Proceedings of the Ocean Drilling Program, Scientific Results*, 129, 169-176.

Vysotsky, E.M. (2001). Geomorphology of the region of Lake Teletskoye. *Geological Sciences Annals of the Royal Museum for Central Africa, Tervuren, Belgium*, 105, 163-181.

Wagemans, C., Schillebeeckx, P., Deruytter, A.J., Barthélémy, R. (1988). Subthermal fission cross-section measurements for ^{233}U, ^{235}U and ^{239}Pu. *Proceedings of the International Conference on Nuclear Data for Science and Technology (Mito, Japan),* Saikon Publishers, Tokyo, 91-95.

Wagner, G.A. (1968). Fission track dating of apatites. *Earth and Planetary Science Letters*, 4, 411-415.

Wagner, G.A. (1972). The geological interpretation of fission track ages. *Transactions of the American Nuclear Society*, 15, 117.

Wagner, G.A. (1981). Fission-track ages and their geological interpretation. *Nuclear Tracks*, 5, 1/2, 15-25.

Wagner, G.A., Reimer, G.M. (1972). Fission track tectonics: the tectonic interpretation of fission track apatite ages. *Earth and Planetary Science Letters*, 14, 263-268.

Wagner, G.A., Van den haute, P. (1992). *Fission Track-Dating.* Kluwer Academic Publishers, Dordrecht, 285 pp.

Wagner, G.A., Reimer, G.M., Jäger, E. (1977). Cooling ages derived by apatite fission-track, mica Sr-Rb and K-Ar dating: the uplift and cooling history of the Central Alps. *Memorie degli Instituti di Geologia e Mineralogia dell'Università di Padova*, 30, 1-27.

Wagner, G.A., Gleadow, A.J.W., Fitzgerald, P.G. (1989). The significance of the partial annealing zone in apatite fission-track analysis: projected track length measurements and uplift chronology of the Transantarctic Mountains. *Chemical Geology (Isotope Geoscience Section)*, 79, 295-305.

Wang, L.M., Wang, S.X., Lian, J., Ewing, R.C. (1999). TEM study of radiation effects in inorganic materials (abstract). *University of Michigan, Ann Arbor, USA 1st Annual Michigan Materials Research Symposium (MMRS), May 5 - 6, 1999*.

Wang, C., Liu, Z., Hébert, R. (2000). The Yarlung-Zangbo paleo-ophiolite, southern Tibet: implications for the dynamic evolution of the Yarlung-Zangbo Suture Zone. *Journal of Asian Earth Sciences*, 18, 651-661.

Wang, Q., Zhang, P.-Z., Freymueller, J.T., Bilham, R., Larson, K.M., Lai, X., You, X., Niu, Z., Wu, J., Li, Y., Liu, J., Yang, Z., Chen, Q. (2001). Present-day crustal deformation in China constrained by Global Positioning System measurements. *Science*, 294, 574-577.

Washburn, Z., Arrowsmith, J.R., Forman, S.L., Cowgill, E., Wang, X., Zhang, Y., Chen, Z. (2001). Late Holocene earthquake history of the central Altyn Tagh fault, China. *Geology*, 29 (11), 1051-1054.

Wendt, A.S., Vidal, O., Chadderton, L. (2002): Experimental evidence for the pressure dependence of fission track annealing in apatite. *Earth and Planetary Science Letters,* 201, 593-607.

Weinberg, R.F., Dunlap, W.J. (2000). Growth and deformation of the Ladakh batholith, northwest Himalayas: Implications for timing of continental collision and origin of calc-alkaline batholiths. *Journal of Geology*, 108, 303-320.

Willems, H., Zhou, Z., Zhang, B., Gräfe, K.U. (1996). Stratigraphy of the Upper Cretaceous and Lower Tertiary strata in the Tethyan Himalayas of Tibet (Tingri area, China). *Geologische Rundschau*, 85, 723-754.

Willet, S.D. (1992). Modelling thermal annealing of fission tracks in apatite. *In*: Zentilli, M., Reynolds, P.H. (Eds.). Short course handbook on low-temperature thermochronology. Mineralogical Society of Canada, 43-72.

Willet, S.D. (1997). Inverse modeling of annealing of fission tracks in apatite 1: A controlled random search method. *American Journal of Science*, 297, 939-969.

Willet, S.D. (1999). Orogeny and orography: the effects of erosion on the structure of mountain belts. *Journal of Geophysical Research*, 104, B12, 28957-28981.

Willett, S.D., Beaumont, C. (1994). Subduction of Asian lithospheric mantle beneath Tibet inferred from models of continental collision. *Nature*, 369, 642-645.

Williams, I.S., Tetley, N.W., Compston, W., McDougall, I. (1982). A comparison of K-Ar and Rb-Sr ages of rapidly cooled igneous rocks: two points in the Paleozoic time scale r-evaluated. *Journal of the Geological Society London*, 139, 557-568.

Windley, B.F., Allen, M.B. (1993). Mongolian Plateau: evidence for a late Cenozoic mantle plume under Central Asia. *Geology*, 21, 295-298.

Windley, B.F., Allen, M.B., Zhang, C., Zhao, Z-Y., Wang, G-R. (1990). Paleozoic accretion and Cenozoic redeformation of the Chinese Tien Shan Range, Central Asia. *Geology*, 18, 128-131.

Wittlinger, G., Tapponnier, P., Poupinet, G., Mei, J., Danian, S., Herquel, G., Masson, F. (1998). Tomographic evidence for localized lithospheric shear along the Altyn Tagh fault. *Science*, 282, 74-76.

Wolf, R.A., Farley, K.A., Kass, D.M. (1998). Modeling of the temperature sensitivity of the apatite (U-Th)/He thermochronometer. *Chemical Geology*, 148, 105-114.

Worrall, D.M., Kruglyak, V., Kunst, F., Kuznetsov, V. (1996). Tertiary tectonics of the Sea of Okhotsk, Russia: Far-field effects of the India-Eurasia collision. *Tectonics*, 15 (4), 813-826.

Wu, Y., Cui, Z., Liu, G., Ge, D., Yin, J., Xu, Q., Pang, Q. (2001). Quaternary geomorphological evolution of the Kunlun Pass area and uplift of the Qinghai-Xizang (Tibet) Plateau. *Geomorphology*, 36, 203-216.

Xiao, W., Windley, B.F., Hao, J., Li, J. (2002). Arc-ophiolite obduction in the Western Kunlun Range (China): implications for thr Palaeozoic evolution of Central Asia. *Journal of the Geological Society, London*, 159, 517-528.

Xu, G., Kamp, P.J.J. (2000). Tectonics and denudation adjacent to the Xianshuihe fault, eastern Tibetan Plateau: constraints from FT thermochronology. *Journal of Geophysical Research*, 105, B8, 19231-19251.

Xu, X., Harbert, W., Dril, S., Kravchinsky, V. (1997). New paleomagnetic data from the Mongol-Okhotsk collision zone, Chita region, south-central Russia: implications for Paleozoic paleogeography of the Mongol-Okhotsk Ocean. *Tectonophysics*, 269, 113-129.

Xue, F., Kröner, A., Reischmann, T., Lerch, F. (1996). Palaeozoic pre- and post-collision calc-alkaline magmatism in the Qinling orogenic belt, central China, as documented by zircon ages and granitoid rocks. *Journal of the Geological Society, London*, 153, 409-417.

Yamamoto, H., Nakamura, E. (1996). Sm-Nd dating of garnet granulites from the Kohistan complex, northern Pakistan. *Journal of the Geological Society, London*, 153, 965-969.

Yang, J.-S., Robinson, P.T., Jiang, C.-F., Xu, Z.-Q. (1996). Ophiolites of the Kunlun Mountains, China and their tectonic implications. *Tectonophysics*, 258, 215-231.

Yang, T.F., Wang, J.R., Lo, C.H., Chung, S.L., Tien, R.L., Xu, R., Deng, W. (1999). The thermal history of the Lhasa block, south Tibetan Plateau based on FTD and Ar-Ar dating. *Radiation Measurements*, 31, 627-632.

Yin, A. (2000). Mode of Cenozoic east-west extension in Tibet suggesting a common origin of rifts in Asia during the Indo-Asian collision. *Journal of Geophysical Research* 105, B9, 21745-21759.

Yin, A. (2003). Cenozoic deformation history of Asia and its relationship to igneous activities (abstract). *EGS-AGU-EUG Joint Assembly, Nice, France, 06-11 April 2003,* Abstract Volume, EAE03-A-03799, TS34-1WE2O-003.

Yin, A., Harrison, T.M. (2000). Geological evolution of the Himalayan-Tibetan orogen. *Annual Review in Earth and Planetary Sciences*, 28, 211-280.

Yin, A., Kapp, P.A., Murphy, M.A., Manning, C.E., Harrison, T.M., Grove, M., Lin, D., Xi-Guang, D., Cun-Ming, W. (1999). Significant late Neogene east-west extension in northern Tibet. *Geology*, 27 (9), 787-790.

Yolkin, E.A., Sennikov, N.V., Buslov, M.M., Yazikov, A. Yu., Gratsianova, R.T., Bakharev, N.K. (1994). Paleogeographic reconstruction of the western Altai-Sayan area in the Ordovician, Silurian, and Devonian and their geodynamic interpretation. *Russian Geology and Geophysics*, 35 (7/8), 100-124.

Young, E.J., Myers, A.T., Munson, E.L., Conklin, N.M. (1969). Mineralogy and geochemistry of fluorapatite from Cerro de Mercado, Durango, Mexico. *U.S. Geological Survey Professional Paper*, 650-D, D84-D93.

Zeitler, P.K. (1985). Cooling history of the NW Himalaya, Pakistan. *Tectonics*, 4 (1), 127-151.

Zeitler, P.K., Tahirkheli, R.A.K., Naeser, C.W., Johnson, N.M. (1982). Unroofing history of a suture zone in the Himalaya of Pakistan by means of fission-track annealing ages. *Earth and Planetary Science Letters*, 57, 227-240.

Zhalkovskii, N.D., Kuchai, O.A., Muchnaya, V.I. (1995). Seismicity and some characteristics of the stress state of the Earth's crust in the Altai-Sayan region. *Russian Geology and Geophysics*, 36 (10), 16-25.

Zhang, C., Zhai, M., Allen, M.B., Saunders, A.D., Wang, G., Huang, X. (1993). Implications of Palaeozoic ophiolites from western Junggar, NW China, for the tectonics of Central Asia. *Journal of the Geological Society, London*, 150, 551-561.

Zhang, Y.Q., Mercier, J.L., Vergély, P. (1998). Extension in the graben systems around the Ordos (China), and its contribution to the extrusion tectonics of south China with respect to Gobi-Mongolia. *Tectonophysics*, 285, 41-75.

Zhao, G. (2001). Palaeoproterozoic assembly of the North China craton. *Geological Magazine*, 138 (1), 89-91.

Zhao, W., Morgan, W.J. (1987). Injection of Indian crust in Tibetan lower crust. *Tectonics*, 6, 489-504.

Zhao, X., Coe, R., Wu, H., Zhao, Z. (1993). Silurian and Devonian paleomagnetic poles from North China and implications for Gondwana. *Earth and Planetary Science Letters*, 117, 497-506.

Zhisheng, A., Kutzbach, J.E., Prell, W.L., Porter, S.C. (2001). Evolution of Asian monsoon and phased uplift of the Himalaya-Tibetan plateau since Late Miocene times. Nature, 411, 62-66.

Zhu, Y., Sun, S., Gu, L., Ogasawara, Y., Jiang, N., Honma, H. (2001). Permian volcanism in the Mongolian orogenic zone, northeast China: geochemistry, magma sources and petrogenesis. *Geological Magazine*, 138 (2), 101-115.

Zonenshain, L.P., Kuzmin, M.I., Natapov, L.M. (1990). Geology of the USSR: a plate-tectonic synthesis. *American Geophysical Union*, Geodynamics Series, Vol. 21, Washington D.C., 242 pp.

Zorin, Yu.A. (1999). Geodynamics of the western part of the Mongolia-Okhotsk collisional belt, Trans-Baikal region (Russia) and Mongolia. *Tectonophysics*, 306, 33-56.

Zorin, Yu.A., Belichenko, V.G., Turutanov, E.K., Kozhevnikov, V.M., Ruzhentsev, S.V., Dergunov, A.B., Filippova, I.B., Tomurtogoo, O., Arvisbaatar, N., Bayasgalan, T., Biambaa, C., Khosbayar, P. (1993). The South Siberia – Mongolia transect. *Tectonophysics*, 225, 361-378.